ISLAND DYNAMICAL SYSTEMS: ATMOSPHERE, OCEAN AND BIOGEOCHEMICAL PROCESSES

EDITED BY: Rui Caldeira, Miguel A. C. Teixeira and Charitha Bandula Pattiaratchi
PUBLISHED IN: Frontiers in Marine Science

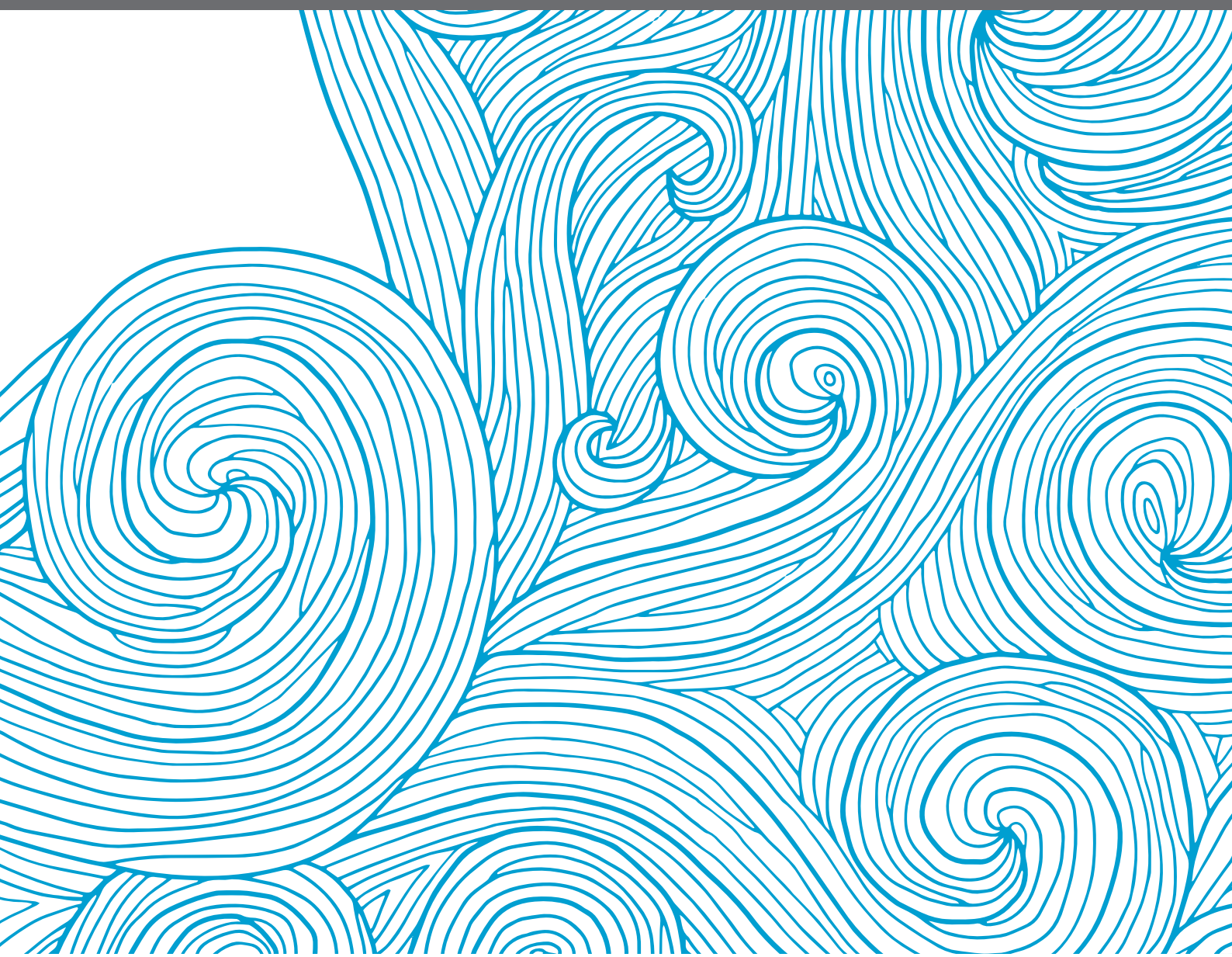

frontiers Research Topics

ISSN 1664-8714
ISBN 978-2-88974-707-8
DOI 10.3389/978-2-88974-707-8

About Frontiers

Frontiers is more than just an open-access publisher of scholarly articles: it is a pioneering approach to the world of academia, radically improving the way scholarly research is managed. The grand vision of Frontiers is a world where all people have an equal opportunity to seek, share and generate knowledge. Frontiers provides immediate and permanent online open access to all its publications, but this alone is not enough to realize our grand goals.

Frontiers Journal Series

The Frontiers Journal Series is a multi-tier and interdisciplinary set of open-access, online journals, promising a paradigm shift from the current review, selection and dissemination processes in academic publishing. All Frontiers journals are driven by researchers for researchers; therefore, they constitute a service to the scholarly community. At the same time, the Frontiers Journal Series operates on a revolutionary invention, the tiered publishing system, initially addressing specific communities of scholars, and gradually climbing up to broader public understanding, thus serving the interests of the lay society, too.

Dedication to Quality

Each Frontiers article is a landmark of the highest quality, thanks to genuinely collaborative interactions between authors and review editors, who include some of the world's best academicians. Research must be certified by peers before entering a stream of knowledge that may eventually reach the public - and shape society; therefore, Frontiers only applies the most rigorous and unbiased reviews.
Frontiers revolutionizes research publishing by freely delivering the most outstanding research, evaluated with no bias from both the academic and social point of view. By applying the most advanced information technologies, Frontiers is catapulting scholarly publishing into a new generation.

What are Frontiers Research Topics?

Frontiers Research Topics are very popular trademarks of the Frontiers Journals Series: they are collections of at least ten articles, all centered on a particular subject. With their unique mix of varied contributions from Original Research to Review Articles, Frontiers Research Topics unify the most influential researchers, the latest key findings and historical advances in a hot research area! Find out more on how to host your own Frontiers Research Topic or contribute to one as an author by contacting the Frontiers Editorial Office: frontiersin.org/about/contact

ISLAND DYNAMICAL SYSTEMS: ATMOSPHERE, OCEAN AND BIOGEOCHEMICAL PROCESSES

Topic Editors:
Rui Caldeira, Agência Regional para o Desenvolvimento da Investigação Tecnologia e Inovação (ARDITI), Portugal
Miguel A. C. Teixeira, University of Reading, United Kingdom
Charitha Bandula Pattiaratchi, University of Western Australia, Australia

Citation: Caldeira, R., Teixeira, M. A. C., Pattiaratchi, C. B., eds. (2022). Island Dynamical Systems: Atmosphere, Ocean and Biogeochemical Processes. Lausanne: Frontiers Media SA. doi: 10.3389/978-2-88974-707-8

Table of Contents

frontiers in Marine Science

ORIGINAL RESEARCH
published: 25 November 2020
doi: 10.3389/fmars.2020.609156

Three-Dimensional Evolution of Mesoscale Anticyclones in the Lee of Crete

Artemis Ioannou[1]*, *Alexandre Stegner*[1], *Franck Dumas*[2] and *Briac Le Vu*[1]

[1] Laboratoire de Météorologie Dynamique, CNRS, Ecole Polytechnique, Palaiseau, France, [2] Service Hydrographique et Océanographique de la Marine (SHOM), Brest, France

Motivated by the recurrent formation of mesoscale anticyclones in the southeast of Crete, we investigated with a high resolution model the response of the ocean to orographic wind jets driven by the Cretean mountain range. As shown in the dynamical process study of Ioannou et al. (2020) which uses a simplified shallow-water model, we confirm here, using the CROCO (Coastal and Regional Ocean COmmunity) model, that the main oceanic response to the Etesian wind forcing is the formation of mesoscale anticyclones. Moreover, we found that the intensity of the wind-induced Ekman pumping acting on the eddies, once they are formed, modulates their intensity. Among the various coastal anticyclones formed during summer and fall 2015, only one of them will correspond to a long lived structure (M_IE15) which is similar to the Ierapetra Eddy detected in 2015 (O_IE15) on the AVISO/DUACS products. Thanks to the DYNED-Atlas data base, we were able to perform a quantitative comparison of the vertical structure of such long-lived anticyclone between the numerical model and the *in-situ* measurements of the various Argo profilers trapped inside the eddy core. Even without assimilation or any nudging, the numerical model was able to reproduce correctly the formation period, the seasonal evolution and the vertical structure of the O_IE15. The main discrepancy between the model and the altimetry observations is the dynamical intensity of the anticyclone. The characteristic eddy velocity derived from the AVISO/DUACS product for the O_IE15 is much lower than in the numerical model. This is probably due to the spatio temporal interpolation of the AVISO/DUACS altimetry products. More surprisingly, several coastal anticyclones were also formed in the model in the lee of Crete area during summer 2015 when the Etesian winds reach strong values. However, these coastal anticyclones respond differently to the wind forcing since they remain close to the coast, in shallow-waters, unlike the M_IE15 which propagates offshore in deep water. The impact of the bottom friction or the coastal dissipation seems to limit the wind amplification of these coastal anticyclones.

Keywords: wind-forced anticyclones, orographic wind forcing, Ierapetra eddies, Ekman pumping, Island wakes, coastal eddies

OPEN ACCESS

Edited by:
Miguel A. C. Teixeira, University of Reading, United Kingdom

Reviewed by:
Jesus Dubert, University of Aveiro, Portugal
Ivica Vilibic, Institute of Oceanography and Fisheries, Croatia

***Correspondence:**
Artemis Ioannou
innartemis@gmail.com

Specialty section:
This article was submitted to Coastal Ocean Processes, a section of the journal Frontiers in Marine Science

Received: *22 October 2020*
Accepted: *03 November 2020*
Published: *25 November 2020*

Citation:
Ioannou A, Stegner A, Dumas F and Le Vu B (2020) Three-Dimensional Evolution of Mesoscale Anticyclones in the Lee of Crete. Front. Mar. Sci. 7:609156. doi: 10.3389/fmars.2020.609156

1. INTRODUCTION

Even if the generation of coastal eddies induced by orographic winds have been documented in several studies, it is still difficult to identify what are the main mechanisms that drive their dynamical characteristics (size and intensity) and their vertical extent. The simultaneous combination of several extra processes (coastal currents, bottom friction, tides...) is often a source of complexity for the analysis of real wind-induced eddies. Such eddies could be very intense and/or long-lived, therefore they have a strong impact on the export of coastal nutrients or biogeochemical species into the open sea or the ocean.

The formation of both cyclonic and anticyclonic eddies was frequently observed in the lee of oceanic mountainous islands (Barton et al., 2000; Caldeira, 2002; Jiménez et al., 2008; Piedeleu et al., 2009; Yoshida et al., 2010; Jia et al., 2011; Kersalé et al., 2011; Caldeira and Sangrà, 2012; Couvelard et al., 2012; Caldeira et al., 2014). The Hawaiian archipelago was one of the first case studies that required the use of high-resolution numerical models. The interaction between the North-Equatorial Current and the archipelago is enough to generate eddies, but the use of higher spatial ($1/4^\circ$ degrees instead of $1/2^\circ$) and temporal (daily instead of monthly) resolution of wind forcing for the regional models was shown to capture eddy intensities in agreement with the observations (Calil et al., 2008; Jia et al., 2011; Kersalé et al., 2011). For Madeira Island, both numerical simulations (Couvelard et al., 2012) and oceanic observations (Caldeira et al., 2014) indicate that the wind wake induced by the mountain orography could be the dominant mechanism of coastal eddy generation. Larger mountain chains, gaps or valleys could locally amplify the upstream synoptic winds and lead to strong wind-jets on the sea. The numerical study of Pullen et al. (2008) has shown that intensified wind jets in the lee of Mindoro and Luzon Islands induce the generation and the migration of a pair of counter-rotating oceanic eddies. In a similar way, the complex orography of Crete island acts as an obstacle for the wind propagation inducing channeling and deflection of the Etesian winds that impact the regional circulation in the south Aegean Sea and the Levantine basin. This study focuses on this specific area where intense coastal anticyclones are formed recurrently during the summer months (Larnicol et al., 1995; Matteoda and Glenn, 1996; Hamad et al., 2005, 2006; Taupier-Letage, 2008; Amitai et al., 2010; Menna et al., 2012; Mkhinini et al., 2014; Ioannou et al., 2017).

Kotroni et al. (2001) performed simulations with and without Crete and they concluded that the Crete mountain ranges (three mountains in the row with height around $2,000\,m$ in **Figure 1A**) modify the Etesian intensity and pathways. The work of Bakun and Agostini (2001) extracts and computes the composite mean wind stress estimates for each one-half degree latitude-longitude quadrangle for the long-term mean seasonal cycle. This observational data-set confirms that the wind-stress curl drives an intense oceanic downwelling at the southeast tip of Crete. Miglietta et al. (2013) simulated the influence of the orography in the same area, capturing the lee waves patterns in the wakes of the Crete, Karpathos, Kasos, and Rhodes islands. The statistical analysis of the monthly surface wind of the ERA-Interim reanalysis (at grid resolution of $1/12^\circ$) performed by Mkhinini et al. (2014) exhibits a seasonal correlation between strong negative wind stress curl and the formation of long-lived anticyclones in the eastern Mediterranean Sea. However, correlation does not imply causation and the recent work of Ioannou et al. (2020) provides a dynamical understanding for the formation of long-lived mesoscale anticyclones induced by a seasonal wind-jet that mimics the Etesian winds deflected by Crete island. This study shows that the oceanic response to a symmetric wind jet could be a symmetric dipole or a strongly asymmetric structure dominated by an intense and robust anticyclone. Since, the anticyclonic wind shear, for the mean summer Etesian wind jet, is two times larger than the cyclonic one, the asymmetry of the oceanic response is enhanced and the formation of large mesoscale anticyclones is expected to be favored in this area. Nevertheless, the reduced-gravity rotating shallow-water model used by Ioannou et al. (2020) might be too simple to reproduce the complexity of the oceanic response to the Etesian winds in the southeast of Crete. In order to better understand the different mechanisms involved in the formation of the real wind-induced anticyclones, we performed a high-resolution numerical modeling of the Mediterranean circulation using the CROCO model forced by realistic winds from August 2012 to December 2016. The main advantage of such high-resolution simulation is to describe the rapid dynamics of meso- and sub-mesoscale vortex structures and to have a precise view of their vertical structure. We focus especially on summer and fall 2015 when several Argo floats were present in this area and allowed for a quantitative comparison between the regional model and the *in-situ* observations. Our main goal is to investigate how the variability of the wind forcing, the complex bathymetry of the shelf or the local outflow impacts on the dynamical characteristics and the vertical extent of these coastal anticyclones.

The paper is organized as follows. In section 2, we describe the various data-sets used in this study, the ARPEGE winds, the DYNED-Atlas eddy data base and the CROCO ocean model used for our realistic numerical simulations of the Mediterranean Sea in 2015 and 2016. Section 3 presents the dynamical characteristics and the vertical structure of the robust coastal anticyclones which formed at the southeast tip of Crete during summer and fall 2015. Throughout comparisons are carried out between the regional model and remote sensing or *in-situ* observations. We then discuss, in section 4, the impact of various forcing on the vertical extent of these coastal anticyclones. Finally, we sum up our results and conclude in section 5.

2. DATA AND METHODS

2.1. Regional Wind Forcing

We used the ARPEGE data-set to provide the most realistic wind-forcing for our regional simulations of the Mediterranean Sea. This data-set is based on 4-D variational assimilation of wind observations into the Meteo-France system of Forecast and Analysis ARPEGE. This reanalysis provides the atmospheric fields at high spatial $(1/10)^\circ$ and temporal (hourly $1\,h$) resolution. To test the accuracy of the ARPEGE data-set in the Crete area

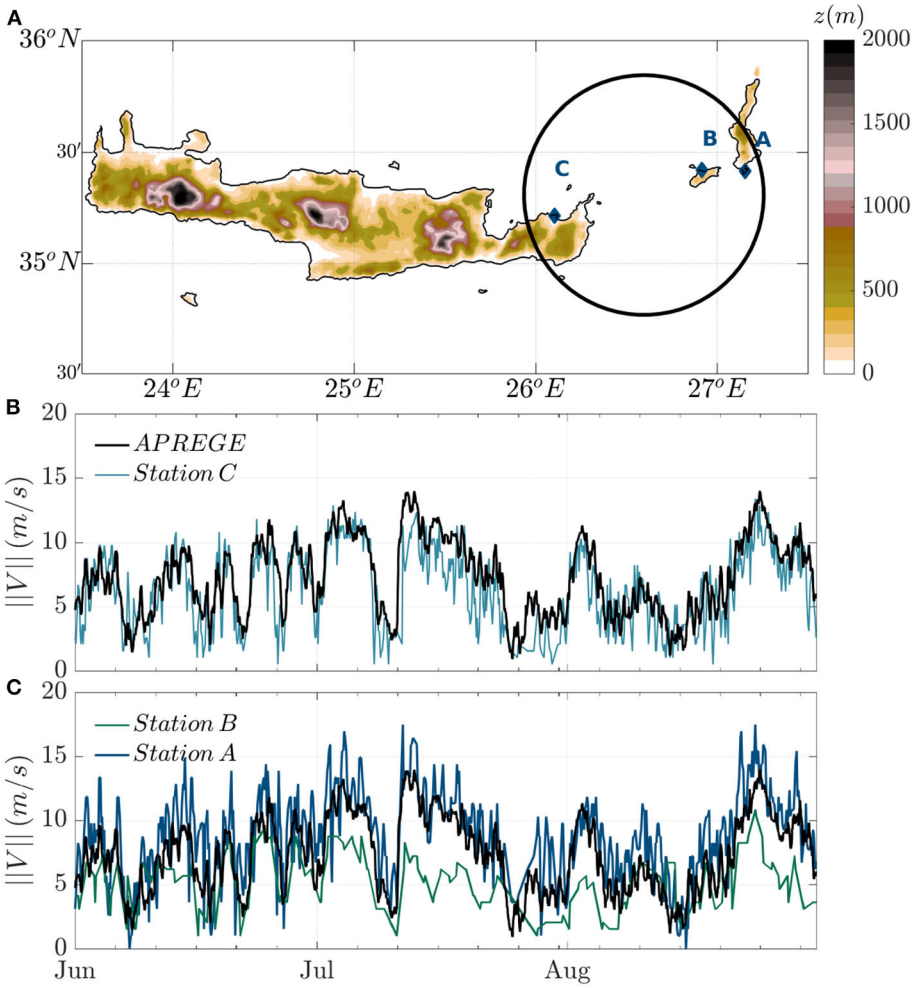

FIGURE 1 | (A) Elevation map (m) of Crete island from ETOPO2 dataset. The locations of the meteorological stations (HNMS); Karpathos (A), Kasos (B), and Sitia (C) are displayed with the blue diamond points. The selected area for analyzing the ARPEGE wind forcing climatology is illustrated with the black circle of $R = 60\,km$. Time-series of wind speed (m/s), as extracted from the three meteorological stations (Station A, B, and C), are shown against the mean wind speed variations from ARPEGE data in **(B,C)**.

and especially in the Kasos strait we collected regional wind speed data from three Meteorological stations of the Hellenic National Meteorological Service (HNMS) located on the islands of Kasos, Karpathos, and Crete at heights 15, 17, and 114 m, respectively. We first build the time series of the mean wind speed in the Kasos strait (inside the black circle of **Figure 1A**) and compare the temporal variability with the *in-situ* data of HNMS. We found that the synoptic variability of the ARPEGE data in 2015 and 2016 is in good agreement with the local observations (see **Figure 1** for summer 2015). However, if we compare the wind intensities we could find some local discrepancies. There is a correct agreement with the Sitia weather station, which is located at the southeast of Crete, but a slight overestimation is found with the Karpathos station and an underestimation with the Kasos station. Hence, if the main components of the synoptic wind variability in the Kasos area are accurate in the ARPEGE data-set, the local intensities of the surface winds, which are strongly impacted by the complex orography of Crete, should always be taken with care. Nevertheless, as far as we know, this is the best wind data-set available at high resolution for this specific area in 2015 and 2016. The ALADIN data-set used by Mkhinini et al. (2014) has a slightly higher resolution but it ends in 2012.

2.2. CROCO Ocean Model

We use outputs of realistic numerical simulations that were carried out for the Mediterranean Sea using the CROCO numerical model (http://www.croco-ocean.org). We refer to Shchepetkin and McWilliams (2005) and Debreu et al. (2012) as well as to Auclair et al. (2018) for details regarding the CROCO inherited numerics from ROMS, its barotropic time-stepping set-up and its solver. The simulation under investigation, CROCO-MED60v40-2015, was forced at the ocean top with ARPEGE wind forcing, thanks to the classical bulk COARE formula (Fairall et al.,

2003) that takes into account the wind stress acting on the ocean surface as

$$\underline{\tau}(x, y, t) = \rho_{air}\, C_d\, |\underline{\mathbf{U}}|\underline{\mathbf{U}} \quad (1)$$

where $\rho_{air} = 1.25\, kg\, m^{-3}$ is the air density, C_d the drag coefficient that varies based on the exchanges between the atmosphere-ocean turbulent surface heat fluxes and $\underline{\mathbf{U}}$ the surface wind. The simulation domain covers the total Mediterranean Sea, extending from $7°W$ to $36.23°E$ and from $30.23°S$ to $45.82°N$. The model configuration solves the classical primitive equations in an horizontal resolution of $1/60°$ in both longitudinal and latitudinal directions, a well fitted resolution to capture the dynamics of interest. The vertical coordinate used is a generalized terrain following one. It is a stretched coordinate that allows to keep flat levels near the surface whatever the bathymetry gradient. The stretching coordinate parameters at the surface (θ_s) and at the bottom (θ_b), are set to $\theta_s = 6$ and $\theta_b = 0$, respectively. Forty unevenly distributed vertical levels discretized the water column. They are closer one from each other next to the surface and more spaced by the bottom where the vertical gradients of hydrology parameters (temperature or salinity) are weak. This distribution was designed in order to properly catch the intense surface dynamics. Moreover, the bathymetry has been produced at SHOM for modeling purposes (http://www.10.12770/50b46a9f-0c4c-4168-9d1c-da33cf7ee188, http://www.data.datacite.org/10.6096/MISTRALS.1341) and was built up from DTM at 100 and 500 m resolution that was optimally interpolated at first and then smoothed to control the pressure gradient truncation error associated with the terrain following coordinate system (Shchepetkin and McWilliams, 2003). The bottom viscous stress has a quadratic form of variable drag coefficient (C_d) computed with the log law approximation. The initial and boundary conditions were built from CMEMS global system analysis (GLOBAL OCEAN $1/12°$ PHYSICS ANALYSIS AND FORECAST UPDATED DAILY), optimally interpolated on the computational grid. CROCO-MED60v40-2015 is a result of a free run simulation (no nudging nor assimilation of any kind) that started on the 1st of August 2012 when the water column stability is at its maximum to avoid static instability in the spinning up phase of three years. It ran till the end of December 2016. For the purposes of this paper, we extracted oceanic numerical fields for the year 2015. To track and quantify full trajectories of mesoscale eddies reproduced in the model, we used AMEDA eddy detection algorithm (Le Vu et al., 2018). Adapted to CROCO $1/60°$ numerical fields, AMEDA can identify the eddy characteristics from the daily mean surface geostrophic velocities derived from Sea Surface Height of the model averaged during 24 h.

2.3. Eddy Database DYNEDAtlas

In order to compare the mesoscale eddies formed in the southeast of Crete in the regional simulation CROCO-MED60v40-2015 with both remote sensing and *in-situ* observations, we used the dynamical eddy data-base DYNED-Atlas (https://www.lmd.polytechnique.fr/dyned/). This recent data-base provides 17 years (2000–2017) of eddy detection and tracking in the Mediterranean Sea along with the co-localization of Argo floats for each detected eddy (https://doi.org/10.14768/2019130201.2). The dynamical characteristics of the eddies contained in the DYNED-Atlas database were computed by the AMEDA eddy detection algorithm (Le Vu et al., 2018) applied on daily surface velocity fields. The latter were derived from the Absolute Dynamic Topography (ADT) maps produced by Salto/Duacs and distributed by CMEMS with a spatial resolution of $1/8°$ which is much coarser than the spatial resolution of the numerical simulations. Hence, we will compare in this study only the characteristics of mesoscale eddies having a characteristic radius R_{max} (i.e., the radius where the azimuthal velocity V_{max} is maximal) higher than 15 km. In order to estimate the vertical structures of the detected eddies, DYNED-Atlas uses all the Argo profiles available since 2000 in the Mediterranean Sea. Once all the detected eddies are identified during the 2000–2017 period, we can separate the Argo profiles in two groups: the ones that are located inside an eddy (i.e., inside the last closed streamline) and the ones which are outside of all the detected eddies. With the second group we can build unperturbed climatological profiles (T, S and ρ) around a given position and a given date. We consider here all the Argo profiles (out of eddies) located at $<150\, km$ around the selected position and at ± 30 days from the target day during the 17 years. Such climatological profiles (plotted in black) give a reference for the T, S and ρ profiles associated to an unperturbed ocean (i.e., without coherent eddies). Hence, the difference between this climatological density profile with the Argo profile taken inside an eddy allows us to compute the profile of the density anomaly $\sigma_A(z)\, (kg\, m^{-3})$ and estimate its vertical extent as shown in **Figure 2**. We use the depth of the maximal density anomaly Z_{max} to quantify the vertical extent of the eddy. A similar methodology was used to estimate the depth of the coastal anticyclones in the regional simulation CROCO-MED60v40-2015 and perform quantitative comparisons with the DYNED-Atlas data. Since all the physical fields are available in the numerical model, the core eddy density profile corresponds to an average of all profiles located at $<10\, km$ from the eddy center. The background profile corresponds to an average of all the vertical profiles located along the last closed streamline.

3. RESULTS

3.1. Etesian Wind-Forcing and Formation of Coastal Anticyclones

The Etesian winds blowing across the complex orography of Crete induce strong wind jets in its wake. As shown by Ioannou et al. (2020) such orographic winds could lead to the formation of long-lived mesoscale anticyclones in this area. We show in **Figure 3** the seasonal variations of both the surface wind stress and the wind stress curl of the ARPEGE wind reanalysis for the year 2015. We note that the intensity of the negative wind stress curl in the Kasos strait (area inside the circle of **Figure 3**) is not strictly correlated to the wind intensity (**Figures 3E,F**). For this specific year, the maximum wind intensity occurs in February while intense negative wind stress curls occur in July. During the summer months, strong wind jets occur with

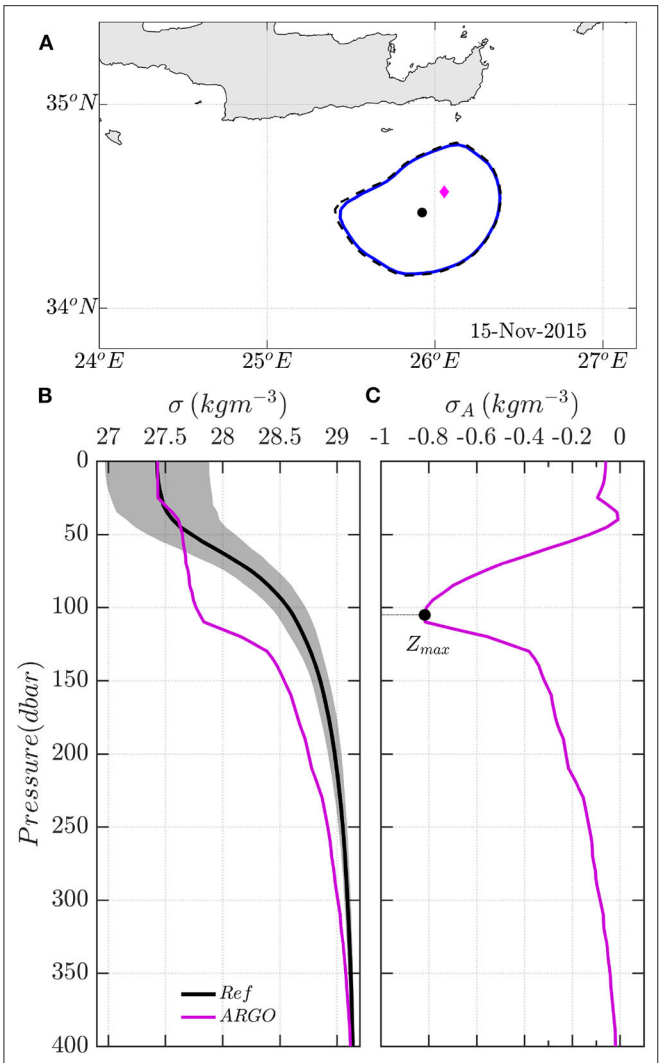

FIGURE 2 | (A) Position of the O_IE15 in November 2015. The eddy characteristic and last contour are illustrated with the blue solid and black dashed lines. The position of an Argo float trapped inside the eddy is shown with the magenta diamond. Vertical **(B)** density σ and **(C)** density anomaly σ_A profile of the Argo float trapped inside the O_IE15 (magenta color). The black line shows the mean climatological profile as computed by Argo profiles that are detected outside of eddies.

a large area of negative Ekman pumping (deep blue area in **Figure 3C**) that extents a hundred of kilometers away from the Kasos strait and tends to favor the formation of coastal anticyclones. It can therefore be expected that the long-lived Ierapetra anticyclone (IE15) will form in July or early August this year. However, this was not the case. Indeed, a long-lived anticyclone that survives more than 6 months was formed in late September in the numerical simulation CROCO-MED60v40-2015 while a similar eddy was detected in early October in the DYNED-Atlas database. Such long-lived and robust anticyclone, which is formed in the Southeast of Crete, is usually called an Ierapetra anticyclone and will be labeled M_IE15 in what follows. Nevertheless, according to CROCO-MED60v40-2015, several other anticyclones were formed in the same area during summer 2015. These coastal anticyclones (labeled AE1, AE2, and AE3) were formed the 9 of June, the 14 of August, and the 12 of September, respectively (**Figure 4**). The lifetime of these robust eddies does not exceed 3 months. This is still low compared to the M_IE15, which survives more than 15 months. Hence, the realistic simulation CROCO-MED60v40-2015 reveals that several coastal anticyclones are formed in the Kasos strait area when intense wind-jets, driven by the Etesian winds, occur. Among all these robust coastal anticyclones, only one will survive more than 6 months and will have the dynamical characteristics of an Ierapetra eddy.

3.2. Comparison Between the CROCO Model and the DYNED-Atlas Data-Base

A regional model that runs without assimilation, such as the CROCO-MED60v40-2015 is very unlikely to reproduce the exact dynamics and trajectory of mesoscale eddies. However, if the wind forcing is correct in the Kasos strait (as shown in the **Figure 1**), the wind-induced coastal anticyclones should have similar characteristics both in the model and the observations. Therefore, a systematic comparison is made between the dynamical eddy characteristics of the CROCO-MED60v40-2015 numerical model and the observations compiled in the Mediterranean eddy data-base: DYNED-Atlas. Besides, such analysis will help to quantify the dynamical differences between the numerous coastal anticyclones which are formed during summer months and the long-lived Ierapetra Eddy (IE15).

3.2.1. Dynamical Characteristics and Trajectories

The **Figure 5** compares the temporal evolution of the characteristic radius (R_{max}) and the intensity (V_{max}) of the long-lived M_IE15 formed in CROCO-MED60v40-2015 with the O_IE15 detected in DYNED-Atlas. These two mesoscale anticyclones were formed mid-fall at the end of September or early October, respectively. Since the spatial resolution of the numerical model (1/60°) is seven times greater than that of merged altimetry products (1/8°), it makes sense that the initial formation of such coastal eddy is better detected in the regional simulation CROCO-MED60v40-2015. If we assume that the model simulates correctly the IE formation, the AMEDA algorithm will detect it earlier in the regional model than in the coarse AVISO/CMEMS data set. In both cases, the radius of the M_IE15 and the O_IE15 exceeds the local deformation radius ($R_d = 10 - 12\,km$) by at least a factor three (**Figure 5B**). Such large radius is in good agreement with previous observations of Ierapetra Eddies (Matteoda and Glenn, 1996; Hamad et al., 2006; Taupier-Letage, 2008; Mkhinini et al., 2014; Ioannou et al., 2017, 2019).

However, the eddy intensity seems to reach higher values in the numerical model than in the eddy database. The maximal azimuthal velocity V_{max} could reach up to $70\,cm/s$ in the CROCO-MED60v40-2015 while it never exceeds $40\,cm/s$ in the DYNED-Atlas data base (**Figure 5A**). The underestimation of the IE's intensity in AVISO/CMEMS products, in comparison with *in-situ* measurements, was previously documented in Ioannou et al. (2017) and typical velocity values of $60\,cm/s$ were confirmed

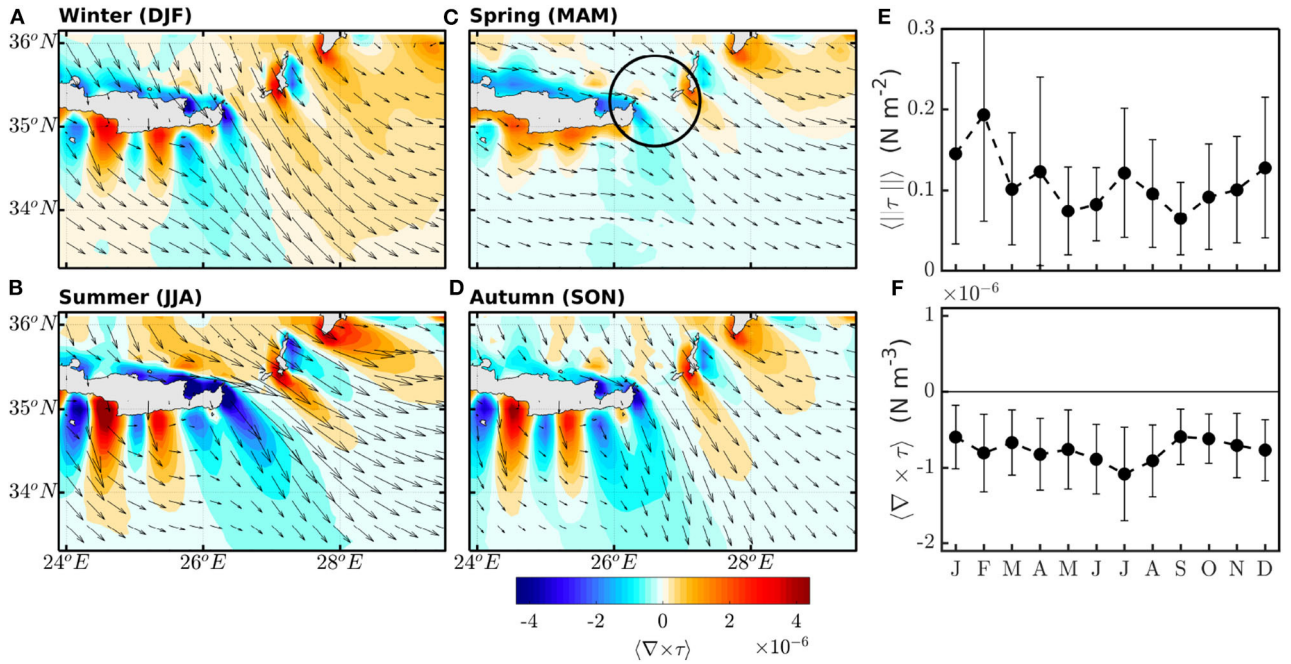

FIGURE 3 | Climatological wind stress $\langle\tau\rangle$ (vectors) and wind stress curl $\langle\nabla\times\tau\rangle$ (colors) during 2015 for the winter **(A)**, spring **(B)**, summer **(C)**, and autumn **(D)** months based on ARPEGE wind data. The selected area for analyzing the wind forcing climatology is illustrated with the black circle in **(B)**. The mean monthly climatological variations of wind stress $\langle\tau\rangle$ and wind stress curl $\langle\nabla\times\tau\rangle$ are shown in **(E,F)**, respectively.

by VMADCP measurements for IE eddies (Ioannou et al., 2017, 2019). The trajectory of the simulated (M_IE15) and the observed one (O_IE15) also differs, even if both of them quickly propagate offshore 60 *km* south of the Kasos strait (**Figure 5C**).

As in the numerical model, a shorter-lived coastal anticyclone, that remained close to the shore in the southeast of Crete, was also detected the 29 of July according to the DYNED Atlas data-base. Such coastal anticyclone was detected from altimetry despite its decreased accuracy near the coast. The formation and the location of the short-lived anticyclone was also confirmed by a careful analysis of SST images. Hence, both remote sensing data sets, visible images, and altimetry maps, show that coastal anticyclones could be formed in this area earlier during the summer months. We compare in the **Figure 6**, the dynamical characteristics of this coastal anticyclone detected in the DYNED-Atlas with the three structures formed by the regional simulation in June, August, and early September. These anticyclones are smaller and weaker than the IE15, their characteristic radius R_{max} does not exceed 25 *km* while the maximal azimuthal velocities V_{max} remain in the range of $20-40\,cm/s$. More strikingly, they all seem to follow the same type of trajectory. The centers of these eddies remain attached to the coastline of Crete and the anticyclone stays above shelf even if they propagate westward, far away from their formation area (**Figure 6C**). Hence, the dynamical characteristics of these wind-induced eddies differ significantly from the long-lived Ierapetra anticyclone.

3.2.2. Comparison of Vertical Eddy Characteristics

The growing number of Argo floats deployed in the Mediterranean Sea in recent years makes it possible to characterize more precisely the three-dimensional evolution of long-lived eddies. Fortunately, the Ierapetra Eddy was sampled by several Argo profiles in the autumn of 2015 just after its formation and later on during winter 2016. The **Figure 7** shows the temporal evolution of the density anomaly in the core of the Ierapetra anticyclone according to the Argo profiles taken in November 2015, in January 2016, and in February 2016. We select here only the profiles that were located at a distance of $<35\,km$ from the eddy center (**Figure 7A**). The maximal density anomaly induced by the eddy on the climatological density background that contains no eddy signature was then estimated. As expected for an anticyclonic eddy, the density anomaly is negative. Moreover, we compute the depth of the maximal density anomaly Z_{max} (black dots in **Figures 7B–D**) to quantify the vertical extent of the O_IE15.

According to **Figure 7B**, one month after its first detection, the density anomaly is confined between 50 and 125 *m*, with a maximum anomaly of $\sigma_A = -1\,kg\,m^{-3}$ located at $-100\,m$. Few months later, in January and in February 2016, the maximal density anomaly propagated in depth, down to $Z_{max} = -150\,m$ and $Z_{max} = -225\,m$, respectively, but decreased in amplitude. The significant deepening of the O_IE15, during the winter months, coincides with the seasonal deepening of the mixed layer depth in the Mediterranean Sea (Moschos et al., 2020). During winter months, when the air-sea interactions are strong, the mixed layer could reach deeper values in the anticyclonic eddy core in comparison with the surroundings (Kouketsu et al., 2011; Dufois et al., 2016). We found that the mixed layer could go down to 200 *m* inside the Ierapetra eddy in February 2016. It is then very simple to quantify the vertical extent of the M_IE15

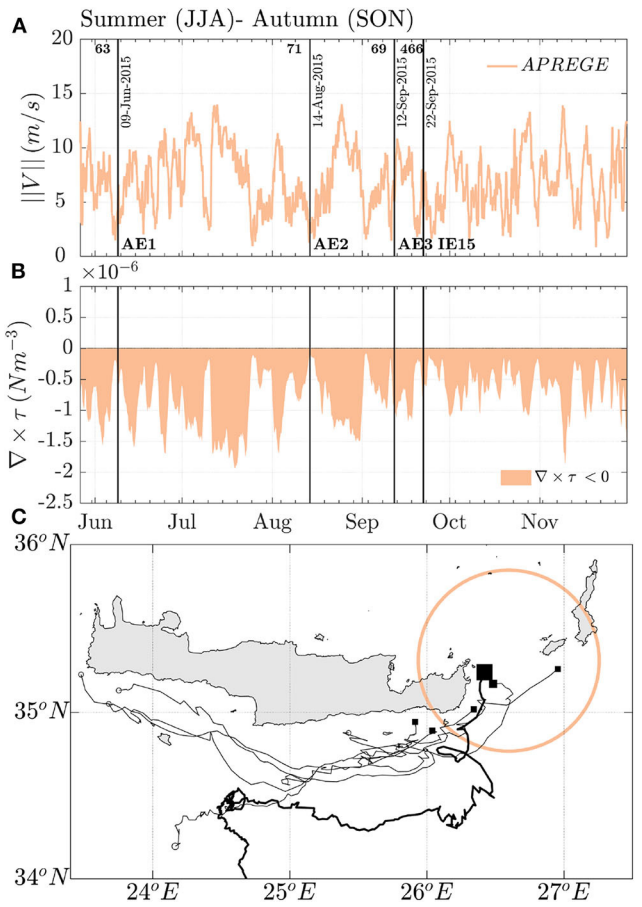

FIGURE 4 | Time-series of **(A)** wind speed (m/s) and **(B)** negative wind stress curl ($\langle \nabla \times \tau \rangle$) are shown with the orange color as extracted from ARPEGE wind data. The selected area for analyzing the wind forcing climatology is illustrated with the orange circle in **(C)**. Trajectories of long-lived (> 2 weeks) eddies (gray colors) detected in CROCO model in the southeastern lee of Crete island during the summer and autumn of 2015. The first points of the eddy detection are plotted with the black square points while the points of last detection are illustrated with the open white circles. The longest-lived detected anticyclone is illustrated with the thick black line.

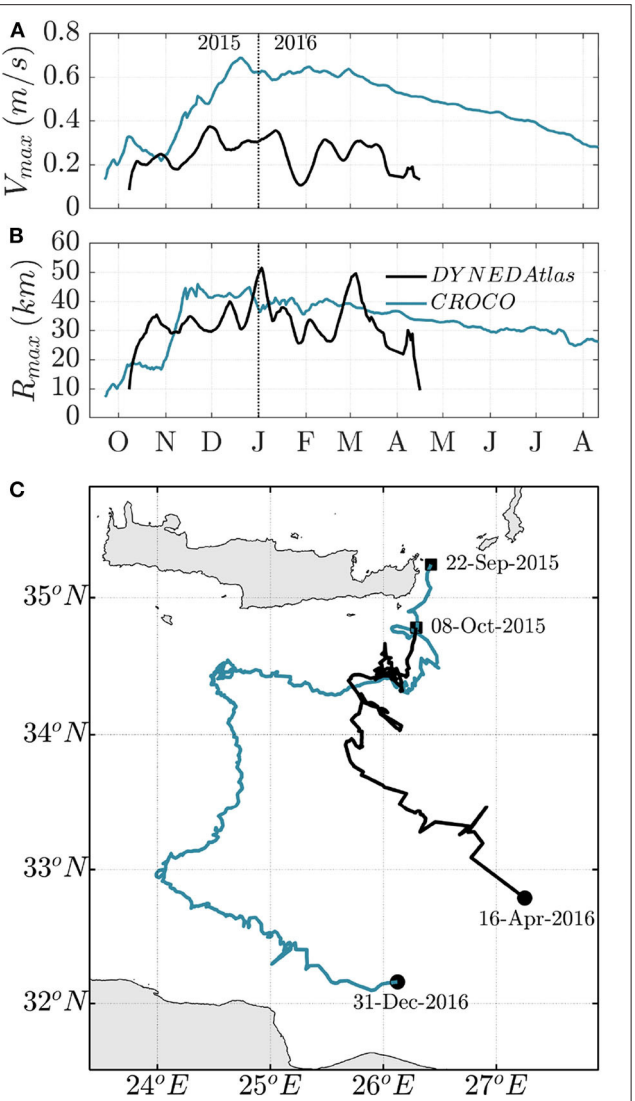

FIGURE 5 | (A) Temporal evolution of long-lived Ierapetra anticyclones as detected in 2015 with AMEDA algorithm from DYNED-Atlas eddy database and from CROCO-MED60v40-2015 simulation. The dynamical characteristics of the eddy velocity V_{max} (m/s) and eddy radius R_{max} (km) are shown in **(A,B)**, respectively while their trajectories are illustrated in **(C)**.

that is formed in the CROCO-MED60v40-2015 and compare them with the *in-situ* observations. Since we can track the eddy center with a high accuracy in the model, we can easily follow the temporal evolution of the density anomaly within the eddy core. The **Figure 8** presents the monthly average of this anomaly for M_IE15 in comparison with the Argo profiles in November 2015, January 2016, and February 2016. The model is in correct agreement with the *in-situ* observations (**Figures 8B–D**) and exhibits the same trend: a significant deepening of the M_IE15 during winter months. However, the maximal density anomaly reaches deeper values, down to $Z_{max} = -220\,m$ and $Z_{max} = -240\,m$ in January and February 2016, in CROCO-MED60v40-2015. The main advantage of such a realistic regional model is that it is possible to follow the three-dimensional evolution of all eddies and to compare them with each other. We could then check how the vertical structure of the coastal anticyclones, that are formed during summer months, differs from the long-lived Ierapetra anticyclone. The **Figure 9** shows the temporal evolution of the size, the intensity, and the vertical core density anomaly of one short-lived coastal anticyclone (AE3) in comparison with the M_IE15. We observe that during the initial stage of formation (the month that follows the first detection) these two types of anticyclones exhibit the same vertical structure and a moderate value of the radius R_{max} around $20\,km$. It is about a month later (in November 2015) that the Ierapetra anticyclone changes its structure: it increases in size and intensity as it expands in depth. Hence, it appears that the deepening of this long-lived anticyclone is induced by a dynamical process which is independent from its initial generation. The initial structure

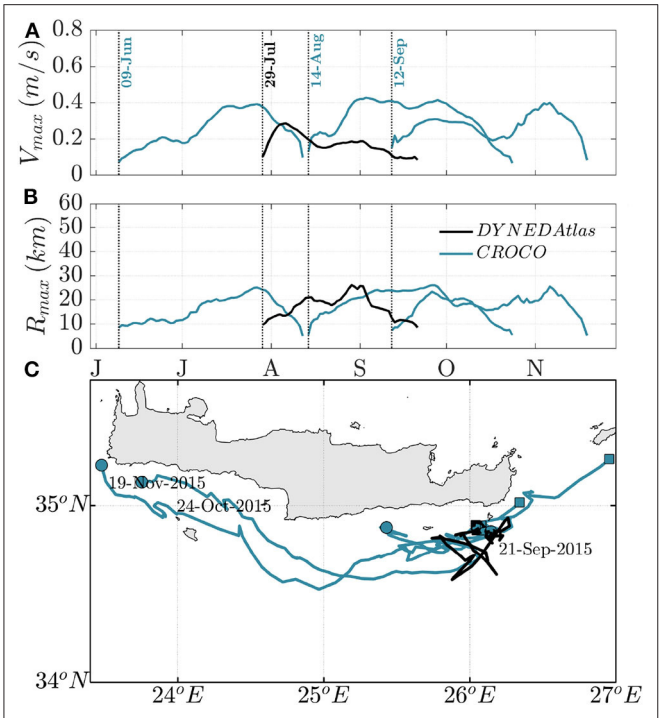

FIGURE 6 | (A) Temporal evolution of short-lived coastal anticyclones detected in 2015 with AMEDA algorithm from DYNED-Atlas eddy database and from CROCO-MED60v40-2015 simulation. The dynamical characteristics of the eddy, its velocity V_{max} (m/s) and radius R_{max} (km) are shown in **(A,B)**, respectively while their trajectories are illustrated in **(C)**. The evolution and the trajectory of the anticyclones AE1, AE2, and AE3 tracked in the regional model are plotted with blue lines while the observed anticyclone (DYNED-Atlas data-base) is plotted with a black line.

and the dynamical characteristics of the Ierapetra eddy, few weeks after its formation, does not differ significantly from the coastal anticyclones that are generated in summer by the wind-jet channelized by the Kasos strait. It is later on, during the winter months, that another mechanism leads to a drastic change in the vertical and the horizontal extent of the M_IE15.

4. DISCUSSION

Several coastal anticyclones were formed during summer and fall 2015 at the southeast tip of Crete, but only one of them will evolve into a large, deep, and long-lived Ierapetra Eddy. Distinct physical processes could lead to this dynamical evolution. On one hand, the orographic wind-jets that occur in the wake of Crete induce strong and localized Ekman pumping. These upwelling or downwelling could then re-intensify or attenuate some coastal eddies. The intensification of a pre-existing mesoscale anticyclone was confirmed by *in-situ* observations (Ioannou et al., 2017) and idealized numerical simulations (Ioannou et al., 2020). If all these coastal anticyclones seem to be wind driven, their lifetime does not seem to be correlated with the wind-jet intensity in the Kasos strait and probably some more complex mechanisms should be considered to explain the robustness and the lifetime of the M_IE15. On the other hand, the Aegean outflow through the Kasos strait (Kontoyiannis et al., 1999, 2005) may also contribute to the formation of coastal eddies or interact with them in this area and therefore modify their intensity and their vertical extent. Both processes are discussed in what follows.

4.1. Wind-Eddy Interactions

We first investigate the impact of local winds on coastal anticyclones once they are formed. We track these eddies with the AMEDA algorithm and compute for each of them the evolution of the daily averaged surface wind-stress inside the eddy contour. The local wind-stress curl will drive horizontal divergence and convergence of the Ekman transport and induce a mean vertical Ekman pumping inside the eddy (Ekman, 1905; Stern, 1965). The cumulative effect of this local Ekman pumping could lead to a significant isopycnal displacement. In order to take into account the core vorticity of the coastal anticyclones we use the non-linear relation derived by Stern (1965). Assuming a quasi-steady response (i.e., neglecting inertial waves generation) the additional isopycnal displacement $\Delta\eta$ induced by the cumulative wind-forcing is given by the following relation:

$$\Delta\eta = \int_{t_0}^{t} W_E \, dt = \int_{t_0}^{t} \frac{1}{A} \iint -\frac{1}{\rho} \nabla \times \left(\frac{\underline{\tau}}{f+\zeta} \right) dA \, dt \qquad (2)$$

where $t = t_0$ is the beginning of the eddy detection, ρ the density of water, f the Coriolis parameter, ζ the vorticity within the eddy core and A the area enclosed by a radial distance of 1.5 R_{max} of the maximum eddy contour. The surface wind stress $\underline{\tau}$ is estimated by the bulk formula:

$$\underline{\tau} = \rho C_D V_{wind} \underline{V_{wind}} \qquad (3)$$

where the drag coefficient C_d is set constant $C_d = 1.6\,10^{-3}$ and V_{wind} is the 10 m wind speed. We plot in **Figure 10A** the temporal evolution of the cumulative isopycnal displacement induced in the core of the three coastal anticyclones (AE1, AE2, and AE3) in comparison with the Ierapetra anticyclone M_IE15. For all the anticyclones, the vortex intensity V_{max} follows the temporal evolution of the cumulative Ekman pumping (**Figures 10A,B**). Indeed, the azimuthal velocity V_{max} of AE1, AE3, and M_IE15 reached their highest values, respectively in July, November and December 2015 when the wind-induced isopycnal displacement reaches its maximum value for each eddy. For AE2, the wind-stress curl, in the eddy core, is zero or negative and therefore, unlike the other ones, the intensity of AE2 stays roughly constant in August and starts to decay in September. However, if the short-lived anticyclones AE1 and AE3 experienced a similar Ekman pumping than the long-lived M_IE15, their intensity and their vertical extents differ strongly from Ierapetra 2015. Thus, for the same wind-stress curl amplitude, the dynamic response can be very different from one anticyclone to another. It seems that the intensity and vertical extent of the Ierapetra anticyclone is more strongly intensified by the local wind forcing than of the other eddies.

One of the main differences between the M_IE15 and the other coastal anticyclones lies in their trajectories. Quite rapidly,

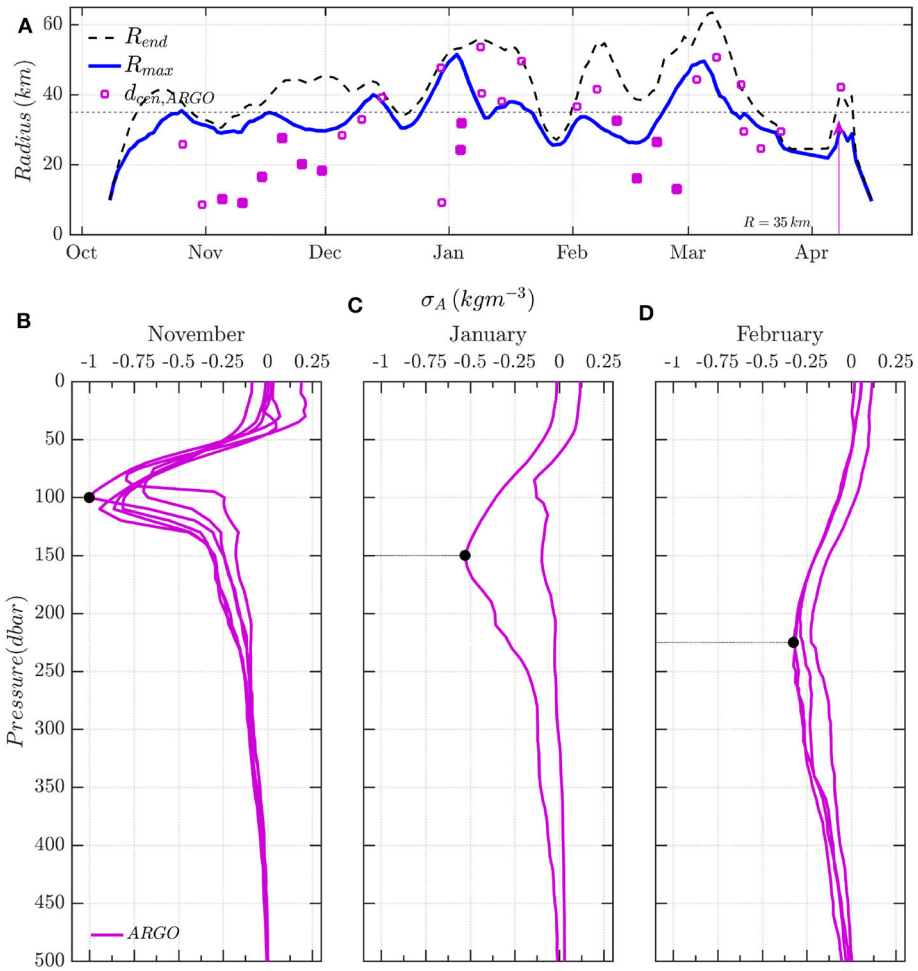

FIGURE 7 | (A) Temporal evolution of the O_IE15 eddy characteristic contour (blue line) and the last contour (black dashed line) as extracted from the DYNED-Atlas eddy database. The squared points illustrate the position of the Argo profiles as a function of their distance from the eddy center. Vertical profiles of density anomaly σ_A (kgm^{-3}) are shown for the months of **(B)** November 2015, **(C)** January 2016, and **(D)** February 2016 as obtained from the Argo float profiles that were trapped in the O_IE15.

after its formation, the Ierapetra eddy escapes from the shore and propagates into deep water unlike other eddies that travel along the Crete coast. The seabed under the eddies AE1, AE2, and AE3 is between -600 and $-1,000\,m$, when the wind forcing is strong, while, in November–December 2015, when Ierapetra anticyclone intensifies, the seabed stays below $-2,000\,m$ and may reaches $-3,000\,m$ depth (**Figures 10C,E**). Hence, the bottom friction could be a possible explanation of the limitation of the intensity and the isopycnal downwelling of these short-lived coastal eddies. Moreover, according to the **Figure 10D**, the characteristic eddy contours of AE1 and AE3 tangent the Crete coastline in July and November 2015 when the cumulative Ekman pumping is maximum for these eddies. The alongshore dissipation could also attenuate the wind induced intensification of these coastal eddies.

The temporal evolution of the vertical density structure and the cumulative isopycnal displacement $\eta = Z_{max}(t_0) + \Delta\eta$, induced by the local Ekman pumping, are shown in **Figure 11** for AE1, AE2, AE3, and M_IE15, respectively. We find that the depth of maximal density anomaly Z_{max} follows roughly the evolution of η. Even if the numerical values are not strictly equal, these two characteristic depths are very close in the first months of the eddy lifetime. This correct agreement between the temporal evolution of $\Delta\eta$ (given by the Equation 2) and Z_{max} confirms that the local wind-stress curl drives the vertical structure of these anticyclones few months after their formation. However, we note for the Ierapetra eddy that during winter months (December, January, and February) the density anomaly deepens while the isopycnal downwelling, induced by the wind-stress curl (i.e., $\Delta\eta$), does not increase. We also notice, during this period, that the intensity of the maximal density anomaly weakens from $\sigma_A = -1\,kgm^{-3}$ mid-November to $\sigma_A = -0.3\,kgm^{-3}$ mid-February. Such an evolution is probably due to air-sea fluxes at the surface that tend to extract a significant amount of heat from the mixed layer that deepens into the anticyclonic core (Donners et al., 2004). Such heat fluxes are not taken into account in the Equation (2). Hence, in addition to the local wind-shear, the air-sea fluxes could

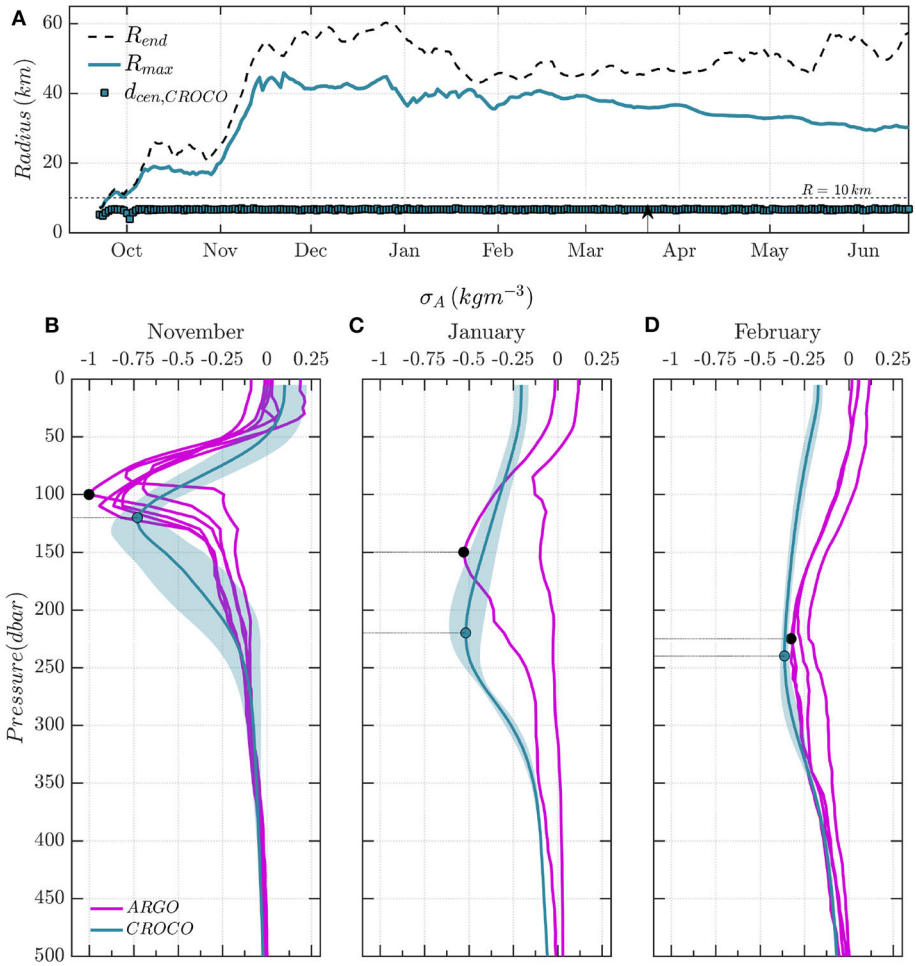

FIGURE 8 | (A) Temporal evolution of the M_IE15 eddy characteristic contour (solid line) and the last contour (black dashed line) computed with AMEDA algorithm applied on CROCO geostrophic fields. Vertical profiles of density anomaly σ_A (kgm^{-3}) for the months of **(B)** November 2015, **(C)** January 2016, and **(D)** February 2016 as obtained from the Argo float profiles that were trapped in the O_IE15 (shown with magenta color) and as obtained from the M_IE15 in CROCO-MED60v40-2015 simulation for the same period (shown with the blue color).

have a significant impact, especially during winter months, on the vertical structure of long-lived mesoscale anticyclones.

4.2. Kasos Strait Outflow

Another forcing mechanism that could generate strong anticyclonic eddies is the density bulge induced by river or strait outflows. A well-know example, at the entrance of the Mediterranean Sea, is the intense Alboran gyre which is forced by the fresh Atlantic water which enters through the Gibraltar strait. Such anticyclone is mainly driven by the amplitude of the inflow rather than the local wind forcing (Viúdez et al., 1996a,b; Viúdez, 1997; Gomis et al., 2001; Flexas et al., 2006).

It is therefore questionable whether the flow out of the Kasos Strait can control the formation of the long-lived Ierapetra anticyclones. Some snapshots of the surface circulation show that the jet corresponding to the Kasos strait outflow, seems to be connected with the periphery of the Ierapetra anticyclone (**Figure 12A**). Therefore, we first quantify the Kasos strait outflow and its variability in CROCO-MED60v40-2015 (**Figures 12B,C**) both in the surface ($0 - 200\,m$) and the subsurface layers (below $-200\,m$). This outflow of lighter water coming from the Aegean Sea could be quite significant with a total flow rate that could exceed 2.4 *Sv* during few days, in July, August, or November 2015. We then compare the variability of this outflow with the intensity of the coastal anticyclones (AE1, AE2, AE3) and the M_IE15 that stays in the vicinity of the Kasos strait (i.e., the area delimited by the black box in **Figure 12A**). We find that the intensification of the AE1 in July and the M_IE15 in November seems to be both correlated to the outflow intensity according to the **Figures 12C,D**. We should note that the eddy intensification is always associated to an amplification of the density anomaly (**Figure 12E**). However, the outflow is relatively strong during the whole period and we can also observe the intensification of AE3 without a significant change in the outflow of the Kasos strait. Hence, there is no systematic correlation between the variations of the outflow and the intensification (of V_{max} or σ_A) of pre-existing anticyclones in this area.

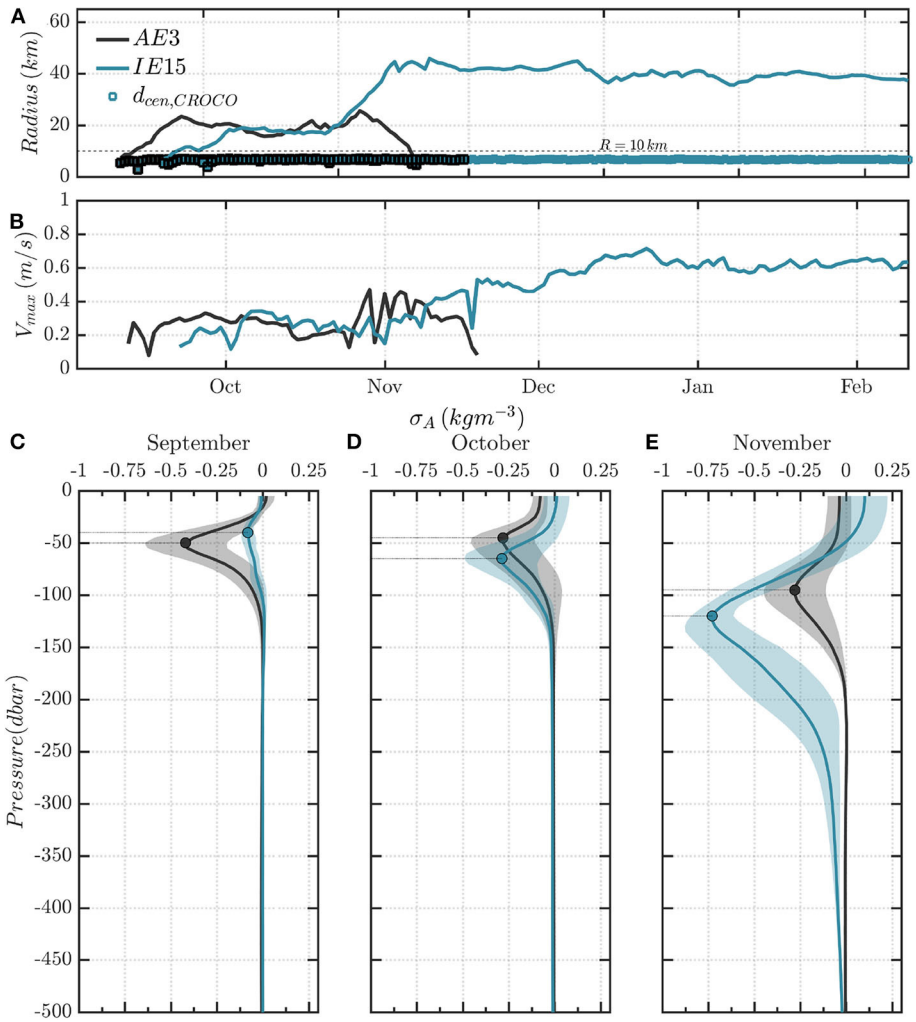

FIGURE 9 | Temporal evolution of dynamical characteristics of **(A)** velocity V_{max} (m/s) and **(B)** radius R_{max} (km) for the coastal eddies AE3 and M_IE15 as computed with AMEDA algorithm applied on CROCO geostrophic fields. Comparison between the vertical profiles of density anomaly σ_A (kgm^{-3}) are shown for the months of **(C)** September 2015, **(D)** October 2015, and **(E)** November 2015 for the two anticyclones AE3 and M_IE15 from the CROCO-MED60v40-2015 simulation.

5. SUMMARY AND CONCLUSIONS

Using a high-resolution (1/60°) regional model CROCO-MED60v40, we analyzed the formation of a coastal eddy in the southeastern wake of Crete island. It is in this area that an intense, large-scale and long-lived anticyclone is formed almost every year, commonly known as the Ierapetra eddy (Hamad et al., 2005, 2006; Taupier-Letage, 2008; Amitai et al., 2010; Menna et al., 2012; Mkhinini et al., 2014; Ioannou et al., 2017). Our previous studies (Mkhinini et al., 2014; Ioannou et al., 2020) have confirmed that the intensity of the summer wind jets (i.e., Etesian winds) blowing through the Kasos strait is one of the main reasons for the formation of robust anticyclones in this area. Motivated by the fact that the regional model CROCO-MED60v40 was driven by the ARPEGE hourly wind reanalysis (at 1/10°), which are the most accurate wind dataset in this region, we study the relation between the wind forcing and the dynamical characteristics of the wind-induced eddies. More specifically, we focus on the year 2015 where an Ierapetra eddy was formed both in the observational as well as in the numerical fields. During that year, Argo profilers were trapped for several months (October 2015–April 2016) in the core of the Ierapetra anticyclone, allowing us to compare the evolution of the vertical structure of the anticyclone from the *in-situ* data with the numerical outputs.

Even without *in-situ* data assimilation, the numerical model was able to reproduce the formation and the dynamical evolution of a long-lived and robust anticyclone (M_IE15) similar to the Ierapetra eddy (O_IE15) that was detected this specific year. The M_IE15 was formed at the end of September while the O_IE15 was detected in early November according to the DYNED-Atlas eddy data-base. The temporal evolution of the characteristic radius and the vertical extent of the M_IE15 are also very close to the observations. However, the trajectories of these two

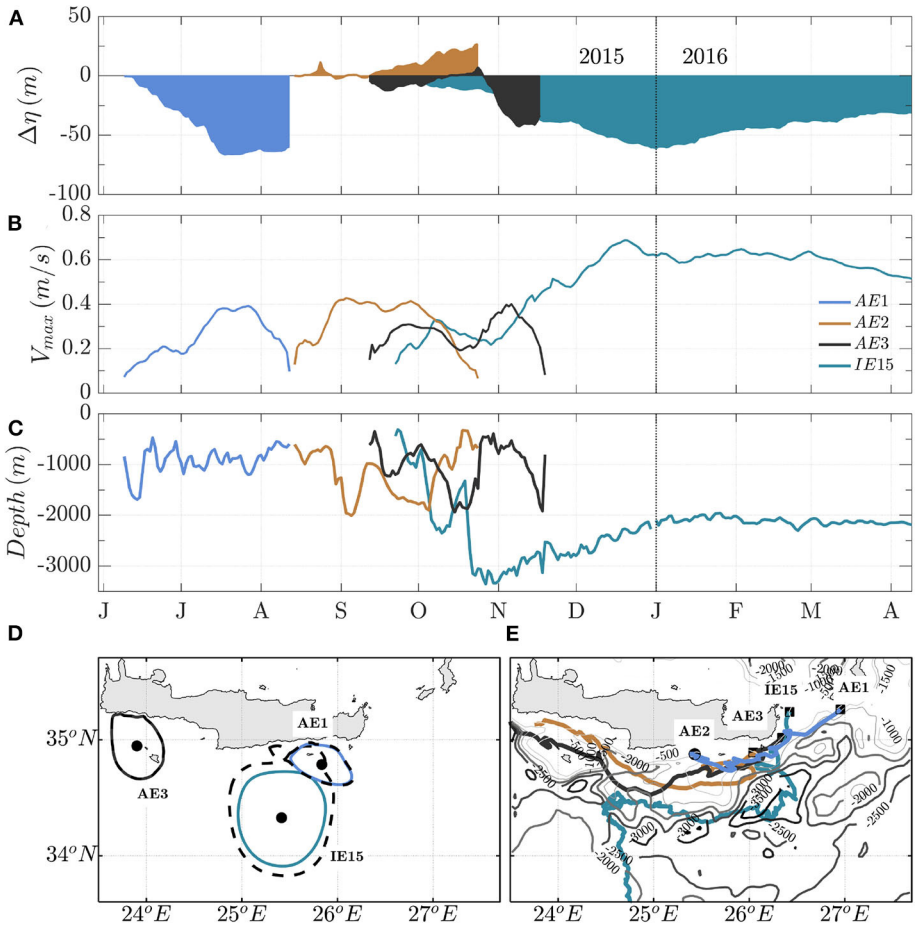

FIGURE 10 | Comparison between the temporal evolution of the anticyclones AE1, AE2, AE3, and M_IE15. The isopycnal displacements after generation $\Delta\eta\,(m)$, associated with the wind stress curl $\langle\nabla\times\tau\rangle$ extracted above the eddies (in an area of 30 *km* from the eddy center) are illustrated in **(A)**. The temporal evolution of the eddy characteristic velocities V_{max} and the mean depth along the eddy trajectories are shown in **(B,C)** for the different anticyclones. The eddy contours and trajectories of the different anticyclones are shown in **(D)** and **(E)**. The background map shown in **(E)** corresponds to the CROCO model bathymetry.

eddies diverge after a few weeks and the eddy intensity reach higher values in the numerical model than in the eddy database. The latter could be due to a systematic under-evaluation of the eddy amplitude when we use the sea surface height or the surface velocity field derived from the altimetry data-set. Indeed, similar under-evaluation in comparison with local VMADCP measurements were found by Ioannou et al. (2017, 2019).

More surprisingly, according to CROCO-MED60v40-2015, several other anticyclones were formed in the same area during summer 2015 when the Etesian winds reach strong values. Three of them survive more than 2 months but their trajectories differ from the M_IE15. These coastal anticyclones travel along the Crete shelf while the Ierapetra eddy propagates offshore after its formation. A careful analysis of the DYNED-Atlas eddy data base reveals that a similar coastal anticyclone was also detected, during August and September 2015, on the standard AVISO/CMEMS Mediterranean altimetry data. Hence, such coastal anticyclones that propagate along the south coast of Crete are both present in the model and the observations. Thus, even if it does not exactly reproduce the observed ocean circulation (since there is no data assimilation), the regional simulation CROCO-MED60v40-2015 seems to provide a realistic description of the formation and the evolution of coastal eddies in the south of Crete island. Therefore, we can rely on this high-resolution model to study the impact of the orographic wind forcing on the formation and the subsequent evolution of realistic coastal anticyclones.

We do find that the intensity of the wind-induced Ekman pumping acting on the eddies, once they are formed, modulates their intensity. However, these coastal anticyclones respond differently to the wind forcing if they remain close to the coast, in shallow-waters, or if they propagate offshore in deep water. The impact of the bottom friction or the coastal dissipation seems to limit the wind amplification of coastal eddies. Among all the coastal anticyclones, which are formed by the summer intensification of the wind jet, only the one that escapes from the shelf will lead to a deep and long-lived eddy. Hence, a strong surface wind-jet is not enough to form an Ierapetra anticyclone and several others

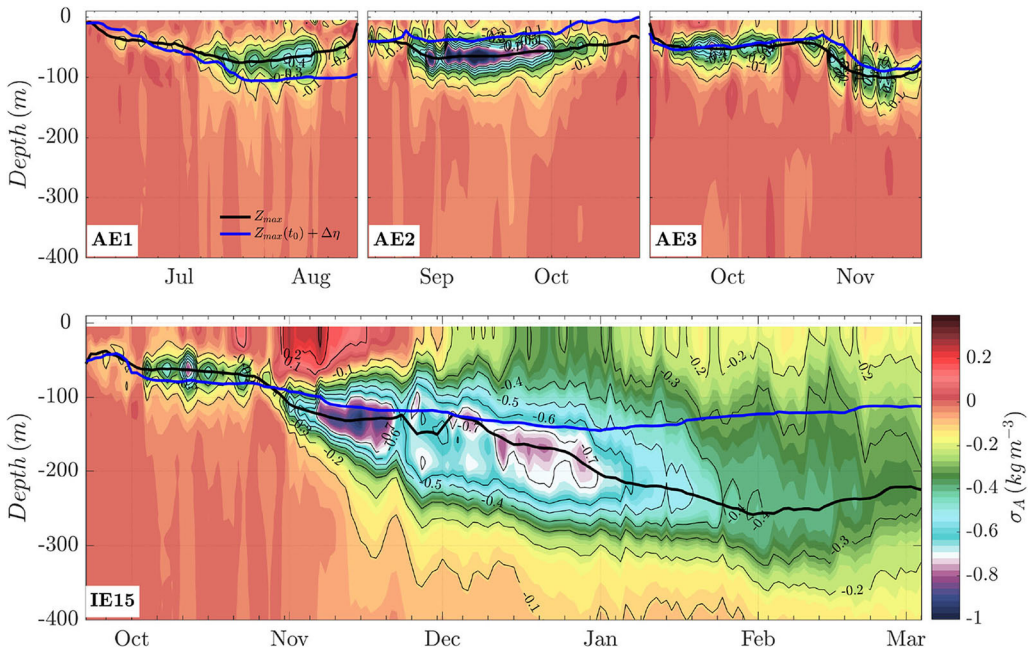

FIGURE 11 | Comparison between the vertical profiles of density anomaly σ_A (kgm^{-3}) for the AE1, AE2, AE3, and M_IE15 anticyclones generated during summer and fall period in the CROCO-MED60v40-2015 simulation southeast of Crete. The temporal evolution of the minimum density anomaly Z_{max} and the isopycnal displacement $\Delta\eta$ associated with the wind stress curl above the eddies are illustrated with the black and blue lines, respectively.

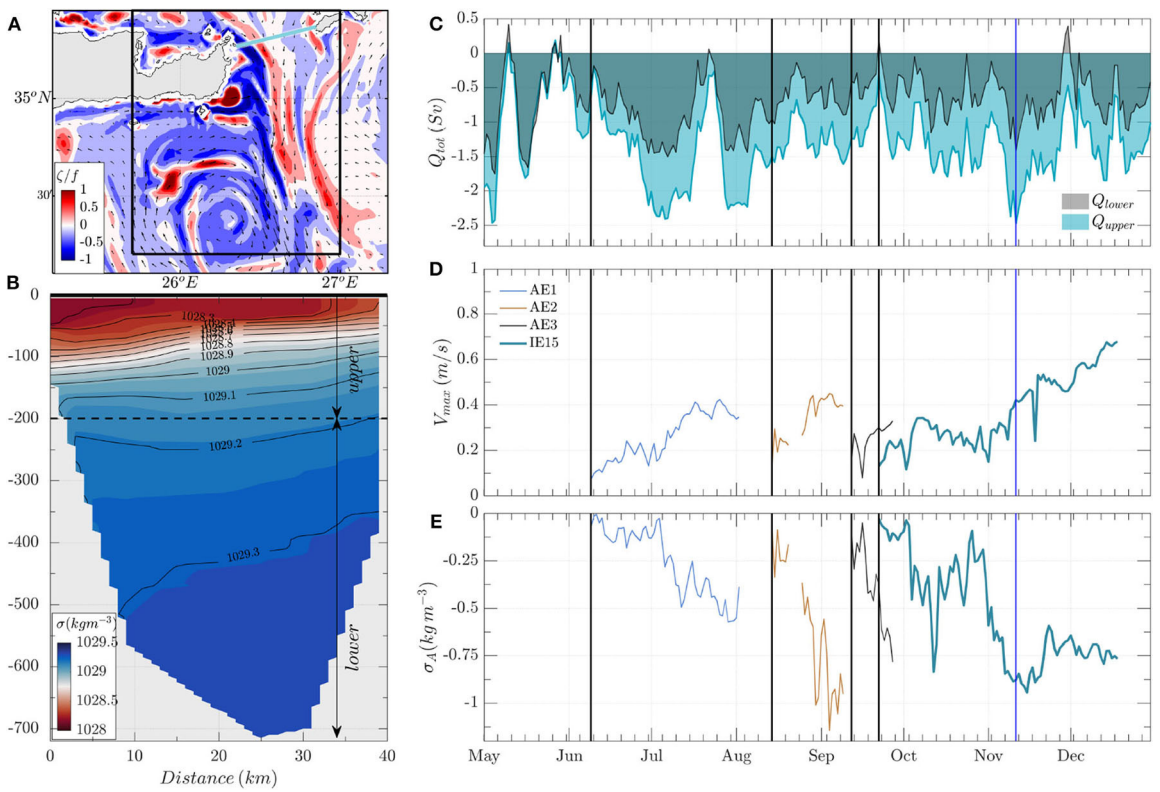

FIGURE 12 | (A) Surface vorticity fields ζ/f and **(B)** vertical section of the density σ (kg/m^{-3}) in the Kasos Strait for the 11 November 2015. Temporal evolution of the Kasos Strait outflow Q separated in surface ($0-200\,m$) and subsurface outflow ($200-700\,m$) in **(C)**. The dates shown with the vertical black lines indicate the first detection of long-lived anticyclones during the same period. The temporal evolution of the eddy characteristic velocity V_{max} and the density anomaly σ_A is shown for the different anticyclones AE1, AE2, AE3, and M_IE15 in **(D,E)**.

factors play a role. The wind-induced Ekman pumping should occur when the eddy is in deep waters and presumably the outflow from the Kasos strait reinforces this mechanism. Moreover, during winter, strong air-sea fluxes could result in a significant upper-layer oceanic heat loss, that could enhance the vertical mixing within the eddy core and deepen its mixed layer. However, these assumptions must be confirmed by a longer numerical simulation that will allow to investigate the formation of different Ierapetra anticyclones several years in a row.

DATA AVAILABILITY STATEMENT

The raw data supporting the conclusions of this article will be made available by the authors, without undue reservation.

AUTHOR CONTRIBUTIONS

AI and AS designed the study, performed the data analysis, and contributed to the writing. FD performed the numerical simulation CROCO-MED60v40 and provided guidance in the interpretation of the results of the numerical simulation. BL adapted the AMEDA algorithm to perform the automatic eddy detection on the numerical simulations. All authors contributed to the article and approved the submitted version.

ACKNOWLEDGMENTS

This work and especially AI and BL were funded by the SHOM with research contract Catoobs 18CP01. The Hellenic National Meteorological Service (HNMS) is kindly acknowledged for providing the wind observations used in this study.

REFERENCES

Amitai, Y., Lehahn, Y., Lazar, A., and Heifetz, E. (2010). Surface circulation of the eastern Mediterranean Levantine basin: insights from analyzing 14 years of satellite altimetry data. *J. Geophys. Res.* 115:C10058. doi: 10.1029/2010JC006147

Auclair, F., Bordois, L., Dossmann, Y., Duhaut, T., Paci, A., Ulses, C., et al. (2018). A non-hydrostatic non-Boussinesq algorithm for free-surface ocean modelling. *Ocean Model.* 132, 12–29. doi: 10.1016/j.ocemod.2018.07.011

Bakun, A., and Agostini, V. N. (2001). Seasonal patterns of wind-induced upwelling/downwelling in the Mediterranean Sea. *Sci. Mar.* 65, 243–257. doi: 10.3989/scimar.2001.65n3243

Barton, E. D., Basterretxea, G., Flament, P., Mitchelson-Jacob, E. G., Jones, B., Arístegui, J., et al. (2000). Lee region of Gran Canaria. *J. Geophys. Res.* 105, 17173–17193. doi: 10.1029/2000JC900010

Caldeira, R., and Sangrá, P. (2012). Complex geophysical wake flows Madeira Archipelago case study. *J. Ocean Dyn.* 62, 683–700. doi: 10.1007/s10236-012-0528-6

Caldeira, R. M. A., and Marchesiello, P. (2002). Ocean response to wind sheltering in the Southern California Bight. *Geophys. Res. Lett.* 29, 1–4. doi: 10.1029/2001GL014563

Caldeira, R. M. A., Stegner, A., Couvelard, X., Araújo, I. B., Testor, P., and Lorenzo, A. (2014). Evolution of an oceanic anticyclone in the lee of Madeira Island: *in situ* and remote sensing survey. *J. Geophys. Res.* 119, 1195–1216. doi: 10.1002/2013JC009493

Calil, P. H., Richards, K. J., Jia, Y., and Bidigare, R. R. (2008). Eddy activity in the lee of the Hawaiian Islands. *Deep Sea Res. II* 55, 1179–1194. doi: 10.1016/j.dsr2.2008.01.008

Couvelard, X., Caldeira, R., Araújo, I., and Tomé, R. (2012). Wind mediated vorticity-generation and eddy-confinement, leeward of the Madeira Island: 2008 numerical case study. *Dyn. Atmos. Oceans* 58, 128–149. doi: 10.1016/j.dynatmoce.2012.09.005

Debreu, L., Marchesiello, P., Penven, P., and Cambon, G. (2012). Two-way nesting in split-explicit ocean models: algorithms, implementation and validation. *Ocean Model.* 49–50, 1–21. doi: 10.1016/j.ocemod.2012.03.003

Donners, J., Drijfhout, S., and Coward, A. (2004). Impact of cooling on the water mass exchange of Agulhas rings in a high resolution ocean model. *Geophys. Res. Lett.* 31:L16312. doi: 10.1029/2004GL020644

Dufois, F., Hardman-Mountford, N. J., Greenwood, J., Richardson, A. J., Feng, M., and Matear, R. J. (2016). Anticyclonic eddies are more productive than cyclonic eddies in subtropical gyres because of winter mixing. *Sci. Adv.* 2:e1600282. doi: 10.1126/sciadv.1600282

Ekman, W. (1905). On the influence of the Earth's Rotation on Ocean-Currents. *Arkiv Fur Matematik Astronomi Och Fysik* 11, 355–367.

Fairall, C. W., Bradley, E. F., Hare, J. E., Grachev, A. A., and Edson, J. B. (2003). Bulk parameterization of air-sea fluxes: updates and verification for the COARE algorithm. *J. Clim.* 16, 571–591. doi: 10.1175/1520-0442(2003)016<0571:BPOASF>2.0.CO;2

Flexas, M., Gomis, D., Ruiz, S., Pascual, A., and León, P. (2006). *In situ* and satellite observations of the eastward migration of the Western Alboran Sea Gyre. *Prog. Oceanogr.* 70, 486–509. doi: 10.1016/j.pocean.2006.03.017

Gomis, D., Ruiz, S., and Pedder, M. (2001). Diagnostic analysis of the 3D ageostrophic circulation from a multivariate spatial interpolation of CTD and ADCP data. *Deep Sea Res. I* 48, 269–295. doi: 10.1016/S0967-0637(00)00060-1

Hamad, N., Millot, C., and Taupier-Letage, I. (2005). A new hypothesis about the surface circulation in the eastern basin of the Mediterranean sea. *Prog. Oceanogr.* 66, 287–298. doi: 10.1016/j.pocean.2005.04.002

Hamad, N., Millot, C., and Taupier-Letage, I. (2006). The surface circulation in the eastern basin of the Mediterranean Sea. *Sci. Mar.* 70, 457–503. doi: 10.3989/scimar.2006.70n3457

Ioannou, A., Stegner, A., Dubos, T., Le Vu, B., and Speich, S. (2020). Generation and intensification of mesoscale anticyclones by orographic wind jets: the case of Ierapetra eddies forced by the etesians. *J. Geophys. Res.* 125:e2019JC015810. doi: 10.1029/2019JC015810

Ioannou, A., Stegner, A., Le Vu, B., Taupier-Letage, I., and Speich, S. (2017). Dynamical evolution of intense ierapetra eddies on a 22 year long period. *J. Geophys. Res.* 122, 9276–9298. doi: 10.1002/2017JC013158

Ioannou, A., Stegner, A., Tuel, A., Le Vu, B., Dumas, F., and Speich, S. (2019). Cyclostrophic corrections of AVISO/DUACS surface velocities and its application to mesoscale eddies in the Mediterranean Sea. *J. Geophys. Res.* 124, 8913–8932. doi: 10.1029/2019JC015031

Jia, Y., Calil, P. H. R., Chassignet, E. P., Metzger, E. J., Potemra, J. T., Richards, K. J., et al. (2011). Generation of mesoscale eddies in the lee of the Hawaiian Islands. *J. Geophys. Res.* 116:C11009. doi: 10.1029/2011JC007305

Jiménez, B., Sangrá, P., and Mason, E. (2008). A numerical study of the relative importance of wind and topographic forcing on oceanic eddy shedding by tall, deep water islands. *Ocean Model.* 22, 146–157. doi: 10.1016/j.ocemod.2008.02.004

Kersalé, M., Doglioli, A. M., and Petrenko, A. A. (2011). Sensitivity study of the generation of mesoscale eddies in a numerical model of Hawaii islands. *Ocean Sci.* 7, 277–291. doi: 10.5194/os-7-277-2011

Kontoyiannis, H., Balopoulos, E., Gotsis-Skretas, O., Pavlidou, A., Assimakopoulou, G., and Papageorgiou, E. (2005). The hydrology and biochemistry of the Cretan Straits (Antikithira and Kassos Straits) revisited in the period June 1997–May 1998. *J. Mar. Syst.* 53, 37–57. doi: 10.1016/j.jmarsys.2004.06.007

Kontoyiannis, H., Theocharis, A., Balopoulos, E., Kioroglou, S., Papadopoulos, V., Collins, M., et al. (1999). Water fluxes through the Cretan Arc Straits, Eastern Mediterranean Sea: March 1994 to June 1995. *Prog. Oceanogr.* 44, 511–529. doi: 10.1016/S0079-6611(99)00044-0

Kotroni, V., Lagouvardos, K., and Lalas, D. (2001). The effect of the island of Crete on the Etesian winds over the Aegean Sea. *Q. J. R. Meteorol. Soc*. 127, 1917–1937. doi: 10.1002/qj.49712757604

Kouketsu, S., Tomita, H., Oka, E., Hosoda, S., Kobayashi, T., and Sato, K. (2011). The role of meso-scale eddies in mixed layer deepening and mode water formation in the western North Pacific. *J. Oceanogr*. 68, 63–77. doi: 10.1007/s10872-011-0049-9

Larnicol, G., Traon, P.-Y. L., Ayoub, N., and Mey, P. D. (1995). Mean sea level and surface circulation variability of the Mediterranean Sea from 2 years of TOPEX/POSEIDON altimetry. *J. Geophys. Res*. 100:25163. doi: 10.1029/95JC01961

Le Vu, B., Stegner, A., and Arsouze, T. (2018). Angular momentum eddy detection and tracking algorithm (AMEDA) and its application to coastal eddy formation. *J. Atmos. Ocean. Technol*. 35, 739–762. doi: 10.1175/JTECH-D-17-0010.1

Matteoda, A. M., and Glenn, S. M. (1996). Observations of recurrent mesoscale eddies in the eastern Mediterranean. *J. Geophys. Res*. 101, 20687–20709. doi: 10.1029/96JC01111

Menna, M., Poulain, P.-M., Zodiatis, G., and Gertman, I. (2012). On the surface circulation of the Levantine sub-basin derived from Lagrangian drifters and satellite altimetry data. *Deep Sea Res. Part I* 65, 46–58. doi: 10.1016/j.dsr.2012.02.008

Miglietta, M. M., Zecchetto, S., and Biasio, F. D. (2013). A comparison of WRF model simulations with SAR wind data in two case studies of orographic lee waves over the Eastern Mediterranean Sea. *Atmos. Res*. 120–121, 127–146. doi: 10.1016/j.atmosres.2012.08.009

Mkhinini, N., Coimbra, A. L. S., Stegner, A., Arsouze, T., Taupier-Letage, I., and Béranger, K. (2014). Long-lived mesoscale eddies in the eastern Mediterranean Sea: analysis of 20 years of AVISO geostrophic velocities. *J. Geophys. Res*. 119, 8603–8626. doi: 10.1002/2014JC010176

Moschos, E., Stegner, A., Schwander, O., and Gallinari, P. (2020). Classification of eddy sea surface temperature signatures under cloud coverage. *IEEE J. Select. Top. Appl. Earth Observ. Rem. Sens*. 13, 3437–3447. doi: 10.1109/JSTARS.2020.3001830

Piedeleu, M., Sangrá, P., Sánchez-Vidal, A., Fabrés, J., Gordo, C., and Calafat, A. (2009). An observational study of oceanic eddy generation mechanisms by tall deep-water islands (Gran Canaria). *Geophys. Res. Lett*. 36, 1–5. doi: 10.1029/2008GL037010

Pullen, J., Doyle, J. D., May, P., Chavanne, C., Flament, P., and Arnone, R. A. (2008). Monsoon surges trigger oceanic eddy formation and propagation in the lee of the Philippine Islands. *Geophys. Res. Lett*. 35:L07604. doi: 10.1029/2007GL033109

Shchepetkin, A. F., and McWilliams, J. C. (2003). A method for computing horizontal pressure-gradient force in an oceanic model with a nonaligned vertical coordinate. *J. Geophys. Res*. 108:3090. doi: 10.1029/2001JC001047

Shchepetkin, A. F., and McWilliams, J. C. (2005). The regional oceanic modeling system (ROMS): a split-explicit, free-surface, topography-following-coordinate oceanic model. *Ocean Model*. 9, 347–404. doi: 10.1016/j.ocemod.2004.08.002

Stern, M. E. (1965). Interaction of a uniform wind stress with a geostrophic vortex. *Deep Sea Res. Oceanogr. Abstracts* 12, 355–367. doi: 10.1016/0011-7471(65)90007-0

Taupier-Letage, I. (2008). "On the use of thermal images for circulation studies: applications to the eastern Mediterranean basin," in *Remote Sensing of the European Seas*, eds V. Barale and M. Gade (La Seyne/Mer: Springer Netherlands), 153–164. doi: 10.1007/978-1-4020-6772-3_12

Viúdez, Á. (1997). An explanation for the curvature of the Atlantic jet past the strait of Gibraltar. *J. Phys. Oceanogr*. 27, 1804–1810. doi: 10.1175/1520-0485(1997)027<1804:AEFTCO>2.0.CO;2

Viúdez, Á., Haney, R. L., and Tintoré, J. (1996a). Circulation in the Alboran Sea as determined by quasi-synoptic hydrographic observations. Part II: mesoscale ageostrophic motion diagnosed through density dynamical assimilation. *J. Phys. Oceanogr*. 26, 706–724. doi: 10.1175/1520-0485(1996)026<0706:CITASA>2.0.CO;2

Viúdez, Á., Tintoré, J., and Haney, R. L. (1996b). Circulation in the Alboran Sea as determined by quasi-synoptic hydrographic observations. Part I: three-dimensional structure of the two anticyclonic gyres. *J. Phys. Oceanogr*. 26, 684–705. doi: 10.1175/1520-0485(1996)026<0684:CITASA>2.0.CO;2

Yoshida, S., Qiu, B., and Hacker, P. (2010). Wind generated eddy characteristics in the lee of the island of Hawaii. *J. Geophys. Res*. 115:C03019. doi: 10.1029/2009JC005417

Conflict of Interest: The authors declare that the research was conducted in the absence of any commercial or financial relationships that could be construed as a potential conflict of interest.

frontiers in Marine Science

ORIGINAL RESEARCH
published: 13 January 2021
doi: 10.3389/fmars.2020.595294

Long-Term Presence of the Island Mass Effect at Rangiroa Atoll, French Polynesia

Carleigh Vollbrecht[1], Paula Moehlenkamp[1], Jamison M. Gove[2], Anna B. Neuheimer[1,3] and Margaret A. McManus[1]*

[1] Department of Oceanography, School of Ocean Earth Science and Technology, University of Hawaii, Honolulu, HI, United States, [2] Ecosystem Sciences Division, Pacific Islands Fisheries Science Center, Honolulu, HI, United States, [3] Department of Biology, Aarhus University, Aarhus, Denmark

Enhancement of phytoplankton biomass near island and atoll reef ecosystems—termed the Island Mass Effect (IME)—is an ecologically important phenomenon driving marine ecosystem trophic structure and fisheries in the midst of oligotrophic tropical oceans. This study investigated the occurrence of IME at Rangiroa Atoll in the French Polynesian Tuamotu archipelago, and the physical mechanisms driving IME, through the analysis of satellite and *in situ* data. Comparison of chlorophyll-a concentration near Rangiroa Atoll with chlorophyll-a concentration in open ocean water 50 km offshore, over a 16-year period, showed phytoplankton enhancement as high as 130% nearshore, over 75.7% of the study period. Our statistical model examining physical drivers showed the magnitude of IME to be significantly enhanced by higher sea surface temperature (SST) and lower photosynthetically active radiation (PAR). Further, *in situ* measurements of water flowing through Tiputa Channel revealed outflowing lagoon water to be warmer, lower in salinity, and higher in particulate load compared to ocean water. We suggest that water inside Rangiroa's lagoon is enriched in nutrients and organic material by biological processes and advected as a result of tidal and wave forcing to coastal ocean waters, where it fuels primary production. We suggest that a combination of oceanographic and biological mechanisms is at play driving frequency and magnitude of IME at Rangiroa Atoll. Understanding the underlying processes driving IME at Rangiroa is essential for understanding future changes caused by a warming climate and changing environmental conditions for the marine ecosystem.

Keywords: Island Mass Effect, Rangiroa atoll, phytoplankton biomass, Chlorophyll-a enhancement, IME

OPEN ACCESS

Edited by:
Charitha Bandula Pattiaratchi, University of Western Australia, Australia

Reviewed by:
Zhongxiang Zhao, University of Washington, United States
Adam Thomas Devlin, The Chinese University of Hong Kong, China

****Correspondence:***
Paula Moehlenkamp
pmoehlen@hawaii.edu

Specialty section:
This article was submitted to Physical Oceanography, a section of the journal Frontiers in Marine Science

Received: *15 August 2020*
Accepted: *04 December 2020*
Published: *13 January 2021*

Citation:
Vollbrecht C, Moehlenkamp P, Gove JM, Neuheimer AB and McManus MA (2021) Long-Term Presence of the Island Mass Effect at Rangiroa Atoll, French Polynesia. Front. Mar. Sci. 7:595294. doi: 10.3389/fmars.2020.595294

INTRODUCTION

Phytoplankton production at the base of the food web provides a fundamental source of energy fueling entire marine ecosystems and production of the world's fisheries (Duarte and Cebrian, 1996). In the midst of oligotrophic waters, biological biomass has been found to be significantly enhanced around coral reef islands and atolls across the Pacific basin supporting productive local ecosystems with high fish biomass and thriving reef communities (Doty and Oguri, 1956; Signorini et al., 1999; Palacios, 2002; Andrade et al., 2014; Gove et al., 2016; James et al., 2020). The increase in phytoplankton biomass near island and atoll reef ecosystems—termed the Island

Mass Effect (IME)—has been attributed to an increase in available nutrients in the euphotic zone (Doty and Oguri, 1956).

Mechanisms contributing to enhancement of phytoplankton biomass in these regions have been found to be diverse and to vary locally. Important sources of nutrients and organic material are inputs from island terrestrial sources such as rivers or submarine groundwater discharge (Dandonneau and Charpy, 1985). In the water surrounding the islands of Tahiti, increased nutrients were found to occur after rain events caused runoff of nutrient-rich land sediment (Sauzède et al., 2018). Further, populated islands and atolls may cause anthropogenic inputs such as human waste or agricultural fertilizer enhancing nutrient and organic matter inputs to nearshore waters (Dandonneau and Charpy, 1985; Gove et al., 2016). Besides direct inputs from land, coral reef organisms can modify biogeochemical characteristics of water flowing over reefs through a multitude of biochemical mechanisms (e.g., Wyatt et al., 2010, 2012; Nelson et al., 2011), such as nitrogen fixation, nutrient regeneration, and recycling from other biota (Atkinson, 2011) and increase nutrient availability surrounding oceanic islands. Physical processes play an essential role in local mixing, transport, and retention of water masses near islands and atolls (Gilmartin and Revelante, 1974; Heywood et al., 1990; Palacios, 2002). Organic material and other sources of nutrients generated via coral reef ecosystem processes can be flushed out of the atoll via wave forcing (Callaghan et al., 2006) and tides (Chevalier et al., 2017) and provide nutrients to the surrounding oligotrophic waters. In tropical lagoons, water renewal time—regulated mainly by the flows through the passages and, when the reef is partially submerged, over the coral reef—strongly affects water quality, biological productivity, and ecological resilience (Delesalle and Sournia, 1991; Chevalier et al., 2017). Further, island and atoll bathymetry and slope can impact ocean currents and cause upwelling of cold nutrient enriched waters around islands and atolls (Hamner and Hauri, 1981; Gove et al., 2016). Internal waves interacting with bathymetry can lead to instabilities in the otherwise stably stratified water column and deliver nutrient rich water from below to the euphotic zone (Carter et al., 2006). Many studies have presented significant spatial and temporal variations in IME, as well as diversity in key forcing mechanisms and their importance in driving IME (Dandonneau and Charpy, 1985; Charpy, 1996; Charpy et al., 1997; Martinez and Maamaatuaiahutapu, 2004; Gove et al., 2016; Sauzède et al., 2018). Gove et al. (2016) analyzed chlorophyll-a measurements recorded over 10 years via satellite for 24 islands and 11 atolls in the tropical western Pacific and found the primary drivers of IME magnitude to be reef area, bathymetric slope, geomorphic type, and population status.

Here we present an investigation of the prevalence of IME at Rangiroa Atoll in French Polynesia. We use long-term satellite-derived observations of chlorophyll-a (a proxy for phytoplankton biomass) to show IME is a near-ubiquitous feature and identify key physical drivers of variations in the magnitude of IME at Rangiroa Atoll. Our findings of IME are contextualized with *in situ* data collected in Tiputa Channel, the main exchange point for water between Rangiroa Lagoon and the ocean. As our global climate changes, atoll ecosystems are increasingly affected by rising ocean temperatures, changes in wave, wind and light fields, as well as rising sea levels. Understanding the environmental factors that drive fluctuations in phytoplankton biomass can provide a basis for predicting food web shifts occurring as a result of climate change in this region. Understanding the relative influence of environmental mechanisms driving IME at Rangiroa Atoll is crucial in order to predict how atoll systems, such as those in the Tuamotu Archipelago, will respond to environmental changes in the future.

MATERIALS AND METHODS

Study Site

Rangiroa Atoll is located in the northwest of the Tuamotu Archipelago at 15.1°S, 147.6°W (**Figure 1A**). The atoll is the largest in the French Polynesia Tuamotu archipelago with a lagoon surface area of 1446 km^2, a maximum depth of 38 m, and an estimated volume of 37.71 km^3 (Kumar et al., 2013). The atoll perimeter extends ∼ 200 km consisting of 415 reef islands and fringing reef. Rangiroa's total land area covers 170 km^2 (Kumar et al., 2013) with a population of 2709 inhabitants recorded in the 2017 census (Institute of Statistics of French Polynesia, 2017). In addition to ∼100 small passes in the fringing reef, two large passes connect the lagoon to the open ocean in the northwest of the atoll rim: Tiputa Channel is 310 m wide at the narrowest point and between 10 m (lagoon side) and 45 m (oceanside) deep with a steep drop off at the mouth to ocean depths below 60 m. Avatoru Pass is a wider, shallower pass located 9 km to the northwest of Tiputa Channel (Kumar et al., 2013).

The southern perimeter of Rangiroa Atoll is primarily comprised of fringing reef and the northern perimeter has more islands. The atoll parameter has been estimated to have ∼22% of the perimeter open to exchange with the ocean (Andréfouët et al., 2001a). Thus, the porous rim allows both predominant southern and northern swells to exchange water to the lagoon, while atolls located to the east and west of Rangiroa Atoll block or reflect waves (Andréfouët et al., 2012). Rangiroa Atoll is classified as a partially enclosed atoll with tides and waves being primary mechanisms forcing circulation and exchange. Using water volume flux calculations and wave heights acquired by satellite altimetry data, residence time at Rangiroa Atoll was estimated to be between 130 and 155 days for wave heights in the range of 1.5–3.5 m (Andréfouët et al., 2001b; Pagès and Andréfouët, 2001). Additionally, water residence in Rangiroa's lagoon was found to decrease linearly with wave forcing above 1.7 m (Andréfouët et al., 2001b).

Data

Chlorophyll-a (mg m^{-3}): Long-term (January 2003 to February 2019) chlorophyll-a data were retrieved from NASA's Moderate Resolution Imaging Spectroradiometer (MODIS) instrument using the 8-day, 4-km data product. Comparison of chlorophyll-a data sets 23 km north, 50 km north, and 23 km to the south of the atoll, using the Mann–Whitney *U* test (a non-parametric test used to indicate the probability that two independent samples are from the same distribution, Spiegel and Stephens, 2011), indicated that these locations are statistically of the same set,

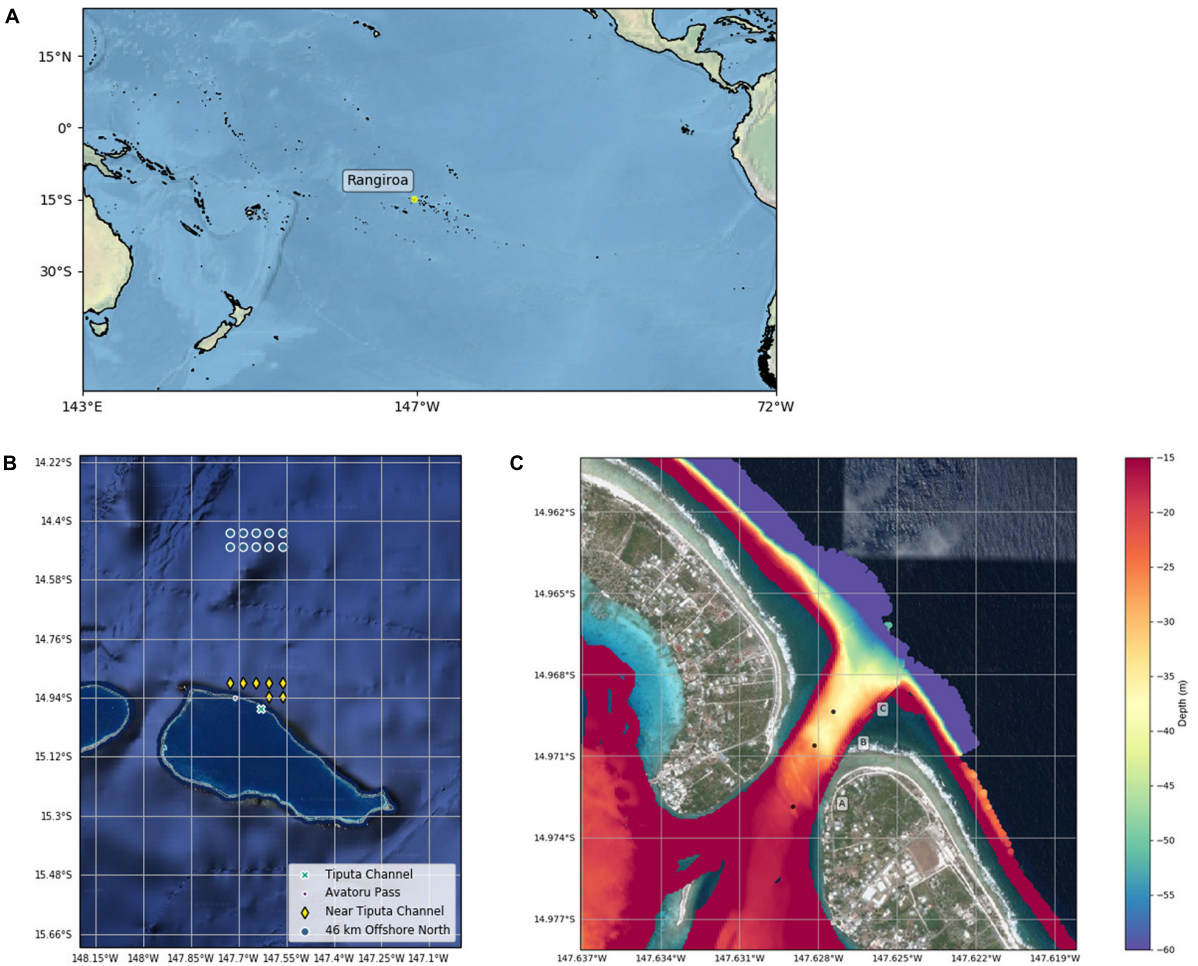

FIGURE 1 | (A) Southern Pacific Ocean map with Rangiroa. **(B)** Satellite image of Rangiroa with Tiputa Channel, Avatoru Pass, and MODIS data near and approximately 50 km north of Tiputa Channel. **(C)** Bathymetric data from Tiputa Channel collected by the Secretariat of the Pacific Community Applied Geoscience Division (SOPAC) overlaid on a Google satellite image. Deployment locations of three moorings are marked A, B, and C. The color bar shows depth in meters.

eliminating the sets 23 km north and south. Further, chlorophyll-a measurements near Tiputa Channel and near the southern fringing reef were found to be statistically of the same set, eliminating the set near the southern fringing reef. For that reason, we focused our analysis of IME at Rangiroa on two locations using 7 MODIS data points (center of each pixel) near the Tiputa Channel and 10 MODIS data points located approximately 50 km offshore and to the north of Rangiroa Atoll (**Figure 1B** and **Table 1**). To assess IME, the difference between average chlorophyll-a concentration at these two locations (near Tiputa Channel and offshore of Rangiroa Atoll) was calculated (**Figure 1B**). Data within ∼3.27 km of the 30 m isobath were removed to avoid optically shallow water and errors induced by terrigenous input, resuspended material, or bottom substrate properties (sensu Gove et al., 2013). Due to sensor limitations, any data points with chlorophyll differences less than 0.005 mg m^{-3} were excluded reducing the data set from 507 to 317 data points. Latitude and longitude of MODIS data locations near Tiputa Channel and offshore are given in **Table 1**.

Sea surface temperature (°C): SST data were retrieved from the same instrument as chlorophyll-a using the 8-day, 4-km data product near Tiputa Channel.

TABLE 1 | Latitude and longitude of MODIS data near Tiputa Channel and approximately 50 km offshore of Tiputa Channel.

Latitude/Longitude Tiputa Channel	Latitude/Longitude 50 km offshore
1. 14.896°S, 147.729°W	1. 14.479°S, 147.729°W
2. 14.896°S, 147.688°W	2. 14.479°S, 147.688°W
3. 14.896°S, 147.646°W	3. 14.479°S, 147.646°W
4. 14.896°S, 147.604°W	4. 14.479°S, 147.604°W
5. 14.896°S, 147.563°W	5. 14.479°S, 147.563°W
6. 14.938°S, 147.604°W	6. 14.438°S, 147.729°W
7. 14.938°S, 147.563°W	7. 14.438°S, 147.688°W
	8. 14.438°S, 147.646°W
	9. 14.438°S, 147.604°W
	10. 14.438°S, 147.563°W

MODIS data is centered at these points.

Photosynthetically active radiation (Einstein m^{-2} d^{-1}): PAR data were analyzed to identify the optimal amount required for peak chlorophyll-a. PAR data were retrieved from the same instrument as chlorophyll-a using the 8-day, 4-km data product near Tiputa Channel.

Wind forcing: An 8-day average of daily wind direction (°) and magnitude (m s^{-1}) was calculated from NASA SeaWinds sensor on the QuikSCAT satellite[1] (data are 0.125° spaced) from January 2003 to November 2009 and NOAA ASCAT sensor on the METOP satellite[2] (data are 0.25° spaced) from November 2009 to February 2019. For each 8-day segment, the mean value of the box bounded by latitudes 14.5°S and 15°S and longitudes 147.25°W 147.5°W (to the east of the chlorophyll-a locations) was computed. Interference with winds caused by topography was not of significant concern as Rangiroa Atoll or neighboring atolls do not contain substantial vertical relief (highest point is ∼12 m). For alignment purposes, all wind data were time centered and averaged using the same time window that was used for chlorophyll-a.

Rainfall (in mm): Daily rainfall totals were downloaded from the multi-satellite Global Precipitation Measurement (GPM) mission, version 5. Data were available in a 0.1° × 0.1° grid. Area rainfall data were downloaded for the period 18–22 April 2014, to correspond with the *in situ* data[3].

Wave forcing: Wave data were obtained from the WaveWatch III model from two sources: CAWCR Wave Hindcast 1979–2010[4] and the CAWCR wave Hindcast extension. Wave data past June 2013 is from WaveWatch III (WW3) Global Wave Model[5]. An 8-day average of daily maximum wave significant wave height, peak wave period, and peak wave direction was calculated from hourly wave data. Wave data were centered (south of the atoll, 15.5°S, 147.5°W) and aligned with chlorophyll-a dates. This location presented the closest model grid cell to the atoll that would capture the biggest swell during the winter months. Mean significant wave height (H_s) and peak period (t_p) were used to calculate wave power (E_f) in kW m^{-1} using Eq. 1 below:

$$E_f = \frac{\rho g^2}{64\pi} H_s^2 t_p / 1000 \quad (1)$$

where ρ is the density of seawater (1024 kg m^{-3}) and g is the acceleration of gravity (9.8 m s^{-2}). The combination of mean significant wave height and peak wave period into wave power allows wave events to be identified in a single predictor variable.

Multivariate ENSO index: Multivariate ENSO Index Version 2 (MEI) data were retrieved from NOAA[6]. MEI has a range of -2.4 to 2.2 and is used to characterize the magnitude of ENSO events with positive MEI values indicating an El Niño event (warming) and negative values indicating a La Niña event (cooling). MEI combines oceanic and atmospheric variables [sea level pressure (SLP), sea surface temperature (SST), zonal and meridional components of the surface wind, and outgoing longwave radiation (OLR)] into a single index computed 12 times a year in overlapping two-month periods to account for seasonality.

In situ Measurements

To measure the current velocity in Tiputa Channel, three SonTek Acoustic Doppler Profilers (ADPs) were deployed in consecutively deeper locations from the lagoon to the ocean (Moorings A, B, and C at 22.5, 29.5, and 38 m, respectively) along the primary axis of the channel. A Sea-Bird Electronics 19plus CTD[7] measuring conductivity, temperature, and pressure; a Wet Labs C-Star transmissometer[8] measuring light transmittance (a proxy for water clarity); and a BioSpherical Instruments QSP-2200PD PAR Sensor[9] measuring photosynthetically active radiation (PAR) were deployed on Mooring C to assess water conditions. Moving from mooring A to B the channel narrows and the seafloor depth drops from 22.5 to 25.9 m, continuing to mooring C the channel opens to the ocean and seafloor depth continues to drop to 38 m. Between moorings A and C spaced 0.4208 km apart, depth drops to a total of 15.5 m. Net water exchange through Tiputa Channel was calculated over a 24-h period following methods used by after Moehlenkamp et al. (2019). In brief, along channel water volume flux was calculated using Eq. 2:

$$\text{Flux} = \text{Width} \times \text{Depth} \times \text{Velocity}, \quad (2)$$

where width is the channel width (175 m at mooring B), depth the channel depth (varies with tide, ∼29.5 m), and velocity the vector of measured along channel current velocity. Water velocity was recorded at mooring B due to its central location in the channel and its constant cross-channel depth. The flow was unidirectional, and the rate of flow for each time point was averaged over the recorded water column measurements (23 bins with 1 m vertical spacing, from a depth of 4.5–26.5 m were averaged to a single flow rate). This flow rate was then applied to the entire depth of 29.5 m.

Statistical Analysis

Our research explores factors affecting the difference in chlorophyll-a concentration (mg m^{-3}) between Rangiroa Atoll (near Tiputa Channel; **Figure 1B**) and waters offshore (i.e., onshore–offshore). Here, IME can be seen as a positive difference in chlorophyll-a concentration (Δchl, mg m^{-3}) between these onshore and offshore locations. We test the hypothesis that Δchl varies with sea surface temperature (SST; °C), photosynthetically available radiation (PAR; Einstein m^{-2} d^{-1}), wind magnitude (m s^{-1}), wind direction (°), wave power (kW m^{-1}), wave direction (°), and the multivariate ENSO index (MEI). Note that MEI and wind magnitude are inherently correlated with one

[1]https://coastwatch.pfeg.noaa.gov/erddap/griddap/erdQSwind1day.html
[2]https://coastwatch.pfeg.noaa.gov/erddap/griddap/erdQAwind1day.html
[3]https://pmm.nasa.gov/data-access/downloads/gpm
[4]https://www.pacificclimatechange.net/document/cawcr-wave-hindcast-1979-2010
[5]http://oos.soest.hawaii.edu/erddap/griddap/NWW3_Global_Best.html
[6]https://www.esrl.noaa.gov/psd/enso/mei/
[7]http://www.seabird.com
[8]http://www.wetlabs.com
[9]http://www.biospherical.com

another. We choose to include both in our model to allow us to assess both wind effects (a combined effect of wind magnitude and direction), as well as more general ENSO forcing effects. To account for covariate collinearity, we model with a combination effect of wind direction and magnitude and use generalized additive modeling (more below) where the non-linear fitting is more robust (vs. linear modeling) to collinearity among predictor variables. Each predictor variable was averaged over the same 8-day period as the chlorophyll-a data with no lag between response and predictor variables. Entries missing a value were removed from the dataset, resulting in 310 time points for analysis. The response (Δchl_i) was modeled as observations from a normal distribution as they are continuous and can be both positive and negative. The expected value of the response was modeled as a function of the predictors using a generalized additive model (GAM). GAMs do not assume *a priori* any specific form of the relationship between the dependent variable and the covariates and can be used to reveal and estimate non-linear effects of the covariate on the dependent variable. To account for temporal autocorrelation, a variable (SampleDay) containing the number of days since the first sample was included in the model. Our GAM was:

$$\Delta\text{chl}_i \sim N(\mu_i, \sigma)$$

and

$$\begin{aligned}\mu_i \sim & f(\text{SST}_i) + f(\text{PAR}_i) + f(\text{WindMagnitude}_i, \\ & \text{WindDirection}_i) \\ & + f(\text{WindPower}_i, \text{WindDirection}_i) + f(\text{MEI}_i) \\ & + f(\textit{SampleDay}_i)\end{aligned} \quad (3)$$

Effects of wind magnitude and direction were assessed via a two-dimensional smoother with magnitude smoothed using a thin plate regression spline and direction smoothed with a cyclic cubic regression spline (the latter reflecting the cyclical nature of wind direction). The link function, $g(\ldots)$, providing the relationship between the expected value of the response and the linear predictor was set as the canonical identity link function, and model residuals were assessed regarding this assumption by inspecting residuals and determining the ability for the model to give rise to the data by comparing residuals to those simulated from the model. The importance of predictors in explaining response variability was assessed by comparing models representing all possible combinations of predictors via corrected Akaike Information Criteria (AICc). Models always included the SampleDay predictor to help adjust for temporal autocorrelation (as mentioned above). All statistical analysis was fit using R (R Core Team, 2018) via the mgcv, lubridate, ggplot2, DHARMa, MuMIn, visreg, reshape2, and metR packages (Wickham, 2007, 2016; Barton, 2009; Grolemund and Wickham, 2011; Wood, 2011; Breheny and Burchett, 2017).

To test correlations among the predictors, a Pearson's pairwise correlation test was performed to test for a linear relationship between two sets of data. Equation 4 below calculates the correlation coefficient or *r*-value (r) using each sample point (i) in the two datasets (x and y)

$$r = \frac{\sum(x - m_x)(y - m_y)}{\sqrt{\sum(x - m_x)^2}\sqrt{\sum(y - m_y)^2}} \quad (4)$$

where m_x is the mean of the set x and m_y is the mean of the set y. Positive signs of R values indicate a positive correlation, negative signs indicate a negative correlation. The magnitude spans from 0 to 1 with larger numbers showing a higher correlation. *P*-values range from 0 to 1 and indicate the probability that the *r*-value relationship is not true (significant if $p < 0.05$, Abbott, 2017).

RESULTS

Nearshore Phytoplankton Enhancement

We found that during 75.7% of the 16-year study period (from January 2003 to February 2019), Rangiroa Atoll displayed localized nearshore enhancement in chlorophyll-a, which is the IME, Δchl. Averaged chlorophyll-a concentration at Tiputa Channel was 16% greater than the concentration offshore to the north with a maximum enhancement nearshore as high as 130%. The chlorophyll-a difference between nearshore and offshore ranged from -0.043 mg m^{-3} (no IME) to 0.091 mg m^{-3} with a mean value of 0.008 mg m^{-3} (**Figure 2**). The mean positive chlorophyll-a difference (i.e., IME) was 0.015 mg m^{-3}, and the mean negative chlorophyll-a difference was -0.013 mg m^{-3} (**Figure 2A**). Chlorophyll-a near Tiputa Channel and offshore followed similar, though not identical, patterns of both increases and decreases through the record (**Figure 2B**).

We investigated the factors that influence the nearshore to offshore chlorophyll-a difference via a suite of physical predictor variables using a GAM with normal error distribution assumption. The resulting statistical model exhibited relatively uniform residuals with only a slightly skewed distribution from the expected (likely due to an outlier). The model was refit with a "log" link function but the change did not improve residual behavior.

A comparison of models representing all possible predictor combinations (but always including SampleDay; see Materials and Methods) revealed five models within ΔAICc < 2 of the lowest AICc model (**Table 2**). Best-specified models also exhibited well-behaved uniform residuals with no significant outliers. SST and PAR appeared in all best-specified models resulting in an importance estimate (via sum of model weights) of 1 for each (**Table 2**). Wind effects (magnitude and direction) appeared in three best-specified models with an importance estimate of 0.66. Wave effects (power and direction) appeared in two best-specified models with an importance estimate of 0.35. MEI effects appeared in one best-specified model with an importance estimate of 0.17. Effect plots were drawn from Model 1 in **Table 2** which had the highest weight (0.337) relative to other best-specified models and explained 18% of the variation in Δchl. The highest proportion of variation in Δchl was explained by wind effects (magnitude and direction; 5.8%).

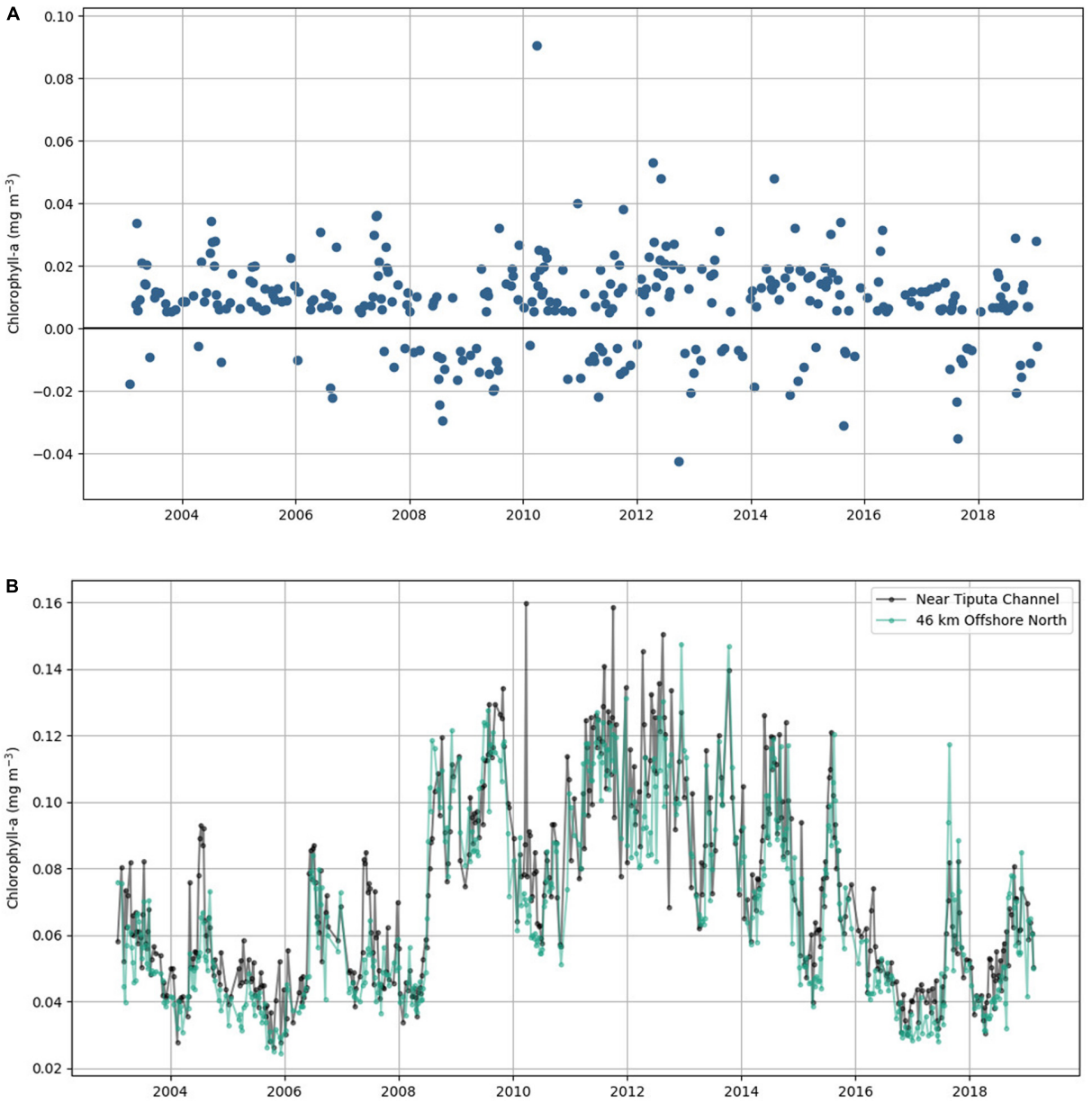

FIGURE 2 | (A) Eight-day average of chlorophyll-a difference between near Tiputa Channel and offshore from January 2003 to February 2019. Positive values represent times when the IME was present; negative values represent times when the IME was not present. **(B)** Eight-day average of chlorophyll-a data near Tiputa Channel (black) and offshore (aqua).

TABLE 2 | Five models resulting from a comparison of models investigating Δchl representing all possible predictor combinations within ΔAICc < 2 of the lowest AICc model.

	Model	Explained variation	Log likelihood	AICc	ΔAICc	Weight
1	$\mu_i \sim f(SST_i) + f(PAR_i) + f(WindMagnitude_i, WindDirection_i) + f(SampleDay_i)$	0.18	892.296	−1735.7	0.00	0.337
2	$\mu_i \sim f(SST_i) + f(PAR_i) + f(WavePower_i, WaveDirection_i) + f(SampleDay_i)$	0.14	884.531	−1734.8	0.97	0.208
3	$\mu_i \sim f(SST_i) + f(PAR_i) + f(WindMagnitude_i, WindDirection_i) + f(MEI_i) + f(SampleDay_i)$	0.18	892.226	−1734.4	1.34	0.172
4	$\mu_i \sim f(SST_i) + f(PAR_i) + f(WindMagnitude_i, WindDirection_i) + f(WavePower_i, WaveDirection_i) + f(SampleDay_i)$	0.19	894.165	−1734.1	1.67	0.147
5	$\mu_i \sim f(SST_i) + f(PAR_i) + f(SampleDay_i)$	0.13	881.498	−1733.9	1.82	0.136

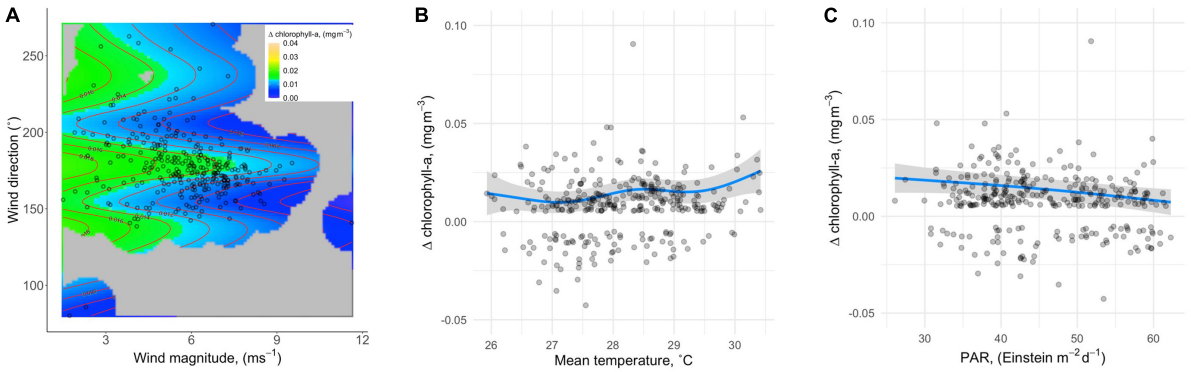

FIGURE 3 | Effect plots from Model 1 in **Table 2**, which had the highest weight (0.337) relative to other best-specified models **(A)** IME magnitude as a function of wind. **(B)** IME magnitude as a function of SST. **(C)** IME magnitude as a function of PAR. As all modeled effects have the prediction estimate above the 0 Δchl line on the *y*-axis, they are describing effects on the magnitude of IME for Rangiroa.

Δchl declined with increasing wind magnitude and showed the highest values over a mid-range in wind directions (**Figure 3A**). SST explained the second highest proportion of variation in Δchl (4.7%). Δchl increased with increasing mean temperature (**Figure 3B**). Finally, PAR explained 3.3% of the variation in Δchl with declining Δchl with increasing PAR (**Figure 3C**). As all modeled effects have the prediction estimate above the 0 Δchl line on the *y*-axis, they are describing effects on the magnitude of IME for Rangiroa.

Seasonal Patterns in the Island Mass Effect

Chlorophyll-a difference data was plotted on 8-day increments across 16 years (January 2003 to February 2019) to investigate seasonality (**Figure 4**). IME across years was variable (**Figure 4A**): the mean value of IME was 0.008 mg m^{-3} with a large standard deviation of 0.015 mg m^{-3}. The highest value 0.091 mg m^{-3} was recorded in March 2010, and the lowest value -0.043 mg m^{-3} was recorded in September 2012 (**Figure 4B**). The month with the highest chlorophyll-a difference across the 16-year time span was May with a mean chlorophyll-a difference of 0.014 mg m^{-3}. The month with the lowest chlorophyll-a difference across the 16-year time span was September with a mean chlorophyll-a difference of 0.002 mg m^{-3}. March had the highest variability with the standard deviation of 0.020 mg m^{-3}, and February had the lowest variably with the standard deviation of 0.009 mg m^{-3} (**Figure 4B**). Data were spaced unevenly throughout the year due to clouds during the rainy summer season resulting in fewer chlorophyll-a records in the months of October through March. Chlorophyll-a near Tiputa Channel and offshore both showed a gradual rise in chlorophyll-a from March through August when all years are averaged; however, when comparing year to year, this pattern was not consistent and there was considerable variability across the years for each month (**Figure 4**). While seasonal trends in chlorophyll-a difference can be identified, these were not consistent across years. Mean chlorophyll-a concentration nearshore and offshore of Tiputa Channel visualized across the entire study period from January 2003 to February 2019 showed a clear IME (i.e., the enhancement of chlorophyll-a concentration nearshore) (**Figure 5A**). However, the degree to which IME was present varied strongly across years, with strong magnitudes in 2013 (**Figure 5B**) and weaker magnitudes in 2016 (**Figure 5C**).

In situ Observations in Tiputa Channel

In situ observations of pressure (water depth), PAR, light transmittance, temperature, conductivity (salinity), and current velocity in Tiputa Channel (18–22 April 2014) revealed strong influence of tidal forcing (**Figure 6**). PAR followed a typical diurnal pattern with solar insolation increasing after sunrise and decreasing before sunset (**Figure 6A**). Water leaving the atoll on ebb tide was higher in turbidity indicating a higher concentration of particulate matter compared to ocean water flooding into the atoll (**Figure 6B**). In addition, water flowing into the atoll on the flood tide was colder, saltier, and denser compared to water flowing out of the atoll with the low tide (**Figures 6C,D**). Current flow at the three moorings was predictable, primarily following the tide (**Figure 7A**). Horizontal currents at moorings A, B, and C flowed in the along channel direction, oriented at 32.2° (true; northeast) for outgoing low tide, and for 212.2° (true; southwest) incoming high tide. Outgoing current speeds had a higher velocity than incoming velocities given the additional pressure gradient between the lagoon and the ocean (**Table 3**). During the sensor deployment period, the maximum outgoing current speed was 2.594 m s^{-1} recorded at mooring B; the maximum incoming current speed was 1.813 m s^{-1} recorded at mooring A. Water balance over the 24-h period summed 969,000 m^3 entering the atoll and 2,810,000 m^3 exiting the atoll highlighting a significant difference between inflow and outflow with more water exiting than entering Rangiroa Atoll through the Tiputa Channel at each tidal cycle. The net water exchange between Rangiroa lagoon and the ocean was 1,841,000 m^3 (outward) for the 24-h period 20 April 2014 00:00 through 23:59. During the flood tide, as the water level increases so does the volume flux, until reaching the midpoint or highest water level at which point it decreases. On ebb tide the flow reverses following the same pattern (**Figure 7B**).

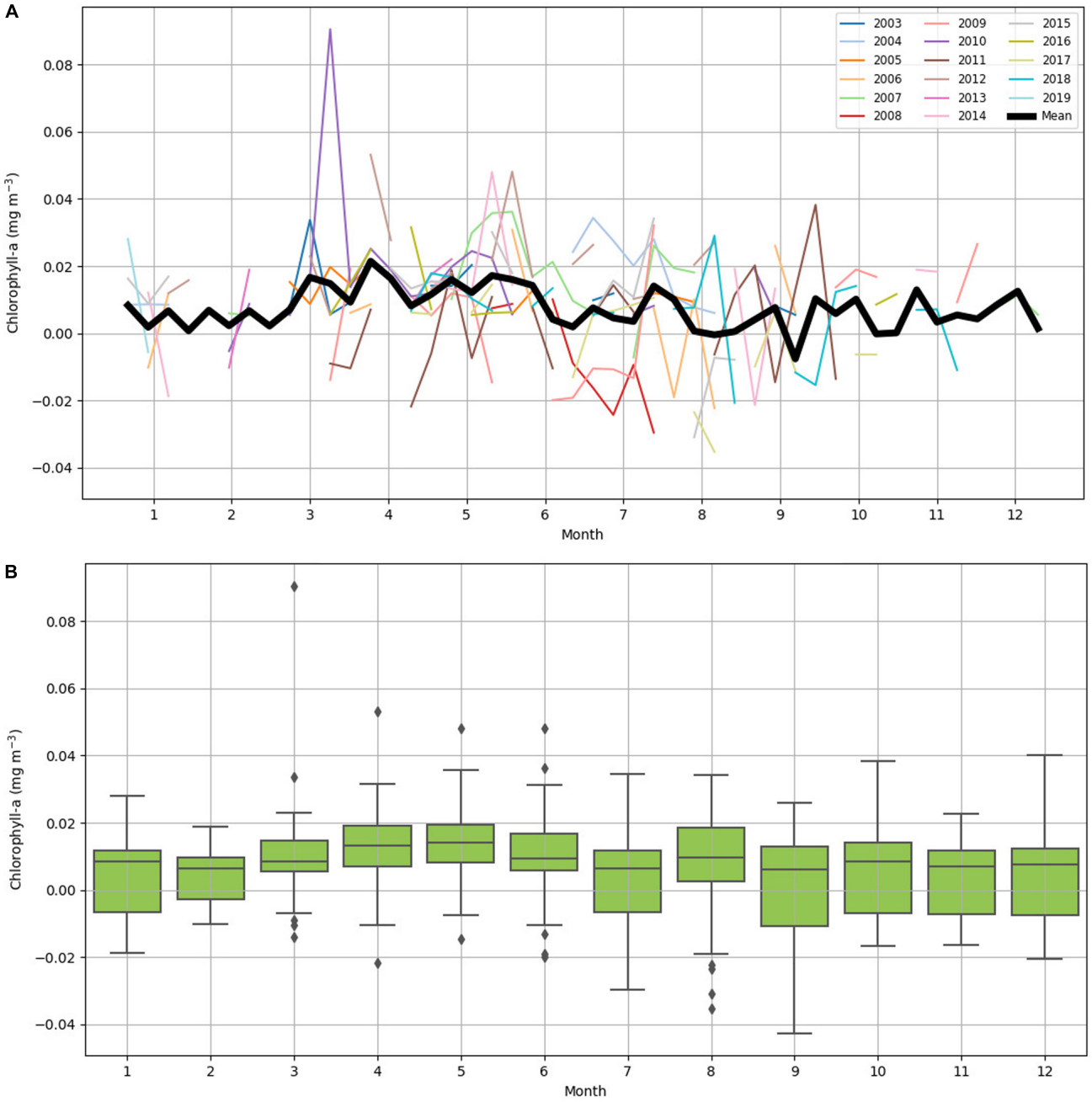

FIGURE 4 | (A) Yearly 8-day mean of chlorophyll-a difference from January 2003 to February 2019. Each year has a color-coordinated line. The dark black line is the collective mean for all years. **(B)** Box plot of 8-day average chlorophyll-a difference between near Tiputa Channel and offshore by month, derived from data between January 2003 and February 2019. The central mark in each box is the median, the bottom and top edges of the box are the 25th and 75th percentiles. Diamonds indicate outliers.

DISCUSSION

IME Present at Rangiroa Atoll

Our investigation of IME demonstrated that nearshore phytoplankton enhancement is a long-term, near-persistent feature at Rangiroa Atoll. IME is present in waters outside Tiputa Channel, Rangiroa Atoll 75.7% of a 16-year period with phytoplankton enhancement as high as 130% and an average enhancement of 16% near Rangiroa Atoll compared to offshore. The magnitude and frequency of enhanced chlorophyll-a concentration clearly indicate presence of the Island Mass Effect (IME) in coastal waters offshore of Tiputa Channel. These results agree with past studies that found increased phytoplankton biomass around islands and atolls in the Tuamotu Archipelago

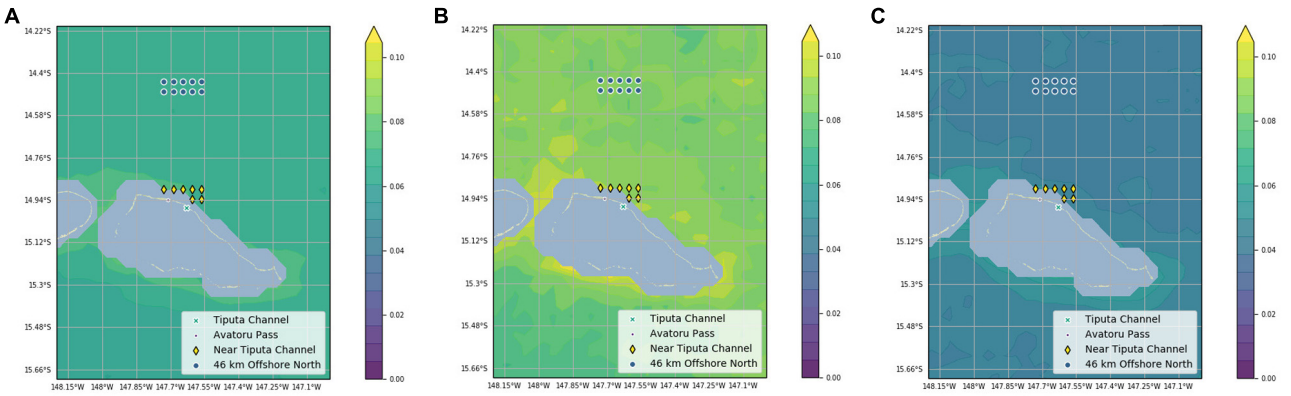

FIGURE 5 | (A) Chlorophyll-a averaged across the entire study period (2003–2019). **(B)** Chlorophyll-a averaged across the year of 2013. **(C)** Chlorophyll-a averaged across the year of 2016. Chlorophyll-a concentration was projected onto a terrain map and plotted using filled contours. Contours are drawn in 0.005 increments from 0 to 0.12 mg m^{-3}. Study points are marked along with Tiputa Channel and Avatoru Pass. Pixels with land or within the 30-m isotherm are masked.

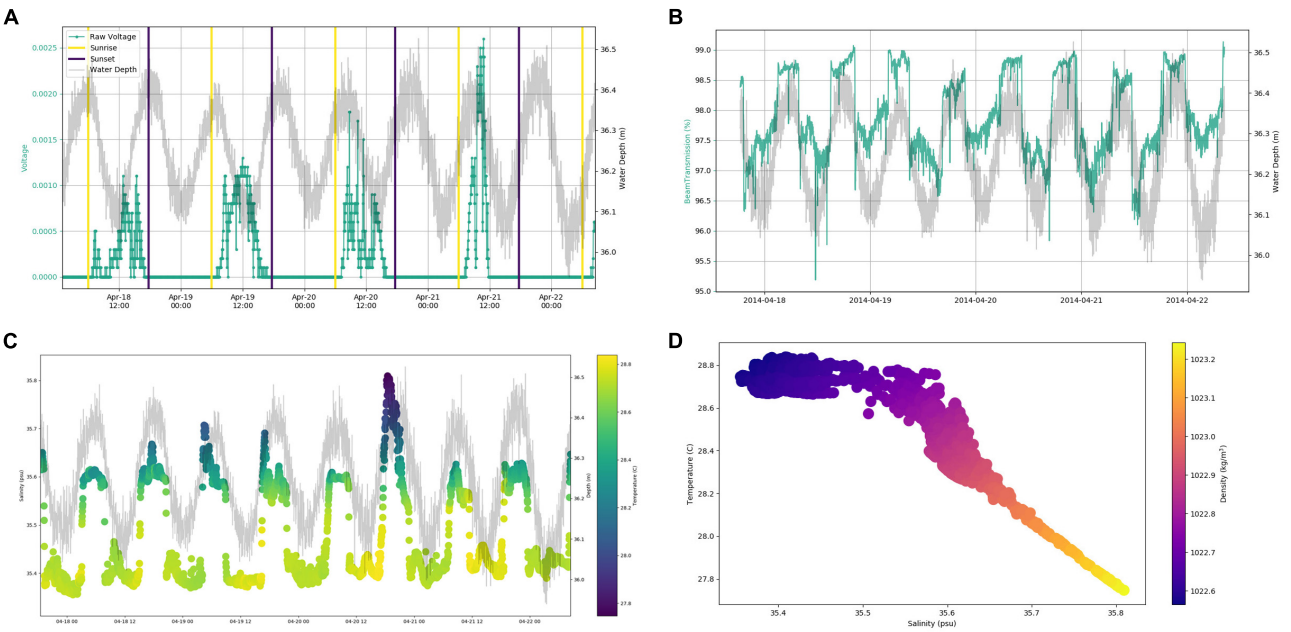

FIGURE 6 | (A) Raw voltage from BioSpherical Instruments QSP-2200PD PAR sensor. Voltage indicated by aqua line. Yellow lines indicate sunrise. Dark blue lines indicate sunset. Sunrise and sunset are from the NOAA Solar Calculator (http://www.esrl.noaa.gov/gmd/grad/solcalc/). Gray line indicates water depth in meters derived from Sea-Bird Electronics 19plus CTD. **(B)** Light transmittance (%) over time with water depth in Tiputa Channel at mooring C. Light transmittance data from Wet Labs C-Star transmissometer. Transmittance (aqua) values. Gray line indicates water depth in meters derived from Sea-Bird Electronics 19plus CTD. **(C)** Temperature and salinity plotted with water depth over time. Color indicates temperature in °C with yellow being warmer and blue colder. Salinity is in psu. Water depth is (in m) is indicated by gray line. Temperature, salinity, and pressure data from Sea-Bird Electronics 19 plus CTD. **(D)** Temperature, salinity, and density. Temperature is in °C. Salinity is in psu. Colors indicate density in kg m^{-3} with yellow being denser and blue being less dense. Data for **A–C** were retrieved from mooring C (depth 37 m) from 18 April 2014 through 22 April 2014.

despite the surrounding oligotrophic waters of the South Pacific Subtropical Gyre (Ferrier-Pagès and Furla, 2001). Studies found enhanced biomass inside atoll lagoons with particulate organic matter to be 2–5 times higher inside the atolls compared to the open ocean (Charpy et al., 1997; Ferrier-Pagès and Furla, 2001). The Island Mass Effect was first described over 70 years ago (Doty and Oguri, 1956), since then, IME has been documented for numerous island-reef ecosystems (e.g., Signorini et al., 1999; Palacios, 2002; Andrade et al., 2014; Gove et al., 2016). In a 10-year study investigating IME across the tropical Pacific, Gove et al. (2016) found an increase of phytoplankton biomass in 91% of the 32 islands and atolls surveyed.

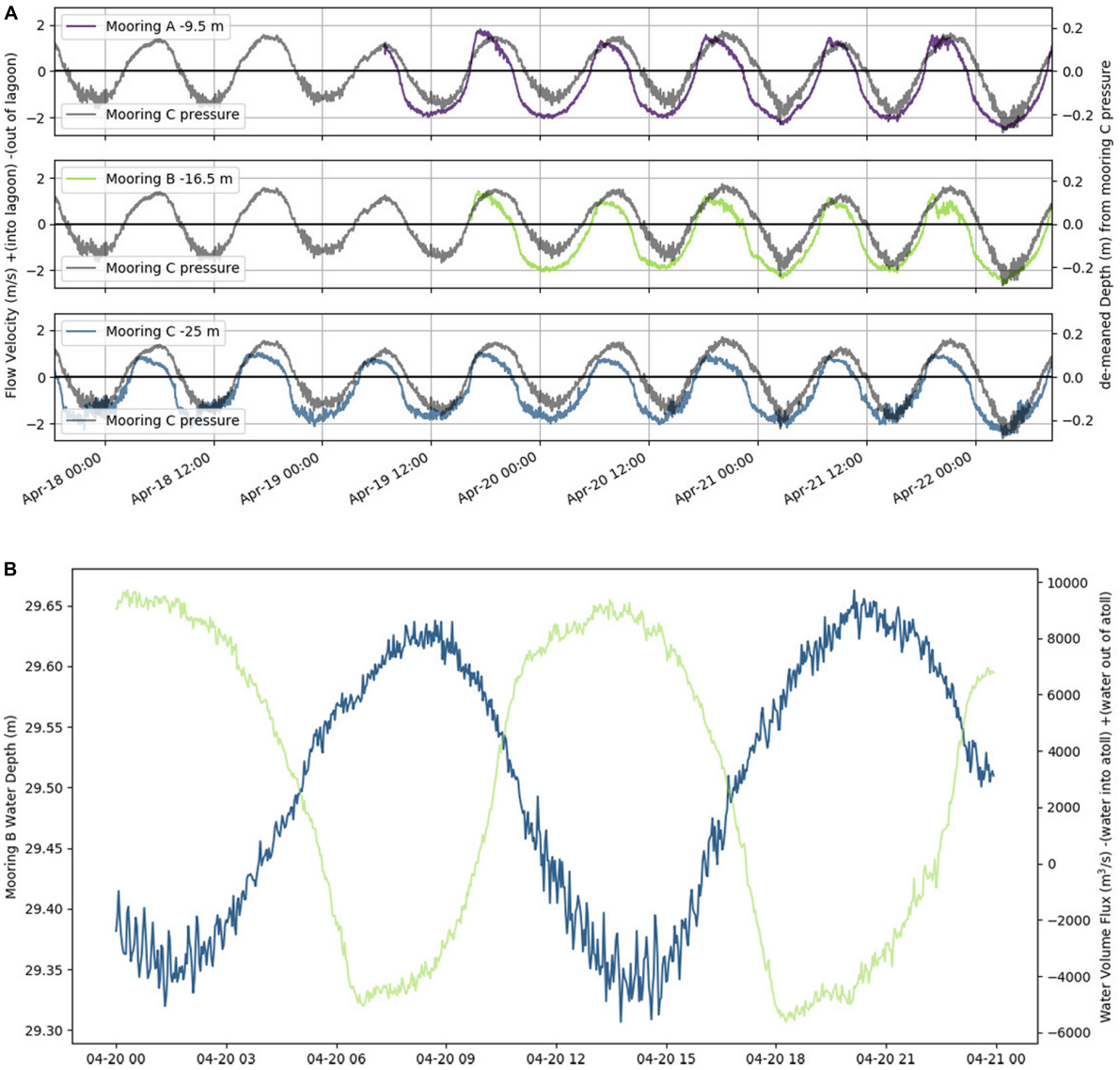

FIGURE 7 | (A) Horizontal channel flow at a single water depth plotted with a demeaned tide taken from pressure at mooring C (gray line in each panel in April 2014). Top panel is mooring A; flow is at 9.5 m depth (purple). Middle panel is mooring B; flow is at 16.5 m depth (green). Bottom panel is mooring C; flow is at 25 m depth (blue). Flow velocity is in m s^{-1}. Relative water depth in m. **(B)** Water level (m, blue) and water flux (m^3 s^{-1}, green) at mooring B over 24-h period on 20 April 2014. Negative water flux indicates water flowing into the lagoon, positive water flux indicates water flowing out of the lagoon.

SST and PAR Are Significant Drivers of IME Magnitude

We found that SST was a significant driver of IME. Multiple studies have documented an important relationship between SST and chlorophyll-a (Lo-Yat et al., 2011; Uz et al., 2017; Dunstan et al., 2018). Dunstan et al. (2018) found that chlorophyll-a change, as a response to SST, is highly heterogeneous with large regional differences: some regions showed increased chlorophyll-a with increased SST; other regions in contrast showed decreased chlorophyll-a with increased SST. Our study indicated a positive relationship between IME (the positive chlorophyll-a difference between coastal Rangiroa waters and offshore) and SST with increasing IME as a result of increasing SST. Chlorophyll-a concentration in coastal Rangiroa waters and offshore of Tiputa Channel are likely influenced by different mechanisms. Chlorophyll-a offshore can be influenced by broad scale climate forcing such as ENSO that lead to changes in SST (McPhaden, 2012). Uz et al. (2017) identified changes in the thermocline and upwelling intensity related to El Niño and La Niña in the equatorial Pacific between 10°N and 10°S. During an El Niño event, enhanced SST can lead to more stable stratification in the upper ocean and a reduction in surface mixing depth resulting in lower chlorophyll-a concentrations (Uz et al., 2017). The relationship of enhanced SST leading to decreased chlorophyll-a in oligotrophic waters offshore was also confirmed by Lo-Yat et al. (2011), who investigated satellite

TABLE 3 | Measurement of current velocity at moorings A, B, and C.

	Mooring A	Mooring B	Mooring C
Max out	2.594	2.636	2.556
Max in	−1.813	−1.444	−1.215
Max up	0.292	0.267	0.238
Max down	−0.140	−0.298	−0.211
Mean out	1.467	1.393	1.323
Mean in	−0.931	−0.675	−0.582
Mean up	0.028	0.053	0.038
Mean down	−0.016	−0.084	−0.033

Current speeds in m s^{-1}.

chlorophyll-a data between January 1996 and March 2000 in a study 124 km (14.1°S, 147.1°W) outside Rangiroa Atoll and found a strong relationship between the timing of an El Niño warming event and satellite-derived chlorophyll-a. While not a statistically significant driver of IME, the relationship between the Multivariate ENSO Index (MEI) and IME was found to be positive in this study (**Figure 8**). While open ocean chlorophyll-a can be depressed during strong warming events as a result of more stable stratification, chlorophyll-a in Rangiroa's coastal waters may be affected less by this dynamic due to its proximity to the lagoon and atoll. Hence, increased SST could lead to a stronger IME (the positive chlorophyll-a difference between coastal Rangiroa waters and offshore). Pearson's pairwise correlation on SST and chlorophyll-a (not IME) near Tiputa Channel (*r*-value -0.29) and offshore (*r*-value -0.37) found a negative linear relationship (increased SST, decreased chlorophyll-a) for both locations (**Figure 8**). However, this trend is more pronounced for the offshore location compared to near Tiputa Channel, supporting the hypothesis that warming water affects chlorophyll-a offshore and close to the coast differently.

While IME increased with increasing SST, IME decreased with increasing PAR (**Figure 3**). High light levels driving reduced chlorophyll-a biomass has been documented in other studies (Flombaum et al., 2013; Jyothibabu et al., 2018). High levels of PAR can cause photoinhibition, which has been observed in *Prochlorococcus* with cell abundance reduced 31% off-peak in a global study (Flombaum et al., 2013). In contrast, cloud cover in the Bay of Bengal causing lower levels of PAR was found to increase chlorophyll-a (Jyothibabu et al., 2018). While sunlight is crucial for photosynthesis of phytoplankton, PAR may reduce surface chlorophyll-a concentration by causing photoinhibition both near and offshore of Rangiroa Atoll, hence reducing the magnitude of IME.

Other Mechanisms Contributing to IME

The total statistical model explains 18% of the variation in Δchl and SST and PAR explain 8% of the variation in Δchl. Therefore, 44% (i.e., 8%/18%) of the total variation explained by the model can be attributed to effects of SST and PAR. 5.8% of variation in Δchl was explained by wind effects (magnitude and direction). However, 82% of the variation in Δchl remains unexplained by the model, suggesting that a combination of biophysical drivers shape IME at Rangiroa. Autochthonous nutrient sources in coral reef ecosystems present one primary driver for increased phytoplankton biomass at island and atoll ecosystems. Processes including nitrogen fixation, regeneration through decomposition of primary producers or from sediment deposition, and recycling from other biota increase the availability of essential limiting nutrients in the water column (Suzuki and Casareto, 2011; Gove et al., 2016). Benthic nitrogen fixation was found to account for 24.4% of benthic primary production requirements at neighboring Tikehau Atoll Lagoon (Charpy-Roubaud et al., 1990, 2001). Further, animal waste products derived from sea birds, reef fish, and marine invertebrates have also been shown to enhance nutrient concentrations in coral reef ecosystems (Williams and Carpenter, 1988; McCauley et al., 2012; Burkepile et al., 2013). Human activities can increase nearshore nutrient concentrations through runoff from urban development and agricultural land use or wastewater (Smith et al., 1999), and population status has been shows to be a significant driver for IME in other studies (Gove et al., 2016). While Rangiroa Atoll is populated (2709 people), it has a flat terrain and lacks rivers, hence the amount of terrigenous material exported via run-off is expected to be limited.

Physical processes such as water residence time and incoming light energy affect biogeochemical processes within coral reefs and can cause variations in total reef-derived nutrients available to phytoplankton (Atkinson, 2011; Suzuki and Casareto, 2011). Wave- and tidal-driven flushing may export nutrient enriched water from lagoons to surrounding waters fueling enhanced nearshore phytoplankton biomass (Gove et al., 2016). Even though statistical analysis did not find wave forcing to be a significant driver of IME ($p > 0.05$) in the present study, wave forcing has been shown in other studies to force atoll flushing, advecting detritus, and other sources of nutrients generated via coral reef ecosystem processes (Callaghan et al., 2006). Further, bathymetric influences on ocean currents can force vertical transport of subsurface nutrient-rich waters that fuel nearshore productivity: divergence of flow around steep island/atoll systems has been documented to cause upwelling of deeper nutrient-rich water near coasts (Caldeira et al., 2002; Spall and Pedlosky, 2013; Gove et al., 2016). Internal waves breaking due to abrupt changes in topography can to play a role in the vertical transport of particles and thus fuel IME (Leichter et al., 2012; Gove et al., 2016; Zhao, 2018). Rangiroa Atoll has been documented to generate internal tides, as a result of tide-bottom interactions (Zhao, 2018). Recent satellite results clearly show that internal tides radiate from Rangiroa and other atolls (Figure 13 in Zhao, 2018). Internal tides may cause pulses of nutrient-rich deep water to be advected up coastal slopes and fuel primary production that enhances IME.

Connecting Satellite Data to *in situ* Measurements

The *in situ* sensors measured warmer, fresher, less transparent water exiting the atoll at each ebb tide (**Figure 6**). This suggests that Rangiroa lagoon provides a source of particulates, chlorophyll-a and likely nutrients into the surrounding oligotrophic ocean. As described previously, we suggest that

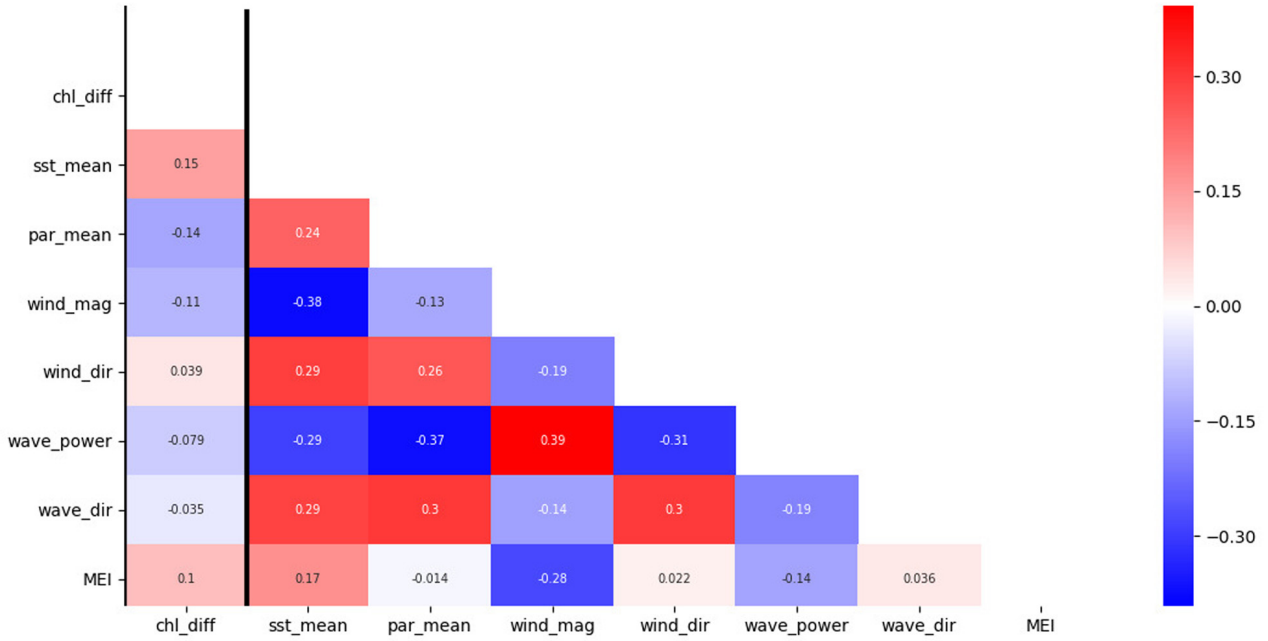

FIGURE 8 | Correlation coefficient (*r*-value) heatmap from data between January 2003 to February 2019. The response variable (chl_diff) is the chlorophyll-a data differences between near Tiputa Channel and offshore. Data are 8-day averages with no lag between variables. The predictor variables are: sea surface temperature (SST) (sst_mean), photosynthetically available radiation (PAR) (par_mean), wind magnitude (wind_mag), wind direction (wind_dir), wave power (wave_power), wave direction (wave_dir), and the multivariate ENSO index (MEI). Colors indicate the correlation coefficient (*r*-value). Red indicates a positive relationship between variables. Blue indicates a negative relationship between variables. The strength of color indicates the strength of the relationship.

benthic processes increasing available nutrients in the lagoon. Water residence time has been found to cause nutrients and organic matter to be recycled multiple times and increase biomass (Chevalier et al., 2017). Rangiroa's long residence time (estimated between 130 and 155 days (Andréfouët et al., 2001b; Pagès and Andréfouët, 2001) could allow nutrients and organic matter to be recycled several times by biota before being exported toward the open ocean. Charpy et al. (1997) found that phytoplankton biomass inside the lagoon was inversely related to the water exchanged between the lagoon and ocean. In contrast, rapid flushing leading to short residence times can inhibit the recycling of nutrients that fuel primary production (Ferrier-Pagès and Furla, 2001). Hence warmer, particulate and likely nutrient enriched water are advected into the oligotrophic waters surrounding Rangiroa, where it fuels phytoplankton production (Kirk, 2011). Over the 5-day span, 18–22 April 2014, 48 mm of precipitation fell on the far west of the lagoon. Lower rainfall amounts were recorded over the remainder of the atoll ranging from 12 mm in the far east upward to 48 mm in the far west. Large fluctuations in daily rainfall (between 0 and 360 mm) observed during the study period did result in a strong salinity signal in our measurements (**Figure 6C**). Instead, fluctuations in salinity were strongly correlated with the tidal cycle (**Figure 6C**). Lower salinity of outgoing lagoon water compared to incoming ocean water can likely be attributed to submarine groundwater discharge (SGD) originating from an atoll fresh water lens. Atoll fresh water lenses have been described to fill during the rainy season (November–April) and discharge freshwater into lagoon and surrounding oceanic water via processes such as SGD (Rougerie et al., 2004). SGD can be enriched in nutrients and may play a significant role in nutrient cycling enriching primary productivity in the coastal ocean (Caroline and Van Cappellen, 2004). Water exchange calculations show that 2.9 times more water volume was exiting than entering Rangiroa Atoll through Tiputa Channel indicating that a large amount of water exchange can be attributed primarily to wave forcing of water over the fringing reef. In a study examining permeability of various atoll rims, Rangiroa was found to have ∼22% of the perimeter open to exchange with the ocean (Andréfouët et al., 2001a). The porous rim allows both predominant southern and northern swells to add water to the lagoon. Other atolls to the east and west block or alter waves from those directions (Andréfouët et al., 2012). A comparison of horizontal current at mooring B to wave power during the deployment period, associated higher wave power with a faster current flow out of Rangiroa Atoll (r^2 values of 0.04). This relationship is supported by Pagès and Andréfouët (2001), who found that net outflow of Tiputa Channel increases with wave heights above 1.4 m.

Future Implications

Climate change has many effects on our oceans including warming sea surface temperatures, sea level rise, and acidification (Goeldner-Gianella et al., 2019), as well as increasing frequencies and intensity of El Niño events (Wang et al., 2019). These changes are likely impacting IME at Rangiroa Atoll, now and will in the

future. Sea level rise threatens to change Rangiroa from a semi-enclosed atoll to a more open atoll, through both erosion and by submerging the southern fringing reef. Open atolls allow lagoon water to be flushed more quickly resulting in shorter residence times and water with properties more similar to the surrounding ocean (Ferrier-Pagès and Furla, 2001). Further, ocean warming and acidification are likely to limit coral growth, prohibiting vertical atoll growth via coral as sea level rises and suppressing an important nutrient source (Goeldner-Gianella et al., 2019). In a study by Andréfouët et al. (2001b), biomass and atoll residence time were found to be linearly related for large Tuamotu atolls, a more open atoll would have a reduced residence time leading to reduced biomass contribution to the coastal ocean and a reduction to IME. Moreover, atmospheric and ocean warming are affecting wind and wave patterns, which may alter atoll reef structure and could affect water residence time (Andréfouët et al., 2001a; Duvat et al., 2017; Goeldner-Gianella et al., 2019).

CONCLUSION

We investigated the occurrence of IME at Rangiroa Atoll and its relationship to physical forcing by analyzing satellite data and *in situ* data. Comparison of chlorophyll-a concentration near Tiputa Channel with offshore resulted in a phytoplankton enhancement nearshore as high as 130% and an average enhancement nearshore of 16% during the 16-year record. Our statistical model examining physical drivers showed the magnitude of IME to be significantly enhanced by higher sea surface temperature (SST) and lower photosynthetically active radiation (PAR). *In situ* measurements and historical studies indicate that the lagoon likely presents a source of increased nutrients for phytoplankton production compared to the oligotrophic ocean that surrounds it. A combination of biological processes and long water residence time in the lagoon causes particulate-rich and likely nutrient-rich water to be advected to surrounding coastal waters by tidal and wave forcing. A biological oasis in the vast oligotrophic Pacific could not exist without increased phytoplankton biomass in Rangiroa's coastal waters. Tourism and pearl farming are the main sources of income in the Tuamotu Archipelago (Chevalier et al., 2017), making the biologically productive lagoon Rangiroa's primary resource. Understanding long term trends of chlorophyll enhancement in Rangiroa as well as the dual impact of physical and biological processes driving enhanced IME has important implications for the marine ecosystem and economy of the entire Tuamotu Archipelago now and in the future.

DATA AVAILABILITY STATEMENT

The raw data supporting the conclusions of this article will be made available by the authors, without undue reservation.

AUTHOR CONTRIBUTIONS

CV contributed with satellite data analysis, observational data analysis, and writing the manuscript. PM conducted the statistical analysis and contributed to writing the manuscript. JG contributed in the formulation of ideas, planning of field study, participation in field study, and writing the manuscript. AN conducted the statistical analysis and contributed to writing the manuscript. MM contributed in the formulation of ideas, planning of field study, and writing the manuscript. All authors contributed to the article and approved the submitted version.

FUNDING

U.S. Veterans Affairs paid CV's tuition through the Post-9/11 GI Bill. This is an earned benefit granted by law to people who served in the US active duty military for at least 90 days.

ACKNOWLEDGMENTS

This work was the basis of the Master thesis of CV. We thank Dr. Brian Powell and Dr. Jeff Drazen for serving on CV's committee and reviewing her thesis. We thank Kamaki Worthington and Brian Zgliczynski for diving support in Rangiroa, Conor Jerolmon for early analysis of the *in situ* CTD data, and Gordon Walker for providing significant logistical support for the field program. Finally, we thank John Hillsman and Howard McPherson for their guidance.

REFERENCES

Abbott, M. L. (2017). *Using Statistics in the Social and Health Sciences with SPSS §and Excel §* . Hoboken, NJ: John Wiley & Sons, Inc.

Andrade, I., Sangrà, P., Hormazabal, S., and Correa-Ramirez, M. (2014). Island mass effect in the Juan Fernández Archipelago (33°S), Southeastern Pacific. *Deep Sea Res. Part I Oceanogr. Res. Pap.* 84, 86–99. doi: 10.1016/j.dsr.2013.10.009

Andréfouët, S., Claereboudt, P., Matsakis, J., Pagès, J., and Dufour, P. (2001a). Typology of atoll rims in Tuamotu Archipelago (French Polynesia) at landscape scale using SPOT HRV images. *Int. J. Remote Sens.* 22, 987–1004. doi: 10.1080/014311601300074522

Andréfouët, S., Pagès, J., and Tartinville, B. (2001b). Water renewal time for classification of atoll lagoons in the Tuamotu Archipelago (French Polynesia). *Coral Reefs.* 20, 399–408. doi: 10.1007/s00338-001-0190-9

Andréfouët, S., Ardhuin, F., Queffeulou, P., and Le Gendre, R. (2012). Island shadow effects and the wave climate of the Western Tuamotu Archipelago (French Polynesia) inferred from altimetry and numerical model data. *Mar. Poll. Bull.* 65, 415–424. doi: 10.1016/j.marpolbul.2012.05.042

Atkinson, M. (2011). "An ecosystem in transition," in *Coral Reefs: An Ecosystem in Transition*, eds Z. Dubinsky and N. Stambler (New York, NY: Springer), 199–206.

Barton, K. (2009). *Mu-MIn: Multi-Model Inference. R Package Version 0.12.2/r18*. Available online at: http://R-Forge.R-project.org/projects/mumin/ (accessed May 8, 2020).

Breheny, P., and Burchett, W. (2017). Visualization of regression models using visreg. *R J.* 9, 56–71. doi: 10.32614/rj-2017-046

Burkepile, D. E., Allgeier, J. E., Shantz, A. A., Pritchard, C. E., Lemoine, N. P., Bhatti, L. H., et al. (2013). Nutrient supply from fishes facilitates macroalgae and suppresses corals in a Caribbean coral reef ecosystem. *Sci. Rep.* 3:1493.

Caldeira, R. M. A., Groom, S., Miller, P., Pilgrim, D., and Nezlin, N. P. (2002). Sea-surface signatures of the island mass effect phenomena around Madeira Island, Northeast Atlantic. *Remote Sens. Environ.* 80, 336–360. doi: 10.1016/s0034-4257(01)00316-9

Callaghan, D. P., Nielsen, P., Cartwright, N., Gourlay, M. R., and Baldock, T. E. (2006). Atoll lagoon flushing forced by waves. *Coast. Eng.* 53, 691–704. doi: 10.1016/j.coastaleng.2006.02.006

Caroline, P., and Van Cappellen, S. P. (2004). Nutrient inputs to the coastal ocean through submarine groundwater discharge: controls and potential impact. *J. Hydrol.* 295, 64–86. doi: 10.1016/j.jhydrol.2004.02.018

Carter, G. S., Gregg, M. C., and Merrifield, M. A. (2006). Flow and mixing around a small seamount on kaena ridge. Hawaii. *J. Phys. Oceanogr.* 36, 1036–1052. doi: 10.1175/jpo2924.1

Charpy, L. (1996). Phytoplankton biomass and production in two tuamotu atoll lagoons (French polynesia). *Mar. Ecol. Progr. Ser.* 145, 133–142. doi: 10.3354/meps145133

Charpy, L., Dufour, P., and Garcia, N. (1997). Particulate organic matter in sixteen Tuamotu atoll lagoons (French Polynesia). *Mar. Ecol. Prog. Ser.* 151, 55–65. doi: 10.3354/meps151055

Charpy-Roubaud, C., Charpy, L., and Cremoux, J. L. (1990). Nutrient budget of the lagoonal waters in an open central South Pacific atoll (Tikehau, Tuamotu, French Polynesia). *Mar. Biol.* 107, 67–73. doi: 10.1007/bf01313243

Charpy-Roubaud, C., Charpy, L., and Larkum, A. W. D. (2001). Atmospheric dinitrogen fixation by benthic communities of Tikehau Lagoon (Tuamotu Archipelago, French Polynesia) and its contribution to benthic primary production. *Mar. Biol.* 139, 991–998. doi: 10.1007/s002270100636

Chevalier, C., Devenon, J. L., Pagano, M., Rougier, G., Blanchot, J., and Arfi, R. (2017). The atypical hydrodynamics of the Mayotte Lagoon (Indian Ocean): effects on water age and potential impact on plankton productivity. *Estuar.Coast. Shelf Sci.* 196, 182–197. doi: 10.1016/j.ecss.2017.06.027

Dandonneau, Y., and Charpy, L. (1985). An empirical approach to the island mass effect in the south tropical Pacific based on sea surface chlorophyll concentrations. *Deep Sea Res. Part I Oceanogr. Res. Pap.* 32, 707–721. doi: 10.1016/0198-0149(85)90074-3

Delesalle, B., and Sournia, A. (1991). Residence time of water and phytoplankton biomass in coral reef lagoons. *Cont. Shelf Res.* 12, 939–949. doi: 10.1016/0278-4343(92)90053-m

Doty, M., and Oguri, M. S. (1956). The Island mass effect. *ICES J. Mar. Sci.* 22, 33–37.

Duarte, C., and Cebrian, J. (1996). The fate of marine autotrophic production. *Limnol. Oceanogr.* 41, 1758–1766. doi: 10.4319/lo.1996.41.8.1758

Dunstan, P. K., Foster, S. D., King, E., Risbey, J., O'Kane, T. J., Monselesan, D., et al. (2018). Global patterns of change and variation in sea surface temperature and chlorophyll a. *Sci. Rep.* 8:14624.

Duvat, V. K. E., Salvat, B., and Salmon, C. (2017). Drivers of shoreline change in atoll reef islands of the Tuamotu Archipelago, French Polynesia. *Glob. Planet. Change.* 158, 134–154. doi: 10.1016/j.gloplacha.2017.09.016

Ferrier-Pagès, C., and Furla, P. (2001). Pico- and nanoplankton biomass and production in the two largest atoll lagoons of French Polynesia. *Mar. Ecol. Prog. Ser.* 211, 63–76. doi: 10.3354/meps211063

Flombaum, P., Gallegos, J. L., Gordillo, R. A., Rincón, J., Zabala, L. L., and Jiao, N. (2013). Present and future global distributions of the marine *Cyanobacteria Prochlorococcus* and *Synechococcus*. *PNAS* 110, 9824–9829.

Gilmartin, M., and Revelante, N. (1974). The 'island mass' effect on the phytoplankton and primary production of the Hawaiian Islands. *J. Exp. Mar. Biol. Ecol.* 16, 181–204. doi: 10.1016/0022-0981(74)90019-7

Goeldner-Gianella, L., Grancher, D., Magnan, A. K., de Belizal, E., and Duvat, V. K. E. (2019). The perception of climate-related coastal risks and environmental changes on the Rangiroa and Tikehau atolls, French Polynesia: the role of sensitive and intellectual drivers. *Ocean. Coast. Manag.* 172, 14–29. doi: 10.1016/j.ocecoaman.2019.01.018

Gove, J. M., McManus, M. A., Neuheimer, A. B., Polovina, J. J., Drazen, J. C., Smith, C. R., et al. (2016). Near-island biological hotspots in barren ocean basins. *Nat. Commu.* 7, 1–8.

Gove, J. M., Williams, G. J., McManus, M. A., Heron, S. F., Sandin, S. A., Vetter, O. J., et al. (2013). Quantifying climatological ranges and anomalies for pacific coral reef ecosystems. *PloS One* 8: e61974. doi: 10.1371/journal.pone.0061974

Grolemund, G., and Wickham, H. (2011). Dates and times made easy with lubridate. *J. Stat. Softw.* 40, 1–25.

Hamner, W. M., and Hauri, I. R. (1981). Effects of island mass: water flow and plankton pattern around a reef in the Great Barrier Reef lagoon, Australia1. *Limnol. Oceanogr.* 26, 1084–1102. doi: 10.4319/lo.1981.26.6.1084

Heywood, K. J., Barton, E. D., and Simpson, J. H. (1990). The effects of flow disturbance by an oceanic island. *J. Mar. Res.* 48, 55–73. doi: 10.1357/002224090784984623

Institute of Statistics of French Polynesia (2017). *French Polynesia Population and Housing Census 2017*. Available online at: http://ghdx.healthdata.org/record/french-polynesia-population-and-housing-census-2017 (accessed October 27, 2020).

James, A. K., Washburn, L., Gotschalk, C., Maritorena, S., Alldredge, A., Nelson, C. E., et al. (2020). An Island mass effect resolved near Mo'orea, French Polynesia. *Front. Mar. Sci.* 7:16. doi: 10.3389/fmars.2020.00016

Jyothibabu, R., Arunpandi, N., Jagadeesan, L., Karnan, C., Lallu, K. R., and Vinayachandran, P. N. (2018). Response of phytoplankton to heavy cloud cover and turbidity in the northern Bay of Bengal. *Sci. Rep*. 8: 11282.

Kirk, J. T. O. (2011). *Light and Photosynthesis in Aquatic Ecosystems*. New York, NY: Cambridge University Press.

Kumar, S., Kruger, J., Begg, Z., Handerson, E., and Alvis, E. (2013). *Multibeam Bathymetry Survey Rangiroa, French Polynesia*. Suva: SPC Applied Geoscience and Technology Division (SOPAC).

Leichter, J. J., Stokes, M. D., Hench, J. L., Witting, W., and Washburn, L. (2012). The island-scale internal wave climate of Moorea, French Polynesia. *J. Geophys. Res. Oceans* 117, 1–16. doi: 10.5479/si.00775630.309.1

Lo-Yat, A., Simpson, S. D., Meekan, M., Lecchini, D., Martinez, E., and Galzin, R. (2011). Extreme climatic events reduce ocean productivity and larval supply in a tropical reef ecosystem. *Glob. Change Biol.* 17, 1695–1702. doi: 10.1111/j.1365-2486.2010.02355.x

Martinez, E., and Maamaatuaiahutapu, K. (2004). Island mass effect in the Marquesas Islands: time variation. *Geophys. Res. Lett.* 31: L18307.

McCauley, D. J., DeSalles, P. A., Young, H. S., Dunbar, R. B., Dirzo, R., Mills, M. M., et al. (2012). From wing to wing: the persistence of long ecological interaction chains in less-disturbed ecosystems. *Sci. Rep.* 2:409.

McPhaden, M. J. (2012). A 21st century shift in the relationship between ENSO SST and warm water volume anomalies. *Geophys. Res. Let.* 39:L09706. doi: 10.1029/2012GL051826

Moehlenkamp, P., Beebe, C. K., McManus, M. A., Kawelo, A. H., Kotubetey, K., Lopez-Guzman, M., et al. (2019). Ku Hou Kuapa: cultural restoration improves water budget and water quality dynamics in He'eia Fishpond. *Sustainability* 11:161. doi: 10.3390/su11010161

Nelson, C. E., Alldredge, A. L., McCliment, E. A., Amaral-Zettler, L. A., and Carlson, C. A. (2011). Depleted dissolved organic carbon and distinct bacterial communities in the water column of a rapid-flushing coral reef ecosystem. *ISME J.* 5, 1374–1387. doi: 10.1038/ismej.2011.12

Pagès, J., and Andréfouët, S. (2001). A reconnaissance approach for hydrology of atoll lagoons. *Coral Reefs* 20, 409–414. doi: 10.1007/s00338-001-0192-7

Palacios, D. M. (2002). Factors influencing the island-mass effect of the Galápagos Archipelago. *Geophys. Res. Lett.* 29, 1–4.

R Core Team (2018). *R: A Language and Environment for Statistical Computing*. Vienna: R Foundation for Statistical Computing.

Rougerie, F., Fichez, R., and Déjardin, R. (2004). "Chapter 15 geomorphology and hydrogeology of selected Islands of French Polynesia: tikehau (Atoll) and tahiti (Barrier Reef)," in *Developments in Sedimentology*, Vol. 54, eds M. Rebesco and A. Camerlenghi Vol (Amsterdam: Elsevier Science & Technology). doi: 10.5479/si.00775630.415-part_iii.1

Sauzède, R., Martinez, E., de Fommervault, O. P., Poteau, A., Mignot, A., Maes, C., et al. (2018). Seasonal dynamics and disturbance of phytoplankton biomass in the wake of Tahiti as observed by biogeochemical-argo floats. *Biogeosci. Discuss.* 1–35. doi: 10.5194/bg-2017-541

Signorini, S. R., McClain, C. R., and Dandonneau, Y. (1999). Mixing and phytoplankton bloom in the wake of the Marquesas Islands. *Geophys. Res. Lett.* 26, 3121–3124. doi: 10.1029/1999gl010470

Smith, V. H., Tilman, G. D., and Nekola, J. C. (1999). Eutrophication: impacts of excess nutrient inputs on freshwater, marine, and terrestrial ecosystems. *Environ. Pol.* 100, 179–196. doi: 10.1016/s0269-7491(99)00091-3

Spall, M. A., and Pedlosky, J. (2013). Interaction of ekman layers and Islands. *J. Phys. Oceanogr.* 43, 1028–1041. doi: 10.1175/jpo-d-12-0159.1

Spiegel, M. R., and Stephens, L. J. (2011). *Schaums Outlines Statistics*. New York, NY: McGraw-Hill, 348–350.

Suzuki, Y., and Casareto, B. E. (2011). "The role of dissolved organic nitrogen (DON) in coral biology and reef ecology," in *Coral Reefs: An Ecosystem in Transition*, eds Z. Dubinsky and N. Stambler (Berlin: Springer).

Uz, S. S., Busalacchib, A. J., Smith, T. M., Evans, M. N., Brown, C. W., and Hackert, E. C. (2017). Interannual and decadal variability in tropical Pacific chlorophyll from a statistical reconstruction: 1958-2008. *J. Clim.* 30, 7293–7315. doi: 10.1175/jcli-d-16-0202.1

Wang, B., Luo, X., Yang, Y. M., Sun, W., Cane, M. A., Cai, W., et al. (2019). Historical change of El Niño properties sheds light on future changes of extreme El Niño. *PNAS* 116, 22512–22517.

Wickham, H. (2007). Reshaping data with the reshape package. *J. Stat. Softw.* 21, 1–20.

Wickham, H. (2016). *ggplot2: Elegant Graphics for Data Analysis*. New York, NY: Springer-Verlag.

Williams, S. L., and Carpenter, R. C. (1988). Nitrogen-limited primary productivity ofcoral reef algal turfs: potential contribution of ammonium excreted by *Diadema antillarum*. *Mar. Ecol. Prog. Ser.* 47, 145–152. doi: 10.3354/meps047145

Wood, S. N. (2011). Fast stable restricted maximum likelihood and marginal likelihood estimation of semiparametric generalized linear models. *J. R. Stat. Soc. Series B Stat. Methodol.* 73, 3–36. doi: 10.1111/j.1467-9868.2010.00749.x

Wyatt, A. S. J., Lowe, R. J., Humphries, S., and Waite, A. M. (2010). Particulate nutrient fluxes over a fringing coral reef: relevant scales of phytoplankton production and mechanisms of supply. *Mar. Ecol. Prog. Ser.* 405, 113–130. doi: 10.3354/meps08508

Wyatt, A. S. J., Falter, J., Lowe, R., Humphries, S., and Waite, A. (2012). Oceanographic forcing of nutrient uptake and release over a fringing coral reef. *Limnol. Oceanogr.* 57, 401–419. doi: 10.4319/lo.2012.57.2.0401

Zhao, Z. (2018). The global mode-2 M2 internal tide. *J. Geophys. Res.* 123, 7725–7746. doi: 10.1029/2018JC014475

Conflict of Interest: The authors declare that the research was conducted in the absence of any commercial or financial relationships that could be construed as a potential conflict of interest.

frontiers in Marine Science

ORIGINAL RESEARCH
published: 18 February 2021
doi: 10.3389/fmars.2021.624392

Asymmetric Ocean Response to Atmospheric Forcing in an Island Wake: A 35-Year High-Resolution Study

José M. R. Alves[1,2], Ricardo Tomé[2], Rui M. A. Caldeira[1,2] and Pedro M. A. Miranda[2]*

[1] Agência Regional Para o Desenvolvimento da Investigação Tecnologia e Inovação, Oceanic Observatory of Madeira, Funchal, Portugal, [2] Instituto Dom Luiz, Faculdade de Ciências, Universidade de Lisboa, Lisbon, Portugal

OPEN ACCESS

Edited by:
Juan Jose Munoz-Perez, University of Cádiz, Spain

Reviewed by:
Alejandro Orfila, Consejo Superior de Investigaciones Científicas (CSIC), Spain
Ivica Vilibic, Institute of Oceanography and Fisheries (IZOR), Croatia

***Correspondence:**
José M. R. Alves
jose.alves@oom.arditi.pt

Specialty section:
This article was submitted to Coastal Ocean Processes, a section of the journal Frontiers in Marine Science

Received: *31 October 2020*
Accepted: *13 January 2021*
Published: *18 February 2021*

Citation:
Alves JMR, Tomé R, Caldeira RMA and Miranda PMA (2021) Asymmetric Ocean Response to Atmospheric Forcing in an Island Wake: A 35-Year High-Resolution Study. Front. Mar. Sci. 8:624392. doi: 10.3389/fmars.2021.624392

The present study assesses the thermal variability of the regional ocean around Madeira Island, in intraseasonal and interdecadal time scales, using a 35-year (1983–2017), 3-km horizontal resolution ocean simulation forced by a co-located atmospheric simulation, with SODA and ERA5 boundary and initial conditions, respectively. Atmosphere–ocean interactions in this region are found to be driven by the variability of two quasi-permanent tip-jets, located at the island west and east tips, especially during the summer months. The ocean response is found to be larger in the regions of higher jets speed variability, but its thermal response is highly asymmetrical. On the interdecadal time scale, a significant intensification of both jets during the analyzed period is more prominent in the east tip, but the thermal signature is mostly associated with a much reduced sea surface temperature trend near the west tip.

Keywords: tip-jets, vorticity, vertical current, mixed layer depth (MLD), numerical modeling

INTRODUCTION

Isolated islands with steep orography and bathymetry constitute major obstacles to the flow, significantly modifying the regional atmospheric and ocean circulations, with an impact that may extend downstream for hundreds or even thousands of kilometers (Xie et al., 2001). For good reason, the structure and dynamics of these island wakes have been the topic of research, focused on its atmospheric (Etling, 1989; Smith et al., 1997, Grubišic et al., 2015) or ocean components (Caldeira and Tomé, 2013; Caldeira et al., 2014, Cardoso et al., 2020), with clear indications of a modified environment in the vicinity of the islands, leading to the establishment of special ecosystems (Narciso et al., 2019). Interactions between the landforms and both the atmosphere and ocean flows, and between the atmosphere and ocean, modify surface fluxes of energy and momentum, conditioning the boundary layers of both media and leading to feedbacks that may reinforce the wakes.

Alves et al. (2020) looked at the regional atmosphere and ocean circulations around Madeira Island during the 2017 summer, using a high-resolution (1 km) fully coupled atmosphere–ocean simulation with the Coupled Ocean-Atmosphere-Wave–Sediment Transport (COAWST) model (Warner et al., 2010), validated against remote sensing sea surface temperature (SST) and wind observations, besides *in situ* observations in coastal weather stations and in an oceanographic field experiment. That study showed a remarkably steady summer flow during that year, with northeasterly trade winds impinging on the island and leading to the establishment of two low-level jets in the wake, emerging from the east and west tips of the island. Alves et al. (2020) argued that those tip-jets are similar to those simulated by Ólafsson and Bougeault (1997) and observed in Greenland (Doyle and Shapiro, 1999), with a much stronger constancy of the flow compensating for its reduced wind speed and that the variability of those jets is a dominant factor in the dynamics of the Madeira wake.

Motivated by Alves et al. (2020) and taking into account their conclusion that the ocean to atmosphere feedback has little impact in the regional atmospheric circulation, Miranda et al. (2021) analyzed results from an extended 40-year atmosphere-only simulation with Weather-Research and Forecasting (WRF), forced by ERA5 reanalysis (1979–2018). That analysis, entirely focused in the summer (JJA) fields, identified the presence of a strong intraseasonal oscillation at the multiweek timescale in the intensity of the tip-jets, correlated with a corresponding oscillation in the atmospheric planetary boundary layer (PBL) height. Furthermore, Miranda et al. (2021) found that both the tip-jet intensity and the regional atmospheric boundary layer height presented significant decadal variability, with recent trends towards a lower PBL height and a faster jet, confirmed by local wind observations at Madeira Airport.

The present study is a follow-up of Miranda et al. (2021), using its low level atmospheric fields to force an ocean simulation with the Regional Oceanic Modeling System (ROMS) model at 3 km resolution, aiming to characterize the ocean temperature and circulation and to assess the decadal variability of the upper ocean. The paper is organized as follows: the setup of numerical simulations and its observational validation are assessed in *Experimental Setup*. Main tip-jets impact on ocean results are present in *Results*. *Discussion and Conclusions* includes a discussion of the ocean asymmetries results and some conclusions.

EXPERIMENTAL SETUP

Data and Numerical Models

The present study is based on the analysis of two numerical simulations: an atmospheric simulation performed by the WRF model forced by ERA5 reanalysis (Hersbach et al., 2020), and an ocean simulation, one-way forced by low level WRF fields, with the ROMS model. The 40-year WRF simulation is described in Miranda et al. (2021), although here the analysis is limited to the 35-year period (1983–2017) due to the time window of the available ocean reanalysis, later described, and the need for an extended spin-up of the ocean model. The one-way coupling from WRF to ROMS is performed by providing the ocean model with three-hourly low-level fields from WRF for wind, relative humidity, air temperature, net shortwave and longwave radiation, pressure, and precipitation, the surface fluxes being computed by ROMS bulk formula. Both simulations (WRF and ROMS) used colocated nested grids, with an inner grid at 3 km and an outer grid at 9 km resolutions, with two-way interaction. The inner domain encloses Madeira and two nearby small islands located to the NW and SW of the main island, Porto Santo and Desertas, respectively. The limits of both computational grids are depicted in **Figure 1A**.

The initial and boundary conditions of the ROMS ocean model were obtained from the Simple Ocean Data Assimilation (SODA v3.4.2) (Carton and Giese, 2008), a global reanalysis with a 0.25° spatial resolution (approximately 24 km, near Madeira), with data every 5 days. That reanalysis assimilated observed data from the World Ocean Database (WOD) and the International Comprehensive Ocean–Atmosphere Dataset (ICOADS). It is forced by the atmospheric ERA-Interim reanalysis (Dee et al., 2011), using the Coupled Ocean–Atmosphere Response Experiment (COARE4) bulk formula. It was recently shown that SODA-v3.4.2. is an accurate reanalysis, particularly near Madeira (Carton et al., 2019), and while an improved product is not available with the new higher-resolution ERA5 dataset, it constitutes the best compromise for the present study.

At the outer ROMS computational grid boundaries, radiation and nudging conditions were imposed for tracers (temperature and salinity) and the baroclinic current (Marchesiello et al., 2001), a Shecheptikin condition for the barotropic current (Mason et al., 2010), and a Chapman condition for free-surface height (Chapman, 1985). Vertical turbulent mixing was parameterized with the Generic Length Scale (GLS) scheme (Umlauf and Burchard, 2003), with a k–ε closure, where k is the turbulent kinetic energy and ε is the dissipation. ROMS used 40 sigma levels, with an increasing vertical resolution near the ocean surface. The sea floor bathymetric grid is based in a 30 arc-second grid spacing data, from the General Bathymetric Chart of the Oceans (GEBCO; Becker et al., 2009). Several passes of a smoothing filter guaranteed a bathymetry r-factor ($r = \nabla h/h$) below 0.2 (Haidvogel and Beckmann, 1999) to avoid pressure gradient errors associated with sigma coordinate calculations. A thorough description of the ROMS model is presented in Shchepetkin and McWilliams (2005, 2009).

Observational Validation

The accuracy of 10-m wind can be assessed from reprocessed Advanced SCATterometer (ASCAT) data, available at a 12.5-km swath grid (Verhoef et al., 2012). Here, we used data from the ascending passage (descending passage gives similar results); that in Madeira occurs between 21 and 23 h UTC and WRF data at 21 h UTC, for the longest available period coincident with the numerical simulation, from 2007 until 2017. After remapping the simulated variables to the satellite grid, the remote-detected values were used to compute the following statistical parameters: bias, time correlation, and normalized standard deviation. The

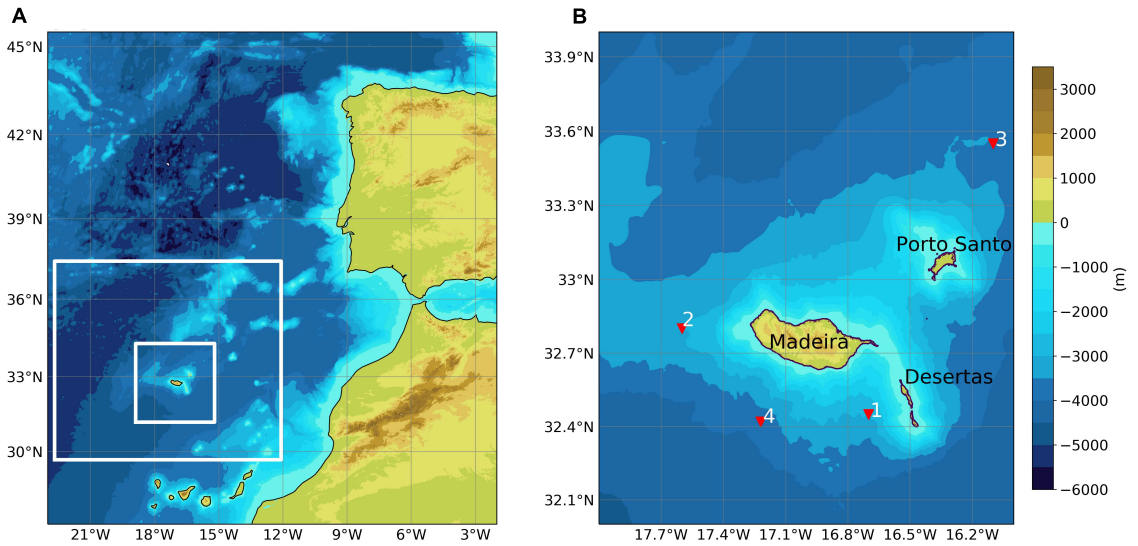

FIGURE 1 | Topography retrieved from Shuttle Radar Topography Mission (SRTM) and sea floor bathymetry near Madeira Island retrieved from General Bathymetric Chart of the Oceans (GEBCO). In panel **(A)**, white rectangles indicate geographical limits of the two domains used in Weather-Research and Forecasting (WRF) and Regional Oceanic Modeling System (ROMS): 9 km (outer) and 3 km resolution (inner), and in panel **(B)**, red triangles indicate locations where some analysis is done.

TABLE 1 | Wind speed statistical parameters, in four points shown in **Figure 1B**, for the 2007–2017 period: bias, Pearson correlation coefficient (*r*), normalized standard deviation (NSD).

Sampling point	Bias (m/s)	*r*	NSD
1	−0.19	0.88	1.11
2	−0.29	0.90	0.99
3	−0.39	0.90	0.94
4	−0.90	0.76	1.13

Model versus satellite data.

TABLE 2 | As in **Table 1** for sea surface temperature (SST) and for the 1983–2017 period.

Sampling point	Bias (K)	*r*	NSD
1	−0.14	0.97	1.04
2	−0.12	0.96	1.04
3	0.03	0.97	1.05
4	−0.22	0.96	1.05

statistical parameters show the high accuracy of the simulated surface wind (**Table 1**), at four locations near Madeira: points 1 and 2 are located near the maximum tip-jets mean wind speed, point 3 in an upstream region not affected by the island influence on surface wind, and point 4 in the wake (see **Figure 1B** for exact position of points). The computed biases vary between −0.19 and −0.90, indicating a very slight underestimation of wind by the model. The time-correlation values are high, varying between 0.90 and 0.76, with the worst value in the wake. The simulated wind speed variability is close to observations.

The simulated SST was compared with the dataset created by the European Space Agency (ESA) Climate Change Initiative/Copernicus Climate Change Service (CCI/C3S), with a 0.05° resolution, combining SST retrievals from the Advanced Very High-Resolution Radiometer (AVHRR) and the Along Track Scanning Radiometer (ATSR) series of satellite sensors. For a full description of the dataset, the reader is referred to Merchant et al. (2019). As for surface wind, the statistical parameters show the robustness of the simulated values (**Table 2**), with an absolute bias lower than 0.23 °C in the four points, a very high synchronization between model and satellite data revealed by time correlations between 0.96 and 0.97, and a realistic simulated variability noted by a ratio of standard deviations of 1.04 or 1.05. The robustness of the simulated SST is also revealed by the mean spatial SST bias and root mean square error (**Figure 2**) with values always lower than 0.3 and 0.8 °C around Madeira, respectively. In both parameters, the highest values are located near the west flank, coinciding with high SST variability and gradients (shown latter) that are not accurately captured by daily 0.05° resolution satellite SST.

RESULTS

Seasonal Variability of the Surface Wind

The presence of Madeira Island is especially clear in the perturbation it imposes to the wind. The seasonal mean wind around Madeira (**Figure 3**) displays a rather constant pattern, with northeasterly flow impinging the island throughout the year, leading to the establishment of two localized wind speed maxima near the east and west island tips. The upstream mean wind speed is stronger in winter (DJF) and weaker in summer (JJA). However, the tip-jets are most prominent in summer.

The establishment of the summer tip-jets was discussed in some detail by Miranda et al. (2021), and both its intraseasonal

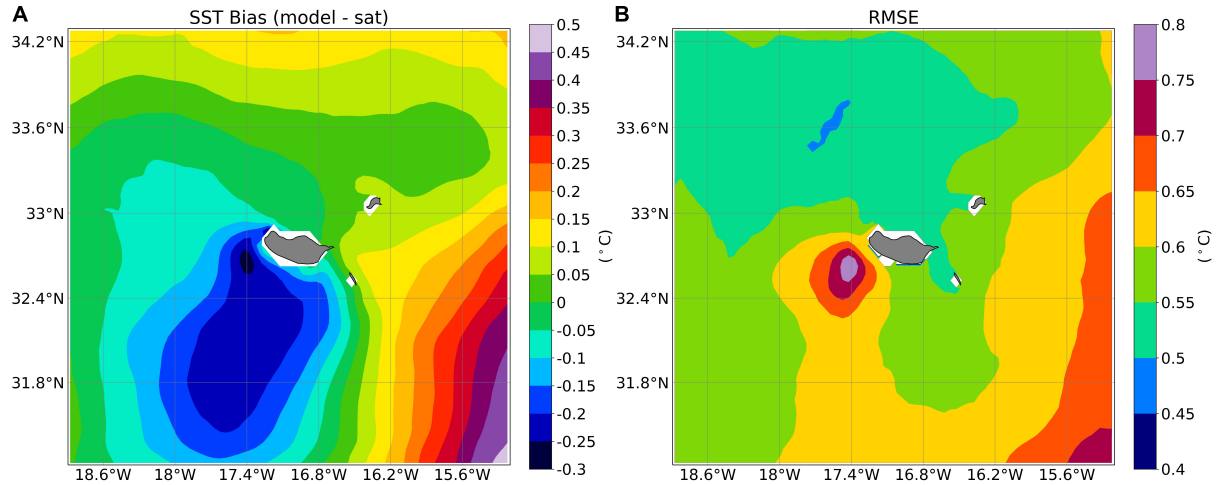

FIGURE 2 | Mean (1983–2017) **(A)** sea surface temperature (SST) bias (model—satellite) and **(B)** root mean square error (RMSE).

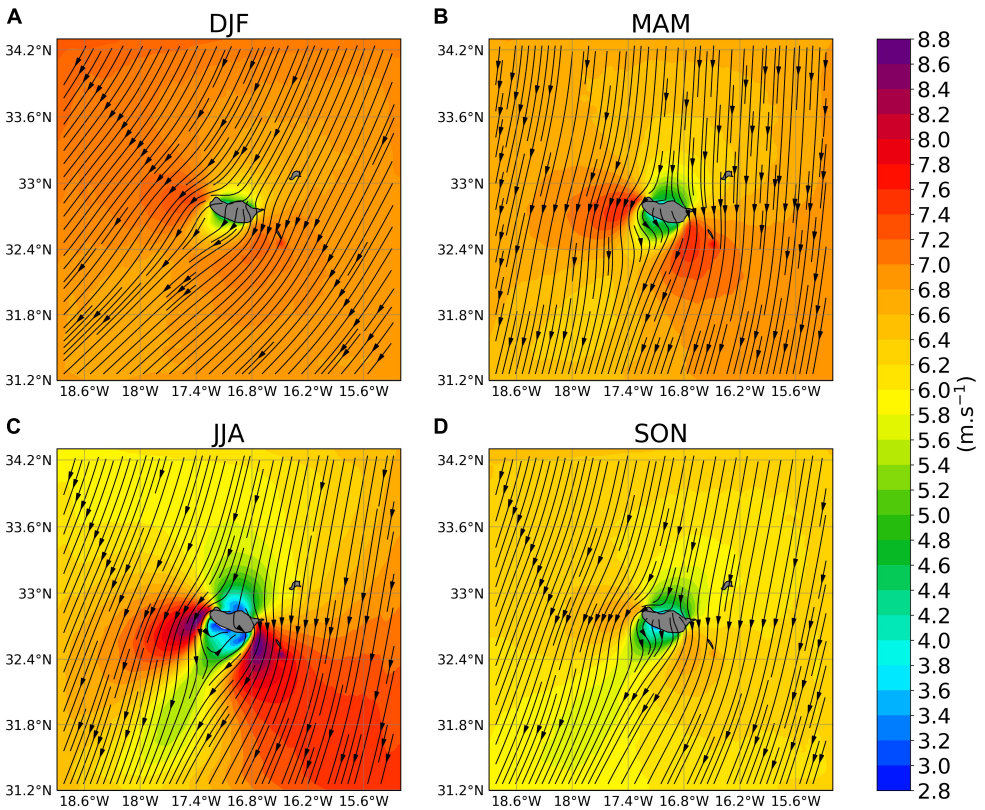

FIGURE 3 | Mean (1983–2017) seasonal [**(A)** DJF, **(B)** MAM, **(C)** JJA, and **(D)** SON] simulated surface (10 m) wind speed and associated streamlines computed with data every 3 h and every four grid cells (12 km), in the 3-km inner domain.

and decadal variability were found to be controlled by the regional PBL height, defined as the height of maximum stability in the low troposphere. **Figure 4** shows the seasonal mean potential temperature gradient in the north upstream sampling point (**Figure 1B**), indicating a much more stable and lower height PBL in summer, lowering from about 1,700 m in winter (DJF) to about 1,000 m in summer (JJA). The lower summer value is below the height of the main island plateau, implying the need for flow deflection around the island with streamline squeezing near the

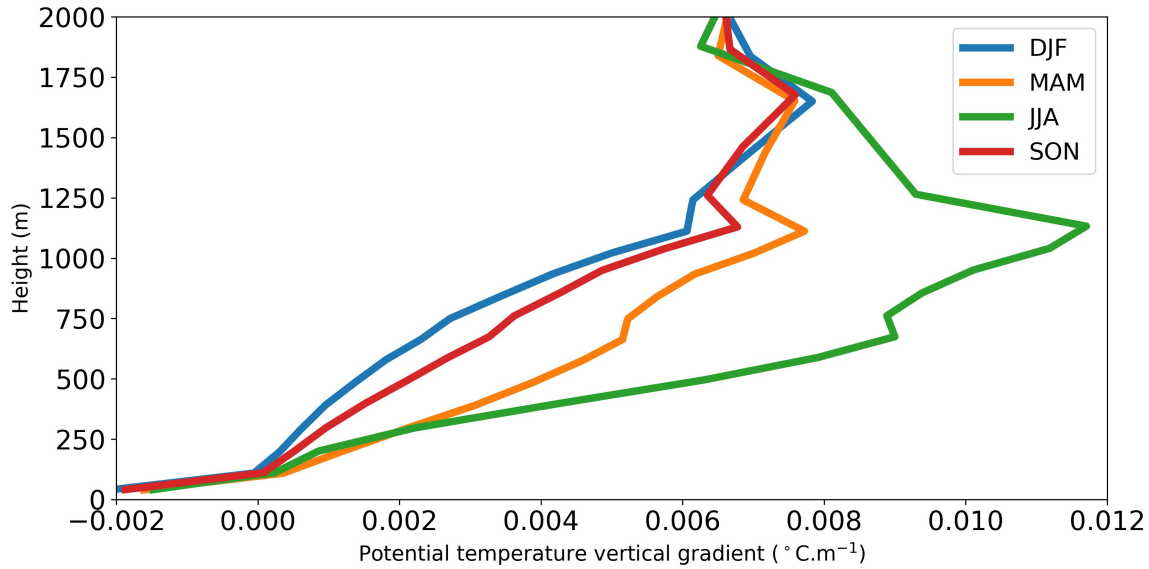

FIGURE 4 | Mean (1983–2017) seasonal potential temperature vertical gradient at point 3 (**Figure 1B**).

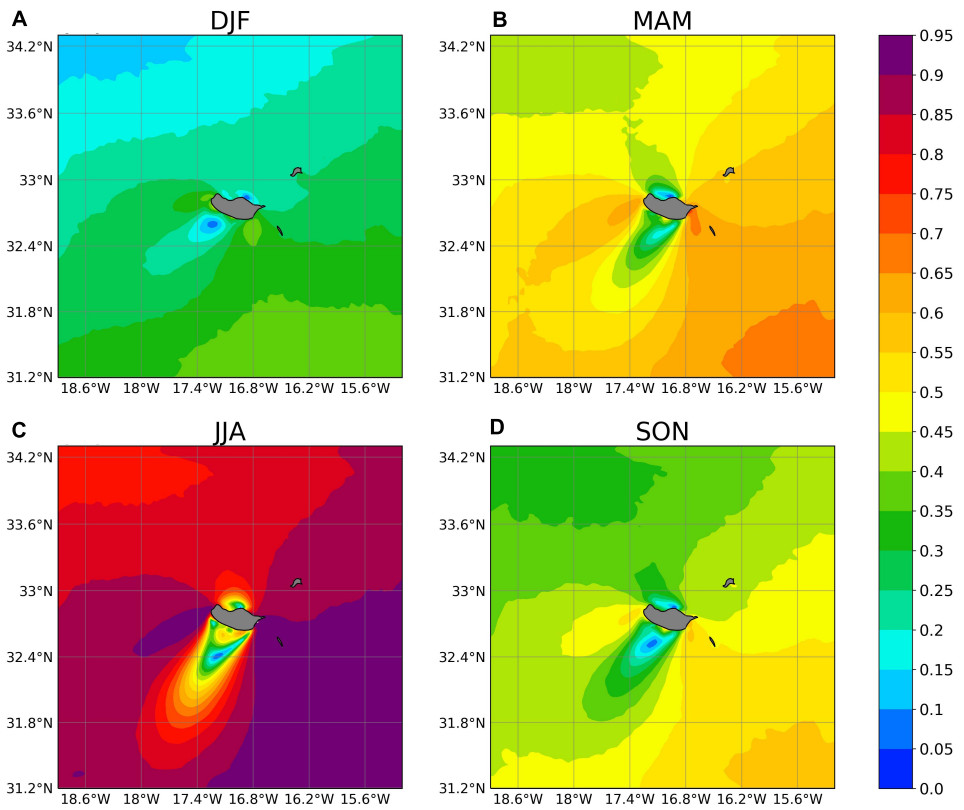

FIGURE 5 | Mean (1983–2017) [**(A)** DJF, **(B)** MAM, **(C)** JJA, **(D)** SON] seasonal wind speed directional constancy (computed following Eq. 1).

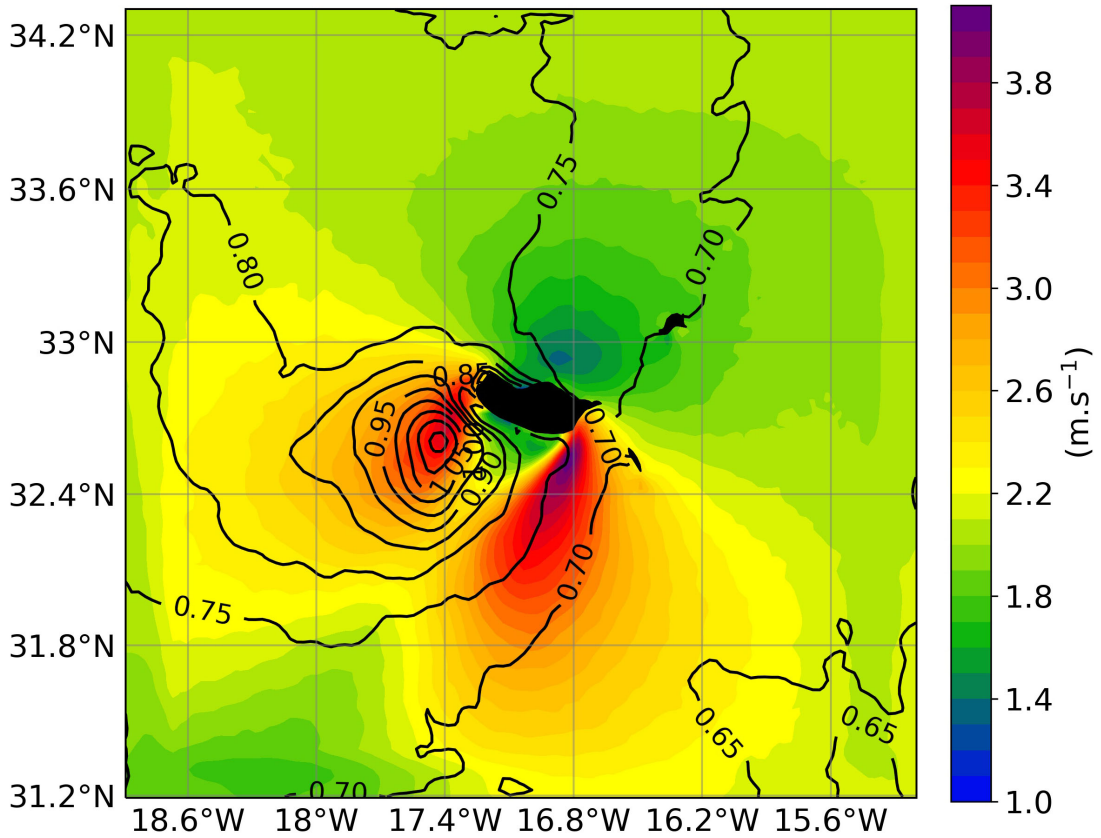

FIGURE 6 | Interannual mean (1983–2017) of the summer (JJA) standard deviations of: wind (shading), and sea surface temperature (SST) (contour lines, °C).

island tips, a simple Bernoulli mechanism to accelerate the flow in the jets.

On the other hand, the seasonal mean wind directional constancy (Bromwich, 1989), computed as the ratio of the magnitude of mean wind vector to the mean wind speed:

$$\mathrm{DC} = \frac{\sqrt{\bar{U}^2 + \bar{V}^2}}{\sqrt{U^2 + V^2}} \quad (1)$$

represented in **Figure 5**, also shows a strong seasonality, with a much stronger constancy in summer (JJA) contributing to more frequent northeasterly flow and favoring the establishment of the tip-jets in their preferred locations.

Summer is also the season with the stronger wind speed variability in the jets, associated with a multiweek oscillation of the jet intensity, driven by a corresponding oscillation in the regional PBL height (Miranda et al., 2021). The seasonal mean intraseasonal variability is shown in **Figure 6**, with the standard deviation of wind speed exceeding 3.5 m/s in the east jet, slightly smaller values in the west jet, and much smaller values in the upstream flow. In the following section, we will concentrate on summer results.

Summer Variability and Its Ocean Impact

Figure 6 also displays the intraseasonal summer variability of SST. While SST variability is driven by wind, there is a clear mismatch between wind variability, with two maxima in the two jets, and SST variability, with a single maximum under the west jet. This asymmetry between atmospheric forcing and the ocean response is explained by the asymmetry in the upper ocean circulation, later discussed, implying a stronger thermal response to wind variability near the west tip-jet.

The perturbed surface wind in the vicinity of Madeira imposes a very heterogeneous forcing on the upper ocean layers, through energy and momentum fluxes, which is reflected in the ocean surface temperature and 3D currents, particularly during summer, with higher wind speed in the tip-jets and lower wind speed in the wake. This wind environment favors the onset of cyclonic current anomalies near the west flank and anticyclonic anomalies near the east flank (**Figure 7**), which are the source of the frequent shedding of ocean eddies usually observed in the lee of Madeira (Caldeira et al., 2014). As also shown in **Figure 7**, this positive (negative) vorticity anomalies imply colocated upward (downward) currents near the west (east) flank. It is interesting to note that the small nearby islands produce qualitatively similar dipolar anomalies of vorticity, of a much smaller horizontal scale, as previously suggested by Caldeira and Sangrà (2012) (numerical) study.

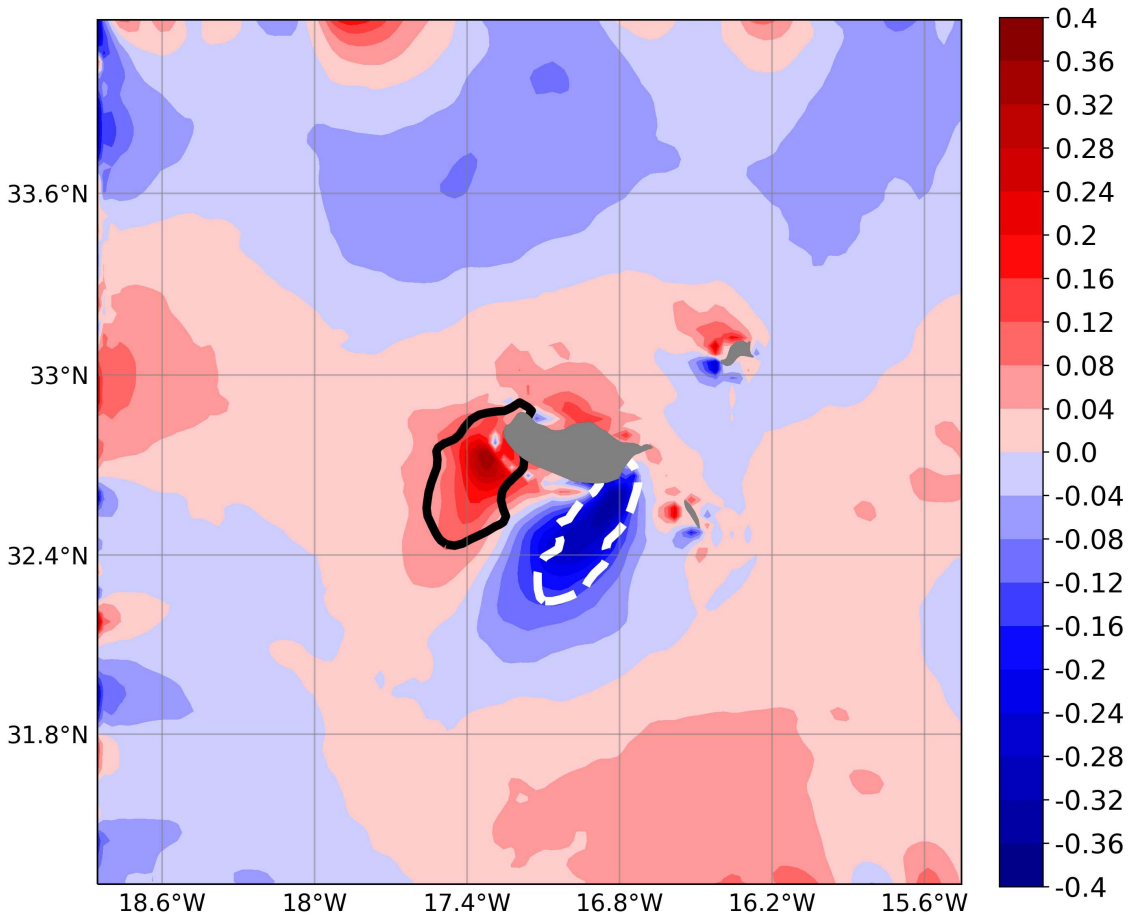

FIGURE 7 | Summer mean (1983–2017) relative vorticity of the surface currents divided by planetary vorticity (*f*) (shading). Thick lines indicate the 20-m depth vertical velocity of +3 m/day (thick solid black line) and −3 m/day (dashed white line).

The asymmetry in the vertical current is also observed in the chlorophyll concentration, assessed by remote sensing data, particularly in the 2016 summer (a summer with intense tip-jets) characterized by high concentration anomaly near the west flank (**Figure 8**). We hypothesize that this may be due to the local upwelling intensification observed in the simulation (not shown).

The effect of the tip-jets is clearly visible in the summer mean SST and mixed layer depth (MLD). The latter was computed considering a threshold of $|\Delta\rho| < \pm 0.3$ kg/m^3 in the upper density vertical profiles (chosen considering the high stratified upper ocean layers near Madeira, during summer). In **Figure 9A**, the ocean surface is locally cooler at both jets, as one would expect from enhanced evaporative cooling, but cooling is much stronger near the west jet because extra cooling is provided there by local upwelling (in a stably stratified ocean), as shown in **Figure 7**, whereas the local downwelling (associated with the east anticyclonic eddies) produces no relevant signature. An asymmetric pattern is also observed in the MLD (**Figure 9B**) with shallower mixed layer in the west upwelling region and a deeper one in the east downwelling sector.

As shown in the MLD spatial distribution and ocean vertical currents, the tip-jets effect on the ocean goes well beyond the ocean surface. To analyze the undersurface effect in the upper ocean stability, **Figure 10** shows vertical cross-sections of ocean static stability, given by squared Brunt–Väisälä frequency in the zonal and meridional directions, following the lines shown in **Figure 9A**. During summer, near the east jet (**Figure 10A**), a locally decreased vertical stability is shown by a deepening of the pycnocline. The opposite is observed near the west jet (**Figure 10B**). At both locations, the perturbations in the top 30 m are compensated by opposite perturbations below, with respect to surrounding water. Below 120 m, the stability field is almost flat (not shown). A detailed look shows that the maximum impact in the upper ocean (black triangles) is located near the maximum wind speed variability and not in the maximum mean wind (red triangles) (cf. **Figure 9A**), since the maximum wind variability coincides with maxima in ocean vorticity and vertical current, showing the importance of the tip-jets and wake for the upper ocean imposed perturbations. This is in line with the Couvelard et al. (2012) study, which suggested that there was a transfer of momentum (wind stress curl) from the atmosphere

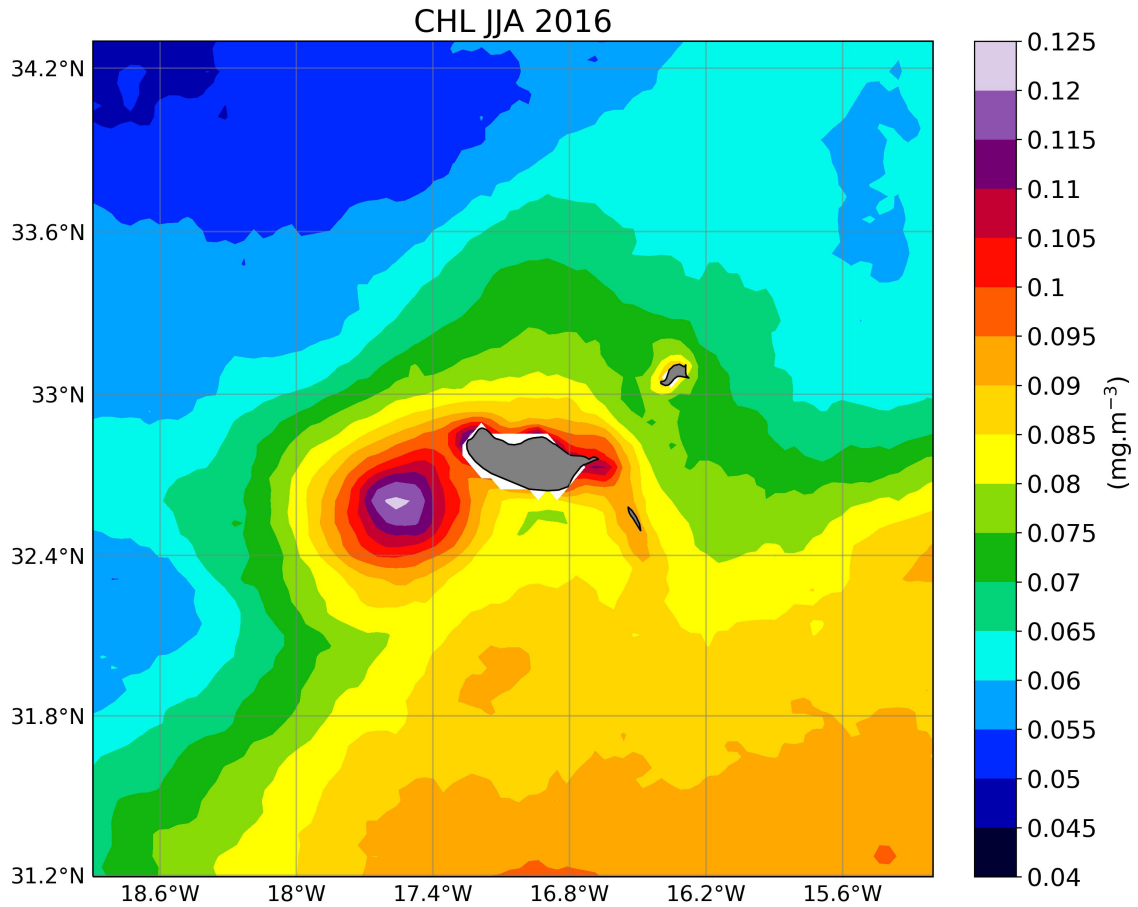

FIGURE 8 | Mean 2016 summer (JJA) remote detected chlorophyll concentration, nearby Madeira, with 4 km resolution, based on the merging of the sensors SeaWiFS, MODIS, MERIS, VIIRS-SNPP&JPSS1, and OLCI-S3A&S3B.

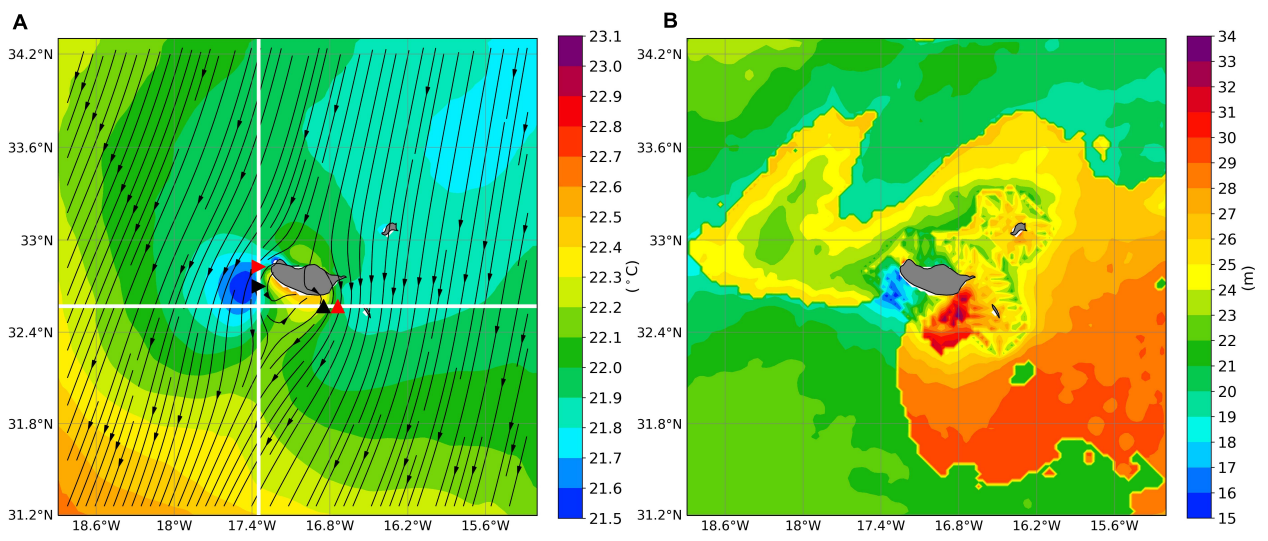

FIGURE 9 | Mean (1983–2017) summer (JJA): **(A)** sea surface temperature (SST) and **(B)** Mixed Layer Depth (MLD). White lines in panel **(A)** indicate **Figure 10** cross-sections, black triangles zone of the maximum perturbed ocean in depth and red triangles maximum wind speed, along each section.

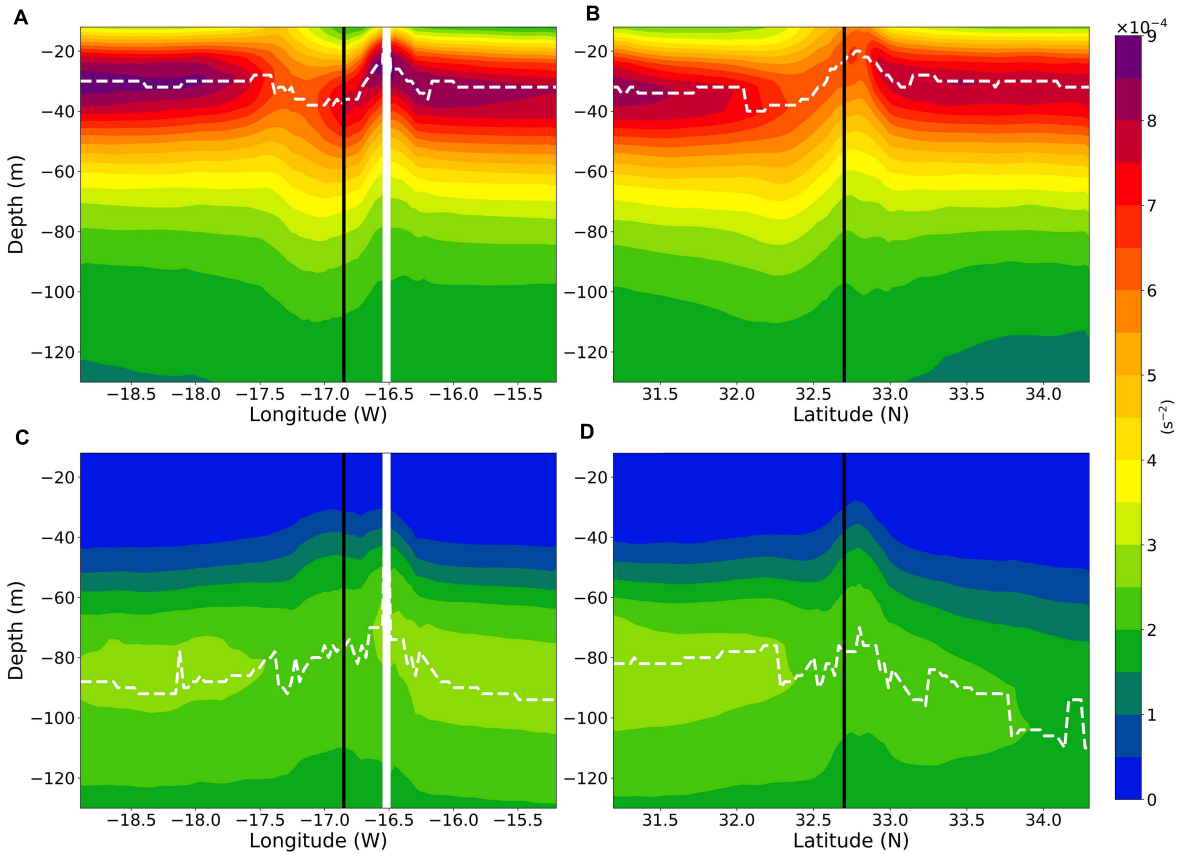

FIGURE 10 | Mean (1983–2017) ocean summer (JJA) cross-sections of squared Brunt–Väissälä frequency (s-2): **(A)** zonal section at 32.6N; **(B)** meridional section at 16.85W. Vertical black lines indicate location of maximum perturbed upper ocean. White bar in **Figure 10A**) is due to Desertas island. White dashed line shows depth of maximum N^2. **(C,D)** similar to **(A,B)**, respectively, but for winter (DJF).

to the ocean, which contributed to the generation of the oceanic eddies at the island flanks. A rather different pattern is shown in the corresponding winter cross-sections (**Figures 10C,D**) with a much better mixed upper ocean and lower pycnocline (dashed line), probably due to the lower incident radiation during winter and the better ocean capacity to transport the heat to its interior. As a consequence, during this season, the tip-jets impact in the upper ocean is attenuated.

Interdecadal Variability and Recent Trends

The shallow MLD observed in summer means a lower ocean heat capacity and consequently a higher SST sensitivity to atmospheric warming. However, there are, at least, two mechanisms that may lead to an attenuation of the ocean surface warming. One is an increased evaporative cooling that would be produced by tip-jet intensification (Miranda et al., 2021); the other is the intensification of the upwelling current associated to cyclonic vorticity near the west tip-jet (not shown), which may lead to a further attenuation of SST warming or even to local cooling. Both processes are controlled by the interdecadal variability of the tip-jets.

Figure 11 shows trends of summer 10-m wind, computed by the nonparametric Theil–Sen estimator (Sen, 1968, Theil, 1992), after filtering time series at each grid point by removing the mean annual cycle. This technique computes a central estimate of the trend and upper and lower estimates at the (chosen) 95% confidence level. In **Figure 11**, the central estimate is only shown when upper and lower estimates have the same sign. That is the case in both jets, which are found to have been intensifying slightly more than 0.7 m/s in 35 years.

Results using the same method (Theil–Sen) applied to summer SST are shown in **Figure 12**. In this case, all estimates are presented, as the underlying positive trend would mostly avoid negative estimates even from the lower estimate. The mean warming trend is found to be around +0.5°C/35 years but with a lot of spatial heterogeneity. Trends in the west jet are, however, much smaller with a minimum approaching zero, indicating that enhanced upwelling at those locations has been able to compensate most of global warming.

The ocean temperature trend at 20 m also shows high spatial heterogeneity, with zones where the warming is more intense than at surface and zones where the inverse is observed, particularly near the west flank upwelling zone. Interestingly, the mean ocean temperature warming trend at 20 m (**Figure 12E**) is

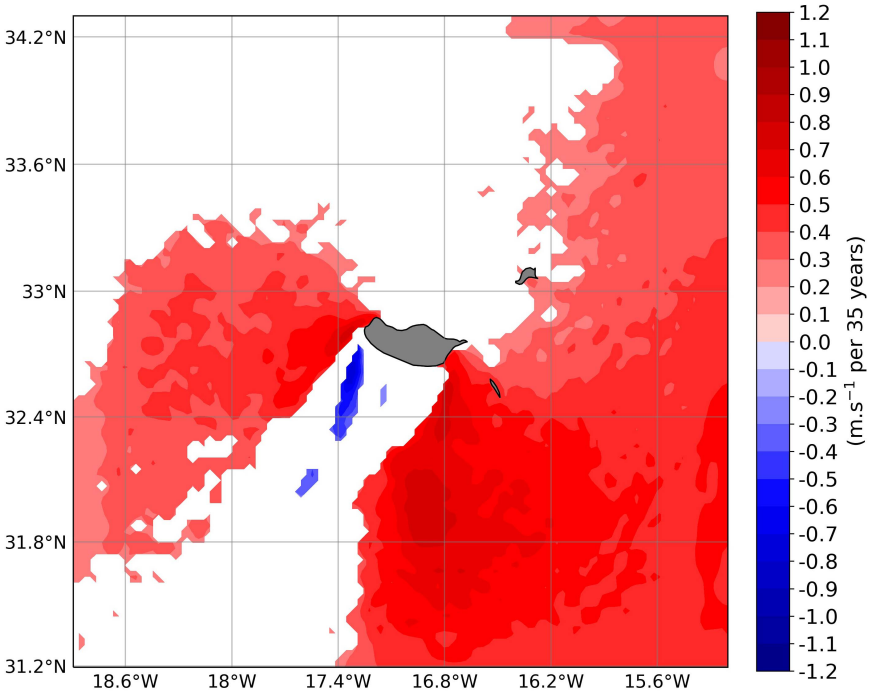

FIGURE 11 | Summer (JJA) (1983–2017) wind speed trend, computed with the Theil–Sen method. Only zones with the same sign in the 95% upper and lower bounds are shown.

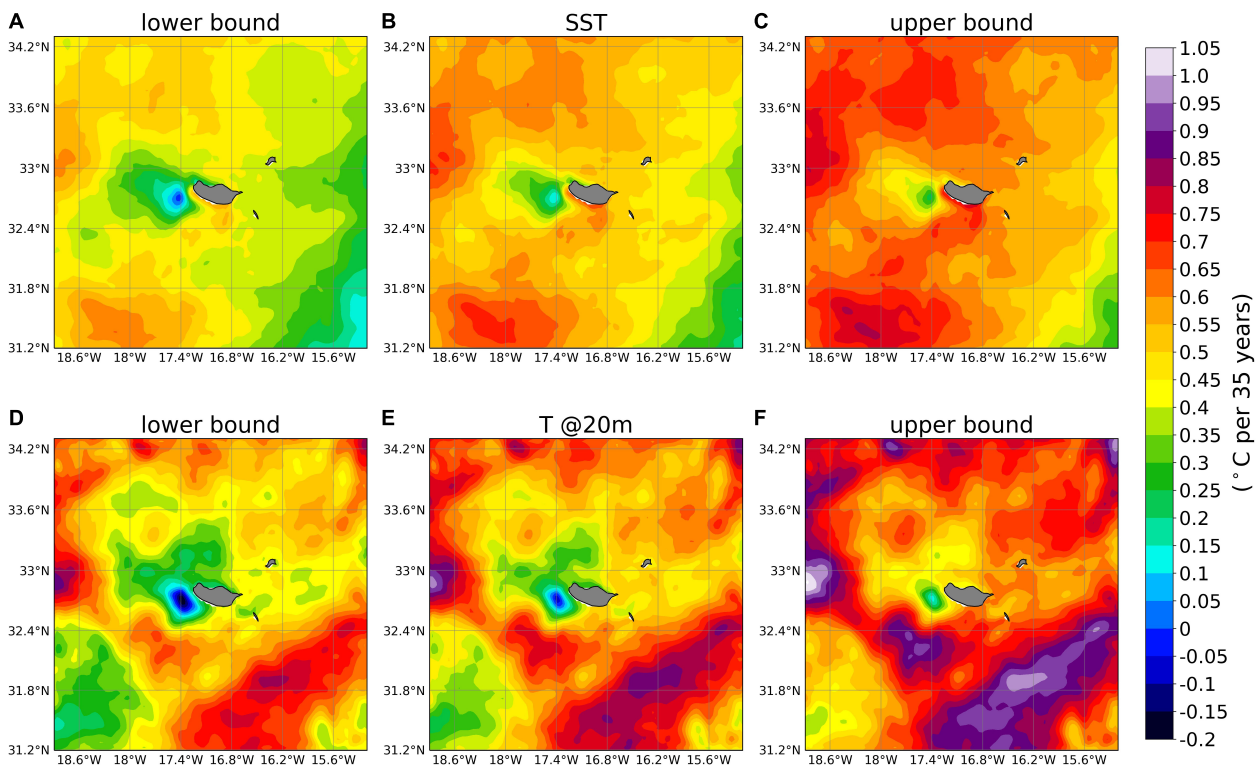

FIGURE 12 | Theil–Sen estimates of the summer (JJA) ocean temperature trend (1983–2017): surface **(A)** Lower bound, **(B)** central estimate, and **(C)** upper bound; 20 m depth **(D)** Lower bound, **(E)** central estimate, and **(F)** upper bound. Upper and lower bounds were estimated at the 95% confidence level.

slightly higher (about +0.06°C per 35 years) than on the surface, suggesting a decoupling between the surface processes expose to daily wind and thermal variations and the interior oceanic mixed layer, as suggested by Azevedo et al. (2021)

DISCUSSION AND CONCLUSION

The complex atmospheric and ocean circulations around Madeira Island, and off many other islands and archipelagos, may interact in unexpected ways with the large-scale circulation. The Madeira location in the NE Atlantic subtropics gives it a rather steady wind regime, under a predominant northeasterly flow, often corresponding to the NE Atlantic trade wind. That flow gives rise to local acceleration near the island tips, especially in summer, where two tip-jets are almost always present, and the flow shows very low values of directional variability but very high values of wind speed variability.

Miranda et al. (2021) have recently shown that the tips-jets are driven by flow acceleration under low PBL height and that such process has intensified significantly in the ERA5 period (1979–2018), due to a progressive lowering of the PBL height. The present study showed that variability in the tip-jets from the intraseasonal to the interdecadal time scale leads to ocean variability with an asymmetric response in the island flanks: while both jets evidence interdecadal intensification, this leads to a much stronger response in the west jet with decreased warming of surface waters driven by enhanced upwelling in a region where cyclonic eddies are often produced. The opposite sign of vorticity produced at the two jets leads to a dipolar response of the summer mixed layer depth: shallower under the west jet; deeper under the east jet. These changes in the ocean environment around Madeira may be relevant for the local marine ecosystem. For instance, the simulated enhanced warming at depth may be important, as mentioned in a modeling study off the west coast of Australia (Ryan et al., 2021), showing that ocean warming events at depth have caused mass die-offs of marine organisms, with coral bleaching, and relevant impact in the fisheries that depend on them. Previous numerical simulations also suggested that submesoscale eddies (1–100 km) can achieve important vertical transports in the upper ocean, contributing to efficient exchanges with the permanent thermocline (Callies et al., 2015), taking heat and atmospheric gases down into the deep ocean and bringing nutrients up into the surface layer and increasing primary production, essential for the maintenance of the Madeira ecosystem (Narciso et al., 2019; Ribeiro and Neves, 2020).

While some of the results presented here were broadly validated against available remote sensing observations, and benefit from the obvious quality of ERA5 forcing fields, it is clear that specific ocean observations would be required to confirm these results, especially in what concerns the subsurface impacts. An extension of the methodology used here for a more extended spatial domain, encompassing the Canary current system, and for climate change scenarios appears justified, as it could help in the discussion of a still open question: the response of the North African upwelling system to climate change (Bakun, 1990; Alves and Miranda, 2013, Barton et al., 2013; Miranda et al., 2013, Sydeman et al., 2014).

DATA AVAILABILITY STATEMENT

The raw data supporting the conclusions of this article will be made available by the authors, without undue reservation.

AUTHOR CONTRIBUTIONS

JA and RT carried out the numerical simulations. JA and PM analyzed the data and wrote the manuscript in close collaboration with RC. All authors participated in the review process and approved the final version.

FUNDING

This work was supported by the Oceanic Observatory of Madeira Project (M1420-01-0145-FEDER-000001-Observatório Oceânico da Madeira-OOM). We also acknowledge the FCT financial support through project UIDB/50019/2020 (IDL).

ACKNOWLEDGMENTS

We acknowledge our data providers, listed in *Experimental Setup*. Finally, we acknowledge IDL for providing the computational resources to perform the numerical simulations.

REFERENCES

Alves, J. M. R., Caldeira, R. M. A., and Miranda, P. M. A. (2020). Dynamics and oceanic response of the Madeira tip-jets. *Q. J. R. Meteorol. Soc.* 146, 3048–3063. doi: 10.1002/qj.3825

Alves, J. M. R., and Miranda, P. M. A. (2013). Variability of Iberian upwelling implied by ERA-40 and ERA-Interim reanalyses. *Tellus A* 65:19245. doi: 10.3402/tellusa.v65i0.19245

Azevedo, C., Camargo, C., Alves, J., and Caldeira, R. M. A. (2021). Convection and heat transfer in island (warm) wakes. *J. Phys. Oceanogr.* doi: 10.1175/JPO-D-20-0103.1

Bakun, A. (1990). Global climate change and intensification of coastal ocean upwelling. *Science* 247, 198–201. doi: 10.1126/science.247.4939.198

Barton, E. D., Field, D. B., and Roy, C. (2013). Canary current upwelling: more or less? *Prog. Oceanogr.* 116, 167–178. doi: 10.1016/j.pocean.2013.07.007

Becker, J. J., Sandwell, D. T., Smith, W. H. F., Braud, J., Binder, B., Depner, J., et al. (2009). Global bathymetry and elevation data at 30 arc seconds resolution: SRTM30_PLUS. *Mar. Geod.* 32, 355–371. doi: 10.1080/01490410903297766

Bromwich, D. H. (1989). An extraordinary katabatic wind regime at Terra-Nova Bay, Antarctica. *Mon. Weather Rev.* 117, 688–695. doi: 10.1175/1520-04931989117<0688:AEKWRA<2.0.CO;2

Caldeira, R. M. A., and Sangrà, P. (2012). Complex geophysical wake flows. *Ocean Dyn.* 62, 683–700. doi: 10.1007/s10236-012-0528-6

Caldeira, R. M. A., Stegner, A., Couvelard, X., Araújo, I. B., Testor, P., and Lorenzo, A. (2014). Evolution of an oceanic anticyclone in the lee of Madeira Island: in situ and remote sensing survey. *J. Geophys. Res. Oceans.* 119, 1195–1216. doi: 10.1002/2013JC009493

Caldeira, R. M. A., and Tomé, R. (2013). Wake response to an ocean-feedback mechanism: Madeira Island case study. *Boundary Layer Meteorol.* 148, 419–436. doi: 10.1007/s10546-013-9817-y

Callies, J., Ferrari, R., Klymak, J., and Gula, J. (2015). Seasonality in submesoscale turbulence. *Nat. Commun.* 6:6862. doi: 10.1038/ncomms7862

Cardoso, C., Caldeira, R. M. A., Relvas, P., and Stegner, A. (2020). Islands as eddy transformation and generation hotspots: Cabo Verde case study. *Prog. Oceanogr.* 184:102271. doi: 10.1016/j.pocean.2020.102271

Carton, J. A., and Giese, B. S. (2008). A reanalysis of ocean climate using simple ocean data assimilation (SODA). *Mon. Weather Rev.* 136, 2999–3017. doi: 10.1175/2007MWR1978.1

Carton, J. A., Penny, S. G., and Kalnay, E. (2019). Temperature and salinity variability in the SODA3, ECCO4r3, and ORAS5 ocean reanalyses 1993–2015. *J. Clim.* 32, 2277–2293. doi: 10.1175/JCLI-D-18-0605.1

Chapman, D. C. (1985). Numerical treatment of cross-shelf open boundaries in a barotropic coastal ocean model. *J. Phys. Oceanogr.* 15, 1060–1075. doi: 10.1175/1520-04851985015<1060:NTOCSO<2.0.CO;2

Couvelard, X., Caldeira, R. M. A., Araújo, I. B., and Tomé, R. (2012). Wind mediated vorticity-generation and eddy-confinement, leeward of the Madeira Island: 2008 numerical case study. *Dyn. Atmos. Oceans.* 58, 128–149. doi: 10.1016/j.dynatmoce.2012.09.005

Dee, D. P., Uppala, S. M., Simmons, A. J., Berrisford, P., Poli, P., Kobayashi, S., et al. (2011). The ERA-Interim reanalysis: configuration and performance of the data assimilation system. *Q. J. R. Meteorol. Soc.* 137, 553–597. doi: 10.1002/qj.828

Doyle, J. D., and Shapiro, M. A. (1999). Flow response to large-scale topography: the Greenland tip jet. *Tellus A* 51, 728–748. doi: 10.1034/j.1600-0870.1996.00014.x

Etling, D. (1989). On atmospheric vortex streets in the wake of large islands. *Meteorol. Atmos. Phys.* 41, 157–164. doi: 10.1007/BF01043134

Grubišic, V., Sachsperger, J., and Caldeira, R. M. (2015). Atmospheric wake of Madeira: first aerial observations and numerical simulations. *J. Atmos. Sci.* 72, 4755–4776. doi: 10.1175/JAS-D-14-0251.1

Haidvogel, D. B., and Beckmann, A. (1999). *Numerical Ocean Circulation Modelling*. London: Imperial College Press, 344.

Hersbach, H., Bell, B., Berrisford, P., Hirahara, S., Horanyi, A., Munoz-Sabater, J., et al. (2020). The ERA5 Global Reanalysis. *Q. J. R. Meteorol. Soc.* 146, 1999–2049. doi: 10.1002/qj.3803

Marchesiello, P., McWilliams, J. C., and Shchepetkin, A. (2001). Open boundary conditions for long-term integration of regional oceanic models. *Ocean Model.* 3, 1–20. doi: 10.1016/S1463-5003(00)00013-5

Mason, E., Molemaker, M. J., Shchepetkin, A., Colas, F., McWilliams, J. C., and Sangra, P. (2010). Procedures for offline grid nesting in regional ocean models. *Ocean Model.* 35, 1–15. doi: 10.1016/j.ocemod.2010.05.007

Merchant, C. J., Embury, O., Bulgin, C. E., Block, T., Corlett, G. K., Fiedler, E., et al. (2019). Satellite-based time-series of sea-surface temperature since 1981 for climate applications. *Sci. Data* 6:223. doi: 10.1038/s41597-019-0236-x

Miranda, P. M. A., Alves, J. M. R., and Serra, N. (2013). Climate change and upwelling: response of Iberian upwelling to atmospheric forcing in a regional climate scenario. *Clim. Dyn.* 40, 2813–2824. doi: 10.1007/s00382-012-1442-9

Miranda, P. M. A., Tomé, R., Frois, L., Nogueira, M., Alves, J. M. R., Prior, V., et al. (2021). Speed-up of the Madeira tip jets in the ERA5 climate highlights the decadal variability of the Atlantic subtropics. *Q. J. R. Meteorol. Soc.* 147, 679–690. doi: 10.1002/qj.3940

Narciso, A., Caldeira, R., Reis, J., Hoppenrath, M., Cachão, M., and Kaufmann, M. (2019). The effect of a transient frontal zone on the spatial distribution of extant coccolithophores around the Madeira archipelago (Northeast Atlantic). *Estuar. Coast. Shelf Sci.* 223, 25–38. doi: 10.1016/j.ecss.2019.04.014

Ólafsson, H., and Bougeault, P. (1997). The effect of rotation and surface friction on orographic drag. *J. Atmos. Sci.* 54, 193–210.

Ribeiro, C., and Neves, P. (2020). Habitat mapping of Cabo Girão Marine Park (Madeira island): a tool for conservation and management. *J. Coast. Conserv.* 24:22. doi: 10.1007/s11852-019-00724-9

Ryan, S., Ummenhofer, C. C., Gawarkiewicz, G., Wagner, P., Scheinert, M., Biastoch, A., et al. (2021). Depth structure of Ningaloo Niño/Niña events and associated drivers. *J. Climate.* 34, 1767–1788. doi: 10.1175/JCLI-D-19-1020.1

Sen, P. K. (1968). Estimates of the regression coefficient based on Kendall's Tau. *J. Am. Stat. Assoc.* 63, 1379–1389. doi: 10.1080/01621459.1968.10480934

Shchepetkin, A. F., and McWilliams, J. C. (2005). The regional oceanic modeling system (ROMS): a split-explicit, free-surface, topography-following-coordinate oceanic model. *Ocean Model.* 9, 347–404.

Shchepetkin, A. F., and McWilliams, J. C. (2009). "Computational kernel algorithms for fine-scale, multiprocess, longtime oceanic simulations," in *Handbook of Numerical Analysis*, Vol. 14, eds R. M. Temam and J. J. Tribbia (New York, NY: Elsevier), 121–183. doi: 10.1016/S1570-8659(08)01202-0

Smith, R. B., Gleason, A. C., Gluhosky, P. A., and Grubišic, V. (1997). The wake of St. Vincent. *J. Atmos. Sci.* 54, 606–623.

Sydeman, W. J., García-Reyes, M., Schoeman, D. S., Rykaczewski, R. R., Thompson, S. A., Black, B. A., et al. (2014). Climate change and wind intensification in coastal upwelling ecosystems. *Science* 345, 77–80. doi: 10.1126/science.1251635

Theil, H. (1992). "A rank-invariant method of linear and polynomial regression analysis," in *Henri Theil's Contributions to Economics and Econometrics. Advanced Studies in Theoretical and Applied Econometrics*, Vol. 23, eds B. Raj and J. Koerts (Dordrecht: Springer). doi: 10.1007/978-94-011-2546-8_20

Umlauf, L., and Burchard, H. (2003). A generic length-scale equation for geophysical turbulence models. *J. Mar. Res.* 61, 235–265. doi: 10.1357/002224003322005087

Verhoef, A., Portabella, M., and Stoffelen, A. (2012). High-resolution ASCAT scatterometer winds near the coast. *IEEE Trans. Geosci. Remote Sens.* 50, 2481–2487. doi: 10.1109/TGRS.2011.2175001

Warner, J. C., Armstrong, B., He, R. Y., and Zambon, J. B. (2010). Development of a coupled ocean–atmosphere–wave–sediment transport (COAWST) modeling system. *Ocean Model.* 35, 230–244. doi: 10.1016/j.ocemod.2010.07.010

Xie, S. P., Liu, W. T., Liu, Q. Y., and Nonaka, M. (2001). Far-reaching effects of the Hawaiian Islands on the Pacific Ocean–atmosphere system. *Science* 292, 2057–2060.

Conflict of Interest: The authors declare that the research was conducted in the absence of any commercial or financial relationships that could be construed as a potential conflict of interest.

frontiers in Marine Science

ORIGINAL RESEARCH
published: 17 March 2021
doi: 10.3389/fmars.2021.592703

Short-Term Spatiotemporal Variability in Picoplankton Induced by a Submesoscale Front South of Gran Canaria (Canary Islands)

Nauzet Hernández-Hernández[1], Yeray Santana-Falcón[2], Sheila Estrada-Allis[3] and Javier Arístegui[1]*

[1] Instituto de Oceanografía y Cambio Global (IOCAG), Universidad de Las Palmas de Gran Canaria (ULPGC), Las Palmas, Spain, [2] CNRM, Université de Toulouse, Météo-France, CNRS, Toulouse, France, [3] Department of Physical Oceanography, CICESE, Ensenada, Mexico

The distribution and variability of phytoplankton in the upper layers of the ocean are highly correlated with physical processes at different time and spatial scales. Model simulations have shown that submesoscale features play a pivotal role on plankton distribution, metabolism and carbon fluxes. However, there is a lack of observational studies that provide evidence for the complexity of short-term phytoplankton distribution and variability inferred from theoretical and modeling approaches. In the present study, the development and decay of a submesoscale front south of Gran Canaria Island is tracked at scales not considered in regular oceanographic samplings in order to analyze the picoplankton response to short-term variability. Likewise, the contribution of each scale of variability to the total variance of the picophytoplankton community has been quantified. We observe statistically different picophytoplankton assemblages across stations closer than 5 km, and between time periods shorter than 24 h, which were related to high physical spatiotemporal variability. Our results suggest that both temporal and spatial variability may equally contribute to the total variance of picoplankton community in the mixed layer, while time is the principal contributor to total variance in the deep chlorophyll maximum (DCM).

Keywords: picoplankton, submesoscale front, spatiotemporal variability, frontogenesis, frontolisis, Canary Islands, subtropical North Atlantic

OPEN ACCESS

Edited by:
Charitha Bandula Pattiaratchi, University of Western Australia, Australia

Reviewed by:
Qian P. Li, Chinese Academy of Sciences, China
Paulo Henrique Rezende Calil, Helmholtz Centre for Materials and Coastal Research (HZG), Germany

****Correspondence:***
Nauzet Hernández-Hernández
nauzet.hernandez@ulpgc.es

Specialty section:
This article was submitted to Coastal Ocean Processes, a section of the journal Frontiers in Marine Science

Received: *07 August 2020*
Accepted: *24 February 2021*
Published: *17 March 2021*

Citation:
Hernández-Hernández N, Santana-Falcón Y, Estrada-Allis S and Arístegui J (2021) Short-Term Spatiotemporal Variability in Picoplankton Induced by a Submesoscale Front South of Gran Canaria (Canary Islands). Front. Mar. Sci. 8:592703. doi: 10.3389/fmars.2021.592703

INTRODUCTION

As higher plants, unicellular marine primary producers' growth mainly depends on nutrient and light availability. Access to these resources may be limited in the highly dynamic oceanic environments, which are dominated by physical processes that generally alter resource availability. Indeed, a large amount of studies has indicated that the distribution and variability of phytoplankton and other biogeochemical parameters like nutrients and organic matter in the upper layers of the ocean are highly correlated in time and space with physical processes (Abraham, 1998; Mahadevan and Campbell, 2002; Lévy and Klein, 2004; Niewiadomska et al., 2008; Omta et al., 2008; Lehahn et al., 2017).

Mesoscale motions have commonly been assumed to be the most important factor modulating the distribution of biogeochemical properties at the upper levels of the ocean (Falkowski et al., 1991; Oschlies and Garçon, 1998; McGillicuddy et al., 2007; Johnson et al., 2010). However, recent theoretical studies (Lévy et al., 2001; Mahadevan and Campbell, 2002; Mahadevan and Tandon, 2006; Klein and Lapeyre, 2009) have highlighted the role played by smaller processes that operate below the local Rossby radius of deformation, referred to here as submesoscale. An estimated 50% of the total variance of vertical velocities in the upper layer of the ocean may be explained by submesoscale processes (Klein and Lapeyre, 2009). These small-scale motions arise from the disruption of the geostrophic balance by mesoscale straining being common in fronts and eddies edges. Vertical motions associated with ageostrophic secondary circulation (ASC) are originated at both sides of the fronts (upward on the warm side and downward on the cold side) leading to small-scale fluxes of biogeochemical properties like nutrients (Mahadevan and Tandon, 2006; Lévy et al., 2012a). Diapycnal mixing has been shown to be a dominant component of the vertical velocity in submesoscales fronts and filaments by destroying the thermal wind and driving intense ASC in the upper layers (Estrada-Allis et al., 2019). Thus, intensification of diapycnal mixing may enhance vertical transport of nutrients (Arcos-Pulido et al., 2014; Corredor-Acosta et al., 2020; Tsutsumi et al., 2020) as well as upwelling/downwelling of phytoplankton communities from sub-surface layers into the euphotic zone and vice versa. These physical cells act to restore the geostrophy by means of restratification in a process known as frontogenesis (Hoskins and Bretherton, 1972; Hoskins, 1982; Capet et al., 2008; McWilliams, 2016). The importance of submesoscale lies in that their spatiotemporal scales are similar to those in which biological process acts, i.e., from 0.1 to tens of kilometers and of the order of 0 (1–10) days. Phytoplankton productivity and growth may thus be influenced by those changes in nutrient and light availabilities (Allen et al., 2005; Lévy et al., 2009, 2018; Lathuiliere et al., 2011; Taylor and Ferrari, 2011; Shulman et al., 2015; Liu and Levine, 2016; Taylor, 2016; Hosegood et al., 2017). Additionally, submesoscale motions may also induce shifts on phytoplankton community structure (D'Ovidio et al., 2010; Lévy et al., 2018) affecting food web dynamics and, ultimately, the carbon cycle (Mayot et al., 2017).

The study of the mechanisms controlling frontogenesis and the associated ASC is a relevant topic due to its potential impact, not only on the short-term modulation of nutrients, organic matter or light, and hence on phytoplankton communities (Mahadevan and Campbell, 2002; Klein and Lapeyre, 2009; Lévy et al., 2009, 2012a), but also because of its role in example global ocean circulation (D'Asaro et al., 2011; Taylor and Ferrari, 2011; Lévy et al., 2012b), heat transport (Siegelman et al., 2020) or fish and marine mammal distribution (Snyder et al., 2017; Siegelman et al., 2020). However, due to the inherent complexity of sampling at such high-resolution levels, only a few studies have reported *in situ* data of submesoscale spatial phytoplankton distribution across a frontal region yet (e.g., Martin et al., 2005; Taylor et al., 2012; Clayton et al., 2014; Cotti-Rausch et al., 2016; Mousing et al., 2016; Hernández-Hernández et al., 2020). Therefore, our knowledge about submesoscale-influenced phytoplankton distribution and variability mostly constrained to the information extracted from theoretical and modeling studies (Lévy et al., 2001, 2012a; Li et al., 2012; Liu and Levine, 2016; Taylor, 2016).

In this study, we provide physical and biogeochemical observations on the development and decay of a submesoscale wind-shear front formed on the wake of Gran Canaria Island. Our overarching objective is to discuss how short-term front-generated physical variability affects the distribution and community structure of picophytoplankton organisms, which are major contributors to total phytoplankton biomass and primary production in the subtropical waters surrounding the Canary archipelago (Zubkov et al., 2000a,b; Arístegui et al., 2009). For that aim, we first study the spatiotemporal evolution of the front and biogeochemical parameters. We then statistically examine the effect of the front over the phytoplankton distribution and community structure via Metric Multidimensional Scaling Analysis. We finally compare the variance induced by the spatial and temporal variabilities to determine which source of variability has major influence over picoplankton community variability.

MATERIALS AND METHODS

Hydrography, Wind and Sampling Design

Data reported in this paper were collected from 9 to 12 of May of 2011 on board R/V *Atlantic Explorer* from a section across a wind-shear convergent front (**Figures 1a,b**). In order to assess both spatial and temporal variability at submesoscale range [horizontal scale of O (1–10 km), vertical scale of O (100 m) and temporal scale of O (1 day)], a section consisting in 6–7 oceanographic stations (**Figures 1a,b**), separated ∼4 km (25 km in total), was entirely sampled every 24 h, during a 96 h period. Unfortunately, intense wind speed (**Figure 1c**) did not allow the sampling of the section at 48 h (May 11th). At each station, conductivity-temperature-depth (CTD) casts were made from surface to 300 m using a SeaBird SBE25 CTD sensor additionally equipped with a Wet Lab ECO-AFL/FL Fluorometer. The CTD was mounted onto an oceanographic rosette implemented with six Niskin bottles of 12 L. Discrete water samples were collected for chlorophyll *a* (Chl *a*), nutrients and picophytoplankton abundances at six levels, from surface to 150 m, including the deep chlorophyll maximum (DCM). TEOS-10 algorithms were used to calculate all physical derived variables. Mixed layer depth (MLD) was calculated following (de Boyer Montégut et al., 2004). Wind velocities and directions every 10 min were obtained from the Meteorological Station based on the Gando Airport, at the wind-exposed eastern coast of the Gran Canaria Island. Raw wind data was averaged every 4 h for plotting (**Figure 1c**).

Satellite-Derived Data

Satellite-derived wind velocities and directions components displayed in **Figures 1a,b** were obtained from the scatterometer mounted on the polar-orbiting satellite MetOp-A (Meteorological Operational satellite) of the European Space Agency (ESA) and provided by Copernicus Marine Environment

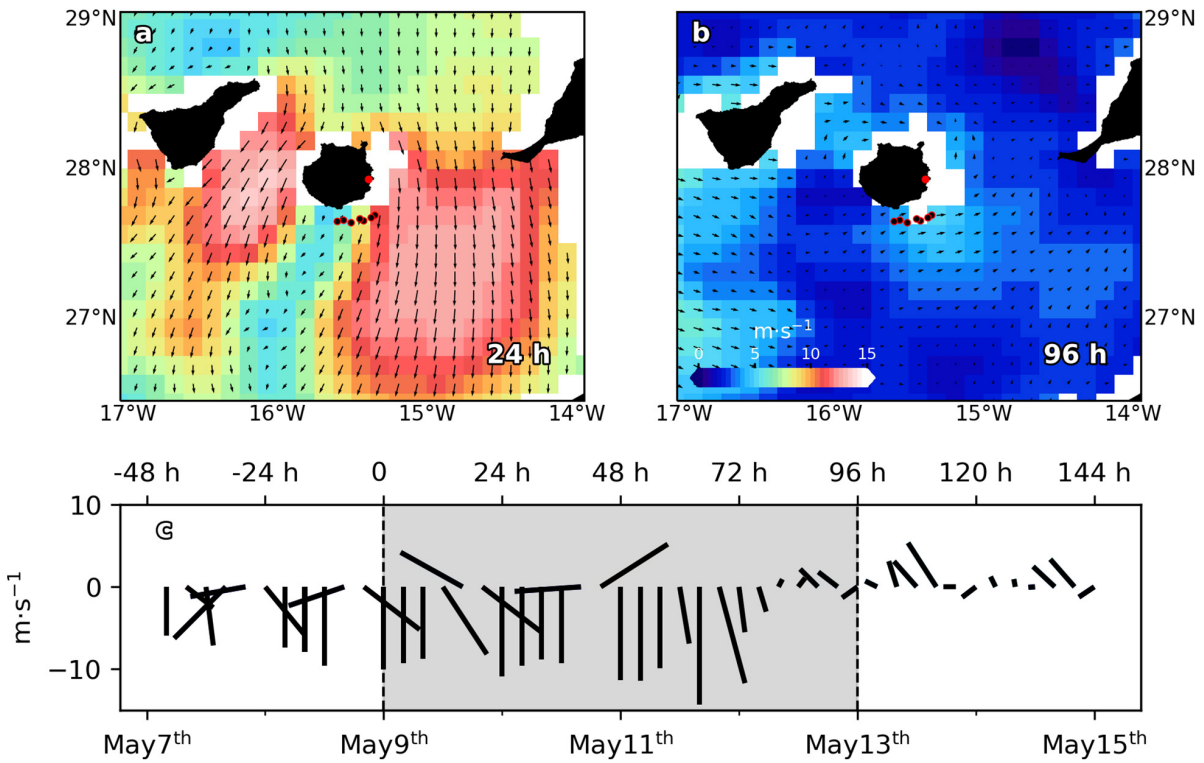

FIGURE 1 | Sea surface winds (m·s^{-1}) and direction (black arrows) from scatterometer on the Meteorological Operational satellite MetOp-A (European Space Agency, ESA), for **(a)** May 10th 2011 (24 h) and **(b)** May 13th 2011 (96 h). Black dots with red borders indicate stations positions. Red dot indicates Gando airport location. **(c)** Wind speed (m·s^{-1}) time series from May 7th to May 15th. Dashed vertical lines delimit sampling period. Negative (positive) values correspond with north (south) and east (west) wind directions.

Monitoring Services (CMEMS). Sea surface temperature (SST) and salinity (SSS) from the CMEMS's product, Atlantic -Iberian Biscay Irish- Ocean Physics Reanalysis accessible through https://resources.marine.copernicus.eu, was used to track the frontal evolution during the cruise. Both data sets present daily temporal resolution, while offering a horizontal resolution of 12.5 × 12.5 km and 8 × 8 km for wind and temperature and salinity, respectively.

Vertical Motions

Vertical velocities associated with diapycnal mixing were calculated under the assumption of negligible viscous forces and important rotation effects. In this case, the ageostrophic Coriolis forcing can be balanced by vertical mixing, and it holds by the scaling of Garret and Loder (1981), w_{GL} hereinafter:

$$w_{GL} \sim \frac{-1}{\rho^2} \frac{\partial}{\partial x}\left(A_v \frac{\partial b}{\partial x}\right)$$

where x is the cross-frontal direction, A_v is the vertical eddy viscosity, and b is the buoyancy in terms of density (ρ), mean density (ρ_o), and gravitational acceleration (g), such as $b = -g(\rho/\rho_o)$.

Though vertical velocities from w_{GL} must not be taken as total vertical velocity, it allows us to compare the magnitude of the diffusive flux and vertical advective flux, i.e., the magnitude of the vertical velocity due diapycnal mixing. Modeling studies have shown that w_{GL} resembles the shape of the total vertical velocity near the surface while differs in its magnitude (Mahadevan and Tandon, 2006; Gula et al., 2014).

Chlorophyll *a*

For Chl *a* analysis, 500 mL of water were filtered through 25 mm Whatman GF/F glass-fiber filters, and then stored frozen at −20°C until their analysis in the land-based laboratory. Pigments were extracted overnight in 10 mL of 90% cold acetone. Chl *a* was measured fluorometrically, before and after acidification (by adding two drops of 37% HCl) by means of a Turner Designs bench fluorometer previously calibrated with pure Chl *a* (Sigma Co.) following Holm-Hansen et al. (1965). Chl *a* data were used to calibrate the Wet Lab ECO-AFL/FL Fluorometer mounted on the oceanographic rosette and connected to the CTD probe.

Inorganic Nutrients

Seawater samples for nitrate + nitrite (NO_x^-) determination were collected in 15 mL polyethylene tubes (Van Waters and Rogers Co., VWR) and preserved frozen at −20°C until their analysis in the land-based laboratory. Nitrite was colorimetrically measured using a Bran+Luebbe Autoanalyzer AA3 model following Hansen and Koroleff (1999) protocol for automated seawater nutrient analysis.

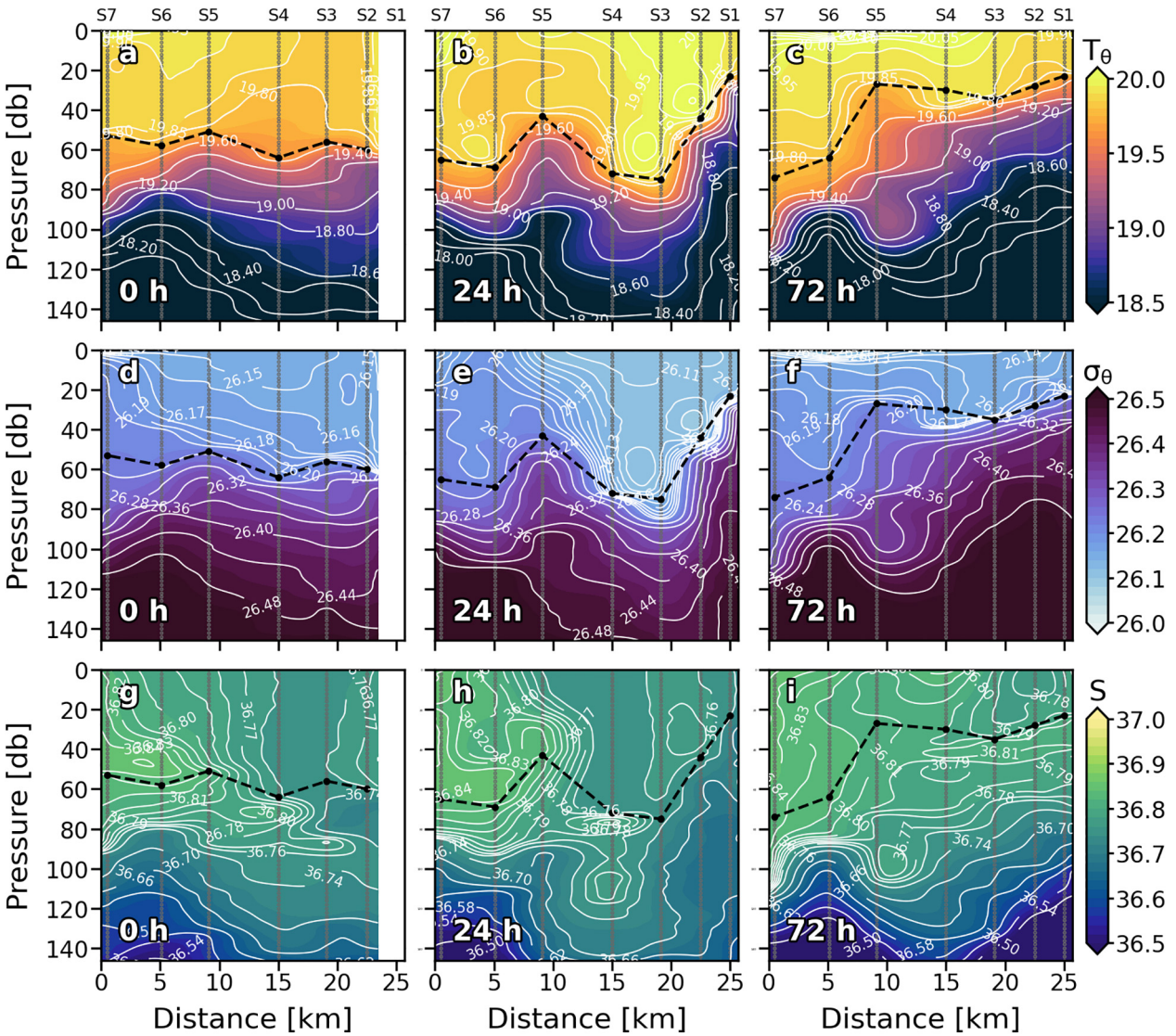

FIGURE 2 | Vertical sections of potential temperature (T_q) (°C) **(a–c)**, potential density (σ_q) (kg·m^{-3}) **(d–f)** and salinity (S) **(g–i)** for every sampling day. Stations are indicated in the upper part of the plot. Isopycnal field is superimposed as solid white lines. Dashed black line indicates the mixed layer depth. Sampling depths are represented by gray dots.

Vertical nutrient fluxes were assessed by following Fick's law:

$$F_{NO_x^-} = -k_z \frac{\partial NO_x^-}{\partial z}$$

where k_z is the vertical eddy diffusivity. Notice that the nature of our survey does not allow us for a direct analysis of the kinetic energy dissipation rates from microstructure profilers to obtain k_z (e.g., Arcos-Pulido et al., 2014; Tsutsumi et al., 2020). Notwithstanding, the increasing interest of the impact of mixing and turbulence in the biological marine systems, prompted a series of studies that compares k_z from microstructure data and fine-structure parameterizations with a reasonable degree of agreement (e.g., Inoue et al., 2007; Arcos-Pulido et al., 2014).

Here, we calculate k_z based on the parameterization of Zhang et al. (1998) validated in Inoue et al. (2007) and Arcos-Pulido et al. (2014), in which both turbulence and double diffusion mixing process are combined to obtain k_z. The approach of Zhang et al. (1998) is valid in a salt-fingering regime as dominance of Turner angles higher than 45° indicates (**Supplementary Figure 2**). The reader could refer to Arcos-Pulido et al. (2014), for a full derivation of the parameterization used here.

Picoplankton Abundances and Biomass Conversion

Cyanobacteria-like *Prochlorococcus* (Pro) and *Synechococcus* (Syn), as well as photosynthetic picoeukaryotes (Euk), were counted with a FACSCalibur (Becton and Dickinson) flow

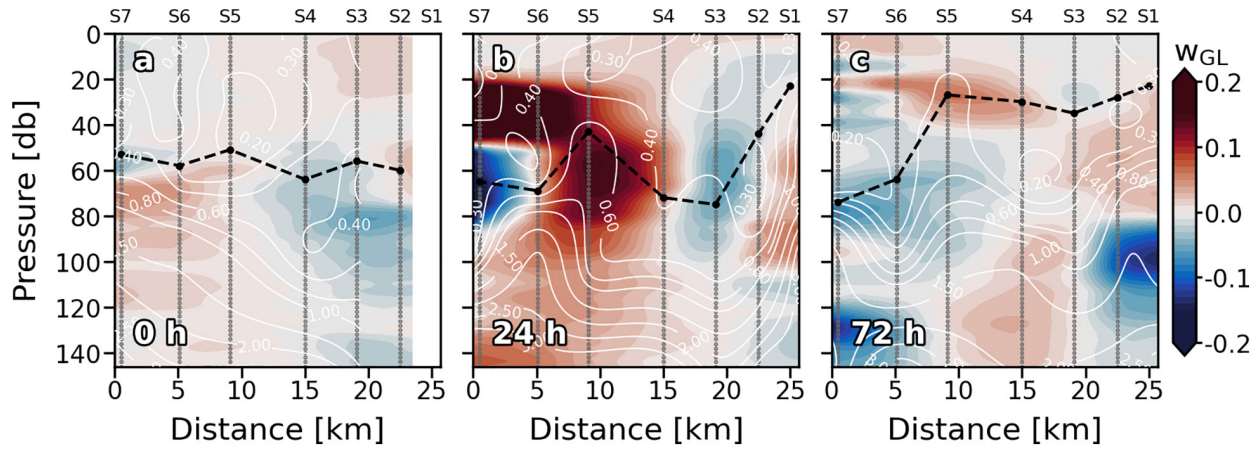

FIGURE 3 | Vertical sections of vertical velocities (w_{GL}; m·day^{-1}) for every sampling days **(a–c)**. Stations are indicated in the upper part of the plot. Nutrient (mmol·m^{-3}) field is superimposed as solid white lines. Sampling depths are represented by gray dots. Positive (negative) values indicate upward (downward) velocities. Dashed black line indicates the mixed layer depth.

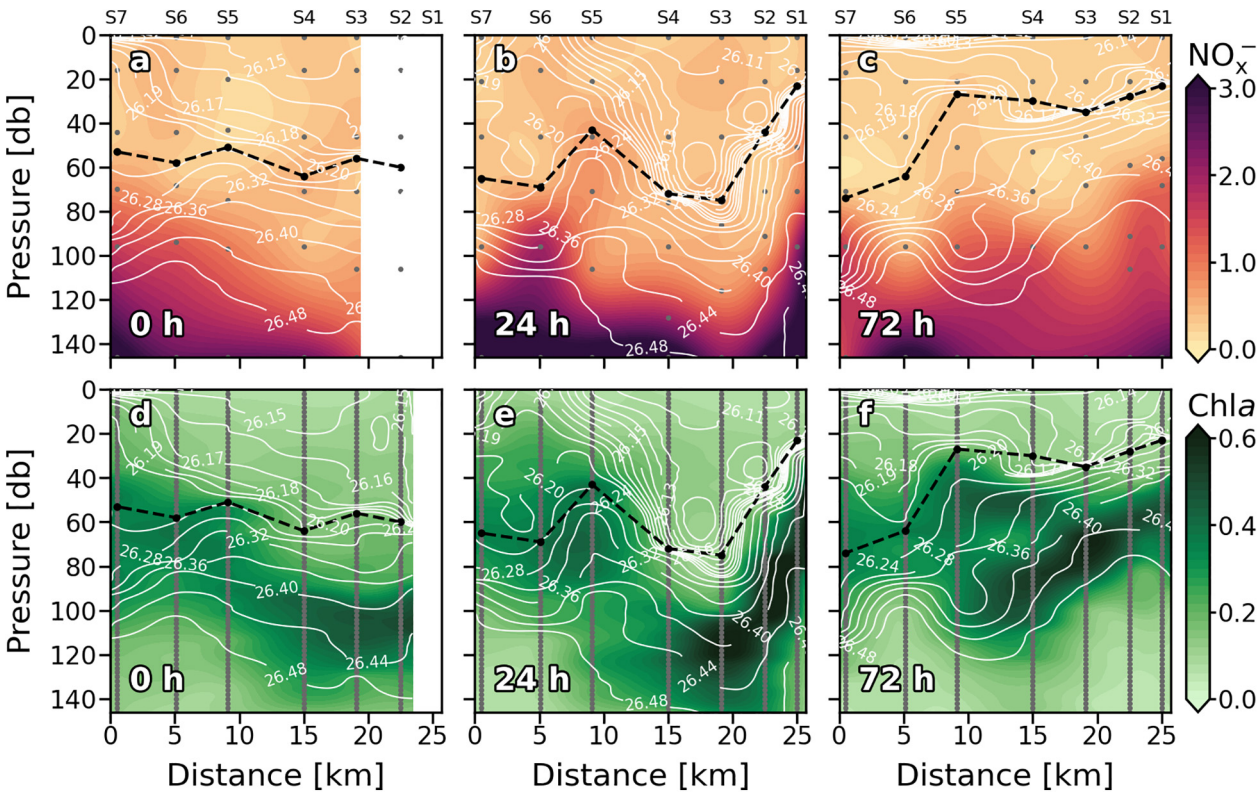

FIGURE 4 | Vertical sections of nitrate + nitrite (NO_x^-) (mmol·m^{-3}) **(a–c)**, and chlorophyll *a* (Chl *a*) (mg·m^{-3}) **(d–f)** for every sampling day. Stations are indicated in the upper part of the plot. Isopycnal field is superimposed as solid white lines. Dashed black line indicates the mixed layer depth. Sampling depths are represented by gray dots.

cytometer. Seawater samples (1.8 mL) were collected on 2 mL cryotubes (VWR) and fixed with 20% paraformaldehyde to 2% of final concentration. Fixed samples were stored at 4°C for 20 min and then frozen and preserved in liquid nitrogen (−196°C) until their analysis. 200 μL of sample were transferred to a flow cytometer tube and inoculated with 4 μL of yellow-green 1 μm ø latex beads suspension, as an internal standard (Polyscience Inc). Samples were run at 60 μL·min^{-1} for 150 s approximately. Groups were identified comparing red (FL3-H) fluorescence versus both

orange (FL2-H) fluorescence and side scatter (SSC-H) in bivariate scatter plots.

Carbon biomasses were estimated using empirical conversion factors provided by M. F. Montero (Montero et al., unpublished data). They carried out more than 60 experiments of sequential filtration (through seven polycarbonate filter from 0.2 to 3 μm) with water from the surface and the DCM of the coastal waters of Gran Canaria island. Picoplankton biovolumes were calculated via sigmoidal fits of cell counts obtained by Flow Cytometry. Spherical shape was assumed for picoplankton. Abundances were then multiplied by its corresponding average carbon content (43 fg C·cell^{-1} for Pro; 100 fg C·cell^{-1} for Syn and 444 fg C cell^{-1} for Euk) obtaining average biomass data for each group. Biomass data were integrated from 0 to 150 m, from 0 to MLD, and in the DCM. Integrated biomass data were then used as input for statistical computations.

Statistical Analysis

In order to identify potential effects of submesoscale processes over picoplankton community structure, a Metric Multidimensional Scaling Analysis (MDS) [also referred to as Principal Coordinate Analysis (PCoA)] was carried out for every sampling day. Ecological distance matrices of integrated picoplankton biomass were calculated by means of Bray-Curtis dissimilarity and then used as inputs for MDS analysis. The two orthogonal axes (MDS1 and MDS2) obtained from the MDS analysis were used as axes for results' scatter plots.

Stations were grouped using K-means clustering method, which aims at partitioning the data into groups such that the sum of squares from data within the assigned cluster is minimized. The value of between-cluster sum square (BSS) divided by the total sum of squares (TSS) was used to decide the optimal number of clusters. The number of clusters that provides higher BSS/TSS ratio was chosen. A first approximation to the optimal number of clusters was also done following the Elbow method.

To quantify the contribution of each scale of variability to the total variance of picoplankton community, a Variance Component Analysis (VCA) was conducted. Previously, the biomass dataset was Winsorized to avoid extreme values. A random effect Linear Mixed Model (LMM) was then fitted to the whole water column, mixed layer (ML) and DCM. Variance components were extracted from fitted LMM. Finally, variances were expressed as the percentage of total variance. R software[1] was used to conduct all statistical analysis.

RESULTS

Spatiotemporal Evolution of the Front

The cruise took place during a highly variable wind regime according to data provided by the Gando Airport meteorological station (**Figure 1c**). During the first 48 h of the experiment, trade winds (northeast) increased from ∼8 m·s^{-1} (0 h) to more than 14 m·s^{-1} (48 h). 72 h on, wind shifted its direction blowing from the south, and its speed dropped down to less than 6 m·s^{-1}. Satellite-derived wind velocities and direction shown in **Figures 1a,b** support the above data. At 24 h, intense (up to ∼14 m·s^{-1}) trade winds are observed at both flanks of the island. However, in the lee of the island winds dropped down to ∼6 m·s^{-1}. Notice that the sample section crossed the wind shear zone. Unfortunately, the studied zone was not in the satellite trajectory at 72 h. Instead, wind velocity and direction for the day after (96 h) are plotted in **Figure 1b**. As **Figure 1c** shows, 72 and 96 h wind conditions were quite similar. At 96 h, due to weak (∼5 m·s^{-1}) northward winds, the windless zone in the lee of the island disappeared and consequently the wind shear front which crossed the section vanished.

Since S1 was not sampled on the first day (0), only the eastern part of the front (S2, S3, and S4) was recorded. It was characterized by doming of the isopleths inside the ML, introducing relatively colder and denser water into shallower depths (**Figures 2a,d,g**). Vertical isopleths at S2 (19.80°C, 26.15 kg·m^{-3}, and 36.77) suggest that the downward branch of the front, which would be on S1, was also affecting this station. Downward movement of the isotherms was observed at S5 and S6 (**Figure 2a**). Highest surface values of T_q, s_q, and S occurred at S7. Vertical velocities tracked pretty well with T_q, s_q, and S fields in the ML (**Figure 3a**). Negative w_{GL} (downward) were associated with the deepening of the isopleths at S5 and S6 while positive w_{GL} (upward) occurred at S2, S3 and S4 where isopleths dome. Thermo and pycnocline were situated at ∼70 m remaining relatively stable along the section as well as MLD.

Wind intensification in the first 24 h (**Figures 1a,c**) strengthened the front that led to a reinforcement of the 19.80°C isotherm, 26.15 kg·m^{-3} isopycnal and 36.77 isohaline, deepening from ∼30 to ∼90 m and spreading from S5 and S6 to S3, S4, and S5 (**Figures 2b,e,h**). A doming of the isopleths associated with the front affected the entire S6. Like at 0 h, w_{GL} field was consistent with the physical structure. Vertical velocities also strengthened at 24 h (**Figure 3b**). Downward velocities were associated with the front-related downwelling whilst upward velocities coupled with isopleths upwelling. Thermocline (pycnocline) reshaped by the downwelling produced by the front, and the upwelling produced by the doming of the isopleths, presenting a vertical zig-zag pattern along the section.

On day 4 (72 h), neither wind intensity nor direction were favorable for front development (**Figures 1b,c**). Indeed, 19.80°C isotherm, 26.15 kg·m^{-3} isopycnal and 36.77 isohaline horizontally crossed the whole section (**Figures 2c,f,i**). Nevertheless, a relative weak zig-zag pattern was still recognizable in the MLD similar to 24 h scenario (upwelling at S5 and S6, downwelling at S3 and S4; **Figures 2b,e,h**); probably a remnant of the thermocline deformation caused by the up- and downwelling fluxes driven by the front the day before. w_{GL} also maintained its bipolar structure between upwelling and downwelling stations above the MLD (**Figure 3c**). Below the isopleth doming observed at S5 and S6, counterpart bowl-shaped structure with negative w_{GL} highlights, both conforming a bipolar lentil-like shaped structure. Thermo and pycnocline were placed at ∼ 40 m at S1, S2, S3, and S4, whilst at ∼100 m at S6 and S7. The

[1]http://www.r-project.org

Shallowest thermo and pycnocline occurred at S5 associated with upwelling motions.

Though satellite-derived data should be used carefully in high-resolution cruises (as is the case) due to their significantly coarse horizontal resolution, a thermo-haline frontal zone is observed crossing through approximately the middle of the sampled section (**Supplementary Figure 1**) supporting our *in situ* observations. SST and SSS data also support the front temporal evolution of the front, showing a moderate intense front is observed at 0 and 24 h (**Supplementary Figures 1A,B**) compared with 72 h (**Supplementary Figure 1D**).

Biogeochemical Features

Nutrients (NO_x^-) present the typical vertical distributions of oligotrophic systems throughout the cruise (**Figures 4a–c**). Low values (<0.5 mmol·m^{-3}) were found at surface waters down to the thermocline, where NO_x^- increased into deeper waters (nitracline), reaching more than 3 mmol·m^{-3} at 150 m. Nevertheless, this typical nutrient distribution is not consistent along the sections. At 0 h (**Figure 4a**), the nutricline did not coincide with the thermocline along the section, being deeper at S3 and S4 (∼120 m) compared with S5, S6, and S7 (∼80 m). Deeper nutricline at S3 and S4 coincides with downward w_{GL} below the MLD while shallower nutricline at S5, S6, and S7 is associated with upward velocities (**Figure 3a**). Highest NO_x^- values were found at S5, S6 and S7 below the MLD and at S3–S4 and S6–S7 above it. Notwithstanding, while high NO_x^- in the first stations seen to be linked to high NO_x^- concentrations below the MLD at S5–S6, high values at S6–S7 are not connected with NO_x^- maximums below the MLD. The most intense upward (positive) F_{NOx} below the MLD (**Table 1**) were observed at S5–S7 (0.039, 0.057, and 0.108 mmol·m^{-2}·d^{-1}, respectively) as well as the nutrient gradients (g_{NOx}). Negative values of g_{NOx} indicates a favorable nutrient gradients for upward fluxes. Comparing NO_x^- and F_{NOx} with the w_{GL} field, it could be observed that the higher values of NO_x^- and F_{NOx} at S5 and S6 were associated with most intense w_{GL} in the MLD as well as that w_{GL} in the MLD at S7 were negative (downward) which may be the reason of the detached high NO_x^- patch observed in the surface waters of S6–S7.

The reshaping of the thermocline (pycnocline) by the reinforcement of the front at 24 h also reshaped the nutricline (**Figure 4b**), which shows the same zig-zag pattern observed in T_q and s_q **Figure 2b**). At S1 and S6, sloping of the isotherms introduced water with concentrations of about 2 mmol·m^{-3} ∼ 40 m above the main thermocline reaching the surface at S6 while deepening of the isopleths at S2–S4 sinks surface waters to ∼ 90 m depth. The both, most intense positive and negative w_{GL} (**Figure 3b**) occurred associated with this isotherm sloping, respectively. The highest F_{NOx} and g_{NOx} were found at S6 and S1 (0.114 mmol·m^{-2}·d^{-1}) while lowest were found at S2–S4 and S7 (**Table 1**). In day four (72 h; **Figure 4c**), the doming of the isopleths below the MLD at S1–S2 and S7 introduced nutrient-richer waters from deeper layers into the bottom of the MLD (**Figure 4b**). Nevertheless, large amounts of NO_x^- inside the ML were observed at S1-S2 and S5 (**Figure 4c**). The highest F_{NOx} and g_{NOx} values right below to the MLD supports the upwelling of nutrients in those stations (**Table 1**), although w_{GL} did not completely agree with NO_x^- and F_{NOx}. Beside NO_x^- distribution suggest that a tongue of nutrient-richer waters outcrop from ∼100 m to about 20 m at S5, upward vertical velocities only dominated on the MLD while downward velocities are presented below the MLD.

TABLE 1 | Values of nutrient gradients (g_{NOx}; mmol·m^{-3}), vertical eddy diffusivity (K_z; m^2·s^{-1}) and nutrient fluxes (F_{NOx}; mmol·m^{-2}·d^{-1}) right below the MLD.

Day	Station	g_{NOx}	K_z	F_{NOx}
0 h	3	−0.117	3.8×10^{-5}	0.013
	4	−0.116	1.71×10^{-5}	0.007
	5	−0.324	3.78×10^{-5}	0.039
	6	−0.429	3.87×10^{-5}	0.057
	7	−0.691	4.69×10^{-5}	0.108
24 h	1	−0.301	3.52×10^{-5}	0.033
	2	−0.120	4.25×10^{-5}	0.013
	3	−0.128	3.19×10^{-5}	0.010
	4	−0.097	1.65×10^{-5}	0.006
	5	−0.270	3.29×10^{-5}	0.031
	6	−0.885	3.72×10^{-5}	0.114
	7	−0.009	3.75×10^{-5}	0.001
72 h	1	−0.422	4.26×10^{-5}	0.066
	2	−0.455	4.13×10^{-5}	0.046
	3	−0.029	3.25×10^{-5}	0.003
	4	0.014	9.11×10^{-5}	−0.004
	5	−0.094	3.75×10^{-5}	0.012
	6	−0.040	3.26×10^{-5}	0.005
	7	−0.707	2.30×10^{-5}	0.056

All values may be found in ***Supplementary Table 1****.*

Similarly, the vertical distribution of Chl *a* follows the characteristic pattern of an oligotrophic system (**Figures 4d–f**), presenting low values (<0.1 mg·m^{-3}) at surface waters, while a DCM was consistently observed over the nitracline. At 0 h (**Figure 4d**), the horizontal distribution of Chl *a* along the section revealed a discontinuity in the DCM between eastern stations (S1, S2, S3, and S4), where a deeper and more intense DCM occurred (0.4–0.5 mg·m^{-3}) and western stations (S5 and S6), as seen in nutricline (**Figure 4a**). This discontinuity became obvious when the front intensified at 24 h (**Figure 4e**). An intense DCM (∼0.6 mg·m^{-3}) due to the front-driven sloping of the isotherms was placed at 40 m at S1 and at ∼150 m at S3 and S4. Relatively high values of Chl *a* were also observed at 24 h in surface waters of S6 and S7, coinciding with nutrient upwelling (**Figure 4b**). In the western stations, the DCM remained centered at 60 m depth. However, a slightly increase in Chl *a* (∼0.45 mg·m^{-3}) coincided with nutrient upwelling in S5. Weakening of the front at 72 h (**Figure 4f**) resulted in an overlap of the two DCM cores at S5 coinciding with the lentil-like shaped structure described in the section above (**Figures 2c,d**).

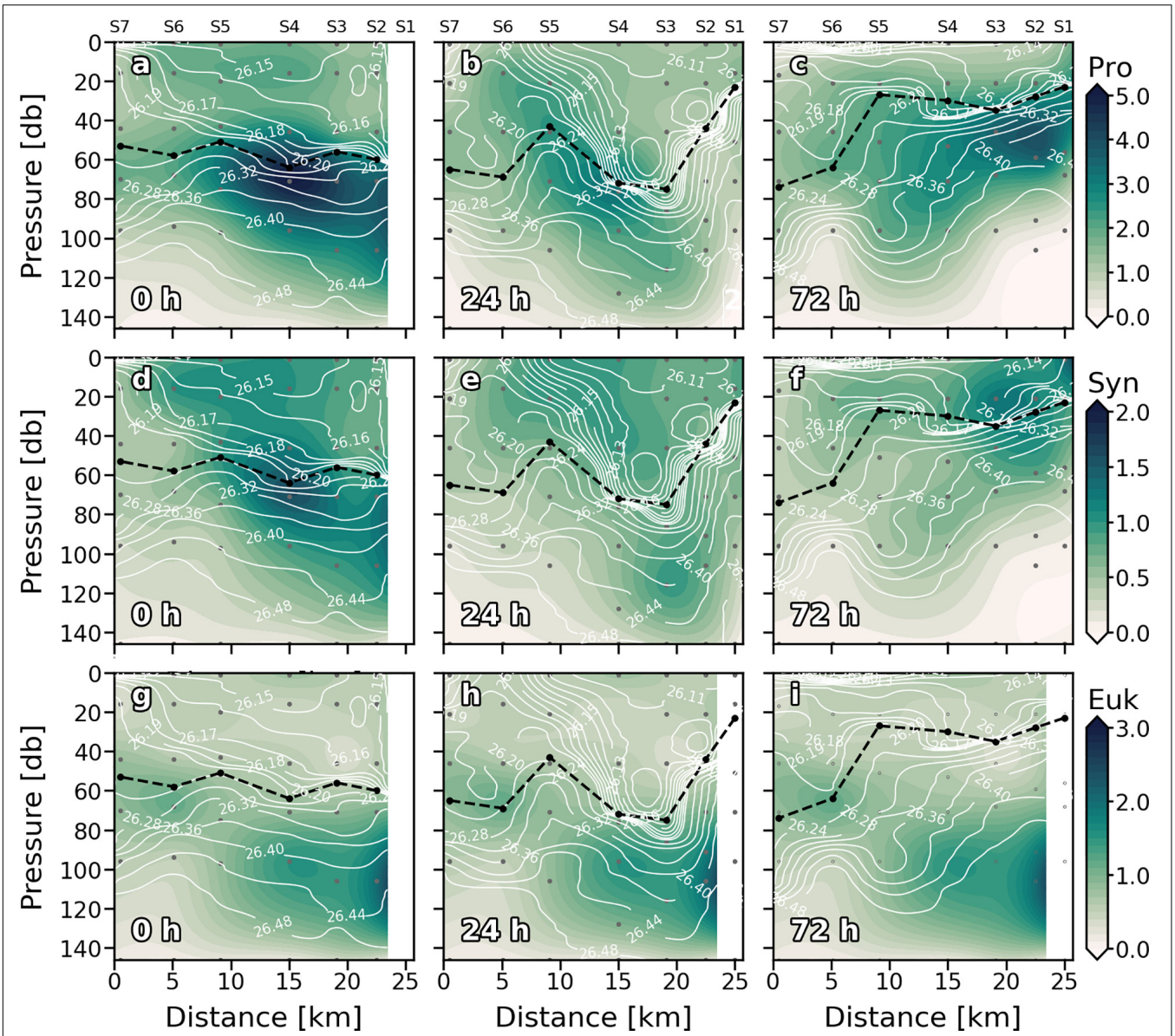

FIGURE 5 | Vertical sections of phytoplankton biomass (mg C·m^{-3}) of *Prochlorococcus* sp. (Pro) **(a–c)**; *Synechococcus* sp. (Syn) **(d–f)** and Eukaryotes (Euk) **(g–i)** for every sampling day. Stations are indicated in the upper part of the plot. Isopycnal field is superimposed as solid white lines. Dashed black line indicates the mixed layer depth. Sampling depths are represented by gray dots.

Picoplankton Distribution and Community Structure

Maximum values of *Prochlorococcus* (Pro) biomass were generally distributed between subsurface waters (>20 m) and just above the DCM throughout the cruise (**Figures 5a–c**). At 0 h (**Figure 5a**), Pro biomass was widely distributed along the section presenting higher values in the MLD of S3, S4, and S5. On the second sampling day (**Figure 5b**), Pro biomass decreased, and the maximum values were associated with upwelling velocities at S4, S5, and S6 (**Figure 3b**). At 72 h (**Figure 5c**), the highest Pro biomass values were found at S2 at 60 m coinciding with positive (upward) w_{GL} and F_{NOx} (**Figure 3c** and **Table 1**). The highest Pro biomass values were consistently placed in nutrient upwelling zones.

Synechococcus (Syn) was generally widely distributed in the well-mixed waters above the thermocline (**Figures 5d–f**). Like Pro, Syn presented its highest biomass at S4 in the first sampling day (**Figure 5d**). At 24 h (**Figure 5e**) the general Syn biomass distribution changed, and high Syn biomass values were found below the thermocline, at the base of the front (∼120 m). Deep high Syn biomass values were also observed on day four (72 h; **Figure 5f**) associated with the downwelling occurred below the MLD at S5. Nevertheless, maximum values at 72 h were found in surface waters of S1 and S2. The distribution of the Euk and

TABLE 2 | Integrated biomass (mg C·m-2) between surface and 150 m depth of Eukaryotes (Euk), *Prochlorococcus* sp. (Pro) and *Synechococcus* sp. (Syn) for the three sampling days (0, 24, and 48 h) and for every station.

Station	0 h			24 h			72 h		
	Euk	*Pro*	*Syn*	*Euk*	*Pro*	*Syn*	*Euk*	*Pro*	*Syn*
1				73.60	107.20	62.33	55.87	168.05	63.11
2	162.19	350.75	134.90	119.36	117.14	71.48	80.69	209.60	73.02
3	112.82	324.36	121.75	90.82	213.89	111.08	85.67	219.19	85.54
4	115.44	394.43	142.35	70.79	267.73	100.08	126.79	250.77	75.48
5	88.29	245.33	91.97	87.65	235.60	74.18	87.11	229.61	64.97
6	84.31	196.21	71.29	91.91	187.65	64.70	58.86	146.51	50.88
7	78.18	146.87	49.74	69.87	106.63	37.49	71.45	133.94	39.95

the DCM resembled throughout the first 24 h (**Figures 5g,h**). At 72 h the relationship between Euk and DCM distribution was observed along S4–S7, while maximum values of Euk biomass were found below the DCM (MLD) in S1–S3 breaking with the observed general pattern (**Figure 5i**).

Water column integrated biomass values are compiled in **Table 2**. At 0 h, all picoplankton groups present higher integrated biomass in the eastern stations, showing Cyanobacteria group differences of up to 3-fold between both ends of the section (S2 and S7). Differences of up to 2-fold between S4 and S6 separated by ∼10 km in Cyanobacteria's biomass can be observed. Pro is the major contributor to picoplankton community biomass along the section at 0 h (56.59 ± 2.64%), while Syn and Euk show similar contributions to total biomass (22.68 ± 3.88% and 20.73 ± 1.43%, respectively; **Figure 6a**). With the enhancement of the front on day two (24 h) the highest Cyanobacteria biomasses are observed at the front-associated stations (S3–S5) while both ends of the section show similar values (**Table 2**). Nevertheless, differences are not as high as at 0 h. Euk presents a consistent integrated biomass along the section at 24 h. Pro still is the major contributor to the total biomass (51.32 ± 7.88%) except in S2 where Euk and Pro show similar contribution rates (38.81% and 38.04%, respectively; **Figure 6b**). At 72 h, both Syn and Euk present similar integrated values among the stations. Pro keeps showing higher values in front-affected stations (S2–S5) as well as in the major contribution percentages to total biomass (48.16 ± 2.51%; **Figure 6c**).

Front Effects Over the Community Structure

Metric Multidimensional Scaling Analysis sorts stations according to differences in picoplankton community structure. Therefore, closer stations present similar picoplankton community assemblages and *vice versa*. At 0 h, three stations groups were obtained from K-means clustering method (**Figure 7A**): (1) S2, S3, and S4 where front-driven up motions occurred; (2) S5 and S6, that were situated at the western boundary of the front; and (3) S7, the farthest from the front. At 24 h (**Figure 7B**), three groups were also observed: (1) S1, S2, and S7, that represent the eastern and western boundaries of the front; (2) S3, S4, and S5 situated at the upwelling front; and (3) S6, where the upwelling front occurs. The vanishing of the front at 72 h also lead to the vanishing of community structure heterogeneity and no significant differences were observed among station in community structure (**Figure 7C**). The selection of three groups at 0 h and 24 h was supported by high BSS/TSS ratio (91.7% and 85.1%, respectively). At 72 h the BSS/TSS ratio is not displayed since there were no differences among stations.

Spatial vs. Temporal Variability

The contributions of every source of variability to total variance are compiled in **Table 3**. Depending on the phytoplankton group, two behaviors may be observed in the entire water column. Cyanobacteria-like Pro and Syn present higher space variability (i.e., among station in the same day), while Euk presents higher temporal variability. This pattern is not observed in the DCM, where all phytoplankton groups show higher temporal than spatial variability. Inside the mixed layer, phytoplankton groups present almost equally spatiotemporal variability. Chl *a* shows higher temporal variability in all cases.

DISCUSSION

Wind Forcing Frontogenesis

Oceanic fronts originated south of Gran Canaria in the area of eddy formation at the wind shear flanks were reported in earlier studies describing the eddy field in the region (Arístegui et al., 1994, 1997; Barton et al., 1998). Later, Barton et al. (2000) and Basterretxea et al. (2002), in more front-focused studies, suggested a potential mechanism for their development. They observed that wind velocities dropped down up to one order of magnitude at the lee region of the island with respect to a station placed in the wind exposed region ∼2 km apart. As a consequence, net westward Ekman transport in the lee region would be practically absent, favoring the convergence (divergence) of water in the eastern (western) side of the wake and its subsequent downwelling (upwelling).

The data presented here fit the Barton et al. (2000) and Basterretxea et al. (2002)'s spatial wind field observations (**Figures 1a,b**) but they also indicate a positive temporal relationship between wind speed and front intensity. During the first 48 h, the increase in down-front blowing winds (**Figure 1c**) strengthened the front signal as seen in T_q, s_q, and S plots (**Figures 2a,b,d,e,g,h**). Conversely, the change in wind direction at 72 h (up-front winds) caused the vanishing of the front signal and the increase in water column stratification, as suggested by the shallowest MLD (**Figures 2c,f,i**). This agrees with the nonlinear Ekman effect theory for frontogenesis of Thomas and Lee (2005), that proposes that winds blowing in the direction of the geostrophic flow generate an Ekman flux that tends to advect colder water from one side of the front over warmer water from the other side, enhancing convective mixing and, thus, strengthening the front. ASC-related upwelling in the warm side of the front and downwelling in the cold side would be triggered as consequence of convective mixing (Nagai et al.,

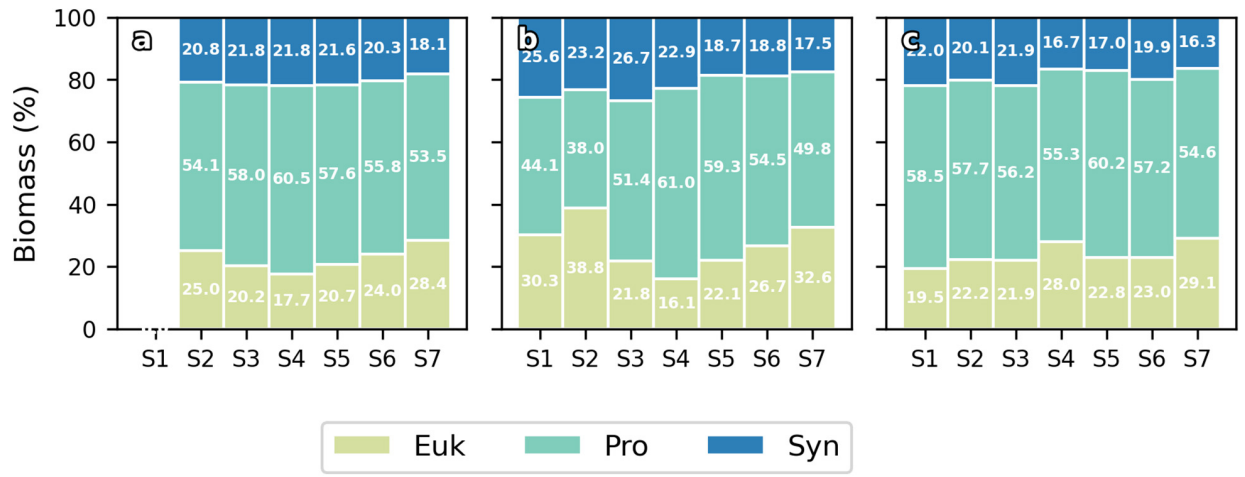

FIGURE 6 | Bar plots of contribution (%) of Eukaryotes (Euk), *Prochlorococcus sp.* (Pro) and *Synechococcus sp*. (Syn) to total integrated biomass at 0 h **(a)**, 24 h **(b)**, and 72 h **(c)** for every station.

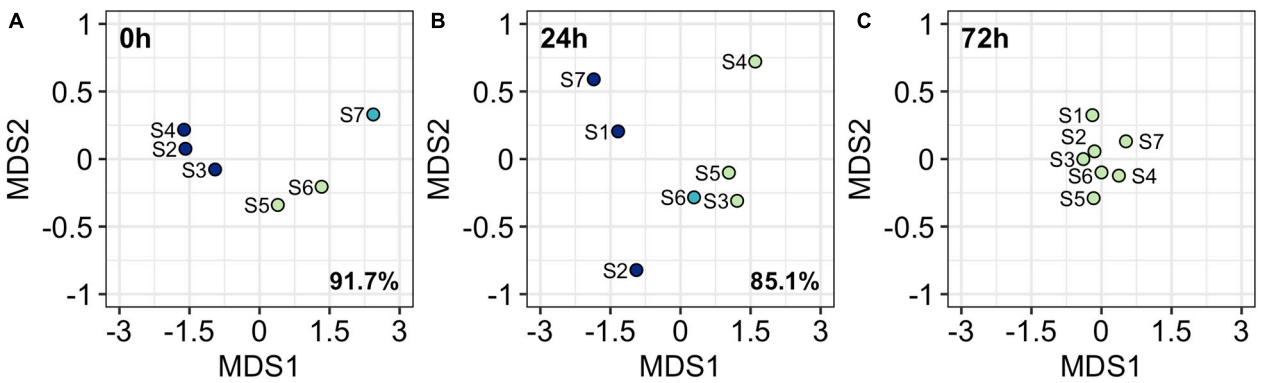

FIGURE 7 | Metric Dimensional Scaling analysis (MDS) ordination plots at 0 h **(A)**, 24 h **(B)**, and 72 h **(C)**. Colors refer to K-mean clustering results. Percentage refers to the BSS/TSS ratio. No BSS/TSS ratio is reported at 72 h since stations are grouped in only one cluster.

TABLE 3 | Percentage of total variance for each source of variability: Distance among stations (Space), daily variability (Time), and the inner variability (Within) for Eukaryotes (Euk), *Prochlorococcus* sp. (Pro), *Synechococcus* sp. (Syn), and Chlorophyll *a* (Chl *a*).

	Water column			DCM			ML		
	Space	**Time**	**Within**	**Space**	**Time**	**Within**	**Space**	**Time**	**Within**
Euk	26.54	64.08	9.38	18.36	72.23	9.41	43.25	48.22	8.53
Pro	68.56	25.32	6.12	17.04	73.62	9.34	51.54	40.58	7.88
Syn	56.63	35.96	7.41	38.69	52.47	8.84	47.78	44.02	8.20
Chl a	<0.01	99.99	<0.01	<0.01	99.99	<0.01	25.53	65.07	9.40

Statistical analysis was carried out for integrated biomass values in the whole water column (0–150 m), for the deep chlorophyll maximum (DCM) and for the mixed layer (ML). Variances were extracted from Variance Component Analysis (VCA).

2006; Pallàs-Sanz et al., 2010). By contrast, winds blowing against geostrophic flow generate the advection of warmer water over colder water favoring vertical stratification and, hence, the weakening of the front (frontolisis). This theory has been later sustained by several modeling and numerical studies (Thomas, 2005; Thomas and Lee, 2005; Thomas and Ferrari, 2008; Mahadevan et al., 2010).

The bipolar structure (upwelling/downwelling; warm/cold) described by the nonlinear Ekman effect theory agrees with the physical structure clearly shown in **Figures 2b**, **3b**. A steep deepening of the isotherm in S2–S4 sinks water in the cold side of the front while doming of the isotherm in S5 and S6 entrained deep waters in the warm side suggesting downwelling and upwelling motions, respectively. This is supported by downward

and upward w_{GL} coinciding with S2–S4 and S5 and S6. At 0 h, only the upwelling side of the front is observed (**Figures 2a**, **3a**), being characterized by a less intense doming of the isotherm in the warm side (S2–S4) compared to the one observed at 24 h. Notwithstanding, positive w_{GL} were also observed at these stations, coinciding with 24 h observations.

Effects of Frontal Dynamics Over Nutrient Distribution

Subtropical oligotrophic areas such as the Canary region are characterized by a well sun light illuminated mixed layer throughout the year, with very low inorganic nutrient concentrations (Levitus et al., 1993) due to the presence of a strong almost permanent thermocline that prevents the outcrop of deeper nutrient-rich waters into the euphotic zone (León and Braun, 1973). It has been suggested that ASC associated with submesoscale fronts may locally alleviate nutrient shortage in oligotrophic surface waters by driving vertical nutrient fluxes into the ML (Mahadevan and Tandon, 2006; Lévy et al., 2012a; Estrada-Allis et al., 2019).

In the present case, the canonical oligotrophic nutrient distribution was broken by high nutrient concentrations that outcropped trough the thermocline into the ML in S4 and S3 at 0 h; S6 at 24 h, and S5 at 72 h (**Figures 4a–c**). In all cases, nutrient intrusions were associated with isopleths doming driven by front-associated upwelling, where positive (upward) w_{GL} and F_{NOx} near the MLD occurred. Though small, the upward fluxes are consistent with other observations in areas of intense mesoscale and submesoscale activity (Arcos-Pulido et al., 2014; Corredor-Acosta et al., 2020). The overlapping of positive w_{GL} with F_{NOx} suggests that diapycnal mixing is acting as an important contributor to the vertical velocity (Ponte et al., 2013) and may be associated with submesoscale process (Estrada-Allis et al., 2019). In summary, upward movements at each side of the front favors the injection of NO_x into the euphotic layer as well as downward motions deepens the nutricline impoverishing the ML, supporting earlier theoretical studies (Lévy et al., 2018 and reference therein).

Does Frontal Dynamics Modulate Picoplankton Distribution and Community Structure?

The picoplankton distribution presented here (see **Figure 5**) largely corroborates the commonly reported distribution described for each group in the region (e.g., Baltar et al., 2009). Syn was abundant in the well-mixed surface layers (Mackey et al., 2013; Grébert et al., 2018), whereas higher amounts of Pro were present in deeper layers (Bouman et al., 2006; Johnson et al., 2006; Biller et al., 2015). Euk were the main contributors to DCM laying close to the nitracline, suggesting that they require higher inorganic nutrients concentrations than prokaryotic phytoplankton for their growth (Painter et al., 2014). Nonetheless, these general distributions were eventually modified by frontal dynamics.

For instance, we observed high Syn concentrations at ∼150 m depth at 24 h coinciding with the downwelling branch of the front. This distribution agrees with the subduction of phytoplankton by submesoscale front-associated downwelling as proposed by several authors (Lévy et al., 2001, 2012a, 2018). Whether the front-driven enlargement of the mixed layer at this station was responsible for the Syn distribution observed or, by contrast, Syn cells found at these depths were dragged from surface waters due to front intensification, is difficult to discern, although front dynamics seem to be behind the distribution patterns in both cases. High Euk biomass at 72 h found below the DCM and the MLD of S1, S2, and S3, is another example of how frontal dynamics subducts phytoplankton biomass. In this case, the high Euk biomass patch appears to be a leftover from the intense DCM observed at 24 h, which has been left out the ML due to frontolisis restratification.

One of the most striking exceptions to the usually reported picoplankton distribution is observed in Pro. The fact that high Pro biomass patches consistently coincided with high nutrient concentrations (**Figures 3a–c**, **4a–c**) differs from the distribution patterns previously reported in the literature. Due to their high nutrient diffusion per unit of cell volume (Raven, 1998; Marañón, 2015) and their capacity of uptake dissolved organic matter (DOC) for growth (Berman and Bronk, 2003; Mulholland and Lee, 2009; Znachor and Nedoma, 2010; Duhamel et al., 2018; osmotrophy), Pro inorganic nutrient requirements are low and thus, they usually present higher abundances in nutrient-poor zones (Bouman et al., 2006; Johnson et al., 2006; Biller et al., 2015). Indeed, several studies have reported low Pro abundances related to eddy-driven nutrient upwelling in the region along with high Pro biomass associated with high dissolved organic matter concentrations (Baltar et al., 2009; Hernández-Hernández et al., 2020). Maximum DOC concentrations along the cruise (not shown here) also coincided with Pro biomass peaks. For these reasons, we considered that Pro and NO_x^- maximums resemblance seems to be a coincidence rather than a causality, and that front-driven accumulation of DOC would be the reason of high abundances of Pro at nutrient upwelling stations.

Besides the general distribution, the data presented in **Figure 5** reveal high biomass patches for every picoplankton group. Several authors have reported local increases of different phytoplankton size groups across frontal zones due to the input of nutrients in a constrained zone, which usually favors the growth of large cells such as diatoms (Abraham, 1998; Rivière and Pondaven, 2006; Mahadevan et al., 2012). D'Ovidio et al. (2010) observed that phytoplankton is organized in submesoscale patches of dominant types separated by physical barriers. Our data reflect two main differences with respect to the studies mentioned above: (1) previous works observed that patches were dominated by different phytoplankton size-groups (i.e., pico, nano, or microplankton; Abraham, 1998; Rivière and Pondaven, 2006; D'Ovidio et al., 2010; Mahadevan et al., 2012), while we observed that patchiness also occurs within the same size-group. This finding raises the question of at what level of organization patchiness actually works. (2) They observed high biomass patches related with local nutrient injection (Abraham, 1998; Rivière and Pondaven, 2006; D'Ovidio et al., 2010; Mahadevan et al., 2012). In our study, by contrast, only Pro high abundance spots are related to high

nutrient concentrations albeit this is probably not due to a causality, as we explained above. While it is true that we only report picoplankton data, the occurrence of these non-nutrient related "hotspots" of high picoplankton biomass suggests that submesoscale dynamics modulates both the hydrographic and biogeochemical fields, favoring the local growth of some groups against others. It is known that although picoplankton groups generally co-occur in subtropical oceans, they present different nutrient requirements, light harvesting, different temperature or physical forcing acclimation (Moore et al., 2002; Scanlan et al., 2009; Mella-Flores et al., 2012; Flombaum et al., 2013; Otero-Ferrer et al., 2018). Therefore, picoplankton groups' distribution across a submesoscale front would be expected to be affected by the front-generated physical and biogeochemical variability (Lévy et al., 2018 and references therein).

A relevant result of our study is the modulation of the picoplankton community structure by the front. Phytoplankton community assemblages were strongly structured in the MDS ordination space in accordance with the frontal structure (**Figure 7**). Few studies have reported the variability in phytoplankton community structures across a frontal systems at submesoscale level (e.g., Taylor et al., 2012; Clayton et al., 2014; Mousing et al., 2016). In all of these studies, different assemblages were observed; at each side of the front and within the front, as the result of the separation of two well-defined water masses and hence two different biomes, with two different communities. Conversely, we observed that picoplankton communities were not separated by the front but showed a mirror-like distribution with respect to the middle of the front. While observations from previously cited authors suggest that fronts work like a physical barrier for different niches, our results suggest that frontal dynamics modulates the phytoplankton community structure. However, it should be noted that while fronts reported by the authors mentioned above were permanent features that separate different water masses, we sampled an ephemeral front that is originated inside the same water mass (Lévy et al., 2018).

Due to section proximity to the coast, tidal forcing was initially considered as another potential driver for the observed picophytoplankton variability. Sangrá et al. (2001) studied the effect of internal waves on Chl *a* in the shelf break of the lee region of Gran Canaria during a spring and a neap tide. They reported an increase in Chl *a* of up to 47% during some pulses of the spring tide from a station situated over the shelf (100 m depth). Notwithstanding, depth integrated Chl a values presented little differences between samplings. Since our section was situated on the 2,000 m isobath (i.e., the island slope), the cruise took place during a full neap tide, and phytoplankton biomass increases were significantly larger than those reported by Sangrá et al. (2001), we considered that the tidal forcing effects if any, they would be negligible compare to front-related effects.

Spatiotemporal Variability

In an earlier study, Martin et al. (2005) observed higher variability in picoplankton community biomass at mesoscale ranges than in the normally used large-scale ranges, arguing that sampling should be done at smaller scales to avoid inaccurate plankton distributions. The integrated biomass data presented here (**Table 2**) reveal that picoplankton biomass varies between 2 and 3-fold on spatial scales of $\sim$ 2.5 km, and temporal scales of $\sim$ 24 h. This variability is comparable to the picoplankton biomass seasonality reported for the region (Zubkov et al., 2000b; Baltar et al., 2009).

In order to assess which source of variability was dominant, we compared the temporal and spatial variances observed during our study (**Table 2**). We found that picoplankton biomass variance is almost equally shared between time and space in the mixed layer, while it mostly depends on time in the DCM, i.e., in the front reported here, picoplankton biomass temporal variability is just as important as, or even more important than spatial variability. Although the front is constrained to a marginal part of the Canary Current region, mesoscale processes and associated submesoscale motions, are ubiquitous around the global ocean (Chelton et al., 2007, 2011). Therefore, our results beg to question whether oceanographic samplings in regions of high mesoscale activity should be designed considering submesoscale spatiotemporal resolutions, in order to gain a more accurate approximation of the biogeochemical fields variability in the region of study.

CONCLUSION

The spatiotemporal development and decay of the convergent wind-driven submesoscale front south of Gran Canaria, as well as their effects on picoplankton community structure and distribution, is reported for the first time through *in situ* measurements. Like in earlier studies in the region (Barton et al., 2000; Basterretxea et al., 2002), our data shows a positive relationship between wind and front development and intensity. Upward diapycnal nutrient flux occurs near the mixed layer of the stations located on the front. This diapycnal mixing was implicated in the observed enhancement of nutrients and chlorophyll in the upper layer advected by positive vertical velocities based on the scaling of Garret and Loder (1981). Conversely, picophytoplankton biomass subduction is also reported. The present study is consistent with model outputs and past predictions, supporting that submesoscale fronts may drive nutrient fluxes into the euphotic layer and subduct picoplankton biomass below it (Mahadevan and Archer, 2000; Lévy et al., 2001, 2012a).

On the other hand, our results also provide new insights in front formation and erosion, pointing out to nonlinear Ekman effects as a potential driver of front dynamics, and their effects on picoplankton community structure. The front favors the patch formation of different picoplankton groups' dominance and modulates the picoplankton community structure. Temporal variability was found to be a significant source of error in phytoplankton variability providing evidence that, at least in regions of high hydrographic variability, plankton, as well as other biogeochemical features, must be sampled at shorter spatial and temporal resolutions than regularly done in order to obtain more accurate datasets. Although daily repeated cruises are in many cases economically unviable and time-consuming, submesoscale measurements would help to get more accurate regional and long-term interpretation of biogeochemical fluxes.

It is worth mentioning that the physical results presented in this study are constrained by the spatiotemporal scales of the survey and the lack of horizontal velocities. However, validated parameterizations and solid scaling of the vertical velocity formulations, allow us to provide a first approximation of submesoscale and diapycnal mixing impact on the biological system in the leeward side of Gran Canaria Island.

DATA AVAILABILITY STATEMENT

The data sets generated for this study are available on request to the corresponding author.

AUTHOR CONTRIBUTIONS

JA conceived and designed the cruise. NH-H, YS-F, and JA carried out the sampling and data analyses. SE-A contributed to the analysis of the physical data. NH-H wrote the manuscript with inputs from all authors. All authors contributed to the article and approved the submitted version.

FUNDING

This work is a contribution to the projects PUMP (CTM2012-33355), FLUXES (CTM2015-69392-C3-1-R), and e-IMPACT (PID2019-109084RB-C2) from the Spanish "Plan Nacional de I+D," co-funded with FEDER funds, and project TRIATLAS (AMD-817578-5) from the European Union's Horizon 2020 Research and Innovation Program. NH-H was supported by a grant (TESIS2015010036) of the Agencia Canaria de Investigación, Innovación y Sociedad de la Información (ACIISI).

ACKNOWLEDGMENTS

We thank to the members of the Biological Oceanography group (GOB-IOCAG) for their help with the analysis of the samples, and Laura Marín for reviewing the English grammar.

SUPPLEMENTARY MATERIAL

The Supplementary Material for this article can be found online at: https://www.frontiersin.org/articles/10.3389/fmars.2021.592703/full#supplementary-material

Supplementary Figure 1 | Sea surface temperature (°C) time series for **(A)** May 09th 2011 (0 h), **(B)** May 10th 2011 (24 h), **(C)** May 11th 2011 (48 h), and **(D)** May 12th 2011 (72 h). Salinity contours are superimposed to SST maps. Black dots with red borders indicate stations positions. Red dot indicates Gando airport location.

Supplementary Figure 2 | Vertical sections of Turner angles (T_U; °) for 0 h **(A)**, 24 h **(B)**, and 72 h **(C)**. Stations are indicated in the upper part of the plot. Dashed black line indicates the mixed layer depth. Sampling depths are represented by gray dots. Angles between −90 and −45 are characteristic of diffusive mode; between −45° and 45° is called doubly stable mode; weak salt fingers mode from 45° to 70° and salt finger mode for angles larger than 70.

Supplementary Table 1 | Values of nutrient gradients (g_{NOx}; $mmol \cdot m^{-4}$), vertical eddy diffusivity (K_z; $m^2 \cdot s^{-1}$), nutrient fluxes (F_{NOx}; $mmol \cdot m^{-2} \cdot d^{-1}$) below the MLD for all sampled depths.

REFERENCES

Abraham, E. R. (1998). The generation of plankton patchiness by turbulent stirring. *Nature* 391, 577–581. doi: 10.1038/35361

Allen, J. T., Brown, L., Sanders, R., Moore, C. M., Mustard, A., Fielding, S., et al. (2005). Diatom carbon export enhanced by silicate upwelling in the northeast Atlantic. *Nature* 437, 728–732. doi: 10.1038/nature03948

Arcos-Pulido, M., Rodríguez-Santana, A., Emelianov, M., Paka, V., Arístegui, J., Benavides, M., et al. (2014). Diapycnal nutrient fluxes on the northern boundary of Cape Ghir upwelling region. *Deep. Res. Part I Oceanogr. Res. Pap.* 84, 100–109. doi: 10.1016/j.dsr.2013.10.010

Arístegui, J., Barton, E. D., Álvarez-Salgado, X. A., Santos, A. M. P., Figueiras, F. G., Kifani, S., et al. (2009). Sub-regional ecosystem variability in the Canary Current upwelling. *Prog. Oceanogr.* 83, 33–48. doi: 10.1016/j.pocean.2009.07.031

Arístegui, J., Sangrá, P., Hernández-León, S., Cantón, M., Hernández-Guerra, A., and Kerling, J. L. (1994). Island-induced eddies in the Canary islands. *Deep. Res. Part I* 41, 1509–1525. doi: 10.1016/0967-0637(94)90058-2

Arístegui, J., Tett, P., Hernández-Guerra, A., Basterretxea, G., Montero, M. F., Wild, K., et al. (1997). The influence of island-generated eddies on chlorophyll distribution: a study of mesoscale variation around Gran Canaria. *Deep. Res. Part I Oceanogr. Res. Pap.* 44, 71–96. doi: 10.1016/S0967-0637(96)00093-3

Baltar, F., Arístegui, J., Montero, M. F., Espino, M., Gasol, J. M., and Herndl, G. J. (2009). Mesoscale variability modulates seasonal changes in the trophic structure of nano- and picoplankton communities across the NW Africa-Canary Islands transition zone. *Prog. Oceanogr.* 83, 180–188. doi: 10.1016/j.pocean.2009.07.016

Barton, E. D., Aristegui, J., Tett, P., Canton, M., García-Braun, J., Hernández-León, S., et al. (1998). The transition zone of the Canary Current upwelling region. *Prog. Oceanogr.* 41, 455–504. doi: 10.1016/S0079-6611(98)00023-8

Barton, E. D., Basterretxea, G., Flament, P., Mitchelson-jacob, E. G., Jones, B., Arístegui, J., et al. (2000). Lee region of Gran Canaria. *J. Geophys. Res.* 105, 173–193.

Basterretxea, G., Barton, E. D., Tett, P., Sangrá, P., Navarro-Perez, E., and Arístegui, J. (2002). Eddy and deep chlorophyl maximum response to wind-shear in the lee of Gran Canaria. *Deep. Res. Part I Oceanogr. Res. Pap.* 49, 1087–1101. doi: 10.1016/S0967-0637(02)00009-2

Berman, T., and Bronk, D. A. (2003). Dissolved organic nitrogen: a dynamic participant in aquatic ecosystems. *Aquat. Microb. Ecol.* 31, 279–305. doi: 10.3354/ame031279

Biller, S. J., Berube, P. M., Lindell, D., and Chisholm, S. W. (2015). Prochlorococcus: the structure and function of collective diversity. *Nat. Rev. Microbiol.* 13, 13–27. doi: 10.1038/nrmicro3378

Bouman, H. A., Ulloa, O., Scanlan, D. J., Zwirglmaier, K., Li, W. K. W., Platt, T., et al. (2006). Oceanographic basis of the global surface distribution of *Prochlorococcus ecotypes*. *Science* 312, 918–921. doi: 10.1126/science.1122692

Capet, X., McWilliams, J. C., Molemaker, M. J., and Shchepetkin, A. F. (2008). Mesoscale to submesoscale transition in the California Current system. Part II: frontal processes. *J. Phys. Oceanogr.* 38, 44–64. doi: 10.1175/2007JPO3672.1

Chelton, D. B., Schlax, M. G., and Samelson, R. M. (2011). Global observations of nonlinear mesoscale eddies. *Prog. Oceanogr.* 91, 167–216. doi: 10.1016/j.pocean.2011.01.002

Chelton, D. B., Schlax, M. G., Samelson, R. M., and de Szoeke, R. A. (2007). Global observations of large oceanic eddies. *Geophys. Res. Lett.* 34, 1–5. doi: 10.1029/2007GL030812

Clayton, S., Nagai, T., and Follows, M. J. (2014). Fine scale phytoplankton community structure across the Kuroshio Front. *J. Plankton Res.* 36, 1017–1030. doi: 10.1093/plankt/fbu020

Corredor-Acosta, A., Morales, C. E., Rodríguez-Santana, A., Anabalón, V., Valencia, L. P., and Hormazabal, S. (2020). The influence of diapycnal nutrient fluxes on phytoplankton size distribution in an area of intense mesoscale and submesoscale activity off Concepción, Chile. *J. Geophys. Res. Ocean* 125:e2019JC015539. doi: 10.1029/2019JC015539

Cotti-Rausch, B. E., Lomas, M. W., Lachenmyer, E. M., Goldman, E. A., Bell, D. W., Goldberg, S. R., et al. (2016). Mesoscale and sub-mesoscale variability in phytoplankton community composition in the Sargasso Sea. *Deep. Res. Part I Oceanogr. Res. Pap.* 110, 106–122. doi: 10.1016/j.dsr.2015.11.008

D'Asaro, E., Lee, C., Rainville, L., Harcourt, R., and Thomas, L. (2011). Enhanced turbulence and energy dissipation at ocean fronts. *Science* 332, 318–322. doi: 10.1126/science.1201515

de Boyer Montégut, C., Madec, G., Fischer, A. S., Lazar, A., and Iudicone, D. (2004). Mixed layer depth over the global ocean: an examination of profile data and a profile-based climatology. *J. Geophys. Res. C Ocean.* 109, 1–20. doi: 10.1029/2004JC002378

D'Ovidio, F., De Monte, S., Alvain, S., Dandonneau, Y., and Lévy, M. (2010). Fluid dynamical niches of phytoplankton types. *Proc. Natl. Acad. Sci. U.S.A.* 107, 18366–18370. doi: 10.1073/pnas.1004620107

Duhamel, S., Van Wambeke, F., Lefevre, D., Benavides, M., and Bonnet, S. (2018). Mixotrophic metabolism by natural communities of unicellular cyanobacteria in the western tropical South Pacific Ocean. *Environ. Microbiol.* 20, 2743–2756. doi: 10.1111/1462-2920.14111

Estrada-Allis, S. N., Barceló-Llull, B., Pallàs-Sanz, E., Rodríguez-Santana, A., Souza, J. M. A. C., Mason, E., et al. (2019). Vertical velocity dynamics and mixing in an anticyclone near the Canary Islands. *J. Phys. Oceanogr.* 49, 431–451. doi: 10.1175/JPO-D-17-0156.1

Falkowski, P. G., Ziemann, D., Kolber, Z., and Bienfang, P. K. (1991). Role of eddy pumping in enhancing primary production in the ocean. *Nature* 352, 55–58. doi: 10.1038/352055a0

Flombaum, P., Gallegos, J. L., Gordillo, R. A., Rincón, J., Zabala, L. L., Jiao, N., et al. (2013). Present and future global distributions of the marine Cyanobacteria *Prochlorococcus* and *Synechococcus*. *Proc. Natl. Acad. Sci. U.S.A.* 110, 9824–9829. doi: 10.1073/pnas.1307701110

Garret, C. J. R., and Loder, J. W. (1981). Dynamical aspects of shallow sea fronts. *Philos. Trans. R. Soc. Lond. Ser. A Math. Phys. Sci.* 302, 563–581. doi: 10.1098/rsta.1981.0183

Grébert, T., Doré, H., Partensky, F., Farrant, G. K., Boss, E. S., Picheral, M., et al. (2018). Light color acclimation is a key process in the global ocean distribution of Synechococcus cyanobacteria. *Proc. Natl. Acad. Sci. U.S.A.* 115, E2010–E2019. doi: 10.1073/pnas.1717069115

Gula, J., Molemaker, J. J., and Mcwilliams, J. C. (2014). Submesoscale cold filaments in the Gulf Stream. *J. Phys. Oceanogr.* 44, 2617–2643. doi: 10.1175/JPO-D-14-0029.1

Hansen, H. P., and Koroleff, F. (1999). "Determination of nutrients," in *Methods of Seawater Analysis*, eds K. Grasshoff, K. Kremling, and M. Ehrhardt (Weinheim: Wiley-VCH), 159–228. doi: 10.1002/9783527613984.ch10

Hernández-Hernández, N., Arístegui, J., Montero, M. F., Velasco-Senovilla, E., Baltar, F., Marrero-Díaz, Á, et al. (2020). Drivers of Plankton distribution across mesoscale eddies at submesoscale range. *Front. Mar. Sci.* 7:667. doi: 10.3389/fmars.2020.00667

Holm-Hansen, O., Lorenzen, C. J., Holmes, R. W., and Strickland, D. H. (1965). Fluorometric determination of chlorophyll. *J. Cons. perm. int. Explor. Mer* 30, 3–15. doi: 10.1093/icesjms/30.1.3

Hosegood, P. J., Nightingale, P. D., Rees, A. P., Widdicombe, C. E., Woodward, E. M. S., Clark, D. R., et al. (2017). Nutrient pumping by submesoscale circulations in the mauritanian upwelling system. *Prog. Oceanogr.* 159, 223–236. doi: 10.1016/j.pocean.2017.10.004

Hoskins, B. J., and Bretherton, F. P. (1972). Atmospheric frontogenesis models: mathematical formulation and solution. *J. Atmos. Sci.* 29, 11–37. doi: 10.1175/1520-0469(1972)029<0011:afmmfa>2.0.co;2

Hoskins, J. B. (1982). The mathematical theory of frontogenesis. *Annu. Rev. Fluid Mech.* 14, 131–151. doi: 10.1146/annurev.fl.14.010182.001023

Inoue, R., Yamazaki, H., Wolk, F., Kono, T., and Yoshida, J. (2007). An estimation of buoyancy flux for a mixture of turbulence and double diffusion. *J. Phys. Oceanogr.* 37, 611–624. doi: 10.1175/JPO2996.1

Johnson, K. S., Riser, S. C., and Karl, D. M. (2010). Nitrate supply from deep to near-surface waters of the North Pacific subtropical gyre. *Nature* 465, 1062–1065. doi: 10.1038/nature09170

Johnson, Z. I., Zinser, E. R., Coe, A., Mcnulty, N. P., Malcolm, E., Woodward, S., et al. (2006). Niche partitioning among ocean-scale environmental gradients *Prochlorococcus* ecotypes along. *Science* 311, 1737–1740. doi: 10.1126/science.1118052

Klein, P., and Lapeyre, G. (2009). The oceanic vertical pump induced by mesoscale and submesoscale turbulence. *Ann. Rev. Mar. Sci.* 1, 351–375. doi: 10.1146/annurev.marine.010908.163704

Lathuiliere, C., Levy, M., and Echevin, V. (2011). Impact of eddy-driven vertical fluxes on phytoplankton abundance in the euphotic layer. *J. Plankton Res.* 33, 827–831. doi: 10.1093/plankt/fbq131

Lehahn, Y., Koren, I., Sharoni, S., D'Ovidio, F., Vardi, A., and Boss, E. (2017). Dispersion/dilution enhances phytoplankton blooms in low-nutrient waters. *Nat. Commun.* 8, 1–8. doi: 10.1038/ncomms14868

León, A. R., and Braun, J. G. (1973). Ciclo anual de la producción primaria y su relación con los nutrientes en aguas Canarias. *Bol. Inst. Esp. Ocean.* 167, 1–24. doi: 10.12795/ie.2017.i90.01

Levitus, S., Conkright, M. E., Reid, J. L., Najjar, R. G., and Mantyla, A. (1993). Distribution of nitrate, phosphate and silicate in the world oceans. *Prog. Oceanogr.* 31, 245–273. doi: 10.1016/0079-6611(93)90003-V

Lévy, M., Ferrari, R., Franks, P. J. S., Martin, A. P., and Rivière, P. (2012a). Bringing physics to life at the submesoscale. *Geophys. Res. Lett.* 39, 1–14. doi: 10.1029/2012GL052756

Lévy, M., Franks, P. J. S., and Smith, K. S. (2018). The role of submesoscale currents in structuring marine ecosystems. *Nat. Commun.* 9:4758. doi: 10.1038/s41467-018-07059-3

Lévy, M., Iovino, D., Resplandy, L., Klein, P., Madec, G., Tréguier, A. M., et al. (2012b). Large-scale impacts of submesoscale dynamics on phytoplankton: local and remote effects. *Ocean Model.* 43–44, 77–93. doi: 10.1016/j.ocemod.2011.12.003

Lévy, M., and Klein, P. (2004). Does the low frequency variability of mesoscale dynamics explain a part of the phytoplankton and zooplankton spectral variability? *Proc. R. Soc. A Math. Phys. Eng. Sci.* 460, 1673–1687. doi: 10.1098/rspa.2003.1219

Lévy, M., Klein, P., and Jelloul, M. B. (2009). New production stimulated by high-frequency winds in a turbulent mesoscale eddy field. *Geophys. Res. Lett.* 36, 1–6. doi: 10.1029/2009GL039490

Lévy, M., Klein, P., and Treguier, A. M. (2001). Impact of sub-mesoscale physics on production and subduction of phytoplankton in an oligotrophic regime. *J. Mar. Res.* 59, 535–565. doi: 10.1357/002224001762842181

Li, Q. P., Franks, P. J. S., Ohman, M. D., and Landry, M. R. (2012). Enhanced nitrate fluxes and biological processes at a frontal zone in the southern California current system. *J. Plankton Res.* 34, 790–801. doi: 10.1093/plankt/fbs006

Liu, X., and Levine, N. M. (2016). Enhancement of phytoplankton chlorophyll by submesoscale frontal dynamics in the North Pacific Subtropical Gyre. *Geophys. Res. Lett.* 43, 1651–1659. doi: 10.1002/2015GL066996

Mackey, K. R. M., Paytan, A., Caldeira, K., Grossman, A. R., Moran, D., Mcilvin, M., et al. (2013). Effect of temperature on photosynthesis and growth in marine *Synechococcus* spp. *Plant Physiol.* 163, 815–829. doi: 10.1104/pp.113.221937

Mahadevan, A., and Archer, D. (2000). Modeling the impact of fronts and mesoscale circulation on the nutrient supply and biogeochemistry of the upper ocean. *J. Geophys. Res. Ocean.* 105, 1209–1225. doi: 10.1029/1999jc900216

Mahadevan, A., and Campbell, J. W. (2002). Biogeochemical patchiness at the sea surface. *Geophys. Res. Lett.* 29, 1–4. doi: 10.1029/2001GL014116

Mahadevan, A., D'Asaro, E., Lee, C., and Perry, M. J. (2012). Eddy-driven stratification initiates North Atlantic spring phytoplankton blooms. *Science* 336, 54–58. doi: 10.1126/science.1218740

Mahadevan, A., and Tandon, A. (2006). An analysis of mechanisms for submesoscale vertical motion at ocean fronts. *Ocean Model.* 14, 241–256. doi: 10.1016/j.ocemod.2006.05.006

Mahadevan, A., Tandon, A., and Ferrari, R. (2010). Rapid changes in mixed layer stratification driven by submesoscale instabilities and winds. *J. Geophys. Res. Ocean.* 115, 1–12. doi: 10.1029/2008JC005203

Marañón, E. (2015). Cell Size as a key determinant of phytoplankton metabolism and community structure. *Ann. Rev. Mar. Sci.* 7, 241–264. doi: 10.1146/annurev-marine-010814-015955

Martin, A. P., Zubkov, M. V., Burkill, P. H., and Holland, R. J. (2005). Extreme spatial variability in marine picoplankton and its consequences for interpreting Eulerian time-series. *Biol. Lett.* 1, 366–369. doi: 10.1098/rsbl.2005.0316

Mayot, N., D'Ortenzio, F., Uitz, J., Gentili, B., Ras, J., Vellucci, V., et al. (2017). Influence of the phytoplankton community structure on the spring and annual primary production in the northwestern mediterranean sea. *J. Geophys. Res. Ocean.* 122, 9918–9936. doi: 10.1002/2016JC012668

McGillicuddy, D. J., Anderson, L. A., Bates, N. R., Bibby, T., Buesseler, K. O., Carlson, C. A., et al. (2007). Eddy/Wind interactions stimulate extraordinary mid-ocean plankton blooms. *Science* 316, 1021–1026. doi: 10.1126/science.1136256

McWilliams, J. C. (2016). Submesoscale currents in the ocean. *Proc. R. Soc. A Math. Phys. Eng. Sci.* 472:20160117. doi: 10.1098/rspa.2016.0117

Mella-Flores, D., Six, C., Ratin, M., Partensky, F., Boutte, C., Le Corguillé, G., et al. (2012). Prochlorococcus and synechococcus have evolved different adaptive mechanisms to cope with light and uv stress. *Front. Microbiol.* 3:285. doi: 10.3389/fmicb.2012.00285

Moore, L. R., Post, A. F., Rocap, G., and Chisholm, S. W. (2002). Utilization of different nitrogen sources by the marine cyanobacteria *Prochlorococcus* and *Synechococcus*. *Limnol. Oceanogr.* 47, 1–8. doi: 10.1007/978-3-319-23534-9_1

Mousing, E. A., Richardson, K., Bendtsen, J., Cetiniæ, I., and Perry, M. J. (2016). Evidence of small-scale spatial structuring of phytoplankton alpha- and beta-diversity in the open ocean. *J. Ecol.* 104, 1682–1695. doi: 10.1111/1365-2745.12634

Mulholland, M. R., and Lee, C. (2009). Peptide hydrolysis and the uptake of dipeptides by phytoplankton. *Limnol. Oceanogr.* 54, 856–868. doi: 10.4319/lo.2009.54.3.0856

Nagai, T., Tandon, A., and Rudnick, D. L. (2006). Two-dimensional ageostrophic secondary circulation at ocean fronts due to vertical mixing and large-scale deformation. *J. Geophys. Res. Ocean.* 111:C09038. doi: 10.1029/2005JC002964

Niewiadomska, K., Claustre, H., Prieur, L., and D'Ortenzio, F. (2008). Submesoscale physical-biogeochemical coupling across the Ligurian Current (northwestern Mediterranean) using a bio-optical glider. *Limnol. Oceanogr.* 53, 2210–2225. doi: 10.4319/lo.2008.53.5_part_2.2210

Omta, A. W., Kooijman, S. A. L. M., and Dijkstra, H. A. (2008). Critical turbulence revisited: the impact of submesoscale vertical mixing on plankton patchiness. *J. Mar. Res.* 66, 61–85. doi: 10.1357/002224008784815766

Oschlies, A., and Garçon, V. (1998). Eddy-influenced enhancement of primary production in a model of the North Atlantic Ocean. *Nature* 394, 266–269. doi: 10.1038/28373

Otero-Ferrer, J. L., Cermeño, P., Fernández-Castro, B., Gasol, J. M., Morán, X. A. G., Marañon, E., et al. (2018). Factors controlling the community structure of picoplankton in contrasting marine environments. *Biogeosci. Discuss.* 15, 6199–6220. doi: 10.5194/bg-2018-211

Painter, S. C., Patey, M. D., Tarran, G. A., and Torres-Valdés, S. (2014). Picoeukaryote distribution in relation to nitrate uptake in the oceanic nitracline. *Aquat. Microb. Ecol.* 72, 195–213. doi: 10.3354/ame01695

Pallàs-Sanz, E., Johnston, T. M. S., and Rudnick, D. L. (2010). Frontal dynamics in a California Current System shallow front: 1. Frontal processes and tracer structure. *J. Geophys. Res. Ocean.* 115:C12067. doi: 10.1029/2009JC006032

Ponte, A. L., Klein, P., Capet, X., Le Traon, P. Y., Chapron, B., and Lherminier, P. (2013). Diagnosing surface mixed layer dynamics from high-resolution satellite observations: numerical insights. *J. Phys. Oceanogr.* 43, 1345–1355. doi: 10.1175/JPO-D-12-0136.1

Raven, J. A. (1998). The twelfth Tansley Lecture. Small is beautiful: the picophytoplankton. *Funct. Ecol.* 12, 503–513. doi: 10.1046/j.1365-2435.1998.00233.x

Rivière, P., and Pondaven, P. (2006). Phytoplankton size classes competitions at sub-mesoscale in a frontal oceanic region. *J. Mar. Syst.* 60, 345–364. doi: 10.1016/j.jmarsys.2006.02.005

Sangrá, P., Basterretxea, G., Pelegrí, J. L., and Arístegui, J. (2001). Chlorophyll increase due to internal waves on the shelf break of Gran Canaria (Canary Islands). *Sci. Mar.* 65, 89–97. doi: 10.3989/scimar.2001.65s189

Scanlan, D. J., Ostrowski, M., Mazard, S., Dufresne, A., Garczarek, L., Hess, W. R., et al. (2009). Ecological Genomics of Marine Picocyanobacteria. *Microbiol. Mol. Biol. Rev.* 73, 249–299. doi: 10.1128/mmbr.00035-08

Shulman, I., Penta, B., Richman, J., Jacobs, G., Anderson, S., and Sakalaukus, P. (2015). Impact of submesoscale processes on dynamics of phytoplankton filaments. *J. Geophys. Res. Ocean.* 120, 2050–2062. doi: 10.1002/2014JC010326. Received

Siegelman, L., Klein, P., Rivière, P., Thompson, A. F., Torres, H. S., Flexas, M., et al. (2020). Enhanced upward heat transport at deep submesoscale ocean fronts. *Nat. Geosci.* 13, 50–55. doi: 10.1038/s41561-019-0489-1

Snyder, S., Franks, P. J. S., Talley, L. D., Xu, Y., and Kohin, S. (2017). Crossing the line: tunas actively exploit submesoscale fronts to enhance foraging success. *Limnol. Oceanogr. Lett.* 2, 187–194. doi: 10.1002/lol2.10049

Taylor, A. G., Goericke, R., Landry, M. R., Selph, K. E., Wick, D. A., and Roadman, M. J. (2012). Sharp gradients in phytoplankton community structure across a frontal zone in the California Current Ecosystem. *J. Plankton Res.* 34, 778–789. doi: 10.1093/plankt/fbs036

Taylor, J. R. (2016). Turbulent mixing, restratification, and phytoplankton growth at a submesoscale eddy. *Geophys. Res. Lett.* 43, 5784–5792. doi: 10.1002/2016GL069106

Taylor, J. R., and Ferrari, R. (2011). Ocean fronts trigger high latitude phytoplankton blooms. *Geophys. Res. Lett.* 38, 1–5. doi: 10.1029/2011GL049312

Thomas, L., and Ferrari, R. (2008). Friction, frontogenesis, and the stratification of the surface mixed layer. *J. Phys. Oceanogr.* 38, 2501–2518. doi: 10.1175/2008JPO3797.1

Thomas, L. N. (2005). Destruction of potential vorticity by winds. *J. Phys. Oceanogr.* 35, 2457–2466. doi: 10.1175/JPO2830.1

Thomas, L. N., and Lee, C. M. (2005). Intensification of ocean fronts by down-front winds. *J. Phys. Oceanogr.* 35, 1086–1102. doi: 10.1175/JPO2737.1

Tsutsumi, E., Matsuno, T., Itoh, S., Zhang, J., Senjyu, T., Sakai, A., et al. (2020). Vertical fluxes of nutrients enhanced by strong turbulence and phytoplankton bloom around the ocean ridge in the Luzon Strait. *Sci. Rep.* 10, 1–12. doi: 10.1038/s41598-020-74938-5

Zhang, J., Schmitt, R. W., and Huang, R. X. (1998). Sensitivity of the GFDL modular ocean model to parameterization of double-diffusive processes. *J. Phys. Oceanogr.* 28, 589–605. doi: 10.1175/1520-0485(1998)028<0589:sotgmo>2.0.co;2

Znachor, P., and Nedoma, J. (2010). Importance of dissolved organic carbon for phytoplankton nutrition in a eutrophic reservoir. *J. Plankton Res.* 32, 367–376. doi: 10.1093/plankt/fbp129

Zubkov, M. V., Sleigh, M. A., and Burkill, P. H. (2000a). Assaying picoplankton distribution by flow cytometry of underway samples collected along a meridional transect across the Atlantic Ocean. *Aquat. Microb. Ecol.* 21, 13–20. doi: 10.3354/ame021013

Zubkov, M. V., Sleigh, M. A., Burkill, P. H., and Leakey, R. J. G. (2000b). Picoplankton community structure on the Atlantic Meridional Transect: a comparison between seasons. *Prog. Oceanogr.* 45, 369–386. doi: 10.1016/S0079-6611(00)00008-2

Conflict of Interest: The authors declare that the research was conducted in the absence of any commercial or financial relationships that could be construed as a potential conflict of interest.

frontiers in Marine Science

ORIGINAL RESEARCH
published: 23 April 2021
doi: 10.3389/fmars.2021.598101

Surface Circulation and Vertical Structure of Upper Ocean Variability Around Fernando de Noronha Archipelago and Rocas Atoll During Spring 2015 and Fall 2017

Alex Costa da Silva[1], Alexis Chaigneau[2,3,4], Alina N. Dossa[1], Gerard Eldin[2], Moacyr Araujo[1,5] and Arnaud Bertrand[6]*

[1] Departamento de Oceanografia da Universidade Federal de Pernambuco – DOCEAN/UFPE, Recife, Brazil, [2] Laboratoire d'Études en Géophysique et Océanographie Spatiale (LEGOS), Université de Toulouse, CNES, CNRD, IRD, UPS, Toulouse, France, [3] Institut de Recherches Halieutiques et Océanologiques du Bènin (IRHOB), Cotonou, Benin, [4] International Chair in Mathematical Physics and Applications (ICMPA–UNESCO Chair), Cotonou, Benin, [5] Brazilian Research Network on Global Climate Change – Rede CLIMA, São José dos Campos, Brazil, [6] Institut de Recherche pour le Développement (IRD), MARBEC, Univ. Montpellier, CNRS, IFREMER, IRD, Sète, France

OPEN ACCESS

Edited by:
Miguel A. C. Teixeira, University of Reading, United Kingdom

Reviewed by:
Zhongxiang Zhao, University of Washington, United States
Xavier Carton, Université de Bretagne Occidentale, France

***Correspondence:**
Alex Costa da Silva
alex.csilva@ufpe.br

Specialty section:
This article was submitted to Physical Oceanography, a section of the journal Frontiers in Marine Science

Received: *23 August 2020*
Accepted: *30 March 2021*
Published: *23 April 2021*

Citation:
Costa da Silva A, Chaigneau A, Dossa AN, Eldin G, Araujo M and Bertrand A (2021) Surface Circulation and Vertical Structure of Upper Ocean Variability Around Fernando de Noronha Archipelago and Rocas Atoll During Spring 2015 and Fall 2017. Front. Mar. Sci. 8:598101. doi: 10.3389/fmars.2021.598101

Using current, hydrographic and satellite observations collected off Northeast Brazil around the Fernando de Noronha Archipelago and Rocas Atoll during two oceanographic cruises (spring 2015 and fall 2017), we investigated the general oceanic circulation and its modifications induced by the islands. In spring 2015, the area was characterized by lower SST (26.6°C) and deep mixed-layer (∼90 m). At this depth, a strong current shear was observed between the central branch of the eastward flowing near-surface South Equatorial Current and the westward flowing South Equatorial Undercurrent. In contrast, in fall 2017, SST was higher (∼28.8°C) and the mixed-layer shallower (∼50 m). The shear between the central South Equatorial Current and the South Equatorial Undercurrent was weaker during this period. Interestingly, no oxygen-rich water from the south (retroflection of the North Brazil undercurrent) was observed in the region in fall 2017. In contrast, we revealed the presence of an oxygen-rich water entrained by the South Equatorial Undercurrent reaching Rocas Atoll in spring 2015. Beside these global patterns, island wake effects were noted. The presence of islands, in particular Fernando de Noronha, strongly perturbs central South Equatorial Current and South Equatorial Undercurrent features, with an upstream core splitting and a reorganization of single current core structures downstream of the islands. Near islands, flow disturbances impact the thermohaline structure and biogeochemistry, with a negative anomaly in temperature (−1.3°C) and salinity (−0.15) between 200 and 400 m depth in the southeast side of Fernando Noronha (station 5), where the fluorescence peak (>1.0 mg m^{-3}) was shallower than at other stations located around Fernando de Noronha, reinforcing the influence of flow-topography. Satellite maps of sea-surface temperature and chlorophyll-a confirmed the presence of several submesoscale features in the study region. Altimetry data suggested the presence of a cyclonic

mesoscale eddy around Rocas Atoll in spring 2015. A cyclonic vortex (radius of 28 km) was actually observed in subsurface (150–350 m depth) southeast of Rocas Atoll. This vortex was associated with topographically induced South Equatorial Undercurrent flow separation. These features are likely key processes providing an enrichment from the subsurface to the euphotic layer near islands, supplying local productivity.

Keywords: mesoscale activity, satellite data, western tropical Atlantic, shipboard measurements, island wake, central South Equatorial Current, South Equatorial Undercurrent

INTRODUCTION

The tropical Atlantic presents a relatively strong static stability with a well-marked thermocline, which is seasonally modulated by the meridional displacement of the Intertropical Convergence Zone (ITCZ), controlling the regime of precipitation and trade winds (Araujo et al., 2011; Nogueira Neto et al., 2018; Assunção et al., 2020). In such regions, vertical mixing, and upwelling are usually restricted to local mechanisms such as divergence of currents, winds and interactions between ocean currents and topography. Interactions between currents and topography, such as oceanic islands and seamounts, can lead to the generation of (sub)mesoscale eddies, changes in current intensity and directions, disturbances of the thermohaline structure, or orographically-induced upwelling [e.g., the special issues dealing with flow encountering abrupt topography (Oceanography, 2019; Vol. 32, No 4) and bio-physical coupling around seamounts (Deep-Sea Research, 2020; Vol. 176)]. This kind of processes is observed in the western tropical Atlantic off northeast Brazil around the oceanic islands of Fernando de Noronha Archipelago (FN) and the Rocas Atoll (RA) (Lessa et al., 1999; Travassos et al., 1999; Chaves et al., 2006; Tchamabi et al., 2017, 2018).

FN and RA, located ∼350 km from the mainland (**Figure 1**) encompass oceanic ecosystems classified as "Ecologically or Biologically significant Marine Areas (EBSAs)"[1]. Oceanic areas nearby FN and RA are energetic regions subjected to strong seasonally driven features, such as the complex system of zonal equatorial currents and countercurrents, the confluence of water masses, or the trade winds systems (Araujo et al., 2011; Tchamabi et al., 2017, 2018; Foltz et al., 2019). The principal currents of the region are the central branch of the South Equatorial Current (cSEC) located north of the South Equatorial Countercurrent, and the South Equatorial Undercurrent (SEUC) centered at about 4°S (**Figure 1**). These zonal currents flow in opposite direction, with cSEC flowing westwards and SEUC flowing eastwards (Silveira et al., 1994; Stramma and Schott, 1999; Lumpkin and Garzoli, 2005). The near-surface circulation in the region is mostly driven by the meridional migration of the ITCZ. In austral winter (June to August), the ITCZ is located north of the equator and trade winds are stronger. Conversely, in austral fall (March-May), the ITCZ is located close to the equator and the winds are relaxed (Servain et al., 2014; Hounsou-Gbo et al., 2015, 2019). The seasonal ITCZ displacement also influences precipitation regime at FN and RA, with a rainy season extending from March to July, and a dry season extending from August to January (Assunção et al., 2016).

In the western tropical Atlantic, many complex physical processes around oceanic island wake are not well described because most of survey efforts have focused on broader processes. The main large-scale currents were well identified by several historical programs developed along the western edge of the tropical Atlantic (e.g., the *Global Atmospheric Research Program—GARP*; *Atlantic Tropical Experiment—GATE*; *Francais Océan Climat Atlantique Equatorial—FOCAL*; *Prediction and Research moored Array in the Tropical Atlantic—PIRATA* programs, and the ETAMBOT and CITHER projects). Although numerous, all those previous initiatives focused on a large-scale picture of the tropical Atlantic circulation and knowledge about the interaction of the large-scale currents with RA and FN is still scarce. To provide a detailed picture of the current-island interactions, here we use current, hydrographic, and satellite data collected during the *Acoustic along the BRAzilian COaSt* (ABRACOS) cruises in Austral spring 2015 and fall 2017 (Bertrand et al., 2015; 2017). These two periods were found to be representative of canonical spring and fall conditions in the area (Assunção et al., 2020; Dossa et al., 2021). More specifically, we describe the upper-ocean circulation around FN and RA and highlight some mesoscale features observed on currents, thermohaline structure and primary productivity.

DATA AND METHODOLOGY

In situ Observations

In situ data were collected during the two ABRACOS surveys carried out onboard the French R/V Antea in austral spring 2015 (ABRACOS 1, 30 September—08 October 2015) and fall 2017 (ABRACOS 2, 26 April—03 May 2017) (**Figure 2**). The *in situ* datasets described below are publically available (Bertrand et al., 2015, 2017).

Vertical profiles of physical and biogeochemical parameters were collected from the surface to 1,000 m depth using a Seabird SBE911+ conductivity temperature depth (CTD) probe equipped with dissolved oxygen (SBE43) and fluorescence (*Wetlabs*®ECO) sensors. Data were acquired at a frequency of 24 Hz and averaged every 0.1 dbar. All the sensors were laboratory-calibrated before and after each cruise. In the study area, a total of 20 (15, respectively) CTD profiles were acquired during ABRACOS 1 (ABRACOS 2) (**Figure 2**). Conductivity, temperature, pressure, and dissolved oxygen accuracies are of 3 mS/m, 0.001°C, 0.7

[1]http://www.cbd.int/marine/doc/azores-brochure-en.pdf

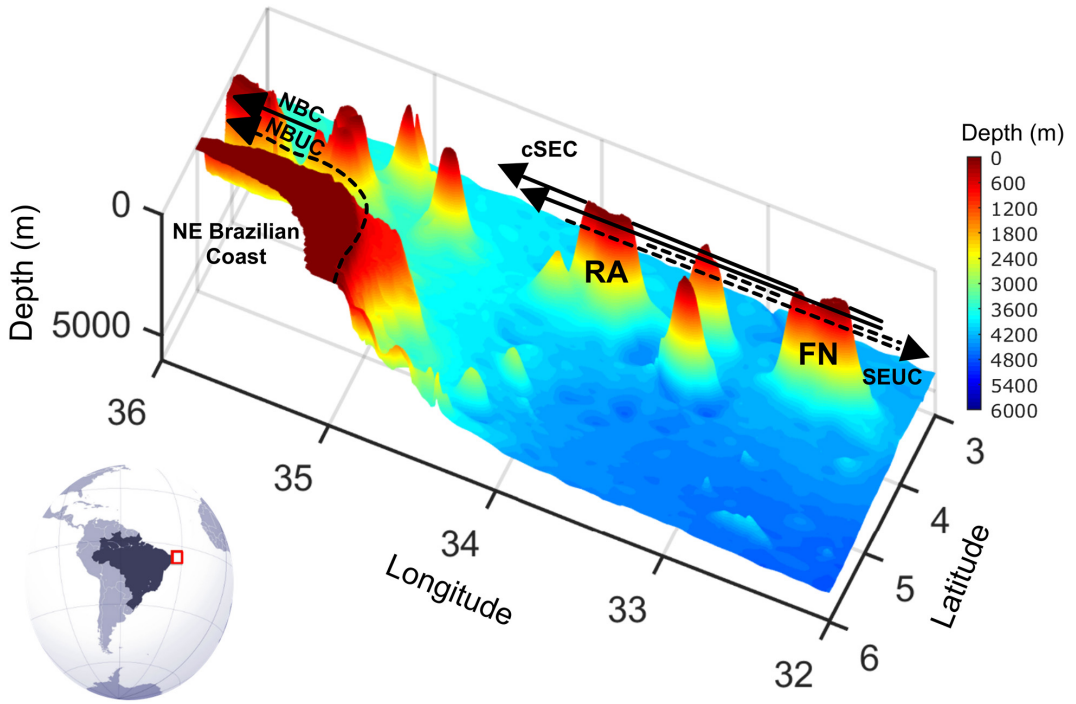

FIGURE 1 | Map of the study area in the western Tropical Atlantic Ocean off northeast Brazil (also indicated by the red box on the globe). General bathymetric (colour scale) is shown at 0–6,000 m depth. Surface and subsurface currents are represented by solid and dashed lines, respectively. RA, Rocas Atoll; FN, Fernando de Noronha Archipelago; cSEC, central branch of the South Equatorial Current, SEUC, South Equatorial Undercurrent, NBC, North Brazil Current; NBUC, North Brazil Undercurrent.

dbar, and 0.09 ml l^{-1}, respectively. The fluorescence sensor measures chlorophyll concentration in the range 0–125 mg m^{-3} with a sensitivity of 0.02 mg m^{-3}. A total of 30 water samples (15 for each survey) were collected using Niskin bottles to determine dissolved oxygen (DO) concentrations using the Winkler titration method (Grasshoff et al., 1983).

In order to investigate the stability of the water column, the Brunt-Väisälä (N) frequency was computed from temperature and salinity profiles, using the equation:

$$N = \sqrt{-\frac{g}{\rho_0}\frac{\partial \rho}{\partial z}} \quad (1)$$

where z is depth (in m), g is gravity, ρ is density and ρ_0 = 1,025 kg m^{-3} is the reference density. Seawater density was based on the atmosphere International Equation of State of Seawater (UNESCO, 1981).

We use vertical profiles of current velocity and hydrographic data to calculate the Richardson number. The Richardson number (Ri) is a measure of the dynamic stability associated with the competing effects of stratification and shear in the flow. It is expressed as the ratio of the vertical gradient of buoyancy over the vertical shear of horizontal velocity:

$$Ri = \frac{N^2}{\left(\frac{dU}{dz}\right)^2\left(\frac{dV}{dz}\right)^2} \quad (2)$$

The vortex Rossby Number (Ro) is used to compare the local relative vorticity of the eddy to the planetary vorticity (Eq. 3). Rossby number and Burger number were used to determine the significance of Coriolis acceleration and stratification, respectively, and their impacts on flow dynamics.

$$Ro = \frac{U}{fL} \quad (3)$$

Where f is the Coriolis parameter, U is the maximum velocity and L is the horizontal length scale of the vortex.

The Burger number (Eq. 4) (Pedlosky, 1987) is a dimensionless parameter related to the aspect ratio (H/L), where H is the vertical length scale of the vortex. The Burger number can also be defined as the square of the ratio of the deformation radius to the horizontal scale of the vortex. The Rossby deformation radius is given in Eq. 5.

$$Bu = (NH/fL)^2 \quad (4)$$

$$Rd = \frac{NH}{f} \quad (5)$$

Vertical profiles of current velocity were continuously acquired along the ship track using a ship-mounted Acoustic Doppler Current Profiler (SADCP) from Teledyne-RDI (OS75 instrument). Raw SADCP data were collected every 3 s in deep water (water-depth < 150 m), and every 1 s in shallow water (water-depth < 150 m) using a vertical bin length of 8 m, and

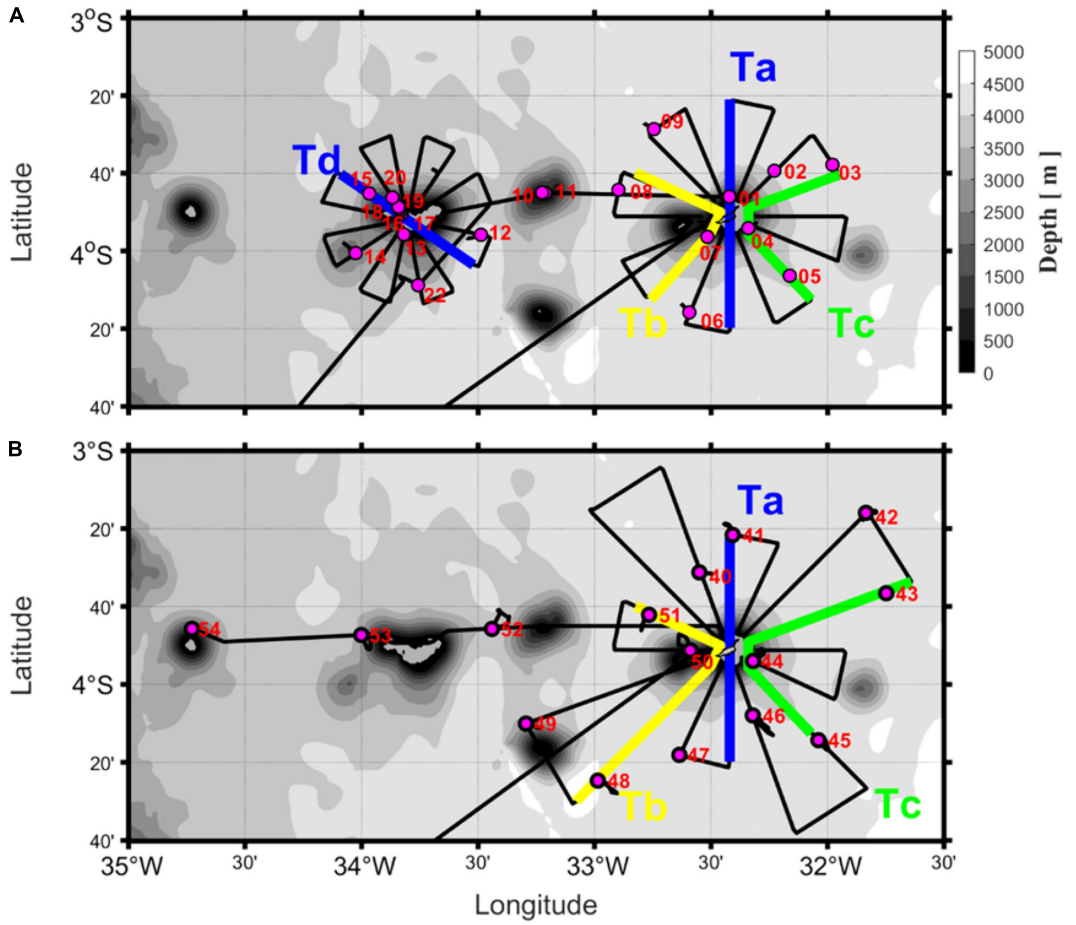

FIGURE 2 | Bathymetric maps of the study area with SADCP sections (black solid lines) acquired during ABRAÇOS 1 in spring 2015 **(A)** and ABRACOS 2 in fall 2017 **(B)**. The thick blue lines (Ta) indicate the transect detailed in section "Circulation Patterns." The thick yellow lines (Tb), the thick green lines (Tc) and the thick blue lines (Td) indicate the transects discussed in section "Discussion." Pink dots show the positions of the CTD profiles.

averaged into 10 min profiles. SADCP data were processed and edited using the Common Ocean Data Access System (CODAS) software package developed by the SOEST, University of Hawaii[2]. The relative velocities were rotated from the transducer to the Earth reference frame using the ship gyrocompass. The global positioning system (GPS) was used to retrieve the absolute current velocities. The orientation of the transducer relative to the gyroscopic compass and an amplitude correction factor for the SADCP were determined by standard calibration procedures (Joyce, 1989; Pollard and Read, 1989). Finally, velocity profiles were averaged hourly, providing profiles in the 19–600 m range.

To better describe the main currents, we separated the data into 2 layers: the surface layer (0–100 m depth), which includes the cSEC, and the subsurface layer (100–400 m depth), where mainly the SEUC is present.

Satellite Data

To provide a more comprehensive image of dynamical processes acting around FN and RA and help the interpretation of results obtained from *in situ* data, several satellite products distributed by the Copernicus Marine Environment Monitoring Service (CMEMS)[3] were extracted in the study region for the periods corresponding to the ABRACOS cruises. The sea surface temperature (SST) product is the so-called OSTIA (Operational SST and Ice Analysis) that combines satellite and *in situ* data. This SST product is daily available from 1 October 1981 to 31 December 2018 on a regular grid of 0.05° resolution (Donlon et al., 2012). Sea-surface chlorophyll-a (Chl-a) concentration maps were from the Copernicus-GlobColour product provided by the ACRI-ST company. Chl-a was obtained from the merging of multi sensors such as SeaWiFS, MODIS, and MERIS. This product is daily available from 2007 to the present with a spatial resolution of 4 km (Garnesson, 2013). Wind-stress data were produced by CERSAT/IFREMER and consist on a blended wind dataset based on remotely sensed surface winds derived from scatterometers and radiometers. It spans from 1992 to present and is daily available on a regular grid of 0.25° (Bentamy and Croizé-Fillon, 2011). Altimetry data is the Salto/Duacs gridded

[2]http://currents.soest.hawaii.edu

[3]http://marine.copernicus.eu

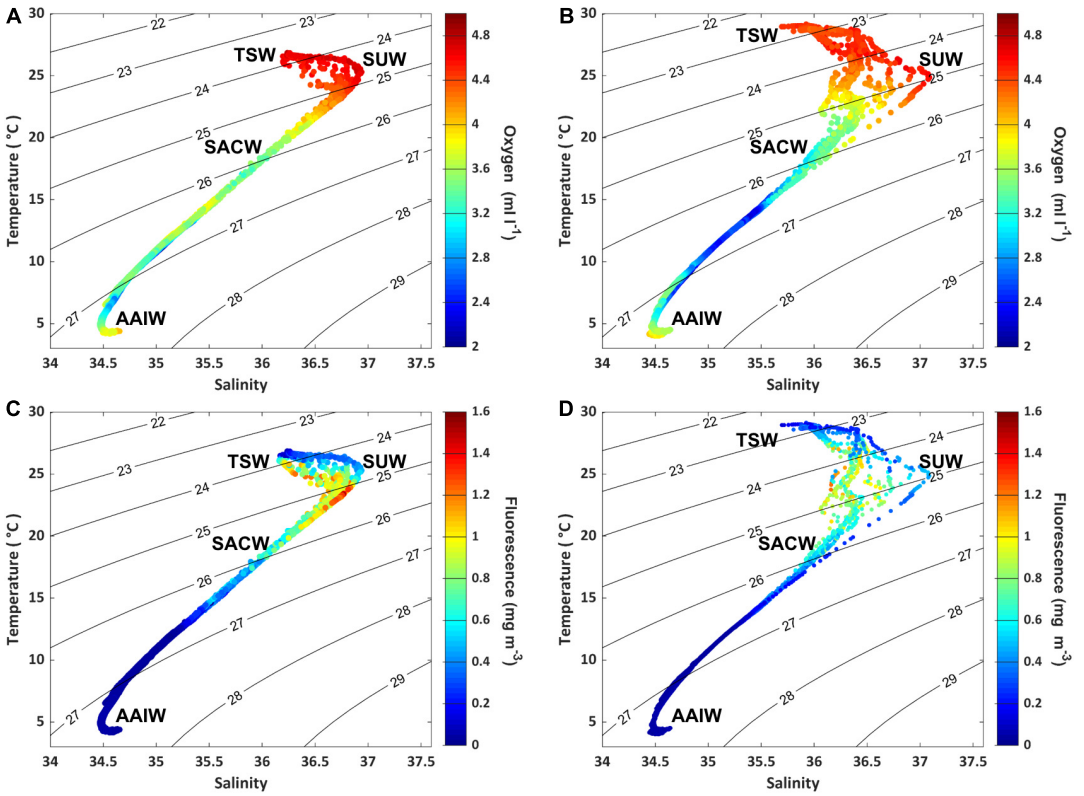

FIGURE 3 | Temperature–salinity diagram obtained from ABRACOS hydrographic stations collected during spring 2015 **(A,C)** and fall 2017 **(B,D)** around RA and FN. Color-coded for dissolved oxygen concentration **(A,B)** and fluorescence **(C,D)**. Isolines are the potential density anomaly contours referenced to the surface pressure.

product of sea-surface height (SSH) and derived geostrophic currents. This product, available from January 1993 to the present, was computed from several multimissions altimeter measurements of SSH, interpolated daily onto a 0.25° × 0.25° longitude/latitude grid (Ducet et al., 2000; Pujol et al., 2016; Taburet et al., 2019).

RESULTS

Water Masses and Thermohaline Structure

Based on the thermohaline properties observed during spring 2015 (**Figures 3A,C**) and fall 2017 (**Figures 3B,D**) and previous works (Schott et al., 1998; Stramma and Schott, 1999) four main water masses were identified in the 0–1,000 m depth-range: the Tropical Surface Water (TSW), the Subtropical Underwater (SUW), the South Atlantic Central Water (SACW), and the Antarctic Intermediate Water (AAIW). The TSW is located on the surface layer above the σ_θ = 24.5 kg m^{-3} isopycnal, located at about 100 m depth. During spring 2015 (**Figures 3A,C**) the TSW was characterized by relatively high values of temperature (>26°C), dissolved oxygen (4.3–5.0 ml l^{-1}), and relatively low values of fluorescence (<1 mg m^{-3}) and salinity (<36.5) in the mixed layer (limited to ∼90 m depth). During fall 2017, the mixed layer was shallower (∼50 m depth), and TSW was characterized by temperature higher than 27°C, salinity lower than 36.5, dissolved oxygen concentrations between 4.3 and 4.7 ml l^{-1} and fluorescence in the range 0–0.9 mg m^{-3} (**Figures 3B,D**). At both seasons, just below the TSW between σ_θ = 24.5 kg m^{-3} and σ_θ = 25.5 kg m^{-3}, lied the SUW characterized by a local maximum in salinity (>36.5) (**Figure 3**). This water-mass, which was more clearly observed in spring 2015 than in fall 2017, is also characterized by relatively high oxygen (>4 ml l^{-1}) and fluorescence (>0.5 mg m^{-3}) values.

Below the SUW, takes place the SACW characterized by a nearly linear temperature-salinity relationship covering wide temperature (10–20°C) and salinity (34.9–36.2) ranges. This water-mass was associated with a relative oxygen minimum of 3.3–3.5 ml l^{-1} (2.3–2.7 ml l^{-1}, respectively) during spring 2015 (fall 2017) at 150–500 m depth. At these depths, fluorescence values were weak due to light limitation. Finally, the isopycnal σ_θ = 27.1 kg m^{-3} (about 500 m) marks the transition between SACW and AAIW. AAIW is characterized by a local salinity minimum of ∼34.5 and a local oxygen maximum of ∼3–3.5 ml l^{-1}. Fluorescence is almost zero at the depth of the AAIW.

In the surface layer, the mixed-layer containing TSW was spatially very homogeneous and characterized by a mean SST of 26.7°C (28.8°C, respectively) in spring 2015 (fall 2017) (**Figures 4A**, **5A**, **6A**). Surface salinity was also higher in spring

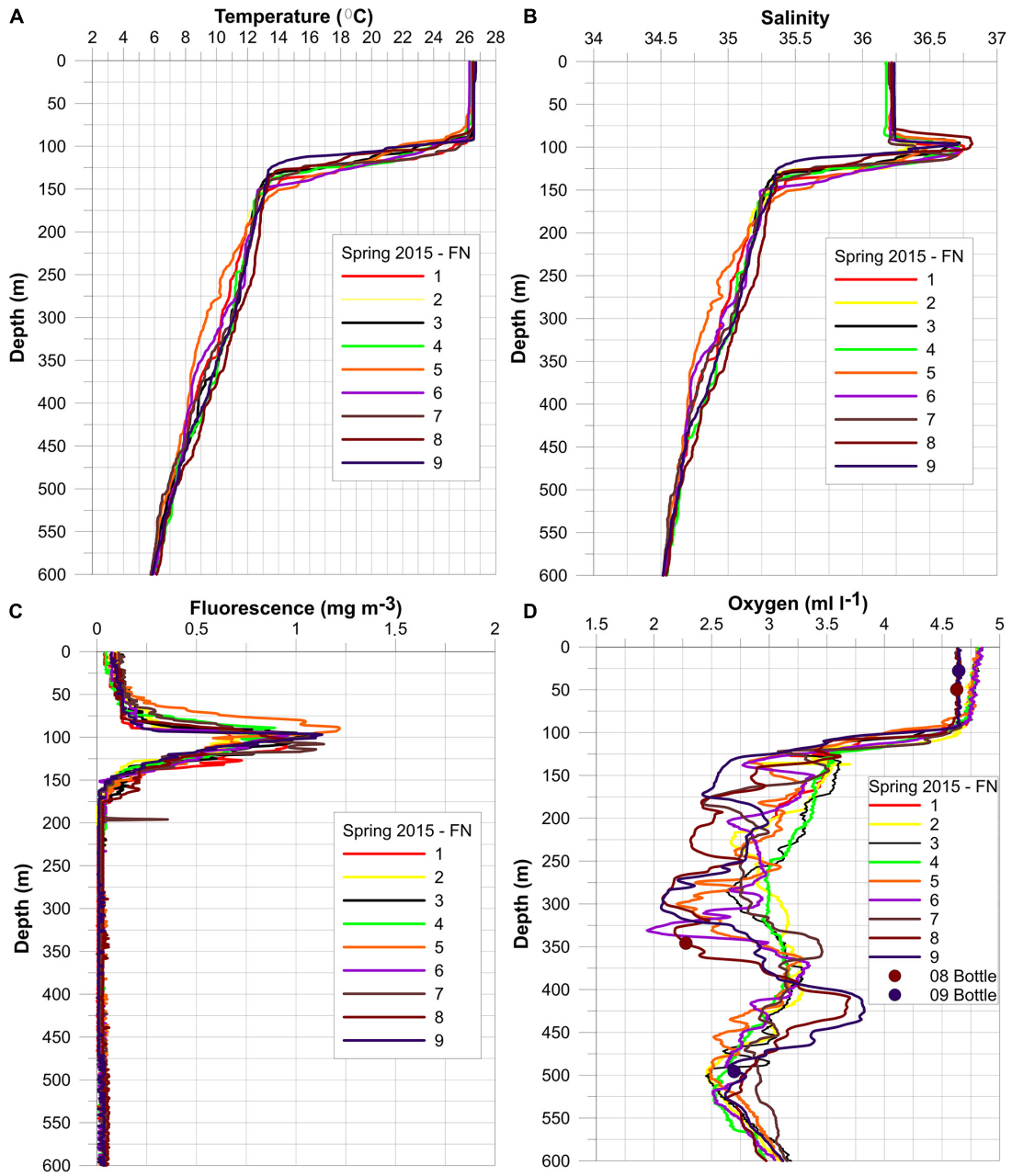

FIGURE 4 | CTD profiles obtained during the ABRACOS surveys in spring 2015 around the Fernando de Noronha Archipelago. Vertical profiles of temperature **(A)**, salinity **(B)**, fluorescence **(C)**, and dissolved oxygen **(D)**.

2015 (∼36.2) than in fall 2017 (∼ 35.9) (**Figures 4B**, **5B**, **6B**). Below, a sharp thermocline-halocline was observed with an upper limit at ∼90 and 50 m in spring 2015 and fall 2017, respectively (**Figures 4A**, **5A**, **6A**). The seasonal thermocline extended down to ∼150 m in spring 2015 and to ∼100 m depth in fall 2017. During both cruises, a thin layer with maximum salinity (≥36.7 and ≥36.3) was present at ∼80–120 m and ∼60–90 m, respectively (**Figures 4B**, **5B**, **6B**), associated with SUW.

Surface fluorescence concentration of the TSW was twice lower in spring 2015 (average: 0.10 mg m^{-3}) than in fall 2017 (average: 0.20 mg m^{-3}) (**Figures 4C**, **5C**, **6C**). Peaks of maximum fluorescence (average: ∼1 mg m^{-3}) were observed in the SUW during spring 2015 and fall 2017 (**Figures 4C**, **5C**, **6C**).

In the surface layer, DO concentrations were similar and of ∼4.5 ml l^{-1} during both cruises (**Figures 4D**, **5D**, **6D**). During spring 2015, CTD stations located north and south of RA also presented higher DO concentrations (≥3.5 ml l^{-1}) below the thermocline layer. During fall 2017 low DO concentrations (∼2.5 ml l^{-1}) were observed in subsurface around FN and RA (**Figures 5D**, **6D**).

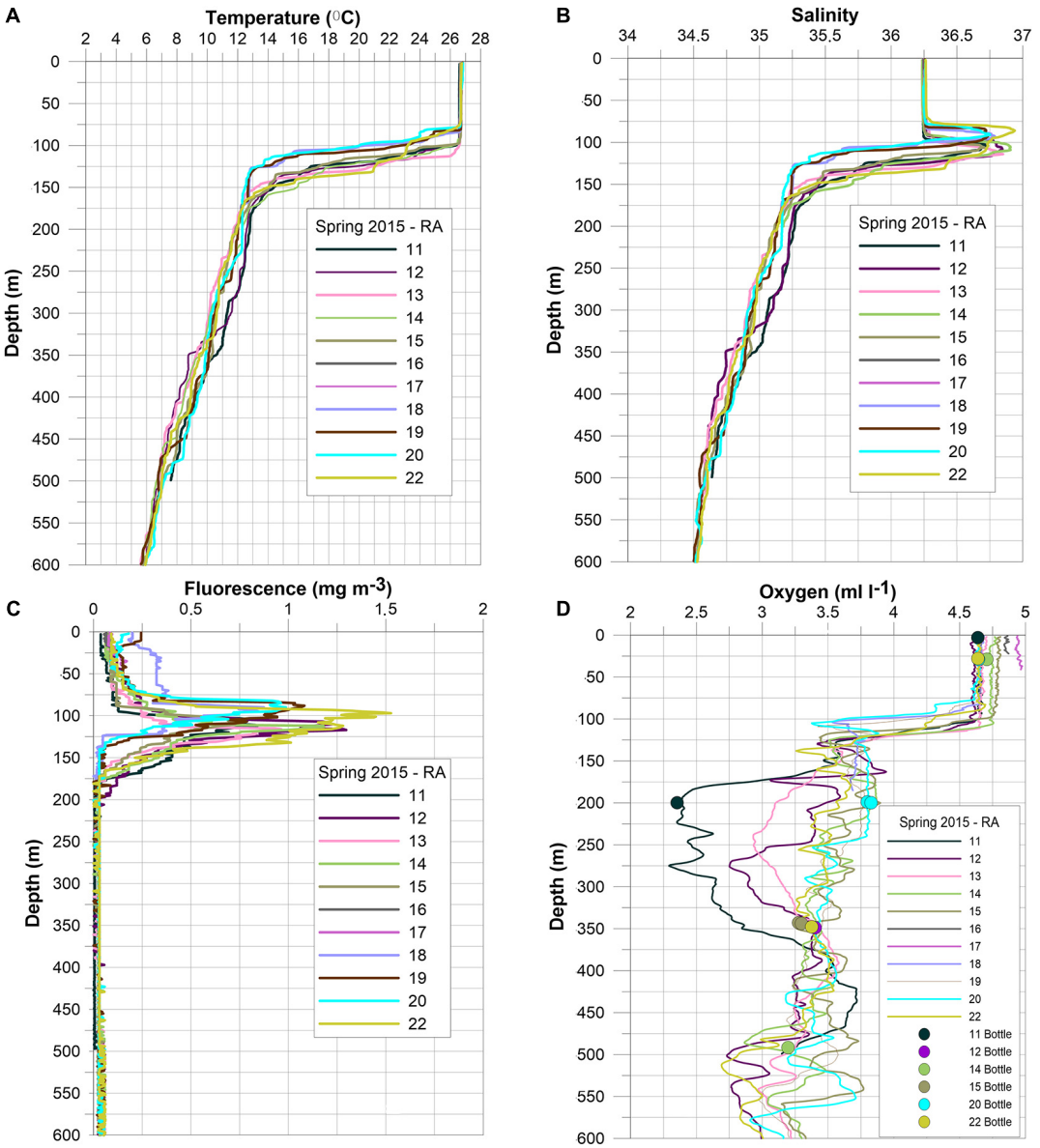

FIGURE 5 | CTD profiles obtained during the ABRACOS surveys in spring 2015 around the Rocas Atoll. Vertical profiles of temperature **(A)**, salinity **(B)**, fluorescence **(C)**, and dissolved oxygen **(D)**.

More specifically, during spring 2015, temperature profiles at stations 11 and 12, close to RA, presented positive temperature (+1°C) and salinity (+0.16) anomalies in the depth range 200–350 m (**Figure 5A**). Corresponding DO concentration were lower than 3.5 ml l^{-1} (**Figure 5D**). Conversely, at station 05 close to FN, a negative anomaly in temperature (−1.3°C) and salinity (−0.15) was observed in the depth range 200–400 m (**Figure 4A**). At this station, the fluorescence peak was shallower than at other stations located around FN (**Figure 4C**). In addition, a shallower thermocline and halocline was observed at stations 18, 19, and 20, located north of RA, when compared to the other stations around RA (**Figure 5A**). In those stations, surface fluorescence concentration was higher (0.18–0.24 mg m^{-3}) and the peaks of maximum fluorescence were shallower (above 100 m) (**Figure 5C**). Finally, stations 14–22 located north and south of RA did not show a marked DO minimum (**Figure 5D**).

During fall 2017, at stations 48 and 54, the thermocline and halocline were deeper than at other stations (**Figure 6A**). In addition, station 42 located north of FN presented a positive temperature (+1°C) and salinity (+0.1) anomaly between 350 and 450 m depth. At this station, in the depth range 425–600 m, DO concentration was higher (>3.2 ml l^{-1}) than at other stations.

Finally, the upper thermocline was deeper in spring 2015 (∼90 m) than fall 2017 (∼50 m). Specifically, in spring 2015, stations 05, 09, 12, 20, and 22 (**Figures 7A–E**) presented deeper

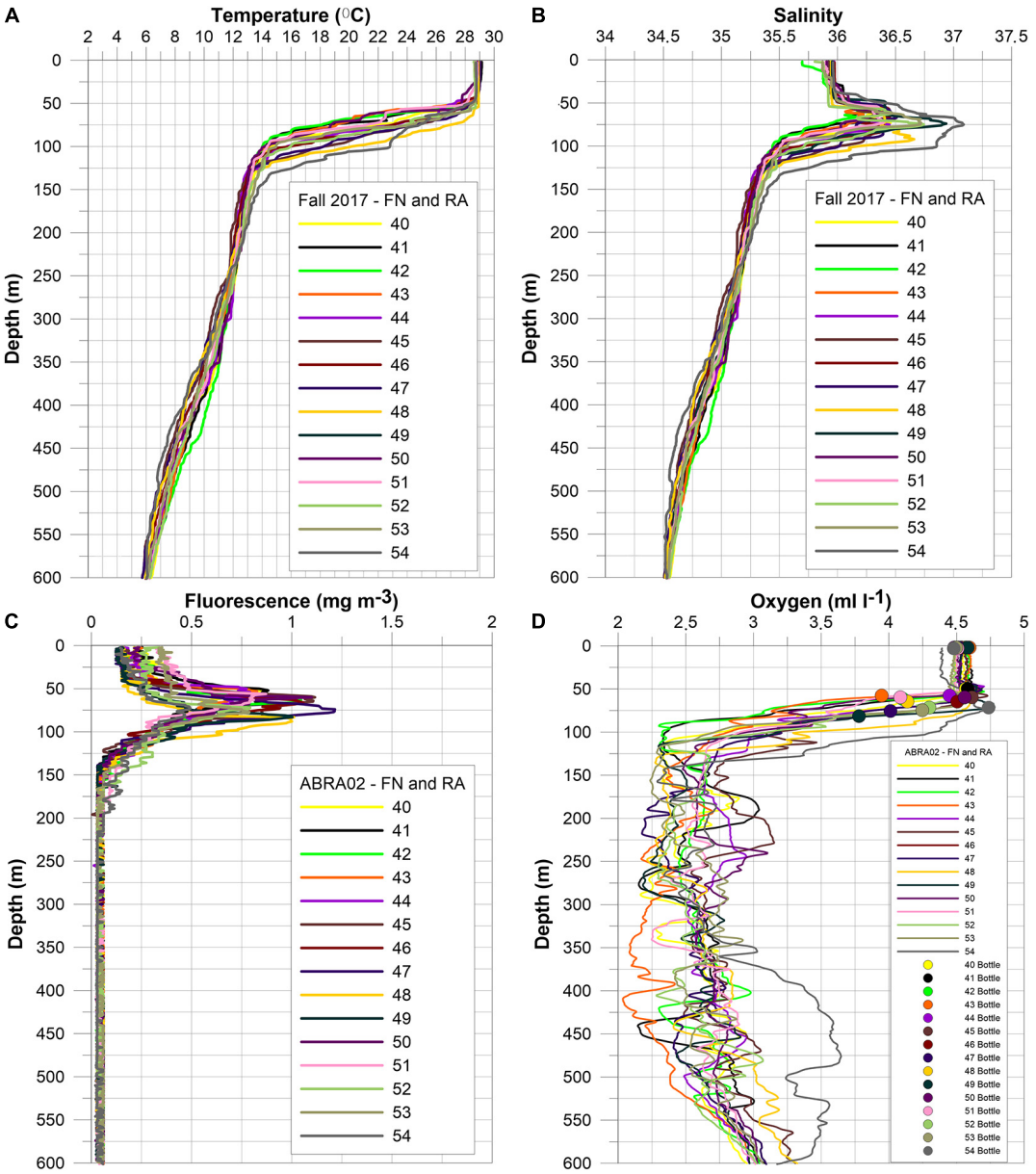

FIGURE 6 | CTD profiles obtained during the ABRACOS surveys in fall 2017 around the Fernando de Noronha Archipelago and Rocas Atoll. Vertical profiles of temperature **(A)**, salinity **(B)**, fluorescence **(C)**, and dissolved oxygen **(D)**.

halocline and thermocline when compared to stations 53 in fall 2017 (**Figures 7E,F**). The area north of FN and RA (stations 09 and 20; **Figures 7B,D**) presented stronger vertical gradients at the lower limit of the mixed layer depth than in the southern area (stations 05 and 12, **Figures 7A,C**). Station 20 located north of RA presented a low Ri between 150 and 250 m depth.

Below the surface layer (near 250 m depth), stations 12 and 22 show low Ri values (<0.5 and <0.3, respectively) in the southeast side of RA (**Figures 7C,E**).

During spring 2015, the upper thermocline and maximum salinity depth (between 50 and 100 m depth) presented a higher peak of Brunt-Väisälä frequency near in surface than in fall 2017 (**Figure 7F**), confirming a stronger vertical stratification and static stability.

Circulation Patterns

cSEC and SEUC Volume Transports Around FN

Although several SADCP sections were performed around FN and RA, we selected a meridional section (crossing FN from North to South (transect Ta in **Figure 2**) to represent the ocean circulation in the region. In spring 2015, the cSEC flowed westward above 100 m depth on both sides of FN (**Figure 8**) but was more intense on the northern side ($U \sim -50$ cm s^{-1})

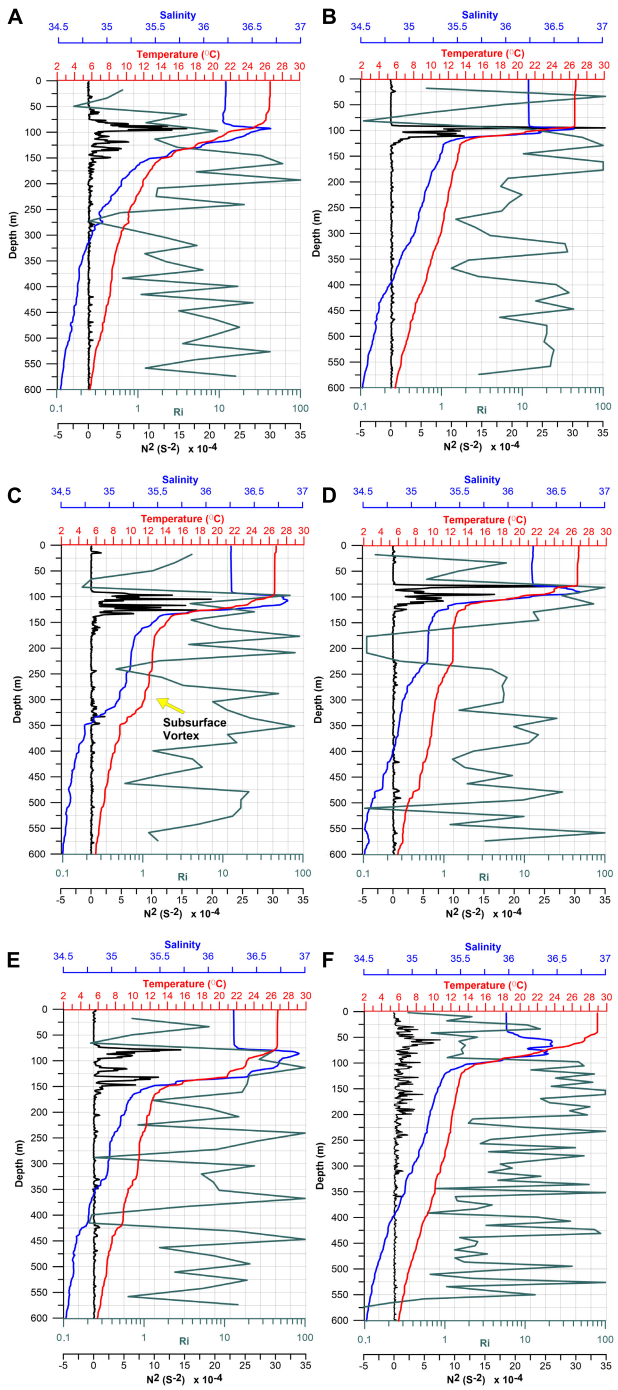

FIGURE 7 | Typical profiles of temperature, salinity, Brunt-Väisälä frequency (N) and Richardson number (Ri) for stations 5 **(A)**, 9 **(B)**, 12 **(C)**, 20 **(D)**, and 22 **(E)** during spring 2015 and for stations 46 **(F)** during fall 2017.

than on the southern side (U $\sim$ $-$20 cm s^{-1}) (**Figure 8A**). The cSEC westward transport was estimated to be of 1.2 $\pm$ 0.1 Sv across this meridional section in spring 2015. In fall 2017, the cSEC was restricted above 70 m (**Figure 8B**) and its zonal velocity component was higher than in spring 2015, with an average of $\sim$$-$60 cm s^{-1} in the surface layer (0–100 m) in both sides of the island (**Figure 8B**). Corresponding westward transport was estimated to be of 4 $\pm$ 0.2 Sv.

In the subsurface layer, between 100 and 400 m depth, the zonal component of the flow reversed and the current was oriented eastward, as is typical of the SEUC. Therefore, a strong current shear occurred between the near-surface cSEC and the subsurface SEUC. In spring 2015, the SEUC presented a maximum zonal velocity of 70 cm s^{-1} south of FN at $\sim$200 m depth (**Figure 8A**). North of FN, the SEUC zonal velocity was weaker ($\leq$40 cm s^{-1}). The SEUC eastward transport, integrated between 100 and 400 m depth along the meridional section, was estimated to 5.6 $\pm$ 0.5 Sv. In fall 2017, the SEUC was weaker than in spring 2015, having a maximum zonal velocity of 30 cm s^{-1} south of FN around 150 m depth (**Figure 8B**). On the northern side of FN, the SEUC velocity was much weaker ($<$10 cm s^{-1}) (**Figure 8B**). In fall 2017, the integrated SEUC transport was estimated to 3.8 $\pm$ 0.7 Sv. Finally, below $\sim$450 m, the circulation was weak and not further investigated in this study.

Near-Surface and Subsurface Circulation Around FN and RA

In order to depict the regional circulation around FN and RA, we divided the circulation into two distinct layers: the near-surface layer (0–100 m depth) that includes the cSEC and the subsurface layer (100–400 m depth) mainly associated with the SEUC.

In spring 2015, the near-surface circulation was dominated by the cSEC (**Figures 8A**, 9A). Around FN, surface currents varied in direction and intensity on both sides (north and south) of the archipelago. On the northern side of the archipelago, surface current was more intense (50 cm s^{-1}) with a prevailing northwestward flow (**Figure 9A**). A similar northwestward flow was also observed on the northern side of RA. In fall 2017, the cSEC had a prevailing westward direction with mean velocities of 50 cm s^{-1} (**Figure 9C**). During this period, no clear current-islands interaction was observed.

In the subsurface layer (100–400 m depth), during spring 2015, the SEUC dominated around FN with maximum velocity (30 cm s^{-1}) south of the island. Near RA, currents flowed predominantly south/southeastwards, being more intense on the western side of the atoll. Between FN and RA (about 33°W), the eastward flow was weaker ($<$10 cm s^{-1}). Interestingly, in spring 2015, a small-scale subsurface cyclonic circulation was observed southeast of RA (illustrated by a black circle in **Figure 9B**). This subsurface cyclonic eddy had an estimated radius of $\sim$28 km and was probably driven by the topographically induced flow separation (**Figure 9B**). This eddy-like structure, centered at 33.38°W and 4°S and having a typical swirl velocity of 20 cm s^{-1}, did not have a signature in the near-surface layer dominated by the cSEC. In fall 2017 the influence of the SEUC was observed in the 100–400 m depth layer around FN, with an average current velocity of 20 cm s^{-1} flowing eastward south of FN. Northwest of FN, the northeast flow was weaker ($\leq$10 cm s^{-1}). Finally, west of RA currents moved southwards (**Figure 9D**).

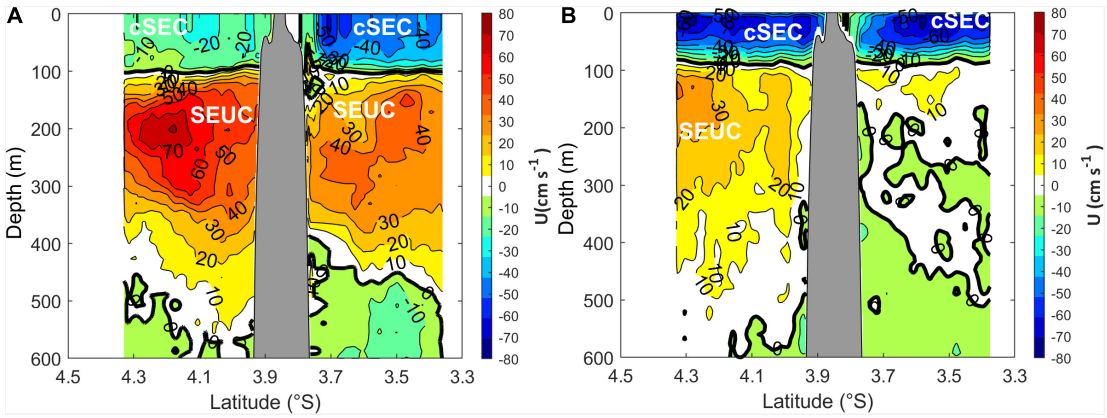

FIGURE 8 | Mean zonal velocity components (in cm s^{-1}) obtained from ABRACOS cruises in spring 2015 **(A)** and fall 2017 **(B)** around Fernando de Noronha archipelago (vertical blue transect Ta in **Figure 2**). The contour interval is 10 cm s^{-1}.

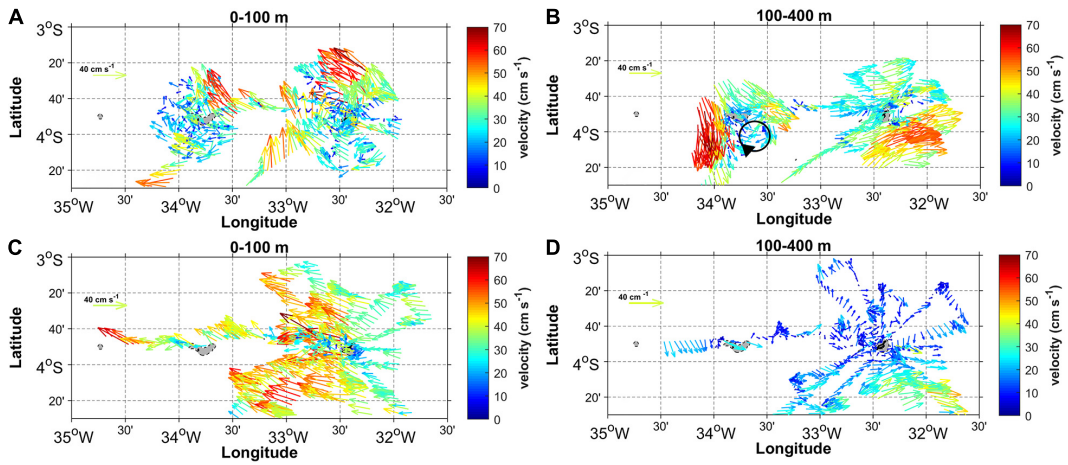

FIGURE 9 | Mean current velocity obtained from ABRACOS cruises at 0–100 m during spring 2015 **(A)** and fall 2017 **(C)**, and at 100–400 during spring 2015 **(B)** and fall 2017 **(D)**. Black circle in **Figure 8B** indicates the cyclonic mesoscale circulation.

Regional Surface Characteristics From Satellite Observations

SST was lower in spring 2015 (<27°C) than in fall 2017 (>28°C) (**Figures 10A,B**), in agreement with the SST values observed from CTD data. In spring 2015, the SST showed a large-scale northwestward gradient, varying from 26°C southeast of FN to 27°C northwest of RA. This SST distribution suggests that the cSEC tended to cool the downstream regions. In fall 2017, the SST was much more homogeneous in the study region and varied by less than 0.4°C. Several mesoscale temperature structures were observed during both seasons (**Figures 10A,B**).

Surface Chl-a concentration was lower in spring 2015 (about 0.1 mg m^{-3}) than in fall 2017 (0.2 mg m^{-3}) (**Figures 10C,D**). Higher surface fluorescence values were also observed in fall 2017 from CTD data. In spring 2015, satellite Chl-a concentrations were higher in the vicinity of FN and RA, suggesting a topographic influence on the primary productivity. In fall 2017, a large-scale northeastward Chl-a gradient was observed, with mean Chl-a concentrations varying from 0.10 to 0.23 mg m^{-3}.

Surface winds blew northwestwards and intensified westwards (**Figures 10E,F** and **Supplementary Figures 1E,F**). It might be related with coastal effects associated with the proximity of land. This intensification was more pronounced in spring 2015 than in fall 2017. Overall surface winds were higher in spring 2015 (≥0.1 N m^{-2}) than fall 2017 (≤0.1 N m^{-2}).

In spring 2015, some changes were observed in the predominant directions of the surface currents (0–100 m depth) around FN and RA, which was not observed in fall 2017. In spring 2015, SSH and associated geostrophic currents depicted a surface current flowing northward on the northern and eastern sides of FN. On the northern side of RA, a northeastward flow was observed (**Figure 10G**). The presence of a mesoscale cyclonic eddy around RA was depicted. In fall 2017, a clear geostrophic westward flow was observed (**Figure 10H**) around FN and RA and no eddy was observed (**Supplementary Figure 1H**).

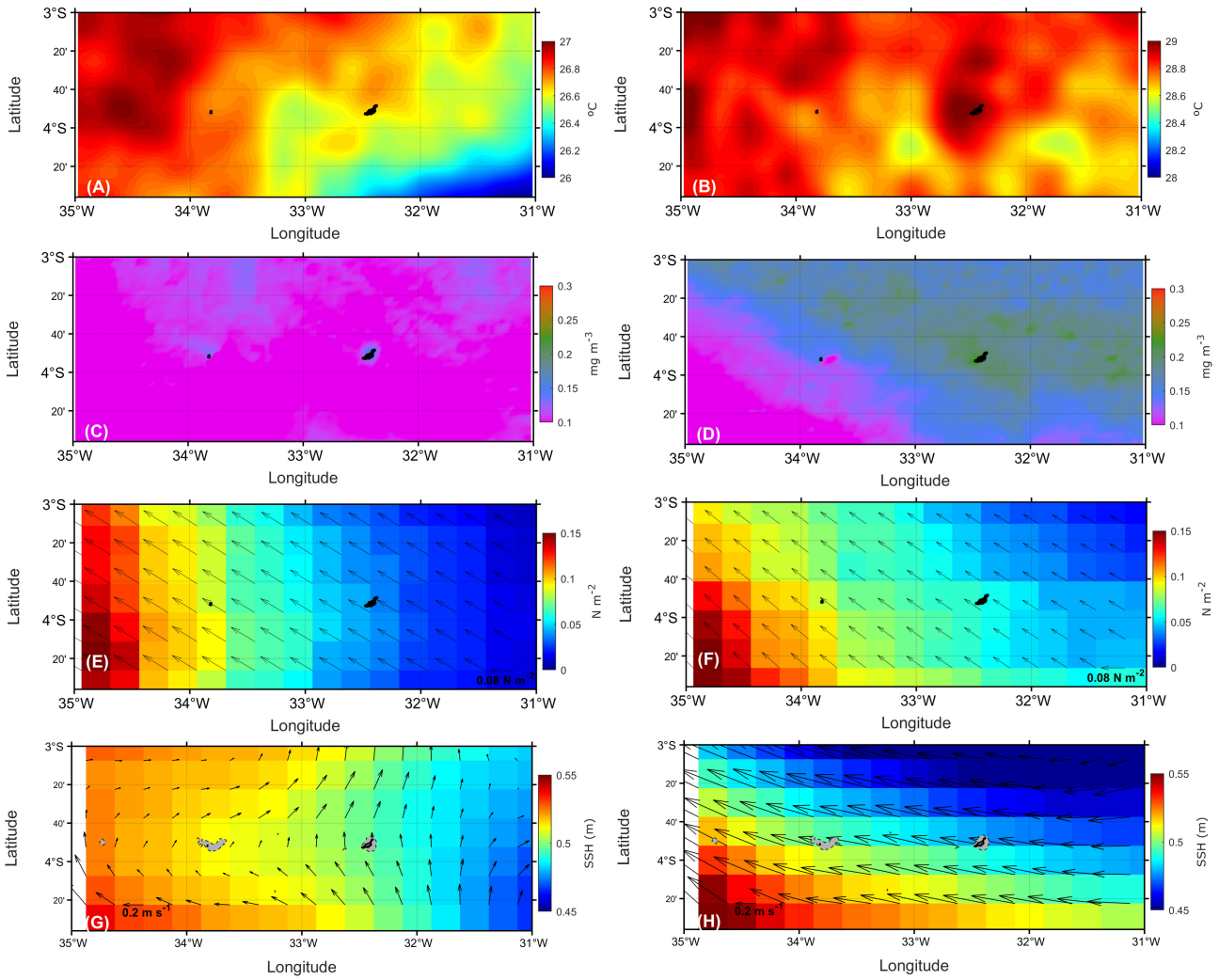

FIGURE 10 | Sea surface temperature in °C **(A,B)**, Sea surface Chl-a concentration in mg m^{-3} **(C,D)**, wind velocity in m s^{-1} (arrows in **E,F**), wind stress in N m^{-2} (colors in **E,F**), surface geostrophic velocities in m s^{-1} (arrows in **G,H**) and sea surface height (colors in **G,H**) in the southwestern tropical Atlantic region (3°S-4.5°S, 35°W-31°), for the time periods of ABRACOS cruises in spring 2015 (left side panels) and fall 2017 (right side panels).

DISCUSSION

I*n situ* and satellite data are used to discuss the temporal variability of the oceanic characteristics around FN and RA in spring 2015 and fall 2017 that have been shown to be representative of canonical spring and fall conditions (Assunção et al., 2020; Dossa et al., 2021). We also discuss the impacts of FN and RA on the thermohaline structure, local circulation, including mesoscale features, primary productivity and dissolved oxygen distribution.

Spatiotemporal Variability of Physical and Biogeochemical Parameters

In the southwestern tropical Atlantic, negative ocean-atmosphere heat fluxes and stronger winds are observed in spring, leading to a lower SST and deeper mixed-layer. In contrast, in fall, positive buoyancy due to positive heat fluxes and the relaxation of southeast trade winds lead to a higher SST and shallower mixed-layer (Araujo et al., 2011; Servain et al., 2014; Nogueira Neto et al., 2018; Assunção et al., 2020). Similarly, *in situ* ABRACOS measurements showed higher SST values in fall 2017 (28.8°C) than in spring 2015 (26.7°C). In fall 2017, during the rainy season, relatively low surface salinity and low wind stress were associated with warmer SST in the western tropical Atlantic (**Supplementary Figure 1**).

Previous studies (Schott et al., 1998, 2003; Stramma and Schott, 1999) described the SEUC characteristics across two meridional sections (35 and 31°W) between 2 and 5°S. These studies underlined the relatively small variability of the SEUC vertical position at 35°W in a depth range of 200–500 m between 2.5 and 4°S. However, using the ABRACOS mesoscale cruises, we showed that the SEUC can exhibit important temporal variability. The SEUC flowed eastward with greater intensity in the southern

part of FN during spring 2015, with a weakening in fall 2017. In the northern part of FN, the influence of the SEUC was not observed in fall 2017.

We observed an influence of the cSEC on the southern and northern sides of the island in the surface layer. This strong surface current was also associated with a variation of the mixed layer depth, which was shallower around FN and RA during fall 2017.

In situ and satellite data revealed a relatively strong variability of near surface fluorescence/Chl-a concentrations in the oceanic area around FN and RA among cruise periods with high concentration in fall 2017 when the mixed layer was shallower. In spring 2015, Chl-a was slightly higher in the northern part of the study area (**Figure 10C** and **Supplementary Figure 1C**), along the equatorial region, which may be associated to equatorial wind-driven upwelling. In fall 2017, a clear surface zonal "tongue" of maximum Chl-a was observed at 3°S, involving FN and RA areas, reaching a maximum of about 0.2 mg m^{-3}. This high productivity may be associated to nutrient rich waters transported westward by the cSEC, which is stronger during fall 2017 reaching a maximum of about 0.2 mg m^{-3} (**Figures 10G,H** and **Supplementary Figures 1G,H**). CTD profiles confirm the increase in fluorescence concentrations around FN and RA during fall 2017, with two to fourfold higher concentrations when compared to spring 2015 (**Figures 4C**, **5C**, **6C**). Note that the Chl-a variability in the equatorial Atlantic can be influenced by several mechanisms, such as the seasonal variations of upwelling driven by the meridional displacement of the ITCZ, the westward advection by the SEC, or the perturbation of the equatorial upwelling by eastward propagating Kelvin waves (Servain et al., 1982; Grodsky et al., 2008). We here highlighted that FN and RA can also locally impact the Chl-a distribution.

Around FN and RA, DO concentration was lower than ∼3 ml l^{-1} in the depth range 150–350 m in fall 2017 (**Figure 6D**). In spring 2015, this pattern was observed around FN but 5 out of 8 profiles around AR presented DO > 3 ml l^{-1} in this depth range (**Figures 4D**, **5D**). These oxygen maxima have been reported in the SEUC farther east (Tsuchiya, 1986; Schott et al., 1998). These oxygen signatures are used to diagnose the origin of the SEUC. Our results can provide further insight in a current debate. Indeed, according to Bourlès et al. (1999), in the region where the NBC forms, the NBUC weakens and retroflects to feed the SEUC. On the contrary, Schott et al. (1998) indicated that the SEUC is not supplied by the oxygen-rich and high-salinity NBUC waters, but is mostly made up of low-oxygen interior recirculation waters out of the SEC. This was also supported by Goes et al. (2005), that stated that apart from the gyre recirculation, there is a minor contribution from the NBUC to the SEUC. Finally, recently, Dossa et al. (2021) also showed that the NBUC retroflection does not feed the SEUC, which instead originates from the SEC retroflection, at least in fall. Still, the presence of profiles with higher DO concentration in spring 2015 raise again the question about a potential contribution of the NBUC to the SEUC. The orientation of the subsurface currents in the area of RA in spring 2015 may also indicate the presence of a retroflection. In the same sense, using float trajectories (around 200 m depth), Fischer et al. (2008) reported that, in austral spring, a float deployed south of the SEUC followed its eastward flow but then drifted westwards. The float was then entrained by the NBUC and re-entered the SEUC northwest of RA. At 23°W, Brandt et al. (2008) observed an oxygen maximum in the deepest part of the SEUC (∼400 m), indicating either a direct connection to the western boundary flow or a recirculation of oxygen-rich water from the south. Around RA, we observed a south/southeastwards flow (100–400 m depth) (**Figure 9B**). It seems therefore that in spring, the NBUC can retroflect to reach RA. However, the contribution of this retroflection to the SEUC remains unclear since the NBUC signature was lost close to RA and no more observable around FN. Therefore, it seems that as proposed by Goes et al. (2005), the NBUC can retroflect, at least in spring, but the contribution of the NBUC to the SEUC is likely negligible. Further studies are needed to quantify such effects and fully explain the mechanisms potentially involved in the NBUC-SEUC connection.

Island Wake Observed From CTDO and SADCP Data

To study possible effects of local flow-topography interactions over the large-scale circulation patterns, in **Figures 11**, **12**, we examined the vertical zonal velocity profiles (0–600 m depth) in the western and eastern side of FN (transects Tb and Tc in **Figure 2**) and in the northwestern and southeastern side of RA (transect Td in **Figure 2**). The westward near-surface cSEC and eastward subsurface SEUC dominated at both periods, with stronger cSEC velocities in fall 2017 than spring 2015. On the opposite and, the subsurface SEUC transport was stronger in spring 2015 (**Figure 11**). In addition, a quite different circulation patterns was observed west and east of FN for both periods. In spring 2015, near-surface (0–100 m depth) zonal currents undergo important changes in their direction and intensity between upstream and downstream areas near FN, with maximal values higher in the western (U ∼ 20 cm s^{-1}) than the eastern (U ∼ 10 cm s^{-1}) side of FN (**Figures 11A,B**). The presence of the archipelago also induced strong perturbations of the cSEC, with a splitting of the cSEC core upstream of the archipelago in both periods (**Figure 11A** versus **Figure 11B**, and **Figure 11C** versus **Figure 11D**), although higher currents were observed in fall 2017, with maxima intensity (∼80 cm s^{-1}) measured at the western side of FN (**Figure 11C**).

Below the surface layer, between 100 and 400 m depth, the effects of island wake on the SEUC was also visible. A current core splitting was indeed observed in the eastern side of FN, with maximum velocities occurring north of 3.9°S (U ∼30 cm s^{-1}) and a core of 20 cm s^{-1} centered at 3.7°S in spring 2015 (**Figure 11A**). A stronger and single SEUC core was observed downstream of FN, suggesting a reorganization of the eastward subsurface flow in the eastern portion of the archipelago, with eastward velocities higher than 50 cm s^{-1} at 3.9–4.2°S (**Figure 11B**). A similar scenario was observed in fall 2017 west of FN and north of 3.9°S, although with a much less intense and even a reversed transport north of the archipelago (U ∼ −10 cm s^{-1} at 3.7°S). East of FN, the SEUC presented

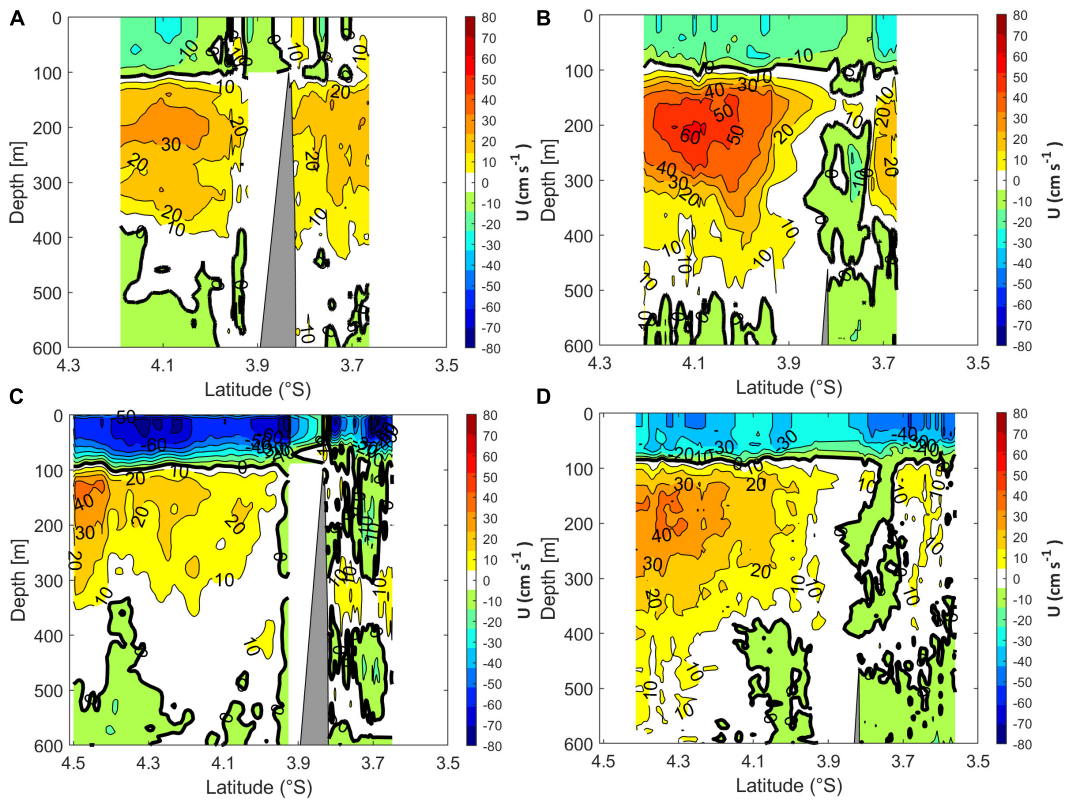

FIGURE 11 | Zonal velocity component (in cm s^{-1}, 0–600 m depth) near FN in the western (left side, see Tb transects in **Figure 2**) and eastern (right side, see Tc transects in **Figure 2**) regions, during spring 2015 **(A,B)** and fall 2017 **(C,D)**. The contour interval is 10 cm s^{-1}. The transects (Tb and Tc) are not along a single straight line, but along two non-meridional line segments.

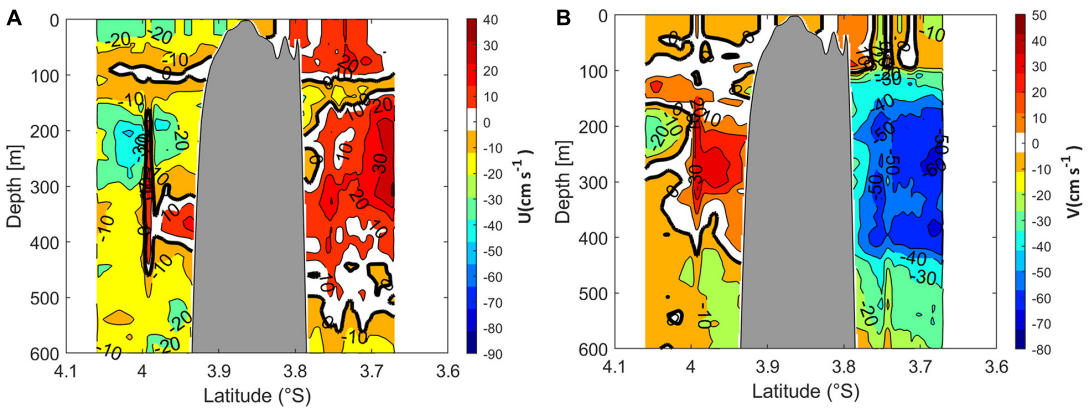

FIGURE 12 | Mean zonal **(A)** and meridional **(B)** velocity components (in cm.s^{-1}) during spring 2015 around RA (see Td transect in **Figure 2**). The contour interval is 10 cm.s^{-1}. In each panel, the bold black solid line contours represents null value of the velocity.

a maximum intensity of 40 cm s^{-1} at ∼4.5°S (**Figure 11C**). In the subsurface layer (100–400 m) SEUC intensity was maximal of 40 cm s^{-1} in the east side of FN at ∼200 m depth (**Figure 11D**).

These changes in the intensity and direction of the currents around the islands can be related to local topography. Cross-sectional vertical profiles of the temperature, salinity, fluorescence/Chl-a and dissolved oxygen concentrations are presented in **Supplementary Figure 2**. Transects were constructed from CTDO stations 05, 04, 01, and 08 (spring 2015), and 45, 44, 50, and 51 (fall 2017), represented by black triangles (see **Figure 2** for the stations position).

Besides currents (intensity and direction) differences, vertical distributions of temperature and salinity are not the same in both sides of FN (Hydrographic transects in

Supplementary Figures 2C,D). During spring 2015, we notice below 100 m depth a deepening of isotherms (see for example 10°C, **Supplementary Figure 2A**) and isohalines (for example 35.2 and 34.9, **Supplementary Figure 2C**) in the west side of FN, which is associated to observed splitting in SEUC structure due to the presence of the island (**Figure 11A**). Although less intense, this scenario is also observed during fall 2017 for the same isotherms and isohalines (**Supplementary Figures 2B,D**), which seems to be also associated to perturbations in SEUC structure imposed by the island wake (**Figure 11C**).

Indeed numerical simulations (e.g., Tchamabi et al., 2017), showed a subsurface cooling around the FN and RA, which was mainly driven by the interruption of cSEC by the bathymetry, enhancing vertical mixing and mesoscale eddy activity in the thermocline. It suggests that the island wake leads to an enrichment from the subsurface to the euphotic layer near FN and RA, supplying the productivity in these regions. This locally enhanced productivity is also visible on the satellite Chl-a observations (**Figure 10C**).

Another section is carried out on the northwestern and southeastern sides of the atoll (transects Td in **Figure 2**). In the surface layer (0–100 m), there is a predominantly eastward flow ($U > 0$ and $V < 0$) and below the surface layer there is an eastward flow centered at 250 meters in the northwestern part of RA (**Figure 12**). As shown later, in the subsurface layer (around 150–350 m depth), a cyclonic vortex structure was observed downstream (southeast side) of RA (red circle in **Figures 9B**, **12**). However, the application of existing Richardson number (station 12 and 22) shows low Ri (<0.3) values around 200–400 m depth indicating the vortex (**Figures 7D,E**).

The maximal vortex velocity Umax $\approx$ 20 cm.s^{-1} is reached for the characteristic radius Rmax $\approx$ 28 km, resulting in a vortex Rossby number Ro $\approx$ 0.7 of this cyclonic vortex. The Rossby radius of deformation (Rd) is 23 km, a value very close to the vortex radius. In the equatorial region, Rd is one order of magnitude larger (Houry et al., 1987; Simoes-Sousa et al., 2021). Strong surface Eddies close to the equator present very small values of the Coriolis parameter f, leading to high Rossby number. Although some of these eddies are also highly circular, most of them have very small amplitudes (Douglass and Richman, 2015). The Burger number of the vortex is about 3. These values are consistent with the processes associated with a cyclonic eddy shedding observed in the Gulf of Guinea (Djakouré et al., 2014).

Corresponding temperature and salinity signatures were observed between 150 and 350 m depth at the same position (station 12 and 22, **Figures 7C,E**). At this depth range, an anomalous (and almost stepwise) increase in temperature and salinity was observed, associated with subsurface mesoscale changes in currents (**Figure 12**) and small Richardson numbers (**Figures 7C,E**). This subsurface vortex structure was also probably generated by the island wake (e.g., Arístegui et al., 1997; Chérubin and Garavelli, 2016). The maximum of subsurface fluorescence was also observed at Station 22, in the edge of the eddy-like feature (**Figure 5A**). Cyclonic and anticyclonic eddies are known to strongly modulate primary production in oligotrophic waters around islands (e.g., Arístegui et al., 1997). Maximum primary productivity is often observed near eddy edges, where numerous filaments are observed due to enhanced lateral straining, stretching and stirring (e.g., Mahadevan, 2016; Lévy et al., 2018).

CONCLUSION

Based on two regional mesoscale cruises realized off the Northeast Brazilian coast, we described the upper-ocean circulation and how island wake impact the main features around Fernando de Noronha island and Rocas Atoll in two contrasted periods, Austral spring 2015 and fall 2017, considered as representative of the mean spring and fall conditions. In spring, the area was characterized by a lower SST (26.6°C) and deeper mixed-layer (∼90 m). At this depth, a strong vertical shear was observed between the surface cSEC and the subsurface SEUC. In contrast, in fall, SST was higher (∼28.8°C), the mixed-layer shallower (∼50 m), and the vertical shear between the cSEC and the SEUC weaker. Our study suggested that SEUC was fed (not fed, respectively) by the NBUC in spring 2015 (fall 2017). However, from the available datasets, it was not possible to quantify how much this retroflection fed the SEUC in spring 2015. To unravel the scientific debate on the NBUC-SEUC connection, dedicated oceanographic cruises and numerical modeling approaches would be needed. Beside these global patterns, the physical processes in the wakes of islands were clear with the splitting of the large-scale currents, the presence of mesoscale meanders and a subsurface eddy-like structure. These features are likely key processes providing an enrichment from the subsurface to the euphotic layer near FN and RA, supplying the local productivity. Enhancement of primary production around the archipelago was also observed from satellite data in spring 2015. In addition to the new information described above, this work enables the planning of future cruises to be carried out for a better understanding of mesoscale vortex processes, water mass transport around the islands and in the tropical Atlantic.

DATA AVAILABILITY STATEMENT

The datasets presented in this study can be found in online repositories. The names of the repository/repositories and accession number(s) can be found below: ABRACOS Data (doi: 10.17600/15005600 and doi: 10.17600/17004100).

AUTHOR CONTRIBUTIONS

ACo and AB planned and organized oceanographic surveys. GE, AB, AD, and ACo worked in data processing and QC. All authors wrote and reviewed the manuscript.

FUNDING

This work was a contribution to the LMI TAPIOCA, the SMAC project (CAPES/COFECUB no. 88881.142689/2017–01),

the PADDLE project (funding by the European Union's Horizon 2020 Research and Innovation Programme—Grant Agreement 73427) and EU H2020 TRIATLAS project under Grant Agreement 817578.

ACKNOWLEDGMENTS

We thank the officers and crew of the R/V Antea for their able assistance and cooperation. MA thanks the Brazilian Research Network on Global Climate Change—Rede CLIMA (FINEP-CNPq 437167/2016-0) and the Brazilian National Institute of Science and Technology for Tropical Marine Environments—INCT AmbTropic (CNPq/FAPESB 565054/2010-4 and 8936/2011) for their support.

SUPPLEMENTARY MATERIAL

The Supplementary Material for this article can be found online at: https://www.frontiersin.org/articles/10.3389/fmars.2021.598101/full#supplementary-material

Supplementary Figure 1 | Sea surface temperature, Sea surface Chl-a concentration, Surface winds stress, and Sea surface height/surface geostrophic velocities, obtained from OSTIA product in the southwestern tropical Atlantic region (4°N-8°S, 39.25°W-27°W), involving Fernando de Noronha Archipelago and Rocas Atoll (rectangle), for the same time periods of ABRACOS cruises: spring 2015 (left side panels), and fall 2017 (right side panels).

Supplementary Figure 2 | Vertical distributions of temperature, salinity, fluorescence, dissolved oxygen concentrations and Brunt-Väisälä frequency (N) near FN, during spring 2015 (left panels) and fall 2017 (right panels). Transects were obtained from CTDO stations 05, 04, 01, and 08 (spring 2015), and 45, 44, 50, and 51 (fall 2017), represented by black triangles. See **Figure 2** for CTDO stations positions (pink dots).

REFERENCES

Araujo, M., Limongi, C., Servain, J., Silva, M., Leite, F. S., Veleda, D., et al. (2011). Salinity-induced mixed and barrier layers in the southwestern tropical Atlantic Ocean off the northeast of Brazil. *Ocean Sci.* 7, 63–73. doi: 10.5194/os-7-63-2011

Arístegui, J., Tett, P., Hernandez-Guerra, A., Basterretxea, G., Montero, M. F., Wild, K., et al. (1997). The influence of island-generated eddies on chlorophyll distribution: a study of mesoscale variation around Gran Canaria. *Deep-Sea Res.* 44, 71–96. doi: 10.1016/S0967-0637(96)00093-3

Assunção, R. V., Silva, A. C., Amédée, R., Bourlès, B., Silva, C. H. S., Ternon, J. F., et al. (2020). 3D characterisation of the thermohaline structure in the southwestern tropical Atlantic derived from functional data analysis of in situ profiles. *Prog. Oceanogr.* 187:102399. doi: 10.1016/j.pocean.2020.102399

Assunção, R. V., Silva, A. C., Martins, J., and Flores, M. M. (2016). Spatial-Temporal variability of the thermohaline properties in the coastal region of Fernando de Noronha Archipelago. *Brazil. J. Coast. Res. Special Issue* 75, 512–516. doi: 10.2112/SI75-103.1

Bentamy, A., and Croizé-Fillon, D. (2011). Gridded surface wind fields from Metop/ASCAT measurements. *Int. J. Remote Sens.* 33, 1729–1754. doi: 10.1080/01431161.2011.600348

Bertrand, A., Alory, G., Chaigneau, A., Eldin, G., Grelet, J., Devesa, J., et al. (2017). *ABRACOS 2 Cruise - Physical Datasets*. SEANOE, doi: 10.17882/76352

Bertrand, A., Costa Da Silva, A., Chaigneau, A., Eldin, G., Roubaut, F., Grelet, J., et al. (2015). *ABRACOS Cruise - Physical Datasets*. SEANOE, doi: 10.17882/76696

Bourlès, B., Molinari, R. L., Johns, E., Wilson, W. D., and Leaman, K. D. (1999). Upper layer currents in the western tropical North Atlantic (1989–1991). *J. Geophys. Res.* 104, 1361–1375. doi: 10.1029/1998JC900025

Brandt, P., Hormann, V., Bourlès, B., Fischer, J., Schott, F. A., Stramma, L., et al. (2008). Oxygen tongues and zonal currents in the equatorial Atlantic. *J. Geophys. Res.* 113:C04012. doi: 10.1029/2007JC004435

Chaves, T. B. C., Mafalda, J. R. P., Santos, C., Souza, C. S., Moura, G., Sampaio, J., et al. (2006). Planktonic biomass and hydrography in the Exclusive Economic Zone of Brazilian Northeast. *Trop. Oceanogr.* 34, 12–30.

Chérubin, L. M., and Garavelli, L. (2016). Eastern Caribbean circulation and island mass effect on St. Croix, US Virgin Islands: a mechanism for relatively consistent recruitment patterns. *PLoS One* 11:e0150409. doi: 10.1371/journal.pone.0150409

Djakouré, S., Penven, P., Bourlés, B., Veitch, J., and Koné, V. (2014). Coastally trapped eddies in the north of the gulf of guinea. *J. Geophys. Res.* 119, 6805–6819. doi: 10.1002/2014JC010243

Donlon, C. J., Martin, M., Stark, J., Roberts-Jones, J., Fiedler, E., and Wimmer, W. (2012). The Operational Sea Surface Temperature and Sea Ice analysis (OSTIA). *Remote Sens Environ.* 116, 140-158, . doi: 10.1016/j.rse.2010.10 017, 2011

Dossa, A. N., Silva, A. C., Chaigneau, A., Eldin, G., Araujo, M., and Bertrand, A. (2021). Near-surface western boundary circulation off Northeast Brazil. *Prog. Oceanogr.* 80:102475. doi: 10.1016/j.pocean.2020.102475

Douglass, E. M., and Richman, J. G. (2015). Analysis of ageostrophy in strong surface eddies in the Atlantic Ocean. *J. Geophys. Res.* 120, 1490–1507.

Ducet, N., Le Traon, P. Y., and Reverdun, G. (2000). Global high-resolution mapping of ocean circulation from TOPEX/Poseidon and ERS-1 and -2. *J. Geophys. Res.* 105, 19477–19498. doi: 10.1029/2000JC900063

Fischer, J., Hormann, V., Brandt, P., Schott, F. A., Rabe, B., and Funk, A. (2008). South Equatorial 834 Undercurrent in the western to central tropical Atlantic. *Geophys. Res. Lett.* 35:L21601. doi: 10.1029/2008GL035753

Foltz, G. R., Brandt, P., Richter, I., Rodriguez-Fonseca, B., Hernandez, F., Dengler, M., et al. (2019). The Tropical Atlantic Observing System. *Front. Mar. Sci.* 6:206. doi: 10.3389/fmars.2019.00206

Garnesson, P. (2013). *Global Ocean Chlorophyll, PP and PFT (Copernicus-GlobColour) From Satellite Observations - Near Real Time*. Available online at: https://sextant.ifremer.fr/record/bc19d37d-fa0d-4035-b80e-33a15e7e29e4/

Goes, M., Molinari, R., Da Silveira, I., and Wainer, I. (2005). Retroflections of the North Brazil Current during February 2002. *Deep-Sea Res. I* 52, 647–667. doi: 10.1016/j.dsr.2004.10.010

Grasshoff, K., Ehrhardt, M., and Kremling, K. (1983). *Methods of Seawater Analysis*. Hoboken NJ: Wiley.

Grodsky, S. A., Carton, J. A., and McClain, C. R. (2008). Variability of upwelling and chlorophyll in the equatorial Atlantic. *Geophys. Res. Lett.* 35:L03610. doi: 10.1029/2007GL032466

Hounsou-Gbo, G. A., Araujo, M., Bourlès, B., Veleda, D. R. A., and Servain, J. (2015). Tropical Atlantic contributions to strong rainfall variability along the Northeast Brazilian coast. *Adv. Meteorol.* 2015:902084. doi: 10.1155/2015/902084

Hounsou-Gbo, G. A., Servain, J., Araujo, M., Caniaux, G., Bourlès, B., Fontenele, D., et al. (2019). SST Indexes in the tropical South Atlantic for Forecasting Rainy Seasons in Northeast Brazil. *Atmosphere* 10:335. doi: 10.3390/atmos10060335

Houry, S., Dombrowsky, E., De Mey, P., and Minster, J. (1987). Brunt-vaisala frequency and rossby radii in the south Atlantic. *J. Phys. Oceanogr.* 17, 1619–1626. doi: 10.1175/1520-04851987017<1619:BVFARR>2.0.CO;2

Joyce, T. M. (1989). On in situ "calibration" of shipboard ADCPs. *J. Atmos. Oceanic Technol.* 6, 169–172.

Lessa, R. P. T., Mafalda, P. Jr., Advincula, R., Lucchesi, R. B., Bezerra, J. L. Jr., Vaskejr, T., et al. (1999). Distribution and abundance of ichthyoneuston at seamounts and islands off North-Eastern Brazil. *Arch. Fish. Mar. Res.* 47, 239–252.

Lévy, M., Franks, P. J. S., and Smith, K. S. (2018). The role of submesoscale currents in structuring marine ecosystems. *Nat. Commun.* 9:4758. doi: 10.1038/s41467-018-07059-3

Lumpkin, R., and Garzoli, S. L. (2005). Near-surface circulation in the tropical Atlantic Ocean. *Deep Sea Res Part I* 52, 495–518. doi: 10.1016/j.dsr.2004.09.001

Mahadevan, A. (2016). The impact of submesoscale physics on primary productivity of plankton. *Ann. Rev. Mar. Sci.* 8, 161–184. doi: 10.1146/annurev-marine-010814-015912

Nogueira Neto, A. V., Giordani, H., Caniaux, G., and Araujo, M. (2018). Seasonal and interannual mixed-layer heat budget variability in the western tropical Atlantic from Argo floats (2007–2012). *J. Geophys. Res. Oceans.* 123, 5298–5322. doi: 10.1029/2017JC013436

Pedlosky, J. (1987). *Geophysical Fluid Dynamics*, 2 Edn. Berlin: Springer, 728.

Pollard, R. T., and Read, J. F. (1989). A method for calibrating ship-mounted acoustic doppler profilers and the limitations of gyro compasses. *J. Atmos. Oceanic Technol.* 6, 859–865.

Pujol, M.-I., Faugère, Y., Taburet, G., Dupuy, S., Pelloquin, C., Ablain, M., et al. (2016). DUACS DT2014: the new multi-mission altimeter data set reprocessed over 20 years. *Ocean Sci.* 12, 1067–1090. doi: 10.5194/os-12-1067-2016

Schott, F. A., Dengler, M., Brandt, P., Affler, K., Fischer, J., Bourlès, B., et al. (2003). The zonal currents and transports at 35W in the tropical Atlantic. *Geophys. Res. Lett.* 30:1349. doi: 10.1029/2002GL016849

Schott, F. A., Fischer, J., and Stramma, L. (1998). Transports and pathways of the upper-layer circulation in the western tropical Atlantic. *J. Phys. Oceanogr.* 28, 1904–1928.

Servain, J., Caniaux, G., Kouadio, Y. K., McPhaden, M. J., and Araujo, M. (2014). Recent climatic trends in the tropical Atlantic. *Clim. Dyn.* 34, 3071–3089. doi: 10.1007/s00382-014-2168-7

Servain, J., Picaut, J., and Merle, J. (1982). Evidence of remote forcing in the equatorial Atlantic Ocean. *J. Phys. Oceanogr.* 12, 457–463.

Silveira, I. C. A., Miranda, L. B., and Brown, W. S. (1994). On the origins of the North Brazil Current. *J Geophys. Res.* 99, 501–522.

Simoes-Sousa, I. T., Silveira, I. C. A., Tandon, A., Flierl, G. R., Ribeiro, C. H. A., and Martins, R. P. (2021). The Barreirinhas Eddies: Stable Energetic Anticyclones in the Near-Equatorial South Atlantic. *Front. Mar. Sci.* 8:617011. doi: 10.3389/fmars.2021.617011

Stramma, L., and Schott, F. (1999). The mean flow field of the tropical Atlantic Ocean. *Deep Sea Res II* 46, 279–303.

Taburet, G., Sanchez-Roman, A., Ballarotta, M., Pujol, M.-I., Legeais, J.-F., Fournier, F., et al. (2019). DUACS DT-2018: 25 years of reprocessed sea level altimeter products. *Ocean Sci.* 15, 1207–1224. doi: 10.5194/os-15-1207-2019

Tchamabi, C., Araujo, M., Silva, M. A., Bourlès, B., and Travassos, P. (2018). Ichthyoplankton transport around the Brazilian Fernando de Noronha archipelago and Rocas Atoll: are there any connectivity patterns ? *Indian J. Geo Mar. Sci.* 47, 812–818.

Tchamabi, C. C., Araújo, M., Silva, M., and Bourlès, B. (2017). A study of the Brazilian Fernando de Noronha Island and Rocas Atoll wakes in the tropical Atlantic. *Ocean Model* 111, 9–18. doi: 10.1016/j.ocemod.2016.12.009

Travassos, P. E. P. F., Hazin, F. H. V., Zagaglia, J. R., Rocha, R. A., and Schober, J. (1999). Thermohaline structure around seamounts and islands off Northeast Brazilian coast. *Arch. Fish. Mar. Res.* 47, 211–222.

Tsuchiya, M. (1986). Thermostads and circulation in the upper layer of the Atlantic Ocean. *Prog. Oceanogr.* 16, 235–267.

UNESCO (1981). *Background Papers and Supporting Data on the International Equation of State of Seawater 1980 (No. 38), UNESCO Technical Papers in Marine Science*. Paris: UNESCO.

Conflict of Interest: The authors declare that the research was conducted in the absence of any commercial or financial relationships that could be construed as a potential conflict of interest.

frontiers in Marine Science

ORIGINAL RESEARCH
published: 30 April 2021
doi: 10.3389/fmars.2021.653502

Modeling the Exposure of the Macaronesia Islands (NE Atlantic) to Marine Plastic Pollution

Cláudio Cardoso [1,2]* *and Rui M. A. Caldeira* [1,2]

[1] *Observatório Oceânico da Madeira, Agência Regional para o Desenvolvimento da Investigação, Tecnologia e Inovação, Funchal, Portugal,* [2] *Instituto Dom Luiz, Faculdade de Ciências, Universidade de Lisboa, Lisbon, Portugal*

The constant increase of marine plastic pollution poses an unprecedented risk to oceanic islands, which become increasingly exposed to a hazard of which they have very little control. Located in the Northeast Atlantic Ocean, the Macaronesia is comprised by the Azores, Madeira, Canary Islands, and Cabo Verde. Although past studies suggest that most plastic items collected on these islands are from offshore regions, their actual sources remain unclear to present date. As such, we focus on the characterization of the potential sources and pathways of plastic particles reaching the Macaronesia archipelagos. This is achieved by combining modeled datasets for ocean currents, winds and waves with a Lagrangian tool used to track virtual particles released around the archipelagos for a 10-year period, making a distinction between surface and submerged particles. Global drifter trajectories are also assessed, selecting those that intercept the archipelagos. Our results demonstrate that the North Atlantic subtropical gyre is the most conspicuous feature in particles and drifter trajectories. The Gulf Stream acts as the main pathway for all archipelagos at a regional scale, though with less significance to Cabo Verde. Surface particles are connected to regional sources in a shorter timescale than mixed particles, mainly because of the wind. Intercepting high-windage particle trajectories are dominant at the center of the North Atlantic subtropical gyre, demonstrating that particles originating from the North Atlantic "garbage patch" are most likely to intercept the archipelagos if considerably exposed to the wind. Regarding the connectivity to sources, all archipelagos are significantly exposed to areas of intensive fishing activity, mainly those located in the Gulf Stream (Azores), in international waters off the Portuguese coast (Madeira and Canary Islands) and along the Northwestern African coast (Cabo Verde). The east coasts of Central and North America are the main sources of land-based particles reaching the Azores, Madeira, and Canary Islands, whereas the Northwestern African coast is the main source for land-based particles reaching Cabo Verde. Our results demonstrate how vulnerable the Macaronesian archipelagos are to marine plastic pollution, highlighting the urgency for international cooperation to mitigate the exposure of oceanic islands to marine plastic pollution.

Keywords: Lagrangian transport, Azores, Madeira, Canary Islands, Cabo Verde, North Atlantic subtropical gyre, surface drifting buoys

OPEN ACCESS

Edited by:
Frédéric Cyr,
Fisheries and Oceans Canada, Canada

Reviewed by:
Erik Van Sebille,
Utrecht University, Netherlands
Annalisa Griffa,
National Research Council (CNR), Italy

***Correspondence:**
Cláudio Cardoso
claudio.cardoso@oom.arditi.pt

Specialty section:
This article was submitted to Physical Oceanography, a section of the journal Frontiers in Marine Science

Received: *14 January 2021*
Accepted: *15 March 2021*
Published: *30 April 2021*

Citation:
Cardoso C and Caldeira RMA (2021) Modeling the Exposure of the Macaronesia Islands (NE Atlantic) to Marine Plastic Pollution. Front. Mar. Sci. 8:653502. doi: 10.3389/fmars.2021.653502

1. INTRODUCTION

The exponential growth of global plastic production from 5 million tons in the 1950s to 322 million tons in 2015 (Andrady, 2011) led to an equally exponential input of plastic objects into the marine environment (Ryan et al., 2009), with estimates between 4 and 12 million tonnes per year (MT.year^{-1}; Jambeck et al., 2015). As a result, marine plastic litter has not only become ubiquitous in the world's oceans in the past few decades (e.g., Cozar et al., 2014; Law, 2017), but also continues to increase at an alarming rate (Lebreton et al., 2018). In fact, it is estimated that plastic items account for up to 80% of marine litter (Barnes et al., 2009), with estimates of abundance ranging from 5.2 trillion pieces (Eriksen et al., 2014) to 15–51 trillion pieces (van Sebille et al., 2015). However, recent studies have argued that the global load of plastic floating at the ocean surface is much lower than predictions (Cozar et al., 2014; Eriksen et al., 2014; van Sebille et al., 2015). Such discrepancy can relate with a variety of factors. For example, although surface-trawling plankton nets are mostly used to sample plastic debris at the ocean surface (e.g., van Sebille et al., 2015; Lebreton et al., 2018; Lacerda et al., 2019), it is now known that a significant amount of small-sized plastic debris are concealed in sub-surface layers, with a exponentially decreasing concentration along depth (Pabortsava and Lampitt, 2020). The vertical displacement of plastic particles can be driven by a variety of mechanisms, such as wind-induced vertical mixing (Kukulka et al., 2012; Reisser et al., 2015) or biofouling, which increases/decreases the average material density of plastic fragments and causes them to sink/re-suspend when the conditions for biological growth are favorable/unfavorable (Fazey and Ryan, 2016; Kooi et al., 2017). Recent studies have also demonstrated that besides being considered hotspots for the degradation of plastic into smaller fragments (Corcoran et al., 2009; Andrady, 2011; Isobe et al., 2014), sandy and rocky beaches can retain significant amounts of plastic fragments stranded at the surface (Thiel et al., 2013), and in deeper layers (Chubarenko et al., 2018; McWilliams et al., 2018). In fact, Turra et al. (2015) found plastic fragments as deep as 2 m, with surface layers accounting for <10% of the total abundance in the sediment column.

The growing accumulation of plastic litter in the marine environment poses an unattended environmental threat to islands, as they become increasingly exposed to pollution of which they have very little control (e.g., Baztan et al., 2014; Monteiro et al., 2018; Pham et al., 2020; Pieper et al., 2020). Its impacts are extensive and can be felt on highly vulnerable socio-economic sectors of which islands depend on, such as tourism, fisheries and shipping industries (Rodríguez et al., 2020). Beach clean-ups are often the only possible remediation measure for the removal of stranded plastic debris from local coastlines, representing an enormous cost to local organizations and governments (Burt et al., 2020; Rodríguez et al., 2020).

Local ecology is also severely impacted by marine plastic pollution through ingestion and entanglement, ranging from zooplankton (Desforges et al., 2015) to cetaceans (Baulch and Perry, 2014), seabirds (Avery-Gomm et al., 2018; Provencher et al., 2018), and marine reptiles (Aguilera et al., 2018). Persistent organic pollutants present in seawater are absorbed very efficiently by plastics and can be transferred into tissues and organs through ingestion (Rochman et al., 2013; Andrady, 2017), having a direct or indirect impact in all trophic-level organisms (Gassel et al., 2013) and potentially on humans (reviewed in Campanale et al., 2020). In addition, floating plastics such as resin pallets and derelict fishing gear have been reported to transport microbial communities (Carson et al., 2013), algae, invertebrates, and fish (Goldstein et al., 2014) to non-native regions (Barnes, 2002; Gregory, 2009). The systematic report of plastic debris stranded in uninhabited islands (e.g., Lavers and Bond, 2017; Fernandes, 2019; Ryan et al., 2019; Burt et al., 2020) further demonstrates how exposed such pristine and often fragile environments are to such hazard, forcing them to act as sentinels of global ocean pollution (Barnes et al., 2018). For all the reasons stated above, it is extremely important to understand how physical processes, such as ocean currents and wind mediate the transport of marine litter to presumably remote insular environments.

The Macaronesia is a biogeographic region located in the Northeast Atlantic Ocean and consists of 31 volcanic islands comprised in four archipelagos (blue polygons in **Figure 1**): the Azores, Madeira (and Selvagens), Canary Islands (hereafter referred as Canaries), and Cabo Verde (Freitas et al., 2019). Politically, Azores and Madeira are under the sovereignty of Portugal, whereas the Canaries are under the sovereignty of Spain. Cabo Verde is the only independent state and the only archipelago outside the European Union. In terms of oceanic and atmospheric conditions, all islands are under the influence of the North Atlantic subtropical gyre (**Figure 1A**) and the Azores High atmospheric pressure system (**Figure 1B**), respectively. For this reason, common patterns in the transport of incoming marine litter are expected to occur between the archipelagos. However, although recent studies strongly suggest that most of the debris collected on the Macaronesian islands come from the open ocean (e.g., Baztan et al., 2014; Fernandes, 2019; Álvarez et al., 2020; Pham et al., 2020), the exposure of the archipelagos to the regional transport of marine litter has, to the best of our knowledge, not been addressed to present date.

Our study focuses on the characterization of the potential sources and pathways of marine plastic litter affecting the archipelagos of the Macaronesia. Special attention was given to the ocean currents and winds responsible for the transport of particles to the archipelagos. Lagrangian simulations were performed, in which particles representative of micro- and macro-plastics (plastic particles smaller and larger than 5 mm in length, respectively; Barnes et al., 2009; Andrady, 2011) with a varying degree of exposure to the wind were released around the archipelagos and tracked backward in time to their origins. Serving as an *in-situ* reference, floating drifter trajectories intersecting the archipelagos were also characterized. As our study focuses primarily on the transport of particles at a regional scale, such as in the connectivity between archipelagos and continental coastal areas, the transport of particles between islands of the same archipelago is beyond the scope of this study and is not considered herein. This article is organized as follows: a brief introduction to the geographic setting of the archipelagos is

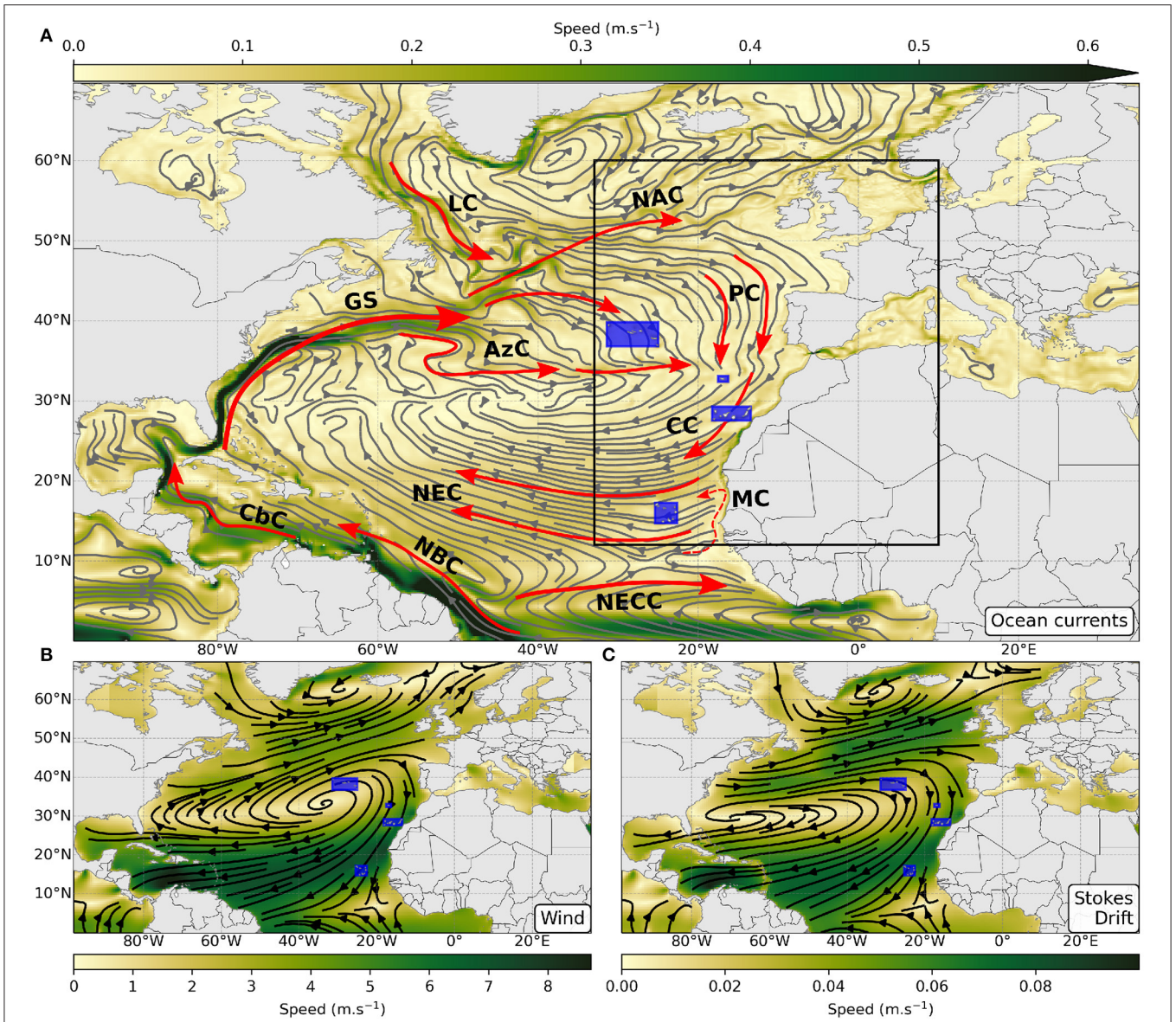

FIGURE 1 | Ten-year climatology (2006–2016) for: **(A)** ocean currents from CMEMS, **(B)** wind from ECMWF, and **(C)** stokes drift from WW3. Black area in **(A)** represents the delimitation of the finer-resolution ocean currents dataset (GLORYS12V1). Blue polygons mark the location of the Azores, Madeira, Canaries, and Cabo Verde archipelagos (from north to south). Red arrows represent the main ocean currents: Gulf Stream (GS), Labrador Current (LC), Azores Current (AzC), North Atlantic Current (NAC), Portugal Current (PC), Canary Current (CC), Mauritania Current (MC), North Equatorial Current (NEC), North Equatorial Counter Current (NECC), the North Brazil Current (BC), and the Caribbean Current (CbC).

presented in section 2; data being used, along with the modeling framework and simulations set-up are described in section 3; the main results and subsequent discussion are presented in section 4; and the main conclusions are summarized in section 5.

2. OCEANOGRAPHIC SETTING

As the north-westernmost islands of the Macaronesia, the Azores archipelago extends for ∼615 km across the Mid-Atlantic Ridge and is composed by nine islands divided in three groups: the western, central and the eastern groups (**Figure 2A**). The Azores is the most remote archipelago of the Macaronesia, being located at ∼1,400 km distance from the nearest continental coast and ∼860 km distance from Madeira (the nearest islands). The archipelago is surrounded by two main large-scale ocean currents: (i) the Gulf Stream and associated bifurcations affect the islands in the form of meanders and eddies from the west and north-west (Caldeira and Reis, 2017); (ii) and the Azores Current that originates from the southern branch of the Gulf Stream and flows south of the archipelago between 32 and 35°N (**Figure 1A**; Gould, 1985). Despite the dominant eastward-flow component, the Azores Current is characterized by the frequent occurrence of

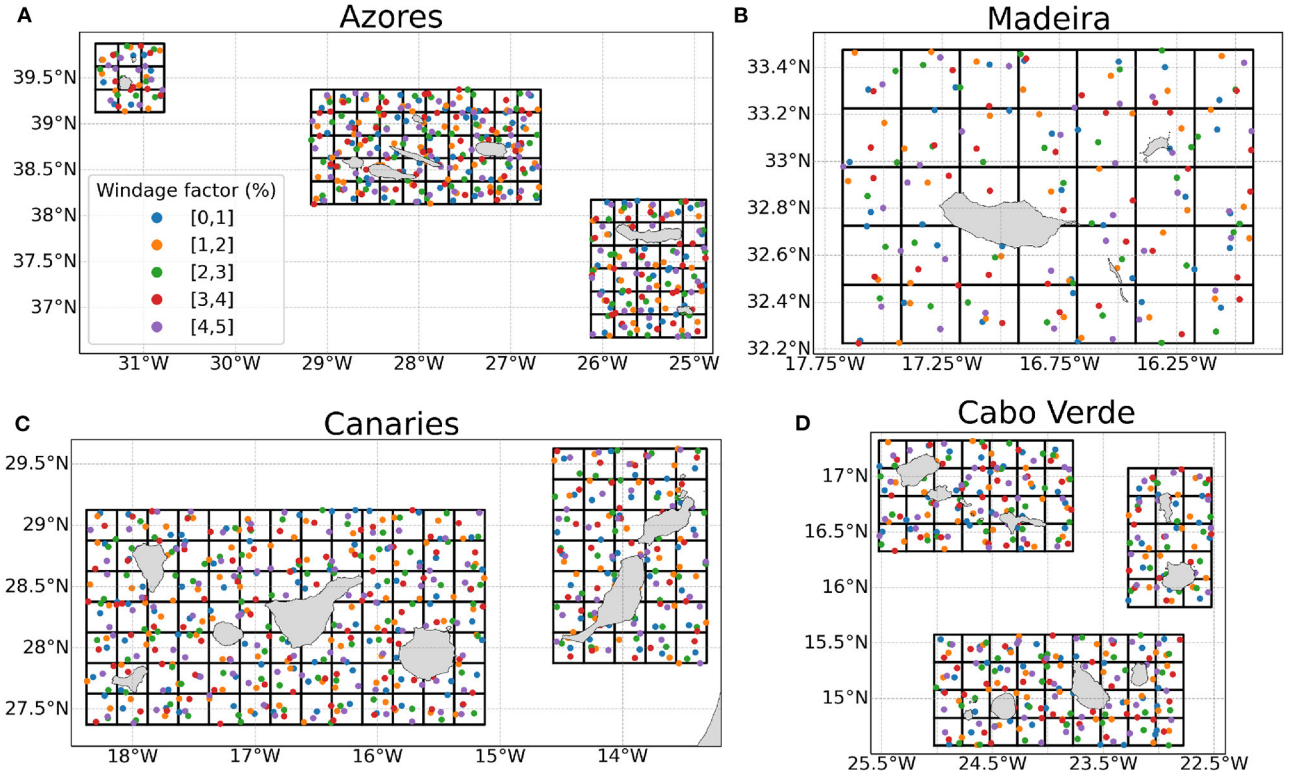

FIGURE 2 | Example of the release location of particles in the **(A)** Azores, **(B)** Madeira, **(C)** Canaries, and **(D)** Cabo Verde archipelagos. Black grids around the islands represent the boundaries in which particles are randomly released. Colors represent the particle windage groups.

eddies (Zhou et al., 2000; Sangrà et al., 2009; Barbosa Aguiar et al., 2011) that often intersect the Azorean islands from the south and from the west (Sala et al., 2016; Caldeira and Reis, 2017).

Along its eastward path, the Azores Current produces three major bifurcations with a southward-flowing component (Klein and Siedler, 1989). At the easternmost bifurcation (∼22°W), one branch meanders eastward toward the Gulf of Cadiz (Johnson and Stevens, 2000), whereas another branch turns southward and reaches the Madeira archipelago through the west/northwest (**Figure 1A**; Zhou et al., 2000). Here, this southward-flowing branch is separated into two branches as it intercepts Madeira (Stramma and Siedler, 1988; Barton, 2001), merging the south/southwestward-flowing Canary Current downstream (Stramma, 1984; Klein and Siedler, 1989; Zhou et al., 2000). Although weaker and wider (Martins et al., 2002), the Portugal Current also feeds the Canary Current as it flows toward Madeira from the north, being strongly influenced by the dominant neighboring Canary and Azores Currents at Madeira's latitude (Pérez et al., 2001). Being the smallest archipelago of the Macaronesia, Madeira is composed by three islands (**Figure 2B**) located at an intermediate geographical position between the Azores and the Canaries (Sala et al., 2013). As a consequence, Madeira is exposed to the seasonal oscillations of the Azores, Portugal, and Canary Currents (Barton, 2001; Caldeira et al., 2002; Martins et al., 2002).

As it progresses southward along the North-Western African coast, the Canary Current intercepts the Canaries at ∼500 km distance from Madeira (**Figure 1A**; Martins et al., 2002). The Canaries are composed by seven major islands extending from near African coast to open ocean with a zonal orientation (**Figure 1C**) and is the largest archipelago of the Macaronesia (in terms of land surface area). These islands act as an obstacle to the propagation of the Canary Current, being partly responsible for the frequent generation of eddies in the lee side (e.g., Arístegui et al., 1994; Barton et al., 2000; Sangrà et al., 2009). Its close proximity to the adjacent African coast (∼94 km) also exposes the Canaries to filaments and eddies pinching off from the Canary Current upwelling system, which often interact with island-induced eddies as they propagate offshore (Barton et al., 2004).

The southern limit of the Canary Current detaches from the continental margin between 25 and 20°N to connect with the wind-driven North Equatorial Current (**Figure 1A**; Mittelstaedt, 1983, 1991). With a initial southwestward flow, the North Equatorial Current intersects the Cabo Verde archipelago from the northeast (Lázaro et al., 2005) and then veers westward to become the southern limb of the North Atlantic subtropical gyre (Bourles et al., 1999), closing the gyre as it intersects the American continent and merges with the Gulf Stream (and associated upstream currents) further west (**Figure 1A**). Composed by 10 islands arrayed in a west-facing horseshoe

disposition (**Figure 2D**, Ramalho, 2011), Cabo Verde marks the southern limit of the Macaronesia region (**Figure 1A**). The oceanographic context surrounding the archipelago is characterized by the complex interaction of several large-scale oceanic currents and features, strongly affected by the seasonal meridional migration of the atmospheric Intertropical Convergence Zone (Stramma and Schott, 1999). South of archipelago, the basin-wide North Equatorial Counter Current flows eastward and leaks Southern Atlantic waters into the North Atlantic as it meanders along the southern limit of the North Equatorial Current (Fratantoni, 2001). As the North Equatorial Counter Current approaches the African coast, part of its flow continues northward along the coast and forms the seasonal-varying Mauritanian Current (**Figure 1A**; Lázaro et al., 2005). Driven by the relaxation of the trade winds and consequent intensification of the North Equatorial Counter Current, the Mauritanian Current reaches its northernmost extension (20°N) during summer and autumn, where it intersects the North Equatorial Current and turns southwestward in the direction of Cabo Verde. During winter and spring the opposite occurs, as the trade winds intensify and force the Canary Current upwelling system to reach its southernmost extension (15°N, Mittelstaedt, 1991; Van Camp et al., 1991). Such dynamic variability at the Mauritania coast is expected to affect the Cabo Verde islands, located 450–600 km west. For example, filaments rich in Chlorophyll *a* have been observed to reach the archipelago during the upwelling season (Lathuilière et al., 2008; Ohde and Siegel, 2010), whereas eddies generated by the dynamic instabilities of the Mauritania Current (Lázaro et al., 2005) and by the interaction of coastal currents with topography (Schütte et al., 2016) are often blocked by the Cabo-Verdian islands as they propagate westward (Cardoso et al., 2020).

3. DATA AND METHODS

3.1. Global Drifter Program

Surface drifting buoys (hereafter referred as drifters) are valuable instruments in providing *in-situ* information on the two-dimensional flow at the ocean surface or near surface, depending on the depth at which the drogue (sea anchor) is located (Lumpkin et al., 2017). As part of the Global Drifter Program (GDP) from the National Oceanic and Atmospheric Administration (NOAA), drifters are deployed throughout the global ocean since 1988, maintaining an array of ∼1,250 drifters throughout the years. These drifters are drogued at 15 m depth so that they follow near-surface currents (Lumpkin and Pazos, 2007). Although their position is received via ARGOS satellite system at an irregular time interval, drifter trajectories are processed for quality-control and interpolated to a six-hourly interval (Lumpkin et al., 2013). A brief analysis of the GDP drifter trajectories that intercept the archipelagos of the Macaronesia is presented in the present study, comprising a total number of 632 trajectories in 32 years (Lumpkin and Centurioni, 2019).

3.2. Lagrangian Model and Forcing Datasets

The transport of marine litter was simulated through the modeling of virtual particles using version 2.0 of the OceanParcels lagrangian ocean analysis framework (Lange and van Sebille, 2017; Delandmeter and van Sebille, 2019). This numerical toolkit takes advantage of the scientific Python ecosystem, but simulations are carried in low-level C code for computational efficiency. In addition, the modular nature of OceanParcels enables the customization of kernels, meaning that particle behavior can be augmented with specific features (e.g., windage, beaching). In the present study, particle trajectories are integrated using a Runge-Kutta 4th order scheme, relying in the combination of ocean currents, wind and stokes-drift.

For the ocean currents we used two eddy-resolving ocean circulation reanalysis developed by Mercator-Océan in the framework of Copernicus Marine Environment Monitoring Service (CMEMS). These reanalysis products are produced with general ocean circulation models that assimilate *in situ* and satellite data, thus more representative of the ocean circulation (van Gennip et al., 2019). With a daily time step, their velocity components are based on the same ocean circulation models as the Nucleus for European Modeling of the Ocean (NEMO) framework, being forced at the surface by the ERA-Interim wind reanalysis from the European Center for Medium-Range Weather Forecasts (ECMWF). The GLORYS12V1 reanalysis is the first domain of the nested grid configuration, covering an area between 12–60°N and 33°W–10°E (black delimited area in **Figure 1A**) with a 1/12° spatial resolution (∼8km at the equator). This area comprises the Macaronesia region and the neighboring continental coasts. The GLORYS2V4 is used for the rest of the study domain, covering an area between 0–70°N and 98°W–40°E with a 1/4° resolution. Although both reanalysis extend up to 5,500 m depth (50 and 75 vertical levels for GLORYS12V1 and GLORYS2V4, respectively), in the scope of this work lagrangian simulations were confined to depths varying from 0 to ∼108 m (23 and 25 vertical levels for GLORYS12V1 and GLORYS2V4, respectively) and neglect vertical flow velocities, following a similar methodology as Delandmeter and van Sebille (2019). For further information on GLORYS12V1 and GLORYS2V4 model configurations and validation, please refer to Garric et al. (2018) and Lellouche et al. (2018), respectively. Sub-grid processes were parameterized using a stochastic zeroth-order Markov model (van Sebille et al., 2018) with a constant horizontal diffusion coefficient of $Kh = 10\mathrm{m}^2.\mathrm{s}^{-1}$, a value well suited for the resolution of the datasets being used (e.g., Lacerda et al., 2019; Kaandorp et al., 2020; van der Mheen et al., 2020). One should note that tidal forcing is not considered in the present study. Sterl et al. (2020) suggested that although barotropic tidal currents can have a significant influence in the transport of marine plastic litter at coastal regions and semi-enclosed seas, such currents have much less impact on the transport and accumulation of marine plastic debris in the open ocean, being thus negligible at the scale of the North Atlantic basin.

The transport of particles driven by the waves (i.e., Stokes drift) was calculated at the ocean surface (i.e., for particles at ≤0.52 m depth) for all simulations with the wave model WaveWatch III (WW3, The WaveWatch III Development Group, 2016), distributed by the Institut Français de Recherche pour l'Exploitation de la Mer (IFREMER). Like CMEMS datasets, this hindcast dataset is forced by the ECMWF ERA-Interim winds and has a 1/2° horizontal resolution. Although it is

distributed with a 3-h temporal resolution, we use a daily average in the present study for consistency.

In order to maintain coherence between forcing mechanisms, the same ECMWF ERA-Interim wind reanalysis (at 10 m above sea surface) that is used to force the WW3 dataset is used to account for direct wind forcing on particles. This data is available with a 1/2° spatial resolution and a 3-h temporal resolution, being subsequently averaged into a daily time step.

3.3. Particle Setup

Marine litter has been reported to appear in various forms throughout the globe (e.g., Enders et al., 2015; Reisser et al., 2015; Pabortsava and Lampitt, 2020), being very difficult to find an universal distribution of their size, material densities and shapes (Kooi and Koelmans, 2019). Morét-Ferguson et al. (2010) argued that most marine litter found in the ocean is millimeter-sized and has an average material density lower than sea water (965 $kg.m^{-3}$). Nevertheless, debris of larger size and material density higher than sea water can still be found floating at the sea, mostly due to air enclosures (e.g., foamed materials; Enders et al., 2015). As the distinction of particle shape and size is beyond the scope of our study, virtual particles are representative of debris with varying buoyancy ratios and neglect inertial forces. Released with a 3-day interval, particles' initial position was randomly generated within every 0.25° cell of equally-spaced grids arranged around the islands (**Figure 2**). Particles are removed from the simulation when initiated on land, exit the domain through an open boundary (Arctic or South Atlantic Ocean) or get stuck in a dry cell (i.e., land) and are considered beached. The verification of beached particles is made after the integration of all velocity fields (i.e., currents, wind, stokes drift, and diffusion) into the particle trajectory.

Most modeling studies attribute hypothetical windage coefficients (also known as wind drag or leeway drift) to their virtual particles in order to simulate the direct wind drag exerted on particles with specific buoyancy ratios (e.g., Gutow et al., 2018; Pereiro et al., 2018). Low windage coefficients are used in particles with low buoyancy and limited surface area exposed to the wind, whereas high windage coefficients are used for highly buoyant particles with large exposed surface area (Chubarenko et al., 2016). Considering the variety of marine plastic litter densities and shapes found in the Macaronesia region (e.g., Ríos et al., 2018; Fernandes, 2019; Herrera et al., 2020; Pham et al., 2020), our model particles were divided into five groups with random windage coefficients ranging from 0 to 1%, 1 to 2%, 2 to 3%, 3 to 4%, and 4 to 5% of the wind at 10 m height. This means that all grid cells arranged around the islands contributed with the release of five particles every 3 days, except when particles were initiated on land (**Figure 2**). A total of ∼1.3 million particles were released in each simulation, from which ∼360,000 were released in Azores, ∼145,000 in Madeira, ∼500,000 in Canaries, and ∼320,000 in Cabo Verde.

3.4. Simulations

Four simulations were carried for a 10-year period between 2006 and 2016 (a summary of the simulations is shown in **Table 1**). To determine the potential sources and pathways of remote particles reaching the archipelagos, simulations $B_{surface}$ and B_{mixed} were conducted in a backward-in-time scenario, in which particles released around the islands between 2009 and 2016 were backtracked in time. This means that the particle's release location corresponds to the their destination, whereas the particles' final position correspond to their origins (e.g., van Gennip et al., 2019). On the other hand, simulations $F_{surface}$ and F_{mixed} were conducted in a forward-in-time scenario, in which particles released around the islands between 2006 and 2013 were tracked to their destinations. As the fate of domestic particles is beyond the scope of the present study, results associated to forward-in-time simulations were used as a complementary information. Following the same temporal resolution of the ocean circulation reanalysis, a daily time step was used for the calculation of particle trajectories. Although the temporal resolution of the forcing datasets may seem limiting, Onink et al. (2019) demonstrated that differences between flow data with 3 and 24 h time steps were not significant at the scale of an oceanic basin.

TABLE 1 | Simulations overview.

Simulation		$B_{surface}$	B_{mixed}	$F_{surface}$	F_{mixed}
Target particles		Remote		Domestic	
Nature		Backward		Forward	
Vertical distribution		Surface	Mixed	Surface	mixed
Particle release period		2016/1/1–2009/1/1		2006/1/1–2013/1/1	
Data	Ocean	GLORYS12V1 & GLORYS2V4			
	Stokes	WW3			
	Wind	ECMWF			
Start date		2006/1/1			
Finish date		2016/1/1			

To elucidate on the differences between particles with strong and weak buoyancy, both backward- and forward-in-time scenarios were run with two configurations. In simulations $B_{surface}$ and $F_{surface}$, particles are transported only at the ocean surface, being thus exposed to direct wind forcing. Such particles (hereafter referred as surface particles) are mostly representative of macro-plastics, known for staying at the surface longer than micro-plastics (Chubarenko et al., 2016). Conversely, particles in simulations B_{mixed} and F_{mixed} have low buoyancy and are immersed in near-surface layers most of the time, being mostly representative of micro-plastics (Wichmann et al., 2019; Pabortsava and Lampitt, 2020). Although the horizontal transport of these submerged particles (hereafter referred as mixed particles) is less affected by direct wind forcing, their vertical positioning is strongly affected by the wind-induced turbulent mixing (Reisser et al., 2015). A brief description of how this vertical mixing is achieved is presented, but for full details please refer to Kukulka et al. (2012) and Wichmann et al. (2019). Considering the principle that the concentration of plastic particles follows an exponential distribution throughout depth (e.g., Reisser et al., 2015; Kooi et al., 2016), mixed particles are randomly displaced in the water column at each time step

according to the exponential probability distribution proposed by Kukulka et al. (2012):

$$p(z) = \lambda e^{-\lambda z} \quad (1)$$

For $\lambda = w_r/A_0$, the particle rise velocity w_r assumes a determinant role, followed by $A_0 = 1.5u_{*w}kH_s$ where u_{*w} is the frictional velocity of water, $k = 0.4$ is the van Karman constant, and H_s is the significant wave height. H_s is parameterized by $H_s = 0.96g^{-1}\sigma^{3/2}U_{*a}^2$, where $g = 9.81$ m.s^{-1} is the gravitational constant, σ the wave age, and u_{*a} the frictional air velocity. As in Kukulka et al. (2012), we assume a fully developed sea with $\sigma = 35$. With the purpose of simulating strong mixing effects, particle rise velocity w_r was set to 0.001 m.s^{-1}, which according to Reisser et al. (2015) is the minimum rise velocities of plastic particles found in the ocean. In this sense, we follow the same methodology of Wichmann et al. (2019), albeit the later authors used a w_r of 0.003 m.s^{-1}. Of course, such vertical positioning of particles is a gross oversimplification of a highly complex process, controlled mainly by particle density, shape, size (Kooi et al., 2017). Considering that the distinction of such particle characteristics is beyond the scope of this study, we believe that this methodology provides an adequate approximation for the proposed objectives.

3.5. Connectivity to Sources of Marine Litter

Understanding the potential sources of marine litter is an essential step in the mitigation of marine pollution (Ryan et al., 2019), especially for islands that are considerably exposed to debris originated elsewhere (e.g., Robinson et al., 2017; Chambault et al., 2018; van Gennip et al., 2019; van Sebille et al., 2019; Burt et al., 2020). As such, two distinct sources of marine litter are assessed in the present study.

3.5.1. Marine-Based Sources

It has been estimated that marine-based human activities, such as fishing, boating, and shipping are responsible for a considerable amount of plastic waste entering the ocean, being fisheries the most relevant activity with proportions ranging from ∼18% (Lebreton et al., 2019) to ∼20% by number of debris collected at the surface of the ocean (or 70% by weigh, Eriksen et al., 2014). Nonetheless, the proportion of fishing gear on stranded debris collected at oceanic islands increases quite significantly (Monteiro et al., 2018; Fernandes, 2019), reaching values as high as 83% (by weight, Burt et al., 2020). As such, it is very important to account for fishing activities as a likely source of marine litter intercepting the Macaronesian islands. Assuming that the quantity of waste particles is a function of the time spent fishing (e.g., van Gennip et al., 2019; van Sebille et al., 2019), we defined areas of intensive fishing activity as sources of marine-based debris using the Global Fishing Watch database (Kroodsma et al., 2018). This database quantifies the time spent fishing in every 0.1° grid cell for the period 2012-2016. As this fine spatial resolution generates many small areas of intensive fishing activity and hampers the definition of intense fishing zones, data was re-sampled to a 0.2° resolution grid and smoothed using a Gaussian filter with a 0.8° standard deviation. Areas of intense fishing were defined as those with >150 of cumulative fishing hours, which corresponds to >50 hours in the original 0.1° resolution (**Supplementary Figure 1**). Areas with <5,000 km^2 were excluded from the analysis for the sake of clarity.

3.5.2. Land-Based Sources

Regions of high population density have been considered as the most probable land sources of marine plastic litter, especially where they are coastal or near rivers (Andrady, 2017). Indeed, ∼12% of plastics entering the marine environment were estimated to come from inland population via riverine transport, whereas ∼60% were estimated to originate from coastal areas (Lebreton et al., 2019). For this reason, population density has been commonly used as an index to estimate the input of marine plastic debris from land (e.g., Lebreton et al., 2012; Maximenko et al., 2012; Eriksen et al., 2014; Robinson et al., 2017; van Gennip et al., 2019). Nevertheless, it is important to note that this relation is overly simplified, as it depends on other factors, such as environmental regulations, solid waste management, and economic status (Jambeck et al., 2015; Kaandorp et al., 2020). Considering that the emission of particles from coastal regions is beyond the scope of this study, we used the population density projections for 2020 from the "Gridded Population of the World" dataset (Version 4, revision 11; Doxsey-Whitfield et al., 2015; CIESIN, 2018) to assess the likelihood of coastal regions to act as sources of marine litter.

It is important to note, however, that the beaching of marine litter at the real ocean/land boundary is a highly complex process. First, it is highly dependent on small-scale coastal dynamics that most ocean circulation models fail to replicate (Isobe et al., 2014; Zhang, 2017). Second, coastal geomorphology (Bowman et al., 1998; Vianello et al., 2013; Jalón-Rojas et al., 2019) and particle shape and size (Hinata et al., 2017) can mediate the rate at which particles are terminally deposited or washed back to sea. Third, physical processes, such as waves, tide, wind, or even UV radiation increase the degradation rate of plastic particles (Corcoran et al., 2009; Carson et al., 2013; Chubarenko et al., 2020), which can facilitate the burial of smaller particles into the sediments (Turra et al., 2015) or their transport to offshore waters (Isobe et al., 2014). As our domain covers a wide range of coastlines with different morphologies and under the influence of coastal dynamics not feasibly represented at this scale, any attempt of using a probabilistic approach to mimic the beaching of marine litter (e.g., Lebreton et al., 2018; Hinata et al., 2020; Kaandorp et al., 2020; van der Mheen et al., 2020) would be very difficult to assess. For this reason, we deem the first contact with dry cells as particle beaching, which depending on the nature of the simulation (i.e., backward- or forward-in-time tracking) represents a source or a sink location.

4. RESULTS AND DISCUSSION

4.1. Drifter Trajectories

The trajectories of drifters that intercept the Macaronesia archipelagos are an important observational evidence for the

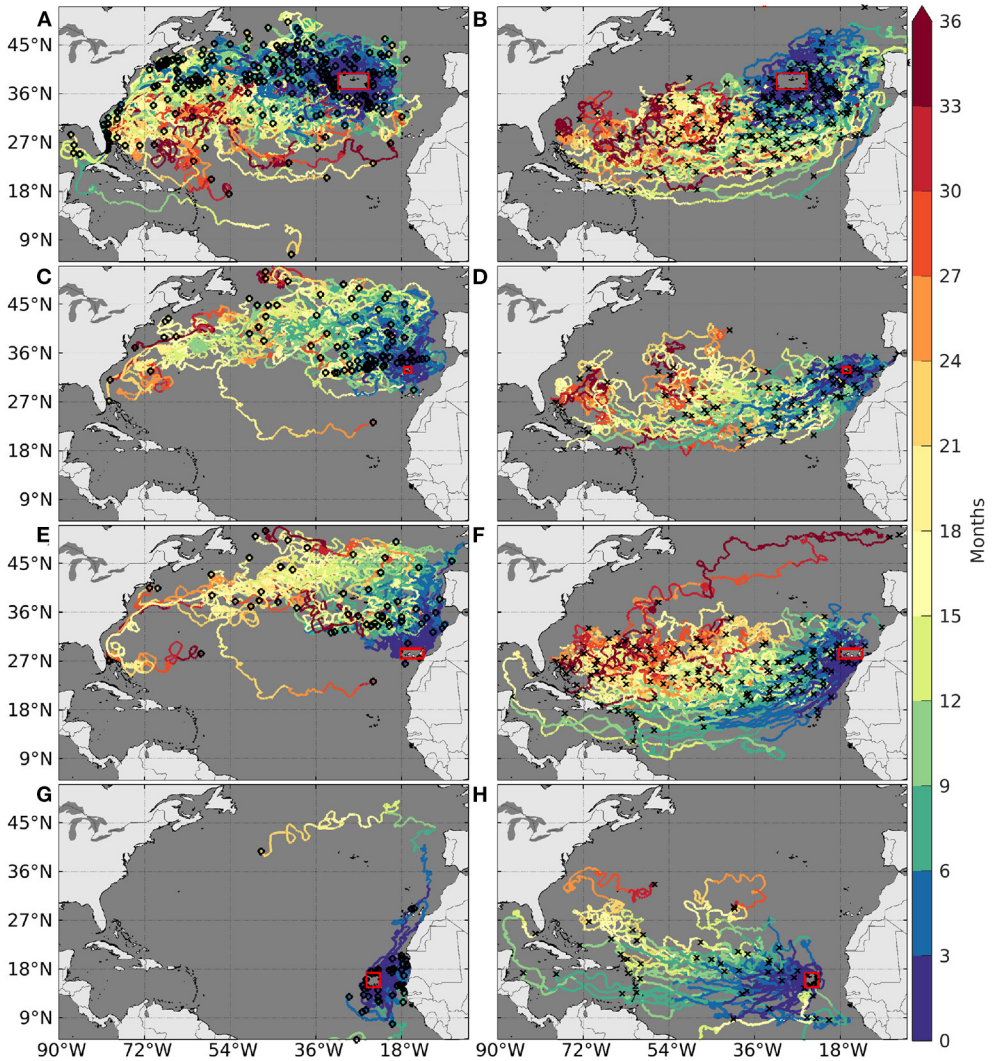

FIGURE 3 | GDP drifter trajectories and age (in months) before (left panels) and after (right panels) intersecting the Azores **(A,B)**, Madeira **(C,D)**, Canaries **(E,F)**, and Cabo Verde **(G,H)**. Red polygons around the archipelagos represent the delimited areas. Black circles and crosses mark the first and last transmitted position, respectively.

analysis of simulated particle trajectories. As such, GDP drifter trajectories before and after intercepting the Macaronesian archipelagos are represented in **Figure 3** left and right panels, respectively. Areas delimiting the archipelagos were defined as the combined grids used to release virtual particles around the islands (**Figure 2**). Because of a mechanical failure of the buoy-drogue connection, nearly 30 and 90% of GDP drifters lose their drogues in the first 3 and 18 months after deployment, respectively (Grodsky et al., 2011), increasing the estimated windage coefficient from 0.1 to 1% of the wind speed (Niiler et al., 1995). Considering that 1% of the wind speed is still at the lower end of the windage interval used in our simulations (0–5%), drogued and undrogued drifter trajectories are not differentiated in **Figure 3**, being mostly representative of submerged and low-windage particles.

The generally long and old drifter trajectories intercepting the Azores (**Figure 3A**) demonstrate that the archipelago is vulnerable to far-field sources. Most of these drifters were deployed along the Gulf Stream and although they intersect the archipelago from all directions, they approach mostly from the west. In fact, the exposure of the Azores islands to the confluence of filaments and eddies pitching off from the Gulf Stream and from the Azores Current led Sala et al. (2016) to propose the archipelago as a potential retention zone for floating particles. Such hypothesis was later reinforced by Pham et al. (2020), who found that the Azorean beaches retain significant quantities of small fragments that are rapidly washed back to sea, acting as transitory repositories of small fragments in the region. After intersecting the Azorean area, drifters are mostly advected southward and eastward with varying meridional deflections,

TABLE 2 | Overview of the GDP drifters intercepting the Macaronesia archipelagos (top rows) and drifter connectivity between archipelagos (bottom rows).

Sink	Azores	Madeira	Canaries	CV
Regional domain (6,536)	269	97	204	62
Beached drifters	42	13	46	16
Azores	–	20	11	0
Madeira	1	–	15	0
Canaries	1	2	–	3
Cabo Verde	0	0	0	–

Rows and columns represent sources and sinks, respectively. White-to-orange color scale is used for the number of drifters intercepting and beaching in the archipelagos. White-to-blue color scale is used for the drifter connectivity between archipelagos.

drifting through the Portugal and Canary currents and eventually closing the North Atlantic Gyre as they follow the North Equatorial Current and reach Central and North American coasts further west (**Figures 3B**, **1A**). From a total of 269 drifters, 42 beached in the archipelago, 20 intersect the Madeira archipelago, and 11 intercept the Canaries (**Table 2**).

Similarly to the Azores, drifter trajectories intercepting Madeira were mostly deployed west and north of the archipelago (**Figure 3C**) but approach mainly from the north. Extending from ∼10 to 24°W (Pérez et al., 2001), the influence of the offshore branch of the Portugal Current (**Figure 1A**) is revealed by the southward trajectories west of the Iberian coast, while the influence of the Azores Current is revealed by the narrow horizontal band of drifter deployments north of Madeira (circles in **Figure 3C**). The Azores Current is still perceivable after drifters intercept the archipelago, evidenced by the eastward trajectories flowing toward Africa and by the swirling westward trajectories passing south of the Azores (**Figure 3D**), likely related with westward-propagating eddies pinching off from the Azores Current (Sangrà et al., 2009; Barbosa Aguiar et al., 2011; Caldeira and Reis, 2017). Nevertheless, most drifters that exit the Madeira delimited area without beaching (84 out of 97) flow south/southwestward, in which 15 cross the Canaries area (**Table 2**), 10 reach the American continent further west and 8 veer north into the Sargasso Sea at the center of the North Atlantic subtropical gyre (often referred as an important area for the accumulation of floating marine litter; e.g., Lebreton et al., 2012; Maximenko et al., 2012; Cozar et al., 2014; Eriksen et al., 2014; van Sebille et al., 2015; Law, 2017; Onink et al., 2019).

Portugal and Azores Currents are also important pathways for drifters intercepting the Canaries (**Figure 3C**). Even though these trajectories are generally very similar to the ones intercepting Madeira, a more careful inspection reveals that some of the drifters that intercept the Canaries are advected closer to the western Iberian coast. Such proximity is likely related with the Portugal Coastal Current which is active when the predominant northward Portugal Coastal Counter Current is suppressed by southward winds (mostly during summer, Martins et al., 2002). After intersecting the Canaries delimited area, most of the drifters that do not beach in the islands (158 out of 204, **Table 2**) continue southward along the Canary Current and then westward along the North Equatorial Current, reaching southern territories of the Central America, such as the Lesser Antilles in ∼9 months (**Figure 3D**).

Three of the drifters leaving Canaries reach the Cabo Verde archipelago as they float in the easternmost branches of the Canary and North Equatorial Currents (**Figures 3A**, **1A**), being the only common trajectories between Cabo Verde and the other archipelagos of the Macaronesia (**Table 2**). Although Cabo Verde lies at the southern limit of the North Atlantic Gyre, the archipelago is predominantly exposed to westward drifters released along the Northwestern African coast, most likely advected by the seasonal Mauritania Current (dashed arrow in **Figure 1A**; Lázaro et al., 2005), upwelling filaments (Lathuilière et al., 2008; Ohde and Siegel, 2010) or coastal-generated eddies (Schütte et al., 2016; Cardoso et al., 2020). Nevertheless, the eastward-flowing North Equatorial Counter Current can still be responsible for the advection of drifters released south of the archipelago. As 16 drifters beached in the islands of Cabo Verde (**Table 2**), some of the remaining 46 drifters followed a general westward trajectory and reached the Lesser Antilles islands, while two drifters crossed the equator (South Atlantic, **Figure 3G**).

To summarize, Azores is the archipelago most intercepted by drifters (269), followed by the Canaries (204), Madeira (97), and Cabo Verde (62, **Table 2**). Even though the number of drifters intercepting the archipelagos is linked to the extension of the delimiting areas, the location where drifters are deployed also play a key role in the pathways they follow (Reisser et al., 2013). For example, Madeira's delimiting area is significantly smaller than Cabo Verde's area, but it is exposed to oceanic currents that cover a broader area (**Figure 1A**) and are thus "seeded" by a larger number of drifters. Drifter trajectories intercepting the Azores are generally older and longer than the ones intercepting Madeira, Canaries, and Cabo Verde. Nevertheless, the exposure of these three archipelagos to far-field sources should not be completely discarded, given the fact that GDP drifters have a limited transmitting lifetime (Lumpkin and Pazos, 2007) which can hinder long-term patterns. Furthermore, Álvarez et al. (2020) argued that the dominance of cold colors (such as white, black, gray, and blue) in micro- and meso-litter collected in Madeira were likely related to the photo degradation of the incorporated pigments (Matsuguma et al., 2017; Syakti et al., 2017). This suggests that the collected fragments were exposed to sunlight for a considerable period of time before intercepting the archipelago (Yu et al., 2018).

4.2. Exposure to Remote Particles

4.2.1. Regional Pathways

In order to assess the potential pathways of remote marine litter affecting the archipelagos of the Macaronesia, we focus our attention in the proportions of $B_{surface}$ and B_{mixed} particles detected in every 0.5° grid cell (**Figure 4**). Corresponding seasonal variations were also assessed, but since the variations were not significant, seasonal $B_{surface}$ particle proportions are included as **Supplementary Figure 2**. It is important to note, however, that as our simulations do not take into account the actual sources and distribution of marine litter in the Atlantic Ocean, the trajectories of particles tracked backward in time can

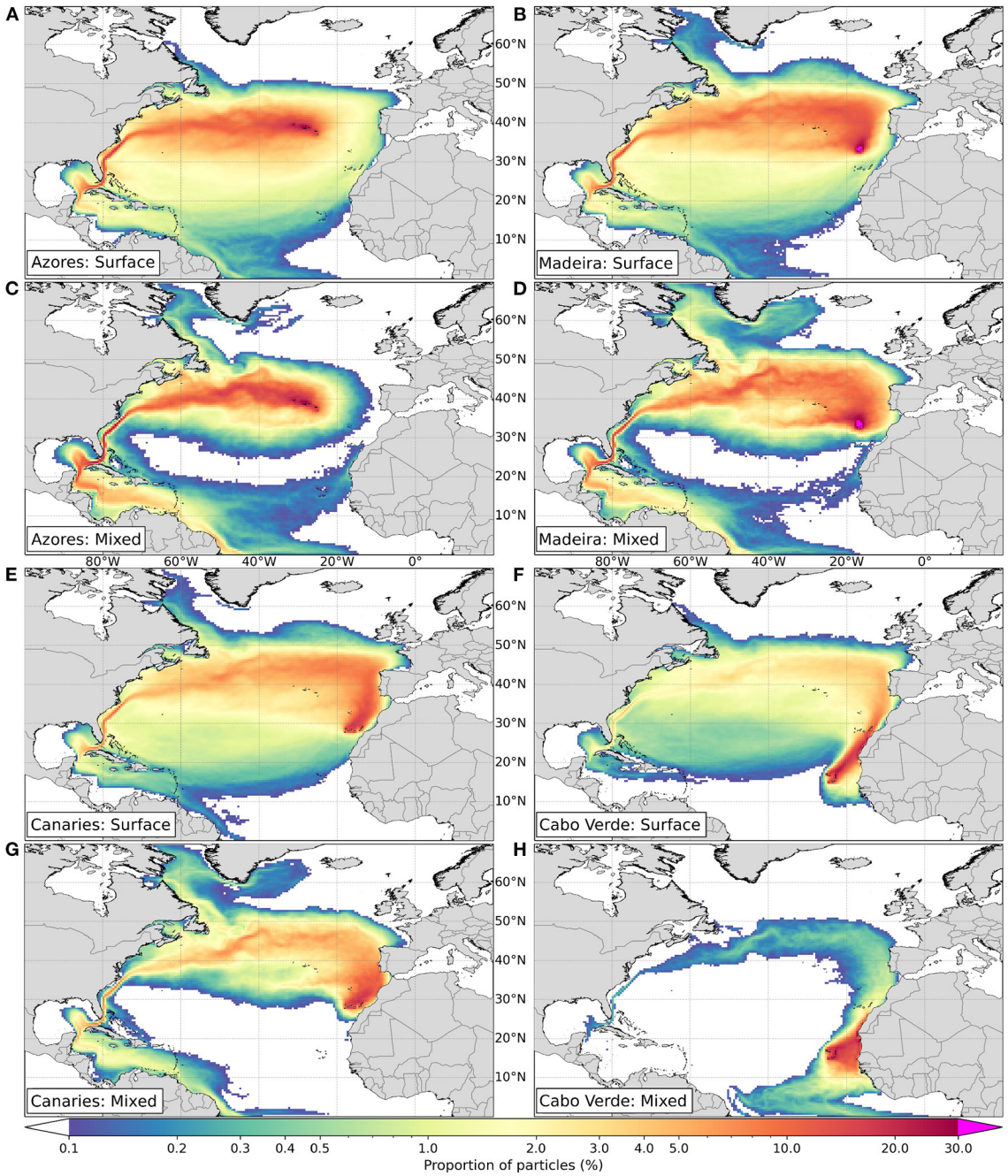

FIGURE 4 | Proportion of $B_{surface}$ **(A,B,E,F)** and B_{mixed} **(C,D,G,H)** particles detected in 0.5° grid cells. Color map is in logarithmic scale, in which cells with < 0.1% are masked.

only serve as an indication of the possible directions taken by particles before reaching the archipelagos (Reisser et al., 2013).

In general, $B_{surface}$ and B_{mixed} particle trajectories have similar patterns (**Figures 4A–H**, respectively), though $B_{surface}$ particles are much more dispersed throughout the North Atlantic basin. In fact, <0.1% of B_{mixed} particles traveled through the Sargasso Sea at the center of the North Atlantic subtropical gyre (between 20–30°N and 70–40°W). Considering that B_{mixed} particles are submerged most of the time and that the inclusion/exclusion of the wind drag from the equation of motion has been linked to the divergence/convergence of particle trajectories (Neumann et al., 2014), it is fair to assume that such spatial differences are caused by the particle exposure to the wind. Furthermore, GDP drifter trajectories before intercepting the archipelagos (**Figure 3** left panels) resemble more closely with B_{mixed} (especially in Cabo Verde, **Figures 3G**, **4H**) than with $B_{surface}$ patterns, reinforcing

the idea that drifter trajectories are mostly representative of submerged and low-windage particles.

The influence of the North Atlantic subtropical gyre is naturally the most evident pattern in the transport of incoming $B_{surface}$ and B_{mixed} particles. The Gulf Stream acts as the dominant pathway for all archipelagos at a regional scale, though with less impact for Cabo Verde (**Figure 4H**). In fact, up tp ∼30% of B_{mixed} particles and ∼20% of $B_{surface}$ particles converge into the initial extension of the Gulf Stream (**Figures 4A,C**, respectively), which is impressive considering the >5,000 km distance from the southeast coast of the United States (US) to the archipelagos of the Macaronesia. The upstream currents that feed the Gulf Stream (i.e., the Florida, Loop, Antilles, Caribbean, and even the North Brazil Currents, **Figure 1A**) are still noticeable in the proportions of particles intercepting the Azores, Madeira, and Canaries (mainly B_{mixed} particles, **Figures 4C,D,G**, respectively). Such signal demonstrates that these archipelagos are significantly exposed to Central and North American sources, which according to Lebreton et al. (2012) account for 64–66% of the debris floating in the North Atlantic. The higher exposure of the Azores archipelago to Central and North American sources is consistent with plastic densities sampled at the beaches of the archipelago (>15,000 items m^{-2}, Pham et al., 2020), which are among the highest densities reported for beaches of oceanic islands in the Atlantic Ocean (Herrera et al., 2018; Monteiro et al., 2018). Flowing southeastward along the northeastern coast of Canada (Lazier and Wright, 1993), the Labrador Current (**Figure 1A**) also acts as a source of particles transported by the offshore extension of the Gulf Stream. Although the Labrador region is less impacted by human activities on land, high levels of small-sized plastic debris were observed along the shoreline (McWilliams et al., 2018) and in gastro-intestinal samples of the Arctic seabird (*Fulmarus glacialis*, Avery-Gomm et al., 2018; Provencher et al., 2018), possibly linked to industrial fishing activity (**Supplementary Figure 1**; Bond et al., 2012).

Similarly to drifter trajectories (**Figure 3A**), $B_{surface}$ and B_{mixed} particles reaching the Azores from the west and from the north are mainly transported by the eastward Gulf Stream and associated branches (**Figures 4A,C**, respectively), whereas particles reaching the archipelago from the south are mainly transported by the eastward Azores Current (**Figure 1A**), more easily depicted in B_{mixed} particle trajectories (**Figure 4C**). Spatial patterns in B_{mixed} particle trajectories are in better agreement with Sala et al. (2016) than $B_{surface}$ particles, which is expected as these authors only considered ocean currents in their simulations. Some of the particles intercepting the Azores were also detected along the eastern boundary of the North Atlantic (0.1–2%), though $B_{surface}$ in higher proportion than B_{mixed} (**Figures 4A,C**, respectively).

Predictably, the main differences between the Azores and Madeira archipelagos appear at the local scale, as $B_{surface}$ and B_{mixed} particles reaching Madeira are mostly transported by the southward Portugal Current and by the eastward Azores Current (**Figures 4B,D**). Due to its seasonal meridional displacement, the Azores Current has an higher impact when the current reaches its southernmost latitude during Summer and Autumn (**Supplementary Figures 2G,H**; Stramma and Siedler, 1988; Klein and Siedler, 1989). In fact, the Azores Current has a bigger influence in particles intercepting Madeira than in particles intercepting the Azores (**Figures 4B,D** and **4A,C** respectively), being more perceptible in B_{mixed} particle trajectories (**Figure 4D**). Although present results demonstrate that Madeira is more frequently exposed to particles intercepting the archipelago from the north and from the west, Álvarez et al. (2020) was unable to find a clear distinction in the accumulation of marine debris between the north and south coasts. Such non-conformity between model results and field surveys can relate to a variety of factors, such as variable beach substrates and exposure to wind and wave action (Herrera et al., 2018; McWilliams et al., 2018; Ríos et al., 2018; Pham et al., 2020) or even the transport of marine litter by coastal currents (Isobe et al., 2014; Pereiro et al., 2018; van Sebille et al., 2020).

Exposed to similar oceanic and atmospheric conditions as Madeira, the Canaries are intercepted by $B_{surface}$ and B_{mixed} particles mostly from the north (**Figures 4E,G**, respectively). These particles are advected by the wind-driven Canary Current, which in turn is fed by the same Portugal and Azores Currents that intercept the Madeira archipelago upstream (Barton, 2001; Martins et al., 2002, **Figure 1A**). Such results are in good agreement with previous studies, that found the highest concentrations of micro-plastics at the beaches directly exposed to the Canary Current and the trade winds (i.e., in the northern side of the islands; Baztan et al., 2014; Herrera et al., 2018). Despite the close proximity between archipelagos, the proportion of particles transiting in the Gulf Stream is lower for particles intercepting the Canaries (**Figures 4E,F**) than for particles intercepting the Azores and Madeira (**Figures 4A–D**, respectively). As first observed in GDP drifter trajectories (**Figure 3E**), such differences can be explained by the higher proportions of Canarian particles transiting closer to the Northwestern African and Western European coasts. As a consequence, such proximity increases the probability for particle beaching (i.e., connectivity to land-based sources) and reduces the number of particles transported by upstream currents.

Clearly, the same is applicable to particles intercepting Cabo Verde, which apart from being the most differentiated archipelago of the Macaronesia, is the archipelago with largest differences between $B_{surface}$ and B_{mixed} particle trajectories (**Figures 4F,H**, respectively). The major pathway for incoming $B_{surface}$ particles is depicted by the high proportions of particles flowing along the Northwestern African coast. Naturally, these particles are exposed to persistent trade winds (**Figure 1B**; Cardoso et al., 2020), which in turn are partly responsible for the equatorward flow of the Canary Current (Barton, 2001) and for the initial southwestward flow of the North Equatorial Current (Lázaro et al., 2005). On the other hand, the major pathway of incoming B_{mixed} particles is depicted by the high proportions of particles that connect the archipelago to the Northwestern African coast in the east. As B_{mixed} particles are less exposed to the wind, the transport of these particles is mainly influenced by: (i) the North Equatorial Current that detaches from the African Coast near Cape Blanc (Mittelstaedt, 1983); (ii) by the wind-driven Ekman currents associated with the seasonal upwelling off the Mauritanian coast (Mittelstaedt, 1991; Van Camp et al., 1991);

(iii) by the Mauritanian Current that is active during summer and autumn (**Supplementary Figures 2O,P**; Lázaro et al., 2005); (iv) or by westward-propagating eddies pinching off from the Northwestern African coast (Schütte et al., 2016; Cardoso et al., 2020). Another characteristic that distinguishes Cabo Verde from the other archipelagos of the Macaronesia is the fact that B_{mixed} particles floating in the South Atlantic or in South American coastal regions can reach the Cabo Verde islands directly through the eastward North Equatorial Counter Current (**Figure 4H**). Such findings are consistent with the detection of plastic additives originated from the Amazon River plume along the entire length of tropical North Atlantic Ocean, reaching the longitudes of Cabo Verde (Schmidt et al., 2019).

4.2.2. Particles Travel Time

As marine plastic litter floats throughout the ocean, it is exposed to several environmental agents that can modify their properties (i.e., density, shape, and size) through fragmentation, weathering, erosion, or biofouling (reviewed in van Sebille et al., 2020). These changes can have profound implications in the transport of plastic debris. For instance, changes in particle buoyancy can lead them to sink/rise, making particles less/more exposed to the wind. For this reason, it is important to account for the estimated time a particle takes to intercept the archipelagos. The median travel time (i.e., particle age) for $B_{surface}$ and B_{mixed} particles detected in every 0.5° grid cell is presented in **Figure 5**, with reference to the moment of particle release (i.e., interception). We choose to present the median instead of the mean because the variability in particles' age passing through each cell is quiet large (>2 years standard deviation, **Supplementary Figure 3**). We suspect this is related with the fact that some particles remain at the ocean for a large period of time before beaching, leading them to pass through the same region more than once. Thus, we believe this analysis prevents an overestimation of the typical travel time a particle takes to intercept the archipelagos.

In general, the timescales associated with the transport of intercepting particles (**Figure 5**) are of the same order of magnitude as the timescales associated with the GDP drifter trajectories before intercepting the archipelagos (**Figure 3** left panels), especially B_{mixed} particles which are less exposed to the wind. $B_{surface}$ and B_{mixed} particles connect the North and Central American east coasts to the Macaronesian archipelagos in ∼1–1.5 and ∼1.5–3 years, respectively (**Figure 5**). On the other hand, the Southwestern European and Northwestern African coasts present a much more variable connectivity timescale, in which $B_{surface}$ and B_{mixed} particles take ∼0.25–4 and ∼0.25–>5 years, respectively, to reach the archipelagos. Naturally, the fact that timescales associated with the B_{mixed} particles are higher than those associated with $B_{surface}$ particles can be explained by the absence of wind advection and by the lower current velocities in subsurface layers.

Besides providing valuable information on the connectivity timescales, particle travel time (**Figure 5**)—in conjunction with particles' pathways (**Figure 4**)—can also indicate the dominant direction taken by the particles before intercepting the archipelagos. For example, **Figures 4A,C** shows that some of the particles intercepting the Azores archipelago were detected off the Southwestern European and Northwestern African coasts. Although $B_{surface}$ and B_{mixed} particles are physically closer to the Azores when transiting through this region, **Figures 5A,C** shows that such particles take >2 and 3 years longer to intercept the archipelago than those detected off the Northeastern American coast. This means that particles from Central and North American sources are less susceptible to fragmentation (e.g., Andrady, 2017; Lebreton et al., 2019) and biofouling (e.g., Fazey and Ryan, 2016; Kooi et al., 2017) before reaching the Azores, whereas particles from Southwestern European and Northwestern African sources have an increased probability of sinking before intercepting the archipelago. The same reasoning can be applied to Madeira, Canaries, and Cabo Verde, considering that the Central and North American coasts are located upstream of all Macaronesian archipelagos, whilst that's not always the case for the Southwestern European and Northwestern African coasts.

As expected, the travel time of $B_{surface}$ and B_{mixed} particles intercepting the archipelagos of Madeira and Canaries have similar patterns at a regional scale, connecting the archipelagos to the Central and North American east coasts in ∼1.5 and 3 years, respectively (**Figures 5B–G**). Nevertheless, a more careful analysis reveals that although the Iberian Peninsula is physically closer to Madeira than to the Canaries, $B_{surface}$ particles take ∼3 months longer to connect the Madeira archipelago to this region (**Figures 5B,E**). Considering that B_{mixed} particles connecting both archipelagos to the Iberian Peninsula share identical travel times (∼0.75–1 year), such disparity in $B_{surface}$ particles can only be related with the wind.

Given the unique exposure of Cabo Verde to the complex interaction of large-scale currents and features (**Figure 1A**; Cardoso et al., 2020), Cabo Verde is the only archipelago in which intercepting particles can approach from very distinct directions (**Figures 5F,H**). Furthermore, $B_{surface}$ particles intercepting Cabo Verde are the ones that cover the broadest area in a relatively short period of time, connecting the archipelago to coastal regions that extend from Guinea (10°N) to the British Isles (50°N) in up to ∼9 months travel time (**Figure 5F**). Naturally, the wind is the main contributor to the high-velocity transport of $B_{surface}$ particles intercepting the archipelago.

4.2.3. Windage Effects on Surface Particles

As demonstrated by the differences between $B_{surface}$ and B_{mixed} particle trajectories (**Figure 4**) and travel time (**Figure 5**), windage effects can have important implications in the distribution of floating marine debris (e.g., Neumann et al., 2014; Maximenko et al., 2018), being even considered the most important mechanism in the transport of light micro-plastics when floating at the surface (Chubarenko et al., 2016). In order to assess how different windage coefficients mediate the transport of particles intercepting the archipelagos of Macaronesia, **Figure 6** illustrates the most frequent windage coefficient group of $B_{surface}$ particles detected in every 0.5° grid cell. Since submerged particles are much less affected by wind drift (Reisser et al., 2015), B_{mixed} particles are excluded from this analysis.

The most frequent occurrence of high-windage particles at the center of the North Atlantic subtropical gyre (**Figure 6**)

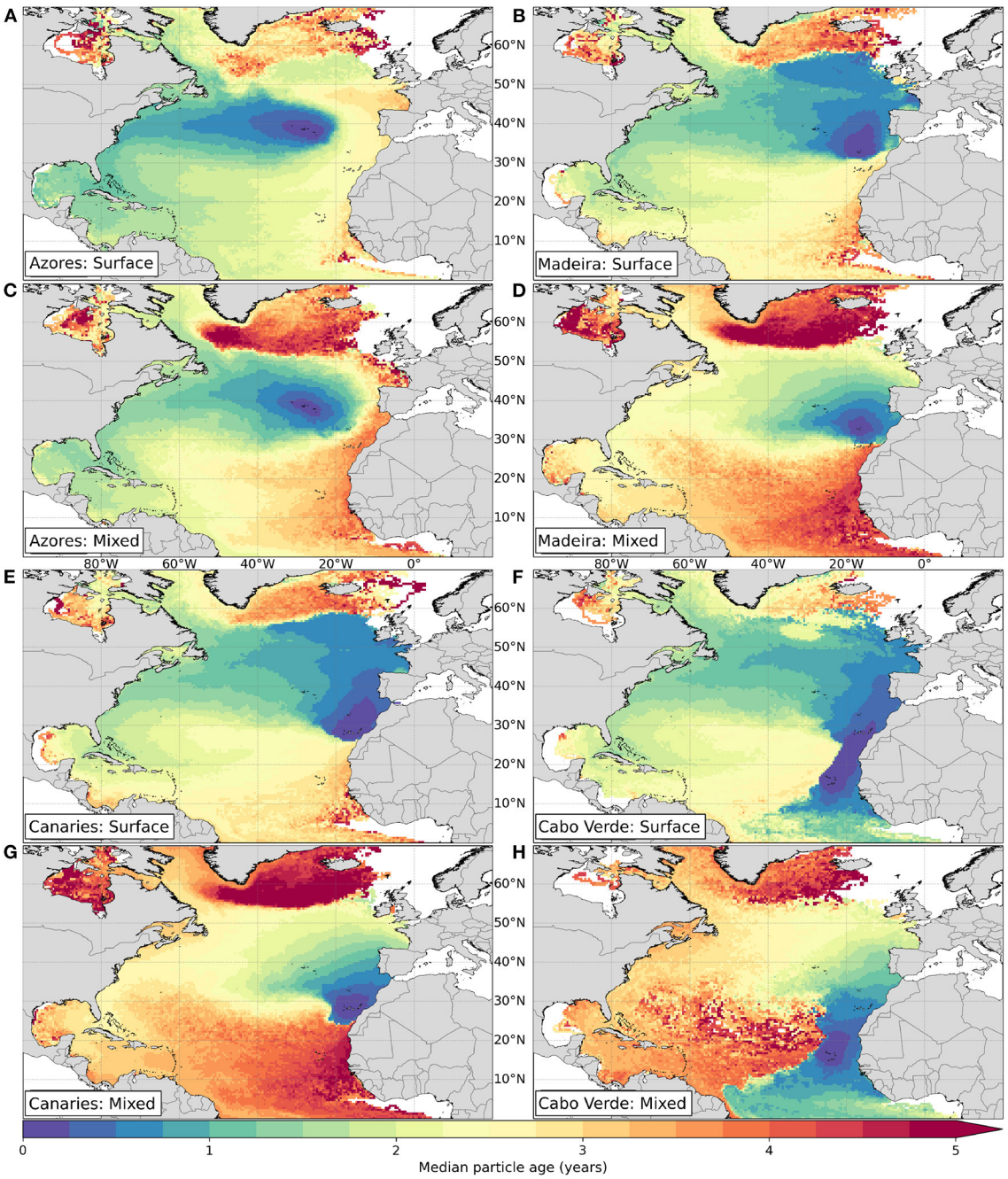

FIGURE 5 | Median age of $B_{surface}$ **(A,B,E,F)** and B_{mixed} **(C,D,G,H)** particles before intercepting the archipelagos, detected in 0.5° grid cells. Color scale is divided with a 3-month interval.

is unquestionably the most conspicuous pattern between archipelagos, revealing the importance of the wind in the transport and delivery of particles from the North Atlantic "garbage patch" to the archipelagos of the Macaronesia. Considering the backward-in-time nature of this simulation, present results are consistent with past studies which reported that low- and null-windage particles tend to accumulate at the so-called "Great Pacific Garbage Patch" (a plastic accumulation zone formed in subtropical waters between California and Hawaii), whereas high-windage particles tend to be pushed out from this region by the wind (e.g., Lebreton et al., 2018; Maximenko et al., 2018). Furthermore, Lebreton et al. (2019) found that most objects captured at the "Great Pacific Garbage Patch" exhibited no or very little air draft when placed in seawater and argued that high-windage particles have higher probability of exiting oceanic "garbage patches" and being transported over larger areas. In

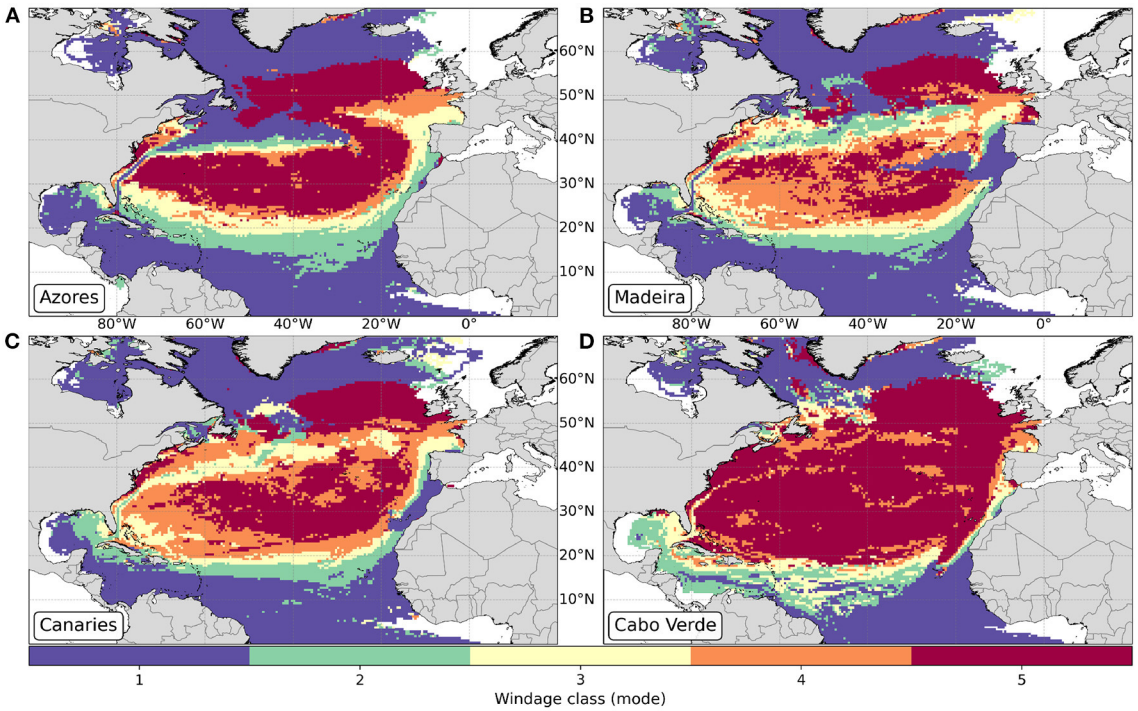

FIGURE 6 | Most frequent occurrence of $B_{surface}$ particle windage class for particles released in the Azores **(A)**, Madeira **(B)**, Canaries **(C)**, and Cabo Verde **(D)**, detected in 0.5° grid cells. Windage coefficient values correspond to the percentage contributions of wind forcing at 10 m above sea level.

fact, such pattern is confirmed by the accumulation of $F_{surface}$ (**Supplementary Figures 4A,B,E,F**) and most significantly F_{mixed} particles (**Supplementary Figures 4C,D,G,H**) at the center of the North Atlantic subtropical gyre, being the particles with low-windage coefficients the most frequent at this location (**Supplementary Figure 5**).

Apart from the regional similarities, a careful inspection at each of the archipelagos reveals distinct pathways of low- and high-windage particles. For instance, particles intercepting the Azores from the north and from the south have mostly low- and high-windage coefficients, respectively (**Figure 6A**). Considering that high-windage particles have the highest probability for beaching (Lebreton et al., 2019), present results corroborate with past studies that found the highest density of plastic debris on Azorean beaches oriented southwestward, facing the predominant wind direction (as illustrated in **Figure 1B**, Ríos et al., 2018; Pham et al., 2020). Furthermore, Pham et al. (2020) found that 59% of plastic items collected at the Azorean beaches were within the dominant size range (2.1–5.0 mm) reported to be floating in the western North Atlantic (Morét-Ferguson et al., 2010) and follow similar sizes and colors as the majority of fragments collected in the same region (Prunier et al., 2019), leading the authors to attribute their origin to the "large offshore plastic soup floating in the wider Atlantic Ocean."

Contrary to the Azores archipelago—that is strongly affected by the Azores high atmospheric pressure system—the Madeira, Canaries, and Cabo Verde archipelagos are exposed to persistent northerly trade winds with varying intensity throughout the year (**Figure 1B**, Barton et al., 2000; Caldeira and Tomé, 2013; Cardoso et al., 2020). For this reason, particles that intercept these archipelagos from the north have mostly high-windage coefficients (**Figures 6B–D**). Indeed, beach surveys conducted in the Canaries (Baztan et al., 2014; Herrera et al., 2018; Álvarez-Hernández et al., 2019) and in a uninhabited island of Cabo Verde (Santa Luzia, Fernandes, 2019) revealed that the north coasts of the islands are accumulating significantly more amounts of macro- and micro-litter (with similar characteristics to those found in the Azores) in comparison with beaches from the south coasts. It is highly likely that the same is occurring in Madeira (**Figure 6B**), but further research is needed to confirm this trend (Álvarez et al., 2020).

Naturally, particles with low-windage coefficients are mostly transported by the currents. Such transport mechanism is easily depicted by the most frequent occurrence of low-windage particles intercepting the Azores from the west/northwest, concurrent to the eastward flow of the Gulf Stream (**Figure 6A**). Similarly, low-windage particles intercept the Madeira archipelago from the west as a result of the eastward-flowing Azores Current (**Figure 6B**), an hypothesis further supported by the high proportions of $B_{surface}$ and B_{mixed} particles that make the Azores Current easily discernible (**Figures 4B,D**). Furthermore, most particles that intercept Madeira and Canaries archipelagos from the east and northeast have predominantly low-windage coefficients (**Figures 6B,C**), demonstrating that the neighboring continental coastal regions (i.e., Morocco, Portugal, and Spain) are more likely to act as sources of low-windage particles than

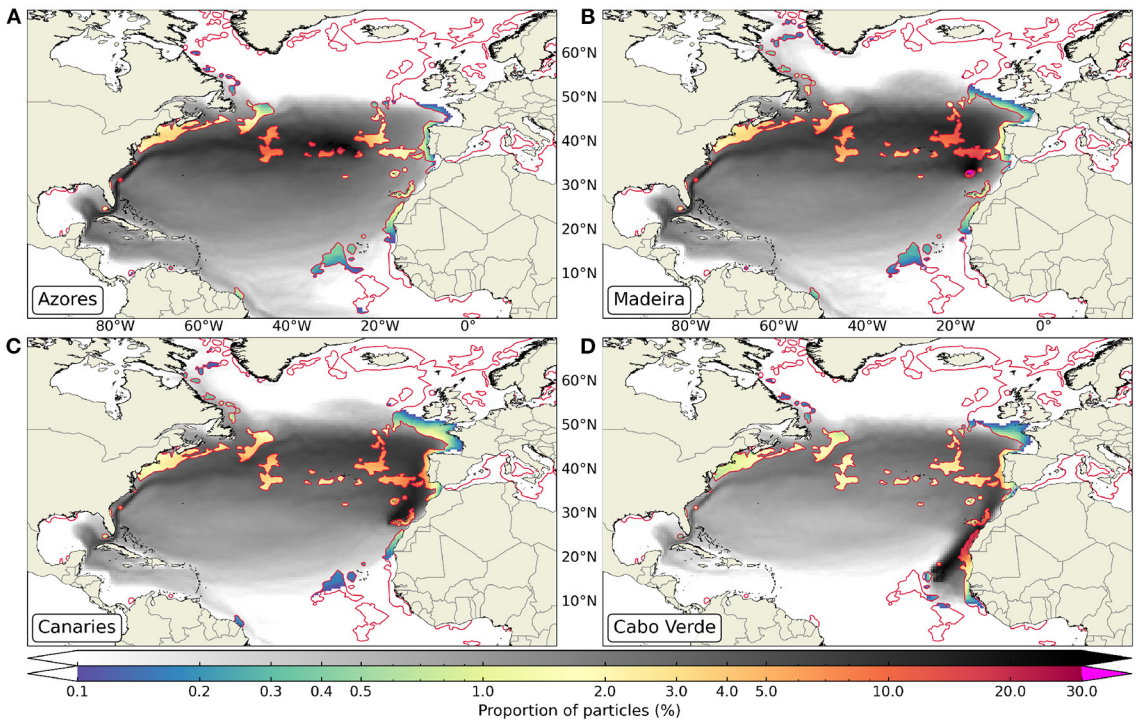

FIGURE 7 | Proportion of $B_{surface}$ particles released in the Azores **(A)**, Madeira **(B)**, Canaries **(C)**, and Cabo Verde **(D)**, detected in 0.5° grid cells and clipped by the areas with >150 h of fishing effort (per 0.2° grid cell) reported in the Global Fishing Watch dataset (Kroodsma et al., 2018). Only fishing areas with >5,000 km^2 are represented by the red contours. Color maps are in logarithmic scale, in which cells with < 0.1% are masked.

high-windage particles. The same applies to Cabo Verde, given the dominance of incoming low-windage particles originating from the adjacent Mauritanian and Senegalese coasts on the east (**Figure 6D**).

4.2.4. Connectivity to Sources of Marine Litter

With the purpose of making a distinction between the two main sources of marine plastic litter affecting the Macaronesian archipelagos, we herein focus our discussion in the connectivity of the archipelagos to marine-based and land-based sources.

4.2.4.1. Marine-Based Sources

Although land-based emissions have been commonly acknowledged as the principal sources of marine litter (Nollkaemper, 1994; Jambeck et al., 2015; Andrady, 2017; Lebreton et al., 2019), recent studies have demonstrated that marine-based sources are generally more important for macro-plastic debris stranded on islands (Unger and Harrison, 2016; Edyvane and Penny, 2017; Burt et al., 2020), being derelict fishing gear the most commonly sampled material on islands of the Atlantic Ocean (up to 40%; Monteiro et al., 2018; Fernandes, 2019). In order to assess the connectivity of the archipelagos to areas of intensive fishing activity, **Figure 7** shows the proportion of $B_{surface}$ particles detected in 0.5° grid cells (following the same methodology as **Figure 4**), highlighting those that transited through these areas. For the sake of brevity, the corresponding analysis for B_{mixed} particles is included in **Supplementary Figure 6**.

In general, all the archipelagos are exposed to common areas of intensive fishing activity, with varying degrees of exposure according to their surroundings and more importantly with their relation with upstream currents. Local fishing activity is relatively intensive around the Azores, Madeira and Canaries, as these archipelagos are almost entirely surrounded by such activity (**Figures 7A–C**). Indeed, surveys conducted at the seafloor of Azorean fishing grounds (around Faial and Pico islands) revealed that macro debris are mainly composed of derelict fishing gear (Pham et al., 2013; Rodríguez and Pham, 2017). Conversely, Chambault et al. (2018) noted that among 2,406 visual transects, derelict fishing gear was the third main type of debris floating around the archipelago, accounting for 18% of the total debris. Still, derelict fishing gear floating at the surface or lost on the seafloor caused the highest number of marine-litter related incidents in the archipelago, which often resulted in the entanglement of ship propellers and fishing gear (Rodríguez et al., 2020).

At a regional scale, the extensive fishing area located off the northeastern coast of the US shows similar proportions of particles intercepting the Azores, Madeira, and Canaries archipelagos (∼2–5%, **Figures 7A–C**). Further to the east, patches of intensive fishing activity located along the offshore extension of the Gulf Stream and along the Azores Current have higher probability of acting as sources of debris reaching the

Azores and Madeira archipelagos (**Figures 7A,B**). Most likely due to their proximity, Madeira and Canaries have very similar proportions of incoming particles (up to ∼3%) passing through areas of intensive fishing activity located in the Labrador and Newfoundland region, but much more significant proportions (up to ∼20%) are observed in offshore regions west of the Iberian Peninsula and in the West European Continental Shelf (**Figures 7B,C**). Such exposure to areas of intensive fishing activity off the Portuguese coast makes Madeira and Canaries archipelagos vulnerable not only to the abundant amount of floating debris observed in that region (likely originated from fisheries), but also to discharges and cargo losses from commercial vessels and cruise ships transiting through the major shipping corridors that connect Mediterranean, Northern European, and African countries (Sá et al., 2016).

As expected, $B_{surface}$ particles intercepting Cabo Verde are more likely to pass through the highly productive (e.g., Mittelstaedt, 1991; Van Camp et al., 1991; Lathuilière et al., 2008) areas of intensive fishing activity along the northwest African coast, extending from the Canaries to the Mauritanian coast (**Figure 7D**). Indeed, Fernandes (2019) found that >60% (by mass) of the plastic debris collected in the northern side of Santa Luzia island in Cabo Verde were fishing gear. Considering that derelict fishing nets can have a draft of several meters and are thus less influenced by the wind (Lebreton et al., 2019), fishing gear with low- or null-windage coefficient collected in Cabo Verde are most likely being discarded by fishing activities off the Western Sahara (disputed territory with Morocco), Mauritanian, and Senegalese coasts (**Figure 4D** and **Supplementary Figure 6D**). In fact, it is possible that the high amounts of octopus traps found in the northern side of Santa Luzia island (Fernandes, 2019) are related with the high abundance of such traps found at the Moroccan seafloor (>75%; Loulad et al., 2017). Octopus traps are normally deployed with a block of cement to fix it in the seafloor, but often loose these blocks due to rough weather conditions or vandalism, making them afloat (Loulad et al., 2017). Important areas of intensive fishing activity are also observed to the south and southwest of Cabo Verde, but as these areas are located downwind of the archipelago (**Figure 1B**), only low- or null-windage debris discarded at this location are able to reach the archipelago due to the advection by the North Equatorial Counter-Current (**Supplementary Figure 6D**).

4.2.4.2. Land-Based Sources

In order to assess the connectivity of the archipelagos to potential sources of marine litter on land, the final location of beached particles (tracked backward in time) was considered as the source, which then served to calculate the proportion of land-based particles emitted by coastal countries. As the exposure to the wind increases the probability of particle beaching (Lebreton et al., 2018, 2019), we choose to present only the proportions of land-based $B_{surface}$ particles per country coastline (represented by the respective Exclusive Economic Zones, **Figure 8**) for the sake of brevity, but the proportions of land-based B_{mixed} particles are included in **Supplementary Figure 7** and in **Table 3** for comparison. Considering that the vulnerability of the archipelagos to land-based sources is not only dependent on the connectivity to land, but also to the respective population size (Jambeck et al., 2015), population density was included in the figures to assess the likelihood of such coastal regions to act as sources of marine litter.

It is important to note that according to Onink et al. (2019), stokes drift is one of the most important drivers for particle beaching when tracked in forward time. This means that the effect of wave-driven particle beaching is reversed for backward-in-time simulations, thus acting as a potential buffer to particles being transported nearshore. Nevertheless, the coarse temporal and spatial resolution of the Stokes Drift data used in the present study are not sufficient to resolve such nearshore wave-related processes. In fact, present results show that almost all $B_{surface}$ and B_{mixed} particles reached land, specifically: 91.94 and 82.55% for Azores; 93.05 and 82.83% for Madeira; 95.30 and 90.39% for Canaries; and 98.00 and 95.24% for Cabo Verde, respectively. For this reason, we believe that the reverse wave-driven beaching effect on particles tracked backward in time are in this case negligible. The reason why the proportions of beached particles are significantly higher in relation to past studies (e.g., Robinson et al., 2017; van Gennip et al., 2019) can be related with the longer simulation period (10 years) and with the fact that the North Atlantic basin is surrounded by land in the west and in the east, constraining particle advection and ultimately leading to beaching.

In terms of $B_{surface}$ particle connectivity between archipelagos, the connectivity between Canaries –> Cabo Verde is the most significant (7.31%), followed by Azores –> Madeira (2.52%), Canaries –> Azores (1.49%) and vice versa (1.37%), and Canaries –> Madeira (1.17%; **Table 3**). The fact that Canaries acts primarily as a source to the Azores and Madeira is quite surprising, considering that the Azores and Madeira are located upstream of Canaries (**Figure 1**). Nevertheless, the Canaries becomes a sink to $F_{surface}$ particles released in the Azores and Madeira archipelagos (**Supplementary Figure 8**). This inconsistency between the two scenarios can be related with the different interpretations associated with backward- (origin) and forward-in-time (fate) simulations, as in the backward-in-time simulations we only track particles that intercept the archipelagos (e.g., van Sebille et al., 2019). Naturally, the proportions of "self-recruited" particles (i.e., the ones beached at the respective archipelago) are proportional to the size of the archipelagos.

In terms of connectivity of the archipelagos to external land-based sources, our results show that the Macaronesia archipelagos can be divided into two groups: the Azores, Madeira, and Canaries constitute one group due to the similar degree of exposure to particles entering the ocean from the Central and North American continent; whereas Cabo Verde is isolated from the other archipelagos due to the higher exposure to particles entering the ocean from the Northwestern African coast (especially B_{mixed} particles, **Table 3**). Curiously, Freitas et al. (2019) found significant differences in marine species between Cabo Verde and the other Macaronesian archipelagos and proposed an identical distinction for the restructuring of the Macaronesia as a biogeographic unit, in which the authors followed previous definitions (Spalding et al., 2007) and deemed

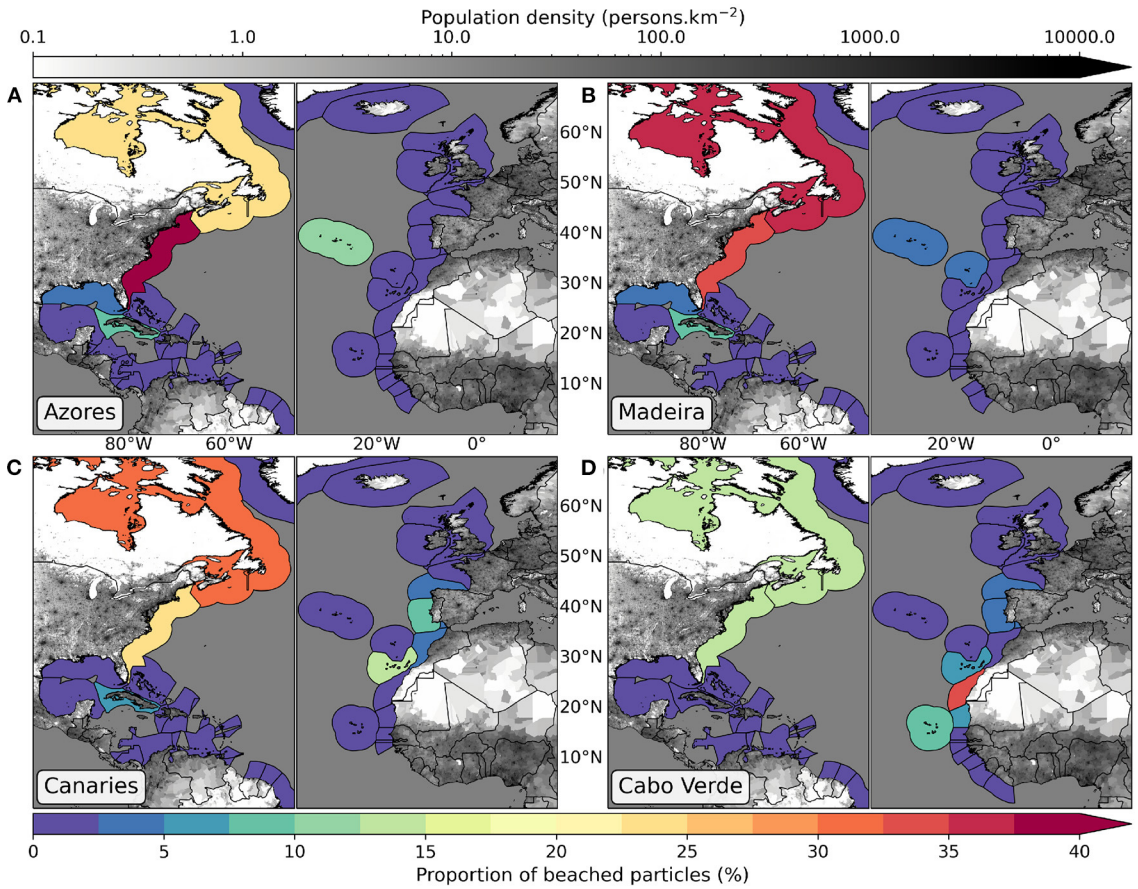

FIGURE 8 | Proportion of $B_{surface}$ particles released in the Azores **(A)**, Madeira **(B)**, Canaries **(C)**, and Cabo Verde **(D)** and beached per country coastline. Countries with coastlines in different seas are divided accordingly (e.g., Atlantic and Mediterranean Spain). On land, gray colors map represents population density.

the Azores, Madeira and Canaries as the Lusitanian archipelagos, whereas Cabo Verde was included in the West African Transition province (along with the Northwest African Upwelling region).

The east coast of North America acts as the primary source of land-based $B_{surface}$ particles to the Azores (69.37%), Madeira (73.73%), and Canaries (56.63%), and the secondary source to Cabo Verde (27.7%; **Figure 8** and **Table 3**). Jambeck et al. (2015) used global solid waste management data compiled by the World Bank for the year of 2010 (Hoornweg and Bhada-Tata, 2012) and showed that although the US had the lowest rate of mismanaged waste (2%) among the top producers of plastic marine litter worldwide, the US had the highest annualized per capita plastic waste generation rate (∼122 kg.person.year^{-1}). This, together with a large coastal population (112.9 million people) lead to an estimated production of 0.04–0.11 MT.year^{-1} of plastic marine debris (Jambeck et al., 2015). As the global plastic production increased by 26% (from 334 to 422 Mt) between 2010 and 2016 (Geyer et al., 2017), Law et al. (2020) used updated data reported by the World Bank for 2016 (Kaza et al., 2018) and found that the US was still the largest producer of waste in the world, increasing the annualized per capita plastic waste generation rate by ∼7% (to ∼130 kg.person.year^{-1}). Although this study does not estimate the amount of plastic debris entering the marine environment, it is highly probable that it followed the same trend as the amount of mismanaged plastic waste, which increased from 0.28 Mt in 2010 to 0.51–1.45 Mt in 2016 (Law et al., 2020). All things considered, it is fair to assume that the east coast of the US is the most probable source of $B_{surface}$ and B_{mixed} land-based particles reaching the Lusitanian archipelagos.

In agreement with **Figure 4**, the Lusitanian archipelagos are also vulnerable to countries from Central America that can act mainly as sources of incoming B_{mixed} particles (**Table 3**). From these countries, and most likely due to its geographic position in relation to the Gulf Stream (and associated upstream currents), Cuba stands out at as the main Central American source of land-based particles to all archipelagos.

Albeit closer to the archipelagos than the American continent, the European continent can be deemed as a secondary and tertiary source of land-based particles to the Lusitanian and to Cabo Verde archipelagos, respectively (**Table 3**). Given the meridionally long coastline facing the North Atlantic, Portugal is the dominant European source for all archipelagos, having a more significant impact for particles reaching the Canaries (especially for $B_{surface}$ particles, **Table 3**).

TABLE 3 | Connectivity between sources (rows) and sinks (columns).

	Azores		Madeira		Canaries		Cabo Verde	
Sink	**AzSurface**	**AzMixed**	**MadeiraSurface**	**MadeiraMixed**	**CanariesSurface**	**CanariesMixed**	**CVSurface**	**CVMixed**
Macaronesia	**13.04**	**11.97**	**7.14**	**7.98**	**16.83**	**26.22**	**17.79**	**15.96**
Azores	11.22	11.65	2.52	1.96	1.37	0.60	0.56	0.02
Madeira	0.12	0.04	3.32	5.72	0.48	0.66	0.16	0.02
Canaries	1.49	0.18	1.17	0.23	14.91	24.93	7.31	2.04
Cabo Verde	0.21	0.10	0.13	0.07	0.08	0.03	9.77	13.88
Europe	**1.17**	**0.25**	**4.68**	**11.37**	**14.24**	**21.41**	**7.22**	**1.51**
Portugal	0.53	0.16	2.13	8.17	8.34	16.32	3.9	1.12
Spain (Atlantic)	0.47	0.06	1.93	3.00	4.69	4.89	2.67	0.38
France (Atlantic)	0.14	0.00	0.56	0.11	0.89	0.14	0.41	0.01
North America	**69.37**	**55.85**	**73.73**	**57.11**	**56.63**	**28.42**	**27.7**	**1.62**
United States (Atlantic)	42.07	12.33	34.28	9.31	24.19	4.47	12.69	0.28
United States (Gulf)	3.78	1.01	3.15	0.67	2.27	0.30	1.01	0.02
Canada	23.34	40.50	36.2	44.17	30.12	22.14	13.99	1.26
Central America	**13.05**	**21.15**	**11.9**	**14.92**	**7.72**	**6.42**	**2.82**	**0.28**
Cuba	8.47	7.05	8.51	5.26	5.7	2.32	2.11	0.11
Haiti	1.23	1.90	0.88	1.19	0.51	0.50	0.14	0.02
Jamaica	0.95	1.99	0.72	1.35	0.42	0.59	0.17	0.02
Bahamas	0.86	4.76	0.75	3.33	0.52	1.55	0.23	0.09
South America	**0.94**	**8.74**	**0.45**	**6.07**	**0.21**	**2.27**	**0.01**	**0.06**
Colombia	0.47	4.24	0.22	2.78	0.1	0.99	0.01	0.02
Venezuela	0.34	2.98	0.17	2.25	0.07	0.91	0	0.03
Africa	**2.32**	**2.04**	**1.58**	**2.56**	**4.11**	**15.26**	**44.4**	**80.56**
Western Sahara	1.65	0.87	1.07	0.62	0.78	0.45	33.93	34.60
Morocco (Atlantic)	0.28	0.09	0.27	1.19	3.23	14.57	1.57	1.49
Mauritania	0.25	0.43	0.15	0.30	0.07	0.10	7.1	29.74
Senegal	0.05	0.12	0.03	0.10	0.01	0.02	1.42	11.38

*Values are expressed as the percentage of land-based particles, represented in **Figure 8** and **Supplementary Figure 7**. White-to-orange color scale is used for the cumulative proportion per continent, whereas white-to-blue color scale is used for the corresponding countries (only the most significant values are shown). Bold values are used to highlight the percentage of beached particles per continent.*

Partly due to their proximity to the continent, Cabo Verde and the Canaries are the only archipelagos considerably exposed to Northwestern African sources (**Table 3**). As previously observed in **Figures 3G**, **4H**, almost all B_{mixed} particles intercepting Cabo Verde (81%; **Table 3**) originated from the Western Sahara, Mauritania, and Senegal. Although coastal population density is relatively low in this region (**Figure 8**), the lack of good waste management policies and infrastructure makes these countries probable sources of land-based marine litter. In fact, Morocco (including Western Sahara) ranks as the 18th country with the highest production of plastic marine debris worldwide (0.05–0.12 MMT.year^{-1}), producing as much as all the coastal European Union countries combined (Jambeck et al., 2015).

5. CONCLUSIONS

Our study focused on the identification of the potential sources and pathways responsible for the transport of land- and marine-based litter to the archipelagos of the Macaronesia. To achieve this, we set up lagrangian simulations with surface particles—representative of floating plastics with a varying exposure to the wind—and mixed particles—representative of submerged plastics due to wind-induced vertical mixing—released around the archipelagos (**Figure 2**) and tracked backward in time to their origins. A forward-in-time scenario was also conducted, but was used as complementary information. As observational evidences, GDP drifter trajectories intercepting the archipelagos were also assessed.

In general, our simulations agreed well with the GDP drifter trajectories. Although the number of intercepting drifters differs quite substantially from the number of particles released in each archipelago (e.g., 269 drifters in comparison to ∼360,000 particles released in the Azores), drifter trajectories and travel time before intercepting the archipelagos (**Figure 3** left panels) show similar patterns as the distributions and the transport timescales of virtual particles, especially B_{mixed} particles that are less impacted by the wind (**Figures 4C,D,G,H**, **5C,D,G,H**). The clockwise-circulating system of ocean currents termed as the North Atlantic subtropical gyre was the most conspicuous

pattern in GDP drifter (**Figure 3**) and particle trajectories in both backward- and forward-in-time scenarios (**Figure 4** and **Supplementary Figure 4**, respectively). Within this system, the Gulf Stream acts as the dominant pathway of particles intercepting all archipelagos at a regional scale, though with less impact for Cabo Verde. At a local scale, however, the Gulf Stream only has a direct impact to the Azores archipelago (**Figures 3A**, **4A,C**). In conjunction with the atmospheric circulation (**Figure 1B**), the southward Portugal and Canary Currents act as important pathways for particles intercepting the Madeira and Canaries, respectively (**Figures 3C,E**, **4B,D,E,G**). The Azores Current also plays an important role in the advection of particles to the Canary Current, having a more and an equally significant impact to the Madeira and Canaries archipelagos, respectively, in comparison to the Azores. For Cabo Verde, the initial extension of the North Equatorial Current acts as the dominant pathway for incoming $B_{surface}$ particles (**Figure 3F**), whereas the seasonal Mauritanian current, upwelling filaments and eddies generated off the Mauritanian coast are the most likely features driving the westward transport of incoming B_{mixed} particles (**Figure 3H**).

Present results also demonstrate that B_{mixed} particles are connected to regional sources in significantly longer timescales than $B_{surface}$ particles (**Figure 5A**), which is naturally related with the absence of wind advection and to the lower current speed along depth. Due to the archipelagos exposure to impinging currents and winds, the Central and North American east coasts are the regions from which plastic marine litter is more likely to reach the Azores in a shorter period of time, whereas Southwestern European and Northwestern African coasts are the closest regions to the other Macaronesian archipelagos time wise. Although counter-intuitive, the fact that $B_{surface}$ and B_{mixed} particles are in some cases physically closer but take significantly longer time to intersect the archipelagos (as it is the case of particles intercepting the Azores from Southwestern European and Northwestern African sources) demonstrate how important it is to account for "oceanographic distances" instead of physical distances in studies of this nature.

As expected, differences in the dispersion of $B_{surface}$ and B_{mixed} particles are mainly related with the exposure to the wind, an hypothesis further supported by the distinct patterns between low- and high-windage particles (**Figure 6** and **Supplementary Figure 5**). In agreement with past studies (e.g., Lebreton et al., 2018; Maximenko et al., 2018), our results demonstrate that particles originating from the center of the North Atlantic subtropical gyre are more likely to intercept the archipelagos of the Macaronesia if considerably exposed to the wind (i.e., high-windage particles). This is further supported by the fact that low-windage particles tend to accumulate at this region and are thus less likely to exit (**Supplementary Figures 4**, **5**). On the other hand, incoming low-windage particles are more likely to originate from distant sources, such as sub-polar regions and the South Atlantic Ocean (**Figure 6**).

In what concerns the connectivity to marine-based sources of marine litter—often deemed as the most important for insular environments (e.g., Monteiro et al., 2018; Fernandes, 2019; Burt et al., 2020)—present results demonstrate that all archipelagos are exposed to common areas of intensive fishing activity (**Figure 7**). Nevertheless, the archipelagos' geographical location ultimately determines the degree of exposure to such areas. For instance, areas of intensive fishing activity located in the offshore extension of the Gulf Stream are much more important to the Azores (**Figure 7A** and **Supplementary Figure 6A**) than to Madeira and Canaries, which are more exposed to fishing activity located offshore and along the western Iberian coast (**Figure 7C** and **Supplementary Figure 6C**). The same applies to Cabo Verde, as the archipelago is mostly affected by different pathways and is thus more exposed intensive fishing activity carried along the Northwestern African coast (**Figure 7D**).

A similar pattern was observed in the connectivity to land-based sources. The west coast of North America is unquestionably the dominant source of land-based particles intercepting the archipelagos of Azores, Madeira and Canaries (**Figures 8A–C**), whereas the Northwestern African coast is the primary source for land-based particles reaching Cabo Verde (**Figure 8D**). This is especially true for B_{mixed} particles intercepting Cabo Verde, as almost all of them originate from the Northwestern African coast (81% of the land-based particles; **Table 3**). In addition, and despite the fact that the Lusitanian archipelagos are also exposed to Southern Atlantic particles (mostly B_{mixed} and low-windage particles; **Figures 4C,D,G**, **6A–C**, respectively), Cabo Verde is the only archipelago directly intercepted by such particles due to its exposure to the North Equatorial Counter Current (**Figures 4H**, **5H**). Such findings reinforce the idea that Cabo Verde is located in a rather complex oceanographic context, which make the archipelago exposed to significantly different sources in relation to the other Macaronesian archipelagos.

Following the same trend as other islands located in different oceanic basins (e.g., Robinson et al., 2017; van Gennip et al., 2019; van Sebille et al., 2019), our study shows that the archipelagos of the Macaronesia are significantly vulnerable to marine litter originating from distant sources. Although at a greater distance from the America than from Europe, these archipelagos are much more exposed to marine litter entering the North Atlantic Ocean at the western boundary, with the exception of Cabo Verde that is much more exposed to Northwestern African sources. It was also demonstrated that the archipelagos are not as exposed to marine litter from the North Atlantic "garbage patch" as previously thought (e.g., Pham et al., 2020), unless these particles are significantly exposed to the wind.

It is important to note that the lagrangian set up used in our simulations is relatively general and uses course resolution. There are also some knowledge gaps associated with the transport of marine plastic particles at the present date. There are several important factors to consider: (i) the coarse temporal and spatial resolution of the ocean circulation and wind datasets is not able to fully resolve sub-mesoscale processes and coastal dynamics; (ii) the fact that our particles do not take into account plastic properties (such as density, shape, and size) that can influence their horizontal and vertical displacement; (iii) the negligence of particle weathering, fragmentation, and biofouling; and (iv) the simplification of highly chaotic (or turbulent) processes associated with particle beaching. Nevertheless, our

modeled results demonstrate the importance of understanding how currents, waves and wind mediate the transport of marine litter from marine- and land-based sources to oceanic islands in the North Atlantic basin. Such understanding is vital, and it is expected that a multi-disciplinary approach between modeling and field-based results can benefit the creation of management and mitigation policies to reduce the vulnerability of oceanic islands to exogenous marine plastic pollution. It is also expected that some of the limitations of our study will be improved with the advent of new products with better resolution and calibration, made possible by future advances in computational power and numerical optimization routines, and by future satellite missions that will measure oceanic parameters with unprecedented precision, such as the Sea surface KInematics Multiscale monitoring (SKIM) concept (Ardhuin et al., 2018).

DATA AVAILABILITY STATEMENT

Particle trajectories files cannot be provided due to size (>100 GB). Python scripts used to run the lagrangian simulations and for the data analysis are available at: https://github.com/claudiofgcardoso/CleanAtlantic_MACARONESIA.git. Global drifter trajectory data are available from the NOAA Global Drifter Program (www.aoml.noaa.gov/phod/gdp/). The ocean circulation datasets GLORYS2V4 and GLORYS12V1 can be found at the CMEMS website (https://resources.marine.copernicus.eu/?option=com_csw&view=details&product_id=GLOBAL_ANALYSIS_FORECAST_PHY_001_024; https://resources.marine.copernicus.eu/?option=com_csw&view=details&product_id=GLOBAL_REANALYSIS_PHY_001_030, respectively). WaveWatch III hindcast and wind dataset used to force the wave model and our virtual particles at the surface (ECMWF ERA-Interim Reanalysis) are available at the IFREMER FTP server (ftp://ftp.ifremer.fr/ifremer/ww3/HINDCAST/GLOBAL/). Shapefiles for the EEZ were made available by the Flanders Marine Institute (https://www.marineregions.org/). The "Gridded population of the world" (Version 4, revision 11) was produced by the centre for International Earth Science Information Network (CIESIN) and the Centro Internacional de Agricultura Tropical (CIAT) and is available online (https://sedac.ciesin.columbia.edu/data/collection/gpw-v4). The "Global Fishing Watch" database was produced by Kroodsma et al. (2018) and is available online (https://globalfishingwatch.org/datasets-and-code/fishing-effort/).

AUTHOR CONTRIBUTIONS

CC assembled most of the writing and was responsible for the modeling and data collection, processing, and analysis. Both authors developed the original ideas, structure of the study, participated in the review process, and approved the final version.

FUNDING

This study was supported by the CleanAtlantic Project from the INTERREG Atlantic Area (EAPA_46/2016) and by the Oceanic Observatory of Madeira (M1420-01-0145-FEDER-000001). CC was funded by the Fundação para a Ciência e a Tecnologia (FCT, SFRH/BD/143792/2019) at the time of publication.

ACKNOWLEDGMENTS

We gratefully thank CESGA (Supercomputing Center of Galicia) for providing the necessary resources for the numerical simulations and data processing. We acknowledge Rui Vieira and Ricardo Faria for the support with computational demands and data processing, as well as Alexandra Rosa, Jesus Reis, Cátia Azevedo, José Alves, Carlos Lucas, and Annalisa Sambolino for the useful and constructive recommendations. We acknowledge the OceanParcels team for making the lagrangian framework available (www.oceanparcels.org) and for the technical support. Comments from Erik van Sebille and from a reviewer helped to improve the original manuscript.

SUPPLEMENTARY MATERIAL

The Supplementary Material for this article can be found online at: https://www.frontiersin.org/articles/10.3389/fmars.2021.653502/full#supplementary-material

REFERENCES

Aguilera, M., Medina-Suárez, M., Pinós, J., Liria-Loza, A., and Benejam, L. (2018). Marine debris as a barrier: assessing the impacts on sea turtle hatchlings on their way to the ocean. *Mar. Pollut. Bull.* 137, 481–487. doi: 10.1016/j.marpolbul.2018.10.054

Álvarez, S., Gestoso, I., Herrera, A., Riera, L., and Canning-Clode, J. (2020). A comprehensive first baseline for marine litter characterization in the Madeira archipelago (NE Atlantic). *Water Air Soil Pollut.* 231, 182. doi: 10.1007/s11270-020-04517-x

Álvarez-Hernández, C., Cairós, C., López-Darias, J., Mazzetti, E., Hernández-Sánchez, C., González-Sálamo, J., et al. (2019). Microplastic debris in beaches of Tenerife (Canary Islands, Spain). *Mar. Pollut. Bull.* 146, 26–32. doi: 10.1016/j.marpolbul.2019.05.064

Andrady, A. L. (2011). Microplastics in the marine environment. *Mar. Pollut. Bull.* 62, 1596–1605. doi: 10.1016/j.marpolbul.2011.05.030

Andrady, A. L. (2017). The plastic in microplastics: a review. *Mar. Pollut. Bull.* 119, 12–22. doi: 10.1016/j.marpolbul.2017.01.082

Ardhuin, F., Aksenov, Y., Benetazzo, A., Bertino, L., Brandt, P., Caubet, E., et al. (2018). Measuring currents, ice drift, and waves from space: the Sea surface KInematics Multiscale monitoring (SKIM) concept. *Ocean Sci.* 14, 337–354. doi: 10.5194/os-14-337-2018

Arístegui, J., Sangrá, P., Hernández-León, S., Cantón, M., Hernández-Guerra, A., and Kerling, J. (1994). Island-induced eddies in the Canary islands. *Deep Sea Res. I* 41, 1509–1525. doi: 10.1016/0967-0637(94)90058-2

Avery-Gomm, S., Provencher, J. F., Liboiron, M., Poon, F. E., and Smith, P. A. (2018). Plastic pollution in the Labrador Sea: an assessment using the seabird northern fulmar *Fulmarus glacialis* as a biological monitoring species. *Mar. Pollut. Bull.* 127, 817–822. doi: 10.1016/j.marpolbul.2017.10.001

Barbosa Aguiar, A. C., Peliz, A. J., Cordeiro Pires, A., and Le Cann, B. (2011). Zonal structure of the mean flow and eddies in the Azores current system. *J. Geophys. Res. Oceans* 116, 1–14. doi: 10.1029/2010JC006538

Barnes, D. K., Galgani, F., Thompson, R. C., and Barlaz, M. (2009). Accumulation and fragmentation of plastic debris in global environments. *Philos. Trans. R. Soc. B Biol. Sci.* 364, 1985–1998. doi: 10.1098/rstb.2008.0205

Barnes, D. K., Morley, S. A., Bell, J., Brewin, P., Brigden, K., Collins, M., et al. (2018). Marine plastics threaten giant Atlantic marine protected areas. *Curr. Biol.* 28, R1137–R1138. doi: 10.1016/j.cub.2018.08.064

Barnes, D. K. A. (2002). Invasions by marine life on plastic debris. *Nature* 416, 808–809. doi: 10.1038/416808a

Barton, E. (2001). "Canary and Portugal currents," in *Encyclopedia of Ocean Sciences*, ed J. H. Steele (Oxford: Academic Press), 380–389. doi: 10.1006/rwos.2001.0360

Barton, E. D., Arístegui, J., Tett, P., and Navarro-Pérez, E. (2004). Variability in the Canary Islands area of filament-eddy exchanges. *Prog. Oceanogr.* 62, 71–94. doi: 10.1016/j.pocean.2004.07.003

Barton, E. D., Basterretxea, G., Flament, P., Mitchelson-Jacob, E. G., Jones, B., Arístegui, J., et al. (2000). Lee region of Gran Canaria. *J. Geophys. Res. Oceans* 105, 17173–17193. doi: 10.1029/2000JC900010

Baulch, S., and Perry, C. (2014). Evaluating the impacts of marine debris on cetaceans. *Mar. Pollut. Bull.* 80, 210–221. doi: 10.1016/j.marpolbul.2013.12.050

Baztan, J., Carrasco, A., Chouinard, O., Cleaud, M., Gabaldon, J. E., Huck, T., et al. (2014). Protected areas in the Atlantic facing the hazards of micro-plastic pollution: first diagnosis of three islands in the Canary Current. *Mar. Pollut. Bull.* 80, 302–311. doi: 10.1016/j.marpolbul.2013.12.052

Bond, A. L., Montevecchi, W. A., Guse, N., Regular, P. M., Garthe, S., and Rail, J. F. (2012). Prevalence and composition of fishing gear debris in the nests of northern gannets (*Morus bassanus*) are related to fishing effort. *Mar. Pollut. Bull.* 64, 907–911. doi: 10.1016/j.marpolbul.2012.03.011

Bourles, B., Molinari, R. L., Johns, E., Wilson, W. D., and Leaman, K. D. (1999). Upper layer currents in the western tropical North Atlantic (1989–1991). *J. Geophys. Res. Oceans* 104, 1361–1375. doi: 10.1029/1998JC900025

Bowman, D., Manor-Samsonov, N., and Golik, A. (1998). Dynamics of litter pollution on Israeli Mediterranean beaches: a budgetary, litter flux approach. *J. Coast. Res.* 14, 418–482.

Burt, A. J., Raguain, J., Sanchez, C., Brice, J., Fleischer-Dogley, F., Goldberg, R., et al. (2020). The costs of removing the unsanctioned import of marine plastic litter to small island states. *Sci. Rep.* 10:14458. doi: 10.1038/s41598-020-71444-6

Caldeira, R., Groom, S., Miller, P., Pilgrim, D., and Nezlin, N. (2002). Sea-surface signatures of the island mass effect phenomena around Madeira Island, Northeast Atlantic. *Rem. Sens. Environ.* 80, 336–360. doi: 10.1016/S0034-4257(01)00316-9

Caldeira, R. M. A., and Reis, J. C. (2017). The Azores confluence zone. *Front. Mar. Sci.* 4:37. doi: 10.3389/fmars.2017.00037

Caldeira, R. M. A., and Tomé, R. (2013). Wake response to an ocean-feedback mechanism: Madeira Island case study. *Bound. Layer Meteorol.* 148, 419–436. doi: 10.1007/s10546-013-9817-y

Campanale, C., Massarelli, C., Savino, I., Locaputo, V., and Uricchio, V. F. (2020). A detailed review study on potential effects of microplastics and additives of concern on human health. *Int. J. Environ. Res. Public Health* 17:1212. doi: 10.3390/ijerph17041212

Cardoso, C., Caldeira, R. M., Relvas, P., and Stegner, A. (2020). Islands as eddy transformation and generation hotspots: Cabo Verde case study. *Prog. Oceanogr.* 184:102271. doi: 10.1016/j.pocean.2020.102271

Carson, H. S., Lamson, M. R., Nakashima, D., Toloumu, D., Hafner, J., Maximenko, N., et al. (2013). Tracking the sources and sinks of local marine debris in Hawai'i. *Mar. Environ. Res.* 84, 76–83. doi: 10.1016/j.marenvres.2012.12.002

Chambault, P., Vandeperre, F., Machete, M., Lagoa, J. C., and Pham, C. K. (2018). Distribution and composition of floating macro litter off the Azores archipelago and Madeira (NE Atlantic) using opportunistic surveys. *Mar. Environ. Res.* 141, 225–232. doi: 10.1016/j.marenvres.2018.09.015

Chubarenko, I., Bagaev, A., Zobkov, M., and Esiukova, E. (2016). On some physical and dynamical properties of microplastic particles in marine environment. *Mar. Pollut. Bull.* 108, 105–112. doi: 10.1016/j.marpolbul.2016.04.048

Chubarenko, I., Efimova, I., Bagaeva, M., Bagaev, A., and Isachenko, I. (2020). On mechanical fragmentation of single-use plastics in the sea swash zone with different types of bottom sediments: insights from laboratory experiments. *Mar. Pollut. Bull.* 150:110726. doi: 10.1016/j.marpolbul.2019.110726

Chubarenko, I. P., Esiukova, E. E., Bagaev, A. V., Bagaeva, M. A., and Grave, A. N. (2018). Three-dimensional distribution of anthropogenic microparticles in the body of sandy beaches. *Sci. Total Environ.* 628–629, 1340–1351. doi: 10.1016/j.scitotenv.2018.02.167

CIESIN (2018). *Gridded Population of the World, Version 4 (GPWV4): Population Density, Revision 11*. Palisades, NY: NASA Socioeconomic Data and Applications Center (SEDAC).

Corcoran, P. L., Biesinger, M. C., and Grifi, M. (2009). Plastics and beaches: a degrading relationship. *Mar. Pollut. Bull.* 58, 80–84. doi: 10.1016/j.marpolbul.2008.08.022

Cozar, A., Echevarria, F., Gonzalez-Gordillo, J. I., Irigoien, X., Ubeda, B., Hernandez-Leon, S., et al. (2014). Plastic debris in the open ocean. *Proc. Natl. Acad. Sci. U.S.A.* 111, 10239–10244. doi: 10.1073/pnas.1314705111

Delandmeter, P., and van Sebille, E. (2019). The Parcels v2.0 Lagrangian framework: new field interpolation schemes. *Geosci. Model Dev. Discuss.* 12, 1–24. doi: 10.5194/gmd-2018-339

Desforges, J. P. W., Galbraith, M., and Ross, P. S. (2015). Ingestion of microplastics by zooplankton in the Northeast Pacific Ocean. *Archiv. Environ. Contamin. Toxicol.* 69, 320–330. doi: 10.1007/s00244-015-0172-5

Doxsey-Whitfield, E., MacManus, K., Adamo, S. B., Pistolesi, L., Squires, J., Borkovska, O., et al. (2015). Taking advantage of the improved availability of census data: a first look at the gridded population of the world, version 4. *Appl. Geogr.* 1, 226–234. doi: 10.1080/23754931.2015.1014272

Edyvane, K. S., and Penny, S. S. (2017). Trends in derelict fishing nets and fishing activity in northern Australia: implications for trans-boundary fisheries management in the shared Arafura and Timor Seas. *Fish. Res.* 188, 23–37. doi: 10.1016/j.fishres.2016.11.021

Enders, K., Lenz, R., Stedmon, C. A., and Nielsen, T. G. (2015). Abundance, size and polymer composition of marine microplastics $\geq$ 10 μm in the Atlantic Ocean and their modelled vertical distribution. *Mar. Pollut. Bull.* 100, 70–81. doi: 10.1016/j.marpolbul.2015.09.027

Eriksen, M., Lebreton, L. C., Carson, H. S., Thiel, M., Moore, C. J., Borerro, J. C., et al. (2014). Plastic pollution in the world's oceans: more than 5 trillion plastic pieces weighing over 250,000 tons afloat at sea. *PLoS ONE* 9:e0111913. doi: 10.1371/journal.pone.0111913

Fazey, F. M., and Ryan, P. G. (2016). Biofouling on buoyant marine plastics: an experimental study into the effect of size on surface longevity. *Environ. Pollut.* 210, 354–360. doi: 10.1016/j.envpol.2016.01.026

Fernandes, M. F. (2019). *Quantification of macro and microplastics on a Desert Island, Santa Luzia, Cabo Verde Archipelago, North East Atlantic Ocean* (Master's thesis), Universidade do Porto, Porto, Portugal.

Fratantoni, D. M. (2001). North Atlantic surface circulation during the 1990's observed with satellite-tracked drifters. *J. Geophys. Res. Oceans* 106, 22067–22093. doi: 10.1029/2000JC000730

Freitas, R., Romeiras, M., Silva, L., Cordeiro, R., Madeira, P., González, J. A., et al. (2019). Restructuring of the 'Macaronesia' biogeographic unit: a marine multi-taxon biogeographical approach. *Sci. Rep.* 9:15792. doi: 10.1038/s41598-019-51786-6

Garric, G., Parent, L., Greiner, E., Drévillon, M., Hamon, M., Lellouche, J.-M., et al. (2018). "Performance and quality assessment of the global ocean eddy-permitting physical reanalysis glorys2v4," in *Proceedings of the Eight EuroGOOS International Conference, 3–5 October 2017, Bergen, Norway*, eds E. Buch, V. Fernández, D. Eparkhina, P. Gorringe, and G. Nolan (Brussels), 215–222.

Gassel, M., Harwani, S., Park, J. S., and Jahn, A. (2013). Detection of nonylphenol and persistent organic pollutants in fish from the North Pacific Central Gyre. *Mar. Pollut. Bull.* 73, 231–242. doi: 10.1016/j.marpolbul.2013.05.014

Geyer, R., Jambeck, J. R., and Law, K. L. (2017). Production, use, and fate of all plastics ever made. *Sci. Adv.* 3:e1700782. doi: 10.1126/sciadv.1700782

Goldstein, M. C., Carson, H. S., and Eriksen, M. (2014). Relationship of diversity and habitat area in North Pacific plastic-associated rafting communities. *Mar. Biol.* 161, 1441–1453. doi: 10.1007/s00227-014-2432-8

Gould, W. (1985). Physical oceanography of the Azores front. *Prog. Oceanogr.* 14, 167–190. doi: 10.1016/0079-6611(85)90010-2

Gregory, M. R. (2009). Environmental implications of plastic debris in marine settings–entanglement, ingestion, smothering, hangers-on, hitch-hiking and alien invasions. *Philos. Trans. R. Soc. B Biol. Sci.* 364, 2013–2025. doi: 10.1098/rstb.2008.0265

Grodsky, S. A., Lumpkin, R., and Carton, J. A. (2011). Spurious trends in global surface drifter currents. *Geophys. Res. Lett.* 38, 1–6. doi: 10.1029/2011GL047393

Gutow, L., Ricker, M., Holstein, J. M., Dannheim, J., Stanev, E. V., and Wolff, J. O. (2018). Distribution and trajectories of floating and benthic marine macrolitter in the south-eastern North Sea. *Mar. Pollut. Bull.* 131, 763–772. doi: 10.1016/j.marpolbul.2018.05.003

Herrera, A., Asensio, M., Martínez, I., Santana, A., Packard, T., and Gómez, M. (2018). Microplastic and tar pollution on three Canary Islands beaches: an annual study. *Mar. Pollut. Bull.* 129, 494–502. doi: 10.1016/j.marpolbul.2017.10.020

Herrera, A., Raymond, E., Martínez, I., Álvarez, S., Canning-Clode, J., Gestoso, I., et al. (2020). First evaluation of neustonic microplastics in the Macaronesian region, NE Atlantic. *Mar. Pollut. Bull.* 153:110999. doi: 10.1016/j.marpolbul.2020.110999

Hinata, H., Mori, K., Ohno, K., Miyao, Y., and Kataoka, T. (2017). An estimation of the average residence times and onshore-offshore diffusivities of beached microplastics based on the population decay of tagged meso- and macrolitter. *Mar. Pollut. Bull.* 122, 17–26. doi: 10.1016/j.marpolbul.2017.05.012

Hinata, H., Sagawa, N., Kataoka, T., and Takeoka, H. (2020). Numerical modeling of the beach process of marine plastics: a probabilistic and diagnostic approach with a particle tracking method. *Mar. Pollut. Bull.* 152:110910. doi: 10.1016/j.marpolbul.2020.110910

Hoornweg, D., and Bhada-Tata, P. (2012). *What a Waste : A Global Review of Solid Waste Management.* Urban development series; knowledge papers no. 15. Washington, DC: World Bank. Available online at: https://openknowledge.worldbank.org/handle/10986/17388

Isobe, A., Kubo, K., Tamura, Y., Kako, S., Nakashima, E., and Fujii, N. (2014). Selective transport of microplastics and mesoplastics by drifting in coastal waters. *Mar. Pollut. Bull.* 89, 324–330. doi: 10.1016/j.marpolbul.2014.09.041

Jalón-Rojas, I., Wang, X. H., and Fredj, E. (2019). A 3D numerical model to Track Marine Plastic Debris (TrackMPD): sensitivity of microplastic trajectories and fates to particle dynamical properties and physical processes. *Mar. Pollut. Bull.* 141, 256–272. doi: 10.1016/j.marpolbul.2019.02.052

Jambeck, J. R., Geyer, R., Wilcox, C., Siegler, T. R., Perryman, M., Andrady, A., et al. (2015). Plastic waste inputs from land into the ocean. *Science* 347, 768–771. doi: 10.1126/science.1260352

Johnson, J., and Stevens, I. (2000). A fine resolution model of the eastern North Atlantic between the Azores, the Canary Islands and the Gibraltar Strait. *Deep Sea Res. I* 47, 875–899. doi: 10.1016/S0967-0637(99)00073-4

Kaandorp, M. L. A., Dijkstra, H. A., and van Sebille, E. (2020). Closing the Mediterranean marine floating plastic mass budget: inverse modeling of sources and sinks. *Environ. Sci. Technol.* 54, 11980–11989. doi: 10.1021/acs.est.0c01984

Kaza, S., Yao, L., Bhada-Tata, P., and Van Woerden, F. (2018). *What a Waste 2.0: A Global Snapshot of Solid Waste Management to 2050*. Washington, DC: World Bank Publications.

Klein, B., and Siedler, G. (1989). On the origin of the Azores Current. *J. Geophys. Res.* 94:6159. doi: 10.1029/JC094iC05p06159

Kooi, M., and Koelmans, A. A. (2019). Simplifying microplastic via continuous probability distributions for size, shape, and density. *Environ. Sci. Technol. Lett.* 6, 551–557. doi: 10.1021/acs.estlett.9b00379

Kooi, M., Reisser, J., Slat, B., Ferrari, F. F., Schmid, M. S., Cunsolo, S., et al. (2016). The effect of particle properties on the depth profile of buoyant plastics in the ocean. *Sci. Rep.* 6:33882. doi: 10.1038/srep33882

Kooi, M., Van Nes, E. H., Scheffer, M., and Koelmans, A. A. (2017). Ups and downs in the ocean: effects of biofouling on vertical transport of microplastics. *Environ. Sci. Technol.* 51, 7963–7971. doi: 10.1021/acs.est.6b04702

Kroodsma, D. A., Mayorga, J., Hochberg, T., Miller, N. A., Boerder, K., Ferretti, F., et al. (2018). Tracking the global footprint of fisheries. *Science* 359, 904–908. doi: 10.1126/science.aao5646

Kukulka, T., Proskurowski, G., Morét-Ferguson, S., Meyer, D. W., and Law, K. L. (2012). The effect of wind mixing on the vertical distribution of buoyant plastic debris. *Geophys. Res. Lett.* 39, 1–6. doi: 10.1029/2012GL051116

Lacerda, A. L., Rodrigues, L. d. S., van Sebille, E., Rodrigues, F. L., Ribeiro, L., Secchi, E. R., et al. (2019). Plastics in sea surface waters around the Antarctic Peninsula. *Sci. Rep.* 9:3977. doi: 10.1038/s41598-019-40311-4

Lange, M., and van Sebille, E. (2017). Parcels v0.9: prototyping a Lagrangian ocean analysis framework for the petascale age. *Geosci. Model Dev.* 10, 4175–4186. doi: 10.5194/gmd-10-4175-2017

Lathuilière, C., Echevin, V., and Lévy, M. (2008). Seasonal and intraseasonal surface chlorophyll-a variability along the northwest African coast. *J. Geophys. Res.* 113:C05007. doi: 10.1029/2007JC004433

Lavers, J. L., and Bond, A. L. (2017). Exceptional and rapid accumulation of anthropogenic debris on one of the world's most remote and pristine islands. *Proc. Natl. Acad. Sci. U.S.A.* 114, 6052–6055. doi: 10.1073/pnas.1619818114

Law, K. L. (2017). Plastics in the marine environment. *Annu. Rev. Mar. Sci.* 9, 205–229. doi: 10.1146/annurev-marine-010816-060409

Law, K. L., Starr, N., Siegler, T. R., Jambeck, J. R., Mallos, N. J., and Leonard, G. H. (2020). The United States' contribution of plastic waste to land and ocean. *Sci. Adv.* 6:eabd0288. doi: 10.1126/sciadv.abd0288

Lázaro, C., Fernandes, M. J., Santos, A. M. P., and Oliveira, P. (2005). Seasonal and interannual variability of surface circulation in the Cape Verde region from 8 years of merged T/P and ERS-2 altimeter data. *Rem. Sens. Environ.* 98, 45–62. doi: 10.1016/j.rse.2005.06.005

Lazier, J. R. N., and Wright, D. G. (1993). Annual velocity variations in the Labrador Current. *J. Phys. Oceanogr.* 23, 659–678. doi: 10.1175/1520-0485(1993)023<0659:AVVITL>2.0.CO;2

Lebreton, L., Egger, M., and Slat, B. (2019). A global mass budget for positively buoyant macroplastic debris in the ocean. *Sci. Rep.* 9:12922. doi: 10.1038/s41598-019-49413-5

Lebreton, L., Slat, B., Ferrari, F., Sainte-Rose, B., Aitken, J., Marthouse, R., et al. (2018). Evidence that the Great Pacific Garbage Patch is rapidly accumulating plastic. *Sci. Rep.* 8:4666. doi: 10.1038/s41598-018-22939-w

Lebreton, L. C., Greer, S. D., and Borrero, J. C. (2012). Numerical modelling of floating debris in the world's oceans. *Mar. Pollut. Bull.* 64, 653–661. doi: 10.1016/j.marpolbul.2011.10.027

Lellouche, J. M., Greiner, E., Le Galloudec, O., Garric, G., Regnier, C., Drevillon, M., et al. (2018). Recent updates to the Copernicus Marine Service global ocean monitoring and forecasting real-time 1/12° high-resolution system. *Ocean Sci.* 14, 1093–1126. doi: 10.5194/os-14-1093-2018

Loulad, S., Houssa, R., Rhinane, H., Boumaaz, A., and Benazzouz, A. (2017). Spatial distribution of marine debris on the seafloor of Moroccan waters. *Mar. Pollut. Bull.* 124, 303–313. doi: 10.1016/j.marpolbul.2017.07.022

Lumpkin, R., and Centurioni, L. (2019). *Global Drifter Program Quality-Controlled 6-Hour Interpolated Data From Ocean Surface Drifting Buoys.* NOAA National Centers for Environmental Information. Dataset. Available online at: https://doi.org/10.25921/7ntx-z961 (accessed July 11, 2020).

Lumpkin, R., Grodsky, S. A., Centurioni, L., Rio, M. H., Carton, J. A., and Lee, D. (2013). Removing spurious low-frequency variability in drifter velocities. *J. Atmos. Ocean. Technol.* 30, 353–360. doi: 10.1175/JTECH-D-12-00139.1

Lumpkin, R., Özgökmen, T., and Centurioni, L. (2017). Advances in the application of surface drifters. *Annu. Rev. Mar. Sci.* 9, 59–81. doi: 10.1146/annurev-marine-010816-060641

Lumpkin, R., and Pazos, M. (2007). "Measuring surface currents with Surface Velocity Program drifters: the instruments, its data and some recent results," in *Lagrangian Analysis and Prediction of Coastal and Ocean Dynamics*, eds A. Griffa, A. D. Kirwan, A. J. Mariano, T. Özgökmen, and H. T. Rossby (Cambridge, MA: Cambridge University Press), 1–56. doi: 10.1017/CBO9780511535901.003

Martins, C. S., Hamann, M., and Fiúza, A. F. (2002). Surface circulation in the eastern North Atlantic, from drifters and altimetry. *J. Geophys. Res. Oceans* 107, 10-1–10-22. doi: 10.1029/2000JC000345

Matsuguma, Y., Takada, H., Kumata, H., Kanke, H., Sakurai, S., Suzuki, T., et al. (2017). Microplastics in sediment cores from Asia and Africa as indicators of temporal trends in plastic pollution. *Archiv. Environ. Contamin. Toxicol.* 73, 230–239. doi: 10.1007/s00244-017-0414-9

Maximenko, N., Hafner, J., Kamachi, M., and MacFadyen, A. (2018). Numerical simulations of debris drift from the Great Japan Tsunami of 2011 and their verification with observational reports. *Mar. Pollut. Bull.* 132, 5–25. doi: 10.1016/j.marpolbul.2018.03.056

Maximenko, N., Hafner, J., and Niiler, P. (2012). Pathways of marine debris derived from trajectories of Lagrangian drifters. *Mar. Pollut. Bull.* 65, 51–62. doi: 10.1016/j.marpolbul.2011.04.016

McWilliams, M., Liboiron, M., and Wiersma, Y. (2018). Rocky shoreline protocols miss microplastics in marine debris surveys (Fogo Island, Newfoundland and Labrador). *Mar. Pollut. Bull.* 129, 480–486. doi: 10.1016/j.marpolbul.2017.10.018

Mittelstaedt, E. (1983). The upwelling area off Northwest Africa—a description of phenomena related to coastal upwelling. *Prog. Oceanogr.* 12, 307–331. doi: 10.1016/0079-6611(83)90012-5

Mittelstaedt, E. (1991). The ocean boundary along the northwest African coast: circulation and oceanographic properties at the sea surface. *Prog. Oceanogr.* 26, 307–355. doi: 10.1016/0079-6611(91)90011-A

Monteiro, R. C., Ivar do Sul, J. A., and Costa, M. F. (2018). Plastic pollution in islands of the Atlantic Ocean. *Environ. Pollut.* 238, 103–110. doi: 10.1016/j.envpol.2018.01.096

Morét-Ferguson, S., Law, K. L., Proskurowski, G., Murphy, E. K., Peacock, E. E., and Reddy, C. M. (2010). The size, mass, and composition of plastic debris in the western North Atlantic Ocean. *Mar. Pollut. Bull.* 60, 1873–1878. doi: 10.1016/j.marpolbul.2010.07.020

Neumann, D., Callies, U., and Matthies, M. (2014). Marine litter ensemble transport simulations in the southern North Sea. *Mar. Pollut. Bull.* 86, 219–228. doi: 10.1016/j.marpolbul.2014.07.016

Niiler, P. P., Sybrandy, A. S., Bi, K., Poulain, P. M., and Bitterman, D. (1995). Measurements of the water-following capability of holey-sock and TRISTAR drifters. *Deep Sea Res. I* 42, 1951–1955, 1957–1964. doi: 10.1016/0967-0637(95)00076-3

Nollkaemper, A. (1994). Land-based discharges of marine debris: from local to global regulation. *Mar. Pollut. Bull.* 28, 649–652. doi: 10.1016/0025-326X(94)90299-2

Ohde, T., and Siegel, H. (2010). Biological response to coastal upwelling and dust deposition in the area off Northwest Africa. *Contin. Shelf Res.* 30, 1108–1119. doi: 10.1016/j.csr.2010.02.016

Onink, V., Wichmann, D., Delandmeter, P., and Sebille, E. (2019). The role of Ekman Currents, geostrophy, and stokes drift in the accumulation of floating microplastic. *J. Geophys. Res. Oceans* 124, 1474–1490. doi: 10.1029/2018JC014547

Pabortsava, K., and Lampitt, R. S. (2020). High concentrations of plastic hidden beneath the surface of the Atlantic Ocean. *Nat. Commun.* 11:4073. doi: 10.1038/s41467-020-17932-9

Pereiro, D., Souto, C., and Gago, J. (2018). Calibration of a marine floating litter transport model. *J. Oper. Oceanogr.* 11, 125–133. doi: 10.1080/1755876X.2018.1470892

Pérez, F. F., Castro, C. G., Álvarez-Salgado, X. A., and Ríos, A. F. (2001). Coupling between the Iberian basin–scale circulation and the Portugal boundary current system: a chemical study. *Deep Sea Res. I* 48, 1519–1533. doi: 10.1016/S0967-0637(00)00101-1

Pham, C. K., Gomes-Pereira, J. N., Isidro, E. J., Santos, R. S., and Morato, T. (2013). Abundance of litter on Condor seamount (Azores, Portugal, Northeast Atlantic). *Deep Sea Res. II* 98, 204–208. doi: 10.1016/j.dsr2.2013.01.011

Pham, C. K., Pereira, J. M., Frias, J. P., Ríos, N., Carriço, R., Juliano, M., et al. (2020). Beaches of the Azores archipelago as transitory repositories for small plastic fragments floating in the North-East Atlantic. *Environ. Pollut.* 263:114494. doi: 10.1016/j.envpol.2020.114494

Pieper, C., Magalhães Loureiro, C., Law, K. L., Amaral-Zettler, L. A., Quintino, V., Rodrigues, A. M., et al. (2020). Marine litter footprint in the Azores Islands: a climatological perspective. *Sci. Total Environ.* 761:143310. doi: 10.1016/j.scitotenv.2020.143310

Provencher, J. F., Vermaire, J. C., Avery-Gomm, S., Braune, B. M., and Mallory, M. L. (2018). Garbage in guano? Microplastic debris found in faecal precursors of seabirds known to ingest plastics. *Sci. Total Environ.* 644, 1477–1484. doi: 10.1016/j.scitotenv.2018.07.101

Prunier, J., Maurice, L., Perez, E., Gigault, J., Pierson Wickmann, A. C., Davranche, M., et al. (2019). Trace metals in polyethylene debris from the North Atlantic subtropical gyre. *Environ. Pollut.* 245, 371–379. doi: 10.1016/j.envpol.2018.10.043

Ramalho, R. A. S. (2011). *Building the Cape Verde Islands*. Berlin; Heidelberg: Springer Berlin Heidelberg.

Reisser, J., Shaw, J., Wilcox, C., Hardesty, B. D., Proietti, M., Thums, M., et al. (2013). Marine plastic pollution in waters around Australia: characteristics, concentrations, and pathways. *PLoS ONE* 8:e80466. doi: 10.1371/journal.pone.0080466

Reisser, J., Slat, B., Noble, K., Du Plessis, K., Epp, M., Proietti, M., et al. (2015). The vertical distribution of buoyant plastics at sea: an observational study in the North Atlantic Gyre. *Biogeosciences* 12, 1249–1256. doi: 10.5194/bg-12-1249-2015

Ríos, N., Frias, J. P., Rodríguez, Y., Carriço, R., Garcia, S. M., Juliano, M., et al. (2018). Spatio-temporal variability of beached macro-litter on remote islands of the North Atlantic. *Mar. Pollut. Bull.* 133, 304–311. doi: 10.1016/j.marpolbul.2018.05.038

Robinson, J., New, A. L., Popova, E. E., Srokosz, M. A., and Yool, A. (2017). Far-field connectivity of the UK's four largest marine protected areas: four of a kind? *Earths Future* 5, 475–494. doi: 10.1002/2016EF000516

Rochman, C. M., Hoh, E., Hentschel, B. T., and Kaye, S. (2013). Long-term field measurement of sorption of organic contaminants to five types of plastic pellets: implications for plastic marine debris. *Environ. Sci. Technol.* 47, 1646–1654. doi: 10.1021/es303700s

Rodríguez, Y., and Pham, C. K. (2017). Marine litter on the seafloor of the Faial-Pico Passage, Azores Archipelago. *Mari. Pollut. Bull.* 116, 448–453. doi: 10.1016/j.marpolbul.2017.01.018

Rodríguez, Y., Ressurreição, A., and Pham, C. K. (2020). Socio-economic impacts of marine litter for remote oceanic islands: the case of the Azores. *Mar. Pollut. Bull.* 160:111631. doi: 10.1016/j.marpolbul.2020.111631

Ryan, P. G., Dilley, B. J., Ronconi, R. A., and Connan, M. (2019). Rapid increase in Asian bottles in the South Atlantic Ocean indicates major debris inputs from ships. *Proc. Natl. Acad. Sci. U.S.A.* 116, 20892–20897. doi: 10.1073/pnas.1909816116

Ryan, P. G., Moore, C. J., Van Franeker, J. A., and Moloney, C. L. (2009). Monitoring the abundance of plastic debris in the marine environment. *Philos. Trans. R. Soc. B Biol. Sci.* 364, 1999–2012. doi: 10.1098/rstb.2008.0207

Sá, S., Bastos-Santos, J., Araújo, H., Ferreira, M., Duro, V., Alves, F., et al. (2016). Spatial distribution of floating marine debris in offshore continental Portuguese waters. *Mar. Pollut. Bull.* 104, 269–278. doi: 10.1016/j.marpolbul.2016.01.011

Sala, I., Caldeira, R. M. A., Estrada-Allis, S. N., Froufe, E., and Couvelard, X. (2013). Lagrangian transport pathways in the northeast Atlantic and their environmental impact. *Limnol. Oceanogr.* 3, 40–60. doi: 10.1215/21573689-2152611

Sala, I., Harrison, C. S., and Caldeira, R. M. (2016). The role of the Azores Archipelago in capturing and retaining incoming particles. *J. Mar. Syst.* 154, 146–156. doi: 10.1016/j.jmarsys.2015.10.001

Sangrà, P., Pascual, A., Rodríguez-Santana, Á., Machín, F., Mason, E., McWilliams, J. C., et al. (2009). The Canary Eddy Corridor: a major pathway for long-lived eddies in the subtropical North Atlantic. *Deep Sea Res. I* 56, 2100–2114. doi: 10.1016/j.dsr.2009.08.008

Schmidt, N., Fauvelle, V., Ody, A., Castro-Jiménez, J., Jouanno, J., Changeux, T., et al. (2019). The Amazon river: a major source of organic plastic additives to the tropical North Atlantic? *Environ. Sci. Technol.* 53, 7513–7521. doi: 10.1021/acs.est.9b01585

Schütte, F., Brandt, P., and Karstensen, J. (2016). Occurrence and characteristics of mesoscale eddies in the tropical northeastern Atlantic Ocean. *Ocean Sci.* 12, 663–685. doi: 10.5194/os-12-663-2016

Spalding, M. D., Fox, H. E., Allen, G. R., Davidson, N., Ferdaña, Z. A., Finlayson, M., et al. (2007). Marine ecoregions of the world: a bioregionalization of coastal and shelf areas. *BioScience* 57, 573–583. doi: 10.1641/B570707

Sterl, M. F., Delandmeter, P., and van Sebille, E. (2020). Influence of barotropic tidal currents on transport and accumulation of floating microplastics in the global open ocean. *J. Geophys. Res. Oceans* 125:e2019JC015583. doi: 10.1029/2019JC015583

Stramma, L. (1984). Geostrophic transport in the Warm Water Sphere of the eastern subtropical North Atlantic. *J. Mar. Res.* 42, 537–558. doi: 10.1357/002224084788506022

Stramma, L., and Schott, F. (1999). The mean flow field of the tropical Atlantic Ocean. *Deep Sea Res. II* 46, 279–303. doi: 10.1016/S0967-0645(98)00109-X

Stramma, L., and Siedler, G. (1988). Seasonal changes in the North Atlantic subtropical gyre. *J. Geophys. Res.* 93:8111. doi: 10.1029/JC093iC07p08111

Syakti, A. D., Bouhroum, R., Hidayati, N. V., Koenawan, C. J., Boulkamh, A., Sulistyo, I., et al. (2017). Beach macro-litter monitoring and floating microplastic in a coastal area of Indonesia. *Mar. Pollut. Bull.* 122, 217–225. doi: 10.1016/j.marpolbul.2017.06.046

The WaveWatch III Development Group (2016). *User Manual and System Documentation of Wavewatch III Version 5.16*. Technical Report 329, NOAA/NWS/NCEP/MMAB, College Park, MD, United States.

Thiel, M., Hinojosa, I. A., Miranda, L., Pantoja, J. F., Rivadeneira, M. M., and Vásquez, N. (2013). Anthropogenic marine debris in the coastal environment: a multi-year comparison between coastal waters and local shores. *Mar. Pollut. Bull.* 71, 307–316. doi: 10.1016/j.marpolbul.2013.01.005

Turra, A., Manzano, A. B., Dias, R. J. S., Mahiques, M. M., Barbosa, L., Balthazar-Silva, D., et al. (2015). Three-dimensional distribution of plastic pellets in sandy beaches: shifting paradigms. *Sci. Rep.* 4:4435. doi: 10.1038/srep04435

Unger, A., and Harrison, N. (2016). Fisheries as a source of marine debris on beaches in the United Kingdom. *Mar. Pollut. Bull.* 107, 52–58. doi: 10.1016/j.marpolbul.2016.04.024

Van Camp, L., Nykjaer, L., Mittelstaedt, E., and Schlittenhardt, P. (1991). Upwelling and boundary circulation off Northwest Africa as depicted by infrared and visible satellite observations. *Prog. Oceanogr.* 26, 357–402. doi: 10.1016/0079-6611(91)90012-B

van der Mheen, M., van Sebille, E., and Pattiaratchi, C. (2020). Beaching patterns of plastic debris along the Indian Ocean rim. *Ocean Sci. Discuss.* 16, 1–31. doi: 10.5194/os-2020-50

van Gennip, S. J., Dewitte, B., Garçon, V., Thiel, M., Popova, E., Drillet, Y., et al. (2019). In search for the sources of plastic marine litter that contaminates the Easter Island Ecoregion. *Sci. Rep.* 9:19662. doi: 10.1038/s41598-019-56012-x

van Sebille, E., Aliani, S., Law, K. L., Maximenko, N., Alsina, J. M., Bagaev, A., et al. (2020). The physical oceanography of the transport of floating marine debris. *Environ. Res. Lett.* 15:023003. doi: 10.1088/1748-9326/ab6d7d

van Sebille, E., Delandmeter, P., Schofield, J., Hardesty, D., Jones, J., and Donnelly, A. (2019). Basin-scale sources and pathways of microplastic that ends up in the Galápagos Archipelago. *Ocean Sci. Discuss.* 15, 1–15. doi: 10.5194/os-2019-37

van Sebille, E., Griffies, S. M., Abernathey, R., Adams, T. P., Berloff, P., Biastoch, A., et al. (2018). Lagrangian ocean analysis: fundamentals and practices. *Ocean Model.* 121, 49–75. doi: 10.1016/j.ocemod.2017.11.008

van Sebille, E., Wilcox, C., Lebreton, L., Maximenko, N., Hardesty, B. D., van Franeker, J. A., et al. (2015). A global inventory of small floating plastic debris. *Environ. Res. Lett.* 10:124006. doi: 10.1088/1748-9326/10/12/124006

Vianello, A., Boldrin, A., Guerriero, P., Moschino, V., Rella, R., Sturaro, A., et al. (2013). Microplastic particles in sediments of Lagoon of Venice, Italy: first observations on occurrence, spatial patterns and identification. *Estuar. Coast. Shelf Sci.* 130, 54–61. doi: 10.1016/j.ecss.2013.03.022

Wichmann, D., Delandmeter, P., and Sebille, E. (2019). Influence of near–surface currents on the global dispersal of marine microplastic. *J. Geophys. Res. Oceans* 124, 6086–6096. doi: 10.1029/2019JC015328

Yu, X., Ladewig, S., Bao, S., Toline, C. A., Whitmire, S., and Chow, A. T. (2018). Occurrence and distribution of microplastics at selected coastal sites along the southeastern United States. *Sci. Total Environ.* 613–614, 298–305. doi: 10.1016/j.scitotenv.2017.09.100

Zhang, H. (2017). Transport of microplastics in coastal seas. *Estuar. Coast. Shelf Sci.* 199, 74–86. doi: 10.1016/j.ecss.2017.09.032

Zhou, M., Paduan, J. D., and Niiler, P. P. (2000). Surface currents in the Canary Basin from drifter observations. *J. Geophys. Res. Oceans* 105, 21893–21911. doi: 10.1029/2000JC900096

Conflict of Interest: The authors declare that the research was conducted in the absence of any commercial or financial relationships that could be construed as a potential conflict of interest.

frontiers in Marine Science

ORIGINAL RESEARCH
published: 20 May 2021
doi: 10.3389/fmars.2021.609113

Ocean Dynamics and Topographic Upwelling Around the Aracati Seamount - North Brazilian Chain From *in situ* Observations and Modeling Results

Marcus Silva[1], Moacyr Araujo[1,2], Fábio Geber[1], Carmen Medeiros[1], Julia Araujo[1,3], Carlos Noriega[1] and Alex Costa da Silva[1]*

[1] *Laboratório de Oceanografia Física Estuarina e Costeira, Departamento de Oceanografia, Universidade Federal de Pernambuco, Recife, Brazil,* [2] *Brazilian Research Network on Global Climate Change — Rede CLIMA, São José dos Campos, Brazil,* [3] *Laboratório de Dinâmica Oceânica, Instituto Oceanográfico, Universidade de São Paulo, São Paulo, Brazil*

OPEN ACCESS

Edited by:
Miguel A. C. Teixeira, University of Reading, United Kingdom

Reviewed by:
José Pinho, University of Minho, Portugal
Antonio Olita, Institute of Atmospheric Sciences and Climate (CNR-ISAC), Italy

***Correspondence:**
Marcus Silva
marcus.asilva@ufpe.br

Specialty section:
This article was submitted to Coastal Ocean Processes, a section of the journal Frontiers in Marine Science

Received: *22 September 2020*
Accepted: *29 March 2021*
Published: *20 May 2021*

Citation:
Silva M, Araujo M, Geber F, Medeiros C, Araujo J, Noriega C and Costa da Silva A (2021) Ocean Dynamics and Topographic Upwelling Around the Aracati Seamount - North Brazilian Chain From in situ Observations and Modeling Results. Front. Mar. Sci. 8:609113. doi: 10.3389/fmars.2021.609113

The hydrodynamics and the occurrence of topographic upwelling around the northern Brazilian seamount chain were investigated. Meteorological and physical oceanographic data collected under the REVIZEE-NE Program cruises around the Aracati Bank, the major and highly productive seamount in the area, were analyzed and used to force and validate simulations using the 3D Princeton Ocean Model (3D POM). The Tropical Water mass in the top 150-m layer and the South Atlantic Central Water (SACW) beneath it and down to a depth of 670 m was present. The thickness of the barrier layer varied seasonally, being thinner (2 m) during the austral spring (October–December) and thicker (20 m) during the austral autumn (April–June) when winds were stronger. The surface mixed and isothermal layers in the austral winter (July–September) were located at depths of 84 and 96 m, respectively. During the austral spring, those layers were located at depths of 6 and 8 m, respectively. The mean wind shear energy was 9.8×10^{-4} m^2 s^{-2}, and the energy of the surface gravity wave break was 10.8×10^{-2} m^2 s^{-2}, and both served to enhance vertical mixing in the area. A permanent thermocline between the 70- and 150-m depths was present throughout the year. The isohaline distribution followed an isotherm pattern of variation, but at times, the formation of low-salinity eddies was verified on the bank slope. The 3D POM model reproduced the thermohaline structure accurately. Temperature and salinity profiles indicated the existence of vertical water displacements over the bank and along the direction of the North Brazil Current, which is the strongest western boundary current crossing the equatorial Atlantic. The kinematic structure observed in the simulations indicated vertical velocities of O (10^{-3} $m.s^{-1}$) in the upstream region of the bank during austral winter and summer seasons. During the summer, the most important vertical velocities were localized below the lower limit of the euphotic zone; while during the austral winter, these velocities were within the euphotic zone, thereby favoring primary producers.

Keywords: seamount upwelling, North Brazilian Current, Aracati Bank, tropical Atlantic, numerical simulation

INTRODUCTION

Oceanic islands, seamounts, and banks are associated with propitious fishing grounds worldwide, hosting abundant and diverse biomass and favoring the congregation of marine predators, such as tunas, dolphins, and seabirds (Morato et al., 2008; Pitcher et al., 2008). These geological features serve as shelter and physical substrates for the development of several species and induce a variety of flow phenomena.

As a current meets a bottom relief, parts of the kinetic energy are transformed into potential energy, promoting turbulence and mixing (Huppert and Bryan, 1976), localized upwelling, and/or the formation of Taylor cones that can increase nutrient transfer from deeper to shallower water layers (Flagg, 1987) and thus enhance primary production (Fonteneau, 1991; Roden, 1991; Cushman-Roisin, 1994; Rogers, 1994; Clark, 1999).

Seamounts, characterized as submerged mountains that rise at least 1,000 m above the surrounding seabed, are one of the most common geological features on our planet. Despite their abundance, they have still been poorly sampled and mapped (Wessel et al., 2010; Yesson et al., 2011; Leitner et al., 2020).

The interaction of marine currents with seamounts results in a complex system of circulation, which has been investigated from laboratory and *in situ* observations (Eiff and Bonneton, 2000; Mourino et al., 2001; Varela et al., 2007; Oliveira et al., 2016), as well as from analytical and numerical modeling studies (Boyer et al., 1987; Morato et al., 2009).

These studies have suggested that the combination of streamline splitting, current intensification, and breaking of internal lee waves plays a significant role as a mixing source in the ocean and may also play a large role in the dissipation of energy from global tides (i.e., Varela et al., 2007; Leitner et al., 2020).

In fact, the circulation patterns modeled and observed suggest that it may be possible that seamounts can increase the amount of chlorophyll in the euphotic zone and that it can be retained locally (White and Mohn, 2004; Lavelle and Mohn, 2010; Watling and Auster, 2017), an effect known in the literature as "SICE–Seamount-Induced Chlorophyll Enhancements" (Leitner et al., 2020).

One of the main mechanisms resulting from flow-topography interactions is the upwelling of nutrient-rich central waters into the euphotic zone, giving rise to mass and energy transfers through the tropical chain. Upwelling phenomena are generally identified by sea surface temperature anomalies, especially in regions that are characterized by a shallow pycnocline and with a relatively low-density gradient (see Mendonça et al., 2010, for seamount examples). This is the classical situation observed on the eastern boundary of the ocean basins along the coasts of the African (Rossi et al., 2008, 2009) and American continents (Hormazábal and Yuras, 2007; Fréon et al., 2009).

A very different scenario is verified at the western boundary of the tropical Atlantic, where the presence of deeper and more intense vertical thermohaline gradients prevents the transport of colder central water masses to the ocean surface (de Boyer Montégut et al., 2004; Araujo et al., 2011; Assunção et al., 2020). In this portion of the ocean, strong oligotrophy takes place.

The Brazilian islands and seamounts are referenced as an "oasis of life in an oceanic desert," representing social and economic stakes for the marine national heritage of Brazil (Hazin et al., 1998; Lessa et al., 1999; Chaves et al., 2006; Tchamabi et al., 2017).

Macedo et al. (1998) and Araujo et al. (2018) observed the occurrence of small-scale upwelling regions surrounding the islands and seamounts of Northeast Brazil's Exclusive Economic Zone (EEZ), and Travassos et al. (1999) indicated that these upwelling phenomena are weak and highly transient.

The North Brazilian Chain (NBCh) Banks are very socially and economically important for supporting almost the entire pelagic fishery production of the area (Hazin et al., 1998). However, the mechanism responsible for sustaining the high production in this area is not well-known.

The aim of this article was to investigate the effects of the flow-topography interaction on the thermohaline structure around the Aracati Bank, NBCh, analyzing potential locations where an enrichment of the mixed layer may occur.

STUDY AREA

Many islands, rocks, and banks are present in the northern-northeastern Brazilian area, among which the shallow oceanic banks, located at 2°–5° S, and 36°–39° W, belong to the NBCh. These banks are of volcanic origin, of various sizes, shapes, and depths, and currently covered by calcareous algae, mainly by *Lithothamnium*, and arranged along a stretch of 1,300 km, 150–200 km offshore the base of the continental slope (Coutinho, 1996).

The NBCh Banks (**Figures 1A,B**) are limited northward by the region where the South American and African continents are closer to each other and southward by subtropical convergence.

The major current system in the western tropical Atlantic in the top 100-m layer and the 100–500-m layer is presented in **Figure 1A**. The currents present in the NBCh domain are the North Brazil Current (NBC), the North Brazil Undercurrent (NBUC), the Central South Equatorial Current (CSEC), the Equatorial South Equatorial Current (ESEC), and the South Equatorial Undercurrent (SEUC) (Richardson and McKee, 1984; Peterson and Stramma, 1991; Stramma and England, 1999).

The NBUC and NBC follow the Brazilian coast and are characterized by a strong northwest acceleration inshore (Richardson and Walsh, 1986; Krelling et al., 2020).

The NBC is present all year. The vertical structure of the NBC between 5° and 10° S is characterized by the existence of an undercurrent with an average intensity of 80 $cm.s^{-1}$ in its nucleus, lying at a depth of approximately 200 m (Schott and Böning, 1991; Silveira et al., 1994; Schott et al., 1995, 2002). More recent modeling and observational results show the NBC core with maximum values higher than 1 $m.s^{-1}$ (Stramma et al., 2005; Krelling et al., 2020).

The existence of this structure can be explained because Ekman transport in the western tropical region opposes geostrophic flow, resulting in a typical upwelling situation. Schott et al. (1998) estimated the annual cycle of NBC

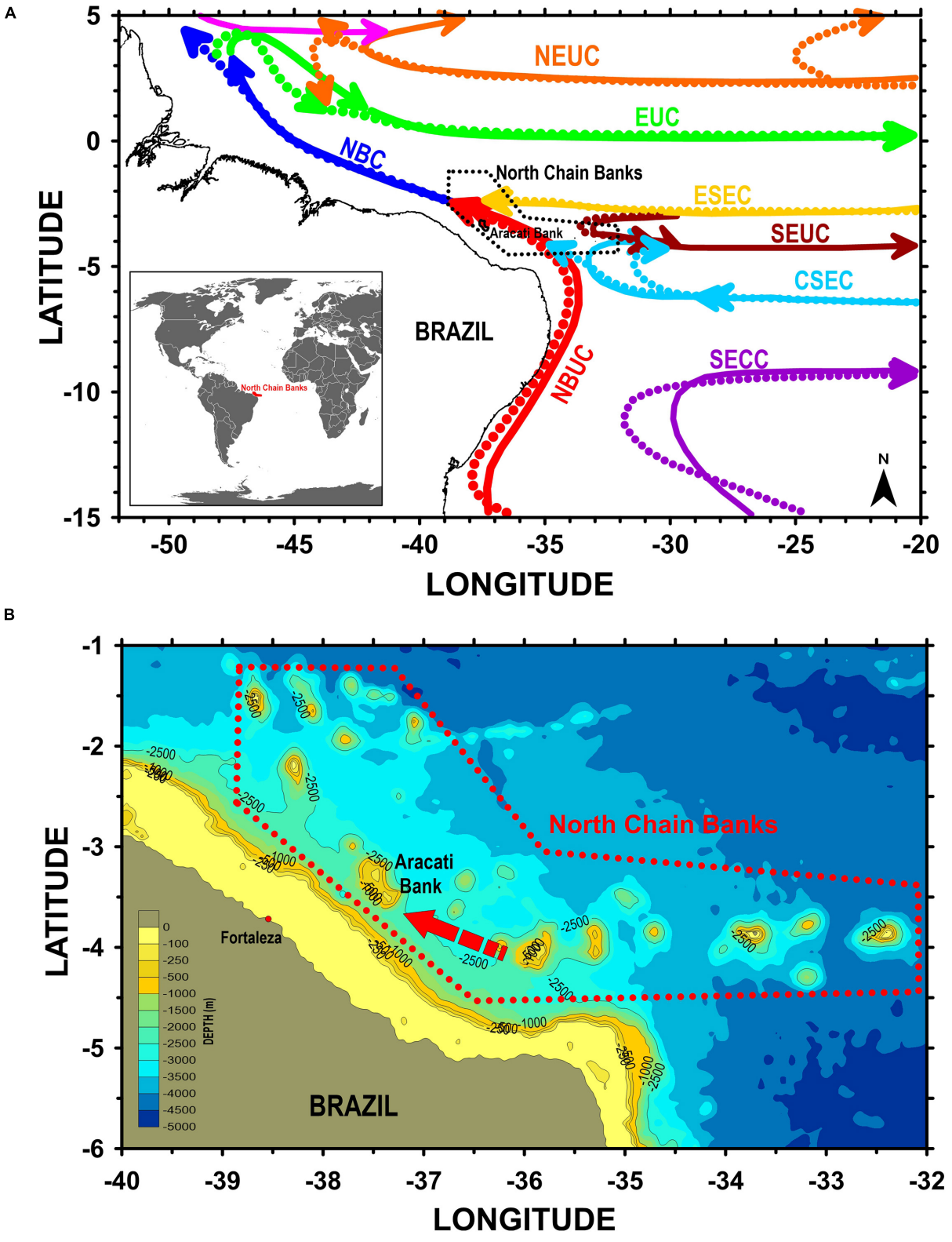

FIGURE 1 | Study area **(A)** general location view of the North Chain Banks and major currents at the top 100 m (solid lines) and at 100- to 500-m layers (dashed lines), both compiled from Stramma and England (1999). **(B)** Detailed view of the North Chain Banks with bathymetric contours and direction of prevailing winds (dashed arrow). NEUC, North Equatorial Undercurrent; NBC, North Brazil Current; EUC, Equatorial Undercurrent; ESEC, Equatorial South Equatorial Current; SEUC, South Equatorial Undercurrent; CSEC, Central South Equatorial Current; NBUC, North Brazil Undercurrent; SECC, South Equatorial Countercurrent.

transport in the oceanic layer between 0- and 500-m depth at coordinates 44° W (0°–5° N) based on the monthly measurement averages from moorings. The NBC transport value was 27.5 Sv, and the transport speed was 0.54 $m.s^{-1}$ in summer and 0.75 $m.s^{-1}$ in winter.

In the NBCh area, the southeast trade wind predominates (**Figure 1B**), which is the main element of the anticyclonic circulation of the South Atlantic Ocean. These winds can be observed between 35° S up to the equator during the summer (February) and between 30° S up to 10° N during winter (August); these winds are dominant throughout the year in the NBCh area.

The Aracati Bank is the larger bank in the NBCh. This bank is 56 km long and 33 km wide and is located in the area where the North Brazilian Current is strongest, exhibiting velocities of 30–50 $cm.s^{-1}$ during the summer and up to 1 $m.s^{-1}$ in August (Richardson and McKee, 1984).

METHODS AND SIMULATIONS

The research method involved the analysis of meteorological and physical oceanographic data gathered under the REVIZEE-NE Program around the Aracati oceanic bank and the performance of simulations with the 3D Princeton Ocean Model (POM).

Dataset

This study was performed using a subset of data gathered under the Project REVIZEE (Living Resources in the Exclusive Economic Zone). This project was a major national sampling joint effort by the Brazilian oceanographic community and Navy, performed between 1995 and 2000. Expeditions were carried out onboard NOc Antares of the Directorate of Hydrography and Navigation (DHN) of the Brazilian Navy to guarantee country sovereignty over a 200-nautical-mile band as an Exclusive Economic Zone. The efforts along the NE-Brazilian coast section comprised four oceanographic expeditions (REVIZEE NE-I, NE-II, NE-III, and NE-IV) corresponding to austral winter, summer, autumn, and spring seasons, respectively. Although a number of years have passed, this dataset remains the most complete and robust dataset available for the study area.

More recent data for the NBCh Bank area also used here correspond to conductivity, temperature, depth (CTD) profiles gathered around the eastern NBCh Banks during the ABRAÇOS II Program and at the Aracati Bank during the CAMADAS FINAS Program in 2017 and 2012, respectively.

The cruise periods, seasons, and number of CTD casts of those expeditions are summarized in **Table 1**, and the locations of the oceanographic sample stations, organized according to season, are shown in **Figures 2A–F**.

We used the data for the sampling stations corresponding to longitudinal and latitudinal transects over the Aracati Bank to investigate the effects caused by the NBC as it encounters this oceanic bank (**Figures 2A–D**).

At each station, wind direction and intensity were recorded using an anemometer, and the wave height and period readings were visually estimated from synoptic satellite data.

TABLE 1 | REVIZEE-NE expeditions organized according to the seasons of the year.

Expedition	Austral season	Record period	NB. CTD profiles
REVIZEE NE-I	Winter	July–September 1995	6
REVIZEE NE-II	Summer	January–March 1997	5
REVIZEE NE-III	Autumn	April–June 1998	5
REVIZEE NE_IV	Spring	October–December 2000	6
ABRAÇOS II	Autumn	April–May 2017	5
CAMADAS FINAS III	Spring	November 2012	1

The thermodynamic dataset for this work comprised CTD continuous profiles taken with a Sea Bird Electronics SBE 911*plus* CTD with conductivity (resolution = 0.00004 $S.m^{-1}$), temperature (resolution = 0.0003°C), and pressure (resolution = 0.068 m) sensors and a centrifugal pump. CTD operated connected to an SBE *11plus* deck unit, allowing real-time control of the data. We use a fall rate of 1 $m.s^{-1}$ and a sampling rate of 24 Hz. The maximum sampling depth around the Aracati Bank area was 800 m, which was 90% of the local depth, where areas were shallower than 800 m.

Conductivity, temperature, depth archives were transferred to a microcomputer and filtered, reduced, and edited (e.g., removing data out of water and faulty data) in preparation for analysis. Only the readings obtained during the descent of the CTD were considered. The recorded values were integrated at 5-m intervals with the first break, referred to as the surface. The calculations of the physical properties were performed in accordance with TEOS-10 (IOC et al., 2010).

T-S diagrams were then derived for the selected CTD data profiles to allow the identification of water masses present in the area, following the criteria of Barnier et al. (2001), who studied the water masses in the NBC retroflection region as described in **Table 2**.

Water Masses and Thermohaline Structure

The stability of the upper surface layer is an important factor that may inhibit (or facilitate) the enrichment of superficial waters. An interesting situation occurs when there are differences between the halocline and thermocline depth. If the isohaline layer is shallower than the isothermal layer, one may observe the formation of a barrier layer (BL). The barrier layer, that is, the layer between the halocline and thermocline (Lukas and Lindstrom, 1991), may isolate the upper isohaline layer from cold nutrient-rich thermocline waters, which also affects the ocean heat budget and ocean exchanges with the atmosphere (Pailler et al., 1999; Swenson and Hansen, 1999).

Most criteria that are used for determining isothermal and mixed layers in the ocean require the deviation of the temperature T (or density, σ_t) from its surface value to be smaller than a certain fixed value (Sprintall and Tomczak, 1990; Brainerd and Gregg, 1995). Normally assumed deviation from surface values for evaluating Z_T varies from 0.5°C (Wyrtki, 1964;

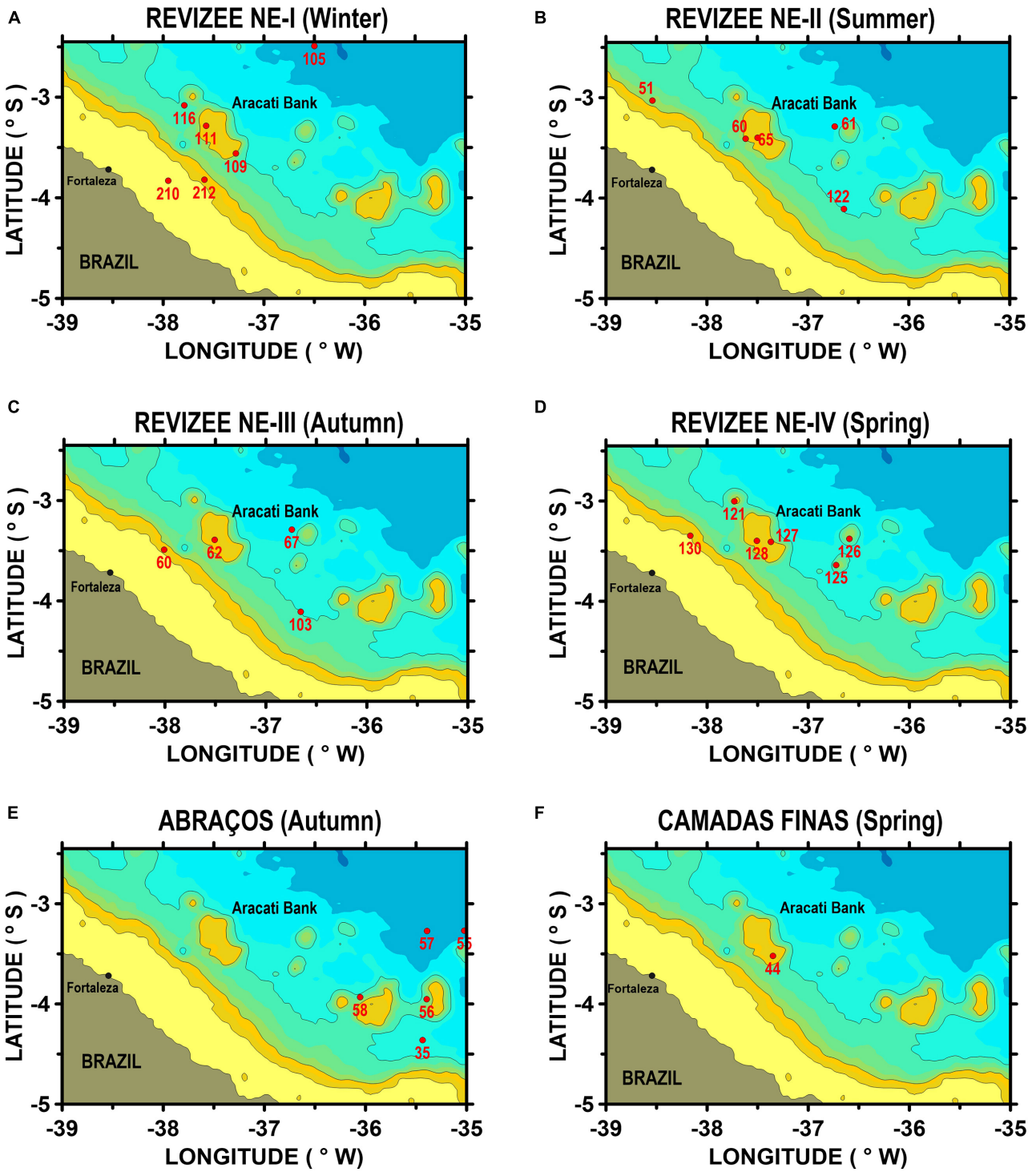

FIGURE 2 | Study area with sampling station locations in the North Brazilian Chain (NBCh) during cruises **(A)** REVIZEE NE-I, winter; **(B)** REVIZEE NE-II, summer; **(C)** REVIZEE NE-III, autumn; **(D)** REVIZEE NE-IV, spring; **(E)** ABRAÇOS II, autumn; and **(F)** CAMADAS FINAS III, spring.

Monterrey and Levitus, 1997) to 0.8°C (Kara et al., 2000). Z_M is estimated as the depth where density is equal to the sea surface value plus an increment $\Delta\sigma_t$ equivalent to a desired net decrease in temperature. Miller (1976) and Spall (1991), e.g., use $\Delta\sigma_t = 0.125\,\sigma_t\,(0)$ for determining the mixed layer depth, while Sprintall and Tomczak (1992) and Ohlmann et al. (1996) adopt $\Delta\sigma_t = 0.5^oC\ (\partial\sigma_t/\partial T)$, where $\partial\sigma_t/\partial T$ is the coefficient of thermal expansion.

TABLE 2 | Density range and depth limits of the water mass in the region of the Aracati Bank (Barnier et al., 2001).

Density range	Water masses	Depth range at 30° W
$\sigma_\theta < 24.500$	Tropical Water	0–75 m
$24.500 < \sigma_\theta < 27.125$	South Atlantic Central Water	75–450 m
$27.125 < \sigma_\theta < 27.450$	Intermediate Antarctica Water	450–1,000 m
$27.450 < \sigma_\theta$	Deep Atlantic Water	Below 1,000 m

Following Sprintall and Tomczak (1992), we evaluate isothermal and mixed layer depths (Z_T and Z_M) in terms of temperature and density steps (ΔT and $\Delta\sigma_t$) from the sea surface temperature and density [$T(0)$ and $\sigma_t(0)$]:

$$Z_T = z\left(T = T(0) - \Delta T\right) \tag{1}$$

$$Z_M = z\left(\sigma_t = \sigma_t(0) + \frac{\partial \sigma_t}{\partial T}\Delta T\right) \tag{2}$$

where $\partial\sigma_t/\partial T$ is calculated as a function of the surface temperature and salinity (Blank, 1999). The SBE 911*plus* CTD has two thermometers, whose accuracy is approximately 0.001°C. Thus, for a $\Delta T = 0.5^oC$, the error in computing Z_T is approximately 0.2% of local Z_T. The barrier layer thickness (BLT) may be easily calculated as:

$$BLT = Z_M - Z_T \tag{3}$$

When density stratification is exclusively controlled by temperature, the isothermal layer depth becomes equivalent to the mixed layer depth and $BLT = 0$. A particular situation occurs when the near-surface distribution of salinity is sufficiently strong to induce a pycnocline inside of the isothermal layer, or $|Z_M| < |Z_T|$. In this case, $BLT > 0$ and surface warm waters may be maintained isolated from cool thermocline waters.

Surface Energy Forcings

The upper mixed layer in the open ocean is characterized by an almost homogeneous configuration, showing reduced variations in temperature, salinity, and density profiles. This homogeneity is a result of several processes, including mixing induced by surface turbulent kinetic energy (TKE) production, such as wind- and current-driven shear and gravity wave breaking. Wind and waves in the Aracati Bank region are approximately 50% stronger during austral autumn–winter (March–August) periods than during spring–summer periods (September–February) (Geber, 2001). These distinct seasonal forcings may be evaluated by calculating the surface TKE input produced by wind shear and gravity wave breaking.

Surface TKE production by wind shear may be estimated from the analogy to the near-wall logarithmic region derived from the boundary layer theory (Klebanoff, 1955; Schilchting, 1979), where an overall balance between the production and dissipation of TKE is observed. This behavior is translated in the following form:

$$E_W = \frac{u_*^2}{\sqrt{C\mu}} \tag{4}$$

where E_W is the wind-driven TKE ($m^2.s^{-2}$), $C\mu$ is the diffusivity coefficient ($C\mu \cong 0.09$, e.g., Rodi, 1972), and u_* is the water friction velocity, which can be estimated from classical drag coefficient formulations (Pond and Pickard, 1983, among others).

Zero-order surface wave parameters can be estimated from semiempirical formulations proposed by Stewart (1967) and Leibovich and Radhakrishnan (1977) as follows:

$$a \approx 0.1\,\frac{W^2}{g}; \quad T \approx 2\pi\,\frac{W}{g}; \quad k \approx \frac{g}{W^2} \tag{5}$$

where a is the wave amplitude (m), T is the wave period (s), k is the wave number (m^{-1}), g is the gravity acceleration ($g \cong 9.81\ m.s^{-2}$), and W is the wind speed ($m.s^{-1}$). These formulations are supposed to improve wave data by providing the characteristics of surface equivalent monochromatic waves as a function of measured wind speed. The results obtained from these expressions showed good agreement with field human observations and satellite synoptic wave data (Rocha, 2000).

Other than wind shear energy, theoretical and experimental works (*in situ* and laboratory measurements) have shown that an important portion of TKE production at the air–water interface is associated with the presence of surface gravity waves (Gargett, 1989). This extra TKE source originates from the "wave break" phenomenon (Kitaïgorodskii et al., 1983) or is even caused by possible effects of rotational behavior in orbital movement (Cheung, 1985; Cavaleri and Zecchetto, 1987). This extra source of TKE can be evaluated from the equation proposed by Araujo et al. (2001). This formulation was obtained by using a fitting method of the field (Kitaïgorodskii et al., 1983; Drennan et al., 1992) and laboratory measurements (Cheung and Street, 1988; Thais and Magnaudet, 1996) involving the estimation of TKE intensities beneath wind waves, in the following form:

$$\mathrm{Ewa} = 0.12\ (\sigma\,\mathrm{a})^2 \tag{6}$$

where *Ewa* is the wave-driven TKE ($m^2.s^{-2}$) and σ is the intrinsic wave frequency (s^{-1}). Eqs. (4, 6) give the total TKE produced at the ocean surface (E_T), or $E_T = E_W + \mathrm{Ewa}$.

Numerical Simulation

The ocean model used was the POM. It is a three-dimensional ocean model developed by Blumberg and Mellor (1987). A modified version of the POM (Mellor, 1998) is employed to solve the primitive equations within a closed domain. This model uses curvilinear orthogonal horizontal coordinates, a horizontal numerical staggered "C" grid (Arakawa and Lamb, 1977), and employs a terrain-following σ-coordinate system in the vertical direction, making it well suited for the resolution of the bottom boundary layer.

Meshgrid Definition and Simulated Scenarios

The numerical study area includes a rectangular domain with four open boundaries with the Aracati Bank near the southeastern boundary. The bottom topography was defined

using a nautical chart # 700 (Diretoria de Hidrografia e Navegação [DHN], 1974). The horizontal model grid includes 41 × 61 grid cells with a constant grid size of $\Delta x = \Delta y = 2$ km, and the maximum depth is H_{max} = 3,000 m.

The vertical grid includes 21 σ-layers exponentially distributed at the surface and bottom to obtain better results in the vertical layer due to the formation of important pressure gradients around and over the bank (Tchamabi et al., 2017).

All experimental data and the temperature and salinity profiles were associated with the bank shape from REVIZEE-NE cruises and used in the simulation conditions. Two seasons were considered for simulation: the austral winter season (March–August) and the austral summer season (September–February).

In a preliminary analysis of the thermodynamic properties in the study area, the simulation was enabled to verify that the information relative to the rainy season (austral autumn and winter) could be grouped into a single scenario, denoted as winter. In the same way, it was possible to group the data of the austral spring and summer periods for the numerical representation of the dry scenario, denoted as summer.

Boundary Conditions

The boundary conditions used were capable of representing the two chosen seasons. At NE and SW boundaries, symmetry conditions of *von Neumann* were applied. The SE boundary was laterally forced by the North Brazilian Current radiation combined with sponge layer conditions, and on the surface, the model was forced with averages of wind and heat for the grid area for both seasons from the Copernicus: Global Ocean Physics Reanalysis System Product (GLOBAL-REANALYSIS-PHY-001-030). A summary of the boundary conditions is given in **Table 3**.

RESULTS AND DISCUSSION

Water Masses and Thermohaline Structure

The analysis and treatment of *in situ* data allowed the identification of two main water masses in the Aracati Bank area (**Table 4**).

Figures 3A–F presents the T/S diagram obtained from the field CTD profiles. The red ellipses in **Figures 3A,C** indicate major dispersion of the thermodynamic data near the interface between the Tropical Water and the South Atlantic Central Water masses (TW–SACW). These dispersed cloud points correspond to oceanographic data obtained from the sample stations located in the upstream region of the Aracati Bank (Geber, 2001), suggesting that it may be associated with the "deformations" in the TW–SACW interface.

Eqs. (1–3) are used in this work to evaluate the seasonal variability of the isothermal (Z_T), mixed (Z_M), and BLTs in the study area. **Figure 4** presents the seasonally averaged values calculated from the CTD profiles. The results indicate higher values of Z_T, Z_M, and BLT during autumn and winter and the presence of considerably shallower layers during summer and (mainly) austral spring. The mixed layer (Z_M) depth, for example, ranged from 6 m (spring) to 84 m (winter). Following the same tendency, the isothermal layer (Z_T) was limited to 8 m during spring and reached a most important value of 96 m during winter. The resulting BLT values indicated the presence of significant BL during autumn (20 m thick), contributing to isolating surface warmer waters from deeper and colder nutrient-rich waters. Otherwise, negligible values of BLT are found during summer and (mainly) spring seasons. These periods of the year are characterized by the action of less intense winds and lower precipitation rates, while stronger surface forcings (wind and waves) observed during autumn and winter contribute to sinking the isothermal and mixed layers in the Aracati Bank area.

Surface Energy Forcings

The TKE induced by wind shear and wave breaking processes in the Aracati Bank region are calculated from Eqs. (4) to (6), respectively. These expressions result in wind-induced E_W values ranging between 3.5×10^{-4} m^2.s^{-2} (summer) and 2.3×10^{-3} m^2.s^{-2} (winter) and wave-induced E_{WA} values ranging from 4.6×10^{-2} m^2.s^{-2} (summer) to 2.1×10^{-1} m^2.s^{-2} (winter). This yields $\frac{E_W}{E_{WA}} = o(1)$, which is in agreement with field (Kitaïgorodskii et al., 1983; Drennan et al., 1992) and laboratory (Cheung and Street, 1988; Thais and Magnaudet, 1996) measurements obtained beneath energetically wavy surfaces. This result suggests that gravity waves are the prime candidate for driving the erosion/deepening of seasonal pycnoclines in the study area.

If one chooses wind shear energy (E_W) and wave number (k) as normalization scales, it is possible to establish a linear ratio between the total TKE ($E_T = E_W + EWA$) and its capacity for mixing the upper surface layers (Z_M). This relationship is

TABLE 3 | Boundary conditions considered in simulations according to the seasons of the year.

	Simulation scenario	
Geophysical forcing	**Summer**	**Winter**
Average North Brazilian Current (m.s^{-1})	0.54	0.75
Average wind stress (Pa)	2.3×10^{-4}	3.3×10^{-4}
Average heat flux (K.m.s^{-1})	2.4×10^{-6}	9.6×10^{-7}

TABLE 4 | Characteristics of the water masses identified in the Aracati Bank area.

Water masses	**Literature data (Barnier et al., 2001) – 40° W**	**Aracati Bank area – 38° W**
TW Tropical Water	Temperature and salinity are greater than 18°C and 36 psu, respectively, extending from the surface to approximately 80 m.	From surface down to approximately 90-m depth.
SACW South Atlantic Central Water	Temperature range between 5 and 18°C, and salinity range between 34 and 36 psu, limited to approximately 450-m depth.	From lowest TW boundary to approximately 650-m depth.

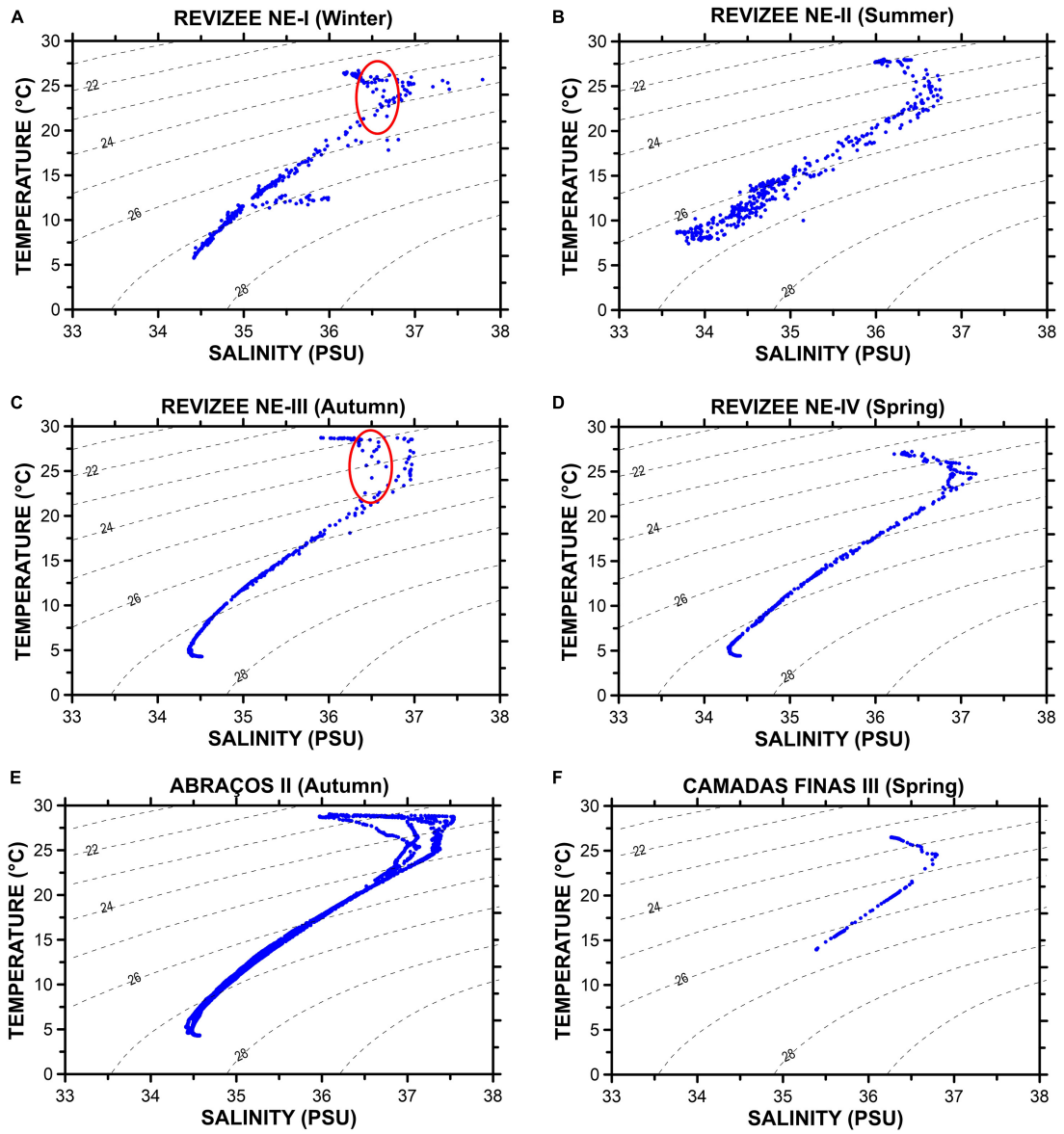

FIGURE 3 | Seasonal variability in T/S diagrams in the Aracati Bank area during cruises **(A)** REVIZEE NE-I, winter; **(B)** REVIZEE NE-II, summer; **(C)** REVIZEENE-III, autumn; **(D)** REVIZEE NE-IV, spring; **(E)** ABRAÇOS II, autumn; and **(F)** CAMADAS FINAS III, spring. Blue dots are T and S field CTD data for upstream region of the Aracati Bank (Geber, 2001). The red ellipses indicate the dispersion of the termodynamical characteristics of the waters near the interface between the Tropical Water and the South Atlantic Central Water masses (TW-SACW).

represented in **Figure 5**. It was determined using the least-squares curve fitting method for wind speeds between 6.2 and 13.4 m.s^{-1} (87% of overall field data) as follows:

$$k\,Z_M = -0.09084\,\frac{E_T}{E_W} + 2.093 \qquad \text{or}$$
$$\hat{Z}_M = -0.09084\,\hat{E}_T + 2.093 \qquad (7)$$

where *small hats* represent non-dimensional variables.

A simple scale analysis involving energy and wind/wave parameters may also be performed to show that the mixing layer depth is proportional to the wave height in the following form:

$$\mathrm{E_T} = \mathrm{E_W} + \mathrm{Ewa} \equiv \mathrm{Ewa} = \mathrm{O}\left(\sigma^2\,\mathrm{a}^2\right) \qquad (8)$$

$$\mathrm{k\,Z_M} = \mathrm{O}\left(\frac{\sigma^2\,\mathrm{a}^2}{\mathrm{u}_*^2}\right) \quad \therefore \quad \mathrm{Z_M} = \mathrm{O\,(a)} = \mathrm{O}\left(\mathrm{W}^2\right) \qquad (9)$$

Expression (9) also states that the upper mixed layer depth is proportional to the square of the wind speed. Wind speeds registered during autumn–winter in the Aracati Bank region are approximately 50% higher than the measured values for

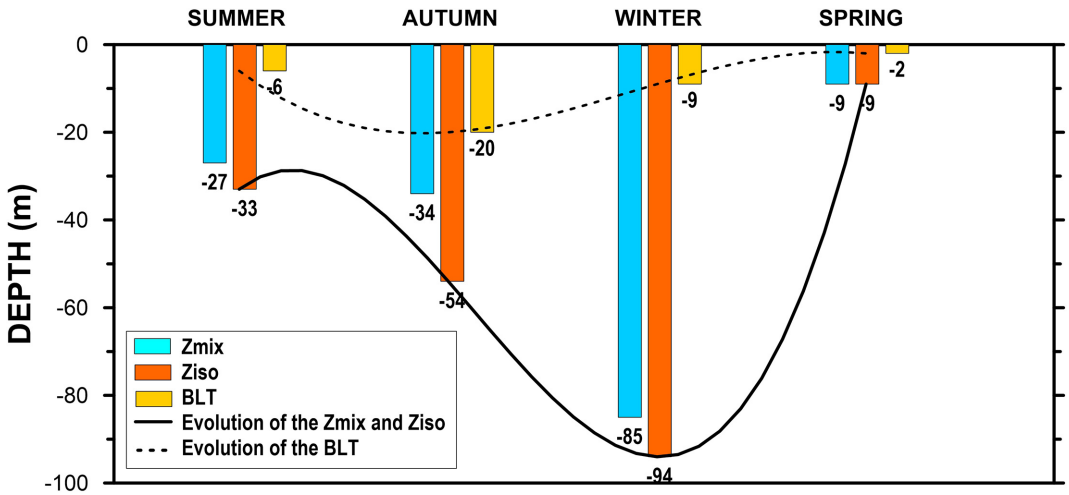

FIGURE 4 | Seasonal variation of the average isothermal, mixed, and barrier layer thickness in the Aracati Bank area.

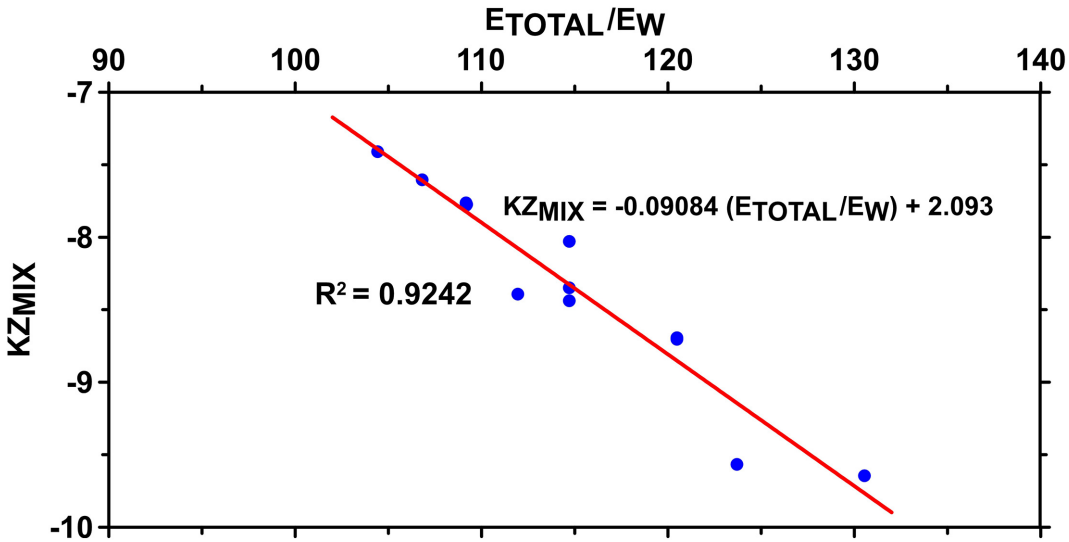

FIGURE 5 | Values of surface energy and mixing layer depth in the Aracati Bank area (blue dots) and adjusted linear regression (red line). Linear ratio between the total TKE (ET = EW + EWA) and its capacity for mixing the upper surface layers (ZM).

spring–summer periods (Geber, 2001). These differences may then explain the seasonal evolution of mixed layer depths previously stressed from field data (**Figure 4**).

Model "Spin-Up" and Comparison With T/S Field Data

During the adjustment process in POM, the time step for numerical stability in the winter for the 15th day was an average global energy of 9.7×10^3 J, and in the summer simulation, the energy stabilized for the 10th day with an average of 7.8×10^3 J. The energy in the summer was lower, as well as the time step needed for model "spin-up." For both winter and summer scenarios, only numerical results corresponding to the numerical time 21st day were considered, despite the fact that the model stability was being achieved before this delay.

The numerical T/S profiles were systematically compared with experimental data. **Figure 6** gives some typical examples of the parallel between temperature and salinity profiles issued from numerical simulations and T/S distributions obtained from a field CTD device. The comparison of T/S profiles shows that the model is able to generate profiles correctly, even the maximum salinity at the surface that was observed in the field. This result also suggests that the model supplies good descriptions of the thermohaline structure observed from field measurements.

Horizontal Cinematic Structure

To analyze the horizontal circulation in the area of Aracati Bank, horizontal velocity fields were traced at depths of 50, 100, 250, 500, and 1,000 m. **Figures 7A–J** show the numerical velocity fields generated by the model for the winter and summer seasons.

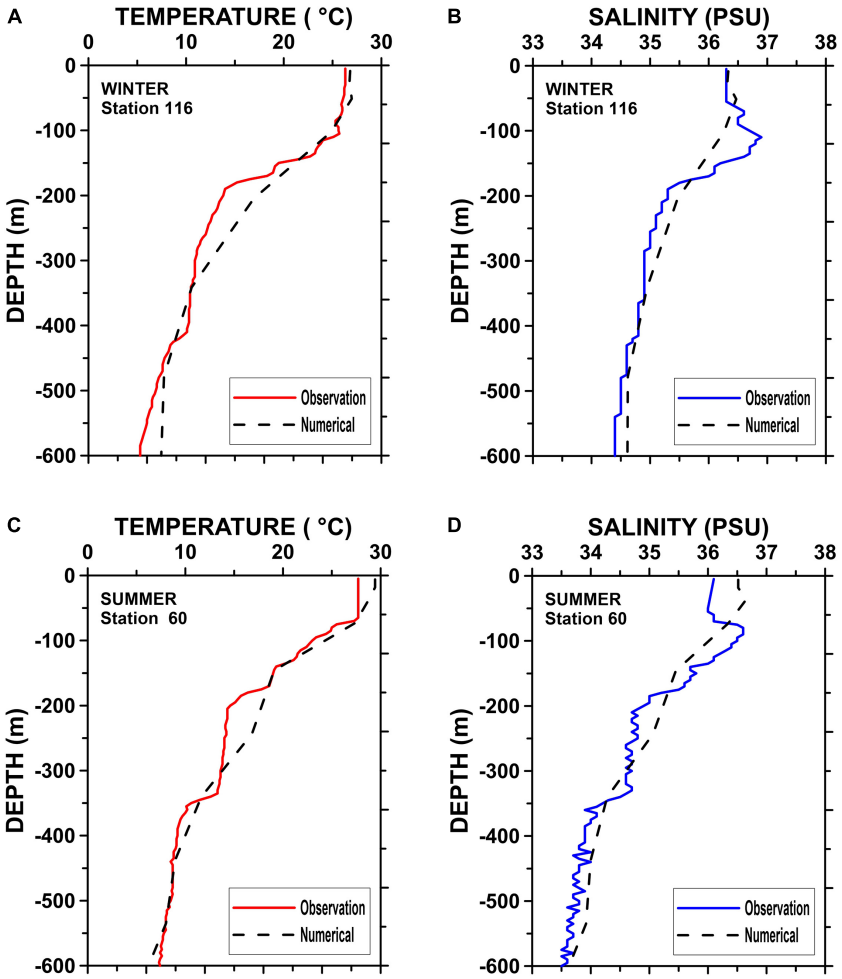

FIGURE 6 | Comparison between experimental data and numerical simulation results for temperature and salinity profiles in the winter **(A,B)** and summer **(C,D)** seasons.

Figures 7A–J show that the velocity vectors turn around the bank, producing eddies in the bank vicinity, especially in the upstream area, where the horizontal velocity gradients between the bank and the frontal slope are stronger.

However, in the summer season (**Figures 7F–J**), changes in current vector directions in the upstream bank area are less pronounced relative to winter simulations (**Figures 7A–E**).

Eddies made by horizontal velocities could "arrest" nutrients, plankton, and larvae that are important for increasing marine productivity. To analyze the Aracati Bank potential in producing eddies in its vicinity, the vertical component of the vorticity in the bank area was calculated as follows:

$$\vec{\Omega} = \frac{\partial \vec{V}}{\partial x} - \frac{\partial \vec{U}}{\partial y} \tag{10}$$

where $\vec{\Omega}$ is the relative vertical vorticity (s^{-1}).

Figures 8A–J present the vertical vorticity field calculated from the horizontal velocity vectors $\vec{U}$ and $\vec{V}$. The negative results indicate clockwise vorticity, while positive results indicate counterclockwise vorticity. **Figures 8A–E** show that the Aracati Bank has higher potential to generate positive vorticity at depths of 50, 100, and 250 m than deeper depths. **Figures 8A,B,F,G** show positive vorticity values for the winter and summer seasons, indicating the potential to reduce isothermal and mixed layer depths over the bank. A comparison between the velocity fields for both the winter and summer seasons indicates that the rotational field is very similar at depths shallower than 250 m. However, at a depth of 500 m, the negative vorticity found during the winter season (**Figure 8D**) was not generated with the same intensity during the summer season (**Figure 8I**).

Vertical Temperature and Velocity Structure

Figure 9 presents the temperature and vertical velocity (w) profiles obtained from simulations for both winter (**Figure 9A**) and summer (**Figure 9B**) seasons across the Aracati Bank section along the NBC. In these panels, the NBC crosses the bank from right to left.

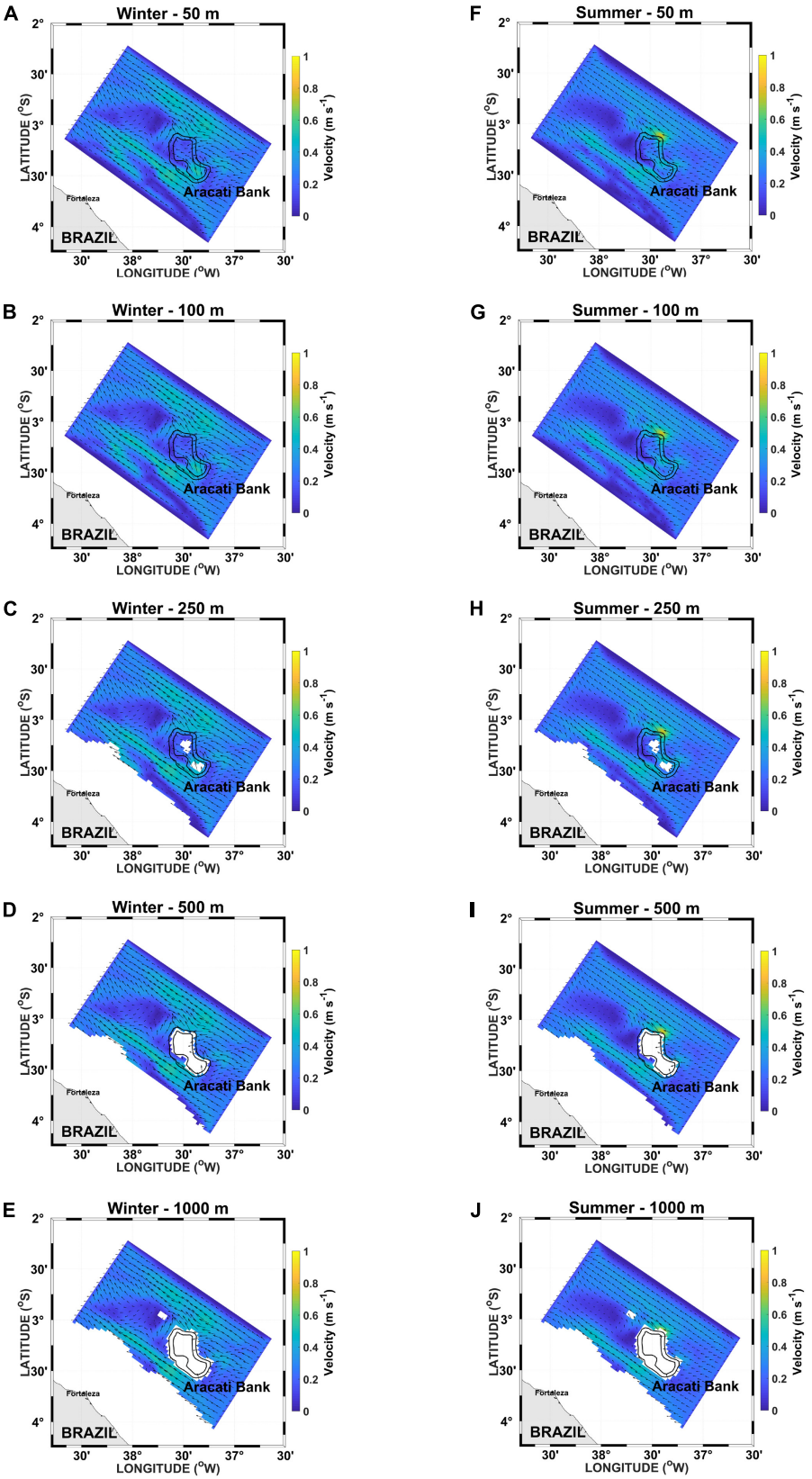

FIGURE 7 | Horizontal velocity (m.s^{-1}) fields in the Aracati Bank area at depths of 50, 100, 250, 500, and 1,000 m during winter **(A–E)** and summer **(F–J)** seasons.

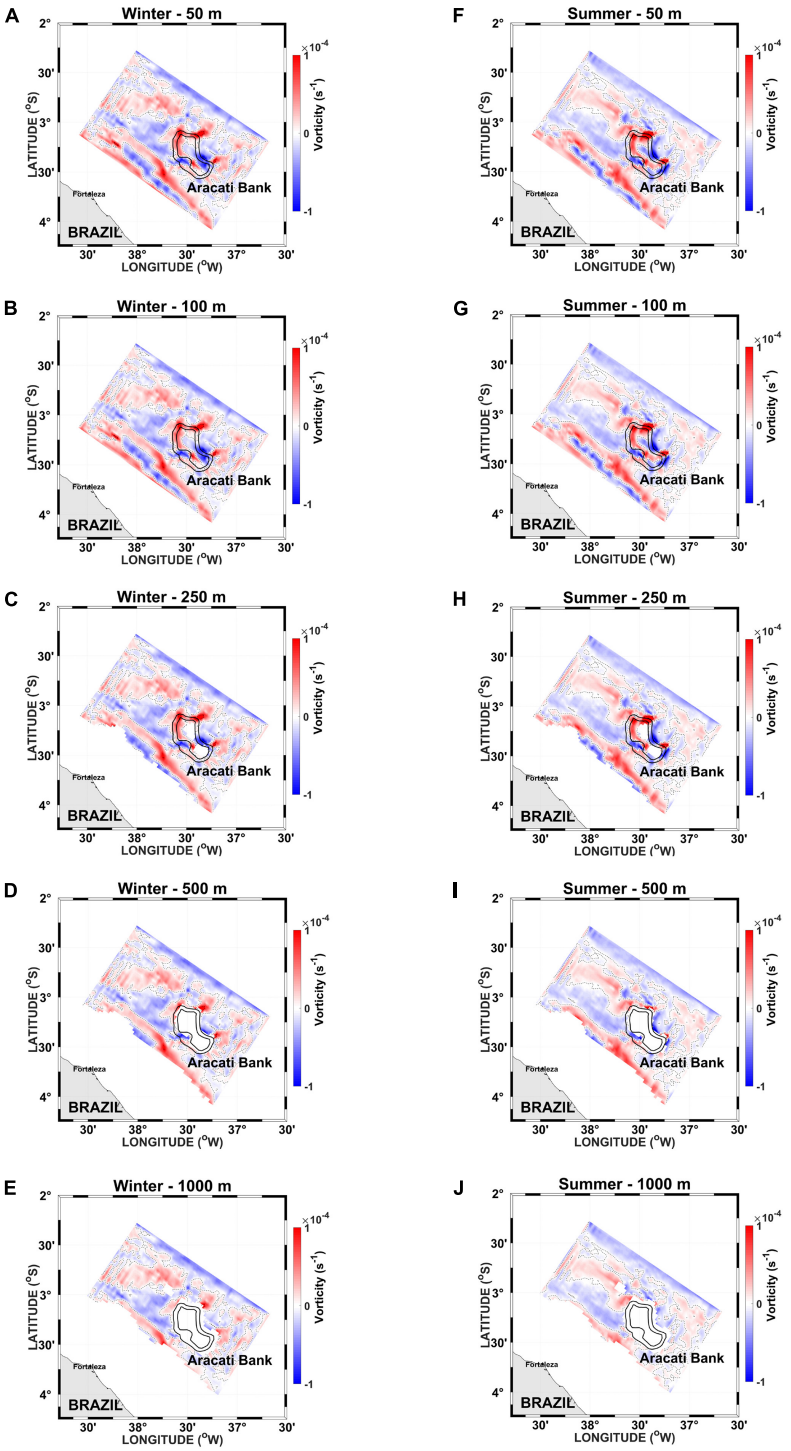

FIGURE 8 | Vertical vorticity (s^{-1}) in the Aracati Bank area at depths of 50, 100, 250, 500, and 1,000 m during winter **(A–E)** and summer **(F–J)** seasons.

As a result of the flow-topography interaction, upstream isotherm perturbation and upwelling and downstream leeward and eddy generation were verified during both seasons.

The highest intensities in vertical velocity (**Figures 9A,B**) are located in the upstream bank region and tend to decrease toward the surface. The minor vertical velocity during the winter was 0.003×10^{-3} m.s^{-1} near the surface, and the major value was 8.4×10^{-3} m.s^{-1} at a 370 depth, with an average velocity of 2.2×10^{-3} m.s^{-1}.

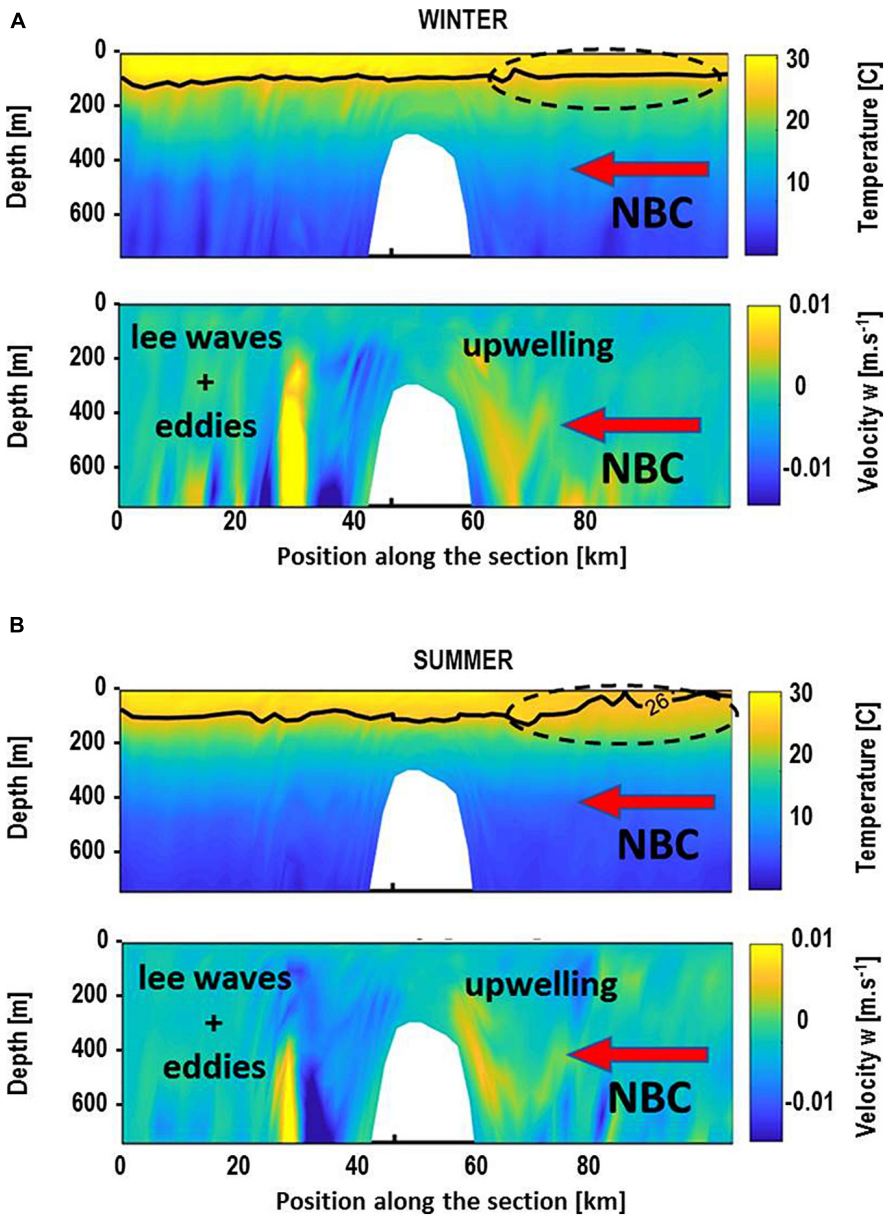

FIGURE 9 | Temperature and w vertical velocity along a section crossing the Aracati Bank area during winter **(A)** and summer **(B)** seasons. North Brazil Current (NBC) crosses the bank from the right to the left side.

In the summer situation, these values were 0.0004×10^{-3} m.s^{-1} (near the surface) and 7.8×10^{-3} m.s^{-1} at a 266-m depth, with an average of 2.6×10^{-3} m.s^{-1}. Despite being less intense, these shallower maximum vertical currents result in a more pronounced near-surface isothermal perturbation.

All values are in global agreement with different field/geophysical and theoretical studies found in the literature. For example, Chen and Beardsley (1995) performed a numerical study of stratified tidal rectification over symmetric banks and observed the presence of vorticity in the upstream bank region promoting upwelling to the surface along the bottom slope with a maximum vertical velocity of approximately 5.0×10^{-3} m.s^{-1} at 56-m depth and 1.8×10^{-3} m.s^{-1} at 83-m depth during a more energetic winter situation; while in the summer season, the vertical velocity was 1.0×10^{-3} m.s^{-1} at 120-m depth. Franks and Cheng (1996) studied the influence of physical forcing over plankton production on Georges Bank during the summer. These authors found vertical velocities of approximately 0.1×10^{-3} m.s^{-1}, concluding that the phytoplankton in the well-mixed waters of the Georges Bank are nutrient replete, with an excess of nutrients supplied by physical processes. In another numerical study of stratified tidal rectification over the same bank, Cheng et al. (1995) found that, in summertime, cross-bank circulations exhibit a strong asymmetry with respect to the two

sides of the bank. In this case, they observed that when the side of the bank was much steeper, the water became shallower, and the vertical mixing increased by approximately 0.1×10^{-3} m.s^{-1} at a depth of 120 m.

CONCLUSION

The temperature CTD profiles indicated the presence of a permanent thermocline throughout the year, located between 70- and 150-m depth. The pattern of isohaline distribution followed that of isotherm variation. At times, the formation of low-salinity eddies was verified on the Aracati Bank slope. The 3D model used was able to accurately reproduce the thermohaline structure in the Aracati Bank area. The kinematic structure observed in the performed simulations indicated vertical velocities of 10^{-3} m.s^{-1} in the upstream region of the bank during winter and summer seasons. During the austral summer, the most important vertical velocities were localized below the lower limit of the euphotic zone, while during the austral winter, these velocities were within the euphotic zone, favoring primary producers.

The data recorded for the Aracati Bank provided clear evidence that upwelling and consequent enrichment of the surface layer can result from a flow-topography interaction in this area, especially during the winter season. Similar uplift of isotherms was observed in October 1990 during fishing surveys near the Aracati, Guará, and Sírius seamounts (Hazin et al., 1990), reinforcing the notion that this process could occur in fairly regular basis and that they are linked in some way to the Aracati Bank topography and NBC interaction. The strong physical forcing by the NBC and southeast trade winds over the Aracati Bank contributes significantly to possible rises in thermodynamic parameters in the study region.

While the results presented here provide evidence to show that the interaction between Aracati Bank and the NBC promotes vertical mixing, the observations are limited to the relatively small spatial and temporal scales examined. Further research is still required to determine the influences of the thermodynamic parameters and analysis of complementary chemical and biological variables across different spatial and temporal scales.

DATA AVAILABILITY STATEMENT

The raw data supporting the conclusions of this article will be made available by the authors, without undue reservation.

AUTHOR CONTRIBUTIONS

All authors listed have made a substantial, direct and intellectual contribution to the work, and approved it for publication.

FUNDING

MA and CN acknowledge the support of the Brazilian Research Network on Global Climate Change-Rede CLIMA (FINEP grants 01.13.0353-00). This work is a contribution to the Projects INCT AmbTropic–Brazilian National Institute of Science and Technology for Tropical Marine Environments (grants 565054/2010-4, 625 8936/2011, and 465634/2014-1, CNPq/FAPESB/CAPES), International Joint Laboratory TAPIOCA (IRD-UFPE-UFRPE), and to the TRIATLAS project, which has received funding from the European Union's Horizon 2020 Research and Innovation Program under grant agreement no. 817578.

ACKNOWLEDGMENTS

We thank the scientific and crew members of the NOc Antares/Brazilian Navy for their efforts during the oceanographic expedition.

REFERENCES

Arakawa, A., and Lamb, V. R. (1977). Computational design of the basic processes of the UCLA general circulation model. *Methods Comput. Phys.* 17, 174–265.

Araujo, M., Dartus, D., Maurel, P. H., and Masbernat, L. (2001). Langmuir circulations and enhanced turbulence beneath wind-waves. *Ocean Modell.* 3, 109–126. doi: 10.1016/s1463-5003(01)00004-x

Araujo, M., Limongi, C. M., Servain, J., Silva, M. A., Leite, F. S., Veleda, D. R. A., et al. (2011). Salinity-induced mixed and barrier layers in the Southwestern tropical Atlantic Ocean off the Northeast of Brazil. *Ocean Sci.* 7, 63–73. doi: 10.5194/os-7-63-2011

Araujo, M., Noriega, C., Medeiros, C., Lefèvre, N., Ibánhez, J. S. P., Montes, M. F., et al. (2018). On the variability in the CO_2 system and water productivity in the western tropical Atlantic off North and Northeast Brazil. *J. Mar. Syst.* 1:1.

Assunção, R. V., Silva, A. C., Roy, A., Bourlès, B., Silva, C., Ternon, J.-F., et al. (2020). 3D characterisation of the thermohaline structure in the southwestern tropical Atlantic derived from functional data analysis of in situ profiles. *Prog. Oceanogr.* 187:102399. doi: 10.1016/j.pocean.2020.102399

Barnier, B., Reynaud, T., Beckmann, A., Böning, C., Molines, J. M., Barnard, S., et al. (2001). On the seasonal variability and eddies in the North Brazil Current: insights from model intercomparison experiments. *Prog. Oceanogr.* 48, 195–230. doi: 10.1016/s0079-6611(01)00005-2

Blank, H. F. (1999). *Using TOPEX Satellite El Niño Altimetry Data to Introduce Thermal Expansion and Heat Capacity Concepts in Chemistry Courses*. Department of Chemistry thesis, Clarksville: Austin Peay State University Clarksville.

Blumberg, A., and Mellor, G. L. A. (1987). "Description of a three-dimensional coastal ocean circulation model," in *Three-Dimensional Coastal Ocean Models*, ed. N. Heaps (Washington, DC: American Geophysical Union).

Boyer, D., Davies, P., Holland, W., Biolley, F., and Honji, H. (1987). Stratified rotating flow over and around isolated three-dimensional topography. *Phil. Trans. R. Soc. London A* 322:213. doi: 10.1098/rsta.1987.0049

Brainerd, K. E., and Gregg, M. C. (1995). Surface mixed and mixing layer depths. *Deep-Sea Res. I: Oceangr. Res. Papers* 42, 1521–1543. doi: 10.1016/0967-0637(95)00068-h

Cavaleri, O., and Zecchetto, S. (1987). Reynolds stress under wind waves. *J. Geophys. Res.* 92, 3894–3904. doi: 10.1029/jc092ic04p03894

Chaves, T. B. C., Mafalda, J. R. P., Santos, C., Souza, C. S., Moura, G., Sampaio, J., et al. (2006). Planktonic biomass and hydrography in the Exclusive Economic Zone of Brazilian Northeast. *Trop. Oceanogr. Online* 34, 12–30.

Chen, C., and Beardsley, R. C. (1995). A numerical study of stratified tidal rectification over finite-amplitude banks. Part I: Symmetric bank. *J. Phys. Oceanogr.* 25, 2090–2110.

Cheng, C., Beardsley, R. C., and Limeburner, R. A. (1995). Numerical study of stratified tidal rectification over finite – amplitude banks. *Part II: Georges Banks. J. Phys. Oceanogr.* 25, 2111–2128. doi: 10.1175/1520-0485(1995)025<2111:ansost>2.0.co;2

Cheung, T. K. (1985). *A study of the Turbulent Layer in the Water at an Air-Water Interface*. Technical Report 287, Department of Civil Engineering, Stanford University. Stanford, CA: 229.

Cheung, T. K., and Street, R. L. (1988). Wave-following measurements in the water beneath an air-water interface. *J. Geophys. Res.* 93, 14689–14993.

Clark, M. (1999). Fisheries for orange roughy (*Hoplostethus atlanticus*) on sea mounts in New Zealand. *Oceanol. Acta* 22, 596–602.

Coutinho, P. N. (1996). *Levantamento do Estado da Arte da Pesquisa dos Recursos Vivos Marinhos do Brasil–Oceanografia Geológica. Região Nordeste. Programa REVIZEE*. Brasília: Ministério do Meio Ambiente, dos Recursos Hídricos e da Amazonia Legal (MMA), 97.

Cushman-Roisin, B. (1994). *Introduction to Geophysical Fluid Dynamics*. Hoboken, NJ: Prentice Hall International, 320.

de Boyer Montégut, C., Madec, G., Fischer, A. S., Lazar, A., and Iudicone, D. (2004). Mixed layer depth over the global ocean: an examination of profile data and a profile-based climatology. *J. Geophys. Res. C Ocean* 109, 1–20.

Diretoria de Hidrografia e Navegação [DHN] (1974). *Carta Náutica No. 700. Brazil Costa Norte – De Fortaleza à Ponta dos Três Irmãos. Escala 1:316220, Diretoria de Hidrografia e Navegação – DHN, Marinha do Brasil*, 2a Edn, ed. R. J. Rio de Janeiro (Brasil: Diretoria de Hidrografia e Navegação [DHN]).

Drennan, K. L., Kahma, K. K., Terray, E. A., Donelan, M. A., and Kitaïgorodskii, S. A. (1992). "Observation of enhancement of kinetic energy dissipation beneath breaking wind waves," in *Breaking Waves*, eds M. L. Banner and R. H. J. Grimshaw (Berlin: Springer), 95–101. doi: 10.1007/978-3-642-84847-6_6

Eiff, O. S., and Bonneton, P. (2000). Lee-wave breaking over obstacles in stratified flow. *Phys. Fluids* 12:1073. doi: 10.1063/1.870362

Flagg, C. N. (1987). "Hydrographic structure and variability," in *Georges Banks*, ed. H. Backus (Cambridge, MA: The MIT Press), 108–124.

Fonteneau, A. (1991). Monts sous-marinset thons dansl'atlantique tropical est. *Aquatic Living Resour.* 4, 13–25. doi: 10.1051/alr:1991001

Franks, P. J. S., and Cheng, C. (1996). Plankton production in tidal fronts: a model of Georges Bank in summer. *J. Mar. Res.* 54, 631–651. doi: 10.1357/0022240963213718

Fréon, P., Barrange, M., and Aristegui, J. (2009). Eastern boundary upwelling ecosystems: integrative and comparative approaches. *Progr. Oceanogr.* 83, 1–14. doi: 10.1016/j.pocean.2009.08.001

Gargett, A. E. (1989). Ocean Turbulence. *Ann. Ver. Fluid Mech.* 21, 419–451.

Geber, F. O. (2001). *Dinâmica de Bancos Oceânicos da Cadeia Norte do Brasil: Caracterização Experimental e Simulação Numérica. dissertação (Mestrado) do Departamento de Oceanografia da Universidade Federal de Pernambuco, Brasil*. 98.

Hazin, F. H. V., Couto, A. A., Kihara, K., Otsuka, K., and Ishino, M. (1990). Distribution and abundance of pelagic sharks in the southwestern equatorial. *Atl. J. Tokio Univ. Fish.* 77, 51–64.

Hazin, F. H. V., Zagaglia, J. R., Broadhurst, M. K., Travassos, P. E. P., and Bezerra, T. R. Q. (1998). Review of a small-scale pelagic logline fishery off Northeastern Brazil. *Mar. Fisheries Rev.* 60, 1–8. doi: 10.1007/s12562-019-01360-w

Hormazábal, S., and Yuras, G. (2007). Mesoscale eddies and high chlorophyll concentrations off central Chile (29o S–39o S). *Geophys. Res. Lett.* 34:L12604.

Huppert, H. E., and Bryan, K. (1976). Topographically generated eddies. *Deep-Sea Res.* 23, 655–679. doi: 10.1016/s0011-7471(76)80013-7

IOC, SCOR, and IAPSO (2010). *The International Thermodynamic Equation of Seawater – 2010: Calculation and Use of Thermodynamic Properties*. Intergovernmental Oceanographic Commission, Manuals and Guides No. 56, UNESCO (English). Paris: UNESCO, 196.

Kara, A. B., Rochford, P. A., and Hurlburt, H. E. (2000). Mixed layer depth variability and barrier layer formation over the north Pacific Ocean. *J. Geophys. Res.* 105, 16783–16801. doi: 10.1029/2000jc900071

Kitaïgorodskii, S. A., Donelan, A. A., Lumley, J. L., and Terray, E. A. (1983). Wave-turbulence interaction in upper ocean. Part II. Statistical characteristics of wave and turbulent components of the random velocity field in the marine surface layer. *J. Phys. Oceanogr.* 13, 1988–1989. doi: 10.1175/1520-0485(1983)013<1988:wtiitu>2.0.co;2

Klebanoff, P. S. (1955). Characteristics of turbulence in a boundary layer flow with zero pressure gradient. *Natl. Acad. Sci. Rep. U.S.A.* 1247:19.

Krelling, A. P. M., Gangopadhyay, A., Silveira, I., and Vilela-Silva, F. (2020). Development of a feature-oriented regional modelling system for the North Brazil Undercurrent region (1°–11°S) and its application to a process study on the genesis of the Potiguar Eddy. *J. Operational Oceanogr.* 13, 1–13. doi: 10.1080/1755876X.2020.1743049

Lavelle, W. J., and Mohn, C. (2010). Motion, commotion, and biophysical connections at deep ocean seamounts. *Oceanography* 23, 90–103. doi: 10.5670/oceanog.2010.64

Leibovich, S., and Radhakrishnan, K. (1977). On the evolution of the system of wind drift currents and Langmuir circulations in the ocean. Part II: Structure of Langmuir vortices. *J. Fluid Mech.* 80, 481–507. doi: 10.1017/s0022112077001803

Leitner, A. B., Neuheimer, A. B., Jeffrey, C., and Drazen, J. C. (2020). Evidence for long-term seamount-induced chlorophyll enhancements. *Sci. Rep.* 10:12729.

Lessa, R. P., Mafalda, J. R. P., Advincula, R. B., Lucchesi, R. B., Bezerra, J. L. Jr., Vaske, T. Jr., et al. (1999). Distribution and abundance od icchthyoneuston at Seamounts and Island off nrth-eastern Brazil. *Arch. Fish. Mar. Res.* 47, 239–252.

Lukas, R., and Lindstrom, E. (1991). The mixed layer of the western equatorial pacific ocean. *J. Geophys. Res.* 96, 3343–3357. doi: 10.1029/90jc01951

Macedo, S. J., Montes, M. J. F., Lins, I. C., and Costa, K. M. P. (1998). *Programa de Avaliação do Potencial Sustentável dos Recursos Vivos da Zona Economica Exclusiva. SCORE/NE Relatório da Oceanografia Química*. Recife: UFPE.

Mellor, G. L. (1998). *A User's Guide for A Three – Dimensional, Numerical Ocean Model.* New Jersey, NJ: Princeton University Report. 41. Available at: http://www.researchgate.net/publication/242777179

Mendonça, A. P., Martins, A. M., Figueiredo, M. P., Bashmachnikov, I. L., Couto, A., Lafon, V. M., et al. (2010). Evaluation of ocean color and sea surface temperature sensors algorithms using in situ data: a case study of temporal and spatial variability on two northeast Atlantic seamounts. *J. Appl. Remote Sens.* 4:043506. doi: 10.1117/1.3328872

Miller, J. R. (1976). The salinity effect ion a mixed layer ocean model. *J. Phys. Oceanogr.* 6, 29–35. doi: 10.1175/1520-0485(1976)006<0029:tseiam>2.0.co;2

Monterrey, G., and Levitus, S. (1997). *Seasonal variability of mixed layer depth for the world ocean. NOAA Atlas NESDIS 14, U.S. Department of Commerce*. Washington, DC: U.S. Department of Commerce, 100.

Morato, T., Bulman, C., and Pitcher, T. J. (2009). Modelled effects of primary and secondary production enhancement by seamounts on local fish stocks. *Deep Sea Res. Part II* 56, 2713–2719. doi: 10.1016/j.dsr2.2008.12.029

Morato, T., Varkey, D. A., Damaso, C., Machete, M., Santos, M., Prieto, R., et al. (2008). Evidence of a seamount effect on aggregating visitors. *Mar. Ecol. Prog. Series* 357, 23–32. doi: 10.3354/meps07269

Mourino, B., Fernandez, E., Serret, P., Harbour, D., Sinha, B., Pingree, R., et al. (2001). Variability and seasonality of physical and biological fields at the Great Meteor Tablemount (subtropical NE Atlantic). *Oceanol. Acta* 24, 167–185. doi: 10.1016/s0399-1784(00)01138-5

Ohlmann, J. C., Siegel, D. A., and Gautier, C. (1996). Ocean mixed layer depth heating and solar penetration: a global analysis. *J. Clim.* 9, 2265–2280. doi: 10.1175/1520-0442(1996)009<2265:omlrha>2.0.co;2

Oliveira, A. P., Coutinhoa, T. P., Cabeçadasa, G., Brogueiraa, M. J., Cocab, J., Ramos, M., et al. (2016). Primary production enhancement in a shallow seamount (Gorringe—Northeast Atlantic). *J. Mar. Syst.* 164, 13–29. doi: 10.1016/j.jmarsys.2016.07.012

Pailler, K., Bourlès, B., and Gouriou, Y. (1999). The barrier layer in the western Atlantic Ocean. *Geophys. Res. Lett.* 26, 2069–2072. doi: 10.1029/1999gl900492

Peterson, R. G., and Stramma, L. (1991). Upper-level circulation in the South Atlantic Ocean. *Prog. Oceanogr.* 26, 1–73. doi: 10.1016/0079-6611(91)90006-8

Pitcher, T. J., Morato, T., Hart, P. J. B., Clark, M. R., Haggan, N., and Santos, R. S. (eds) (2008). *Seamounts: Ecology, Fisheries and Conservation. Fish and Aquatic Resources Series*. Hoboken, NJ: Blackwell Publishing, 24.

Pond, S., and Pickard, G. L. (1983). *Introductory Dynamic Oceanography*. Oxford: Pergamon Press, 329.

Richardson, S. G. H., and McKee, T. K. (1984). Average seasonal variation of the Atlantic equatorial currents from historical ship drifts. *J. Phys. Oceanogr.* 17, 1226–1238. doi: 10.1175/1520-0485(1984)014<1226:asvota>2.0.co;2

Richardson, S. G. H., and Walsh, D. (1986). Mapping climatological season variations of surface currents in the tropical Atlantic using ship drifts. *J. Geophys. Res.* 91, 10537–10550. doi: 10.1029/jc091ic09p10537

Rocha, R. A. (2000). *Elementos Micronutrientes na Camada Eufótica da Região Oceânica Entre Recife (PE) e Salvador (BA): Distribuição Espacial e Mecanismos Físicos Influentes na Fertilização Das Águas. Dissertação (Mestrado) do*. Brasil: do Departamento de Oceanografia da Universidade Federal de Pernambuco, 129.

Roden, G. I. (1991). "Effect of seamounts and seamounts chains on ocean circulation and thermohaline structure," in *Seamounts, Island and Atolls. Geophysical Monograph*, Vol. 43, eds B. H. Keating, P. Fryer, R. Batiza, and G. W. Boehlert (Washington, DC: American Geophysical Union), 335–354. doi: 10.1029/gm043p0335

Rodi, W. (1972). *The Prediction of Free Turbulent Boundary Layers by Use of a Two-Equation Model of Turbulence*. Ph.D. thesis. London: University of London, 310.

Rogers, A. D. (1994). "The biology of seamounts," in *Advances in Marine Biology*, ed. M. Lesser (London: Academic Press), 305–350. doi: 10.1016/s0065-2881(08)60065-6

Rossi, V., López, C., Hernández-García, E., Sudre, J., Garçon, V., Morel, Y., et al. (2009). Surface mixing and biological activity in the four Eastern boundary upwelling systems. *Nonlinear Process. Geophys.* 16, 557–568. doi: 10.5194/npg-16-557-2009

Rossi, V., Lopez, C., Sudre, J., Hernandez-Garcia, E., and Garçon, V. (2008). Comparative study of mixing and biological activity of the Benguela and Canary upwelling systems. *Geophys. Res. Lett.* 35:L11602.

Schilchting, H. (1979). *Boundary layer theory*. New York, NJ: McGraw-Hill B. C, 489.

Schott, F. A., and Böning, W. (1991). The WOCE model in the western equatorial Atlantic: upper-layer circulation. *J. Geophys. Res.* 96, 6993–7004. doi: 10.1029/90jc02683

Schott, F. A., Brandt, P., Hamann, M., Fischer, J., and Stramma, L. (2002). On the boundary flow off Brazil at 5-10o S and its connection to the interior tropical Atlantic. *Geophys. Res. Lett.* 29, 21–21. doi: 10.1029/2002gl014786

Schott, F. A., Fischer, J., and Stramma, L. (1998). Transports and pathsways of the upper-layer circulation in the western tropical Atlantic. *J. Phys. Oceanogr.* 28, 1904–1928. doi: 10.1175/1520-0485(1998)028<1904:tapotu>2.0.co;2

Schott, F. A., Stramma, L., and Fischer, J. (1995). The warm water inflow into the western tropical Atlantic boundary regime, spring 1994. *J. Geophys. Res.* 100, 24745–24760. doi: 10.1029/95jc02803

Silveira, I. C. A., Miranda, L. B., and Brown, W. S. (1994). On the origins of the North Brazil Current. *J. Geophys. Res.* 99, 22501–22512. doi: 10.1029/94jc01776

Spall, M. A. (1991). A diagnostic study of wind- and buoyancy- driven north Atlantic circulation. *J. Geophys. Res.* 96, 18509–18518. doi: 10.1029/91jc01957

Sprintall, J., and Tomczak, M. (1990). *Salinity Considerations in the Oceanic Surface Mixed Layer*. Ocean Sciences Institute Rep. 36. Sidney: University of Sidney, 170.

Sprintall, J., and Tomczak, M. (1992). Evidences of the barrier layer in the surface layer of the tropics. *J. Geophys. Res.* 97, 7305–7316. doi: 10.1029/92jc00407

Stewart, R. W. (1967). Mechanics of the air-sea interface. *Phys. Fluids Suppl.* 10, 47–55.

Stramma, L., and England, M. (1999). On the water masses and mean circulation of the South Atlantic Ocean. *J. Geophys. Res.* 104, 20863–20883. doi: 10.1029/1999jc900139

Stramma, L., Rhein, M., Brandt, P., Dengler, M., Böning, C., and Walter, M. (2005). Upper ocean circulation in the western tropical Atlantic in boreal fall 2000. *Deep Sea Res. Part I* 52, 221–240. doi: 10.1016/j.dsr.2004.07.021

Swenson, M. S., and Hansen, D. V. (1999). Tropical Pacific Ocean mixed layer heat budget: the Pacific cold tongue. *J. Phys. Oceanogr.* 29, 69–81. doi: 10.1175/1520-0485(1999)029<0069:tpomlh>2.0.co;2

Tchamabi, C. C., Araujo, M., Silva, M., and Bourlès, B. (2017). A study of the Brazilian Fernando de Noronha island and Rocas atoll wakes in the tropical Atlantic. *Ocean Modell.* 111, 9–18. doi: 10.1016/j.ocemod.2016.12.009

Thais, L., and Magnaudet, J. (1996). Turbulent structure beneath surface gravity waves sheared by the wind. *J. Fluid Mec.* 328, 313–344. doi: 10.1017/s0022112096008749

Travassos, P., Hazin, F. H. V., Zagaglia, J. R., Advincula, R., and Schober, J. (1999). Thermohaline structure around seamounts and islands off North-Brazil. *Arch. Fishery Mar. Res.* 47, 211–222.

Varela, J., Araújo, M., Bove, I., Cabeza, C., Usera, G., Martí, A. C., et al. (2007). Instabilities developed in stratified flows over pronounced obstacles. *Physica A : Stat. Mech. Appl.* 386, 681–685. doi: 10.1016/j.physa.2007.08.051

Watling, L., and Auster, P. J. (2017). Seamounts on the high seas should be managed as vulnerable marine ecosystems. *Front. Mar. Sci.* 4:14. doi: 10.3389/fmars.2017.00014

Wessel, P., Sandwell, D. T., and Kim, S.-S. (2010). The global seamount census. *Oceanography* 23, 24–33. doi: 10.5670/oceanog.2010.60

White, M., and Mohn, C. (2004). Seamounts: a review of physical processes and their influence on the seamount ecosystem. *OASIS Rep.* 38, 1–40. doi: 10.1002/9780470691953.ch1

Wyrtki, K. (1964). The thermal structure of the eastern Pacific Ocean. *Deutsche Hydrographische Zeitung Ergänzungsheft A* 6:84.

Yesson, C., Clark, M. R., Taylor, M. L., and Rogers, A. D. (2011). The global distribution of seamounts based on 30 arc seconds bathymetry data. *Deep. Res. Part I* 58, 442–453. doi: 10.1016/j.dsr.2011.02.004

Conflict of Interest: The authors declare that the research was conducted in the absence of any commercial or financial relationships that could be construed as a potential conflict of interest.

frontiers in Marine Science

ORIGINAL RESEARCH
published: 08 June 2021
doi: 10.3389/fmars.2021.645578

Disease Outbreak in a Keystone Grazer Population Brings Hope to the Recovery of Macroalgal Forests in a Barren Dominated Island

Francesca Gizzi[1†], João Gama Monteiro[1*†], Rodrigo Silva[1], Susanne Schäfer[1,2], Nuno Castro[1,3], Silvia Almeida[1], Sahar Chebaane[1], Alejandro Bernal-Ibáñez[1], Filipe Henriques[1], Ignacio Gestoso[1,4] and João Canning-Clode[1,4]*

[1] MARE–Marine and Environmental Sciences Centre, Agência Regional para o Desenvolvimento da Investigação, Tecnologia e Inovação (ARDITI), Funchal, Portugal, [2] GEOMAR, Marine Ecology Department, Helmholtz Centre for Ocean Research Kiel, Kiel, Germany, [3] MARE–Marine and Environmental Sciences Centre, Faculdade de Ciências da Universidade de Lisboa, Lisbon, Portugal, [4] Smithsonian Environmental Research Center, Edgewater, MD, United States

OPEN ACCESS

Edited by:
Charitha Bandula Pattiaratchi, University of Western Australia, Australia

Reviewed by:
Yining Chen, Second Institute of Oceanography, Ministry of Natural Resources, China
Nuno Vaz Álvaro, Instituto de Investigação e Tecnologia da Agronomia e Meio Ambiente (IITAA), Portugal

***Correspondence:**
Francesca Gizzi
francesca.gizzi@mare-centre.pt
João Gama Monteiro
joao.monteiro@mare-centre.pt

† These authors have contributed equally to this work and share first authorship

Specialty section:
This article was submitted to Coastal Ocean Processes, a section of the journal Frontiers in Marine Science

Received: 23 December 2020
Accepted: 14 May 2021
Published: 08 June 2021

Citation:
Gizzi F, Monteiro JG, Silva R, Schäfer S, Castro N, Almeida S, Chebaane S, Bernal-Ibáñez A, Henriques F, Gestoso I and Canning-Clode J (2021) Disease Outbreak in a Keystone Grazer Population Brings Hope to the Recovery of Macroalgal Forests in a Barren Dominated Island. Front. Mar. Sci. 8:645578. doi: 10.3389/fmars.2021.645578

Macroalgal forests play a key role in shallow temperate rocky reefs worldwide, supporting communities with high productivity and providing several ecosystem services. Sea urchin grazing has been increasingly influencing spatial and temporal variation in algae distributions and it has become the main cause for the loss of these habitats in many coastal areas, causing a phase shift from macroalgae habitats to barren grounds. The low productive barrens often establish as alternative stable states and only a major reduction in sea urchin density can trigger the recovery of macroalgal forests. The present study aims to assess if the 2018 disease outbreak, responsible for a strong reduction in the sea urchin *Diadema africanum* densities in Madeira Island, was able to trigger a reverse shift from barren grounds into macroalgae-dominated state. By assessing the diversity and abundance of benthic sessile organisms, macroinvertebrates and fishes before, during and after that particular mass mortality event, we evaluate changes in benthic assemblages and relate them to variations in grazer and herbivore densities. Our results revealed a clear shift from barren state to a macroalgae habitat, with barrens characterized by bare substrate, sessile invertebrate and Crustose Coralline Algae (CCA) disappearing after the mortality event. Overall variations in benthic assemblages was best explained by four taxa (among grazers and herbivores species). However, it was the 2018 demise of *D. africanum* and its density reduction that most contributed to the reverse shift from a long stable barren state to a richer benthic assemblage with higher abundance of macroalgae. Despite this recent increase in macroalgae dominated habitats, their stability and persistence in Madeira Island is fragile, since it was triggered by an unpredictable disease outbreak and depends on how *D. africanum* populations will recover. With no control mechanisms, local urchin populations can easily reach the tipping point needed to promote a new shift into barren states. New conservation measures and active restoration are likely required to maintain and promote the local stability of macroalgal forests.

Keywords: sea urchin, *Diadema africanum*, alternative stable state, phase-shift, microalgae restoration, tipping point, rocky reef, Madeira Island

INTRODUCTION

Coastal habitats represent one of the most productive and valued ecosystems of our planet (Costanza et al., 1997) but they are also seriously threatened by multiple factors and compounding pressures such as habitat loss and degradation, pollution, overexploitation, species introductions and climate change (see Solan and Whiteley, 2016 and references therein). Shallow marine coastal habitats are often dominated by macroalgae, where canopy and erect algae forests support biodiverse communities with high productivity (Graham, 2004; Ling, 2008; Christie et al., 2009; Tamaki et al., 2009). Macroalgae communities play a central role in the shallow temperate benthic ecosystems, representing the primary producers in the coastal zone as an important source of carbon sequestration (Krause-Jensen and Duarte, 2016) and providing valuable ecosystem services in shallow coastal systems (Muguerza et al., 2017; Ware et al., 2019; Edwards et al., 2020). In macroalgal forests, local herbivore populations are often able to drive fluctuations in spatial and temporal distribution of algal communities (Stachowicz et al., 2007; Schmitz, 2008; Owen-Smith, 2014), determine algal abundance and species composition (Van Alstyne, 1989), influence algal growth rates and reproductive output (Shurin et al., 2002; Steneck et al., 2002). For this reason, major increases in local populations of key grazers and herbivores can lead to the replacement of productive macroalgae forests with impoverished barrens dominated by encrusting organisms (Pinna et al., 2020 and references therein). These phase-shifts often occur with variation in sea urchin grazing intensity (Melis et al., 2019) as their feeding activity can play a major role in the stability, biodiversity, production and functioning of these ecosystems (Duffy and Hay, 1990; Poore et al., 2009; Korpinen et al., 2010; Kraufvelin, 2017). Sea urchins can thrive at very high population densities (Lawrence, 1975; Alves et al., 2001; Gizzi et al., 2020), possess limited mobility and a powerful excavating mouth providing them the ability to regulate the distribution, abundance, and diversity of benthic marine algae communities, influencing the establishment, spread and persistence of algal species (e.g., Steneck, 2013; Filbee-Dexter and Scheibling, 2014; Friedlander et al., 2017; Melis et al., 2019). Numerous studies have unequivocally demonstrated an inverse relationship between urchin density and algal biomass as well as their role in promoting a shift of habitats with complex macroalgae forests into urchin barrens (e.g., Filbee-Dexter and Scheibling, 2014; Ling et al., 2015; Hernández, 2017; Melis et al., 2019; Pinna et al., 2020).

With several natural factors influencing the intensity of urchin grazing (e.g., population density, food availability, and predation pressure), anthropogenic pressures such as overfishing (and consequent reduction in urchin predators) and global warming (and consequent changes in recruitment, physiology and distribution) can favor the proliferation of sea urchins and the spread of barren grounds worldwide (Filbee-Dexter and Scheibling, 2014; Ling et al., 2015; Melis et al., 2019; Pinna et al., 2020). The geographically widespread increase of barren grounds (Feehan et al., 2012; Filbee-Dexter and Scheibling, 2014; Perreault et al., 2014) and the persistence of this alternate state in some areas where the causes for sea urchin proliferation have been removed, give cause for concern (see Filbee-Dexter and Scheibling, 2014 and references therein). The occurrence of hysteresis mechanisms promote a self-perpetuating positive feedback that maintain the barrens even if the initial conditions are restored, reducing habitat complexity and ecosystem services (Scheffer et al., 2001; Filbee-Dexter and Scheibling, 2014). This loss in complexity and services leads to a crucial need in better understanding the mechanisms involved in forward and reverse shifts between algae dominated and barren states. Previous studies have consistently demonstrated that the threshold (i.e., urchin density or biomass) for a forward shift into barren state to occur is much higher than that of a reverse shift (Filbee-Dexter and Wernberg, 2018; Guarnieri et al., 2020). This non-linearity in triggering thresholds implies that once the barren ground is formed, a major reduction in urchin density is required for a reversal of a barren state into an erect algae dominated one (Ling et al., 2010; Trowbridge et al., 2011; Piazzi and Ceccherelli, 2019; Guarnieri et al., 2020). In some circumstances, multiple phase shifts between macroalgae forests and urchin barrens can go back and forward, driven by various factors such as fisheries targeting urchins or their predators, storm events, temperature increases or urchin diseases (Filbee-Dexter and Scheibling, 2014 and references therein). In contrast, they have consistently required a major decrease in urchin populations to achieve a tipping point and reverse into an algae-dominated state (Scheibling et al., 2013). This non-linear nature of phase shifts can be particularly relevant in coastal marine habitats that are especially vulnerable or under pressure from other stressors such as coastal development, pollution and overfishing. Forward shifts can be easily triggered whereas state reversal toward habitats with higher complexity and diversity may be hampered and barrens may become alternative stable states (Claisse et al., 2013; Filbee-Dexter and Scheibling, 2014; Cabanillas-Terán et al., 2015; Ling et al., 2015).

In the northeastern Atlantic archipelagos of Madeira and Canary Islands (Macaronesian region), populations of the long-spined sea urchin *Diadema africanum* with average densities of 10 individuals/m^2 have been responsible for the persistence of vast urchin barrens (Alves et al., 2001; Hernández et al., 2013). Several ecological and physical processes are involved in the structure and abundance of local *D. africanum* populations, including water turbulence (Alves et al., 2001), environmental parameters (e.g., nutrient and temperature; Hernández et al., 2006a,b), abundance of top-predators (Tuya et al., 2004b), substrate complexity (Tuya et al., 2004a) and mass mortality events (Clemente et al., 2014; Gizzi et al., 2020), but evidence suggests a general stability in the barren state of shallow coastal habitats across multiple islands of these archipelagos.

In Madeira Island, shallow rocky reef bottoms appear to have been the stage for a phase shift from algae dominated bottoms (Augier, 1985) toward *D. africanum* barrens (Alves et al., 2001; Hernández et al., 2008b). In 2009, a *D. africanum* mass-mortality event was first registered off the coasts of Madeira (Clemente et al., 2014) and resulted in a reduction of 65% of sea urchins abundance (Hernández et al., 2013; Clemente et al., 2014). At that time, the lack of long term monitoring and historical data series have hampered dedicated studies on how it may have triggered

an increase of algae cover and a phase shift from barren to algae dominated bottoms during the following months. In the summer of 2018 (early August, late September), a second mass mortality event was recorded in Madeira, with a major drop of approximately 90% in population density (described in detail in Gizzi et al., 2020). A disease outbreak that had been initially detected in the Canary Islands during February 2018 (Hernández et al., 2020), took more than 4 months to reach Madeira (where mortality was first detected in late July) but disrupted the local population of *D. africanum* across the entire archipelago.

Like many oceanic islands, Madeira Island is particularly vulnerable due to its offshore location, high level of endemisms and limited spatial extent suitable for macroalgal forests (Nunn et al., 1999; Mata et al., 2013). For this reason, it is of crucial importance that efforts are made to restore the macroalgal forests once present in the archipelago and thus protect local marine biodiversity.

There is typically a strong inverse correlation between *D. africanum* urchin density and erect algae abundance (Alves et al., 2001; Hernández et al., 2008b) due to the grazing pressure associated with urchin populations (Brito et al., 2004; Tuya et al., 2004a; Hernández et al., 2008b). The 2018 disease outbreak and urchin mass-mortality (Gizzi et al., 2020) provided an unique opportunity to leverage census data from annual monitoring surveys along the south coast of Madeira Island (2017–2019) to assess if *D. africanum* mortality had reduced grazing pressure for long enough to allow an increase in algal cover.

In this context, the present study aims to assess whether the 2018 abrupt reduction in *D. africanum* densities (Gizzi et al., 2020) triggered areas that were previously barren to transform into algae dominated areas by correlating urchin densities with the occurrence of distinct benthic assemblages. Additionally we discuss the role that periodic natural events and disease outbreaks may have in controlling *D. africanum* populations in Madeira and allow reverse phase-shifts and recovery of macroalgae communities. Finally, we suggest active conservation and habitat restoration practices that may apply toward preserving macroalgal forests in the region.

MATERIALS AND METHODS

Study Area

Madeira is a Portuguese archipelago located in the warm-temperate waters of the Northeast Atlantic Ocean within the Macaronesia area, together with the Azores, the Canary Islands and Cabo Verde, and is located about 650 km west of Morocco at its closest point to the mainland (**Figure 1**). The archipelago consists of two main populated islands, Madeira and Porto Santo, and five uninhabited islands (Desertas and Selvagens Islands). This study was conducted in the main island of Madeira, where the coastline and shallow waters (0–12 m) are dominated by rocky shores and reefs (Canning-Clode et al., 2008; Schäfer et al., 2020). The archipelago is influenced by north currents (Portuguese, Azorean and Canary currents; Caldeira et al., 2002), resulting in oligotrophic waters with high salinity, high temperature and low-nutrient regime waters (Johnson and Stevens, 2000; New et al., 2001). In the summers of 2017, 2018, and 2019, benthos and associated motile fauna were monitored in 10 sites along the south coast of the island (**Figure 1**). Sites

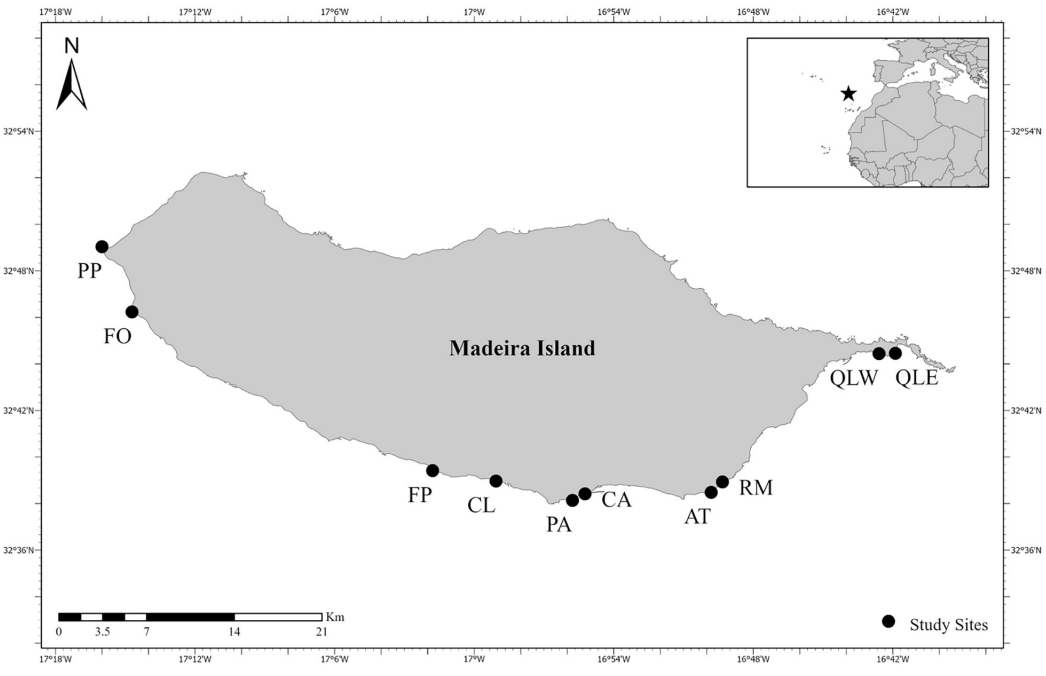

FIGURE 1 | Study area (Madeira Island, Portugal) and study sites represented by dots. PP, Ponta do Pargo; FO, Fajã da Ovelha; FP, Fajã dos Padres; CL, Câmara de Lobos; PA, Palms; CA, Carlton; AT, Atalaia; RM, Reis Magos; QLW, Quinta do Lorde West; QLE, Quinta do Lorde East.

were selected to include surveys along the entire south coast; whereas no sites were selected along the north coast due to difficulties in systematically access these sites due to strong prevailing winds and swells from the north quadrant, especially in the early summer months (Caldeira et al., 2002). Surveys targeted shallow rocky bottoms from the extreme western tip (Ponta do Pargo), to the easternmost part of the island (Quinta do Lorde), covering a range of different constraints (e.g., coastal development, population density, fishing, coastal runoff). With the exception of Ponta do Pargo, most sites are fairly protected from the prevailing north winds and currents with no major differences in salinity or temperature regimes (Caldeira et al., 2002).

Benthic Community Distributions and Associated Motile Fauna

Changes in benthic communities subsequent to the 2018 *D. africanum* mortality event (Gizzi et al., 2020) were assessed by: (i) identifying existing distinct assemblages; (ii) inspecting their occurrence in each summer (2017, 2018, and 2019), and (iii) assessing the influence of *D. africanum* density reduction in the occurrence of each unique assemblage.

Data on the abundance and density of sessile organisms, fish and macroinvertebrates were compiled from Underwater Visual Census (UVC) yearly surveys, performed by scientific divers along the south coast of Madeira Island (**Figure 1**). For each study site three transects were performed at 9–11 m depth. Benthic sessile diversity and relative abundance was assessed using 10 m point-intersect transects with 100 points (10 cm each), whereas fish and conspicuous macro-invertebrates diversity and abundance were recorded by counting individuals along a 50 × 4 m transect. Both the benthos and motile transects had the same starting point, georeferenced with a GPS equipped buoy, and with perpendicular orientation to the depth gradient.

During benthic surveys, sessile organisms under each intersection point were identified *in situ* to the highest taxonomic resolution possible and macro-photographs were collected when identification was uncertain or unknown. Imagery was later inspected to resolve uncertainties. All point-intersect data were grouped into nine categories, adapted from Friedlander et al. (2017, 2018): Crustose Coralline Algae (CCA), encrusting algae (non-CCA), filamentous microalgae (i.e., diatoms and cyanobacteria), turf algae (<3 cm in height), erect algae, canopy algae, sessile invertebrates, motile invertebrates and bare substrate (**Supplementary Table 1**).

Motile organisms abundance data were collected by two divers counting all fishes from 0 to 2 m above the rocky reef and all conspicuous macroinvertebrates (including *D. africanum* individuals) exposed over rocky reefs and in holes and crevices. Identified taxa were later grouped into the following five functional groups (based on their feeding guild): grazer, herbivore, omnivore, invertivore and macro carnivore. For subsequent analysis, motile data were pruned to select herbivores and grazers (as these are the organisms that can directly affect macro-algae abundance and promote phase shifts; e.g., Filbee-Dexter and Scheibling, 2014; Filbee-Dexter and Wernberg, 2018; **Supplementary Table 2**). Finally, all sessile and motile data and metadata were compiled and labeled for analysis.

Statistical Analysis

To identify and assess changes in the occurrence of significantly different sessile assemblages, the relative abundance of major sessile functional groups in each transect (see above) was standardized (to exclude all remaining uncertainties) and square-rooted (to minimize weight of dominant taxa in similarity based analysis). A Bray-Curtis similarity matrix was constructed and a cluster analysis with a Similarity Profile (SIMPROF) routine with 9999 permutations was used to visualize (dis)similarity in benthic structure between transects and identify significantly different groups of samples based solely on taxa group composition and data ordination (Clarke et al., 2008). SIMPROF generated groups (SFG) composition and occurrence over the 3 year period was inspected by plotting a shade plot, while a one-way Analysis of Similarity (ANOSIM) was used to test differences between years and confirm significant differences occurred after the 2018 *D. africanum* mortality event. The contributions of sessile taxonomic categories to the SIMPROF generated grouping were assessed with a Similarity Percentage routine (SIMPER), illustrating the typical composition of each assemblage.

Having established significant differences in sessile data over the 3 year period, a Distance-based Linear Model (DistLM) with the Akaike information criterion (AICc) was constructed to establish if and which herbivores and grazers were most contributing to the shape of the sessile assemblages identified with SIMPROF. Density data on all herbivore and grazer taxa was included as trial predictors, selecting BEST procedure to generate the top 10 best solutions to explain sessile data ordination. Lastly, Principal Coordinates Ordination (PCO) and non-metric Multi-Dimensional Scaling (nMDS) plots of the sessile Bray-Curtis similarity matrix were constructed with vector and bubble overlays to illustrate how variations in DistLM selected motile taxa related to the sessile functional groups ordination and grouping. Data analyses were performed and figures generated in Primer v7 (Clarke and Gorley, 2015) with PERMANOVA + add-on (Anderson et al., 2008).

RESULTS

Inspection of the abundance of sessile functional groups (**Figure 2**) occurring in the summers of 2017, 2018, and 2019 suggests a shift from a barren state to a macroalgae habitat, with a general decrease in relative abundance of bare substrate, sessile invertebrates and CCA and an increase in turf, erect and canopy forming algae (**Figure 2**). The general decreasing trend in the abundance of benthos categories and sessile functional groups that are typically dominant in barren states, were accompanied by a yearly decrease in the density of individuals from grazer taxa (**Figure 3**). Based on a hierarchical cluster analysis of Bray-Curtis similarity matrix with SIMPROF routine, three significantly different groups of sessile organisms were identified (**Figure 4** and **Supplementary Table 3**): a typical barren state assemblage (SFG = a), an intermediate state with no clear dominance of

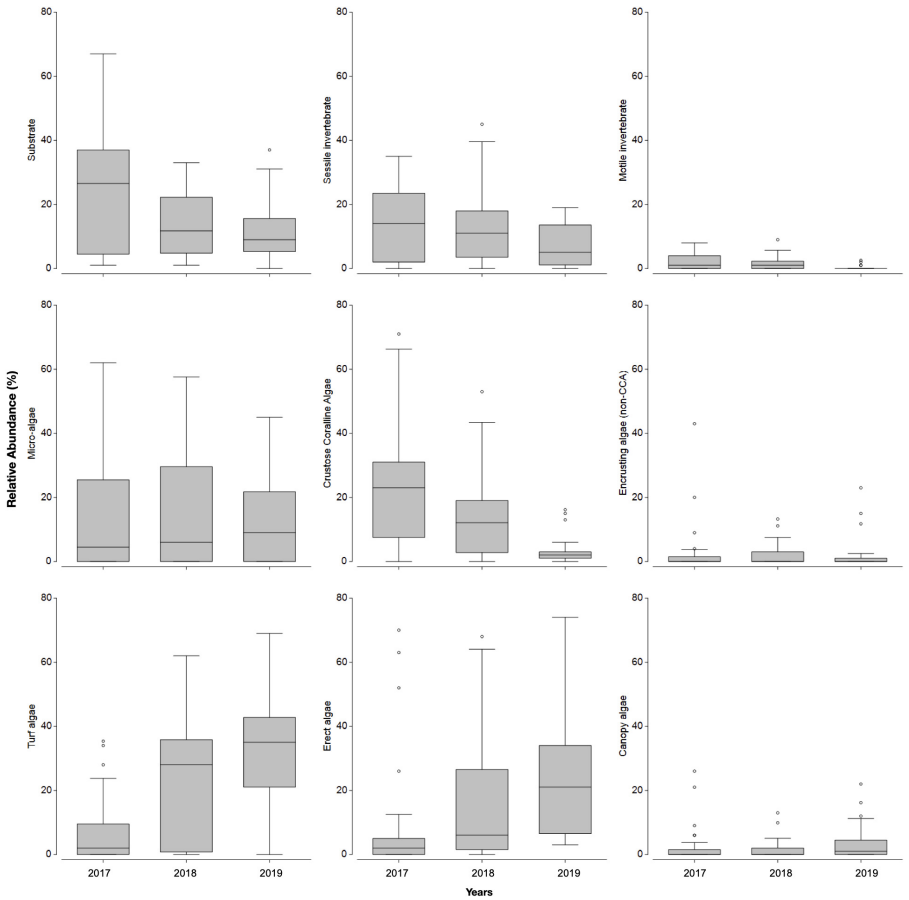

FIGURE 2 | Sessile functional group average relative abundance (%) in each of the three considered years (2017, 2018, 2019); boxplot with first quartile, median and third quartile, minimum and maximum as whiskers and points as outliers.

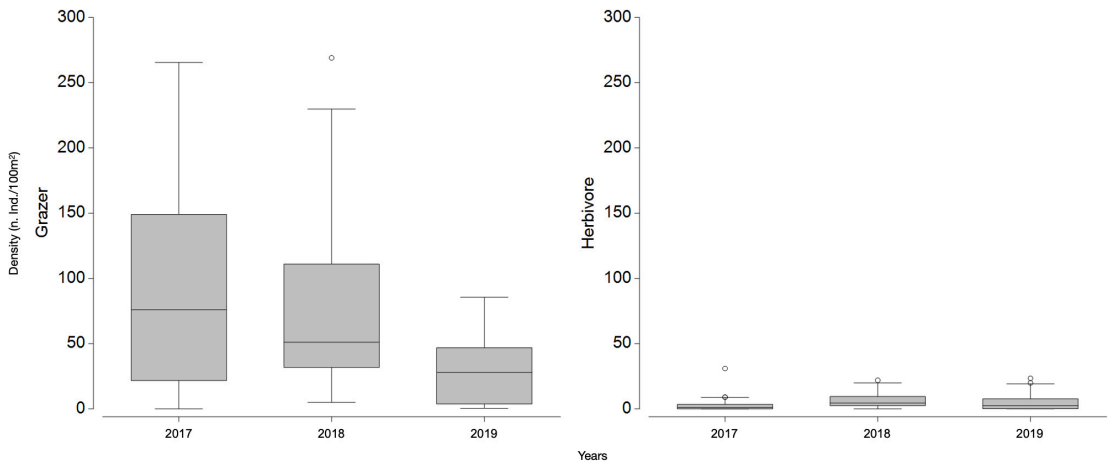

FIGURE 3 | Grazer and herbivore densities (individuals/100 m^2) in each of the three considered years (2017, 2018, 2019); boxplot with first quartile, median and third quartile, minimum and maximum as whiskers and points as outliers.

any functional groups (SFG = b) and a macroalgae dominated assemblage (SFG = c). The identification of these three distinct assemblages is independent of any factor or pre-deterministic grouping (e.g., year, site or location), as it is generated by permutation and profiling Bray-Curtis similarity among samples (Clarke et al., 2008, 2014). While samples with typical barren state

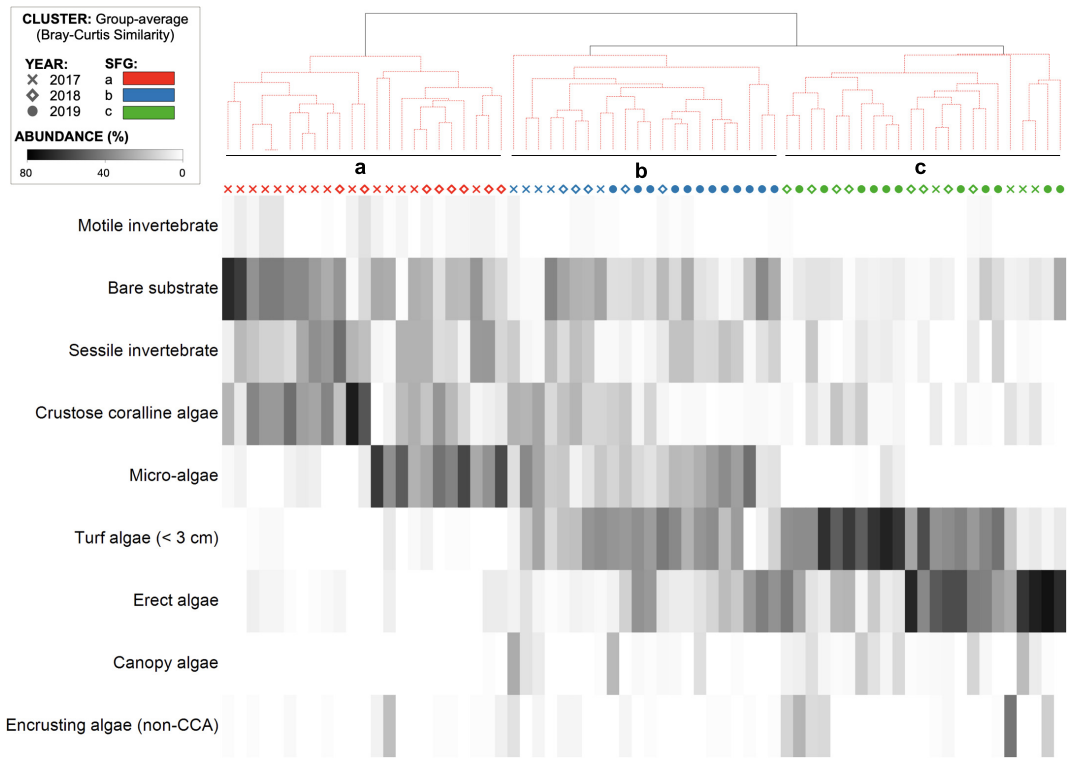

FIGURE 4 | Hierarchical cluster analysis (top) of Bray-Curtis similarities in benthic transect samples for each of the three considered years (2017, 2018, 2019; shapes) with SIMPROF-routine generated groups (SFG = a, b, and c; colors) and sessile functional groups relative density (individuals/100 m^2; shade plot).

assemblage, where bare substrate is more common and CCA, sessile invertebrates and filamentous microalgae dominated living cover (SFG = a) occurred in 2017 and 2018 (n = 15 and n = 8, respectively), 2019 was characterized by the absence of this assemblage (**Figure 4**). Remaining assemblages characterized by higher algal cover (SFG = b and c) were identified in samples from all years. However, with the disappearance of barren grounds (SFG = a), they become increasingly more common over time (**Figure 4**). This post-mortality change in the frequency and occurrence of the three identified assemblages was further assessed by testing years as a factor in a one-way ANOSIM. The only significant differences in sessile functional groups' ordination were those between 2019 and remaining years (**Table 1**), supporting the hypothesis that *D. africanum* density reduction in 2018 has enabled a reverse phase shift.

TABLE 1 | One-way ANOSIM of year as a significant factor in the ordination of Bray-Curtis similarities between benthic transect samples (n = 68) with pairwise tests (significant differences in bold).

	R	Significance (%)	Permutations
Overall test	**0.185**	**0.01**	**9,999**
Pairwise tests			
2017, 2018	0.05	7.8	9,999
2017, 2019	**0.385**	**0.01**	**9,999**
2018, 2019	**0.12**	**0.8**	**9,999**

A Distance-based Linear Model, using herbivore and grazer taxa densities as possible predictors, supported that the reduction in *D. africanum* density following the 2018 mass mortality event had a major role in the absence of typical urchin barren state in 2019 (**Tables 2**, **3**). The model that best explained the variation in benthic assemblages included four taxa: two grazer sea urchins *D. africanum* and *Paracentrotus lividus,* one herbivore crab *Percnon gibbesi* and the grazer fish *Ophioblennius atlanticus.* The four-axis model explained over 41% of the variability in sessile assemblages and benthic sample ordination (**Table 4**) with axis 1 being responsible for more than 88% of the fitted model. With *D. africanum* density variation having stronger correlation with axis 1 than any of the other taxa, it has a greater weight in explaining sessile sample ordination. This greater influence and stronger correlation of *D. africanum* densities, and sessile assemblages and sample ordination can be further illustrated by inspecting a Principal Coordinate Ordination plot with vector overlays displaying correlations with the four selected grazer and herbivore taxa (**Figure 5**). Beside the stronger correlation, fluctuations and variation range of *D. africanum* density was also considerably greater than those observed in the remaining three taxa (**Supplementary Figure 1**).

The distribution of identified sessile assemblages (SFG = a, b, c) during annual surveys (**Figure 6**) also illustrates a clear reverse shift from barren state (SFG = a) to intermediate or algae dominated state (SFG = b, c) in sites where it had been previously identified. Similarly, some locations where an

TABLE 2 | Marginal tests for distance-based linear modeling to predict Bray-Curtis similarities between benthic transect samples (n = 68) with herbivore and grazer taxa densities as predictors (significant predictors in bold; SS, Sum of Squares; Prop., proportion).

Predictor	SS (trace)	Pseudo-F	p	Prop.
Arbacia lixula	2442.4	2.17	0.09	0.03183
Diadema africanum	**22895**	**28.076**	**0.001**	**0.29837**
Ophioblennius atlanticus	2122.5	1.878	0.132	0.02766
Paracentrotus lividus	**5252.3**	**4.85**	**0.001**	**0.06845**
Patella aspera	216.4	0.187	0.966	0.00282
Percnon gibbesi	**8368.3**	**8.079**	**0.001**	**0.10906**
Sarpa salpa	808.3	0.703	0.568	0.01053
Sphaerechinus granularis	935.8	0.815	0.453	0.01220

TABLE 3 | DistLM top solutions predicting Bray-Curtis similarities between benthic transect samples (n = 68) with herbivore and grazer taxa densities as predictors (overall best solution in bold; AICc, Akaike information criterion; RSS, R Sum of Squares).

N° predictors	Predictor	AICc	R^2	RSS
1	*D. africanum*	458.03	0.29837	53839
2	*D. africanum* + *O. atlanticus*	454.59	0.35411	49562
3	*D. africanum* + *O. atlanticus* + *P. lividus*	453.88	0.38175	47441
4	***D. africanum* + *O. atlanticus* + *P. lividus* + *P. gibbesi***	**452.93**	**0.41085**	**45208**

TABLE 4 | Variation in benthic transect explained by each coordinate axis of the best DistLM solution (%) and correlations with orthonormal variables (predictor taxa).

	Axis 1	Axis 2	Axis 3	Axis 4
Explained variation (%)	36.37	2.84	1.65	0.23
Predictor	**Partial correlations**			
Diadema africanum	0.881	−0.454	−0.002	−0.134
Percnon gibbesi	−0.293	−0.436	−0.727	−0.441
Paracentrotus lividus	−0.267	−0.347	0.676	−0.593
Ophioblennius atlanticus	−0.258	−0.695	0.120	0.66

intermediate state (SFG = b) occurred in 2017 and 2018 shifted to an algae dominated state (SFG = c) in the following year. An inspection of matching *D. africanum* densities further supports the role of the urchin grazing pressure in the shaping of benthic assemblages (**Figure 6**). In addition, despite spatial variation in urchin densities, the 2018 disease outbreak had a clear impact in *D. africanum* population along the entire south coast of the island, confirming the severity and extent of the mortality event described in Gizzi et al. (2020).

By inspecting *D. africanum* densities found in each assemblage (**Figures 6**, **7**) it is also clear that the urchin density was considerably higher in barren areas (SFG = a) where values are typically above 50 individuals per 100 m^2. Opposingly, intermediate and algae dominated assemblage (SFG = b and c) were typically below this value (**Figures 6**, **7**), suggesting that 50 ind./100 m^2 can be empirically perceived as the threshold (i.e., maximum density) to reduce grazing pressure and trigger reverse phase shift from a barren state.

DISCUSSION

Worldwide, temperate rocky reef ecosystems with macroalgae forests host numerous diverse communities of marine organisms. However, kelp and other algae rich biotopes have been increasingly under pressure by compounding stressors such as climate change, eutrophication, coastal development, and pest species proliferation (Steneck et al., 2002; Koch et al., 2012; Borja et al., 2013; Ling et al., 2015). The uncontrolled proliferation of keystone gazers, such as sea urchins, has been reported to be an increasing problem for kelp forests and other algae rich habitats (Feehan et al., 2012; Cabanillas-Terán et al., 2015; Ling et al., 2015). In fact, temperate shallow benthic communities often present one of two ecological states: macroalgae forests with high densities of urchin predators, or; barrens where urchins overgraze algae and predators are typically scarce (reviewed in Lawrence, 1975; Steneck et al., 2002; Konar and Estes, 2003; Ling et al., 2015). In north Atlantic coasts, cyclical alternation between kelp beds and urchin barren seems to occur every 10–20 years, thanks to recurrent sea urchin mass mortality events (Scheibling et al., 2013). The role of macroalgae can be especially relevant in oceanic islands, where productivity can be low and shallow complex habitats scarce. Consequently, local populations of sea urchins (or other keystone herbivores or grazers) can have a particularly nefarious effect on local biodiversity when they become a threat to algae-dominated habitats.

In the northeast Atlantic archipelagos of Madeira and Canary Islands, previous studies describe *D. africanum* as a keystone species, exhibiting a key role in controlling fleshy macroalgae on rocky bottoms and promoting a barren state, through intense grazing activity (Alves et al., 2001; Brito et al., 2004; Tuya et al., 2004b; Hernández et al., 2007). The genera *Halopteris, Lobophora,* and *Dyctiota* have been identified as the preferred algae, followed by *Padina* and *Cystoseira* (Tuya et al., 2001). However, when the habitat is in the barren state, *D. africanum* shifts from specialist to generalist feeding, and survives eating all available algae (Tuya et al., 2004b), including CCA, microbial films, drift algae and even consuming animals (Hernández et al., 2007).

In Madeira, the southeast coast has been characterized by urchin barrens as an alternative stable state for more than 20 years (Augier, 1985; Alves et al., 2001). In theory, reverse phase shifts may occur after a major reduction in urchin population (Filbee-Dexter and Scheibling, 2014; Ling et al., 2015), however, the lack of long term datasets has hampered the ability to assess if and how mortality events and reductions in *D. africanum* densities may locally facilitate the recovery of macroalgae. In 2018, thanks to a yearly monitoring program of Madeira coastal habitats, it was possible to detect an ongoing *D. africanum* mortality event (Gizzi et al., 2020). Mass mortality events represent a natural removal experiment that eliminates many of the artifacts associated with experimental manipulations and are useful to study the effect of natural control mechanisms, sea urchin

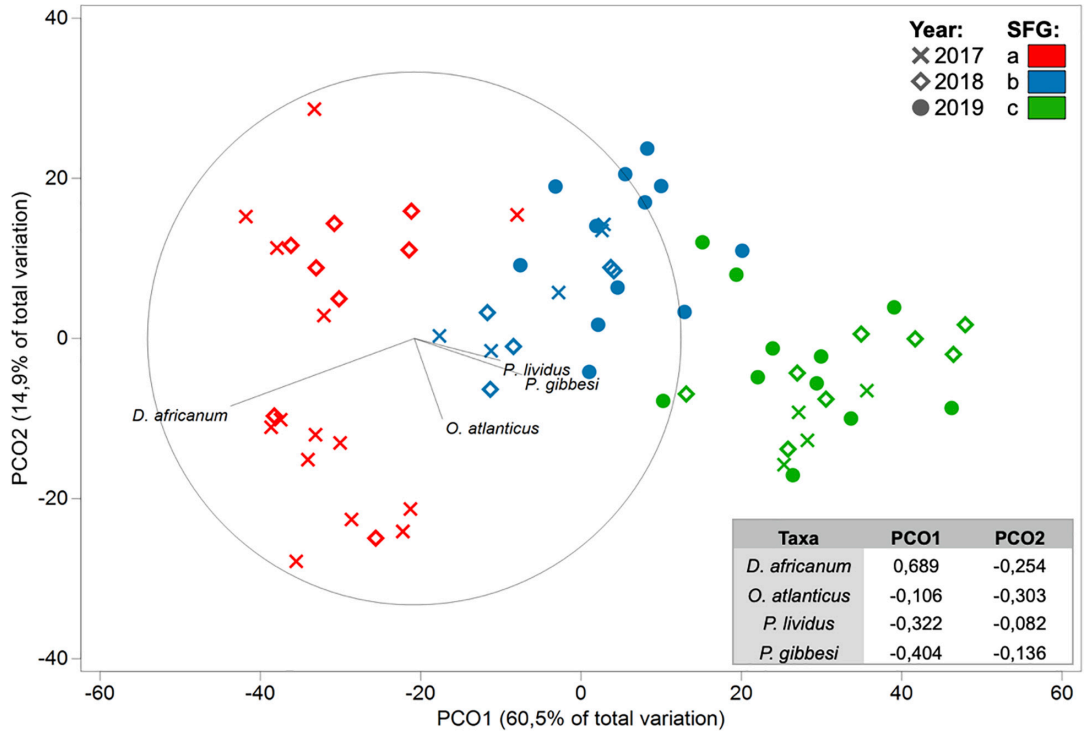

FIGURE 5 | Principal Coordinate Ordination (PCO) plot of benthic transect samples for each of the three considered years (2017, 2018, 2019; shapes) with SIMPROF-routine generated Functional Groups (SFG = a, b, and c; colors) and correlations between the four DistLM selected taxa (vectors) and PCO axes (bottom-right table).

removal and consequences to algal abundance and composition. The present study investigates the variability and distribution of distinct benthic assemblages before (2017), during (2018) and after the mortality event (2019) and explores the relation between algal composition and variations in herbivore and grazer densities.

Our findings support that the reduction of *D. africanum* density following the 2018 mortality, was strongly correlated with shifts in benthic community structure and increase in algal cover (**Figures 2–6**). A non-deterministic analysis of the entire pool of samples identified three significantly different assemblages of benthic functional-groups (**Figure 4**). There is spatial variation in the distribution of the identified assemblages (SFG = a, b and c) in each year, however the frequency of transects with barren state assemblage (SFG = a) reduces from most common, in 2017, to absent in 2019 (**Figure 6**). Many factors are likely to contribute to the spatial variability in benthic assemblages and *D. africanum* densities (e.g., fishing, urban and coastal development, turbidity, exposure). However, an inspection and analysis of our data clearly demonstrates that locations that had a barren state assemblage prior to the disease outbreak have shifted to intermediate or algae dominated states (**Figures 4**, **6**). Similarly, some areas also shifted from intermediate to an algae dominated state, suggesting an overall increase in macroalgal cover. These changes over time and the overall influence of *D. africanum* mortality in sample ordination was further confirmed by ANOSIM, with 2019 benthic data being significantly different from remaining years. Results from ANOSIM (**Table 1**) also support that reverse shifts (from barren to algae dominated states) can take several months to occur (Ling et al., 2015), explaining why, despite the reduction in barren state areas, no significant differences were found between 2017 and 2018 samples.

The use of a Distance-based Linear Model (Anderson et al., 2008; Clarke et al., 2014) assisted in understanding how herbivore and grazer taxa were correlated with the benthic sample ordination and grouping (SFG), with variations in benthic community structure being best explained in a model with contributions of *D. africanum*, and three additional taxa (**Tables 2–4**). The higher contribution of *D. africanum* (**Table 2**) and the stronger correlation with benthic data ordination (**Figure 5**) can be easily explained by the greater variance in density (**Supplementary Figure 1**) compounded by his voracious appetite and a mean daily algal consumption of 0.5–0.7 gDW/ind./day (Tuya et al., 2004a). This is in agreement with findings in the neighboring Canary Islands, where *D. africanum* is able to maintain barren rocky reefs (Tuya et al., 2004a). The characteristics of this species, including the high level of daily consumption, the ability to change its diet depending on habitat, the capacity to live at high population densities and the lack of predators, makes *D. africanum* determinant in shaping rocky reef communities and the stability of barren states in Madeira.

Overall, the strong correlation between *D. africanum* density and benthic data ordination (**Tables 2**, **4** and **Figure 5**) coupled with the significant differences in benthic data (**Table 1** and

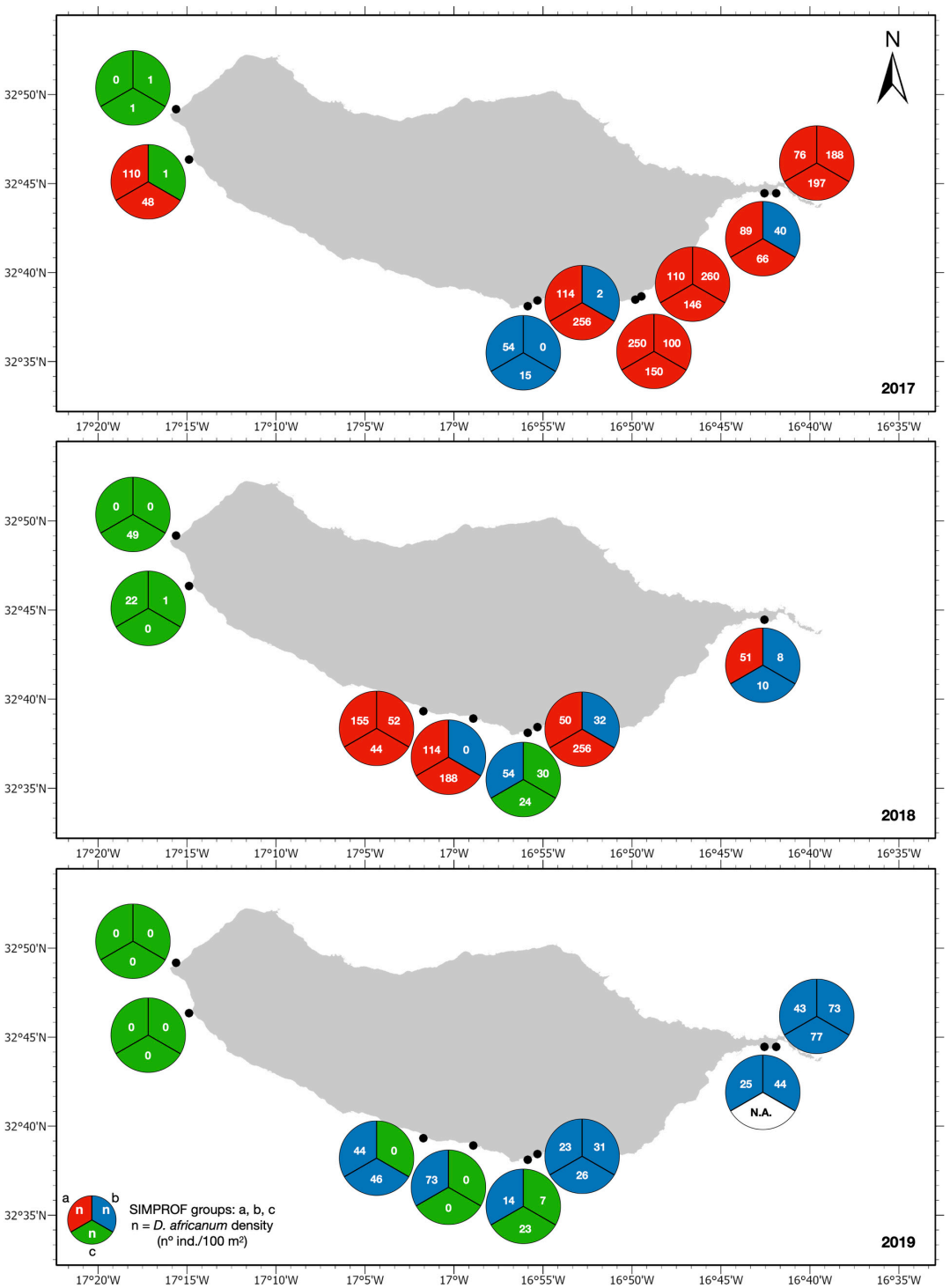

FIGURE 6 | Identified assemblages (SFG = a, b, c; colors) and *D. africanum* density (individuals/100 m^2) in each transect (pie chart slices) for sites surveyed in 2017 (top), 2018 (middle), and 2019 (bottom).

Figure 4) and the reductions in the urchin numbers and barren areas following the 2018 disease outbreak (**Figures 2**, **3**, **6**) support that the mass mortality event has indeed triggered a reverse shift and increase in macroalgae cover. The severe reduction in the numbers of *D. africanum* appear to have reached a tipping point that enabled the recovery of algal cover within 12 months. A close inspection of urchin densities in the three distinct assemblages (SFG = a, b and c) can assist in

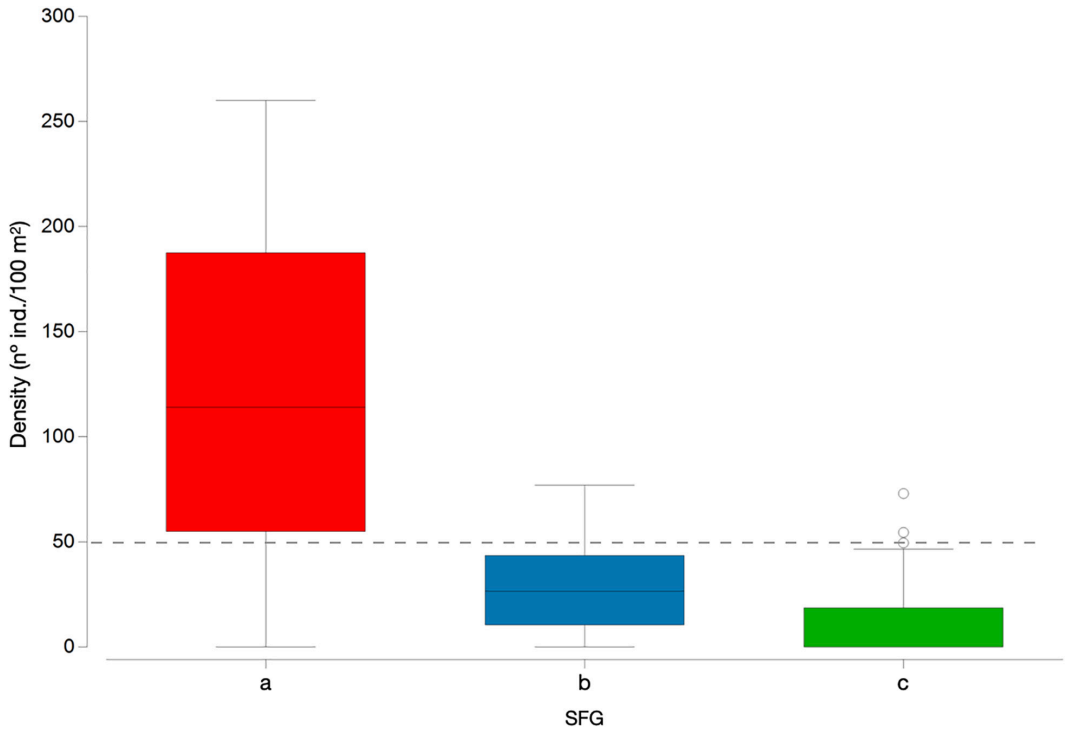

FIGURE 7 | *Diadema africanum* density (individuals/100 m^2) in each of the three identified assemblages (SFG = a, b, c); boxplot with first quartile, median and third quartile, minimum and maximum as whiskers and points as outliers.

identifying the density tipping point for a reverse shift to occur (**Figure 7**). With the lower quartile in barren state (SFG = a) above 50 individuals per 100 m^2 and both intermediate and algae dominated states (SFG = b and c) upper quartile below this density, it is possible to empirically identify the triggering threshold to allow a reverse shift from a stable barren state at 0.5 ind./m^2. This critical tipping point is considerably lower than the 2 ind./m^2 density threshold of urchin barren grounds suggested for the Canary Islands (Clemente and Hernández, 2008), but is in agreement with findings in other locations, where barrens formation occur at higher densities than reverse shifts (Ling et al., 2009, 2015).

Despite the 2018 disease outbreak and *D. africanum* mass mortality in the archipelago, a recovery of mature local urchin populations may indeed promote a regression in algal cover and easily return coastal habitats to a stable barren state (Filbee-Dexter and Scheibling, 2014; Ling et al., 2015). Urchin populations recovery can require years to pass before urchins emerge from crypsis to graze (Ling et al., 2009; Ling and Johnson, 2009; Ling, 2013). However, the 6-month recovery density values in local *D. africanum* populations reported in Gizzi et al. (2020), suggest that the algae dominated state may not be stable for long. If urchin densities reach the forward-shift critical threshold and grazing intensity is restored, barren formation can occur in a short period of time (Ling et al., 2015). As such, the stability of macroalgal forest habitats in Madeira will be partly dependent on control mechanisms keeping local *D. africanum* populations below the tipping point required for a forward shift. Even if assuming the 2 ind./m^2 density threshold reported in barren grounds of Canary Islands (Clemente and Hernández, 2008), local populations of *D. africanum* are expected to easily reach this density in many areas of the island.

Predation is one of the main controlling mechanisms in the recovery of sea urchin populations (e.g., Halpern et al., 2006; Clemente et al., 2011; Medrano et al., 2019). The intensive fishing activity in Madeira (Martínez-Escauriaza et al., 2020a,b), has not only reduced local fish stocks, but also the number of sea urchin predators (Friedlander et al., 2017). In fact, previous studies in the archipelagos of Madeira and Canary Islands had already reported that local reductions in predator numbers, such as *Balistes capriscus, Bodianus scrofa, Canthidermis sufflamen,* and *Sparisoma cretense*, likely contributed to the proliferation of *D. africanum* and promoted urchin barrens (Tuya et al., 2004b, 2005; Hernández et al., 2008a,b; Clemente et al., 2010, 2011; Sangil et al., 2011; Friedlander et al., 2017). With a low number of natural predators due to its long spines, the reduction of predation pressure associated with fishing activities can disproportionately favor *D. africanum* proliferation and consequently result in a damaging effect on local macroalgae forests. Spatial variation in fishing efforts will likely have a major influence in predatory pressure and the recovery of *D. africanum,* but adequate management and marine spatial planning can contribute to reduce chances of new barren formations and contribute to the conservation of macroalgae dominated habitats.

In view of the ecological importance of macroalgal forests and that erect macroalgae provides nursery areas and shelter to numerous organisms in the eastern Atlantic (Hernández et al., 2008a; Sangil et al., 2014; Friedlander et al.,

2017), it is of the utmost importance to take action toward the conservation and even restoration of this important habitat (Rice and Smith, 2017; Verdura et al., 2018; Melis et al., 2019). Despite the occurrence of disease outbreaks as natural control mechanisms of urchin populations, the unpredictable frequency and possible impacts on other marine species (Boudouresque and Verlaque, 2007; Rogers-Bennett, 2007; Jurgens et al., 2015; Gizzi et al., 2020; Hernández et al., 2020) makes them unreliable controlling agents for future conservation efforts of macroalgae forests. Effective management of local coastal habitats that aim to enhance marine biodiversity need to prioritize measures toward the conservation and restoration of macroalgal forests (Melis et al., 2019; Pinna et al., 2020). The present study illustrates that a severe reduction in urchin population can trigger the return of macroalgae dominated states, but to assure its stability urgent action will be required to assure that: (i) urchin densities stay below the tipping point that initiates phase shift toward barren state, and (ii) macroalgae fronds are not facing catastrophic collapse from other pressure sources such as eutrophication, sedimentation and siltation, contamination and physical damage from activities such as marine construction or dredging (Filbee-Dexter and Scheibling, 2014; Schäfer et al., 2020).

General measures for macroalgae conservation include: improvements in local fishery management policies to account for recreational fishing activities and reduce chances of overfishing; closely monitor wastewater treatment plants and other potential sources of marine pollution; regulate and enforce strict measures to reduce the impact of coastal and urban development, and; establish long-term monitoring programs to assess the status of marine coastal habitats. Management programs that target urchin control are likely the most reliable way to assure low urchin population densities and the stability and restoration of local macroalgal forests. However, the establishment of marine protected areas can simultaneously favor urchin predator pressure (by imposing fishing restrictions; Medrano et al., 2019) and reduce chances of damage to algae populations from other sources (by banning human activities that may have negative impacts), making it a preferable approach in promoting habitat and biodiversity conservation. Finally, targeted pilot-studies should explore the feasibility and success of *D. africanum* selective harvesting and other culling methods as proactive restoration initiatives to maintain and promote the stability of local macroalgae forests.

DATA AVAILABILITY STATEMENT

The raw data supporting the conclusions of this article will be made available by the authors, without undue reservation.

ETHICS STATEMENT

Ethical review and approval was not required for the animal study because Scientific divers just counted all the macro invertebrates and fishes presented along underwater transects.

AUTHOR CONTRIBUTIONS

FG and JM: conceptualization, analysis, and writing—original draft. FG, JM, RS, SS, NC, FH, and IG: fieldwork. JM and SA: visualization. JM, IG, and JC-C: resources and funding acquisition. FG, JM, RS, SS, NC, SA, SC, AB-I, FH, IG, and JC-C: writing—review and editing. All authors contributed to the article and approved the submitted version.

FUNDING

FG was supported by a post-doctoral research fellowship granted by ARDITI in the framework of project RAGES (ARDITI-RAGES-2019-001). JM and IG were supported by a post-doctoral research fellowship by Agência Regional para o Desenvolvimento da Investigação, Tecnologia e Inovação (ARDITI–M1420-09-5369-FSE-000002). RS was supported by a research fellowship in the framework of project PLASMAR+ (MAC2/1.1a/347). SS was supported through a federal state scholarship by the Kiel University, Germany and is currently funded by an ARDITI research fellowship in the scope of the H2020 project GoJelly. NC was funded by a doctoral grant (SFRH/BD/146881/2019) awarded by Fundação para a Ciência e Tecnologia (FCT). SA was supported by the CleanAtlantic INTERREG (Atlantic Area) project. AB and SC were financially supported by doctoral fellowships by Agência Regional para o Desenvolvimento da Investigação, Tecnologia e Inovação (ARDITI–M1420-09-5369-FSE-000002). JC-C was funded by national funds through FCT—Fundação para a Ciência e a Tecnologia, I.P., under the Scientific Employment Stimulus–Institutional Call–(CEECINST/00098/2018). Activities within this study were partially supported by projects MIMAR (MAC/4.6.d/066) and Project Observatório Oceânico da Madeira-OOM (M1420-01-0145-FEDER-000001). Finally, this study also had the support of Fundação para a Ciência e Tecnologia (FCT), Portugal, through the strategic project (UIDB/04292/2020) granted to MARE UI&I. This is contribution 74 from the Smithsonian's MarineGEO Network.

ACKNOWLEDGMENTS

We thank the Captain and 2017–2018 crews of the research vessel NRP Auriga (Instituto Hidrográfico/Marinha Portuguesa) and local dive operators Atalaia Diving Center, Madeira Diving Center, Azul Diving, Madeira Divepoint and Scuba Madeira for their logistic support.

SUPPLEMENTARY MATERIAL

The Supplementary Material for this article can be found online at: https://www.frontiersin.org/articles/10.3389/fmars.2021.645578/full#supplementary-material

REFERENCES

Alves, F. M. A., Chicharo, L. M., Serrão, E., and Abreu, A. D. (2001). Algal cover and sea urchin spatial distribution at Madeira Island (NE Atlantic). *Sci. Mar.* 65, 383–392. doi: 10.3989/scimar.2001.65n4383

Anderson, M. J., Gorley, R. N., and Clarke, K. R. (2008). *PERMANOVA+ for PRIMER: Guide to Software and Statistical Methods*. Plymouth: PRIMER-E.

Augier, H. (1985). Première contribution a l'étude et à la cartographie des biocénoses marines benthiques de l'île de Madère. *Bol. Mus. Mun. Funchal.* 37, 86–129.

Borja, Á, Fontán, A., and Muxika, I. (2013). Interactions between climatic variables and human pressures upon a macroalgae population: implications for management. *Ocean Coast. Manag.* 76, 85–95. doi: 10.1016/j.ocecoaman.2013.02.023

Boudouresque, C., and Verlaque, M. (2007). "Chapter 13 Ecology of *Paracentrotus lividus*," in *Edible Sea Urchins: Biology and Ecology*, ed. J. M. Lawrence (Amsterdam: Elsevier), 243–285. doi: 10.1016/S0167-9309(07)80077-9

Brito, A., Hernández, J. C., Falcón, J. M., García, N., González-Lorenzo, G., Gil-Rodríguez, M. C., et al. (2004). El Erizo de lima (*Diadema antillarum*) una especie clave en los fondos rocosos litorales de Canarias. *Makaronesia* 6, 68–86.

Cabanillas-Terán, N., Martín, J. A., Rodríguez-Barreras, R., and Luque, Á (2015). Size-density strategy displayed by *Diadema africanum* linked with the stability of urchin-barrens in the Canary Islands. *J. Mar. Biol. Assoc. U. K.* 95, 145–151. doi: 10.1017/S0025315414001246

Caldeira, R. M. A., Groom, S., Miller, P., Pilgrim, D., and Nezlin, N. P. (2002). Sea-surface signatures of the island mass effect phenomena around Madeira Island, Northeast Atlantic. *Remote Sens. Environ.* 80, 336–360. doi: 10.1016/S0034-4257(01)00316-9

Canning-Clode, J., Kaufmann, M., Molis, M., Wahl, M., and Lenz, M. (2008). Influence of disturbance and nutrient enrichment on early successional fouling communities in an oligotrophic marine system. *Mar. Ecol.* 29, 115–124. doi: 10.1111/j.1439-0485.2007.00210.x

Christie, H., Norderhaug, K. M., and Fredriksen, S. (2009). Macrophytes as habitat for fauna. *Mar. Ecol. Prog. Ser.* 396, 221–233. doi: 10.3354/meps08351

Claisse, J. T., Williams, J. P., Ford, T., Pondella, D. J., Meux, B., and Protopapadakis, L. (2013). Kelp forest habitat restoration has the potential to increase sea urchin gonad biomass. *Ecosphere* 4, 1–19. doi: 10.1890/ES12-00408.1

Clarke, K. R., and Gorley, R. N. (2015). *Getting STARTED with PRIMER v7*. Plymouth: PRIMER-E. Plymouth Mar. Lab., 20.

Clarke, K. R., Gorley, R. N., Somerfield, P. J., and Warwick, R. M. (2014). *Change in Marine Communities: An Approach to Statistical Analysis and Interpretation*, 3rd Edn. Plymouth: PRIMER-E Ltd.

Clarke, K. R., Somerfield, P. J., and Gorley, R. N. (2008). Testing of null hypotheses in exploratory community analyses: similarity profiles and biota-environment linkage. *J. Exp. Mar. Bio. Ecol.* 366, 56–69. doi: 10.1016/j.jembe.2008.07.009

Clemente, S., and Hernández, J. C. (2008). Influence of wave exposure and habitat complexity in determining spatial variation of the sea urchin *Diadema aff. antillarum* (*Echinoidea*: Diadematidae) populations and macro algal cover (Canary Islands-Eastern Atlantic Ocean). *Rev. Biol. Trop.* 56, 229–254. doi: 10.15517/RBT.V56I3.27088

Clemente, S., Hernández, J. C., Rodríguez, A., and Brito, A. (2010). Identifying keystone predators and the importance of preserving functional diversity in sublittoral rocky-bottom areas. *Mar. Ecol. Prog. Ser.* 413, 55–67. doi: 10.3354/meps08700

Clemente, S., Lorenzo-Morales, J., Mendoza, J. C., López, C., Sangil, C., Alves, F., et al. (2014). Sea urchin *Diadema africanum* mass mortality in the subtropical eastern Atlantic: role of waterborne bacteria in a warming ocean. *Mar. Ecol. Prog. Ser.* 506, 1–14. doi: 10.3354/meps10829

Clemente, S., Rodríguez, A., Brito, A., Ramos, A., Monterroso, Ó, and Hernández, J. C. (2011). On the occurrence of the hydrocoral *Millepora* (Hydrozoa: Milleporidae) in the subtropical eastern Atlantic (Canary Islands): is the colonization related to climatic events? *Coral Reefs* 30, 237–240. doi: 10.1007/s00338-010-0681-7

Costanza, R., D'Arge, R., de Groot, R., Farber, S., Grasso, M., Hannon, B., et al. (1997). The value of the world's ecosystem services and natural capital. *Nature* 387, 253–260. doi: 10.1038/387253a0

Duffy, J. E., and Hay, M. E. (1990). Seaweed adaptations to herbivory. *Bioscience* 40, 368–375. doi: 10.2307/1311214

Edwards, M., Konar, B., Kim, J.-H., Gabara, S., Sullaway, G., McHugh, T., et al. (2020). Marine deforestation leads to widespread loss of ecosystem function. *PLoS One* 15:e0226173. doi: 10.1371/journal.pone.0226173

Feehan, C., Scheibling, R. E., and Lauzon-Guay, J. S. (2012). Aggregative feeding behavior in sea urchins leads to destructive grazing in a Nova Scotian kelp bed. *Mar. Ecol. Prog. Ser.* 444, 69–83. doi: 10.3354/meps09441

Filbee-Dexter, K., and Scheibling, R. E. (2014). Sea urchin barrens as alternative stable states of collapsed kelp ecosystems. *Mar. Ecol. Prog. Ser.* 495, 1–25. doi: 10.3354/meps10573

Filbee-Dexter, K., and Wernberg, T. (2018). Rise of turfs: a new battlefront for globally declining kelp forests. *Bioscience* 68, 64–76. doi: 10.1093/biosci/bix147

Friedlander, A. M., Ballesteros, E., Clemente, S., Gonçalves, E. J., Estep, A., Rose, P., et al. (2017). Contrasts in the marine ecosystem of two Macaronesian islands: a comparison between the remote Selvagens Reserve and Madeira Island. *PLoS One* 12:e0187935. doi: 10.1371/journal.pone.0187935

Friedlander, A. M., Ballesteros, E., Clemente, S., Gonçalves, E. J., Estep, A., Rose, P., et al. (2018). Data from: contrasts in the marine ecosystem of two Macaronesian islands: a comparison between the remote Selvagens Reserve and Madeira Island. *Dryad Digital Repository* doi: 10.5061/dryad.322q2

Gizzi, F., Jiménez, J., Schäfer, S., Castro, N., Costa, S., Lourenço, S., et al. (2020). Before and after a disease outbreak: tracking a keystone species recovery from a mass mortality event. *Mar. Environ. Res.* 156:104905. doi: 10.1016/j.marenvres.2020.104905

Graham, M. H. (2004). Effects of local deforestation on the diversity and structure of southern California giant kelp forest food webs. *Ecosystems* 7, 341–357. doi: 10.1007/s10021-003-0245-6

Guarnieri, G., Bevilacqua, S., Figueras, N., Tamburello, L., and Fraschetti, S. (2020). Large-Scale Sea urchin culling drives the reduction of subtidal barren grounds in the mediterranean sea. *Front. Mar. Sci.* 7:519. doi: 10.3389/fmars.2020.00519

Halpern, B. S., Cottenie, K., and Broitman, B. R. (2006). Strong top-down control in southern california kelp forest ecosystems. *Science* 312, 1230–1232. doi: 10.1126/science.1128613

Hernández, J. C. (2017). Influencia humana en las fluctuaciones poblacionales de erizos de mar. *Rev. Biol. Trop.* 65, S23–S34. doi: 10.15517/RBT.V65I1-1.31663

Hernández, J. C., Brito, A., Cubero, E., García, N., Girard, D., González-Lorenzo, G., et al. (2006a). Temporal patterns of larval settlement of *Diadema antillarum* (Echinodermata: *Echinoidea*) in the Canary Islands using an experimental larval collector. *Bull. Mar. Sci.* 78, 271–279.

Hernández, J. C., Brito, A., García, N., Gil-Rodríguez, M. C., Herrera, G., Cruz-Reyes, A., et al. (2006b). Spatial and seasonal variation of the gonad index of *Diadema antillarum* (Echinodermata: *Echinoidea*) in the Canary Islands. *Sci. Mar.* 70, 689–698. doi: 10.3989/scimar.2006.70n4689

Hernández, J. C., Clemente, S., Sangil, C., and Brito, A. (2008a). Actual status of the sea urchin *Diadema aff. antillarum* populations and macroalgal cover in marine protected areas compared to a highly fished area (Canary Islands-eastern Atlantic Ocean). *Aquat. Conserv. Mar. Freshw. Ecosyst.* 18, 1091–1108. doi: 10.1002/aqc.903

Hernández, J. C., Clemente, S., Sangil, C., and Brito, A. (2008b). The key role of the sea urchin *Diadema aff. antillarum* in controlling macroalgae assemblages throughout the Canary Islands (eastern subtropical Atlantic): an spatio-temporal approach. *Mar. Environ. Res.* 66, 259–270. doi: 10.1016/j.marenvres.2008.03.002

Hernández, J. C., Gil-Rodríguez, M. C., Herrera-López, G., and Brito, A. (2007). Diet of the key herbivore *Diadema antillarum* in two contrasting habitats in the Canary Islands (Eastern Atlantic). *Vieraea* 35, 109–120.

Hernández, J. C., Sangil, C., and Clemente, S. (2013). "Sea urchins, natural events and benthic ecosystems functioning in the Canary Islands," in *Climate Change Perspectives From the Atlantic: Past, Present and Future*, eds J. M. Fernández-Palacios, L. Nascimento, J. C. Hernández, S. Clemente, A. González, and J. P. Díaz-González (Spain: Universidad de La Laguna), 487–512.

Hernández, J. C., Sangil, C., and Lorenzo-Morales, J. (2020). Uncommon southwest swells trigger sea urchin disease outbreaks in Eastern Atlantic archipelagos. *Ecol. Evol.* 10, 7963–7970. doi: 10.1002/ece3.6260

Johnson, J., and Stevens, I. (2000). A fine resolution model of the eastern North Atlantic between the Azores, the Canary Islands and the Gibraltar Strait. *Deep Sea Res. Part I Oceanogr. Res. Pap.* 47, 875–899.

Jurgens, L. J., Rogers-Bennett, L., Raimondi, P. T., Schiebelhut, L. M., Dawson, M. N., Grosberg, R. K., et al. (2015). Patterns of mass mortality among rocky

shore invertebrates across 100 km of northeastern Pacific coastline. *PLoS One* 10:e0126280. doi: 10.1371/journal.pone.0126280

Koch, M., Bowes, G., Ross, C., and Zhang, X.-H. (2012). Climate change and ocean acidification effects on seagrasses and marine macroalgae. *Glob. Change Biol.* 19, 103–132. doi: 10.1111/j.1365-2486.2012.02791.x

Konar, B., and Estes, J. A. (2003). The stability of boundary regions between kelp beds and deforested areas. *Ecology* 84, 174–185.

Korpinen, S., Jormalainen, V., and Pettay, E. (2010). Nutrient availability modifies species abundance and community structure of Fucus-associated littoral benthic fauna. *Mar. Environ. Res.* 70, 283–292. doi: 10.1016/j.marenvres.2010.05.010

Kraufvelin, P. (2017). Macroalgal grazing by the green sea urchin: born to consume resources. *Mar. Biol.* 164, 1–3. doi: 10.1007/s00227-017-3161-6

Krause-Jensen, D., and Duarte, C. M. (2016). Substantial role of macroalgae in marine carbon sequestration. *Nat. Geosci.* 9, 737–742. doi: 10.1038/ngeo2790

Lawrence, J. M. (1975). On the relationship between marine plants and sea urchins. *Oceanogr. Mar. Biol. Ann. Rev.* 13, 213–286.

Ling, S. D. (2008). Range expansion of a habitat-modifying species leads to loss of taxonomic diversity: a new and impoverished reef state. *Oecologia* 156, 883–894. doi: 10.1007/s00442-008-1043-9

Ling, S. D. (2013). "Pushing boundaries of range and resilience: a review of range-extension by a barrens-forming sea urchin," in *Climate Change Perspectives From the Atlantic: Past, Present and Future*, eds J. M. Fernández-Palacios, L. Nascimento, J. C. Hernández, S. Clemente, A. González, and J. P. Díaz-González (Spain: Universidad de La Laguna), 411–442.

Ling, S. D., Ibbott, S., and Sanderson, J. C. (2010). Recovery of canopy-forming macroalgae following removal of the enigmatic grazing sea urchin *Heliocidaris erythrogramma*. *J. Exp. Mar. Bio. Ecol.* 395, 135–146. doi: 10.1016/j.jembe.2010.08.027

Ling, S. D., and Johnson, C. R. (2009). Population dynamics of an ecologically important range-extender: kelp beds versus sea urchin barrens. *Mar. Ecol. Prog. Ser.* 374, 113–125. doi: 10.3354/meps07729

Ling, S. D., Johnson, C. R., Frusher, S. D., and Ridgway, K. R. (2009). Overfishing reduces resilience of kelp beds to climate-driven catastrophic phase shift. *Proc. Natl. Acad. Sci. U.S.A.* 106, 22341–22345. doi: 10.1073/pnas.0907529106

Ling, S. D., Scheibling, R. E., Rassweiler, A., Johnson, C. R., Shears, N., Connell, S. D., et al. (2015). Global regime shift dynamics of catastrophic sea urchin overgrazing. *Philos. Trans. R. Soc. B Biol. Sci.* 370, 1–10. doi: 10.1098/rstb.2013.0269

Martínez-Escauriaza, R., Hermida, M., Villasante, S., Gouveia, L., Gouveia, N., and Pita, P. (2020a). Importance of recreational shore angling in the archipelago of Madeira, Portugal (northeast Atlantic). *Sci. Mar.* 84, 331–341. doi: 10.3989/scimar.05046.30A

Martínez-Escauriaza, R., Vieira, C., Gouveia, L., Gouveia, N., and Hermida, M. (2020b). Characterization and evolution of spearfishing in Madeira archipelago. *Eastern Atlantic. Aquat. Living Resour.* 33:12. doi: 10.1051/alr/2020015

Mata, J., Fonseca, P. F., Prada, S., Rodrigues, D., Martins, S., Ramalho, R., et al. (2013). "O Arquipélago da Madeira," in *Geologia de Portugal, Volume II Geologia Meso-Cenozóica de Portugal*, eds R. Dias, A. Araújo, P. Terrinha, and J. C. Kullberg (Lisboa: Escolar Editora), 691–746.

Medrano, A., Linares, C., Aspillaga, E., Capdevila, P., Montero-Serra, I., Pagès-Escolà, M., et al. (2019). No-take marine reserves control the recovery of sea urchin populations after mass mortality events. *Mar. Environ. Res.* 145, 147–154. doi: 10.1016/j.marenvres.2019.02.013

Melis, R., Ceccherelli, G., Piazzi, L., and Rustici, M. (2019). Macroalgal forests and sea urchin barrens: structural complexity loss, fisheries exploitation and catastrophic regime shifts. *Ecol. Complex.* 37, 32–37. doi: 10.1016/j.ecocom.2018.12.005

Muguerza, N., Díez, I., Quintano, E., Bustamante, M., and Gorostiaga, J. M. (2017). Structural impoverishment of the subtidal vegetation of southeastern Bay of Biscay from 1991 to 2013 in the context of climate change. *J. Sea Res.* 130, 166–179. doi: 10.1016/j.seares.2017.06.006

New, A. L., Jia, Y., Coulibaly, M., and Dengg, J. (2001). On the role of the azores current in the ventilation of the north atlantic ocean. *Prog. Oceanogr.* 48, 163–194. doi: 10.1016/S0079-6611(01)00004-0

Nunn, P. D., Veitayaki, J., Ram-Bidesi, V., and Vunisea, A. (1999). Coastal issues for oceanic islands: implications for human futures. *Nat. Resour. Forum* 23, 195–207. doi: 10.1111/j.1477-8947.1999.tb00909.x

Owen-Smith, N. (2014).). Spatial ecology of large herbivore populations. *Ecography* 37, 416–430. doi: 10.1111/j.1600-0587.2013.00613.x

Perreault, M.-C., Borgeaud, I. A., and Gaymer, C. F. (2014). Impact of grazing by the sea urchin Tetrapygus niger on the kelp *Lessonia trabeculata* in Northern Chile. *J. Exp. Mar. Bio. Ecol.* 453, 22–27. doi: 10.1016/j.jembe.2013.12.021

Piazzi, L., and Ceccherelli, G. (2019). Effect of sea urchin human harvest in promoting canopy forming algae restoration. *Estuar. Coast. Shelf Sci.* 219, 273–277. doi: 10.1016/j.ecss.2019.02.028

Pinna, S., Piazzi, L., Ceccherelli, G., Castelli, A., Costa, G., Curini-Galletti, M., et al. (2020). Macroalgal forest vs sea urchin barren: patterns of macro-zoobenthic diversity in a large-scale Mediterranean study. *Mar. Environ. Res.* 159:104955. doi: 10.1016/j.marenvres.2020.104955

Poore, A. G. B., Campbell, A. H., and Steinberg, P. D. (2009). Natural densities of mesograzers fail to limit growth of macroalgae or their epiphytes in a temperate algal bed. *J. Ecol.* 97, 164–175. doi: 10.1111/j.1365-2745.2008.01457.x

Rice, J., and Smith, A. D. M. (2017). "Ecosystem-based management: opportunities and challenges for application in the ocean forest," in *Marine Animal Forests*, eds S. Rossi, L. Bramanti, A. Gori, and C. Orejas (Cham: Springer), 965–988. doi: 10.1007/978-3-319-21012-4_26

Rogers-Bennett, L. (2007). "Chapter 19 the ecology of *Strongylocentrotus franciscanus* and *Strongylocentrotus purpuratus*," in *Edible Sea Urchins: Biology and Ecology*, ed. J. M. Lawrence (Amsterdam: Elsevier), 393–425. doi: 10.1016/S0167-9309(07)80083-4

Sangil, C., Sansón, M., and Afonso-Carrillo, J. (2011). Spatial variation patterns of subtidal seaweed assemblages along a subtropical oceanic archipelago: thermal gradient vs herbivore pressure. *Estuar. Coast. Shelf Sci.* 94, 322–333. doi: 10.1016/j.ecss.2011.07.004

Sangil, C., Sansón, M., Clemente, S., Afonso-Carrillo, J., and Hernández, J. C. (2014). Contrasting the species abundance, species density and diversity of seaweed assemblages in alternative states: urchin density as a driver of biotic homogenization. *J. Sea Res.* 85, 92–103. doi: 10.1016/j.seares.2013.10.009

Schäfer, S., Monteiro, J., Castro, N., Gizzi, F., Henriques, F., Ramalhosa, P., et al. (2020). Lost and found: a new hope for the seagrass *Cymodocea nodosa* in the marine ecosystem of a subtropical Atlantic Island. *Reg. Stud. Mar. Sci.* 41:101575. doi: 10.1016/j.rsma.2020.101575

Scheffer, M., Carpenter, S., Foley, J. A., Folke, C., and Walker, B. (2001). Catastrophic shifts in ecosystems. *Nature* 413, 591–596. doi: 10.1038/35098000

Scheibling, R. E., Feehan, C. J., and Lauzon-Guay, J.-S. (2013). "Climate change, disease and the dynamics of a kelp-bed ecosystem in Nova Scotia," in *Climate Change Perspectives From the Atlantic: Past, Present and Future*, eds J. M. Fernández-Palacios, L. Nascimento, J. C. Hernández, S. Clemente, A. González, and J. P. Díaz-González (Spain: Universidad de La Laguna), 361–387.

Schmitz, O. J. (2008). Herbivory from individuals to ecosystems. *Annu. Rev. Ecol. Evol. Syst.* 39, 133–152. doi: 10.1146/annurev.ecolsys.39.110707.173418

Shurin, J. B., Borer, E. T., Seabloom, E. W., Anderson, K., Blanchette, C. A., Broitman, B., et al. (2002). A cross-ecosystem comparison of the strength of trophic cascades. *Ecol. Lett.* 5, 785–791. doi: 10.1046/j.1461-0248.2002.00381.x

Solan, M., and Whiteley, N. (2016). *Stressors in the Marine Environment: Physiological and Ecological Responses; Societal Implications*. Oxford: Oxford University Press.

Stachowicz, J. J., Bruno, J. F., and Duffy, J. E. (2007). Understanding the effects of marine biodiversity on communities and ecosystems. *Annu. Rev. Ecol. Evol. Syst.* 38, 739–766. doi: 10.1146/annurev.ecolsys.38.091206.095659

Steneck, R. S. (2013). "Chapter 14 sea urchins as drivers of shallow benthic marine community structure," in *Sea Urchins: Biology and Ecology*, ed. J. M. Lawrence (Amsterdam: Elsevier), 195–212. doi: 10.1016/B978-0-12-396491-5.00014-9

Steneck, R. S., Graham, M. H., Bourque, B. J., Corbett, D., Erlandson, J. M., Estes, J. A., et al. (2002). Kelp forest ecosystems: biodiversity, stability, resilience and future. *Environ. Conserv.* 29, 436–459. doi: 10.1017/S0376892902000322

Tamaki, H., Kusaka, K., Fukuda, M., Arai, S., and Muraoka, D. (2009). *Undaria pinnatifida* habitat loss in relation to sea urchin grazing and water flow conditions, and their restoration effort in Ogatsu Bay. *Japan. J. Water Environ. Technol.* 7, 201–213. doi: 10.2965/jwet.2009.201

Trowbridge, C. D., Little, C., Pilling, G. M., Stirling, P., and Miles, A. (2011). Decadal-scale changes in the shallow subtidal benthos of an Irish marine reserve. *Bot. Mar.* 54, 497–506. doi: 10.1515/BOT.2011.057

Tuya, F., Boyra, A., Sanchez-Jerez, P., Barbera, C., and Haroun, R. (2004a). Can one species determine the structure of the benthic community on a temperate

rocky reef? The case of the long-spined sea-urchin *Diadema antillarum* (Echinodermata: *Echinoidea*) in the eastern Atlantic. *Hydrobiologia* 519, 211–214. doi: 10.1023/B:HYDR.0000026599.57603.bf

Tuya, F., Boyra, A., Sanchez-Jerez, P., Barbera, C., and Haroun, R. J. (2004b). Relationships between rocky-reef fish assemblages, the sea urchin *Diadema antillarum* and macroalgae throughout the Canarian Archipelago. *Mar. Ecol. Prog. Ser.* 278, 157–169. doi: 10.3354/meps278157

Tuya, F., Martín, J. A., Reuss, G. M., and Luque, A. (2001). Food preferences of the sea urchin *Diadema antillarum* in Gran Canaria (Canary Islands, central-east Atlantic Ocean). *J. Mar. Biol. Assoc. U. K.* 81, 845–849.

Tuya, F., Sanchez-Jerez, P., and Haroun, R. J. (2005). Influence of fishing and functional group of algae on sea urchin control of algal communities in the eastern Atlantic. *Mar. Ecol. Prog. Ser.* 287, 255–260. doi: 10.3354/meps287255

Van Alstyne, K. L. (1989). Adventitious branching as a herbivore-induced defense in the intertidal brown alga *Fucus distichus*. *Mar. Ecol. Prog. Ser. Oldend.* 56, 169–176.

Verdura, J., Sales, M., Ballesteros, E., Cefalì, M. E., and Cebrian, E. (2018). Restoration of a canopy-forming alga based on recruitment enhancement: methods and long-term success assessment. *Front. Plant. Sci.* 9:1832. doi: 10.3389/fpls.2018.01832

Ware, C., Dijkstra, J. A., Mello, K., Stevens, A., Brien, B. O., and Ikedo, W. (2019). A novel three-dimensional analysis of functional architecture that describes the properties of macroalgae as a refuge. *Mar. Ecol. Prog. Ser.* 608, 93–103. doi: 10.3354/meps12800

Conflict of Interest: The authors declare that the research was conducted in the absence of any commercial or financial relationships that could be construed as a potential conflict of interest.

frontiers in Marine Science

ORIGINAL RESEARCH
published: 11 June 2021
doi: 10.3389/fmars.2021.645531

Strain Evolution and Instability of an Anticyclonic Eddy From a Laboratory Experiment

Guoqing Han[1,2,3], Changming Dong[1,2], Jingsong Yang[3], Joel Sommeria[4], Alexandre Stegner[5] and Rui M. A. Caldeira[6]*

[1] School of Marine Sciences, Nanjing University of Information Science and Technology, Nanjing, China, [2] Southern Marine Science and Engineering Guangdong Laboratory (Zhuhai), Zhuhai, China, [3] State Key Laboratory of Satellite Ocean Environment Dynamics, Second Institute of Oceanography, Ministry of Natural Resources, Hangzhou, China, [4] Laboratoire des Ecoulements Géophysiques et Industriels (LEGI), Université Grenoble Alpes, CNRS, Grenoble, France, [5] Laboratoire de Metéorologie Dynamique, École Polytechnique, Palaiseau Cedex, France, [6] Agência Regional para o Desenvolvimento da Investigação Tecnologia e Inovação, Observatório Oceânico da Madeira (OOM), Funchal, Portugal

OPEN ACCESS

Edited by:
Frédéric Cyr, Fisheries and Oceans Canada, Canada

Reviewed by:
Nicolas Grisouard, University of Toronto, Canada
Stefania Espa, Sapienza University of Rome, Italy

****Correspondence:***
Changming Dong
cmdong@nuist.edu.cn

Specialty section:
This article was submitted to Physical Oceanography, a section of the journal Frontiers in Marine Science

Received: *18 January 2021*
Accepted: *14 May 2021*
Published: *11 June 2021*

Citation:
Han G, Dong C, Yang J, Sommeria J, Stegner A and Caldeira RMA (2021) Strain Evolution and Instability of an Anticyclonic Eddy From a Laboratory Experiment. Front. Mar. Sci. 8:645531. doi: 10.3389/fmars.2021.645531

Using the 13 m diameter LEGI-Coriolis rotating platform, the evolution processes of a generated anticyclonic eddy throughout its lifecycle are analyzed. Experimental results have shown that the eddy lasted for approximately $3T_0$, where T_0 is the rotating period of 90 s. After $T = 0.3T_0$, the eddy enters its mature phase, whereby following this event, eddy intensity slowly decreases from its maximum rotation speed. By $T = 2.6T_0$, the eddy enters a stage of rapid weakening. In its decay period, two underlying mechanisms for this decay have been identified as inertial instability and eddy–eddy interactions.

Keywords: laboratory experiment, inertial instability, eddy–eddy interaction, anticyclonic eddy, island wakes

INTRODUCTION

The presence of islands significantly affects the surrounding hydrological environment, especially with regards to the physical processes occurring in the lee of the island (Coutis and Middleton, 2002; Doglioli et al., 2004; Neill and Elliott, 2004; Caldeira et al., 2005; Dong et al., 2007, 2018; Han et al., 2019). Island wake eddies are one of the most common dynamic processes in the island wake region. Island wakes can be further differentiated into two types based on their vorticity generation mechanisms: deep-water and shallow-water island wakes (Tomczak, 1988; Dong et al., 2007, 2018). The difference between shallow-water and deep-water island wakes (with/without the shelf-slope) is the source of vorticity (i.e., lateral horizontal gradients, bottom stress irregularity, and tilting of the baroclinic flow). If the primary vorticity source comes from the lateral stress gradient, the island wake is considered deep-water; when the bottom stress irregularity is dominant, the wake is shallow-water, where the horizontal vorticity can be tilted into the vertical component through baroclinic processes.

Previous studies show that the shedding of eddies tends to be inhibited by increasing rotation rate (e.g., Boyer and Davies, 1982; Page, 1985; Heywood et al., 1996). At different background rotation frequencies (i.e., $\beta \neq 0$), the wake can develop a standing Rossby wave structure (McCartney, 1975), and the flow separation and eddy formation are affected by the direction of

the incident current with respect to the wave propagation (e.g., Johnson and Page, 1993; Tansley and Marshall, 2001). The proposed mechanisms of eddy decaying include damping by ocean bottom drag (Sen et al., 2008; Arbic et al., 2009) and sea surface wind stresses (Duhaut and Straub, 2006; Hughes and Wilson, 2008), generating lee-waves over small-scale bottom topography (Marshall and Garabato, 2008; Sheen et al., 2014), radiating near-inertial waves through loss of balance (Molemaker et al., 2005; Alford et al., 2013), and instability processes in eddies (Lazar et al., 2013a,b).

Following eddy generation in an island's lee, the eddy could experience instability. Eddy inertial instability is due to a centrifugal instability mechanism as originally proposed by Rayleigh (1916) where in the presence of the Coriolis force when there is an imbanlance between the centrifugal and Coriolis forces, in addition to the radial pressure gradient. As previously highlighted by Dong et al. (2007); Kloosterziel et al. (2007) and Lazar et al. (2013a,b), inertial instability plays a crucial role in the decaying process of eddies in island wakes. For a steady, cylindrical, inviscid rotating fluid, the rotation rate $V(r)$ is unstable when the absolute angular momentum ($L = V \cdot r$) decreases with the increase of radius r in some parts of the fluid.

In addition to inertial instability processes, eddy–eddy interactions also play a crucial role in eddy evolution, especially in decaying processes. Fang and Morrow (2003) investigate the characteristics of eddies in the Leeuwin Current, finding that eddy interaction with topography can induce splitting or merging which further affects eddy decay. Eddies generated from different processes may coalesce and form a single eddy due to complicated eddy–eddy interactions (Dritschel and Waugh, 1992; Nan et al., 2011; Cui et al., 2019). Zhai et al. (2010) model a random sea of westward-propagating eddies and in that simulation, it is demonstrated that eddies interact with one another and cascade to larger scales through the merging of eddies of the same parity and finally dissipate near the western boundary. de Marez et al. (2020) present an analysis of merging events in the global ocean that are influenced by the β-effect and the presence of neighboring eddies.

According to the literature review, one can see that the eddy decaying process is very complicated and requires further investigation. To further our understanding of the decaying processes of anticyclonic eddies, we conduct a series of laboratory experiments to investigate the roles of both inertial instability and eddy–eddy interaction in the eddy dissipation. Using the 13-m diameter (world's largest) LEGI-Coriolis rotating platform, we conducted a series of island wake simulation experiments. In a strongly stratified experiment, the evolution processes of a generated anticyclonic eddy are analyzed throughout its lifecycle. The decaying period of this anticyclonic eddy can be divided into two parts: slow decay period and rapid decaying period. This study reveals the influence of inertial instability and eddy–eddy interaction on the anticyclonic's cycle evolution from the perspective of laboratory observation.

The rest of the paper is organized as follows: section "Experimental Settings and Method" describes the experimental settings and the eddy detection method. In section "Results," the statistical characteristics and decaying mechanism of an identified anticyclonic are analyzed. Section "Conclusion and Discussion" is the conclusion and discussion.

EXPERIMENTAL SETTINGS AND METHOD

Experimental Settings

We conduct a series of laboratory experiments on island wakes in the currently world's largest rotating tank, the LEGI-Coriolis rotating tank that possess a diameter of 13 m and a depth of 1.2 m. Parts of the laboratory experimental results have been analyzed and led to publications (Lazar et al., 2013a,b). We conducted many island wake simulation experiments in the LEGI-Coriolis platform, and only a few experiments have found the eddy–eddy interaction phenomena.

To mimic the oceanic density stratification we used salt stratification. We first filled the tank with a deep (∼50 cm) salty layer, $\rho_{\text{bottom}} = 1,040\ \text{gl}^{-1}$. Due to the slow Ekman recirculation, it took 1 day for this thick layer to reach a solid body rotation. We then used the double bucket technique (Oster, 1965) to create a thin surface layer with linear stratification. To avoid residual motions it was then necessary to wait at least one to 2 h between consecutive experiments. The configuration of the laboratory experiments is shown in **Figures 1A,B**. We used a conductivity and temperature profiler (125MicroScale)[1] to accurately measure the vertical density profile **Figure 1C**. In the present study, an anticyclonic eddy (A_0) is identified from the series of laboratory experiments and used for the investigation of the underlying mechanisms for the eddy decaying processes.

The rotating platform rotates counter-clockwise, and the corresponding Coriolis parameter is:

$$f = \frac{4\pi}{T_0} = 2\omega = 0.139\,\text{s}^{-1} \quad (1)$$

where f is the Coriolis parameter, T_0 is the rotating period (T_0 = 90 s), ω is the angular velocity. We used a cylinder with a diameter of 25 cm and a towing speed of 4 cm/s to mimic ocean circulation interacting with a cylindrical island. In this experiment, we produce intense eddies in a shallow strongly stratified (N/f = 10) layer at high Reynolds numbers (Re = 10,000) (avoiding excessive dissipation). Generally, for high Reynolds number eddies, the nonlinear evolution of three-dimensional inertial perturbations induces a redistribution of the angular momentum (Kloosterziel et al., 2007; Carnevale et al., 2011). However, for a strong stratification, the redistribution of angular momentum is weak and barely affects the velocity profile (Kloosterziel et al., 2007; Lazar et al., 2013b).

The surface stratification layer (h_s) is 6.7 cm. The height of the cylinder (h_c) is slightly smaller than h_s. We assume that the cylinder (i.e., island) mainly transfers momentum in the upper stratified layer, Hence, the dynamic state is mainly the first baroclinic mode (thus, the barotropic mode can be ignored). This is true in the case of $h_s \approx h_c << H_c$ (Hc represent

[1] http://www.pme.com

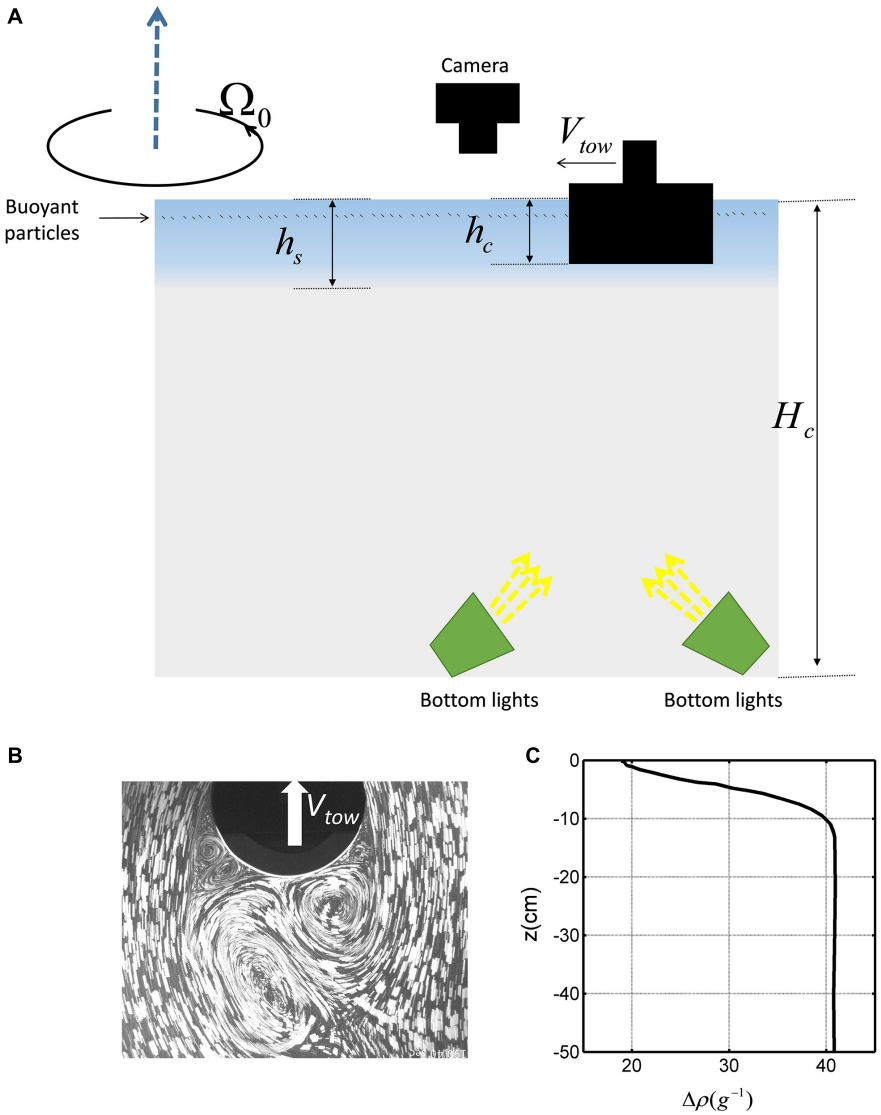

FIGURE 1 | (A) Side view of the experimental setup, **(B)** top view of the particle visualization of the surface wake, and **(C)** a typical density anomaly induced by salinity stratification.

the depth of the flow) as demonstrated by Perret et al. (2006) and Teinturier et al. (2010). The deformation radius of the first baroclinic mode is defined as $R_d = \frac{N \cdot hc}{f}$ and the value of Rd = 68 cm is larger than the eddies' radius. The Burger number $(Bu = (\frac{N}{f}\frac{h_s}{r_{island}})^2)$ is 28.88 and the Rossby number $(Ro = \frac{V_{tow}}{f \cdot r_{island}})$ is 2.29. R_d is larger than A_0's radii, and much smaller than the barotropic radius R_d^* $(R_d^* = \frac{\sqrt{g \cdot H_c}}{f}$, $H_c \sim 1$ m in our experiment, g is the gravity). Therefore, the barotropic mode is ignored in our study. Perret et al. (2006); Lazar et al. (2013b), and Stegner (2014) showed, for baroclinic island wake laboratory experiments, that the isopycnal displacement is inversely proportional to the Burger number, which is quite large, and directly proportional to the Rossby number, which in our experiments is moderate. Therefore, the displacement of the isopycnal interface between the thin stratified layer and the deep barotropic layer is expected to be small or moderate. The main parameters of this experiment are listed below in **Table 1**.

In our experiment, the effective measuring area is 2 m·2 m. To perform quantitative velocity measurements we used several powerful waterproof lamps to illuminate small plastic particles of a buoyancy corresponding to 5–10 mm below the surface. To enhance the contrast, the bottom of the platform was painted black. We used two 1,024 × 1,024 pixels CCD cameras to record the particle motions. The surface velocities were analyzed using uvmat software (a PIV software used in the LEGI-Coriolis platform)[2]. The spatial resolution of velocities is 1 cm, which is

[2]http://servforge.legi.grenoble-inp.fr/projects/soft-uvmat

TABLE 1 | Experimental settings.

Parameters	Value	Symbol
Radius for the island	12.5 cm	R_{island}
Rotating period	90 s	T_0
Density layer thickness	6.7 cm	*hs*
Height of the cylinder	4 cm	*hc*
Coriolis parameter	0.1396 s^{-1}	*f*
Towing speed	4 cm/s	V_c
Reynolds number	10,000	*Re*
Brunt-Väisälä frequency	1.4 s^{-1}	*N*
Burger number	28.88	*Bu*
Rossby number	2.29	*Ro*
the 1st baroclinic deformation radii	68 cm	*Rd*

enough to use for our study (the generated eddy is nearly equal to the R_{island}, R_{island} = 12.5 cm).

Angular Momentum Eddy Detection and Tracking Algorithm

In the present study, we apply an eddy detection tracking algorithm (Angular Momentum Eddy Detection and Tracking Algorithm, AMEDA), developed by Le Vu et al. (2018). AMEDA improves upon a hybrid algorithm originally proposed by Mkhinini et al. (2014), and combines a physical parameter, the local normalized angular momentum (LNAM), with the geometric characteristics of streamlines to determine the center and dynamic characteristics of eddies. LNAM will be maximized at the center of the eddy, that is, the center of swirling motion $_{G_i}$. For each grid point $_{G_i}$, the *LNAM* value can be calculated according to the following equation:

$$LNAM(G_i) = \frac{\sum_j G_i X_j \times V_j}{\sum_j G_i X_j V_j + \sum_j |G_i X_j| \, |V_j|} \quad (2)$$

where X_j and V_j are the position and velocity vector, on a grid point neighbor of G_i.

The selected vortex center is the extremum of the region where $[|LNAM|\,(LOW < 0)] \geq K = 0.7$, where K is a selected threshold and *LOW* is the local Okubo-Weiss (OW) parameter. In addition, only when there is a closed streamline outside the selected extreme value can it be left as the center of the vortex.

For each closed streamline around the center of the vortex, the radius corresponding to the circle is equal to the square root of the area corresponding to the closed streamline:

$$\langle R \rangle = \sqrt{A/\pi} \quad (3)$$

The average velocity can be calculated by the integral along the closed streamline:

$$\langle V \rangle = \frac{1}{L_p} \oint V dl \quad (4)$$

where L_p is the circumference of the closed streamline. Through this method, the maximum average velocity$V_{\max} = \max(\langle V \rangle)$ can be obtained and corresponds to the radius R_{max}, that is to say$\langle V \rangle$ $(r = R_{\max}) = V_{\max}$. The closed streamline corresponding to V_{max} serves as the boundary of the eddy.

In this study, we also use the OW parameter to detect the eddies. The OW parameter evaluates the relative amplitude between the local deformation and local rotation. The eddy center is dominated by vorticity and the negative values of the OW parameter are expected in the core of the eddy. However, the OW parameter is quite sensitive to the threshold value used to identify and characterize the eddy boundary when quantifying eddy intensity. On the one hand, weak eddies could be excluded, while on the other hand, intense eddies could lead to multiple contours. Moreover, the geometry of the OW contours could strongly differ from the geometry of the velocity vector field. In our case, when $T > 2.93T_0$, we cannot find A_0's closed streamline. As AMEDA can only be used in eddy detection when closed streamlines are present, the algorithm can no longer be used and thus instead, we used the OW parameter to define the position and shapes of the eddy to examine the eddy–eddy interaction in the end stage of A_0.

RESULTS

Evolution of an Anticyclonic Eddy

We conducted a series of island wake experiments in the LEGI-Coriolis platform, and only a few experiments yielded the eddy–eddy interaction phenomena. In the present study, the anticyclonic eddy A_0 is the only one whose whole lifetime was observed in the experiments. In this laboratory experiment, when the cylinder (the ideal island) is towed azimuthally through the water surface layer, cyclonic-anticyclonic eddy pairs are generated on the leeward side of the island (**Figure 1B**). Three pairs of cyclonic and anticyclonic eddies are detected, shown in **Figure 2f**. To better show the results, we do not show all three pairs in other panels of **Figure 2**. In **Figure 2f**, C_1 and A_1 represent a pair of cyclonic and anticyclonic eddies generated before A_0 and C_0 are generated, respectively, C_2 and A_2 are another pair of cyclonic and anticyclonic eddies, respectively, after A_0 and C_0 are generated. In the present study, we focus on the anticyclonic eddy A_0 because the experiment encapsulates the complete eddy lifecycle.

Figure 2 shows a complete life evolution process of an anticyclonic eddy, denoted as A_0. The vectors in **Figure 2** represent the normalized velocity (V_n) which is the water particles velocity (V) relative to the cylinder moving velocity (V_{tow}), and normalized by V_{tow}: $V_n = V/V_{tow}$. The color in **Figure 2** represents the relative vorticity ζ_n ($\zeta_n = \zeta/f$, $\zeta = \partial_x v - \partial_y u$, u and v are the x-direction and y-direction components of V_n, respectively.).

The red circles denote the boundaries of the anticyclonic eddy A_0, and the red solid lines are the tracks of A_0. When the cylinder is towed through $y = 0$, the time is recorded as $T = 0$. During the early stage of the formation of A_0 (**Figures 2a–b**), its elliptical shape becomes unstable. As time progresses, the form of A_0 develops into a regular circle and moves to the positive y-direction (**Figures 2c–g**).

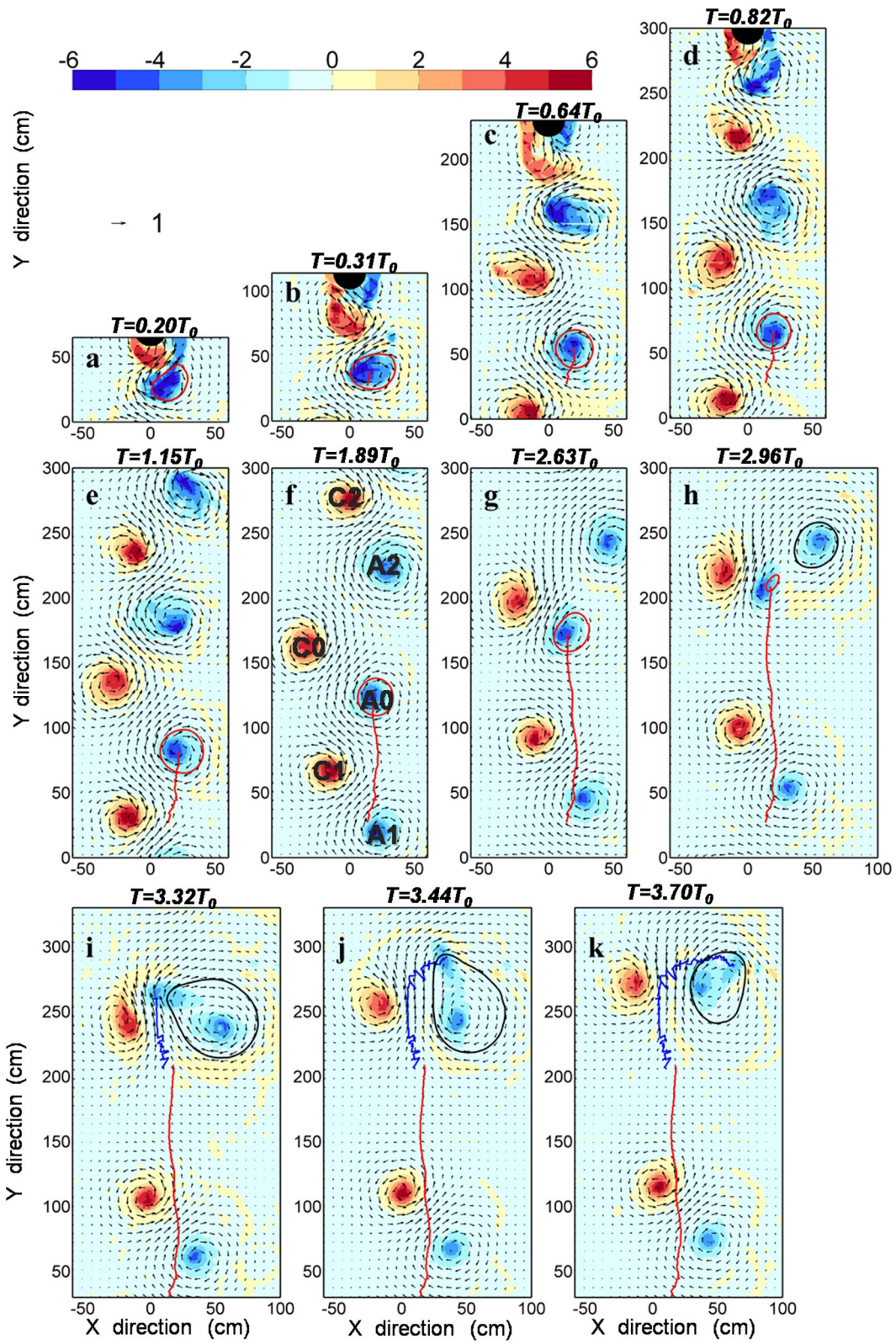

FIGURE 2 | Time evolution of the anticyclonic eddy A_0. Shading represents relative vorticity and vectors represent relative velocity. Panels **(a–k)** correspond to different times. Red circles **(a–h)** represent the shapes of anticyclonic eddy A_0. The red solid line indicates the tracks of A_0. Black circles (**h–k**) represent the shapes of anticyclonic eddy A_2. The blue solid lines (**i–k**) indicate the moving path of the maximum negative vorticity value after A_0 disappears.

The size of A_0 does not noticeably change, but its vorticity decreases gradually (inertial instability to be discussed later). However, in the late stage of A_0 (**Figure 2h**), after being affected by the C_0 cyclonic eddy (i.e., eddy–eddy interaction), its size rapidly decreases, inducing significant eddy-core deformation. Moreover, its translation speed in the y-direction accelerates, approaching C_0 (**Figure 2f–h**). Thereafter, the anticyclonic eddy, A_0, is severely deformed. In a later stage, the A_0 anticyclonic eddy is strongly affected by another anticyclonic eddy (A_2), causing further deformation. Although there is still negative vorticity at its core, no closed streamlines can be drawn and thus no significant vorticity can be measured for A_0.

As shown in **Figures 2i–k**, A_0 is wrapped around A_2 in a clockwise manner, as can be observed in the vorticity field. From the closed streamline drawn in **Figures 2i–k**, it can be seen that A_0 and A_2 tend to merge to form another anticyclonic, significantly increasing A_2's size.

Under the influence of C_0, the combined eddy A_2 (merged with A_0) is irregular in shape and stretches significantly in the direction of C_0. At the time $T = 3.70\ T_0$, the last record for the A_0, the A_0 is almost completely merged into A_2.

To better understand the life evolution process of the anticyclonic eddy A_0, the azimuthal averaged relative velocity and relative vorticity profiles of A_0 at four-time steps ($T = 0.31T_0$, $1.15T_0$, $1.89T_0$, and $2.78T_0$) are presented in **Figure 3**. **Figure 3A** shows that at $T = 0.31T_0$, V_n reaches a maximum value of 0.89 during its whole lifetime. The radius corresponding to the maximum speed is 1.25, which is normalized by the radius of the cylinder (12.5 cm). The eddy radius is defined as the distance between the location of the maximum speed and eddy center, as shown in section "Angular Momentum Eddy Detection and Tracking Algorithm." It is observed that A_0's speed and its radius both decrease with time. The vorticity normalized by f near the center of A_0 can reach -5.3 at $T = 0.3T_0$, accompanied by a sharp vorticity gradient (**Figure 3B**). As time progress, the relative vorticity decreases, and the vorticity profiles of A_0's asymptote to a maximum value.

To show the temporal evolution of A_0 in more details, we use the AMEDA eddy detection method (as detailed in section "Angular Momentum Eddy Detection and Tracking Algorithm") to obtain time series of four physical parameters about A_0: (i) the maximum normalized velocity V_{nmax}; (ii) the maximum relative radius R_{nmax} ($R_{nmax} = R_{max}/R_{island}$); (iii) the area-averaged normalized kinetic energy [$KE_n = \frac{1}{n}\sum_{i=1}^{n}\frac{1}{2}Vn_i^2$, ($i$ is the grid point inside A_0)]; and (iv) the ellipticity (E, $E = 1 - \frac{a}{b}$, where a and b are the semi-major and semi-minor axes of A_0, respectively).

In **Figure 4a** one can see that the V_{nmax} reaches the maximum value of 0.89 in the early stages of its formation, i.e., at $T = 0.3T_0$. Thereafter, between $T > 0.3T_0$ and $T \leq 2.6T_0$, V_{nmax} gradually decreases. After $T = 2.6\ T_0$, V_{nmax} enters a rapidly decaying period. All the four-time series in **Figure 4** show that the lifetime of A_0 can be divided into three periods: (1) the early turbulence stage (0–$0.3T_0$), in which the unstable processed is dominated; (2) the slow decaying period (0.3–$2.6T_0$), which is controlled by inertial instability, to be discussed in section "Internal Factor: Inertial Instability for the Slow Decaying Period"; (3) the rapid decaying period ($T > 2.6T_0$), which is controlled by eddy–eddy interaction, to be discussed in section "External Factor: Eddy–Eddy Interactions for the Rapid Decaying Period."

Figure 4b shows that R_{nmax} of A_0 fluctuates around $R_{nmax} = 1.2$ during the slow decaying period ($0.3T_0 < T \leq 2.6T_0$). During the slow decaying period, the maximum R_{nmax} is 1.4, and the minimum R_{nmax} is 1, which is approximately equal to the radius of the cylinder used in the experiment. In the period of rapid decaying, the maximum velocity of the eddy decays with its radius.

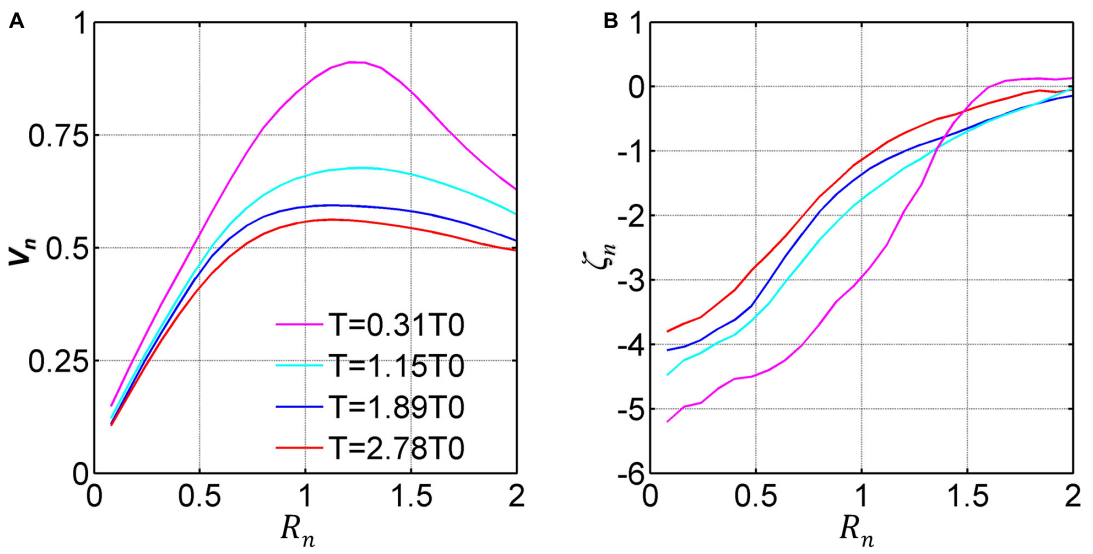

FIGURE 3 | Circle averaged of **(A)** relative velocity (V_n) and **(B)** relative vorticity (ζ_n) for A_0 at different intervals.

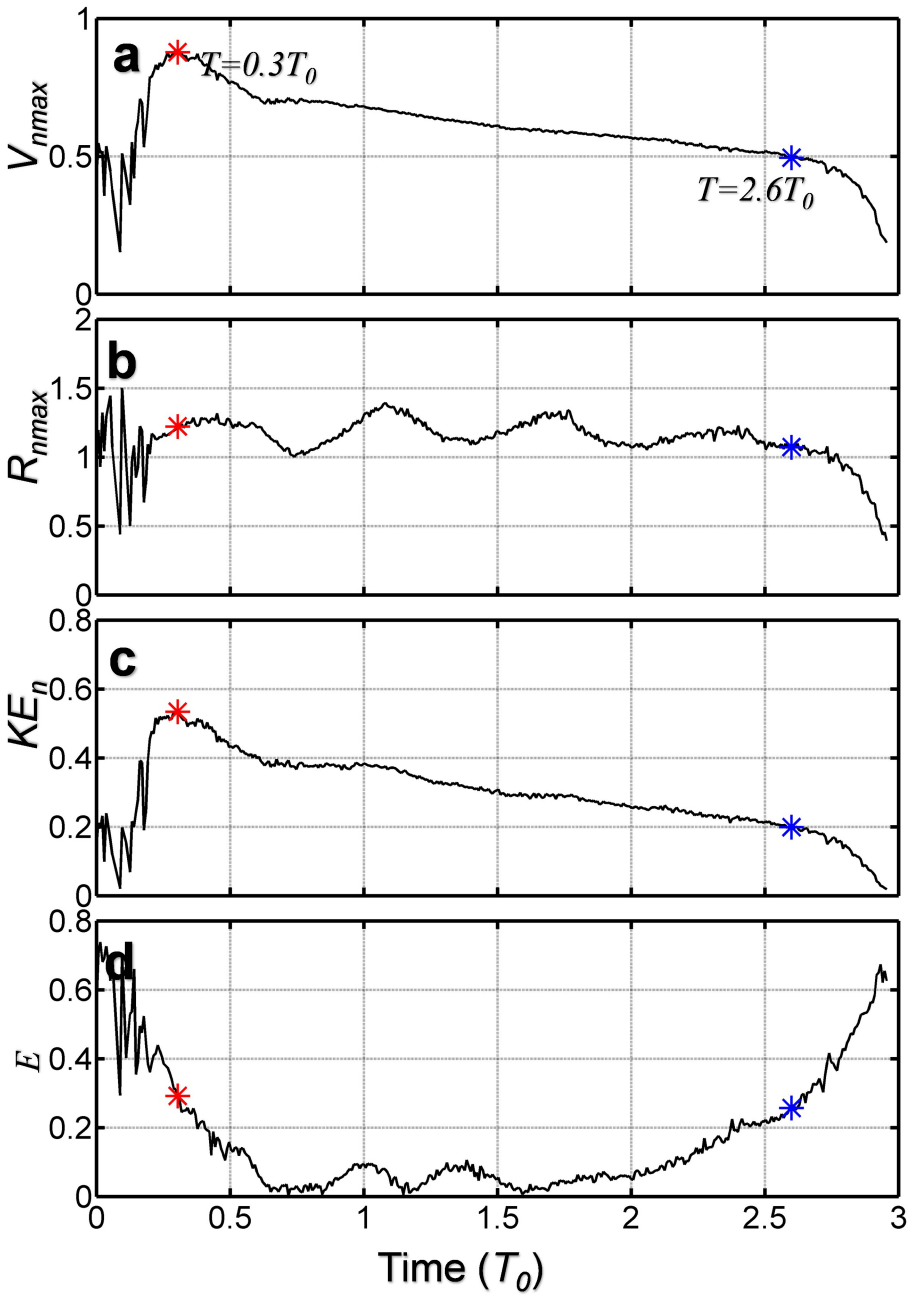

FIGURE 4 | Time evolution of **(a)** maximum relative velocity V_{nmax}, **(b)** maximum relative radius R_{nmax}, **(c)** local mean relative KE_n, and **(d)** local mean ellipticity E for A_0, respectively. The red asterisk and the blue asterisk indicate the beginning of A_0 slow and rapid weakening, respectively.

From **Figure 4c**, it can be shown that the maximum value of KE_n of A_0 can reach the value of 0.5. It should be noted that, as discussed above, the KE_n is calculated using normalized velocity, which is normalized by towing speed. The maximum value of KE_n can reach 0.5, that is to say, the area-averaged kinetic energy of A_0 could reach half of the background current.

During the early stages of the eddy formation, the eddy velocity is slow and highly unstable, concurrent with a strong variability of its form ("elliptical pumping"). The island boundary layer strongly interacts with the eddy during its formation. After shedding from the island, the eddy vorticity holds its elliptical for a while. After A_0 starts decaying slowly ($0.3T_0 < T \leq 2.6T_0$), the eddy elliptical shape (E) is small (**Figure 4d**), whereas during its last stages ($T > 2.6T_0$), the ellipticity increases rapidly, suggesting that the anticyclone becomes severely deformed. Nevertheless, the main difference between the early and last stages of the eddy formation is that during its turbulent birth, pumping might occur inducing strong vertical motions before shedding takes place,

whereas at the end of its life, the "eddy pumping" no longer occurs (Casella et al., 2014; Meunier et al., 2018; Perfect et al., 2018).

In the following two sections, we examine the potential mechanisms causing the eddy decaying: inertial instability and eddy–eddy interaction.

Internal Factor: Inertial Instability for the Slow Decaying Period

The Rayleigh criterion is used to determine whether or not inertial instability occurs (Rayleigh, 1916; Kloosterziel and Van Heijst, 1991; Mutabazi et al., 1992). The Rayleigh criterion is a sufficient condition for the inertial instability for an eddy, which can be expressed as:

$$\chi(r) = [\zeta + f]\left[\frac{2V(r)}{r} + f\right] < 0 \tag{5}$$

where $V(r)$ is the azimuth velocity $V(r)$ is negative (positive) for the clockwise (counter-clockwise) flow, r is the radius of the eddy. The inertial instability can induce three-dimensional turbulence in the edge of anticyclonic eddies (Kloosterziel et al., 2007), which can weaken the intensity of the anticyclones (Dong et al., 2007). However, the Rayleigh criterion does not takes into account the stratification and the dissipation. The stratification induces a low wavenumber cutoff (confining the instability to wavelengths below a threshold) for the inertial instability of jets (Plougonven and Zeitlin, 2009) or circular eddies (Billant and Gallaire, 2005; Kloosterziel et al., 2007; Lazar et al., 2013a). Short vertical wavelength perturbations are also damped by the vertical dissipation, reducing their growth rate. Hence, new marginal stability criterions, taking into account the dissipation, were proposed recently (Lazar et al., 2013a; Yim et al., 2019). Moreover, stability analysis have investigated the impact of the baroclinic structure on the inertial instability of vortices (Lahaye and Zeitlin, 2015; Mahdinia et al., 2017; Yim et al., 2019). Nevertheless, the results of Yim et al. (2019) reveal that the growth rates and the marginal stability limit of the centrifugal modes are close to those calculated for an equivalent barotropic columnar eddy.

To examine the mechanism of A_0's slow decay, we plot profiles of the angular average of the relative velocity V_n, relative vorticity ζ_n and the normalized Rayleigh criterion $\chi_n = \chi/f^2$ in **Figure 5**. In **Figures 5a,b**, it can be seen that the normalized azimuth velocity decreases, with the maximum velocity appearing at roughly R_n = 1.2. The magnitude of the normalized relative vorticity also decreases with time while its initial value reaches about −5.0. From **Figure 5c**, one can clearly see that the χ_n is negative between 1 and 2.5 R_n from the beginning to the end, which suggests that inertial instability occurs and causes the slow decaying of A_0. After $T = 2.6T_0$, the value of χ_n is close to zero, and other processes starts to replace the inertial instability to cause the eddy decaying, which is the eddy–eddy interaction (discussed in section "External Factor: Eddy–Eddy Interactions for the Rapid Decaying Period").

Due to the availability of the data from laboratory experiments, the effects of the stratification and baroclinic instability are not applied to the dynamic analysis in the present study. However, from the data analysis based on Rayleigh

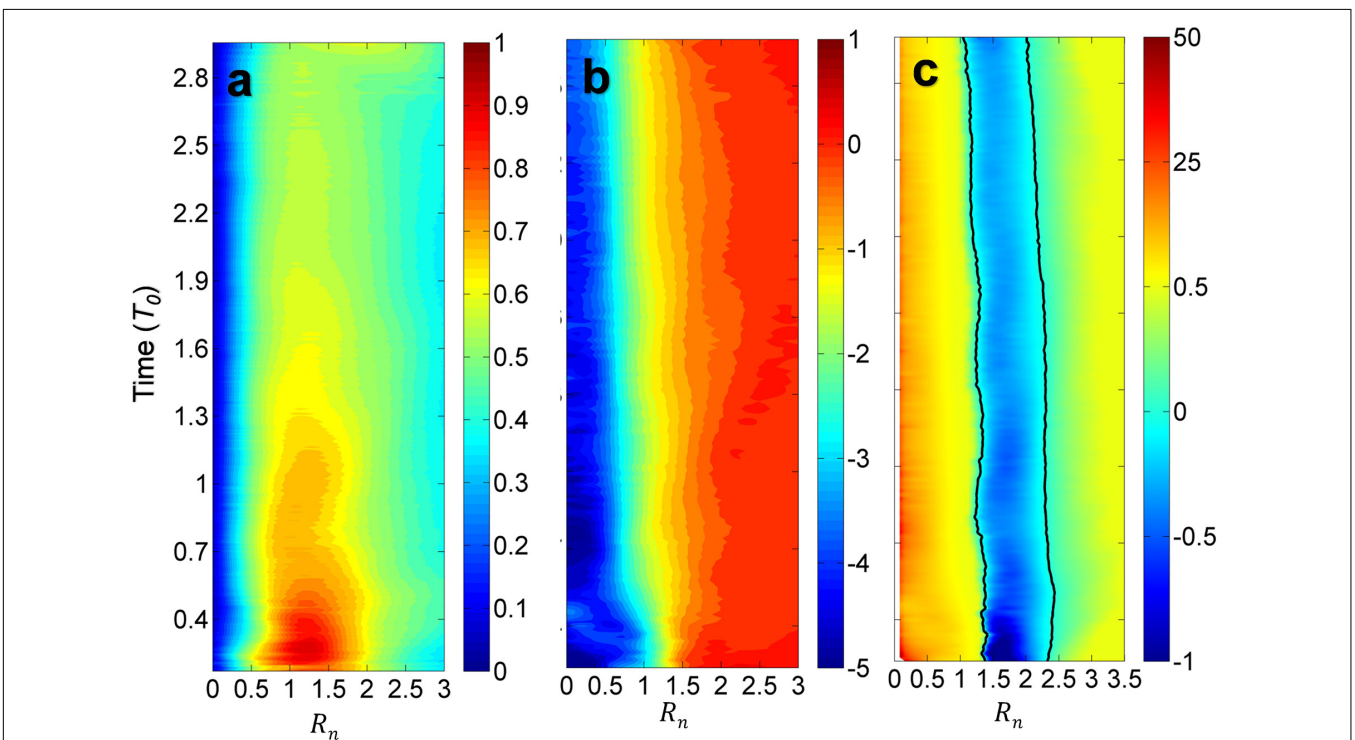

FIGURE 5 | Time evolution of the circular averages of **(a)** relative velocity (V_n), **(b)** relative vorticity (ζ_n), and **(c)** normalized Rayleigh criteria (χ_n) for A_0, respectively.

criteria, inertial instability occurs because of the large magnitude of the relative vertical vorticity. Therefore, it can be concluded that inertial instability plays a key role in the eddy decay in its first phase of instability, and baroclinic instability might play an indirect role, which needs more data of the stratification to justify the argument.

External Factor: Eddy–Eddy Interactions for the Rapid Decaying Period

Phenomenon: A_0 Is Severely Deformed

In the late stage of A_0 evolution (after $T = 2.6T_0$), when A_0 feels the influence from the C_0 (**Figure 2h**), the size of A_0 rapidly decreases and its shape changes significantly. Moreover, its moving speed in the y-direction accelerates when it approaches C_0. After $T = 2.96T_0$, A_0 is severely deformed and the AMEDA method cannot detect its closed streamline. It is visible only in the relative vorticity field.

The strong deformation to the shape of the eddy is evident in the time series of the strain rate. The strain rate is an effective parameter to characterize the eddy shape, which can be expressed as follows:

$$Sr = \sqrt{\left(\frac{\partial u}{\partial x} - \frac{\partial v}{\partial y}\right)^2 + \left(\frac{\partial v}{\partial x} + \frac{\partial u}{\partial y}\right)^2} \tag{6}$$

where u and v are the x-direction and y-direction components of V, the first part $(\frac{\partial u}{\partial x} - \frac{\partial v}{\partial y})$ is the stretching of the flow field and

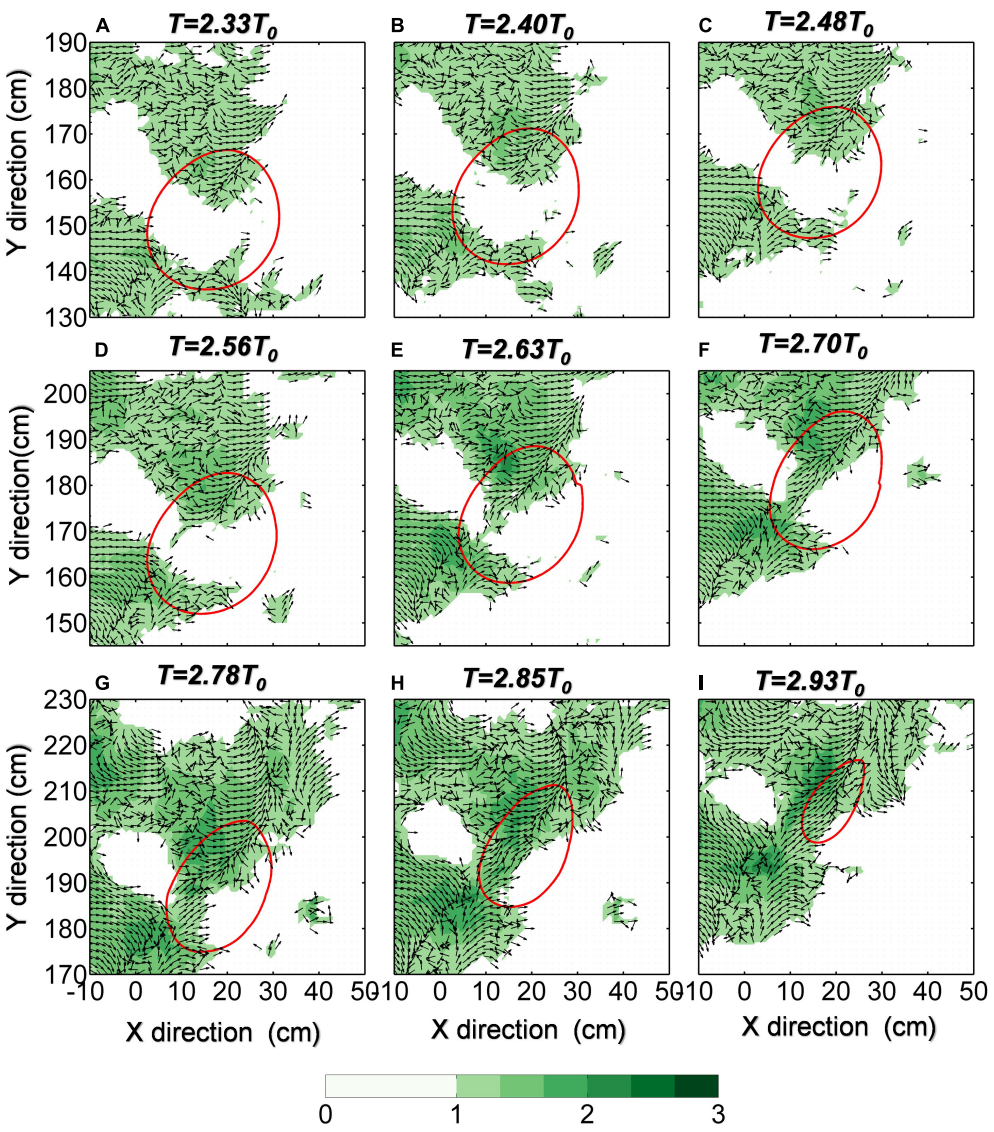

FIGURE 6 | The normalized strain rate field (values less than 1 are not displayed) at different times (Panels **A–I** correspond to $T = 2.33T_0$, $2.40T_0$, $2.48T_0$, $2.56T_0$, $2.63T_0$, $2.70T_0$, $2.78T_0$, $2.85T0$, $2.93T_0$) near A_0. Shading represent the magnitudes and vectors represent directions. Red circles represent the shapes of the anticyclonic eddy A_0.

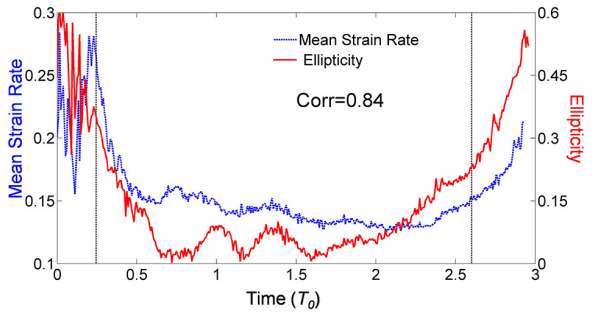

FIGURE 7 | Time evolution of the local mean strain rate (blue dotted line) and ellipticity (red solid line, also shown in **Figure 4d**) for A_0. Two black dotted lines represent the beginnings of slowly weakening and rapidly weakening for A_0, respectively.

the second part ($\frac{\partial v}{\partial x} + \frac{\partial u}{\partial y}$) is the contribution to the strain from flow shearing. The ratio of the two parts represents the stretching direction. The stretching direction can be calculated using the following:

$$\theta = \frac{1}{2}\tan^{-1}\left(\frac{\partial u/\partial y + \partial v/\partial x}{\partial u/\partial x - \partial v/\partial y}\right) \quad (7)$$

Figure 6 shows the time series of the spatial distribution of the normalized strain rate (Sr/f) filed and its direction. In **Figures 6A–E**, one can see that before $T = 2.6T_0$ (before it is affected by C_0), the strain rates near the center of A_0 are small, and their stretching directions are not consistent. By contrast, it can be seen from **Figures 6F–I** that: after $T = 2.6T_0$ (it starts to be affected by C_0), strain rates near the center of A_0 show a rapid increase and the stretching directions are consistent. Since the strain rate direction is equivalent to the stretching direction, A_0 extends along the strain rate's direction (**Figures 6F–I**).

The development of A_0 can also be illustrated by its evolution of the strain rate and ellipticity. **Figure 7** shows the time evolution of the strain rate and the ellipticity of

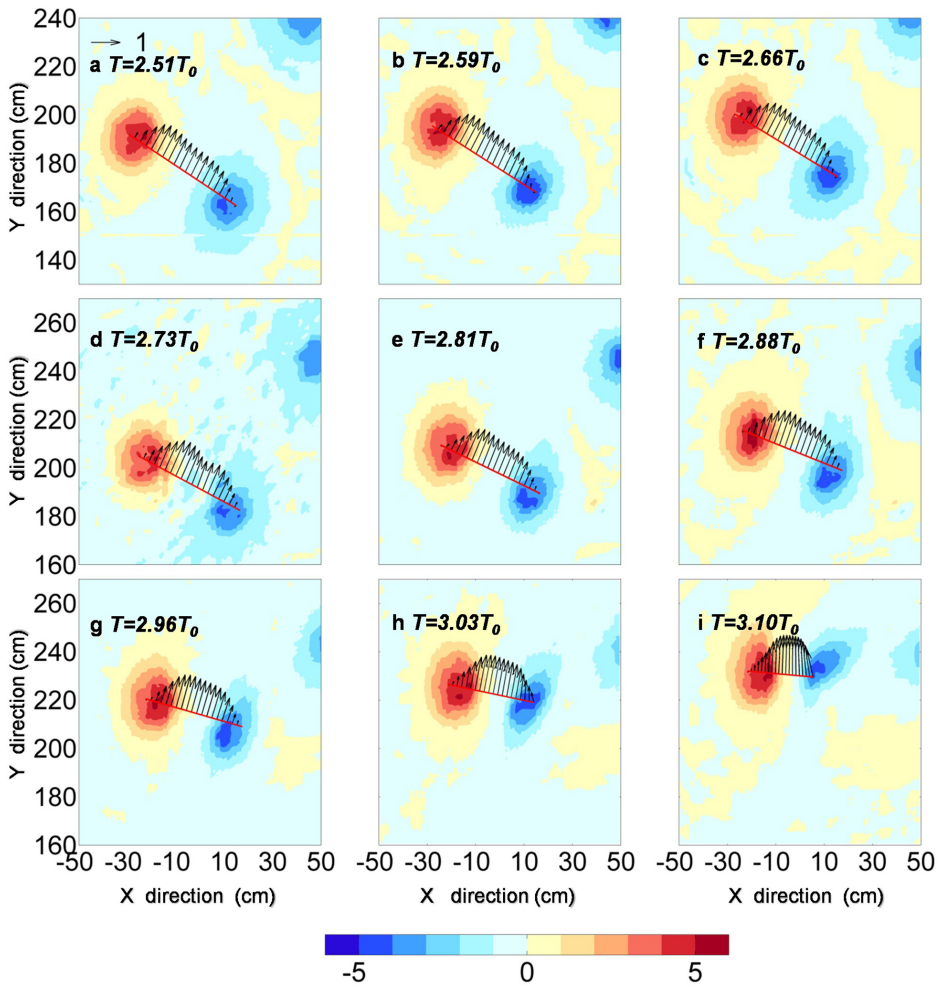

FIGURE 8 | The velocity field between the centers of C_2 and A_0 at different times (Panels **a–i** correspond to $T = 2.51T_0$, $2.59T_0$, $2.66T_0$, $2.73T_0$, $2.81T_0$, $2.88T_0$, $2.96T_0$, $3.03T_0$, and $3.10T_0$). Shading represents relative vorticity, and vectors represents relative velocity.

A_0, both of which can depict the temporal variation of A_0's deformation (their correlation is 0.83). They are in disordered states during A_0's formation stage (before $T = 0.3T_0$). During the slow decaying period, the strain rate and ellipticity values are small, which imply that the A_0 is in a steady state and A_0's shapes is close to circular. During the rapid decaying period, both variables increases rapidly, implying A_0 is severely deformed, see **Figures 2g–h**. From the discussion below (section

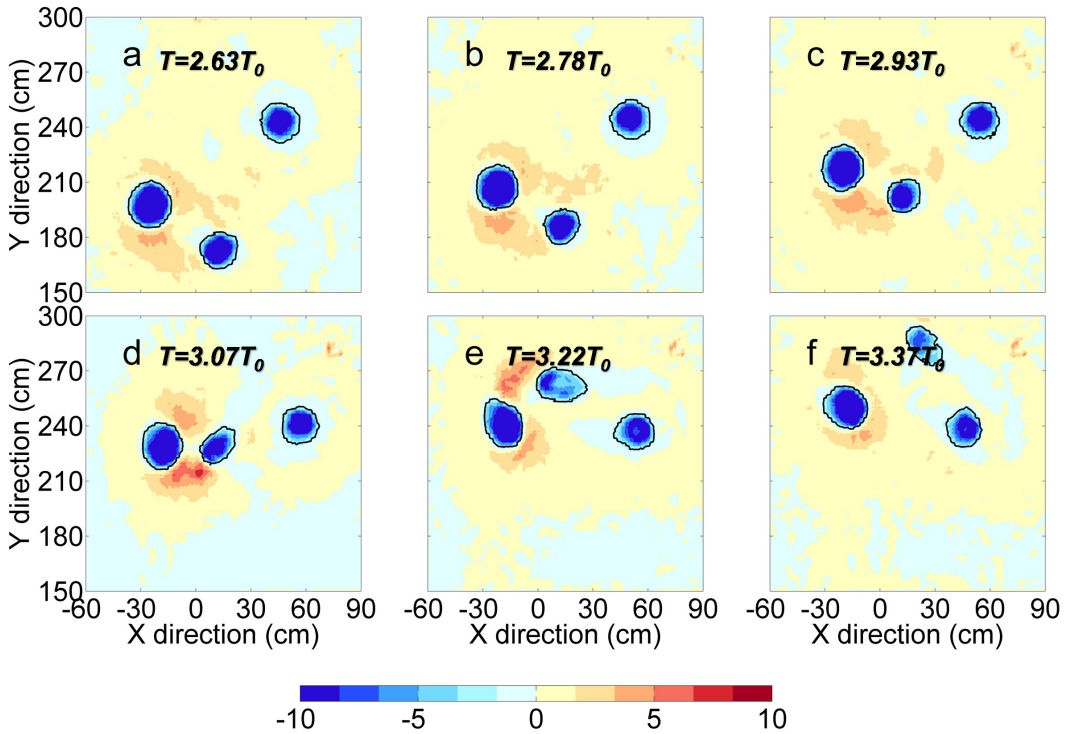

FIGURE 9 | The Okubo-Weiss parameter (Q_n) near A_0 at different times (Panels **a–f** correspond to $T = 2.63T_0$, $2.78T_0$, $2.93T_0$, $3.07T_0$, $3.22T_0$, $3.37T_0$). The black lines represent the isolines ($Q_n = 2$) which demarcate eddy boundaries.

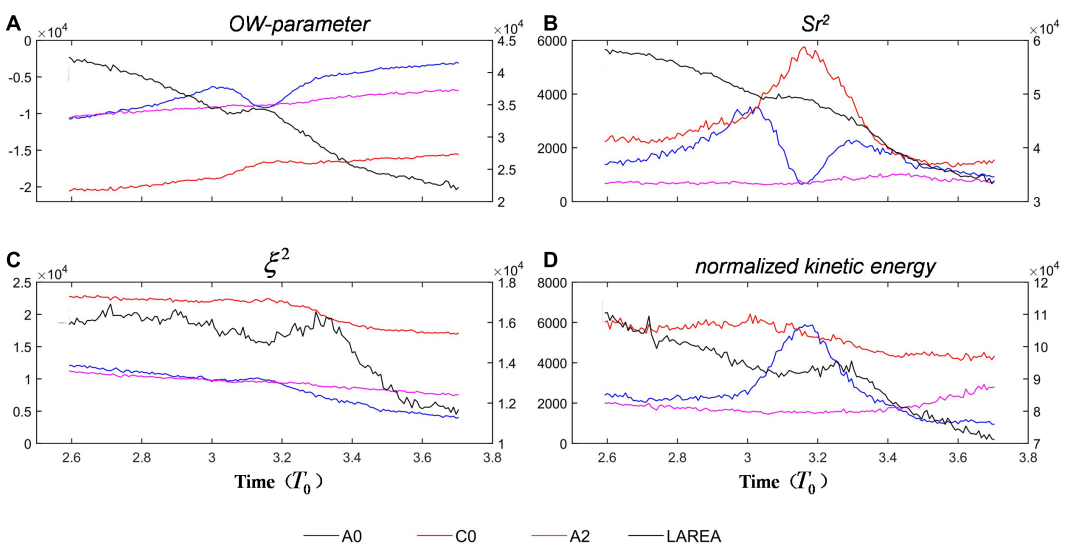

FIGURE 10 | (A) Time evolution of the Okubo-Weiss parameter. The blue, red, and pink lines give the inner eddy local means of A_0, C_0, and A_2, respectively. The black line gives the local mean of area enclosed by X: –60 to 90 cm, Y: 150–300 cm, with the contribution of the A_0, C_0, and A_2 eddies removed. **(B)** The same with panel **(A)** but for Sr^2. **(C)** The same with panel **(A)** but for enstrophy (ξ^2). **(D)** The same with panel **(A)** but for normalized kinetic energy.

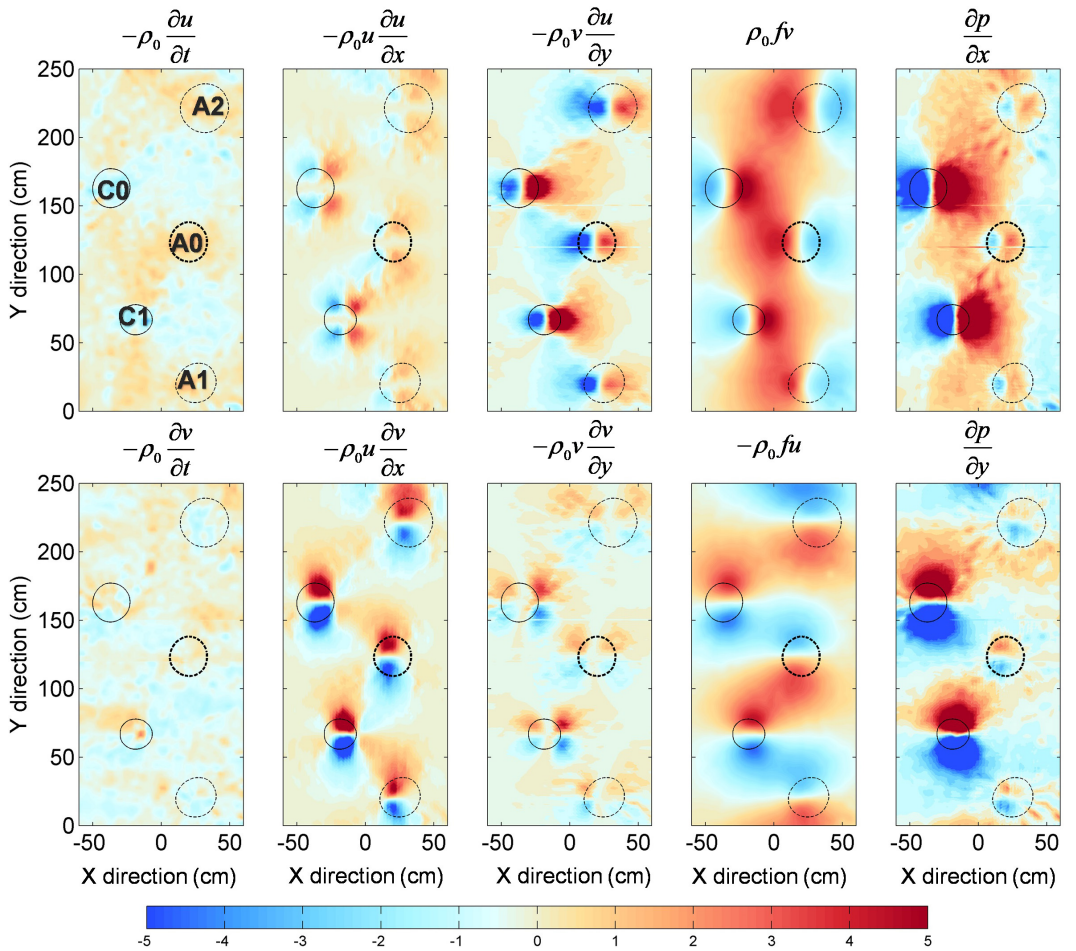

FIGURE 11 | The contributions of different terms in the flow governing equation to the pressure gradient for A_0 at T = 1.52 T_0.

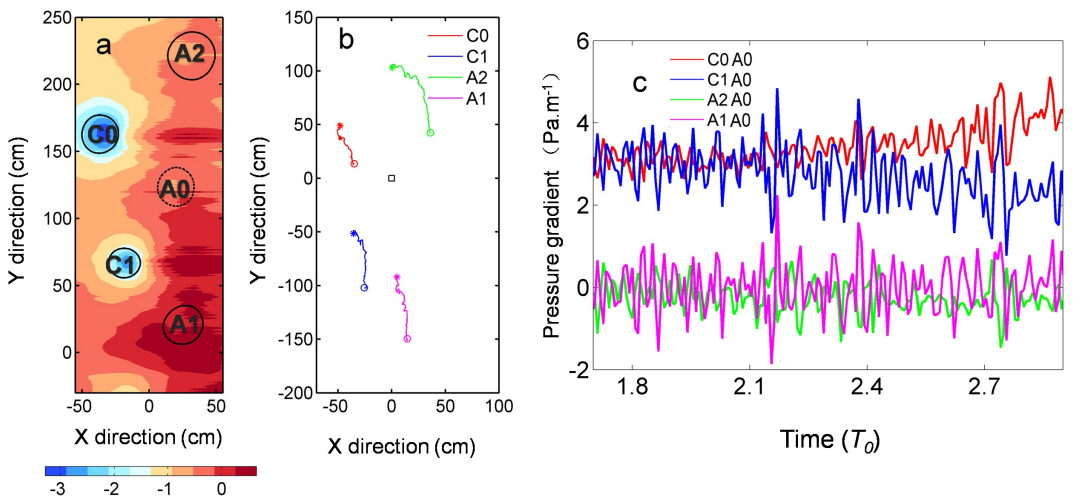

FIGURE 12 | (a) The pressure field estimated using the flow governing equation at T = 1.52 T_0. **(b)** The relative positions of C_0, C_1, A_2, and A_1 with respect to A_0. **(c)** The time evolution of the pressure gradient between C_1 and A_0, C_0 and A_0, A_2 and A_0, A_1 and A_0. The color of the lines is corresponding to panel **(b)**.

"Mechanism: Eddy–Eddy Interaction Between A_0 and C_0"), the strong deformation of A_0 is caused by the interaction between A_0 and C_0.

Mechanism: Eddy–Eddy Interaction Between A_0 and C_0

To explore the reason for the strong deformation of the A_0's shape, the eddy–eddy interaction between A_0 and C_0 is examined. In **Figure 8**, the velocity between the centers of C_0 and A_0 at different time intervals are plotted. It can be seen that A_0 is dragged toward C_0 and simultaneously stretched severely by C_0, and there is a strong velocity shear between them.

When $T > 2.93T_0$, we cannot find A_0's closed streamline. As AMEDA can only be used in eddy detection when closed streamlines are present, the algorithm can no longer be used and thus instead, we used the OW parameter to define the position and shapes of the eddy to examine the eddy–eddy interaction in the end stage of A_0. The normalized OW parameter (McWilliams, 1984; Weiss, 1991; Hua and Klein, 1998) is defined as:

$$Q_n = \frac{Sr^2 - \zeta^2}{f^2} \tag{8}$$

where Sr is the strain rate.

Figure 9 shows the evolution of distribution of Q_n. The isolines ($Q_n = 2$) are selected as eddy boundaries. The geometry of the stream function field (deduced from the horizontal motions) involves elliptical (or circular) and hyperbolic flow structures. When the strain rate exceeds the vorticity, the fluid is in a hyperbolic mode of motion. When the vorticity exceeds the strain, the fluid is in an elliptical mode of motion that advects the vorticity smoothly (Weiss, 1991). Q_n is larger than 0 between A_0 and C_0, which means that strain dominates the region with respect to the hyperbolic structures.

Using the OW parameter, we determine the size and shape of eddies. We then calculate the time evolution of OW parameter and its two parts: the strain energy (Sr^2) and the enstrophy (ζ^2), and the total kinetic energy inside A_0, C_0, A_2 and the left area (X: −60 to 90 cm, Y: 150–300 cm, which shown in **Figure 9**). As can be seen from **Figure 10A**, the OW parameter in the eddy region is negative and approaches 0, while the value in the left area is positive and also close to 0, because both the strain rate and the enstrophy are decreasing. During $3T_0 < T < 3.4T_0$, the OW parameter of A_0, C_0 and left area have large perturbations. This signal can also be clearly seen in **Figures 10B,C**, which corresponding to the period of strongest interaction between A_0 and C_0. In **Figure 10D**, it can be seen that the total kinetic energy in the study area is gradually decreasing, which is mainly affected by friction. However, during $3T_0 < T < 3.4T_0$, the kinetic energy of A_0 first increases rapidly and then decreases rapidly. This is because A_0 enters the strong current region between A_0 and C_0 (where the flow is uniform) and leaves quickly. The rapid increase of A_0's kinetic energy corresponds to the rapid decrease of A_0 strain rate. When the strain rate of A_0 decreases, the strain rate of C_0 increases rapidly, which indicates that the shape of C_0 has changed, and the kinetic energy of C_0 begins to decay. In the left area, the kinetic energy during $3T_0 < T < 3.4\ T_0$ increases slightly. The enhanced kinetic energy in the left area may be the kinetic energy lost by C_0. At the end of the experiment, when $T > 3.4T_0$, the energy of C_0 and A_0 gradually decreased, while the energy of A_2 increased, which is due to the effect of A_0 and A_2 merging.

Here, an interesting question can be raised: why is the anticyclonic eddy A_0 affected by C_0? This can be answered through usage of the flow governing equation (for an incompressible inviscid two-dimensional fluid):

$$\begin{aligned} \frac{\partial u}{\partial t} + u\frac{\partial u}{\partial x} + v\frac{\partial u}{\partial y} - fv &= -\frac{1}{\rho_0}\frac{\partial p}{\partial x} \\ \frac{\partial v}{\partial t} + u\frac{\partial v}{\partial x} + v\frac{\partial v}{\partial y} + fu &= -\frac{1}{\rho_0}\frac{\partial p}{\partial y} \end{aligned} \tag{9}$$

wherein we can calculate each term contribute to the pressure gradient force (**Figure 11**). In our laboratory experiments, the time variation terms ($\frac{\partial u}{\partial t}$, $\frac{\partial v}{\partial t}$) make the least contributions to the pressure gradient. Both anticyclonic eddies and cyclonic eddies show a similar pattern in the nonlinear terms ($u\frac{\partial u}{\partial x}$, $v\frac{\partial u}{\partial y}$; $u\frac{\partial v}{\partial x}$, $v\frac{\partial v}{\partial y}$), and the Lamb vector terms ($v\frac{\partial u}{\partial y}$, $u\frac{\partial v}{\partial x}$) play a more vital role in the pressure gradient than the kinetic energy gradient terms ($u\frac{\partial u}{\partial x}$, $v\frac{\partial v}{\partial y}$). Under in influence of the Coriolis and nonlinear terms, the signals of the anticyclonic eddies are weakened and the signals of the cyclonic eddies are strengthened. Using eq.10, we can estimate the relative pressure field (**Figure 12a**). The cyclonic eddies and the anticyclonic eddies show an asymmetric pattern (Gallet et al., 2014; Liu and Andutta, 2020; Yang et al., 2020). The distance between C_0 and A_0 decreases (**Figure 12b**) resulting in the pressure gradient between them increases (**Figure 12c**). And although C_1 plays an equally important role in A_0 compared to C_0, the pressure gradient decrease between C_1 and A_0 in A_0's rapid decaying period ($T > 2.6T_0$).

CONCLUSION AND DISCUSSION

Through a laboratory experiment carried out on the LEGI-Coriolis rotating platform, the evolutionary lifecycle of an anticyclonic eddy is studied. Observations have suggested that in the early stage of the eddy's formation, turbulence is the main factor affecting the fluid and its shape, though generally elliptical, is not stable. As time passed, the eddy developed a more regular shape and moved to the positive Y-direction. Although the eddy's size did not noticeably change, its vorticity however gradually decreased. Later, the anticyclonic eddy interacted with a cyclonic eddy, leading to a rapid decay of the anticyclonic eddy's size in addition to significant shape deformation. An increase in the y-direction lead to the A_0 anticyclonic eddy to approach the cyclonic eddy, which then resulted in the disappearance of the A_0 eddy. Although negative vorticity continued to persist, we cannot detect closed streamlines. Moreover, the A_0 and A_2 merged to form a large anticyclonic eddy.

Further analyses have uncovered that there are two factors that affect the weakening of the A_0 anticyclonic eddy. In the early stage, the eddy's own inertial instability contributed to slow weakening but after $T = 2.6T_0$, inertial instability itself weakened, but paradoxically, the pace of A_0's decay quickened. In later stages, A_0's rapid decay began to be affected by other eddies. Through a calculation of the strain rate, it is found that in the

A_0's later stages, the eddy is becoming increasingly affected by. This led to the strain rate of the A_0 eddy gradually increasing, leading to the destruction of the eddy's circulation structure and hence, leading to A_0's rapid decay.

Through laboratory experiments, the present study finds that eddy interaction can cause a change in the eddy's strain rate, which results in an eddy decay. We derive the pressure gradient field from the experiments which did not measure the relative pressure fields. The pressure gradient is used to discuss the dynamic cause of eddy motion. This study reveals the influence of inertial instability and eddy–eddy interaction on the anticyclonic eddy's life evolution from the perspective of laboratory observation and contributes to our better understanding of eddy–eddy interaction and mechanisms of eddy decay.

It should be noted that the conclusions are reached based on the analysis of one single experiment. The sensitivity of the conclusions to physical paraments cannot be tested: such as the cylinder size, rotating speed, towering speed, and so on. Without the sensitivity experiments, the generalization of the conclusions is limited. Moreover, such sensitivity is important for one to better understand the physical mechanisms involved in the process. We will continue the study in the future by conducting more lab experiments about the subject.

DATA AVAILABILITY STATEMENT

The original contributions presented in the study are included in the article/supplementary material, further inquiries can be directed to the corresponding author.

AUTHOR CONTRIBUTIONS

GH and CD did literature search, collected the data, processed the data, and wrote the manuscript. JY, JS, AS, RC, and CD contributed to the revision of the manuscript. JS, AS, and RC participated in the data processing. All authors contributed to the article and approved the submitted version.

FUNDING

This work was supported by the National Key Research and Development Program of China (Nos. 2017YFA0604100, 2016YFA0601803, and 2016YFC1401407), the National Natural Science Foundation of China (Nos. 41476022, 41490643, and 41706008), the National Program on Global Change and AirSea Interaction (Nos. GASI-IPOVAI-02 and GASI-03-IPOVAI-05), and the China Ocean Mineral Resources R&D Association (Nos. DY135-E2-2-02 and DY135-E2-3-01). The authors are also grateful to 6th European Commission (EC) framework program – HYDRALAB, for the funding provided.

ACKNOWLEDGMENTS

These successful experiments took place on the Grenoble LEGI-Coriolis Laboratory, thanks to the expertise of Samuel Viboud and Henri Didelle on rotating experiments.

REFERENCES

Alford, M. H., Shcherbina, A. Y., and Gregg, M. C. (2013). Observations of near-inertial internal gravity waves radiating from a frontal jet. *J. Phys. Oceanogr.* 43, 1225–1239. doi: 10.1175/jpo-d-12-0146.1

Arbic, B. K., Shriver, J. F., Hogan, P. J., and Hurlburt, H. E. (2009). Estimates of bottom flows and bottom boundary layer dissipation of the oceanic general circulation from global high-resolution models. *J. Geophys. Res. Atmos.* 114:C02024.

Billant, P., and Gallaire, F. (2005). Generalized Rayleigh criterion for non-axisymmetric centrifugal instabilities. *J. Fluid Mech.* 542, 365–379. doi: 10.1017/s0022112005006464

Boyer, D. L., and Davies, P. (1982). Flow past a cylinder on a beta plane. *Philos. Trans. Roy. Soc. London*. 306A, 33–56.

Caldeira, R. M. A., Marchesiello, P., Nezlin, N. P., Digiacomo, P. M., and McWilliams, J. C. (2005). Island wakes in the southern California Bight. *J. Geophys. Res. Oceans* 110:C11012.

Carnevale, G. F., Kloosterziel, R. C., Orlandi, P., and van Sommeren, D. D. J. A. (2011). Predicting the aftermath of vortex breakup in rotating flow. *J. Fluid Mech.* 669, 90–119. doi: 10.1017/s0022112010004945

Casella, E., Tepsich, P., Couvelard, X., Caldeira, R. M. A., and Schroeder, K. (2014). Ecosystem dynamics in the Liguro-Provençal Basin: the role of eddies in the biological production. *Mediterr. Mar. Sci.* 15, 274–286. doi: 10.12681/mms.520

Coutis, P. F., and Middleton, J. H. (2002). The physical and biological impact of a small island wake in the deep ocean. *Deep-Sea Res. Oceanogr. Res. Pap.* 49, 1341–1361. doi: 10.1016/s0967-0637(02)00029-8

Cui, W., Wang, W., Zhang, J., and Yang, J. (2019). Multicore structures and the splitting and merging of eddies in global oceans from satellite altimeter data. *Ocean Sci.* 15, 413–430. doi: 10.5194/os-15-413-2019

de Marez, C., Xavier, C., L'Hégaret, P., Meunier, T., Stegner, A., Morvan, M., et al. (2020). Oceanic vortex mergers are not isolated but influenced by the β-effect and surrounding eddies. *Sci. Rep.* 10:2897.

Doglioli, A. M., Griffa, A., and Magaldi, M. G. (2004). Numerical study of a coastal current on a steep slope in presence of a cape: the case of the Promontorio di Portofino. *J. Geophys. Res.* 109:C12033. doi: 10.1029/2004JC002422

Dong, C., Cao, Y., and McWilliams, J. C. (2018). Island wakes in shallow water. *Atmos.-Ocean* 56, 96–103. doi: 10.1080/07055900.2018.1448750

Dong, C., McWilliams, J. C., and Shchepetkin, A. F. (2007). Island wakes in deep water. *J. Phys. Oceanogr.* 37, 962–981. doi: 10.1175/jpo3047.1

Dritschel, D. G., and Waugh, D. W. (1992). Quantification of the inelastic interaction of unequal vortices in two-dimensional vortex dynamics. *Phys Fluids A* 4, 1737–1744. doi: 10.1063/1.858394

Duhaut, T., and Straub, D. N. (2006). Wind stress dependence on ocean surface velocity: implications for mechanical energy input to ocean circulation. *J. Phys. Oceanogr.* 36, 202–211. doi: 10.1175/jpo2842.1

Fang, F., and Morrow, R. (2003). Evolution, movement and decay of warm-core Leeuwin Current eddies. *Deep Sea Res. 2 Top. Stud. Oceanogr.* 50, 2245–2261. doi: 10.1016/s0967-0645(03)00055-9

Gallet, B., Campagne, A., Cortet, P. P., and Moisy, F. (2014). Scale-dependent cyclone-anticyclone asymmetry in a forced rotating turbulence experiment. *Phys. Fluids* 26:035108. doi: 10.1063/1.4867914

Han, G., Dong, C., Junde, L., and Yang, J. (2019). SST anomalies in the mozambique channel using remote sensing and numerical modeling data. *Remote Sens.* 11:1112. doi: 10.3390/rs11091112

Heywood, K. J., Stevens, D. P., and Bigg, G. R. (1996). Eddy formation behind the tropical island of Aldabra. *Deep-Sea Res. I* 43, 555–578.

Hua, B. L., and Klein, P. (1998). An exact criterion for the stirring properties of nearly two-dimensional turbulence. *Physica D* 113, 98–110. doi: 10.1016/s0167-2789(97)00143-7

Hughes, C. W., and Wilson, C. (2008). Wind work on the geostrophic ocean circulation: an observational study of the effect of small scales in the wind stress. *J. Geophys. Res.* 113:C02016.

Johnson, E. H., and Page, M. (1993). Flow past a circular cylinder on a beta-plane. *J. Fluid Mech.* 257, 603–626.

Kloosterziel, R. C., Carnevale, G. F., and Orlandi, P. (2007). Inertial instability in rotating and stratified fluids: barotropic vortices. *J. Fluid Mech.* 583, 379–412. doi: 10.1017/s0022112007006325

Kloosterziel, R. C., and Van Heijst, G. J. F. (1991). An experimental study of unstable barotropic vortices in a rotating fluid. *J. Fluid Mech.* 223, 1–24. doi: 10.1017/s0022112091001301

Lahaye, N., and Zeitlin, V. (2015). Centrifugal, barotropic and baroclinic instabilities of isolated ageostrophic anticyclones in the two-layer rotating shallow water model and their nonlinear saturation. *J. Fluid Mech.* 762, 5–34. doi: 10.1017/jfm.2014.631

Lazar, A., Stegner, A., Caldeira, R., Dong, C., Didelle, H., and Vuiboud, S. (2013a). Inertial instability of intense stratified anticyclones. part 2. laboratory experiments. *J. Fluid Mech.* 732, 485–509. doi: 10.1017/jfm.2013.413

Lazar, A., Stegner, A., and Heifetz, E. (2013b). Inertial instability of intense stratified anticyclones. part 1. generalized stability criterion. *J. Fluid Mech.* 732, 457–484. doi: 10.1017/jfm.2013.412

Le Vu, B., Stegner, A., and Arsouze, T. (2018). Angular momentum eddy detection and tracking algorithm (AMEDA) and its application to coastal eddy formation. *J. Atmos. Ocean. Technol.* 35, 739–762. doi: 10.1175/jtech-d-17-0010.1

Liu, Z., and Andutta, F. P. (2020). A Study on an anticyclonic-cyclonic eddy pair off Fraser Island, Australia. *Front. Marine Sci.* 7:594358. doi: 10.3389/fmars.2020.594358

Mahdinia, M., Hassanzadeh, P., Marcus, P. S., and Jiang, C. H. (2017). Stability of three-dimensional gaussian vortices in an unbounded, rotating, vertically stratified, boussinesq flow: linear analysis. *J. Fluid Mech.* 824, 97–134. doi: 10.1017/jfm.2017.303

Marshall, D. P., and Garabato, A. N. (2008). A conjecture on the role of bottom-enhanced diapycnal mixing in the parameterization of geostrophic eddies. *J. Phys. Oceanogr.* 38, 1607–1613. doi: 10.1175/2007jpo3619.1

McWilliams, J. C. (1984). The emergence of isolated coherent vortices in turbulent flow. *J. Fluid Mech.* 146, 21–43. doi: 10.1017/s0022112084001750

McCartney, M. (1975). Inertial Taylor columns on a beta plane. *J. Fluid Mech.* 68, 71–95.

Meunier, T., Pallás-Sanz, E., Tenreiro, M., Portela, E., Ochoa-de-la-Torre, J. L., Ruiz-Angulo, A., et al. (2018). The vertical structure of a Loop Current Eddy. *J. Geophys. Res. Oceans* 123, 6070–6090. doi: 10.1029/2018jc013801

Mkhinini, N., Coimbra, A. L. S., Stegner, A., and Arsouze, T. (2014). Long-lived mesoscale eddies in the eastern Mediterranean Sea: analysis of 20 years of AVISO geostrophic velocities. *J. Geophys. Res. Oceans* 119, 8603–8626. doi: 10.1002/2014jc010176

Molemaker, M. J., Mcwilliams, J. C., and Yavneh, I. (2005). Baroclinic instability and loss of balance. *J. Phys. Oceanogr.* 35, 1505–1517. doi: 10.1175/jpo2770.1

Mutabazi, I., Normand, C., and Wesfreid, J. E. (1992). Gap size effects on centrifugally and .rotationally driven instabilities. *Phys. Fluids A* 4, 1199–1205. doi: 10.1063/1.858238

Nan, F., He, Z., Zhou, H., and Wang, D. (2011). Three long-lived anticyclonic eddies in the northern South China sea. *J. Geophys. Res. Oceans* 116:C05002.

Neill, S. P., and Elliott, A. J. (2004). Observations and simulations of an unsteady island wake in the Firth of Forth, Scotland. *Ocean Dyn.* 54, 324–332.

Oster, G. (1965). Density gradients. *Sci. Am.* 213, 70–76.

Page, M. A. (1985). On the low Rossby number of a rotating fluid past a circular cylinder. *J. Fluid Mech.* 156, 205–221.

Perfect, B., Kumar, N., and Riley, J. J. (2018). Vortex structures in the wake of an idealized seamount in rotating, stratified flow. *Geophys. Res. Lett.* 45, 9098–9105. doi: 10.1029/2018gl078703

Perret, G., Stegner, A., Farge, M., and Pichon, T. (2006). Cyclone-anticyclone asymmetry of large-scale wakes in the laboratory. *Phys. Fluids* 18:036603. doi: 10.1063/1.2179387

Plougonven, R., and Zeitlin, V. (2009). Nonlinear development of inertial instability in a barotropic shear. *Phys. Fluids* 21, 1004–1013.

Rayleigh, L. (1916). On the dynamics of revolving fluids. *Proc. R Soc. Lond. A Math. Phys. Sci.* 93, 148–154. doi: 10.1098/rspa.1917.0010

Sen, A., Scott, R., and Arbic, B. (2008). Global energy dissipation rate of deep-ocean low-frequency flows by quadratic bottom boundary layer drag: computations from current-meter data. *Geophys. Res. Lett.* 35:L09606.

Sheen, K. L., Naveira Garabato, A. C., Brearley, J. A., Meredith, M. P., Polzin, K. L., Smeed, D., et al. (2014). Eddy-induced variability in Southern Ocean abyssal mixing on climatic timescales. *Nature Geosci.* 7, 577–582. doi: 10.1038/ngeo2200

Stegner, A. (2014). "Chapter 14 in modeling atmospheric and oceanic fluid flow: insights from laboratory experiments and numerical simulations, geophysical monograph 205," in *Oceanic Island Wake Flow in Laboratory*, 1st ed., eds T. von Larcher and P. D. Williams (American Geophysical Union, John Wiley and Sons, Inc.)

Tansley, C., and Marshall, D. (2001). Flow past a cylinder on a beta-plane with application to Gulf Stream separation and the Antarctic Circumpolar Current. *J. Phys. Oceanogr.* 31, 3274–3283.

Teinturier, S., Stegner, A., Didelle, H., and Viboud, S. (2010). Small-scale instabilities of an island wake flow in a rotating shallow-water layer. *Dyn. Atmos. oceans* 49, 1–24. doi: 10.1016/j.dynatmoce.2008.10.006

Tomczak, M. (1988). Island wakes in deep and shallow water. *J. Geophys. Res. Oceans* 93, 5153–5154. doi: 10.1029/jc093ic05p05153

Weiss, J. (1991). The dynamics of enstrophy transfer in two-dimensional hydrodynamics. *Physica D* 48, 273–294. doi: 10.1016/0167-2789(91)90088-q

Yang, Q., Liu, H., and Lin, P. (2020). The effect of oceanic mesoscale eddies on the looping path of the Kuroshio intrusion in the Luzon Strait. *Sci. Rep.* 10:636.

Yim, E., Stegner, A., and Billant, P. (2019). Stability criterion for the centrifugal instability of surface intensified anticyclones. *J. Phys. Oceanogr.* 49, 827–849. doi: 10.1175/jpo-d-18-0088.1

Zhai, X., Johnson, H. L., and Marshall, D. P. (2010). Significant sink of ocean-eddy energy near western boundaries. *Nat. Geosci.* 3, 608–612. doi: 10.1038/ngeo943

Conflict of Interest: The authors declare that the research was conducted in the absence of any commercial or financial relationships that could be construed as a potential conflict of interest.

frontiers in Marine Science

ORIGINAL RESEARCH
published: 07 July 2021
doi: 10.3389/fmars.2021.645672

Monsoon Influence on the Island Mass Effect Around the Maldives and Sri Lanka

Danielle Su[1,2,3], Sarath Wijeratne[1,2] and Charitha Bandula Pattiaratchi[1,2]*

[1] Oceans Graduate School, The University of Western Australia, Perth, WA, Australia, [2] The UWA Oceans Institute, Indian Ocean Marine Research Centre, Perth, WA, Australia, [3] LOCEAN Laboratory, Sorbonne Université-CNRS-IPSL, Paris, France

The monsoon circulation in the Northern Indian Ocean (NIO) is unique since it develops in response to the bi-annual reversing monsoonal winds, with the ocean currents mirroring this change through directionality and intensity. The interaction between the reversing currents and topographic features have implications for the development of the Island Mass Effect (IME) in the NIO. The IME in the NIO is characterized by areas of high chlorophyll concentrations identified through remote sensing to be located around the Maldives and Sri Lanka in the NIO. The IME around the Maldives was observed to reverse between the monsoons to downstream of the incoming monsoonal current whilst a recirculation feature known as the Sri Lanka Dome (SLD) developed off the east coast of Sri Lanka during the Southwest Monsoon (SWM). To understand the physical mechanisms underlying this monsoonal variability of the IME, a numerical model based on the Regional Ocean Modeling System (ROMS) was implemented and validated. The model was able to simulate the regional circulation and was used to investigate the three-dimensional structure of the IME around the Maldives and Sri Lanka in terms of its temperature and velocity. Results revealed that downwelling processes were prevalent along the Maldives for both monsoon periods but was applicable only to latitudes above 4°N since that was the extent of the monsoon current influence. For the Maldives, atolls located south of 4°N, were influenced by the equatorial currents. Around Sri Lanka, upwelling processes were responsible for the IME during the SWM but with strong downwelling during the NEM. In addition, there were also regional differences in intra-seasonal variability for these processes. Overall, the strength of the IME processes was closely tied to the monsoon current intensity and was found to reach its peak when the monsoon currents were at the maximum.

Keywords: monsoon currents, Indian Ocean, Island Mass Effect, Regional Ocean Model System, Sri Lanka and Maldives

OPEN ACCESS

Edited by:
Juan Jose Munoz-Perez, University of Cádiz, Spain

Reviewed by:
Rui Caldeira, Agência Regional para o Desenvolvimento da Investigação Tecnologia e Inovação (ARDITI), Portugal
Vanesa Magar, Center for Scientific Research and Higher Education in Ensenada (CICESE), Mexico
Peng Yao, Hohai University, China

****Correspondence:***
Danielle Su
dasu@dhigroup.com

Specialty section:
This article was submitted to Coastal Ocean Processes, a section of the journal Frontiers in Marine Science

Received: *23 December 2020*
Accepted: *31 May 2021*
Published: *07 July 2021*

Citation:
Su D, Wijeratne S and Pattiaratchi CB (2021) Monsoon Influence on the Island Mass Effect Around the Maldives and Sri Lanka. Front. Mar. Sci. 8:645672. doi: 10.3389/fmars.2021.645672

INTRODUCTION

The Maldives island chain and Sri Lanka occupy a unique location within the Northern Indian Ocean (NIO) at the crossroads of water exchange between the higher salinity Arabian Sea (AS) to the west and the freshwater dominated Bay of Bengal (BoB) to the east (**Figure 1**). The NIO's northern boundary is landlocked by the Asian continent and differential heating of the Asian continent creates a strong land-sea contrast, which drives the strongest monsoon system on Earth

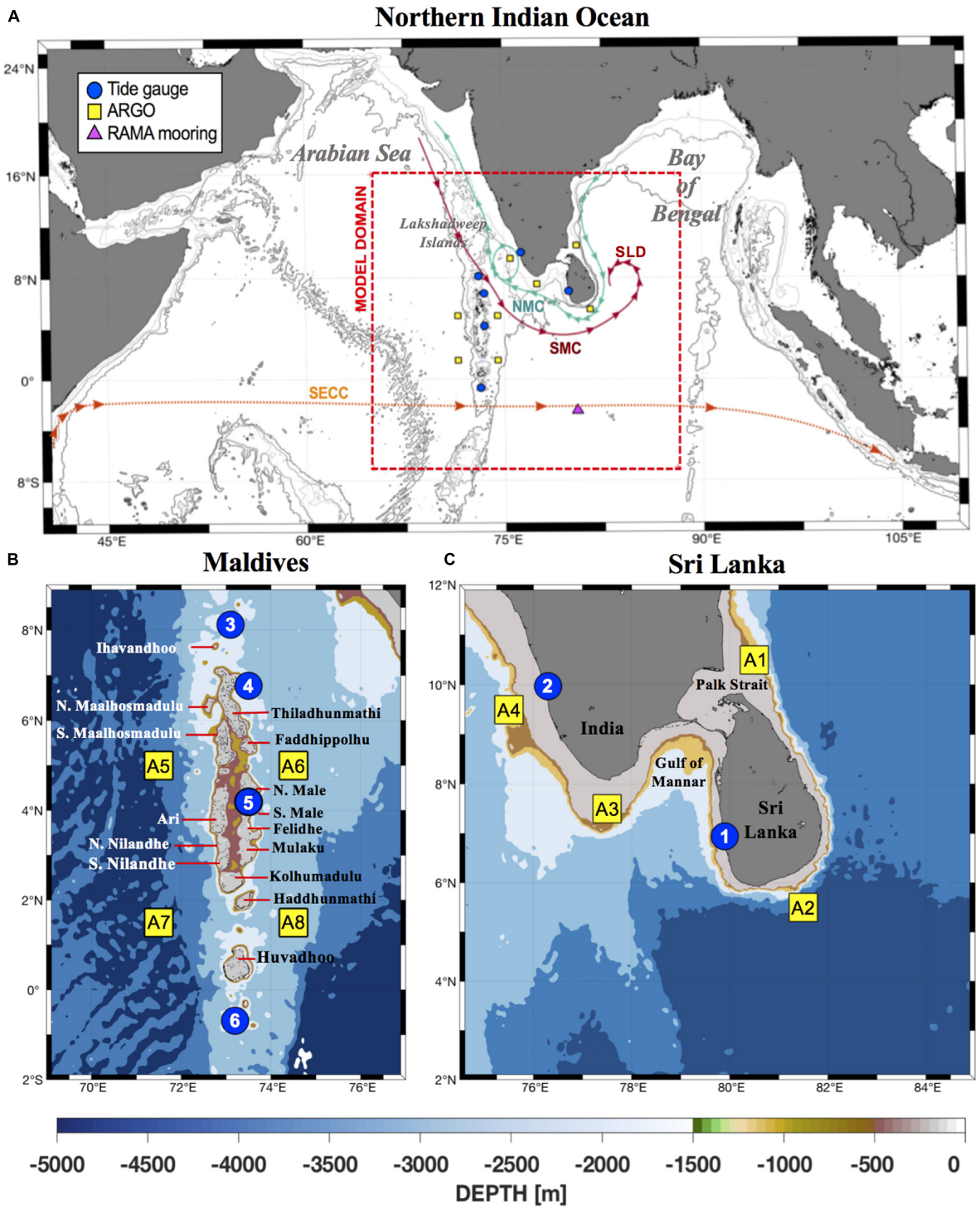

FIGURE 1 | (A) Schematics for the surface circulation in the Northern Indian Ocean (NIO) adapted from Schott and McCreary, 2001. The major currents during the Northeast Monsoon (Dec–Feb) and the Southwest Monsoon (Jun–Aug) are the Northeast Monsoon Current (NMC—green line), the Southwest Monsoon Current (SMC—red line), and the Sri Lanka Dome (SLD), respectively. Also included is the South Equatorial Counter Current (SECC—orange line). The red box represents the boundaries of the model domain. The locations of ARGO profile data (yellow boxes), tide gauges (blue circles), and mooring (pink triangle) used for model validation are also identified. **(B)** Bathymetry map of the Maldives and atoll names. Tide gauge sites are (3) Minicoy, India (4) Male, Maldives (5) Hanimaadho, Maldives (6) Gan, Maldives based on data obtained from the University of Hawaii Sea Level Center (UHSLC—https://uhslc.soest.hawaii.edu/). Locations for ARGO profile data extraction (A5–A8) were selected based on data availability and where the IME has been previously identified from remote sensing data. **(C)** Bathymetry map of India and Sri Lanka. Tide gauge sites are (1) Colombo, Sri Lanka and (2) Cochin, India. Locations for ARGO profile data extraction (A1–A4) were selected to coincide with the main pathways of the monsoon currents, NMC and SMC and where the IME has been previously identified from remote sensing data.

(Schott et al., 2009). These monsoon winds north of 10°S are unique since they reverse twice a year and directly influence the seasonal circulation variability (Schott et al., 2009). The two major monsoon periods in the NIO are the Northeast Monsoon (NEM) from December to April and the Southwest Monsoon (SWM) between June to October, along with two inter-monsoon periods in May and November.

During the NEM, the monsoon winds blow from the northeast toward the southwest direction whilst winds during the SWM come from the opposite direction. This directionality is mirrored by the two monsoon currents, the Northeast Monsoon Current (NMC) and the Southwest Monsoon Current (SMC). The NMC flows westwards from the BoB, past Sri Lanka toward the Maldives, bringing lower salinity (less dense) water from the BoB to the AS during the NEM (**Figure 1A**). In contrast, the Southwest Monsoon Current (SMC) flows eastwards from the AS, past the northern end of the Maldives toward Sri Lanka, transporting higher salinity (more dense) water from the AS to the BoB (**Figure 1A**; de Vos et al., 2014b).

Satellite ocean color imagery revealed higher surface chlorophyll concentrations (SCC) downstream of the Maldives west coast (**Figures 2B**, **3A,C**) and a filament of higher SCC was also observed along the south-west coastline of Sri Lanka during the NEM (**Figure 3B**). Conversely, during the SWM, satellite observations identified higher SCC to the east of the Maldives (**Figures 2A**, **3D,G,H**) and along the south-east coast of Sri Lanka (**Figures 2C**, **3F**). The higher SCC were advected into a recirculation feature along the east coast of Sri Lanka known as the Sri Lanka Dome (SLD) (**Figures 2C**, **3E**, Vinayachandran and Yamagata, 1998). These areas of higher SCC can be attributed to the Island Mass Effect (IME), which has been defined by Doty and Oguri (1956) as an enhancement of primary productivity in the surrounding waters of islands and/or topographic features.

The IME is a geographically ubiquitous phenomenon around island-atoll systems and is analogous to "an oasis in a desert" for the high primary productivity present in the island's nearshore waters in an otherwise oligotrophic ocean (Hamner and Hauri, 1981; Caldeira et al., 2002; Elliott et al., 2012; Andrade et al., 2014; Gove et al., 2016). This increase in primary productivity can be attributed to several non-exclusive mechanisms such as tidal mixing, internal waves and lee eddies formed by flow disturbance or Ekman pumping (Gove et al., 2016). All of them involve mixing processes in the water column to bring deeper, nutrient-rich water into the photic zone, thus stimulating productivity. As such, the IME is characterized by regions of cool sea surface temperature and high current speeds due to these mixing processes (Caldeira et al., 2002). The IME is ecologically significant for its role in supporting higher trophic levels as well as influencing migratory patterns of marine megafauna and localization of fisheries around islands (Palacios, 2002; Anderson et al., 2011). The presence of the IME has been observed in various case studies worldwide such as around the Hawaiian Islands, Barbados (Cowen and Castro, 1994), Cosmoledo atolls (Heywood et al., 1990), Madeira Island (Caldeira et al., 2002), the Great Barrier Reef, Australia (Hamner and Hauri, 1981), and the Galapagos Archipelago (Palacios, 2002).

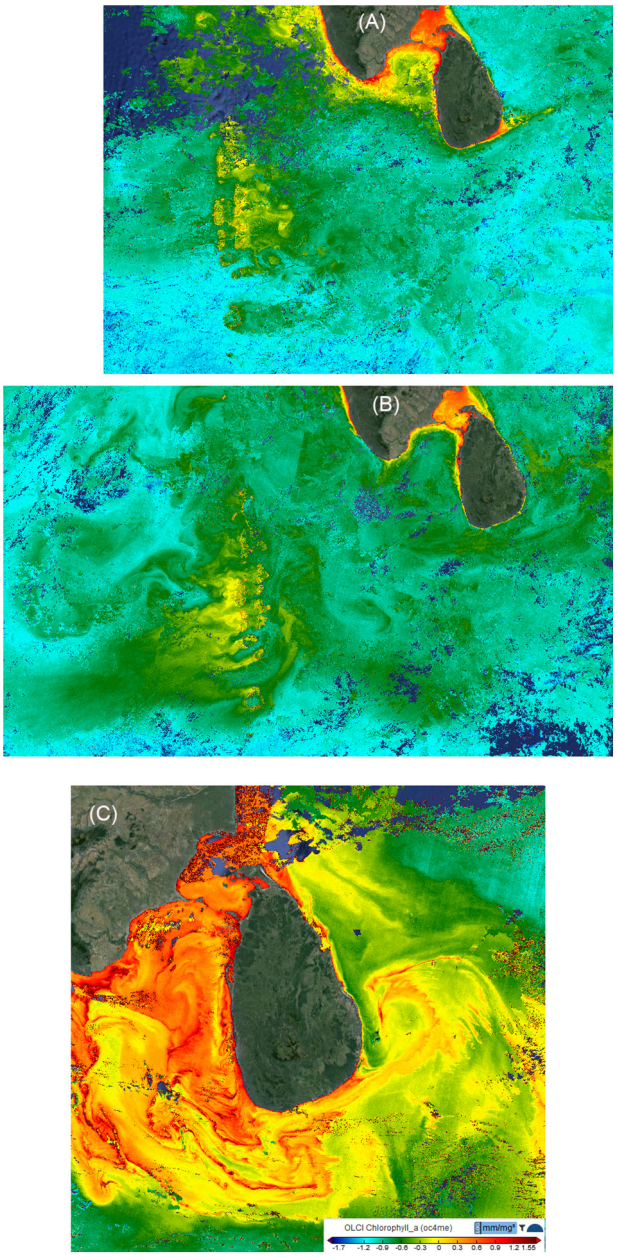

FIGURE 2 | Surface chlorophyll concentrations (SCC) obtained from the Sentinel-3 satellite. **(A)** SWM; 7-day mean 9–15 June 2020; **(B)** NEM; 7-day mean 1–7 February 2020; **(C)** SWM; 3-day mean 10–12 August 2020. The images were sourced from https://s3view.oceandatalab.com/ and display SCC estimated using the oc4me algorithm (Morel et al., 2007).

The seasonality of the NIO circulation is defined by the NEM and SWM. The key difference between the monsoons lie in the dynamics of the monsoon wind forcing, with stronger winds during the SWM (Schott and McCreary, 2001). This directly affects the strength of the monsoon currents, NMC and SMC. The NMC peaks during January with current strength approaching 0.2 ms^{-1} south of Sri Lanka whilst the SMC peaks during July with current strength approaching 0.4 ms^{-1}

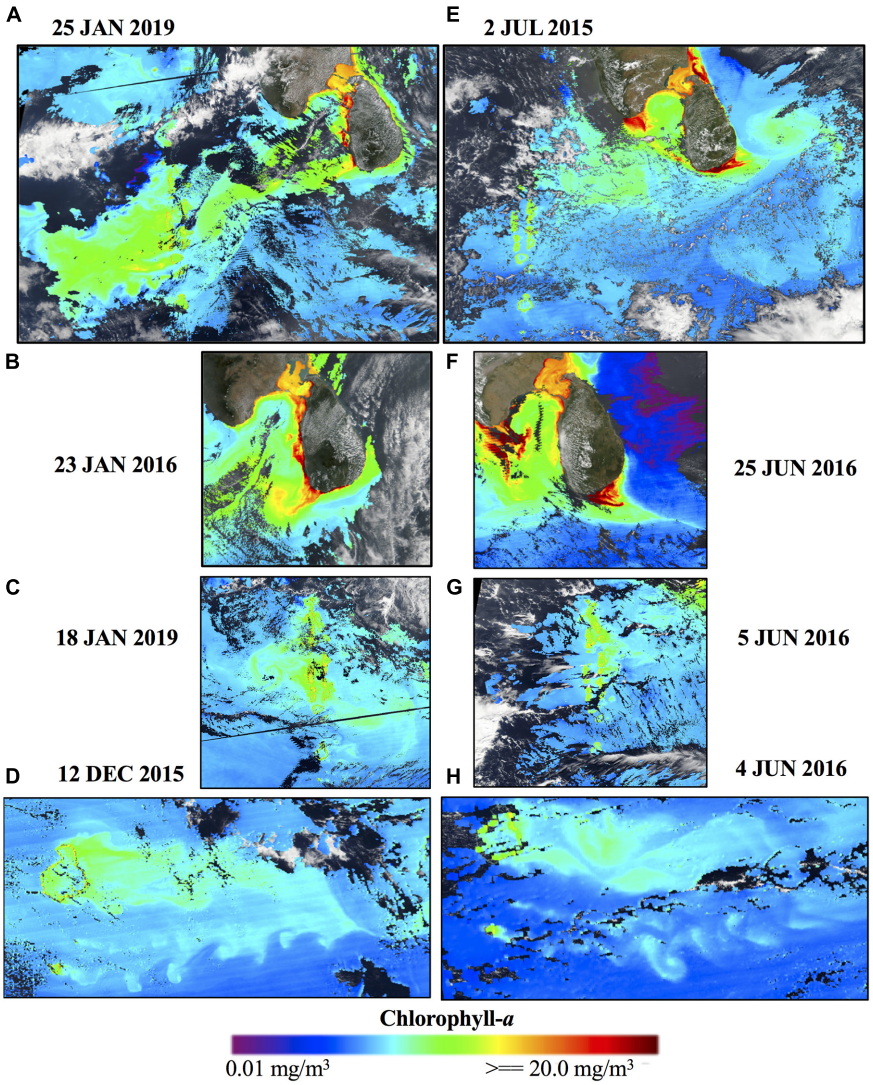

FIGURE 3 | Daily snapshots of surface chlorophyll-*a* concentrations around Sri Lanka and the Maldives during the **(A–D)** Northeast Monsoon (Dec–Feb) and the **(E–H)** Southwest Monsoon (Jun–Aug). **(A,E)** Highlights potential connectivity based on the high chlorophyll-*a* concentrations "advected" from Sri Lanka to the Maldives. **(B,F)** Identifies the location of the IME along the south coast of Sri Lanka during the NEM and SWM, respectively. **(C,G)** Identifies the directionality of the IME along the Maldives island chain. **(D,H)** Displays multiple von Karman vortex streets swirling downstream from the Huvadhoo Atoll during both monsoon periods. Images adapted from EOSDIS Worldview (https://worldview.earthdata.nasa.gov).

(Shankar et al., 2002). Due to this difference in directionality and intensity of wind forcing and currents, the type of circulation features and nature of the IME developed are unique to each monsoon period. The effects of freshwater input rainfall/runoff in the study region are limited to a narrow coastal band along the coast (de Vos et al., 2014a).

To date, there have been several studies by Anderson et al. (2011); de Vos et al. (2014b), and Sasamal (2007) that have identified the IME in the NIO via remote sensing data and numerical modeling. However, the paucity of *in situ* measurements in this region as well as the effect of cloud cover during the SWM meant that there have been limitations in resolving the mechanisms underlying IME development. In addition, coarser global/regional models currently are unable to resolve the fine-scale features implicit to the IME.

The Maldives island chain (**Figure 1B**) is one of the largest and most geologically complex mid-ocean atoll chains in the world. It extends ∼1,000 km from Ihavandhoo (∼8°N) to Gan (∼1°S), and consists of ∼ 1,200 small coral islands and sandbanks (**Figure 1B**). The islands have a mean elevation of 1–1.5 m above sea level. The coral islands are grouped in a double chain of 27 atolls that run north to south (**Figure 1B**). These atolls are situated atop a submarine ridge that rises abruptly from the depths of the Indian Ocean and runs from north to south. The depth of the surrounding ocean are >4,000 m (**Figure 1B**). Along the ridge, there are many coral islands with

intervening channels with depths <50 m where water can flow zonally and allows for the generation of shallow island wakes (**Figures 2A,B**). At the southern end of the Maldives, there are two deep passages between Kolhumadulu, Haddhunmathi, and Huvadhoo (**Figure 1B**). In contrast, although Sri Lanka is an island, from an oceanographic point of view, it behaves as a large headland due to the very shallow waters (<20 m) off the northern section of the island (**Figure 1C**). The continental shelf around Sri Lanka is narrower, shallower and steeper than the global mean (de Vos et al., 2014b) with the width of the shelf along the southern coast less than 10 km (**Figure 1C**). The continental slope around Sri Lanka is a concave feature that extends from 100 m to 4,000 m in depth. Thus, the Maldives and Sri Lanka have similar yet contrasting bathymetric features, i.e., they both have narrow continental shelves/slopes with the surrounding ocean depths generally >4,000 m.

In this paper, we examine the influence of the reversing monsoon currents on the variability of the IME around Sri Lanka and the Maldives archipelago and the IME structure through the water column. Specifically, we focus on the IME developed due to island wakes that have been generated through the interaction between oceanic currents and topography, i.e., the bathymetrically distinct Maldives and Sri Lanka. This was undertaken through the development and application of a high spatial resolution three-dimensional numerical model for the region to characterize the structure of the IME across seasonal time scales.

The paper is organized as follows: section "Materials and Methods" describes the model configuration in detail and evaluates the robustness of the model against observational data; section "Results" examines the variability of the IME at both seasonal and intra-seasonal scales and section "Discussion" is the discussion followed by the concluding remarks and summary in section "Summary and Conclusion."

MATERIALS AND METHODS

Numerical Model Configuration

The numerical model was built using the Rutgers University version of the Regional Ocean Modeling System (ROMS)[1] with significant adaptations for Maldives and Sri Lanka. It has been previously used to study island wake circulation in the southern California Bight (Caldeira et al., 2005; Dong and McWilliams, 2007), the Hawaiian Islands (Kersalé et al., 2011), the Marquesas Archipelago (Raapoto et al., 2018), New Caledonia (Marchesiello et al., 2010), and Fernando de Noronha Island (Brazil) (Tchamabi et al., 2017). It was also used to examine the circulation patterns around Sri Lanka and the SLD (de Vos et al., 2014b). ROMS is a split-explicit free surface, terrain-following vertical coordinate oceanic model, and resolves the incompressible primitive equations (Cushman-Roisin and Beckers, 2011) using the Boussinesq approximation and hydrostatic vertical momentum balance (Shchepetkin and McWilliams, 2003, 2005). These equations are discretized on an orthogonal, curvilinear, Arakawa C-grid and a stretched, terrain-following coordinate system in the vertical direction (Song and Haidvogel, 1994; Shchepetkin and McWilliams, 2003, 2005).

The model grid domain extends from 7°S–15°N, 65°E–88°E (**Figure 1A**). Bathymetry was obtained from the General Bathymetric Chart of the Oceans (GEBCO) 30 arc-second gridded product (Weatherall et al., 2015)[2] and coastline data was extracted from GSHGG coastlines[3]. Potential horizontal gradient errors were minimized by smoothing the bathymetry until the recommended slope factors were obtained for the Beckman and Haidvogel number, rx_0 <0.2 (topographic stiffness ratio) (Beckmann and Haidvogel, 1993) and the Haney number, rx_1 (hydrostatic instability number), was $7 > rx_1 > 5$ (Haney, 1991). The bathymetry was smoothed in the following steps: (1) a Shapiro filter was applied twice across the original bathymetry; (2) High rx_0 areas >0.2 were identified (**Supplementary Figure 1A**). Iterative pointwise smoothing was applied at these high rx_0 areas (**Supplementary Figure 1A**). This was found to achieve a good balance in maintaining realism without compromising grid stability. rx_1 was sensitive to the vertical parametrization in the model which was dependent on the number of vertical layers (N), the thermocline depth (T_{cline}) and the s-coordinate surface (θ_S) and bottom control parameters (θ_b). The representation of surface mixed layer processes was sensitive to the vertical resolution at the surface, which is dependent on the choice of stretching functions, i.e., the vertical terrain-following stretching function ($V_{Stretch}$) and vertical terrain-following transformation function ($V_{Transform}$). A summary of the values used for these parameters are provided in **Supplementary Table 1** and the model's vertical grid resolution in **Supplementary Figure 2**.

The model domain had a depth range of 0–5,000 m with 30 vertical layers (**Supplementary Figure 2**). The thermocline depth was estimated from the ARGO climatology profile averaged across the entire model domain. The resulting horizontal grid resolution was approximately 3 km per cell in the 860 × 860 grid. The higher spatial resolution was necessary since the horizontal scales of these island wake structures have a small Rossby radius of deformation. The initial conditions and open boundary data (salinity, temperature, sea surface height and velocity fields) for the model were obtained from the 1/12° global US Navy Hybrid Coordinate Ocean Model (HYCOM) GLBu0.08 (Expt 19.1–91.2) reanalysis product (Chassignet et al., 2007). It should be noted that this product is without tides.

Due to the difference in bathymetry between the z-coordinate HYCOM reanalysis product and model s-coordinate grid, a hybrid bathymetry was created using both the GEBCO and HYCOM bathymetry to improve interpolation at the boundaries (**Supplementary Figure 3**). The reanalysis product and hybrid bathymetry were then gridded to the model grid boundaries for the final boundary files. Tidal constituents were obtained from the TPXO7 global tide model with a 1/4° resolution (Egbert and Erofeeva, 2002) to generate the tidal forcing and was applied to the four open boundaries using the Flather condition

[1] http://www.myroms.org

[2] https://www.gebco.net/

[3] ngdc.noaa.gov

(Flather, 1976) and Chapman implicit boundary condition for the elevation. For the baroclinic mode (temperature, salinity, and baroclinic momentum), a combination of Orlanski-type radiation boundary conditions were applied with nudging (Marchesiello et al., 2001). Vertical mixing processes were parameterized with the non-local K-profile boundary layer scheme (Large et al., 1994) and implemented for both surface and bottom boundary layers. In addition, a sponge layer was applied across 60 grid points (approximately 180 km) where the viscosity was increased linearly from the interior to a maximum viscosity of 300 m^2 s^{-1} at the exterior. Explicit lateral viscosity was set to zero throughout the model domain, except along the sponge layer near the open boundaries. The model was nudged toward daily HYCOM data along a linearly tapered nudging band along the open boundaries that had the same dimensions as the sponge layer (60 grid points). The model set up and parameters have been similarly applied by Wijeratne et al. (2018) for Australian waters.

At the surface, the model was forced with 3-hourly atmospheric pressure and wind stress at 10 m, net heat and freshwater fluxes at a 1/8° resolution obtained from the European Centre for Medium Range Weather Forecast (ECMWF) ERA-Interim reanalysis dataset (Dee et al., 2011). To prevent the simulation from drifting, the surface data were relaxed to daily surface fields from HYCOM [sea surface temperature (SST), sea surface salinity (SSS)] and a heat flux correction (maximum 37°C) that was derived from the HYCOM SST averaged over the region was applied.

The ROMS simulation, hereafter referred to as SNIO, was run over a 12 year period between the years 2005–2016 with daily outputs saved. The model took about 6 months to reach statistical equilibrium and was dependent on the initial conditions used, in this case the hydrography from HYCOM. To avoid impact from the model spin-up on the results, only model outputs from year 2006 onward were used.

Model Validation

The model results were validated against several observational datasets for the following variables: sea level, temperature, salinity, and surface current velocities. A summary of the observational data, time period and source that were used for model comparison are presented in **Table 1**.

The following statistical metrics were used for validation—Pearson correlation coefficient (Coefficient of determination, R^2), the Root-Mean Square Error (RMSE), the model bias, the mean absolute error (MAE), and Willmott model skill (Willmott, 1982). The statistical metrics for each variable are consolidated in **Table 1**.

Sea Level

Tide gauge data and locations around the Maldives (**Figure 1B**) and Sri Lanka (**Figure 1C**) were obtained from the University of Hawaii Sea Level Centre (UHSLC). The sea level computed from the model were compared to the tide gauge data (**Figure 4**) and the monthly climatologies were averaged between 2006 and 2016 for the Sri Lanka and Maldives stations and 2011–2016 for India (**Table 1**). The higher sea levels associated with the SWM period (June- August) are reproduced in the model. The model generally underestimated the sea level at the specified locations but performed better (**Figure 4** and **Table 1**) around Sri Lanka and India compared to the Maldives (**Figure 4** and **Table 1**). Possible reasons for this error could be due to the complex bathymetry around the Maldives that may have been overly smoothed to avoid potential horizontal pressure gradient errors and that the minimum depth of the model was set to 10 m which was deeper than the actual depth of the tide gauge locations. In addition, some of the locations extracted from the model could not be exactly matched to the locations of the tide gauges since those fell within the land mask area of the model (**Table 1**).

Sea Surface Temperature

Throughout the 11 years of model simulations, the model was able to reproduce the regional seasonal SST pattern but with the largest difference during the SWM. The mean difference between the model and satellite derived observations was <1°C for both monsoons (**Figures 5C,I**). Comparisons between the climatology of the MODIS SST and the model SST indicated that although the bias was low for both monsoon periods (**Table 1**), the general distribution of SST differences were not consistent (**Figures 5C,I**). The model tended to slightly overestimate SST in the region of the South Equatorial Counter Current (SECC) (2°S–2°N) and underestimates SST around the islands (**Figure 5** and **Table 1**) particularly the shelf area between India and Sri Lanka by a mean difference of <2°C (**Figure 5**). This discrepancy could be due to the bottom reflectance from the shallow depth in this shelf region (<10 m) which has been known to affect the estimation of MODIS measurements (Jiang et al., 2017). Conversely, the overestimation of temperatures occurred closer to the SECC region (**Figure 5**). During the NEM, the model has a lower bias (0.18) compared to the SWM (0.24) and the largest difference in SST was localized around the Lakshadweep Islands. However, during the SWM, the largest SST difference was more pronounced between the shelf region of Sri Lanka and the south point of India. Overall, the model exhibits a strong skill (Skill > 0.6, RMSE < 0.5, **Table 1**) to simulate the surface SST.

Current Velocities

The model has higher current speeds than the observational data (**Figures 5F,L**). The model performed slightly better for the zonal velocities (Skill > 0.65, **Table 1**) compared to the meridional velocities (Skill < 0.5, **Table 1**) where the mean difference for the zonal velocities and meridional velocities were 0.03 ms^{-1} and 0.06 ms^{-1} for the NEM and SWM, respectively. This overestimation could be attributed to the higher resolution of the model compared (3 km) to the satellite observations (4 km).

Vertical Temperature Profiles

Model validation with the ARGO vertical profiles were conducted at eight locations around the Maldives and Sri Lanka (**Figure 1**). The mean monthly climatology of ARGO temperature during 2006–2014 was compared with the mean monthly climatology from the model at those areas and plotted with depth (**Figure 6**). Overall, the model had good agreement (RMSE = 1.3°C, Skill > 0.6, **Table 1**) with the Argo data and the simulated profiles were able to represent the changes in the thermocline depth

TABLE 1 | Observational data sets used for model validation and statistical metrics.

Variable	Source	Period	Location	Model location	RMSE	Bias	MAE	R^2	Skill
Sea surface height	UHSLC https://uhslc.soest.hawaii.edu/	Sri Lanka 2006–2016	(1) Colombo	79.9°E, 6.94°N	0.45	−0.05	0.44	0.78	0.62
		India 2011–2016	(2) Cochin	76.2°E, 9.96°N	0.43	−0.06	0.41	0.82	0.60
			(3) Minicoy	73.1°E, 8.11°N	0.41	−0.04	0.41	0.83	0.54
		Maldives 2006–2016	(4) Male	73.5°E, 4.20°N	0.43	−0.04	0.42	0.47	0.12
			(5) Hanimaadhoo	73.2°E, 6.76°N	0.42	−0.04	0.42	0.73	0.32
			(6) Gan	73.1°E, 0.78°S	0.44	−0.43	0.43	0.20	0.24
		Period		**Velocity**	**RMSE**	**Bias**	**MAE**	**R^2**	**Skill**
Current velocities	OSCAR https://www.pmel.noaa.gov/tao/drupal/disdel/	2006–2016	NEM	U	0.19	0.03	0.13	0.60	0.70
				V	0.09	−0.02	0.07	0.44	0.41
			SWM	U	0.25	−0.01	0.18	0.88	0.67
				V	0.13	0.02	0.08	0.39	0.34
Sea surface temperature	MODIS https://modis.gsfc.nasa.gov/data/dataprod/	2006–2016	NEM		0.40	0.18	0.25	0.82	0.79
			SWM		0.43	0.24	0.32	0.65	0.70
Temperature, salinity	ARGO http://www.godac.jamstec.go.jp/argogpv/e/	2006–2016			1.33	−2.5	1.89	0.53	0.66

for the different regions in the model domain. However, the model tended to underestimate temperatures compared to the observational data and this difference is apparent at depths less than 600 m (**Table 1**).

Volume Transport

Volume transport at the RAMA mooring (**Figure 1A**) was calculated from the model at 80.5°E, 2.5°S–2.5°N and depth integrated over 80 m for both the NEM and SWM during 2005–2016. The negative direction of the volume transport indicates that the main directionality of the currents heading westwards and the transport values were in good agreement (**Figure 7**) with McPhaden et al. (2015). The mean transport values were in the range of 9–11 SV (**Figure 7**) while McPhaden et al. (2015) had transports of 5–15 Sv. The westward mean flow was attributed to the mean residual of the monsoon currents above the equator (McPhaden et al., 2015). The SWM had higher volume transport with a mean value of 10 Sv compared with the NEM mean value of 7 Sv (**Figure 7**).

RESULTS

Seasonal Circulation Variability

Surface Circulation

The mean surface current speed for the entire domain during the simulation SWM was 0.3 ms^{-1} whilst the mean speed during the NEM was 0.2 ms^{-1} (**Figure 5**). During the NEM, current speeds >0.3 ms^{-1}, along the east coast of India indicated the presence of the East Indian Coastal Current (EICC) as it flows southwards along the coastlines of eastern India and Sri Lanka. However, along the southern coast of Sri Lanka, current speeds increased to >0.5 ms^{-1} before part of the current continued to form the West Indian Coastal Current (WICC) along the west coast of India (**Figure 5**). Several island wakes developed along the western coastline of the Maldives with the largest, in terms of spatial extent and current speed (>0.5 ms^{-1}), located at 5 and 1°N (**Figure 5**). All the wakes were directed westward and the largest wake at ∼1°N extended up to 780 km. The SECC was also present between ∼4 and 6°S throughout the study region and had a mean current speed of ∼0.4 ms^{-1}.

During the SWM, the SMC (speed $>$ 0.5 ms^{-1}) enters the model domain from 4 to 8°N to flow eastwards past the northern tip of the Maldives archipelago and past the southern coast of Sri Lanka (**Figure 8**). The major flow pathway was such that the currents flowed southwards, parallel to the Maldives in the west and then flowing northwards along the eastern side of the Maldives. This was due to the presence of the submarine ridge. Weaker eastward flow across the atolls were present which developed into island wakes that were visible in satellite imagery (**Figure 2**). There was a distinct separation of the current pathways between Maldives and Sri Lanka. The flow from the west was deflected to the south by the Maldives ridge. The currents that impacted Sri Lanka during the SWM was mainly derived from the WICC with the injection of colder water through upwelling along the southern tip of India (**Figure 8**). The advection of this cold water along the southern coast of the

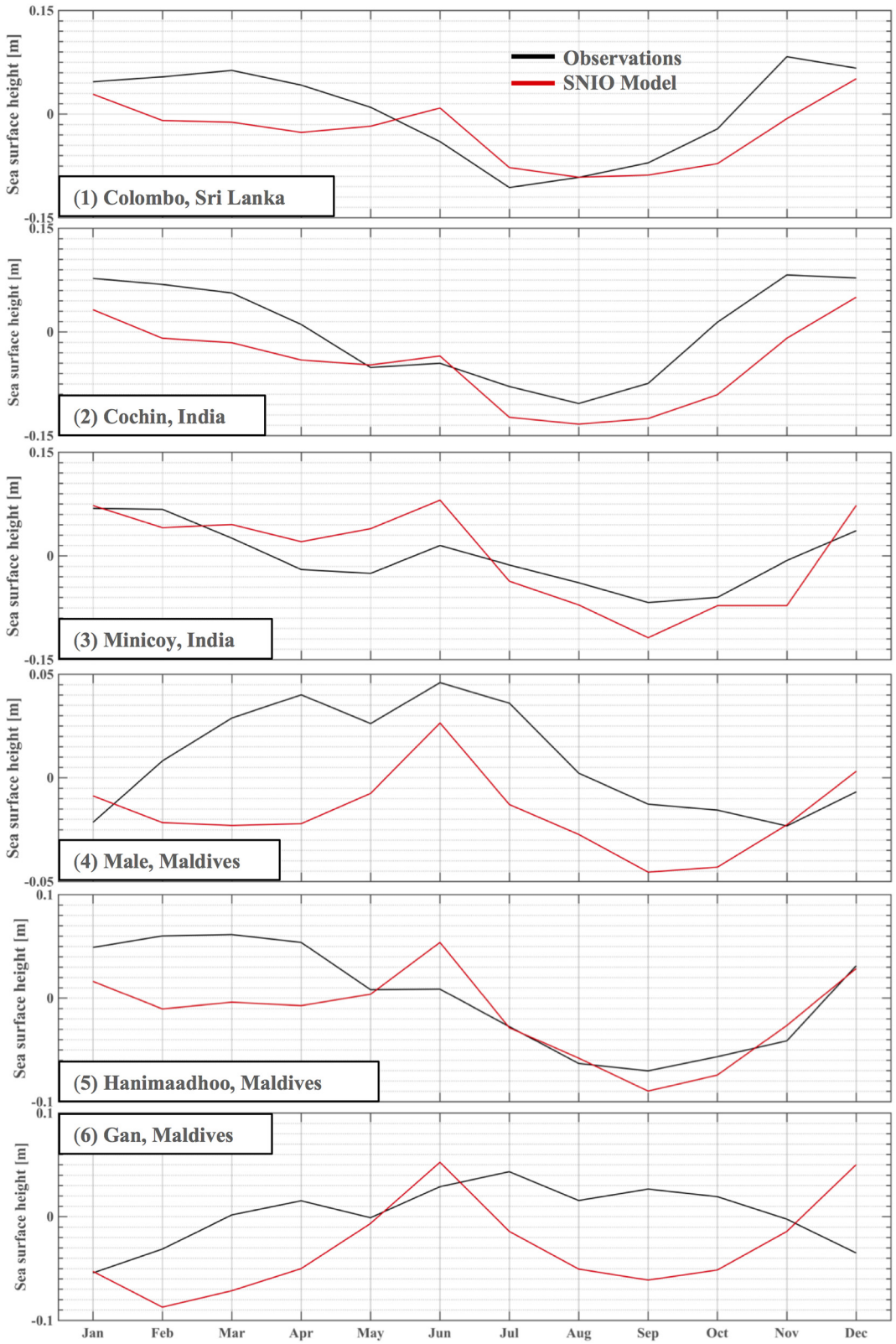

FIGURE 4 | Monthly climatology of observed sea level derived from UHSLC observations (black line) and SNIO model (red) from tide gauge locations at (1) Sri Lanka, Colombo (2) Cochin, India (3) Minicoy, India (4) Male, Maldives (5) Hanimaadhoo, Maldives (6) Gan, Maldives. All units are in (m).

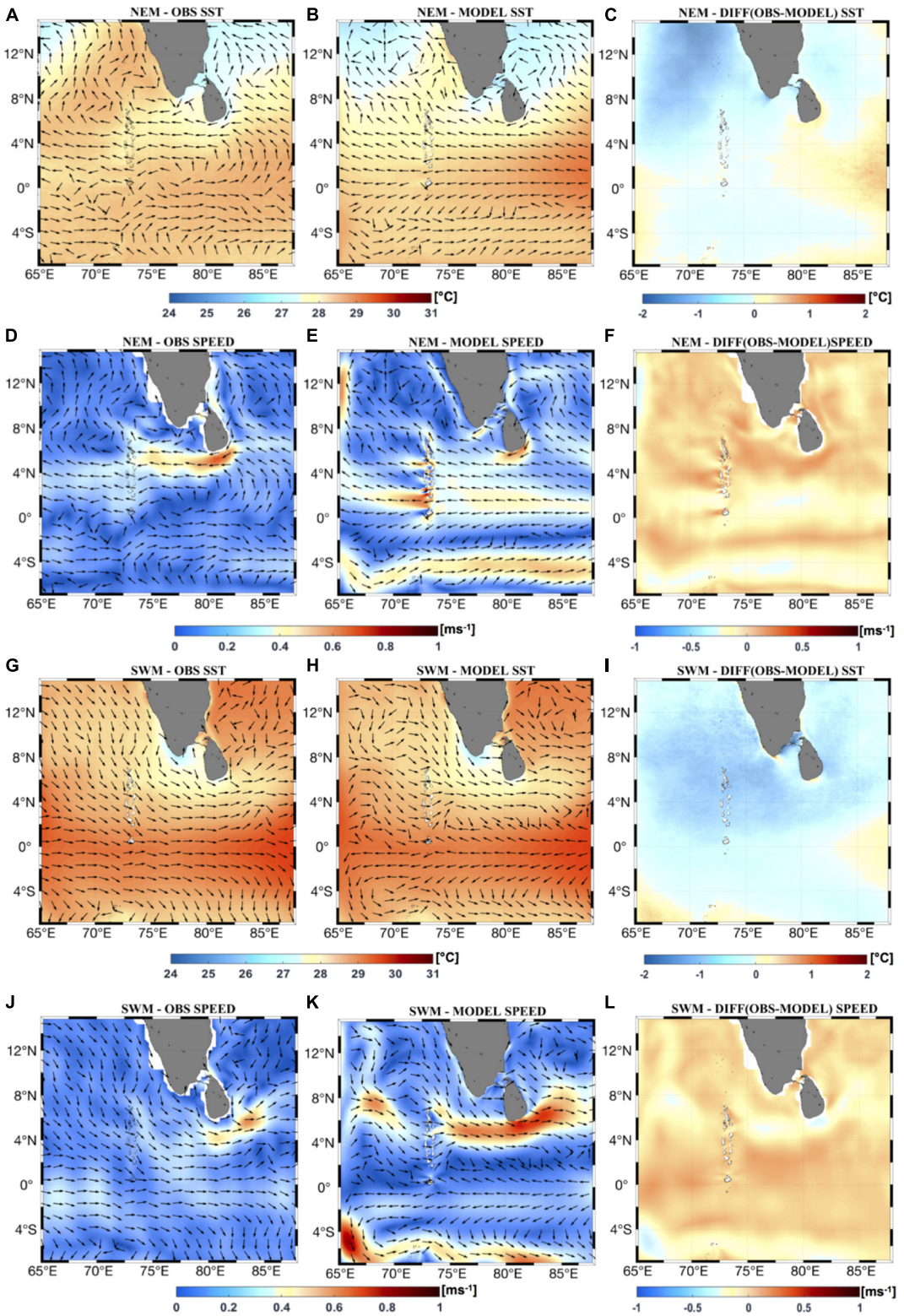

FIGURE 5 | Seasonal climatology of SST and current speeds of observations and model simulations during the NEM **(A–F)** and SWM **(G–L)** averaged over 2006–2016. Observational SST was obtained from MODIS-AQUA and mapped with current velocities from OSCAR (arrows) **(A,G)**. SNIO model SST from were mapped with model current velocities **(B,H)**. The difference between the observations and model SST were also calculated **(C,I)**. Observational current speeds were calculated from OSCAR and mapped with current velocities (arrows) **(D,J)**. SNIO model current speeds from were mapped with model current velocities **(E,K)**. The difference between the observations and model current speeds were also mapped **(F,L)**.

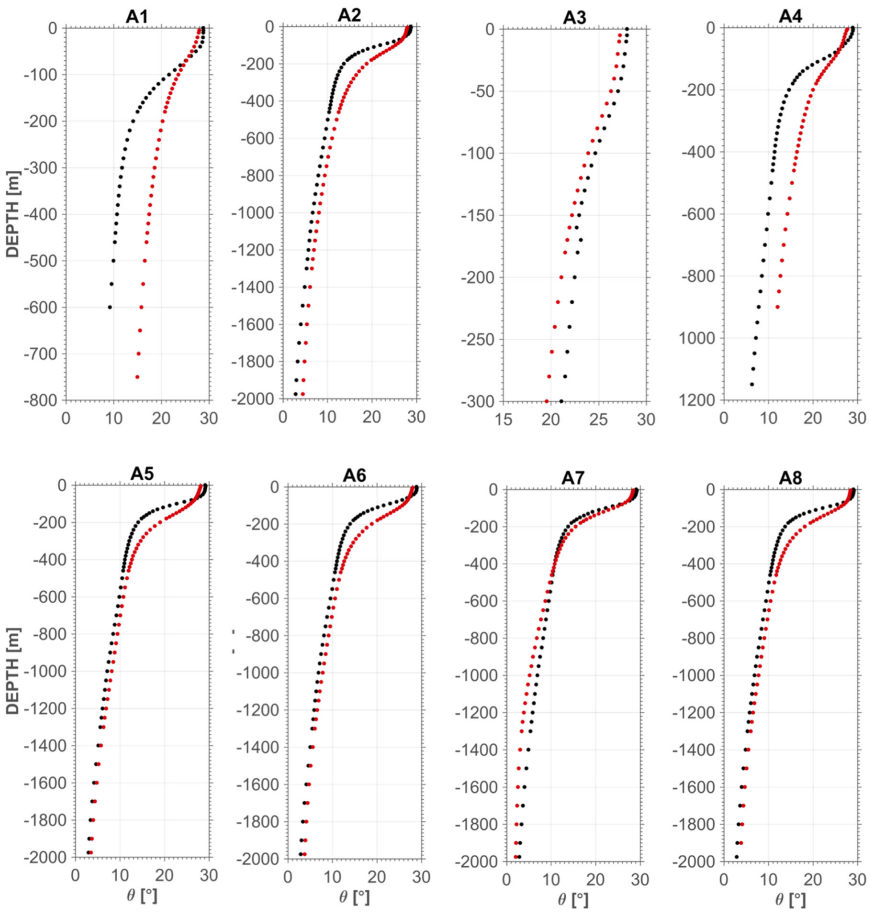

FIGURE 6 | Comparison of Argo (black) and SNIO (red) climatological monthly mean temperature profiles at eight locations identified around Maldives and Sri Lanka (see **Figure 2**). Note that the y-axis are at different scales.

Sri Lanka that acts as a headland resulted in the formation of the recirculation feature identified as the SLD.

Thermocline Variability

To identify locations of upwelling and downwelling, the depth of the 26°C isotherm (henceforth, referred to as D26) was extracted and mapped from the model climatology (**Figure 9**). D26 is often used in the NIO (McCreary et al., 1993; Rao et al., 2006; Ali et al., 2015; McPhaden et al., 2015) whilst D20 (depth of the 20°C isotherm) is used more in the Southern Indian Ocean. Here, we define upwelling (downwelling) processes to be when the local D26 is shallower (deeper) than the domain-averaged mean depth for D26. There are several distinct differences between the NEM and SWM, the first being that downwelling was more prevalent during the NEM and upwelling during the SWM. The mean depth for D26 during the NEM was ∼112 m whilst during the SWM, the mean depth for D26 was ∼100 m.

During the NEM, downwelling occurred on both sides of the Maldives island chain but upwelling occurred within the archipelago and downstream from Kolhumadulu Atoll (73.5°E, 0.5°N). Upwelling occurred along the south coast of Sri Lanka and India (**Figure 9Ai**). D26 reached its shallowest at approximately 83°E, 13°N (D26 < 50 m), indicating the presence of strong upwelling. At the start of the NEM during December, the mean depth of D26 was ∼113 m and downwelling occurred on the western coastline of the Maldives Island chain (**Figure 9Aii**). It was deepest along 3 and 0.5°N. Around the eastern coastline of Sri Lanka, D26 shallowed to depths <50 m from the surface between ∼7 and 13°N. Downwelling intensified during January with D26 being suppressed to depths >160 m and the overall mean depth increasing to ∼115 m (**Figure 9Aiii**). The downwelling signal was strongest along the northern tip of the Maldives at ∼7°N and extended further westward across ∼4°N. In contrast, upwelling strengthened along the east coast of India and downwelling occurred at ∼86°E, 12°N. Upwelling reached its maximum along the southern coast of Sri Lanka during January with D26 being shoaled to less than 80 m from the surface. In February, downwelling intensity subsided (mean depth of D26 at ∼110 m) but was more prevalent across the domain with downwelling occurring both around Maldives and the south coast of Sri Lanka Sri Lanka. However, upwelling also developed along the western coastline of Maldives at ∼5°N and downstream from Kolhumadulu Atoll (**Figure 9Aiv**).

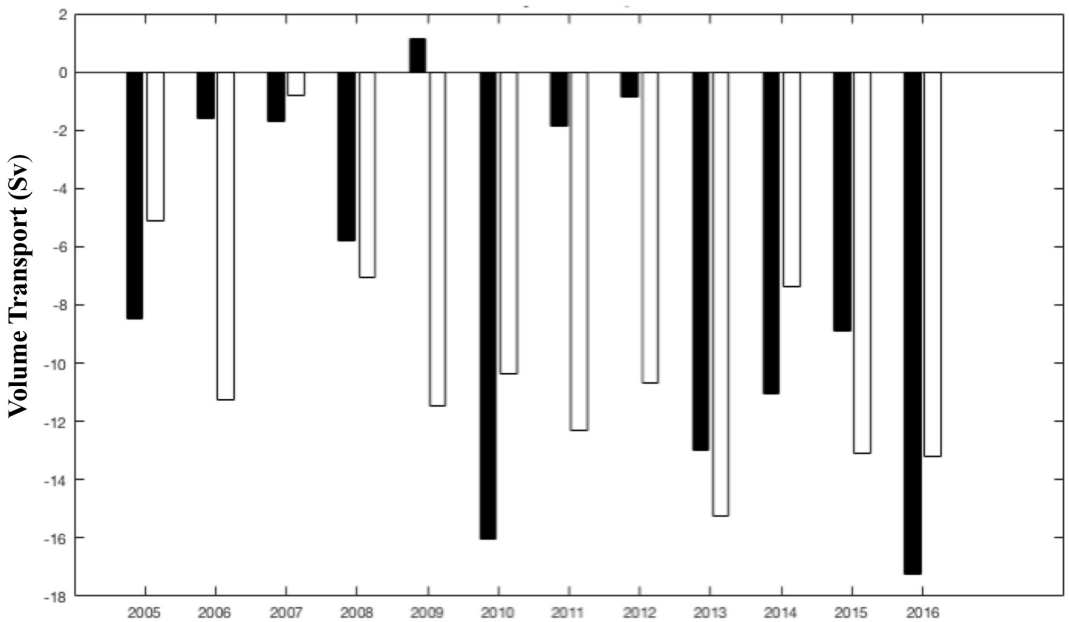

FIGURE 7 | Volume transport from model output at 80.5°E across 2.5°S–2.5°N, relative to a fixed depth of 80 m for the NEM (black) and SWM (white) during 2006–2016.

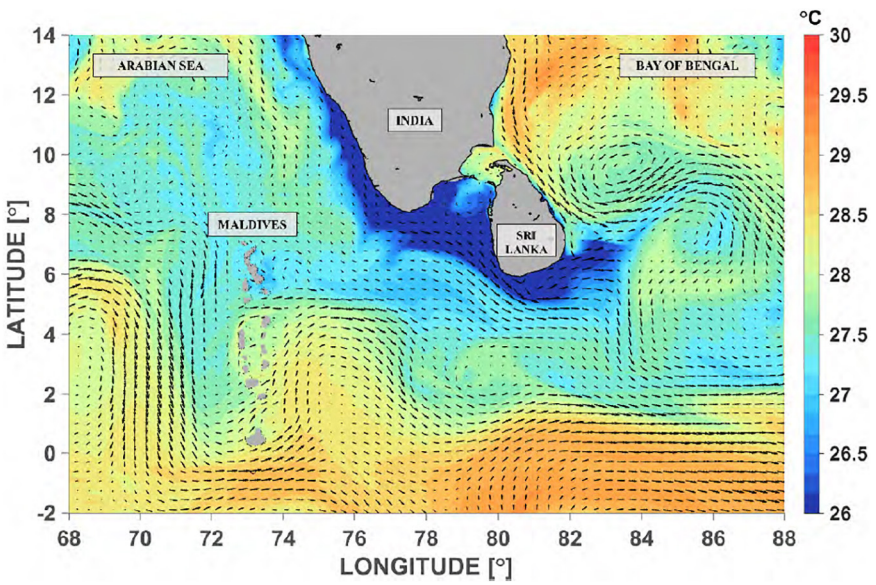

FIGURE 8 | Surface flow patterns (arrows) and sea surface temperature (color) in July, during the SWM showing the circulation around the Maldives and flow separation and the formation of the Sri Lanka Dome to the east of Sri Lanka.

Downwelling during the SWM tends to occur to the south of 5°N for the Maldives but occurs at the northern tip of the Maldives (**Figure 9Bi**). Upwelling intensifies along the south coast of Sri Lanka where the mean depth of D26 has been shoaled by approximately 20 m to the surface. In addition, strong upwelling between 82 and 86°E identify the presence of the Sri Lanka Dome (**Figure 9Bi**). The SWM was characterized by increased wind stress with monsoonal currents flowing eastward and overall upwelling favorable. However, upwelling is continuous throughout the domain and there are key differences around the Maldives and Sri Lanka. The mean depth of D26 across the domain was 105 m in June (**Figure 9Bii**) and shallowed to 100 m in July (**Figure 9Biii**) and shallowest in August at 95 m (**Figure 9Biv**). Upwelling was at a maximum both spatially and in intensity at the northern tip of the Maldives at ∼6°N in June but subsided in July (**Figure 9Biii**).

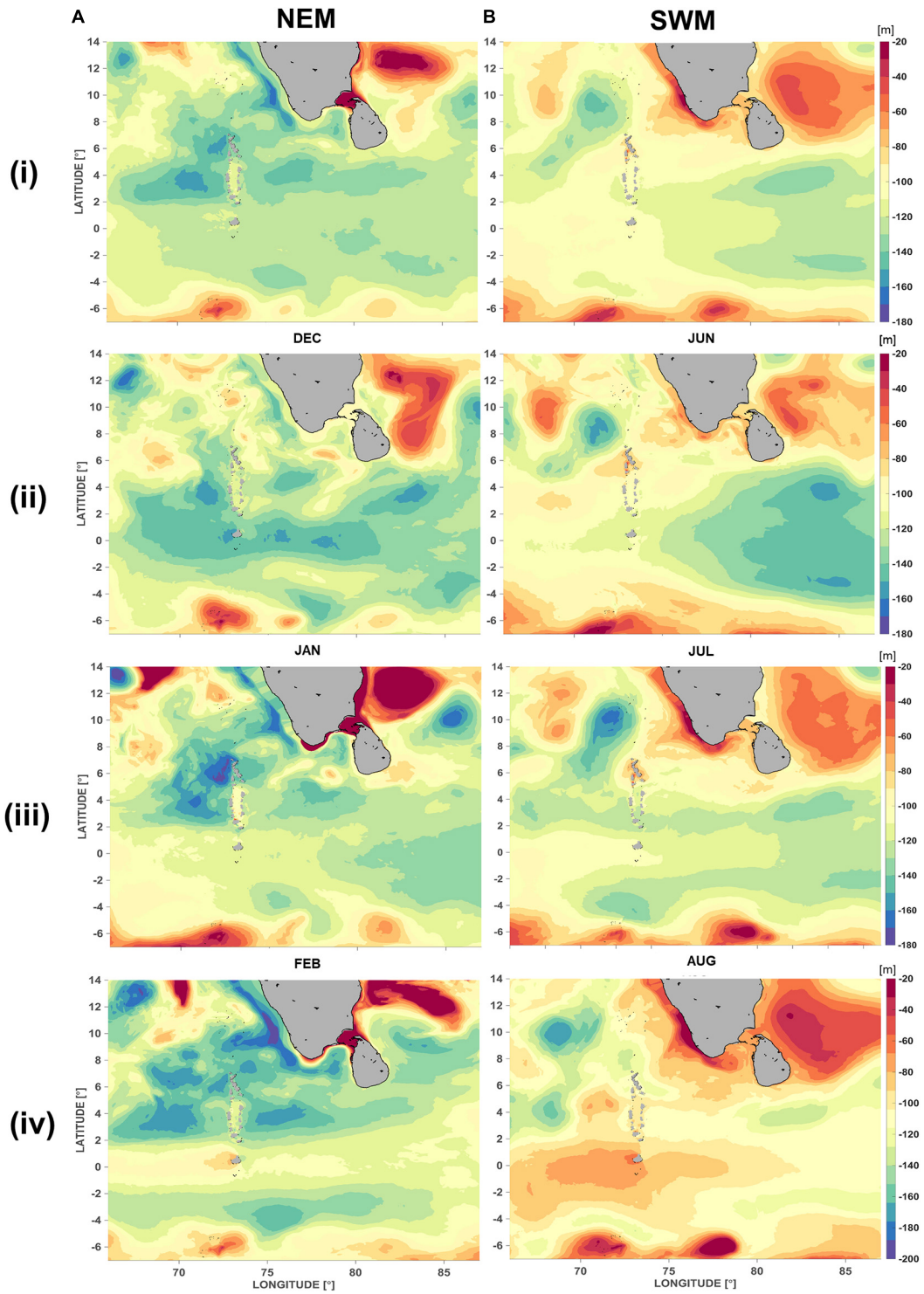

FIGURE 9 | Mapped depths of the 26°C isotherm (D26) relative to the mean during the **(A)** NEM (i) December (ii) January (iii) February and **(B)** SWM—(i) June (ii) July (iii) August. Shallower (deeper) values where the colormap is warmer (cooler) identify locations where the 26°C isotherm (D26) is uplifted (suppressed).

In August, downwelling developed at this location. Below 5°N, downwelling was prevalent along the eastern coastline from June to July but the reverse occurred during August. At ∼1°N, D26 was gradually uplifted from ∼140 m in June to a maximum of ∼50 m in August. Along the south coast of Sri Lanka, upwelling is initiated in June and reached its maximum in August

(**Figure 9Biv**). In the region where the SLD has been known to develop, upwelling started at ∼82°E, 8°N and broadened during July, reaching its maximum at ∼30 m depth from the surface (**Figure 9Biii**).

Intra-seasonal Circulation Variability

Meridional transects of temperature were examined along the eastern coastline of the Maldives at 73 and 74°E, and the south coast of Sri Lanka at 81°E for the monthly mean average from the model output and compared within each monsoon period (**Figures 10**, **11**). The remote sensing data and numerical simulations indicated the formation of island wakes frequently occurs on the downstream of the islands (**Figures 2**, **5**). This was the motivation for the selection of these, hence these sections. For consistency, we define cooler temperatures <27.5°C and warmer temperatures >27.5°C.

Northeast Monsoon (December to February)

At the start of the NEM during December, currents begin the transition from the inter-monsoon period and begin to flow east to west. The EICC strengthens along the east coast of India before making its way to Sri Lanka and the interaction along the curvature of the Sri Lanka coastline is accompanied by cooler SST and strong currents (**Figure 10B**). The EICC follows the coastline tightly and part of it becomes entrained within a recirculation feature along the south coast before the remaining current flows northwards into the Bay of Bengal. From the Sri Lanka transect at 81°E, the D26 isotherm lies between 50 and 110 m and warmer temperatures extended from the surface to ∼40 m depth (**Figure 10C**). At the 73°E Maldives transect, the deepest position of the D26 was at ∼135 m depth with warm temperatures constrained in the upper 50 m of the water column (**Figure 10A**).

During January, the mean sea surface temperatures in the model domain decreased by approximately 2°C (**Figure 10E**). Current velocity speeds increased by 23% with the strongest velocities arriving from the eastern boundary of the model domain (**Figure 10E**). A plume of cool SST leaves the south coast of Sri Lanka and a recirculation feature develops between Sri Lanka and the south tip of India. A warm current between 4 and 6°N dominates the westward flow toward the Maldives and interacts with the recirculation feature at 78°E before flowing through the northern end of the Maldives (**Figure 10E**). An interesting feature of this current is the decrease in SST across longitude after it passes 78°E and brings cooler SST through the Maldives. From the Sri Lanka transect at 81°E, D26 shifts downwards between 90 and 120 m and warmer temperatures extended deeper to 110 m depth, indicating downwelling (**Figure 10F**). At the 73°E Maldives transect, the D26 was uplifted to ∼80 m depth and accompanied by an overall decrease in temperatures throughout the water column, identifying the process of upwelling (**Figure 10D**). Overall, mean SST and current velocities continued to decrease throughout the region in February toward the end of the NEM. The original inflow current between 4 and 6°N reduced in width to 5°N (**Figure 10H**). SST around Sri Lanka and India increased by ∼1.5°C, in contrast to the Maldives where SST along the western coastline decreased by ∼1°C. The spatial structure of the wake becomes more coherent around the Maldives and a fully developed recirculation feature is observed at 72°E, 5°N. Along Sri Lanka at 81°E, D26 remained at a consistent depth of ∼112 m and the isotherm layers become spatially uniform throughout the water column with warmer temperatures in the upper 60 m of the water column (**Figure 10I**). At the 73°E Maldives transect, D26 continues to be uplifted to ∼60 m depth with a continued decrease in temperatures throughout the water column, indicating that the upwelling process has not only continued but strengthened (**Figure 10G**).

Southwest Monsoon (June to August)

The start of the SWM in June begins with warmer SST throughout the study region with mean temperatures of 28.5°C and mean current speeds at ∼0.4 ms^{-1} (**Figure 11B**). Currents flow from west to east and a cold pool was observed downstream at the northern tip of the Maldives at 74°E, 5°N (**Figure 11B**). As the currents interacted with the Maldives, an anticyclonic eddy developed downstream, along the eastern coastline of the Maldives at 76°E, 4°N. The directionality of the WICC reversed direction to flow southwards and part of it remained close to the coastline as it interacted with the southern coast of Sri Lanka before progressing to the east as the EICC. However, at this stage of the SWM, the EICC was still transitory in direction with weak current speeds (∼0.3 ms^{-1}). Lower SST were present along the south coast of Sri Lanka and India and a second anticyclonic eddy developed at 83°E, 10°N. Inflow from the eastern boundary between 0°N and 2°S remained weak with mean current speeds <0.2 ms^{-1} (**Figure 11B**). At 74°E Maldives, the D26 lies at 90 m depth below 4°N. Isotherm layers are spatially uniform and warmer temperatures extended to 70 m depth. D26 shifts downwards from ∼90 to ∼110 m depth above 4.6°N, an indication of downwelling. At the south coast of Sri Lanka, shoaling occurred as the isotherms are uplifted and the D26 isotherm is at its shallowest at ∼40 m depth. Mean temperatures throughout the water column were ∼24°C and the angle of uplift was at its steepest between 4.5 and 5.3°N.

In July, the region cooled by ∼38% along with an increase in current velocities intensified at the south point of India and Sri Lanka. The downstream cold pool at the northern end of the Maldives extends further to continue as a plume toward Sri Lanka. Isotherms begin to dome upwards and the D26 was uplifted by ∼10 m. As the SMC flowed through the Maldives toward Sri Lanka, it merged with the southward flowing WICC and the southward flowing EICC to converge along the south coast of Sri Lanka. The flow convergence resulted in a cyclonic eddy at ∼81°E and a general decrease of SST in the convergence zone (**Figure 11E**). Part of the SMC continued along the Sri Lanka coastline and the shear interaction with the coastline was diverted into the cyclonic SLD at ∼84°E, 8°N. In contrast to the month of June, the WICC strengthened and drove upwelling along the west coast of India and intensified at the southern tip of India. In the convergence zone at ∼81°E Sri Lanka, the D26 was uplifted to the surface and the upwelling zone was at its widest from 4.5 to 6°N with water temperatures in the water column <27°C (**Figure 11F**).

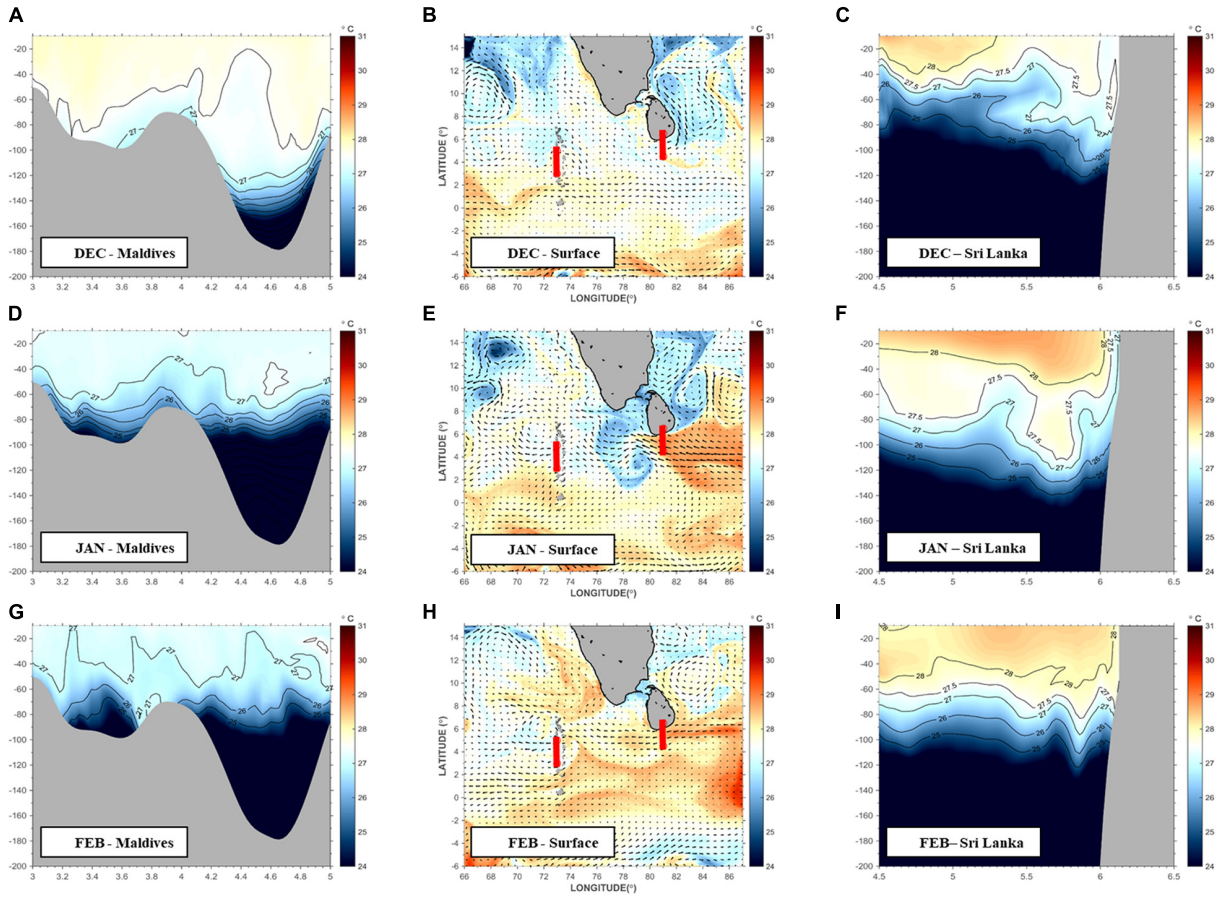

FIGURE 10 | Top to bottom: NEM model output for December, January, and February. Left panel shows the longitudinal temperature transect for Maldives along 73°E and the right panel shows the longitudinal temperature transect for Sri Lanka along 81°E. Surface circulation and temperature for the model domain is shown in the middle panel and red lines indicate transect locations. Intra-seasonal temperature variability during the NEM for Maldives and Sri Lanka during **(A–C)** December, **(D–F)** January, **(G–I)** February. Longitudinal temperature transects for Maldives along 73°E are shown in **(A)** December **(D)** January **(G)** February. Surface circulation and temperature for the model domain is shown **(B)** December **(E)** January **(H)** February. Longitudinal temperature transects for Sri Lanka along 81°E are shown in **(C)** December **(F)** January **(I)** February.

SST continued to decrease throughout August with mean SST at ∼27°C (**Figure 11H**). However, the SMC and SEC current velocities increased, altering the wake structures around the Maldives and Sri Lanka. As the velocities of the westward flowing SEC increased, it advected warmer SST and its interaction with Kolhumadulu Atoll at ∼73.5°E, 0.5°N created a downstream wake with cooler SST (**Figure 11H**). In contrast, the strengthened SMC redefined the structure of the anticyclonic eddy along the east coast of the Maldives to become more coherent, although still spatially smaller than its counterpart in June. At the 74°E zonal transect, the distance between the different isotherms was reduced and D26 continued to be shifted upwards and with its shallowest point at ∼55 m depth (**Figure 11G**). A warm pool (28°C) between 3 and 4°N continued to deepen from the previous ∼20 m in July to ∼40 m but an upwelling signal remained present above 4.6°N (**Figure 11G**). The increase in velocity of the SMC also had implications for the upwelling zone along Sri Lanka by narrowing its width to be between 5.5 and 6°N (**Figure 11I**). The WICC also increased in strength, broadened along the west coast of India, and was accompanied by a decrease in SST. Similarly, the strengthened EICC reversed its directionality and flowed southwards, decreasing SST along the east coast of Sri Lanka and India. The combined increase in strength of the SMC, WICC and directionality of the EICC resulted in the original upwelling zone around the south of Sri Lanka being shifted further eastwards and leaving the Sri Lanka coastline as a filament of cooler SST and high current velocities.

DISCUSSION

Seasonal Variability

The directionality of the island wakes downstream from the islands follows the dominant monsoon currents. The regions where the island wakes develop were characterized by stronger currents, cooler temperatures and higher SCC (**Figures 2**, **3**, 5), identifying the presence of the IME (Caldeira and Sangrà,

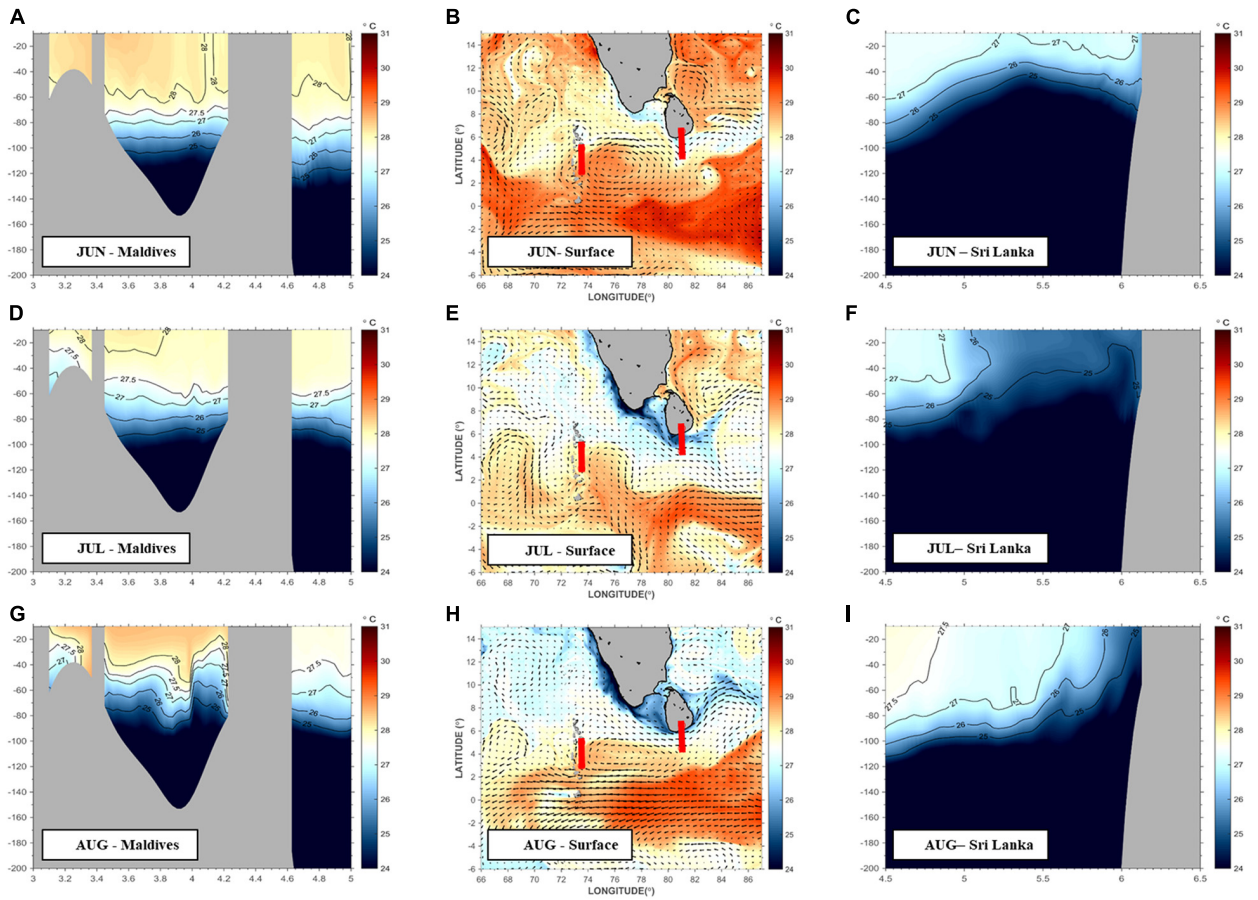

FIGURE 11 | Top to bottom: SWM model output for June, July, and August. Left panel shows the longitudinal temperature transect for Maldives along 74°E and the right panel shows the longitudinal temperature transect for Sri Lanka along 81°E. Surface circulation and temperature for the model domain is shown in the middle panel and red lines indicate transect locations. Intra-seasonal temperature variability during the SWM for Maldives and Sri Lanka during **(A–C)** June, **(D–F)** July, **(G–I)** August. Longitudinal temperature transects for Maldives along 73°E are shown in **(A)** June **(D)** July **(G)** August. Surface circulation and temperature for the model domain is shown in **(B)** June **(E)** July **(H)** August. Longitudinal temperature transects for Sri Lanka along 81°E are shown in the right panel for **(C)** June **(F)** July **(I)** August.

2012). Possible mechanisms for IME development include the passive advection from the deep chlorophyll maximum (George et al., 2013) or via eddy shedding (Sasamal, 2006; Hasegawa et al., 2009). The strength of the wakes varied with the monsoon currents for the period, with stronger wakes occurring during the SWM than the NEM due to the stronger SMC and wind forcing (Schott and McCreary, 2001; de Vos et al., 2014b). The physical mechanisms for IME development were different between the Maldives and Sri Lanka where island wake processes were found to be key to IME development while flow convergence and divergence along the Sri Lanka coastline generated upwelling and downwelling. The directionality of the wake structures along the Maldives island chain varied with latitude and shows the extent of influence of the major monsoon current for the period. Above 4°N, the wakes flow in the same direction of the incoming monsoon current. However, below 4°N, particularly around Kolhumadulu Atoll (**Figure 9**), the direction of the island wakes was unaffected by the monsoon currents and was influenced by the presence of the non-reversing year round equatorial current, SECC.

Intra-seasonal Variability

Intra-seasonal variability was observed within each monsoon period but with regional differences. Along the east coast of Sri Lanka and India, there was shallowing of D26 throughout the NEM (upwelling), while D26 was deepening (downwelling) around the northern end of the Maldives. The maximum intensity for these processes were in January and could be explained by the NMC which reaches its mature phase during January (Shankar et al., 2002). The upwelling along the southern end of the Maldives could be attributed to the end of the NEM and the transition to the inter-monsoon period where the Wrytki jets are the dominant zonal current in the equatorial region (Wyrtki, 1973; Nagura and Masumoto, 2015). In contrast to the NEM, D26 was shallower throughout the SWM for the Maldives region but with increased downwelling at the mid-latitudes during the peak of the SWM. This could be due to

TABLE 2 | Summary of key findings on the IME processes around the Maldives and Sri Lanka.

	NEM	SWM
Overview	• Downwelling throughout the domain • Island wakes flow westwards • Highest current speeds around the eastern coastline of Maldives	• Upwelling throughout the domain • Island wakes flow eastwards • Highest current speeds at the south coast of Sri Lanka
Maldives	• Downwelling begins in December, intensifies in January and broadens in February. • Strong eastward flow at the start of December due to Wrytki jets but reverse at the start of January to flow west. • Downwelling occurs on both sides of the archipelago in January • Upwelling constrained within the archipelago throughout the NEM • Upwelling occurs at Kolhumadulu Atoll due to intensification of SECC at the end of the NEM • Basin warming with increase in SST due to SEC • Upwelling frequency increases at the end of January along with the deepening and increase in velocity of the zonal currents	• Strong upwelling signature at the northern end of the Maldives chain in June but subsides in July. Broadens in August. • Downwelling occurs below 5°N in July • Upwelling occurs at Kolhumadulu Atoll in August with greater intensity compared to upwelling at the end of the NEM • Basin wide cooling with decrease in SST • Upwelling is more prevalent throughout the SWM at the northern end of the Maldives due to higher zonal velocities downwelling occurs at 4°N throughout the first half of the SWM before zonal velocities increase leading to upwelling
Sri Lanka	• Upwelling signal strongest in January around but replaced by downwelling in February	• Upwelling signal strong throughout the SWM with high zonal velocities • Highest velocities in the Sri Lanka Dome region

the SECC which shifts northward during the SWM, with the combined influence of the stronger SMC (Schott and McCreary, 2001; Shankar et al., 2002). At Sri Lanka, D26 shallows and broadens in spatial extent, identifying the presence of the SLD developing (Vinayachandran and Yamagata, 1998). In the nearshore regions around the Maldives, the fine-scale processes provide a similar picture of the IME. The largest intra-seasonal variability in terms of temperature and vertical structure occurs within January to February for both the Maldives and Sri Lanka, during the peak of the NEM. In contrast, during the SWM, upwelling remains prevalent along Sri Lanka and broadens during July whilst downwelling occurs along the Maldives. These processes were closely tied to the onset and phase of the monsoonal currents and reach the maximum variability during mature phases of the NMC (SMC) during the NEM (SWM) (Shankar et al., 2002).

IME and Island Wakes

Many scaling arguments have been proposed to define the circulation patterns in the lee of islands based on the Reynolds number which appear to reproduce the observed circulation in the lee of the island/headland (Wolanski et al., 1984; Tomczak, 1988). The Reynolds number, R_e for the deep ocean is defined by Tomczak (1988) as $R_e = UL/K_h$, where U is the velocity scale, L, a length scale and K_h is the horizontal eddy viscosity. The nature of the wake downstream of an island can be predicted using the Reynolds number with low values of R_e (of ∼1), reflecting no wake with the flow attached to island termed as an "attached" flow condition (Pattiaratchi et al., 1987; Alaee et al., 2007) and for R_e between 1 and 40, the wake consists of attached eddies. Sri Lanka acts as a large headland that extends to the ocean (large scale flows are absent between Sri Lanka and India due to shallow water). Two distinct circulation patterns related to the Reynolds number were identified through the analysis of the predicted flow patterns around Sri Lanka: (1) interaction between SMC and the southern part of the island where the flow followed the curvature of the southern coast of Sri Lanka and generated an eddy to the east, defined as the Sri Lanka Dome (**Figure 2C**). Using the values of L∼200 km; U ∼0.8 ms^{-1}; and $K_h \sim 10^4$ m^2 s^{-1}, yields a Reynolds number ($R_e = UL/K_h$) of ∼20 which predicts an attached eddy which is the SLD. Numerical simulations undertaken by de Vos et al. (2014b) with constant westerly winds predicted a stronger eddy with increasing wind (flow) speeds and the removal of the Sri Lanka land mass resulted in no eddy; (2) During both the SWM and NEM, the model results indicated southward flow along both east and west coasts converging along the south coast. In this case, circulation was similar to that of an island with no discernible wake—defined as attached flow (e.g., Alaee et al., 2004). The currents were now weaker and using values of L∼100 km; U ∼0.1 ms^{-1}; and $K_h \sim 10^4$ m^2 s^{-1}, yields Re = ∼1, in agreement with the theoretical predictions (see also Su, 2020).

SUMMARY AND CONCLUSION

This paper examined the monsoonal variability of IME processes, such as island wake circulation and upwelling around the Maldives and Sri Lanka. A numerical model based on the ROMS framework was implemented for Sri Lanka and the Maldives in the NIO. The model was validated with available *in situ* and remote sensing measurements. It was able to reproduce the unique monsoonal circulation, including the recirculation feature known as the SLD that develops east of Sri Lanka during the SWM. The model simulations also provided further insight into the seasonal and intra-seasonal variation of the three-dimensional structure of the IME around Sri Lanka and the Maldives in terms of its temperature and current velocities.

There is a strong monsoonal influence on the development of the IME which can be characterized by the presence of upwelling or downwelling in the proximity of islands. The monsoon currents influence the directionality and intensity of the downstream wakes but only above latitudes 4°N. Below 4°N, island wake development around the Maldives is influenced by the equatorial currents, the SECC. Due to the different

circulation regimes between the two monsoon periods, there will be potentially different connectivity pathways between Sri Lanka, India and the Maldives. This sets the case for the IME developing via remote enrichment in addition to localized flow topography interactions and can be explored in future work (e.g., Su, 2020). A full breakdown of the IME processes specific to Maldives and Sri Lanka during the NEM and SWM is summarized in **Table 2**.

DATA AVAILABILITY STATEMENT

The raw data supporting the conclusions of this article will be made available by the authors, without undue reservation.

AUTHOR CONTRIBUTIONS

DS: undertaken this study as a part of research, analysis and interpretation, and writing—original draft preparation. DS and CP: conceptualization. DS, SW, and CP: methodology. DS and SW: software. CP: resources. DS, CP, and SW: writing—review and editing. All authors have read and agreed to the published version of the manuscript.

FUNDING

This postgraduate research was part of research by DS that was funded by the Australian government's Research Training Program and Australian postgraduate award. DS was also supported by the *Ad Hoc* Postgraduate Scholarship by the University of Western Australia.

ACKNOWLEDGMENTS

Access to the supercomputing facilities of the Pawsey Centre (Magnus) was enabled through the partner allocation scheme. We would like to thank John Wilkin, Art Miller, and Patrick Marchiesello for their constructive comments and input on the manuscript.

SUPPLEMENTARY MATERIAL

The Supplementary Material for this article can be found online at: https://www.frontiersin.org/articles/10.3389/fmars.2021.645672/full#supplementary-material

REFERENCES

Alaee, J. M., Ivey, G., and Pattiaratchi, C. (2004). Secondary circulation induced by flow curvature and Coriolis effects around headlands and islands. *Ocean Dyn.* 54, 27–38. doi: 10.1007/s10236-003-0058-3

Alaee, M. J., Pattiaratchi, C., and Ivey, G. (2007). Numerical simulation of the summer wake of Rottnest Island, Western Australia. *Dyn. Atmos. Oceans* 43, 171–198. doi: 10.1016/j.dynatmoce.2007.01.001

Ali, M. M., Nagamani, P. V., Sharma, N., Venu Gopal, R. T., Rajeevan, M., and Goni, G. J. (2015). Relationship between ocean mean temperatures and Indian summer monsoon rainfall. *Atmos. Sci. Lett.* 16, 408–413. doi: 10.1002/asl2.576

Anderson, R. C., Adam, M. S., and Goes, J. I. (2011). From monsoons to mantas: seasonal distribution of *Manta alfredi* in the Maldives. *Fish. Oceanogr.* 20, 104–113. doi: 10.1111/j.1365-2419.2011.00571.x

Andrade, I., Sangrà, P., Hormazabal, S., and Correa-Ramirez, M. (2014). Island mass effect in the Juan Fernández Archipelago (33 S), Southeastern Pacific. *Deep Sea Res. I Oceanogr. Res. Papers* 84, 86–99. doi: 10.1016/j.dsr.2013.10.009

Beckmann, A., and Haidvogel, D. B. (1993). Numerical simulation of flow around a tall isolated seamount. part i: problem formulation and model accuracy. *J. Phys. Oceanogr.* 23, 1736–1753. doi: 10.1175/1520-0485(1993)023<1736:nsofaa>2.0.co;2

Caldeira, R. M. A., and Sangrà, P. (2012). Complex geophysical wake flows Madeira Archipelago case study. *Ocean Dyn.* 62, 683–700. doi: 10.1007/s10236-012-0528-6

Caldeira, R. M. A., Groom, S., Miller, P., Pilgrim, D., and Nezlin, N. P. (2002). Sea-surface signatures of the island mass effect phenomena around Madeira Island, Northeast Atlantic. *Remote Sens. Environ.* 80, 336–360. doi: 10.1016/s0034-4257(01)00316-9

Caldeira, R. M. A., Marchesillo, P., Nezlin, N. P., and DiGiacomo, P. M. (2005). Island wakes in the Southern California Bight. *J. Geophys. Res.* 110:11012.

Chassignet, E. P., Hurlburt, H. E., Smedstad, O. M., Hallliwell, G. R., Hogan, P. J., and Wallcraft, A. J. (2007). The HYCOM (hybrid coordinate ocean model) data assimilative system. *J. Mar. Syst.* 65, 60–83.

Cowen, R. K., and Castro, L. R. (1994). Relation of coral reef fish larval distributions to island scale circulation around Barbados, West Indies. *Bull. Mar. Sci.* 54, 228–244.

Cushman-Roisin, B., and Beckers, J.-M. (2011). *Introduction to Geophysical Fluid Dynamics: Physical and Numerical Aspects*. Cambridge: Academic Press.

de Vos, A., Pattiaratchi, C. B., and Wijeratne, E. M. S. (2014a). Inter-annual variability in blue whale distribution off southern Sri Lanka between 2011 and 2012. *J. Mar. Sci. Eng.* 2, 534–550. doi: 10.3390/jmse2030534

de Vos, A., Pattiaratchi, C. B., and Wijeratne, E. M. S. (2014b). Surface circulation and upwelling patterns around Sri Lanka. *Biogeosciences* 11, 5909–5930. doi: 10.5194/bg-11-5909-2014

Dee, D. P., Uppala, S. M., Simmons, A. J., Berrisford, P., Poli, P., Kobayashi, S., et al. (2011). The ERA-interim reanalysis: configuration and performance of the data assimilation system. *Q. R. Meteorol. Soc.* 137, 553–597.

Dong, C., and McWilliams, J. C. (2007). A numerical study of island wakes in the Southern California Bight. *Cont. Shelf Res.* 27, 1233–1248. doi: 10.1016/j.csr.2007.01.016

Doty, M. S., and Oguri, M. (1956). The island mass effect. *ICES J. Mar. Sci.* 22, 33–37.

Egbert, G. D., and Erofeeva, S. Y. (2002). Efficient inverse modeling of barotropic ocean tides. *J. Atmos. Ocean. Technol.* 19, 183–204. doi: 10.1175/1520-0426(2002)019<0183:eimobo>2.0.co;2

Elliott, J., Patterson, M., and Gleiber, M. (2012). "Detecting Island mass effect through remote sensing," in *Proceedings of the 12th International Coral Reef Symposium*, (Australia).

Flather, R. A. (1976). A tidal model of the north-west European continental shelf. *Mém. Soc. R. Sci. Liège* 1, 141–164.

George, J. V., Nuncio, M., Chacko, R., Anilkumar, N., Noronha, S. B., Patil, S. M., et al. (2013). Role of physical processes in chlorophyll distribution in the western tropical Indian Ocean. *J. Mar. Syst.* 113, 1–12. doi: 10.1016/j.jmarsys.2012.12.001

Gove, J. M., McManus, M. A., Neuheimer, A. B., Polovina, J. J., Drazen, J. C., Smith, C. R., et al. (2016). Near-island biological hotspots in barren ocean basins. *Nat. Commun.* 7:10581.

Hamner, W. M., and Hauri, I. R. (1981). Effects of island mass: water flow and plankton pattern around a reef in the great barrier reef lagoon, Australia 1. *Limnol. Oceanogr.* 26, 1084–1102. doi: 10.4319/lo.1981.26.6.1084

Haney, R. L. (1991). On the pressure gradient force over steep topography in sigma coordinate ocean models. *J. Phys. Oceanogr.* 21, 610–619. doi: 10.1175/1520-0485(1991)021<0610:otpgfo>2.0.co;2

Hasegawa, D., Lewis, M. R., and Gangopadhyay, A. (2009). How islands cause phytoplankton to bloom in their wakes. *Geophys. Res. Lett.* 36, 2–5.

Heywood, K. J., Barton, E. D., and Simpson, J. H. (1990). The effects of flow disturbance by an oceanic island. *J. Mar. Res.* 48, 55–73. doi: 10.1357/002224090784984623

Jiang, W., Knight, B. R., Cornelisen, C., Barter, P., and Kudela, R. (2017). Simplifying regional tuning of MODIS algorithms for monitoring chlorophyll-a in coastal waters. *Front. Mar. Sci.* 4:151.

Kersalé, M., Doglioli, A. M., and Petrenko, A. A. (2011). Sensitivity study of the generation of mesoscale eddies in a numerical model of Hawaii islands. *Ocean Sci.* 7, 277–291. doi: 10.5194/os-7-277-2011

Large, W. G., McWilliams, J. C., and Doney, S. C. (1994). Oceanic vertical mixing: a review and a model with a nonlocal boundary layer parameterization. *Rev. Geophys.* 32, 363–403. doi: 10.1029/94rg01872

Marchesiello, P., Lefèvre, J., Vega, A., Couvelard, X., and Menkes, C. (2010). Coastal upwelling, circulation and heat balance around new Caledonia's barrier reef. *Mar. Pollut. Bull.* 61, 432–448. doi: 10.1016/j.marpolbul.2010.06.043

Marchesiello, P., McWilliams, J. C., and Shchepetkin, A. (2001). Open boundary conditions for long-term integration of regional oceanic models. *Ocean Model.* 3, 1–20. doi: 10.1016/s1463-5003(00)00013-5

McCreary, J. P., Kundu, P. K., and Molinari, R. L. (1993). A numerical investigation of dynamics, thermodynamics and mixed-layer processes in the Indian Ocean. *Prog. Oceanog* 31, 181–244. doi: 10.1016/0079-6611(93)90002-u

McPhaden, M. J., Wang, Y., and Ravichandran, M. (2015). Volume transports of the Wyrtki jets and their relationship to the Indian Ocean Dipole. *JGR Oceans* 120, 5302–5317. doi: 10.1002/2015jc010901

Morel, A., Gentili, B., Claustre, H., Babin, M., Bricaud, A., Ras, J., et al. (2007). Optical properties of the "clearest" natural waters. *Limnol. Oceanogr.* 52, 217–229. doi: 10.4319/lo.2007.52.1.0217

Nagura, M., and Masumoto, Y. (2015). A Wake due to the Maldives in the Eastward Wyrtki Jet. *J. Phys. Oceanogr.* 45, 1858–1876. doi: 10.1175/jpo-d-14-0191.1

Palacios, D. M. (2002). Factors influencing the island-mass effect of the Galápagos Archipelago. *Geophys. Res. Lett.* 29, 49-1–49-4.

Pattiaratchi, C. B., James, A. E., and Collins, M. B. (1987). Island wakes and headland eddies: a comparison between remotely sensed data and laboratory experiments. *J. Geophys. Res. Oceans* 92, 783–794. doi: 10.1029/jc092ic01p00783

Raapoto, H., Martinez, E., Petrenko, A., Doglioli, A. M., and Maes, C. (2018). Modeling the wake of the Marquesas Archipelgao. *J. Geophys. Res. Oceans* 123, 1213–1228. doi: 10.1002/2017jc013285

Rao, R. R., Kumar, M. S. G., Ravichandran, M., and Samala, B. K. (2006). Observed mini-cold pool off the southern tip of India and its intrusion into the south central Bay of Bengal during summer monsoon season. *Geophys. Res. Lett.* 33:L06607.

Sasamal, S. K. (2006). Island mass effect around the Maldives during the winter months of 2003 and 2004. *Int. J. Remote Sens.* 27, 5087–5093. doi: 10.1080/01431160500177562

Sasamal, S. K. (2007). Island wake circulation off Maldives during boreal winter, as visualised with MODIS derived chlorophyll-α a data and other satellite measurements. *Int. J. Remote Sens.* Taylor & Francis, 28, 891–903.

Schott, F. A., and McCreary, J. P. (2001). The monsoon circulation of the Indian Ocean. *Prog. Oceanogr.* 51, 1–123. doi: 10.1016/s0079-6611(01)00083-0

Schott, F. A., Xie, S. P., and McCreary, J. P. (2009). Indian Ocean circulation and climate variability. *Rev. Geophys.* 47, 1–46

Shankar, D., Vinayachandran, P. N., and Unnikrishnan, A. S. (2002). The monsoon currents in the north Indian Ocean. *Prog. Oceanogr.* 52, 63–120. doi: 10.1016/s0079-6611(02)00024-1

Shchepetkin, A. F., and McWilliams, J. C. (2003). A method for computing horizontal pressure-gradient force in an oceanic model with a nonaligned vertical coordinate. *J. Geophys. Res.* 10:3090.

Shchepetkin, A. F., and McWilliams, J. C. (2005). The regional oceanic modeling system (ROMS): a split-explicit, free-surface, topography-following-coordinate oceanic model. *Ocean Model.* 9, 347–404. doi: 10.1016/j.ocemod.2004.08.002

Song, Y., and Haidvogel, D. (1994). A semi-implicit ocean circulation model using a generalized topography-following coordinate system. *J. Comput. Phys.* 115, 228–244. doi: 10.1006/jcph.1994.1189

Su, D. L. W. (2020). *Flow Topography Interactions Around Sri Lanka and the Maldives*. Unpubl PhD thesis. Australia: The University of Western Australia.

Tchamabi, C. C., Araujo, A., Silva, M., and Bourles, B. (2017). A study of the Brazilian Fernando de Noronha island and Rocas atoll wakes in the tropical Atlantic. *Ocean Model.* 111, 9–18. doi: 10.1016/j.ocemod.2016.12.009

Tomczak, M. (1988). Island wakes in deep and shallow water. *J. Geophys. Res. Oceans* 93, 5153–5154. doi: 10.1029/jc093ic05p05153

Vinayachandran, P. N., and Yamagata, T. (1998). Monsoon response of the sea around Sri Lanka: generation of thermal domes and anticyclonic vortices. *J. Phys. Oceanogr.* 28, 1946–1960. doi: 10.1175/1520-0485(1998)028<1946:mrotsa>2.0.co;2

Weatherall, P., Marks, K. M., Jakobsson, M., Schmitt, T., Tani, S., Arndt, J. E., et al. (2015). A new digital bathymetric model of the world's oceans. *Earth Space Sci.* 2, 331–345.

Wijeratne, S., Pattiaratchi, C., and Proctor, R. (2018). Estimates of surface and subsurface boundary current transport around Australia. *J. Geophys. Res. Oceans* 123, 3444–3466. doi: 10.1029/2017jc013221

Willmott, C. J. (1982). Some comments on the evaluation of model performance. *Bull. Am. Meteorol. Soc.* 63, 1309–1313. doi: 10.1175/1520-0477(1982)063<1309:scoteo>2.0.co;2

Wolanski, E., Imberger, J., and Heron, M. L. (1984). Island wakes in shallow coastal waters. *J. Geophys. Res. Oceans* 89, 10553–10569. doi: 10.1029/JC089iC06p10553

Wyrtki, K. (1973). An equatorial jet in the Indian ocean. *Science* 181, 262–264. doi: 10.1126/science.181.4096.262

Conflict of Interest: The authors declare that the research was conducted in the absence of any commercial or financial relationships that could be construed as a potential conflict of interest.

The reviewer RC is currently organizing a Research Topic with one of the authors CP.

frontiers in Marine Science

ORIGINAL RESEARCH
published: 08 July 2021
doi: 10.3389/fmars.2021.688248

Modeling Fine-Scale Cetaceans' Distributions in Oceanic Islands: Madeira Archipelago as a Case Study

Marc Fernandez[1,2], Filipe Alves[1,3], Rita Ferreira[1,3], Jan-Christopher Fischer[4,5], Paula Thake[5], Nuno Nunes[6], Rui Caldeira[3] and Ana Dinis[1,3]*

[1] MARE - Marine and Environmental Sciences Centre, Agência Regional para o Desenvolvimento da Investigação Tecnologia e Inovação (ARDITI), Funchal, Portugal, [2] cE3c/Azorean Biodiversity Group, Departamento de Biologia, Faculdade de Ciências e Tecnologia, Universidade dos Açores, Ponta Delgada, Portugal, [3] Oceanic Observatory of Madeira (OOM), Funchal, Portugal, [4] School of Earth Sciences, University of Bristol, Bristol, United Kingdom, [5] Lobosonda - Madeira Whale Watching, Estreito da Calheta, Portugal, [6] ITI/LARSyS, Técnico Lisboa, Universidade de Lisboa, Lisbon, Portugal

OPEN ACCESS

Edited by:
Matthew Lewis, Bangor University, United Kingdom

Reviewed by:
Victoria Paige Van de Vuurst, Virginia Tech, United States
James Waggitt, Bangor University, United Kingdom

***Correspondence:**
Marc Fernandez
marc.fern@gmail.com

Specialty section:
This article was submitted to Coastal Ocean Processes, a section of the journal Frontiers in Marine Science

Received: *30 March 2021*
Accepted: *15 June 2021*
Published: *08 July 2021*

Citation:
Fernandez M, Alves F, Ferreira R, Fischer J-C, Thake P, Nunes N, Caldeira R and Dinis A (2021) Modeling Fine-Scale Cetaceans' Distributions in Oceanic Islands: Madeira Archipelago as a Case Study. Front. Mar. Sci. 8:688248. doi: 10.3389/fmars.2021.688248

Species distributional estimates are an essential tool to improve and implement effective conservation and management measures. Nevertheless, obtaining accurate distributional estimates remains a challenge in many cases, especially when looking at the marine environment, mainly due to the species mobility and habitat dynamism. Ecosystems surrounding oceanic islands are highly dynamic and constitute a key actor on pelagic habitats, congregating biodiversity in their vicinity. The main objective of this study was to obtain accurate fine-scale spatio-temporal distributional estimates of cetaceans in oceanic islands, such as the Madeira archipelago, using a long-term opportunistically collected dataset. Ecological Niche Models (ENM) were built using cetacean occurrence data collected on-board commercial whale watching activities and environmental data from 2003 to 2018 for 10 species with a diverse range of habitat associations. Models were built using two different datasets of environmental variables with different temporal and spatial resolutions for comparison purposes. State-of-the-art techniques were used to iterate, build and evaluate the MAXENT models constructed. Models built using the long-term opportunistic dataset successfully described distribution patterns throughout the study area for the species considered. Final models were used to produce spatial grids of species average and standard deviation suitability monthly estimates. Results provide the first fine-scale (both in the temporal and spatial dimension) cetacean distributional estimates for the Madeira archipelago and reveal seasonal/annual distributional patterns, thus providing novel insights on species ecology and quantitative data to implement better dynamic management actions.

Keywords: whales, dolphins, pelagic, ecological niche modeling, opportunistic data, whale watching

INTRODUCTION

While the construction of species distributional estimates is a crucial topic to conserve, protect, manage and monitor biodiversity (Rodríguez et al., 2007), it stills remains a challenge to obtain accurate and reliable products to ensure practical management actions (Araújo et al., 2019). One of the main tools used for these purposes are ecological miche models (ENMs). A class of methods that use occurrence data together with environmental data to make a correlative model of the environmental conditions that meet a species' ecological requirements and predict the relative suitability of habitat (Warren and Seifert, 2011). Challenges are even more significant when estimating species distributions in the marine environment, where there are many factors to take into account, such as the species mobility and habitat dynamism (Redfern et al., 2006; Fernandez et al., 2017), or the difficulties of sampling at oceanic environments, primarily when referring to cetacean populations (Tyne et al., 2016).

Lately, several studies found that non-traditional data sources (such as opportunistic or citizen science data; e.g., Catlin-Groves, 2012; Embling et al., 2015) can be a cost-effective solution to overcome some of the challenges mentioned, allowing to produce relatively accurate cetacean abundance and distributional estimates (e.g., Fernandez et al., 2018; Robbins et al., 2019). When studying species in dynamic habitats, opportunistic surveys (and citizen science) can have many advantages over traditional methods. Formal and dedicated surveys provide poor coverage in time because of financial and logistic constraints, meaning that they cannot capture long-term variation in species distributions and occurrence.

Oceanic islands are a key actor on pelagic habitats, congregating biodiversity in their vicinity, primarily due to the "island-mass effect" (Doty and Oguri, 1956) or "island stirring" (Mann and Lazier, 1991), which is the topographic disturbance of oceanic flow by an island and its effects on the marine ecosystem. Several oceanographic features, such as wakes and eddies or vortices (e.g., Aristegui et al., 1994; Caldeira et al., 2002), are originated due to the presence of islands and have a direct effect on the local and regional productivity (Barton et al., 2000). Due to their dynamic nature, their effects on marine species are not well understood.

Cetaceans are marine mammals in the order Cetacea, which includes whales, dolphins, and porpoises. They have a strong influence on the marine ecosystems: as consumers of fish and invertebrates, as prey to other predators, as reservoirs of carbon, as vertical and horizontal vectors for nutrients and as detrital sources of energy and habitat in the deep-sea (Roman et al., 2014). Whales and dolphins are essential to ensure the correct functioning of the marine ecosystems worldwide, with a vital role in the biogeochemical cycles at biome and Earth system scale (Albouy et al., 2020; Norris et al., 2020). A high diversity of cetaceans (∼30 species) has been recorded in the Madeira Archipelago (NE Atlantic), including species featured in the Red List of the International Union for Conservation of Nature as Endangered, Vulnerable, and Data Deficient (Freitas et al., 2012; Alves et al., 2018). These waters host populations with some degree of residency, such as the short-finned pilot whale (*Globicephala macrorhynchus*) or the bottlenose dolphin (*Tursiops truncatus*) (Alves et al., 2013b; Dinis et al., 2016a). Other deep-diving cetacean species, such as the sperm whale (*Physeter macrocephalus*) and Blainville's beaked whale (*Mesoplodon densirostris*), are among the most sighted species by commercial whale watching companies with some periodicity.

Moreover, baleen whales occur frequently in the archipelago, especially the Bryde's whale (*Balaenoptera edeni*), with a relatively high occurrence rate but with a very high interannual variation (Alves et al., 2018). Recent studies revealed cetacean interconnectivity among neighboring archipelagos, such as the Canaries and the Azores, with re-sightings of individuals from several species among the three archipelagos (e.g., Alves et al., 2019; Dinis et al., 2021). Additionally, Madeira constitutes an area of interest for several (at least ten) cetacean species due to being used for traveling, feeding, resting, socializing and calving (Alves et al., 2018). However, despite its ecological importance, up to date, there are no reliable spatio-temporal distributional estimates for any of the cetacean species present in the area.

In this study, we provide, for the first time, a fine-scale spatio-temporal approach to obtain distributional estimates of cetaceans around the Madeira archipelago. Having a better knowledge of the species suitability throughout the year is critical for their conservation through maritime spatial planning and management of human activities. We built niche models for the ten most sighted cetacean species in Madeira, using two different datasets of environmental variables with different temporal and spatial resolutions. Models were iterated and selected using several state-of-the-art evaluation techniques.

MATERIALS AND METHODS

Study Area and Data Collection

The Madeira archipelago is in the NE Atlantic (33°N, 17°W) and is mainly influenced by a branch of the Gulf Stream, the Azores Current system. Caldeira et al. (2002) suggested that the archipelago's latitude might be the subtropical front, where cold-temperate waters from the north meet warm tropical waters from the south. The island mass effect of the archipelago is easily noticeable from satellite imagery, with wakes being formed on leeward areas and lee eddies spinning of both flanks of Madeira Island. Moreover, upwelling was detected near the island's coasts, with the region between Madeira and Desertas Islands being particularly dynamic (Caldeira et al., 2002).

Cetacean occurrences were collected in an opportunistically way on-board commercial whale-watching vessels departing from two harbors (Calheta and Funchal) separated over 30 km on the South Coast of Madeira Island (**Figure 1**). The occurrences were collected by three operators (see section "Acknowledgments") during their regular touristic trips from January 2003 until December 2018, with a total of 3,138 days sampled. Experienced observers from the companies collected

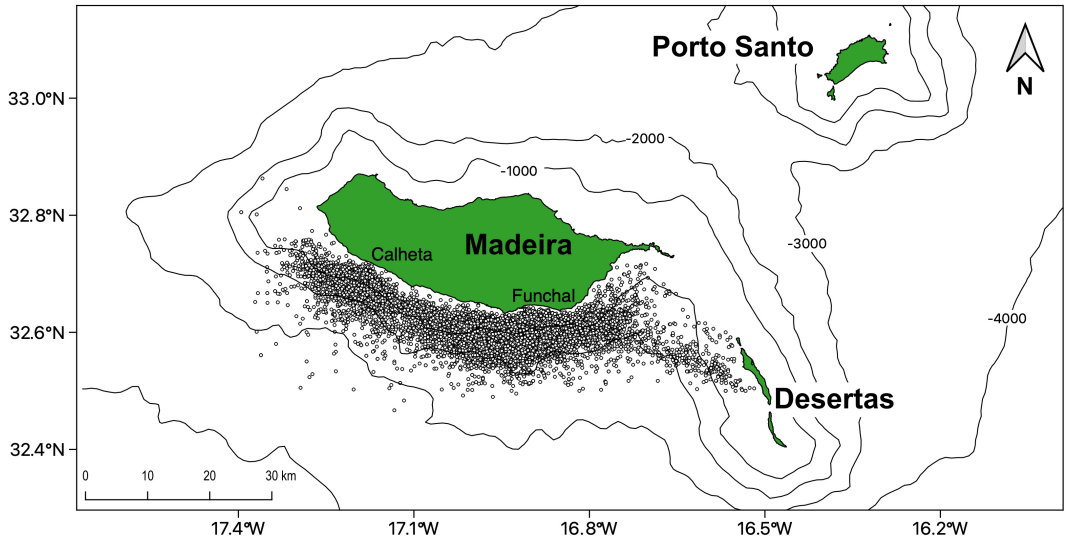

FIGURE 1 | Cetacean sightings for 23 species (n = 8,607) pooled together, collected by the commercial whale watching companies departing from Funchal and Calheta in Madeira Island (Portugal) from 2003 until 2018.

TABLE 1 | Number of sightings for the 10 most sighted species (out of 23) by commercial whale watching companies from 2003 until 2018 used in the present study (n = 8,607).

Species	*N*
Atlantic Spotted dolphin (*Stenella frontalis*)	3040
Bottlenose dolphin (*Tursiops truncatus*)	2733
Short-beaked common dolphin (*Delphinus delphis*)	1936
Short-finned pilot whale (*Globicephala macrorhynchus*)	1503
Bryde's whale (*Balaenoptera edeni*)	931
Sperm whale (*Physeter macrocephalus*)	554
Striped dolphin (*Stenella coeruleoalba*)	292
Blainville's beaked whale (*Mesoplodon densitrostris*)	144
Fin whale (*Balaenoptera physalus*)	130
Rough-toothed dolphin (*Steno bredanensis*)	81

location and species identification of each encounter. We applied a database filtering and cleaning to remove duplicate observations and incorrect GPS points clearly outside of the study area (or on land). A total of 8,607 sightings from 23 different species were selected during this period, from which the ten most sighted species were used in the present study (**Table 1**). Detailed methodological procedures on the data collection on-board commercial whale-watching vessels are given in Alves et al. (2018).

Occurrences and Background Data

All occurrences records were projected onto 2 and 8 km grids to match the resolution of the two environmental datasets. Observations data collected on whale-watching operations might have a different source of biases due to the nature of the touristic activity. For example, it is not unusual that the same group of animals is visited more than once in a very similar location, both in space and time, which creates autocorrelation problems in contiguous grids. Therefore, a filtering approach was applied to remove potentially related sightings. A spatial thinning procedure was applied to all the sightings for both temporal groupings (1- and 8-days), using the spThin R package (Aiello-Lammens et al., 2015). Different sizes of the exclusion radius were tested (2, 4, and 6 km), selecting at the end a value of 2 km, which was the best compromise to reduce related sightings and still keep a good amount of observations. This agrees with the relatively small size of the sampled area (around 2,100 km^2) by the whale-watching boats. Furthermore, during the modeling analysis, occurrences were also resampled to one occurrence per pixel for each temporal grouping.

Due to the sampling effort's opportunistic nature, we applied a Minimum Sampled Area (MSA) approach, as Fernandez et al. (2017) used. All the sightings for each specific temporal scale were pooled together using a Minimum Convex Polygon, adding a 2 km buffer. Grids intersecting the polygon were taken as potentially sampled areas, therefore classified as background. The amount of effort per temporal unit (day or 8-days) was considered using the number of sea trips performed on a specific period. For each analysis, random background datasets (n = 10,000) were created, using the effort as a weighting factor.

Environmental Variables

A set of 19 environmental variables were used to calibrate the models (**Table 2**). Six terrain variables (depth, slope, and distance to the 1,000 m bathymetric lines, valley depth, distance to canyon-like features, and distance to major canyons) were derived from a digital elevation model (DEM) using the bathymetric dataset from the Instituto Hidrográfico of Portugal and interpolated using QGIS 3.1 at a resolution of 1 km. Physical features, such as the depth and the slope, can directly influence the distribution of cetaceans (e.g., Moore et al., 2000;

Azzellino et al., 2008). Depth was directly read from the DEM; slope and distances to the 1,000 m bathymetric lines were calculated using QGIS 3.1. Moreover, other morphological features, such as canyons, can play an essential role in cetacean distributions. Canyons and other similar features can affect cetacean abundance patterns due to a series of physical features that enhance primary productivity and convert it to potential prey biomass (Moors-Murphy, 2014). These effects are even more noticeable when dealing with deep-diving cetacean species, which might directly rely on these areas for feeding purposes (Breen et al., 2020).

We calculated a series of morphological variables to include the effects of morphological features as prey aggregation areas into the models. The valley depth refers to the vertical distance to a channel network base level; it was calculated using the QGIS module "Relative Heights and Slope Positions" based on Boehner and Selige (2006). The canyon-like features were calculated using the topographic position index (TPI), which measures where a point is in the overall landscape/seascape to identify features such as ridges, canyons, or midslopes (Wright and Heyman, 2008). We computed the TPI with the SAGA GIS[1] implementation (based on Guisan et al., 1999; Weiss, 2001), using a radius of 3,000 m. We selected features corresponding to V-shape river valleys and deep narrow canyons (Weiss, 2001). We applied a spatial filter (<3km) to eliminate artifacts and minor features. Another layer focusing only on the major canyon-like features was identified, selecting features with an extension larger than 25 squared km. Distance to the edge of these structures was calculated.

Nine of the surface and deep waters oceanographic variables used for model building were obtained through the Copernicus Marine system, with a daily, 8-day, and monthly temporal resolution; through the IBI (Iberian Biscay Irish) Ocean Reanalysis system (see **Table 2**). The IBI model numerical core is based on the NEMO v3.6 ocean general circulation model run at 1/12° horizontal resolution, assimilating altimeter data, *in situ* temperature, vertical salinity profiles, and satellite sea surface temperature. The surface chlorophyll (Chl-a) data was obtained from the ESA Ocean Color CCI Remote Sensing Reflectance data (by merging layers from SeaWiFS, MODIS-Aqua, MERIS, and VIIRS sensors and realigning the spectra to that of the SeaWiFS sensor) using the regional OC5CCI chlorophyll algorithm. Moreover, the Sea Surface Temperature (SST) was obtained from the Group for High-Resolution Sea Surface Temperature (GHRSST), a global, gap-free, gridded, daily 1 km dataset created by merging multiple Level-2 satellite SST datasets. Depending on the analysis performed, layers were scaled to the desired temporal and spatial resolution.

We applied a variance inflation factor (VIF) approach as implemented in the R package usdm (Naimi, 2015) to test for collinearity. Two of the environmental layers had collinearity issues, the distance to 1,000 m bathymetric line and the distance to major canyons. Due to the potential ecological importance of canyons, we excluded the distance to 1,000 m bathymetric isoline, keeping all the canyon-related variables (see the final variables selected for the analysis in **Table 2**).

Two different sets of environmental layers were constructed. The first assemblage (the daily set) aimed to detect the effect of dynamic variables at a coarse spatial resolution (7.8 km) and included a set of nine oceanographic variables at different depths with a daily resolution. The cumulative effect of variables (temperature and Chl-a) was measured as the mean values for the 30 days previous to the sightings. The second group of layers (the 8-day set) aimed to detect the influence of topographic features on a fine-scale resolution (2 km), including a set of 4 oceanographic variables with an 8-day (**Table 2**). The 30-day mean values of temperature and Chl-a were included to test for those variables' cumulative effects.

Modeling Building and Evaluation

Due to the opportunistic nature of the data used in this study, without real absences, we used a presence-background algorithm MAXENT (Phillips et al., 2006) to infer the ecological niche model of the selected species.

The kuenm package (Cobos et al., 2019a) in R was used to select the most important variables, build and evaluate the MAXENT models. Data was introduced using the sightings with data (SWD) formatting, adding the temporality factor. Models were built with 75% occurrences for training purposes. For each species or family, we created thousands of candidate models (more than 10,000 for each group) by combining all the potential different sets of environmental predictors, three values of regularization multiplier (1, 1.5, 2), and five possible combinations ("l," "lq," "lqp," "lqpt," and "lqpth") of the feature classes (linear = l, quadratic = q, product = p, threshold = t, and hinge = h). The regularization parameter allows MAXENT to limit the model complexity (protecting it against overfitting), adding a penalty for each term included in the model and higher weights given to a term (Phillips et al., 2006). Overfitted models excel in predicting non-independent evaluation data, leading to an inappropriate automatic selection of low regularization values; better model performance is generally achieved at slightly (or substantially) higher regularization parameters (Radosavljevic and Anderson, 2014). Feature classes are used in MAXENT to build the responses curves. Depending on the feature classes selected, different response curves can be obtained, from very simple to highly complex non-linear curves (Merow et al., 2013).

Model evaluation was carried out following the implementation of kuenm based on statistical significance, through partial ROC (Receiver Operator Curve), with 500 iterations and 50% of data for bootstrapping (Peterson et al., 2008), omission rates with a threshold of $E = 5\%$ (Anderson et al., 2003) and model complexity based on the findings of Warren and Seifert (2011) on the AICc index (indicates how well models fit the data while penalizing complexity to favor simple models). Best models were selected according to (1) significant models with (2) omission rates $\leq$5%. Then, from among this model set, models with delta AICc values of $\leq$2 were chosen as final models. The exhaustive method implemented in kuenm ensures better performance of the models selected and reduces

[1] www.saga-gis.org/

TABLE 2 | Variables used to construct the two different assemblages of layers for the present analysis: the (1) "D" set with a spatial resolution of 7.8 km and a temporal resolution of 1 day, and the (2) "8-D" set, with a spatial resolution of 2 km and a temporal resolution of 8-days and 1 month.

ACR	Variables	D set	8-D set	UNITS	Product source/ID
DEPTH	Depth	√	√	m	Resampled from Instituto Hidrográfico
SLOPE	Bottom slope	√	√	°	Calculated and resampled from Instituto Hidrográfico
VALLEY_DEPTH	Vertical distance to a channel network base level		√	m	Calculated and resampled from Instituto Hidrográfico
D_M_CANYONS	Distance to major canyon like features		√	Km	Calculated and resampled from Instituto Hidrográfico
D_CANYONS	Distance to canyon like features		√	Km	Calculated and resampled from Instituto Hidrográfico
SST	Sea surface temperature		√	°C	GHRSST Level 4 MUR Global Foundation Sea Surface Temperature Analysis (v4.1)
TEMP_0.5	Sea water potential temperature at 0.5 m	√		°C	Atlantic-Iberian Biscay Irish-Ocean Physic Reanalysis product: IBI_REANALYSIS_PHYS_005_001
TEMP_100	Sea water potential temperature at 108 m	√		°C	Atlantic-Iberian Biscay Irish-Ocean Physic Reanalysis product: IBI_REANALYSIS_PHYS_005_001
TEMP_700	Sea water potential temperature at 773 m	√		°C	Atlantic-Iberian Biscay Irish-Ocean Physic Reanalysis product: IBI_REANALYSIS_PHYS_005_001
TEMP_PR_0.5	Sea water potential temperature at 0.5 m of the previous month	√		°C	Atlantic-Iberian Biscay Irish-Ocean Physic Reanalysis product: IBI_REANALYSIS_PHYS_005_001
TEMP_PR_100	Sea water potential temperature at 108 m of the previous month	√		°C	Atlantic-Iberian Biscay Irish-Ocean Physic Reanalysis product: IBI_REANALYSIS_PHYS_005_001
TEMP_PR_700	Sea water potential temperature at 773 m of the previous month	√		°C	Atlantic-Iberian Biscay Irish-Ocean Physic Reanalysis product: IBI_REANALYSIS_PHYS_005_001
SAL_S	Sea water salinity at 0.5 m	√		ppt	Atlantic-Iberian Biscay Irish-Ocean Physic Reanalysis product: IBI_REANALYSIS_PHYS_005_001
MIXED_LAYER	Mix layer depth	√		m	Atlantic-Iberian Biscay Irish-Ocean Physic Reanalysis product: IBI_REANALYSIS_PHYS_005_001
SSH	Sea surface height	√		Cm	Atlantic-Iberian Biscay Irish-Ocean Physic Reanalysis product: IBI_REANALYSIS_PHYS_005_001
CHL	Chlorophyll-a concentration in sea water	√	√	$mg{\cdot}m^{-3}$	North Atlantic Chlorophyll Concentration from Satellite observations reprocessed L4 (ESA-CCI) product: OCEANCOLOUR_ATL_CHL_L4_REP_OBSERVATIONS_009_098
LUNAR_IL	Lunar illumination	√	√	Lux	R "lunar" package
CHL_PR	Chlorophyll-a concentration in sea water of the previous month	√	√	$mg{\cdot}m^{-3}$	North Atlantic Chlorophyll Concentration from Satellite observations reprocessed L4 (ESA-CCI) product: OCEANCOLOUR_ATL_CHL_L4_REP_OBSERVATIONS_009_091
SST_PR	Sea surface temperature of the previous month		√	°C	GHRSST Level 4 MUR Global Foundation Sea Surface Temperature Analysis (v4.1)

both overfitting and underfitting when comparing it to a classical heuristic method (Cobos et al., 2019b).

The best models were selected by the kuenm process, only in one case (fin whales on the daily scenario); we did not select the best option given by kuenm, but one of the other potential candidates selected during the process. In this case, the best model was slightly overfitted to coastal areas due to the relatively low number of observations for the species and the bias associated with the whale-wacthing activity. Therefore, we selected a model with no restrictions on the Depth variable, as we know that fin whales are also frequently sighted offshore.

To select between the two different environmental datasets tested (with different temporal and spatial resolution), we used an expert-based omission criterion (areas/time being classified as unsuitable when they are not). Experts evaluation and knowledge were based on empirical observations of the target species around the archipelago in different periods outside the study area. However, as these datasets were not available at the moment of the evaluation, we used the expert-based omission criterion as a complementary validation method.

Projections of the models were made for each combination of year/month from 2003 to 2018 using a clamping approach to avoid extrapolations to areas outside of the range of the training conditions (Merow et al., 2013). Finally, the mean suitability values and standard deviation for all months through all years were calculated.

RESULTS

Model Performance

A total of 87,300 model solutions were generated for the 8-day dataset, and 300,300 were generated for the daily data. The best results were selected according to their relative predictive and explanatory capabilities. According to expert knowledge criteria, models built using the 8-day dataset, with a higher

TABLE 3 | Eight-days models regularization multiplier (REG.), feature classes (linear = l, quadratic = q, product = p, threshold = t, and hinge = h), omission rate at 5% (OR 5%), area under the curve (AUC), and variables selected (with its contribution) for each species.

Species	REG.	FEAT.	OR 5%	AUC	Vars selected
*Globicephala macrorhynchus**	1.5	lqpt	0.048	0.75	Depth (62.5%). SST previous month (17%). SST week (7.4%). Slope (7.3%). Chl-a previous month (3.9%). Distance to major canyons (2%).
*Physeter macrocephalus**	1.5	lqpt	0.045	0.73	Depth (59.3%). SST week (12.4%). Valley depth (11.1%). Slope (6.3%). Distance to canyons (5.9%). Distance to major canyons (4.9%).
*Mesoplodon densirostris**	1.5	lqp	0.032	0.73	Distance to major canyons (36.3%). Slope (31.8%). SST week (20.5%). Chl-a previous month (7%). SST previous month (4.5%).
*Stenella frontalis**	2	lqpth	0.044	0.7	Depth (46.4%). SST previous month (23.3%). Chl-a week (17.9%). SST week (10.5%). Chl-a previous month (2%).
*Tursiops truncatus**	1.5	lqpt	0.046	0.73	Depth (73.4%). Slope (19.6%). Distance to major Canyons (5%). Chl-a previous month (1%). Chl-a week (1%).
*Delphinus delphis**	1	lqpt	0.048	0.81	SST week (30.9%). Chl-a previous month (20.8%). Depth (17%). SST previous month (14.3%). Slope (12.2%). Distance to major canyons (4.8%).
*Stenella coeruleoalba**	1.5	lqpt	0.048	0.80	Depth (59.5%). SST previous month (19.4%). Slope (15.5%). SST week (5.6%).
*Steno bredanensis**	1	lqpt	0	0.90	SST week (57.1%). Slope (23.5%). Lunar illumination (13.9%). Distance to major canyons (5.4%).
Balaenoptera physalus	1.5	lqpt	0.038	0.88	Chl-a week (41.4%). SST previous month (38.1%). Lunar illumination (12.2%). Depth (8.3%).
Balaenoptera edeni	1	lq	0.044	0.75	SST week (50.5%). Depth (43.2%). Chl-a week (6.3%).

Variables are sorted by percent contribution to the final model. Models marked with an asterisk are the ones selected as "Best."

spatial resolution and more topographic-based variables, had a better predictive performance. For 8 of the 10 species considered in the present study (*G. macrorhyncus, P. macrocephalus, M. densirostris, S. frontalis, T. truncatus, D. delphis, S. coeruleoalba,* and *S. bredanensis*), the 8-day scenario produced better results (**Table 3**). Only two species (*B. edeni* and *B. physalus*) produced better estimates when using the daily dataset. The results are presented per functional ecological groups: (i) deep-divers (short-finned pilot whales, sperm whales and Blainville's beaked whale), (ii) delphinids (bottlenose dolphins, rough-toothed dolphins, Atlantic spotted dolphins, short-beaked common dolphins and striped dolphins), and (iii) balaenopterids (fin whales and Bryde's whales).

Deep-Divers

All the deep-diving species higher suitability values were related to the bathymetry or other topographic variables. The short-finned pilot whales (*G. macrorhynchus*) suitable

areas were related with depths between 1,000 and 2,000 m with intermediate slope values and a slight preference for regions closer to major canyons (**Figure 2**). The SST played a relevant role in the species niche, with a preference for warm waters (18–24°C) and low Chl-a values. The daily analysis results showed an influence of the shallow mixed layer in the suitability. Models projections suggest a patched temporal and spatial distribution of the species, with highly suitable areas found at the South-east and North of Madeira. Seasonal variability was found, with lower suitability values from March to July. However, high standard deviation values were found in March and April (**Supplementary Figure 1**). Lastly, the daily models showed a subtle influence of the lunar illumination on the species, with higher suitability indexes with lower values.

Sperm whales (*P. macrocephalus*) habitat was related with waters deeper than 1 km, with an intermediate slope and closer to any type of canyons (**Figure 3**). The analysis suggested a relation with areas with low valley depths and close to canyons on mid-slope areas. Only one oceanographic variable was found relevant for the model selected (the SST), denoting a slight preference of the species for warmer waters. Low standard deviation values of suitability were found (**Supplementary Figure 2**) for all the months.

Blainville's beaked whales (*M. densirostris*) models showed a significant contribution of the major canyons, slope, and SST, with a total contribution of 88.6% on the model construction (**Table 3**). The species was related to areas with major canyons, with high slope values and a positive correlation with warm waters (**Figure 4**). Moreover, a marginal effect of the Chl-a and SST on the previous month was also observed. This species showed a patchy distribution primarily in the vicinity of canyons and a temporal preference for summer and early autumn. Nonetheless, the standard deviation maps (**Supplementary Figure 3**) show relatively high values from January to April.

Delphinids

The suitability for bottlenose dolphins (*T. truncatus*) was found to be primarily related to the bathymetry, slope, and distance to the major canyons, contributing up to 98% to the selected model (**Table 3**). The species suitability was positively linked to relatively shallow waters with high slope values and somehow close to major canyons. Even if marginal, there is also a preference for waters with high Chl-a values (**Figure 5**). These outcomes produced a generalist distribution of the species on Madeira's coastal areas with almost no temporal variability, also reflected on the low values of standard deviation maps (**Supplementary Figure 4**).

The weekly SST was found to be the most influential factor (**Figure 6**) determining the rough-toothed dolphins (*S. bredanensis*) niche, being linked to warmer waters (above 20°C). The daily scenario models also showed a relation between warm waters and shallow mixed layer depth. Topographically, the niche was linked with mid and high slope values in the proximity of major canyons. The results revealed a relation between rough-toothed dolphin niche and low lunar illumination values. Relatively high suitability values for the species were found from July to October, with high standard deviation values in June and November (**Supplementary Figure 5**).

In both of the modeling approaches used in this study, only one topographic variable was identified as an important predictor for the Atlantic spotted dolphins (*S. frontalis*), the bathymetry (**Tables 3**, **4**). The species showed a preference for relatively deep-waters around the 1,000 m isoline. Moreover, both during the 8-day and in the previous month, the temperature was selected as the models' relevant variables. Atlantic spotted dolphins niche was related with temperate/warm waters (over 18°C) with very low productivity values (**Figure 7**), leading to higher suitability values from June until October. However, high standard deviation values are found between February and May (**Supplementary Figure 6**), which denotes the high variability of the suitability indexes in those months.

In contrast, the short-beaked common dolphins (*D. delphis*) presented a strong relation with lower values of SST (both in the weekly and previous month) along with high values of Chl-a during the previous month (**Figure 8**). This delphinid niche was also related to relatively shallow waters, moderate to high slope regions, and areas closer to major canyons. Moreover, the daily model showed an influence of the mixed layer depth on the species niche. Common dolphins had higher suitability values in winter and spring (from December to June), with moderate standard deviation values in June (**Supplementary Figure 7**). The striped dolphins (*S. coeruleoalba*) were predominantly related to deep waters regions (over 1,000 m) and moderate slope values (**Figure 9**), alongside a preference for temperate waters (around 19–20°C). While the suitability values obtained indicate a year-round presence of these delphinids in the archipelago, higher suitability values were found from spring to early summer, with very low standard deviation values (**Supplementary Figure 8**).

Balaenopterids

Oceanographic variables were constantly selected as the most influential variables for the baleen whales' ecological niche in the present study. The fin whales suitability (*B. physalus*) was influenced mainly by moderate values of Chl-a in the previous month, together with high daily Chl-a values and low daily values of temperature in 100 m depth. Topographically, the species niche was related to intermediate bathymetry (with a peak at 2,000 m) and mid-slope values (**Figure 10**). Suitability maps exhibited elevated values from February to May, with high standard deviation values from February to August (**Supplementary Figure 9**).

Conversely, very low values of Chl-a during the previous month were more related to the Bryde's whales (*B. edeni*) niche, together with sea surface temperatures in the previous month between 20 and 24°C (**Figure 11**). This species' results also indicated a relation with waters around 1,000 m depth and a positive correlation with the warmer daily temperature at 100 m. Suitability values for Bryde's whales were relatively low, with a slight increase from June to January; however, high standard deviation values were found from June to November (**Supplementary Figure 10**).

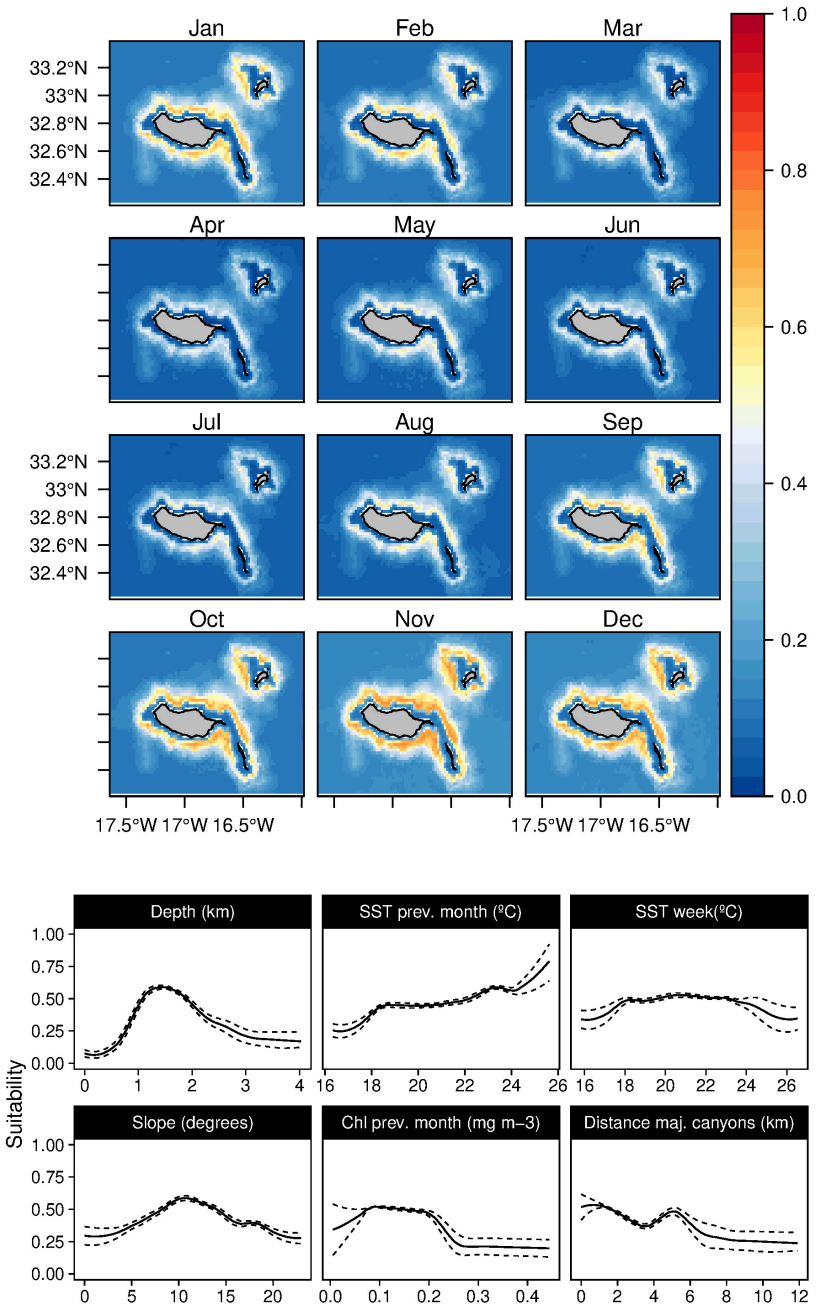

FIGURE 2 | Mean monthly suitability maps **(above)** and smoothed response curves with standard deviation **(below)** in the Madeira archipelago for *Globicephala macrorhynchus* for the "8-days" models. In the maps, red represents more suitable and blue less suitable. Responses curves are ordered by percent contribution of the environmental variables.

DISCUSSION

The long-term opportunistic dataset used in this study provided an excellent opportunity to build reliable ecological niche models with various environmental conditions. Even if the AUC values alone might not be the best model performance indicator (Lobo et al., 2008), all selected models ranged between 0.7 and 0.9, which, together with the low omission rate values, indicates good overall predictive performance. This reinforces the potential of opportunistically collected datasets to produce reliable estimates of habitat suitability, as Henckel et al. (2020) found recently.

While a series of techniques to reduce overfitting and select the best models were applied (e.g., AICc index for model selection), few coincidental relationships between suitability predictions and environmental variables might still be present.

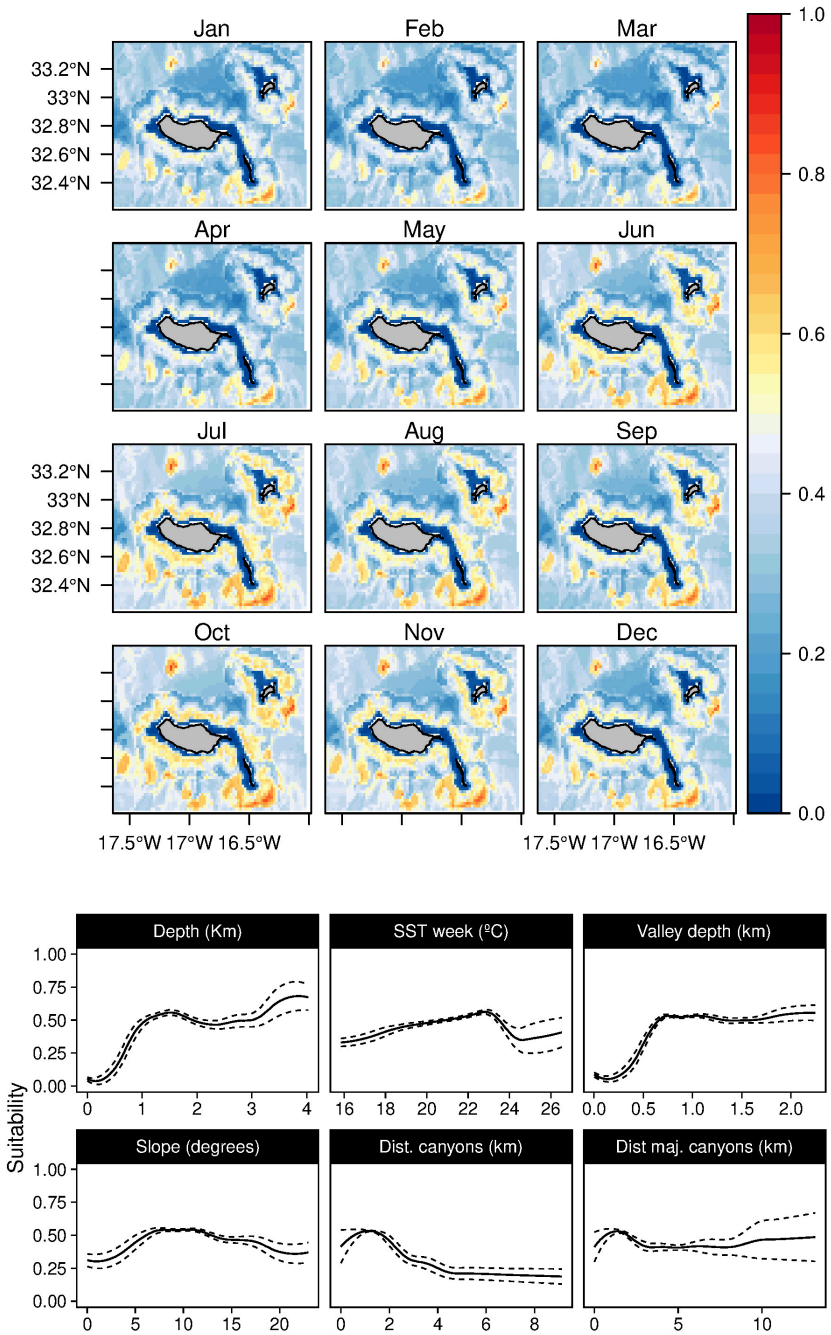

FIGURE 3 | Mean monthly suitability maps **(above)** and smoothed response curves with standard deviation **(below)** in the Madeira archipelago for *Physeter macrocephalus* for the "8-days" models. In the maps, red represents more suitable and blue less suitable. Responses curves are ordered by percent contribution of the environmental variables.

Some of the relations found in the response curves (such as the high suitability predictions on low slope values found for the common dolphins; **Figure 8**) might look odd and spurious, affecting the explanatory power. Explanatory power and predictive accuracy are different qualities; a model will possess some level of each (Shmueli, 2010). Therefore, even if few coincidental relationships might be present, the validation techniques implemented assure good predictive performance for the models built.

Despite the small area where data was collected (limited mainly to the South coast of Madeira and West of Desertas islands), experts confirmed that extrapolated areas agree with their experience. However, using a reduced area to collect training data might result in a truncated response curve

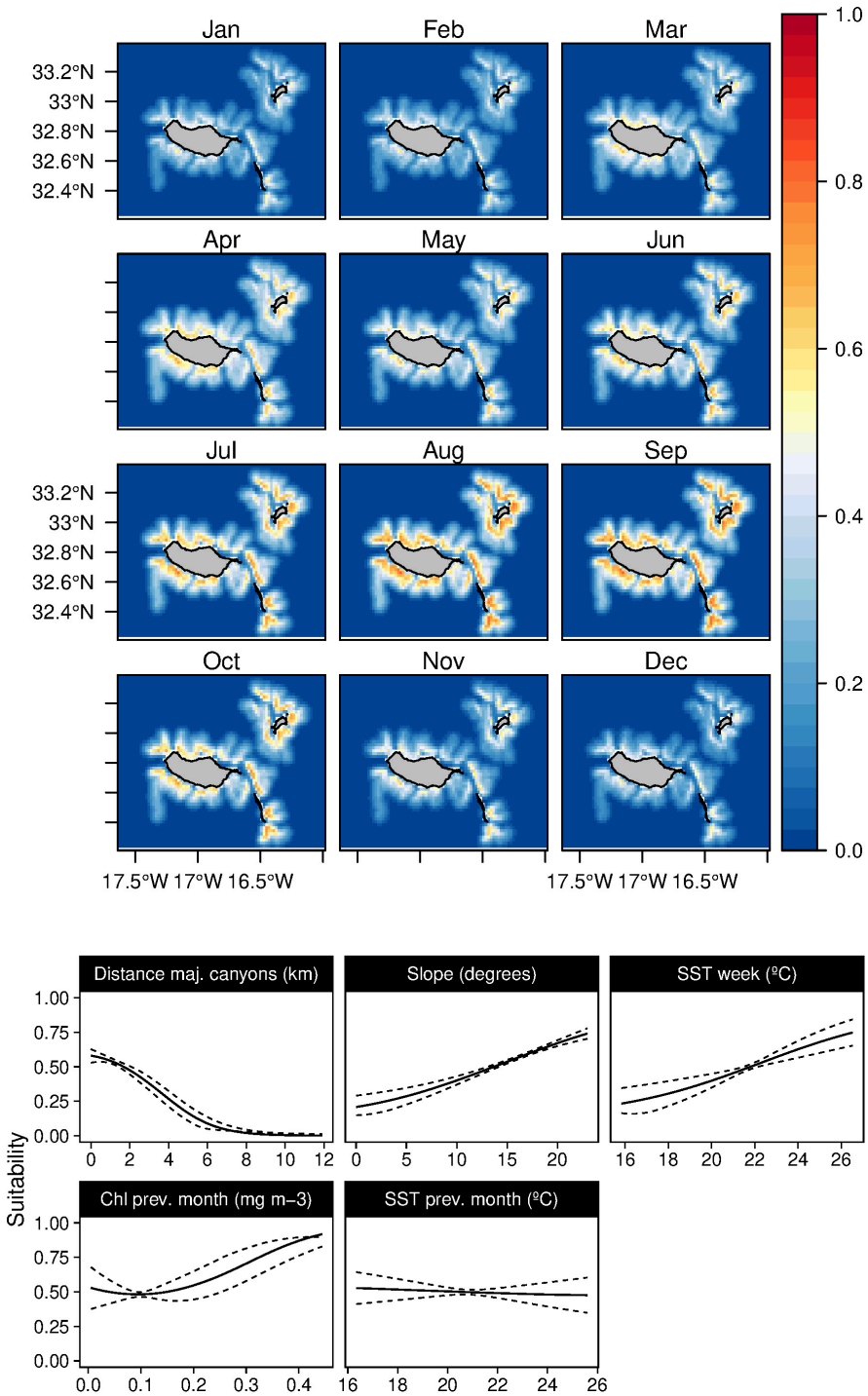

FIGURE 4 | Mean monthly suitability maps **(above)** and smoothed response curves with standard deviation **(below)** in the Madeira archipelago for *Mesoplodon densirostris* for the "8-days" models. In the maps, red represents more suitable and blue less suitable. Responses curves are ordered by percent contribution of the environmental variables.

for some variables, missing fundamental environmental values to fully describe the niche (Thuiller et al., 2004; Williams and Jackson, 2007). This could be the case, especially for those more bottom-related species (such as the sperm whale, the short-finned pilot whale, or the bottlenose dolphin). The Maxent clamping implementation mitigates this issue (Phillips et al., 2006; Anderson and Raza, 2010); however, preferably, a wider sampling area with

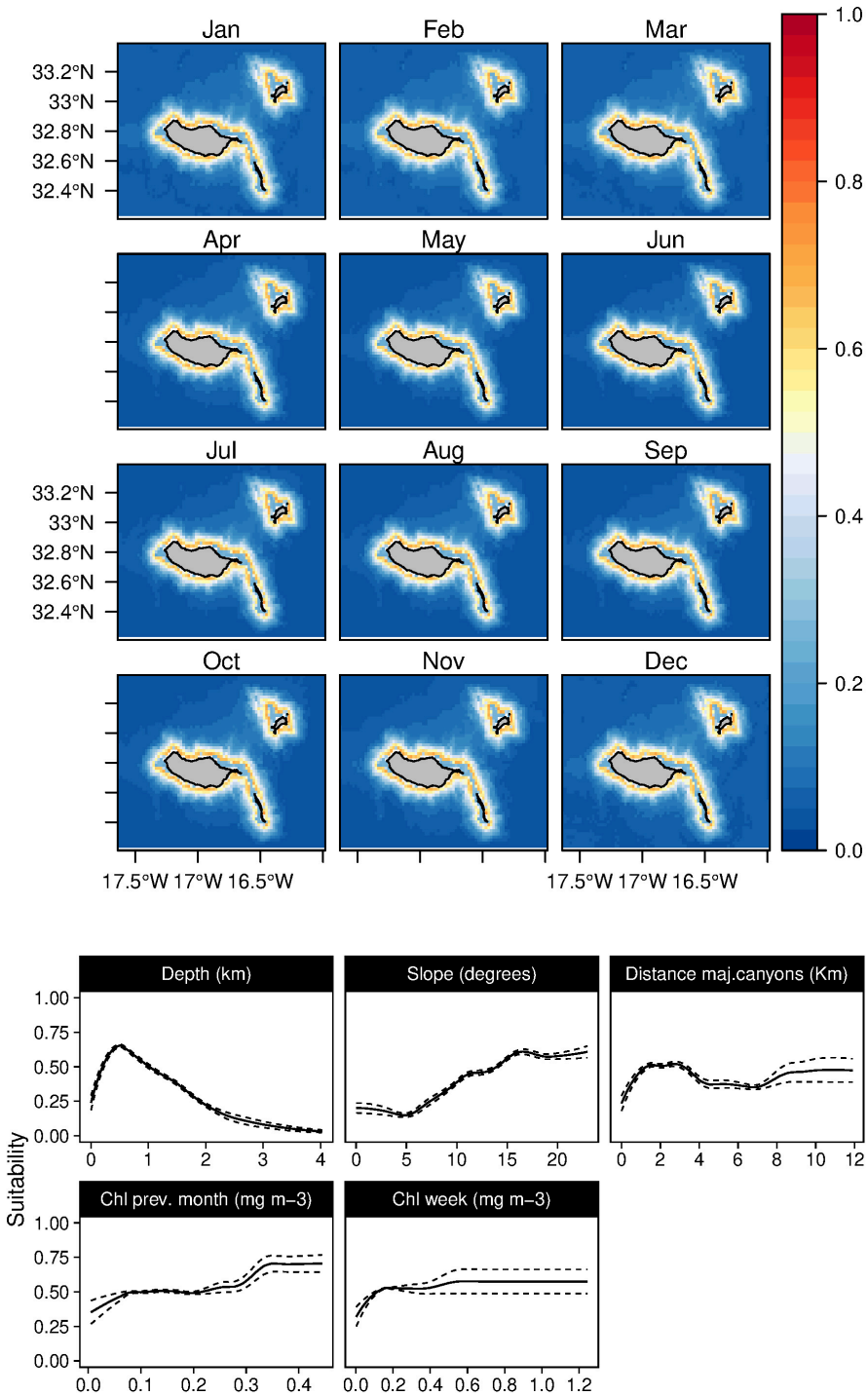

FIGURE 5 | Mean monthly suitability maps **(above)** and smoothed response curves with standard deviation **(below)** in the Madeira archipelago for *Tursiops truncatus* for the "8-days" models. In the maps, red represents more suitable and blue less suitable. Responses curves are ordered by percent contribution of the environmental variables.

different topographic characteristics would be the best way to overcome this concern.

The daily models added some relevant information on species niches, as it considers a broader range of oceanographic variables in the three dimensions. However, its informative potential was primarily reduced due to the dataset's coarse spatial resolution and the use of a broad-scale circulation oceanographic algorithm. Using models with a finer spatial resolution and including

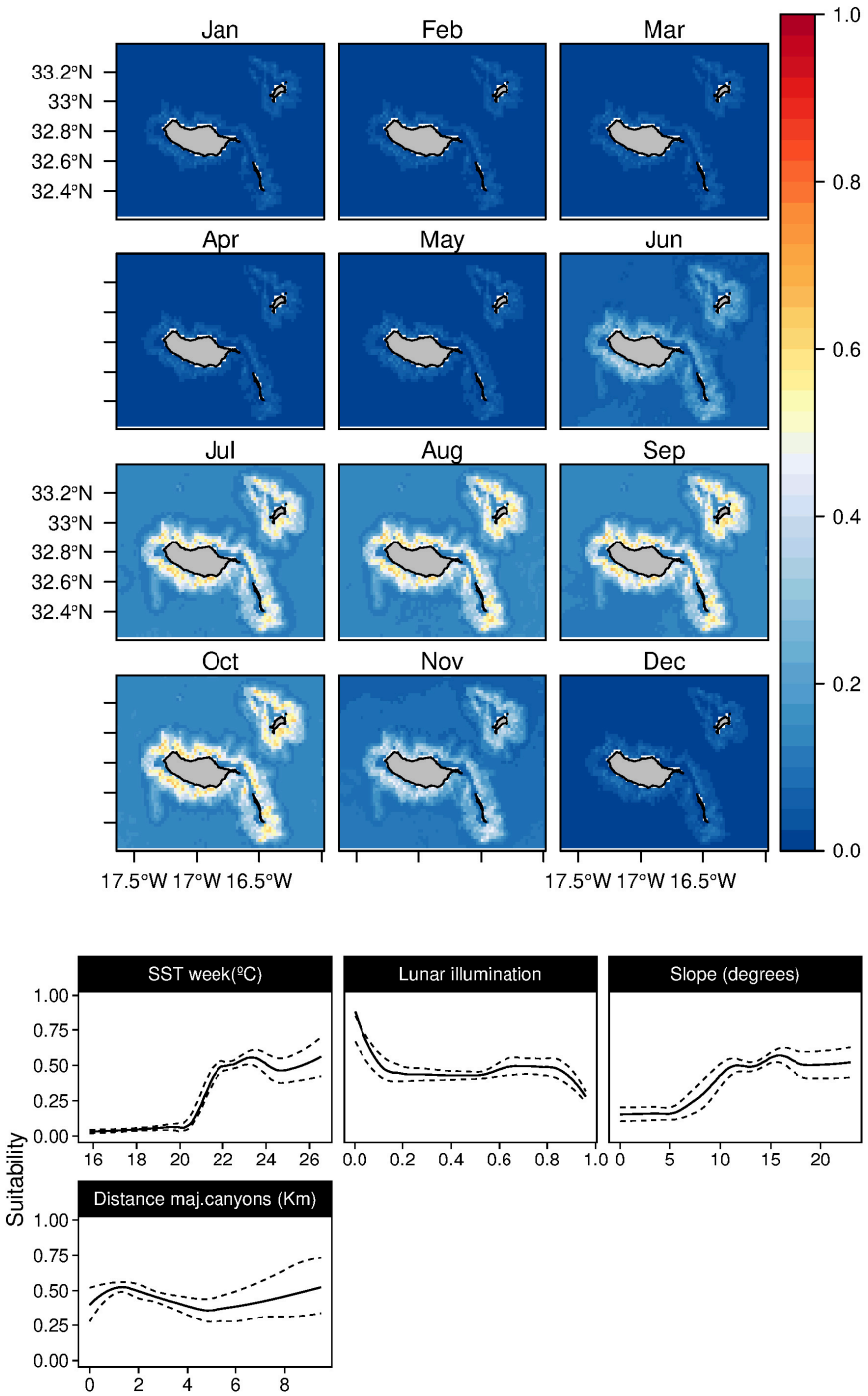

FIGURE 6 | Mean monthly suitability maps **(above)** and smoothed response curves with standard deviation **(below)** in the Madeira archipelago for *Steno bredanensis* for the "8-days" models. In the maps, red represents more suitable and blue less suitable. Responses curves are ordered by percent contribution of the environmental variables.

atmosphere-ocean interactions could improve the results, giving more insights on fine-scale features that can influence cetacean distributions. This fact is especially relevant when considering the fine-scale structures generated by the island in the archipelago (Caldeira et al., 2002).

Species Ecological Findings

Deep-Divers

The three deep-diving species (*G. macrorhynchus*, *P. macrocephalus*, and *M. densirostris*) showed differentiated niches, both in the spatial and temporal dimensions. The

TABLE 4 | Daily models regularization multiplier (REG.), feature classes (linear = l, quadratic = q, product = p, threshold = t, and hinge = h), omission rate at 5% (OR 5%), area under the curve (AUC), and variables selected (with its contribution) for each species.

Species	REG.	FEAT.	OR 5%	AUC	Vars selected
Globicephala macrorhynchus	1	lqpt	0.044	0.74	Depth (62.7%). Slope (19.4%). Mixed layer depth (7.8%). SSH (7.5%). Lunar illumination (2.5%).
Physeter macrocephalus	1.5	lqp	0.047	0.65	Depth (40%). Slope (34.8%). Temp. at 0.5 m previous month (22%). Temp. at 700 m daily (3.2%).
Mesoplodon densirostris	1.5	lqpth	0.034	0.73	Slope (55.5%). Temp. at 0.5 m daily (30%). Temp. at 0.5 m previous month (8%). Chl-a previous month (6.4%).
Stenella frontalis	1.5	lqpth	0.047	0.74	Depth (48.9%). Temp. at 0.5 m daily (20.6%). Temp. at 0.5 m previous month (19.1%). Temp. at 100 m previous month (9.7%). Temp. at 100 m daily (1.8%).
Tursiops truncatus	1	lqpt	0.05	0.68	Slope (60.3%). Depth (25.7%). Temp. at 100 m previous month (9.7%). Temp. at 0.5 m previous month (6.7%).
Delphinus delphis	1.5	lqpt	0.047	0.77	Temp. at 0.5 m previous month (43.2%). Chl-a previous month (24.6%). Slope (23.4%). Mixed layer depth (6.4%). Depth (2.5%).
Stenella coeruleoalba	2	lqpth	0.032	0.76	Depth (52.7%). Temp. at 0.5 m previous month (23.6%). Slope (10.3%). Mixed layer depth (9.6%). SSH (3.8%).
Steno bredanensis	2	lqpth	0	0.86	Temp. at 0.5 m previous month (48%). Mixed layer depth (31.2%). Slope (19.3%). Temp. at 100 m previous month (1.5%).
*Balaenoptera physalus**	2	lqpt	0.038	0.85	Chl-a previous month (52%). Depth (20.5%). Chl-a daily (14.2%). Temp. at 100 m daily (9.4%). Slope (3.9%).
*Balaenoptera edeni**	1	lqpt	0.049	0.85	Temp. at 0.5 m previous month (33.5%). Chl-a previous month (25.6%). Depth (19.7%). Temp. at 100 m daily (11%). SSH (10.2%).

Variables are sorted by percent contribution to the final model. Models marked with an asterisk are the ones selected as "Best."

short-finned pilot whales' ecological niche was clearly described by a preference for warmer waters (over 18°C) and low/moderate chlorophyll values. The species was found to be related to waters slightly deeper than 1,000 m, which agrees with the findings on the diving behavior for the species by Soto et al. (2008) in the Canary Islands and Alves et al. (2013a) in Madeira, with dives between 500 and 1,000 m. While major canyons played a role in the distribution of pilot whales, higher suitability values were found mostly related to moderate slopes. This agrees with Thorne et al. (2017) findings, where canyons and the shelf-break zones were found to be suitable habitat for tracked animals. The temporal occurrence pattern for the species in the archipelago seems to be shaped by the SST and Chl-a, with resultant higher suitability values in late-summer/autumn and winter (**Figure 2**).

These findings are in accordance with the known species' temporal occurrence and might be related to some of the inter-archipelagic movements registered by Alves et al. (2019). Some animals might travel to other areas (such as the Azores or the Canary Islands) using oceanographic features, like the long-lived eddies in the Macaronesian region described by Sangrà et al. (2009) and Caldeira (2019), a behavior already observed for this species by Thorne et al. (2017) when following the Gulf

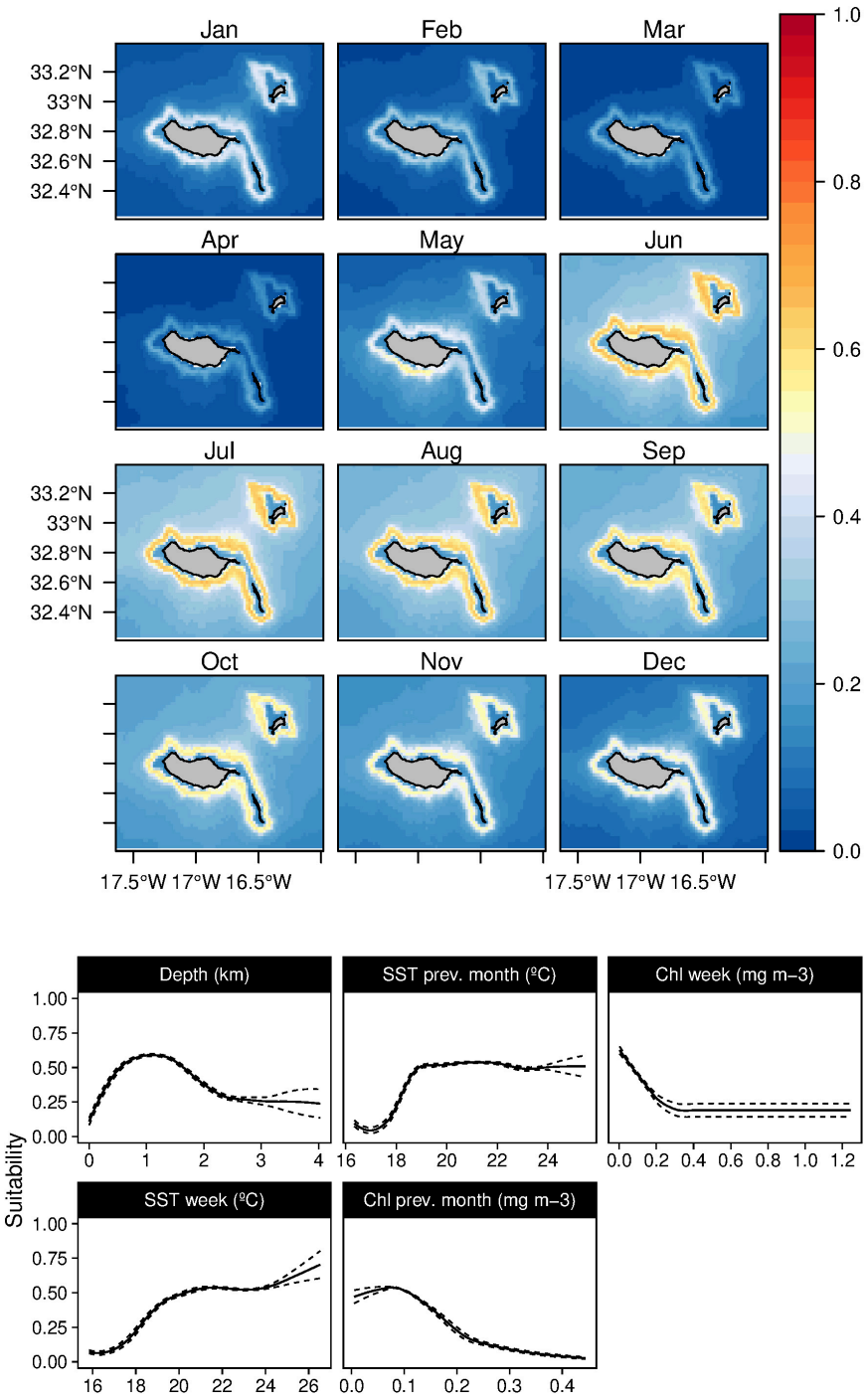

FIGURE 7 | Mean monthly suitability maps **(above)** and smoothed response curves with standard deviation **(below)** in the Madeira archipelago for *Stenella frontalis* for the "8-days" models. In the maps, red represents more suitable and blue less suitable. Responses curves are ordered by percent contribution of the environmental variables.

stream meanders off the Atlantic Coast of the United States. Furthermore, Owen et al. (2019) recently found an influence of the lunar moon on the behavior and distribution of pilot whales in Hawaii, with a displacement toward offshore waters, together with deeper and longer dives during the full moon. These findings might be related to the subtle influence of the lunar illumination we found in the daily models (**Table 3**); results indicated that suitability around the island was lower with higher lunar illumination. Nevertheless, other approaches would be needed to understand this potential effect better.

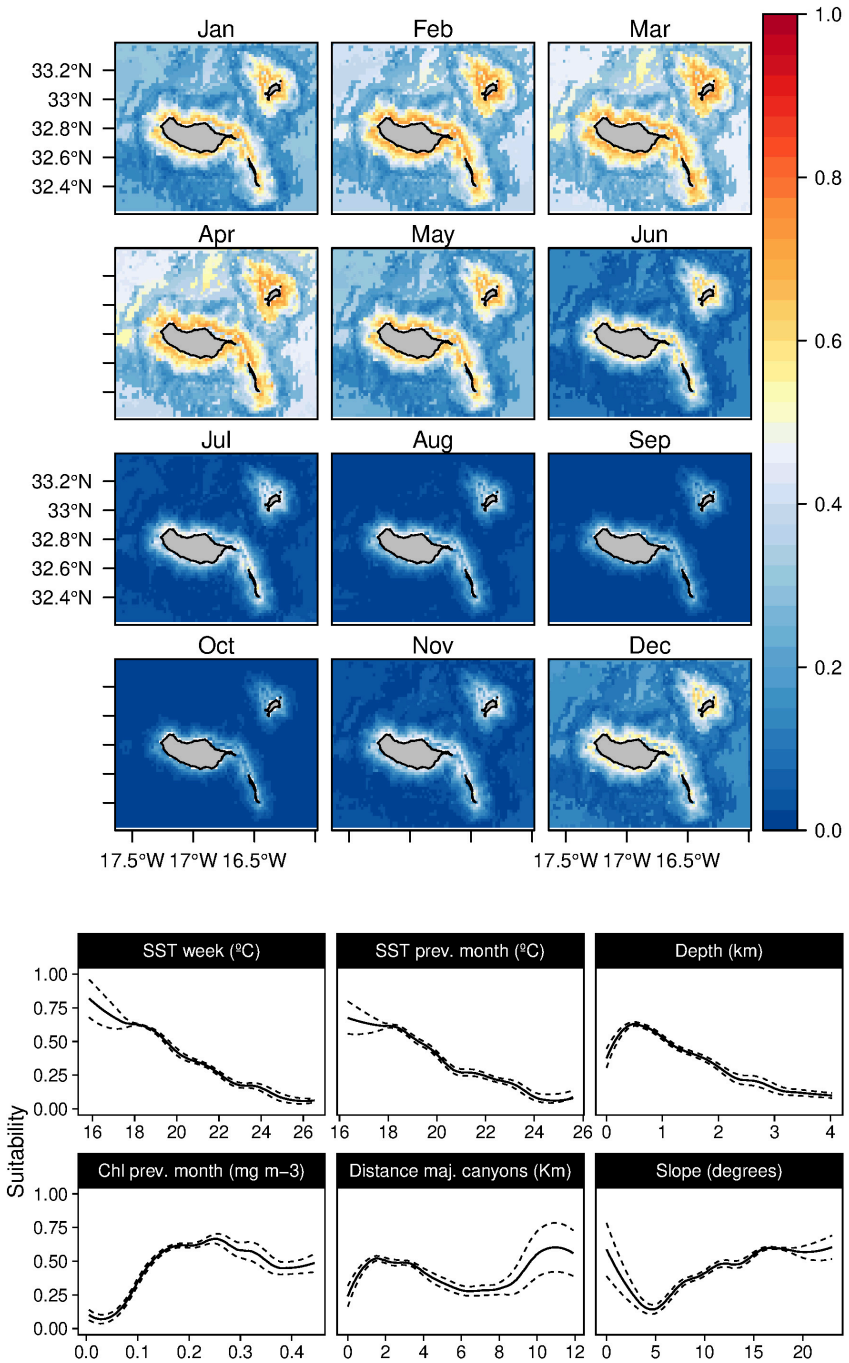

FIGURE 8 | Mean monthly suitability maps **(above)** and smoothed response curves with standard deviation **(below)** in the Madeira archipelago for *Delphinus delphis* for the "8-days" models. In the maps, red represents more suitable and blue less suitable. Responses curves are ordered by percent contribution of the environmental variables.

Sperm whales are known to be a cosmopolitan species (Jefferson et al., 2011). Even if mostly feeding on cephalopods, they can be considered generalist foragers, consuming a wide variety of prey (e.g., Clarke, 1980; Evans and Hindell, 2004). Our results showed a broader niche of the species on the spatial dimension than the short-finned pilot whales, with a preference for waters deeper than 1 km (but not restricted to a specific range) in the proximity of submarine canyons areas. While the species seems to be present in the archipelago throughout the year, there is an apparent increase in suitability from June to November, linked to SST, with a peak around 23°C, similar to other areas, such as the Azores (Fernandez et al., 2018). In Madeiran waters,

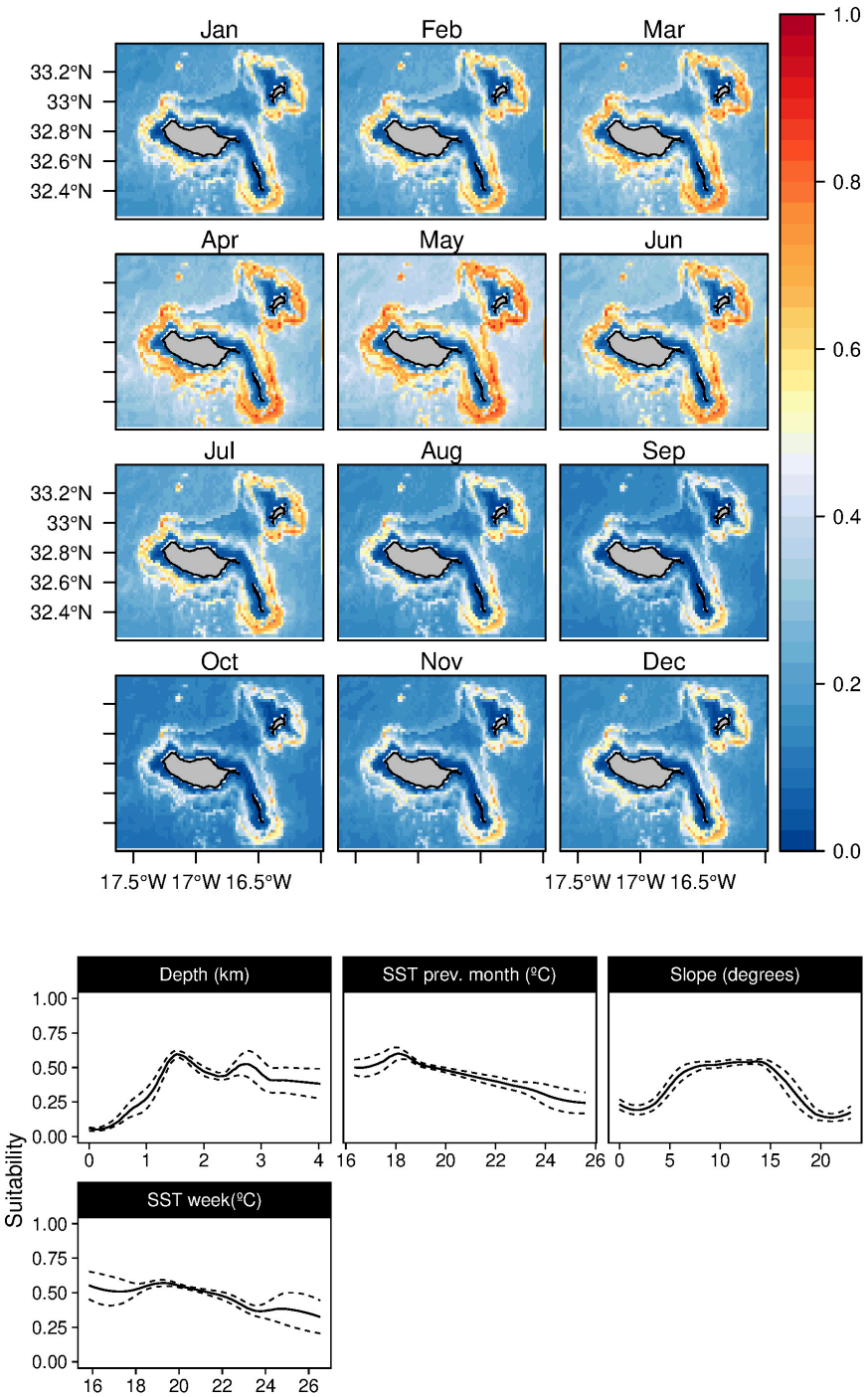

FIGURE 9 | Mean monthly suitability maps **(above)** and smoothed response curves with standard deviation **(below)** in the Madeira archipelago for *Stenella coeruleoalba* for the "8-days" models. In the maps, red represents more suitable and blue less suitable. Responses curves are ordered by percent contribution of the environmental variables.

the group size for the species ranges between 1 and 30 animals, with calves present in 25% of the groups (Alves et al., 2018). Pirotta et al. (2020), found that solitary animals and groups used areas with different characteristics in the Balearic Islands, with groups preferring warmer waters. Therefore, the presence of groups with offspring in the archipelago might be related with the increase of suitability observed from June to December.

Finally, the Blainville beaked whale shows the most restricted ecological niche of the deep-diving species, mainly being linked to steep relief areas in the vicinity of major canyons (**Table 3**).

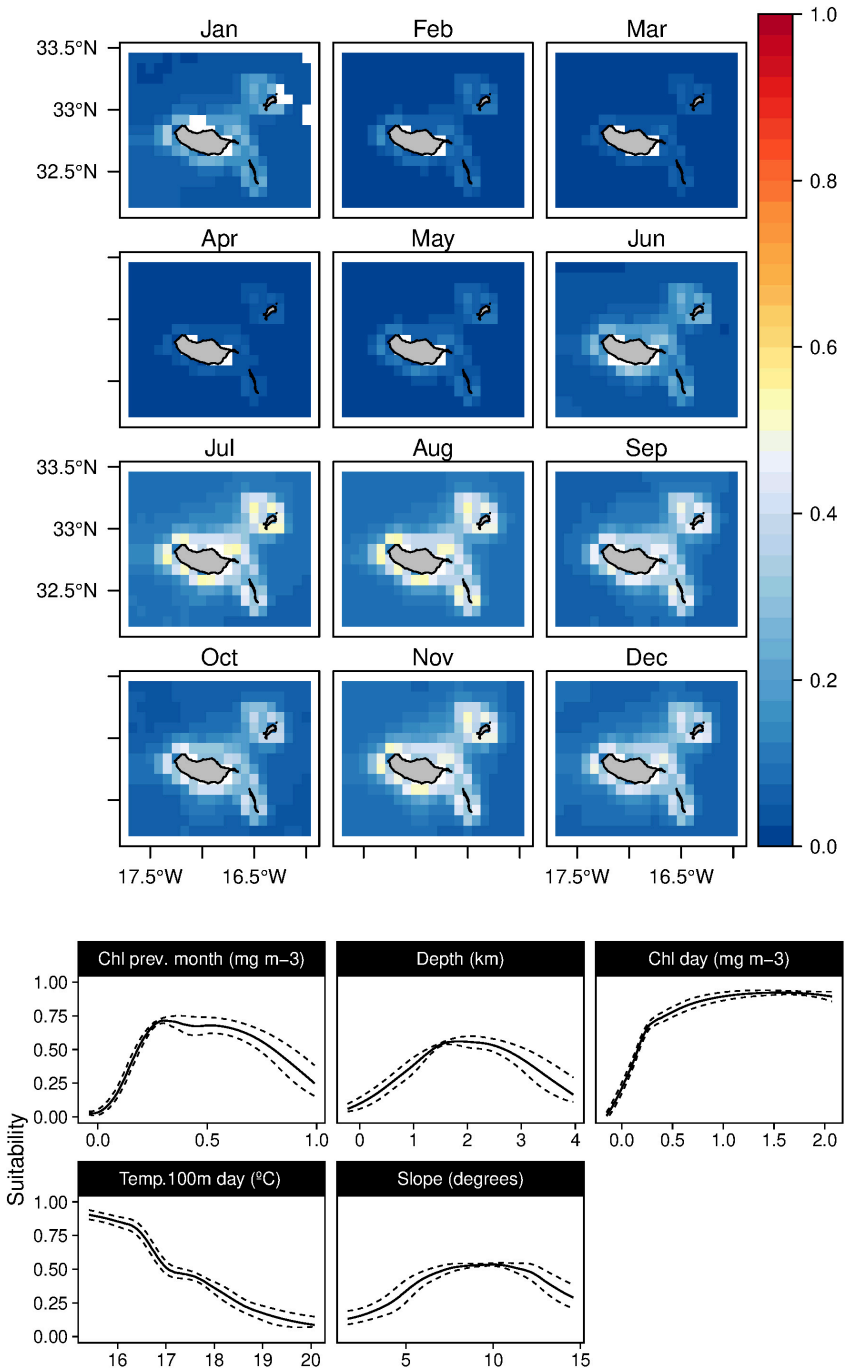

FIGURE 10 | Mean monthly suitability maps **(above)** and smoothed response curves with standard deviation **(below)** in the Madeira archipelago for *Balaenoptera physalus* for the "daily" models. In the maps, red represents more suitable and blue less suitable. Responses curves are ordered by percent contribution of the environmental variables.

This results in a very spatially constrained niche in some areas close to the island's shoreline, which agrees with the findings in other regions, such as the Canary Islands (Ritter and Brederlau, 1999) and Hawaii (Schorr et al., 2009). The strong relation found with steep areas is probably related to the prey aggregation on these specific habitats, representing a reliable food resource for the species (Arranz et al., 2011). Finally, the explicit contribution of the SST to the models suggests a preference for warm waters, as suggested by Macleod (2000). All these results lead to relatively good suitability values almost all year round, peaking in summer and early autumn months, which explains the high site fidelity patterns previously found by Dinis et al. (2017) around Madeira.

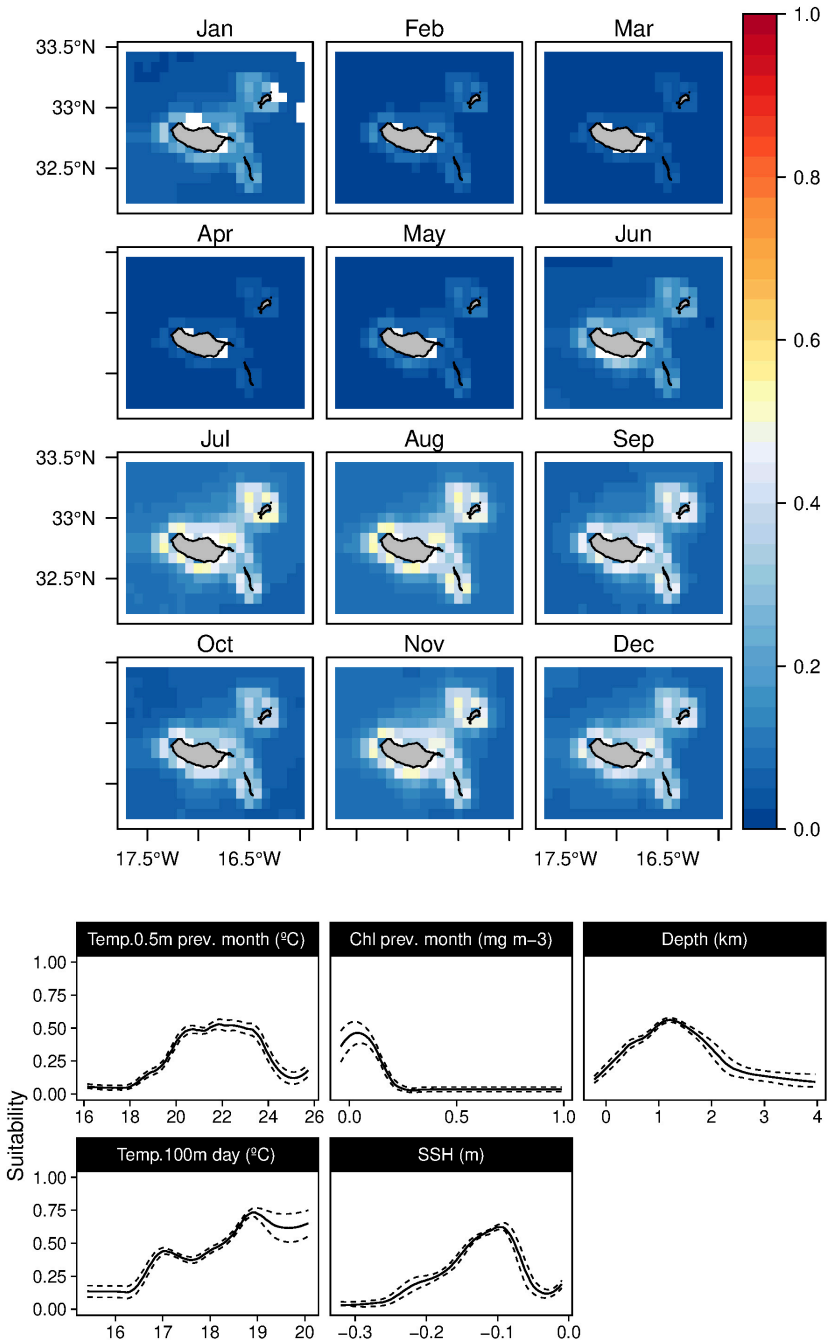

FIGURE 11 | Mean monthly suitability maps **(above)** and smoothed response curves with standard deviation **(below)** in the Madeira archipelago for *Balaenoptera edeni* for the "daily" models. In the maps, red represents more suitable and blue less suitable. Responses curves are ordered by percent contribution of the environmental variables.

Delphinids

Distinct habitat preferences characterized the two medium-sized delphinids (*T. truncatus* and *S. bredanensis*) distributions analyzed; nevertheless, both niches were linked to the island-induced features, reflected in the preference for mid-high slope values. The bottlenose dolphin niche was almost solely influenced by topographic variables (**Table 3**) with a clear preference for shallow coastal waters (<1,000 m), which agrees with the findings of Dinis et al. (2016b), with almost no temporal variation. This relation was also found in other oceanic archipelagos, such as the Azores (Fernandez et al., 2018). Previous studies found that this species might be present in the Madeira archipelago all year round, with no significant difference in the monthly encounter rate (Dinis et al., 2016a), reflected

in the low variability of the suitability values during the year (**Supplementary Figure 4**). Interestingly, we found a marginal effect of the surface chlorophyll on their distribution, which could be related to fine-scale effects of primary productivity on the species distribution, as found for the species in shallow seas (Scott et al., 2010).

While the rough-toothed dolphin was also linked to areas with medium or high bottom inclination (usually associated with islands or seamounts), the temporal distribution for this species mainly was limited due to a preference for warm waters (over 21–22°C), such as those on the warm wake present mostly on summer months on the South Coast of Madeira (Caldeira et al., 2002; Alves et al., 2021).

When looking at the small delphinids an interesting pattern was found, with two species (*D. delphis* and *S. frontalis*) with differentiated ecological niches. Both species have a similar spatial distribution, with a widespread distribution around the islands, clearly demonstrated by the influence of depth. However, differences arise when looking at their temporal distribution; the common dolphin was closely related to lower SST values and high chlorophyll concentrations, while the Atlantic spotted dolphin preferred warm waters and low chlorophyll values (**Figures 7**, **8**). As a result, higher suitability values were found in winter/spring for the former species and summer/autumn for the later species. Au and Perryman (1985) found that in the Eastern Tropical Pacific, common dolphins were found to be associated with upwelling modified waters, while tropical spotted dolphins (*Stenella attenuata*) were associated with tropical waters. In the present study, instead of *S. attenuata,* we have *S. frontalis*; however, a similar pattern seems to occur, with common dolphins preferring "cold" waters rich in nutrients and Atlantic spotted dolphins more associated with warm, and therefore, stratified areas. This is in agreement with the seasonal regimes found in the waters surrounding Madeira, reflected by the ocean static stability, with a much better mixed upper ocean in winter and a more stratified structure present in summer (Alves et al., 2021).

Our findings agree with the observations made by Freitas et al. (2004) for Madeira and are in harmony with the niche segregation hypothesis made by Silva et al. (2014) for the Azores. Nevertheless, it is true that when environmental conditions are suitable for both species, they might occupy the same areas. Furthermore, if we also add the high standard deviation values found in the suitability for the Atlantic spotted dolphins, it is possible that in some years both species might have high suitability values during some months, especially in spring and early summer. Finally, the striped dolphin was found to be an offshore species primarily occurring in deeper waters with a slight preference for lower temperatures and related to mid-slope areas, agreeing with the findings of Fernandez et al. (2018) for the Azores.

Balaenopterids

The two balaenopterids considered herein proved to have very differentiated niches. The fin whale mainly was related to high chlorophyll concentrations during the previous month and on the same day (**Figure 10**). The niche was shaped by the low water temperature preference at 100 m (<18°C), which might be related to the deep-diving foraging behavior previously documented in the Azores (Silva et al., 2013). The 8-day analysis also showed an influence of the previous month SST, peaking around 18–20°C, which agrees with findings by Fernandez et al. (2018) from the Azores. Conversely, in the present study, the chlorophyll levels were also relevant (with a preference of values higher than 0.5 mgm^{-3}), which might be a limiting factor for the species in Madeira. As a result, higher suitability values (and high standard deviation) are found mostly during the spring months, compared to the Azores, where the species has been recorded during winter, spring, and summer (Silva et al., 2014). In the Azores, the combination of the complex topography with the highly energetic eddy field creates a confluence zone between the west and the east North Atlantic (Caldeira and Reis, 2017). Additionally, Caldeira (2019) found that the number of long-lived eddies (lifetime greater than 60 days) generated by the interaction of the oceanic flow with the islands is much larger in the Azores (n = 202) than in Madeira (n = 50). Considering that mesoscale eddies can modulate oceanic productivity in many ways (Dufois et al., 2016), together with the existence of a confluence area, might support the extended temporal presence of fin whales in the Azores compared to Madeira.

While not much is known, the results presented here agree with the Bryde's whales described literature. The species is known to move through tropical and warm-temperate waters, with a specific preferred thermal range (Kato and Perrin, 2018). We found that higher suitability values mainly were related to warm surface waters and low surface chlorophyll concentrations during the previous months (**Figure 11**). This agrees with the higher number of sightings for this species in summer/autumn in the archipelago (Alves et al., 2018). The relatively low suitability values and the high standard deviation we detected could be caused by the high variability of interannual occurrence rates. In the present study, the species was related to a specific SST (between 20 and 24°C). Nevertheless, in California, no significant effect of the temperature occurrence pattern was found, with observations of animals in waters as cold as 15°C (Kerosky et al., 2012). The same authors hypothesize that interannual climate oscillations and oceanographic indexes (such as the ENSO) could explain some of the variability observed, recognizing that other environmental variables rather than the SST might influence the whales' movements. Therefore, depending on general circulation patterns, the animals might move to Madeira, to northern latitudes, up to the Azores (Steiner et al., 2008), or could remain in southern latitudes.

CONCLUSION

The distributional estimates presented here are the first attempt to better understand spatial-temporal patterns of cetaceans in the Madeira archipelago. Except for the fin whale, all the other nine species analyzed in the present study showed a clear relation with specific topographic features, which might be related to the island-mass effect and associated eddies. To better understand how the specific fine-scale island-related oceanographic features might affect cetaceans' populations, we

recommend using coupled atmospheric-ocean models in future studies. The use of fine-scale accurate data (both in the temporal and spatial dimension) is crucial to improve dynamic ocean management actions in cetaceans, as demonstrated recently by Hausner et al. (2021).

Moreover, we acknowledge that some models might greatly benefit from more data, especially from unsampled areas. Ideally, the next steps to obtain better distributional estimates will include data from different sources (such as dedicated surveys, telemetry data, or other platforms of opportunity like fishing boats, ferries, or cargo ships) to cover as much as possible the potential factors influencing the species distribution. However, different datasets might have different biases, and therefore data merging from different sources should be analyzed carefully (Fletcher et al., 2019).

DATA AVAILABILITY STATEMENT

The original contributions generated for this study are included in the article/**Supplementary Material**, further inquiries can be directed to the corresponding author.

AUTHOR CONTRIBUTIONS

MF, AD, and FA conceived the study design. FA, AD, RF, PT, and J-CF supported the data collection and organized the databases. MF analyzed the data and wrote the first draft of the manuscript. All authors actively contributed on the writing and editing of the manuscript.

FUNDING

This study was supported by: (i) INTERTAGUA, MAC2/1.1.a/385 funded by MAC INTERREG 2014-2020, (ii) Oceanic Observatory of Madeira throughout the project M1420-01-0145-FEDER-000001-OOM, and (iii) Fundação para a Ciência e Tecnologia (FCT), Portugal, through the strategic project UID/MAR/04292/2020 granted to MARE UI&I. AD and FA have grants funded by ARDITI—Madeira's Regional Agency for the Development of Research, Technology and Innovation, throughout the project M1420-09-5369-FSE-000002. RF was partially supported by a FCT doctoral grant (SFRH/BD/147225/2019).

ACKNOWLEDGMENTS

We wish to thank to all the people and organizations involved in the collection of data over the years. We thank the whale-watching operators Ventura | Nature Emotions, Lobosonda and Seaborn (especially to Miguel Fernandes).

SUPPLEMENTARY MATERIAL

The Supplementary Material for this article can be found online at: https://www.frontiersin.org/articles/10.3389/fmars.2021.688248/full#supplementary-material

REFERENCES

Aiello-Lammens, M. E., Boria, R. A., Radosavljevic, A., Vilela, B., and Anderson, R. P. (2015). spThin: an R package for spatial thinning of species occurrence records for use in ecological niche models. *Ecography* 38, 541–545. doi: 10.1111/ecog.01132

Albouy, C., Delattre, V., Donati, G., Frölicher, T. L., Albouy-Boyer, S., Rufino, M., et al. (2020). Global vulnerability of marine mammals to global warming. *Sci. Rep.* 10, 1–12.

Alves, F., Alessandrini, A., Servidio, A., Mendonça, A. S., Hartman, K. L., Prieto, R., et al. (2019). Complex biogeographical patterns support an ecological connectivity network of a large marine predator in the north-east Atlantic. *Divers. Distrib.* 25, 269–284. doi: 10.1111/ddi.12848

Alves, F., Dinis, A., Ribeiro, C., Nicolau, C., Kaufmann, M., Fortuna, C. M., et al. (2013b). Daytime dive characteristics from six short-finned pilot whales Globicephala macrorhynchus off Madeira Island. *Arquipélago Life Mar. Sci.* 31, 1–8.

Alves, F., Quérouil, S., Dinis, A., Nicolau, C., Ribeiro, C., Freitas, L., et al. (2013a). Population structure of short-finned pilot whales in the oceanic archipelago of Madeira based on photo-identification and genetic analyses: implications for conservation. *Aquat. Conserv.* 23, 758–776. doi: doi:10.1002/aqc.2332

Alves, F., Ferreira, R., Fernandes, M., Halicka, Z., Dias, L., and Dinis, A. (2018). Analysis of occurrence patterns and biological factors of cetaceans based on long-term and fine-scale data from platforms of opportunity: Madeira Island as a case study. *Mar. Ecol.* 39:e12499. doi: 10.1111/maec.12499

Alves, J., Tomé, R., Caldeira, R., and Miranda, P. (2021). Asymmetric ocean response to atmospheric forcing in an island wake: a 35-year high-resolution Study. *Front. Mar. Sci.* 8:624392. doi: 10.3389/fmars.2021.624392

Anderson, R. P., Lew, D., and Peterson, A. T. (2003). Evaluating predictive models of species distributions: criteria for selecting optimal models. *Ecol. Model.* 162, 211–232. doi: 10.1016/s0304-3800(02)00349-6

Anderson, R. P., and Raza, A. (2010). The effect of the extent of the study region on GIS models of species geographic distributions and estimates of niche evolution: preliminary tests with montane rodents (genus *Nephelomys*) in Venezuela. *J. Biogeogr.* 37, 1378–1393. doi: 10.1111/j.1365-2699.2010.02290.x

Araújo, M. B., Anderson, R. P., Barbosa, A. M., Beale, C. M., Dormann, C. F., Early, R., et al. (2019). Standards for distribution models in biodiversity assessments. *Sci. Adv.* 5:eaat4858. doi: 10.1126/sciadv.aat4858

Aristegui, J., Sangra, P., Hernandez-Leon, S., Canton, M., Hernandez- Guerra, A., and Kerling, J. L. (1994). Island-induced eddies in the Canary Islands. *Deep Sea Res.* 41, 1509–1525. doi: 10.1016/0967-0637(94)90058-2

Arranz, P., De Soto, N. A., Madsen, P. T., Brito, A., Bordes, F., and Johnson, M. P. (2011). Following a foraging fish-finder: diel habitat use of Blainville's beaked whales revealed by echolocation. *PLoS One* 6:e28353. doi: 10.1371/journal.pone.0028353

Au, D. W., and Perryman, W. L. (1985). Dolphin habitats in the eastern tropical Pacific. *Fish. Bull.* 83, 623–644.

Azzellino, A., Gaspari, S., Airoldi, S., and Nani, B. (2008). Habitat use and preferences of cetaceans along the continental slope and the adjacent pelagic waters in the western Ligurian Sea. *Deep Sea Res. I* 55, 296–323. doi: 10.1016/j.dsr.2007.11.006

Barton, E. D., Basterretxea, G., Flament, P., Mitchelson-Jacob, E. G., Jone, B., Aristegui, J., et al. (2000). Lee region of gran canaria. *J. Geophys. Res.* 105, 17173–17193. doi: 10.1029/2000jc900010

Boehner, J., and Selige, T. (2006). "Spatial prediction of soil attributes using terrain analysis and climate regionalisation," in *SAGA - Analysis and Modelling*

Applications, eds J. Boehner, K. R. McCloy, and J. Strobl (Goettingen: Göttinger Geographische Abhandlungen), 13–28.

Breen, P., Pirotta, E., Allcock, L., Bennison, A., Boisseau, O., Bouch, P., et al. (2020). Insights into the habitat of deep diving odontocetes around a canyon system in the northeast Atlantic ocean from a short multidisciplinary survey. *Deep Sea Res. Part I* 159:103236. doi: 10.1016/j.dsr.2020.103236

Caldeira, R. (2019). "Island wakes," in *Encyclopedia of Ocean Sciences*, 3rd Edn, Vol. 3, eds J. K. Cochran, J. H. Bokuniewicz, and L. P. Yager (Amsterdam: Elsevier), 83–91. doi: 10.1016/b978-0-12-409548-9.11614-8

Caldeira, R., Groom, S., Miller, P., Pilgrim, D., and Nezlin, N. P. (2002). Sea-surface signatures of the island mass effect phenomena around Madeira Island, Northeast Atlantic. *Remote Sens. Environ.* 80, 336–360. doi: 10.1016/s0034-4257(01)00316-9

Caldeira, R., and Reis, J. C. (2017). The Azores confluence zone. *Front. Mar. Sci.* 4:37. doi: 10.3389/fmars.2017.00037

Catlin-Groves, C. L. (2012). The citizen science landscape: from volunteers to citizen sensors and beyond. *Int. J. Zool.* 2012, 1687-8477. doi: 10.1155/2012/349630

Clarke, M. R. (1980). Cephalopods in the diet of sperm whales of the Southern Hemisphere and their bearing on sperm whale biology. *Discov. Rep.* 37, 1–324.

Cobos, M. E., Peterson, A. T., Barve, N., and Osorio-Olvera, L. (2019a). kuenm: an R package for detailed development of ecological niche models using Maxent. *PeerJ* 7:e6281. doi: 10.7717/peerj.6281

Cobos, M. E., Peterson, A. T., Osorio-Olvera, L., and Jiménez-García, D. (2019b). An exhaustive analysis of heuristic methods for variable selection in ecological niche modeling and species distribution modeling. *Ecol. Informatics* 53:100983. doi: 10.1016/j.ecoinf.2019.100983

Dinis, A., Alves, F., Nicolau, C., Ribeiro, C., Kaufmann, M., Cañadas, A., et al. (2016a). Bottlenose dolphin *Tursiops truncatus* group dynamics, site fidelity, residency and movement patterns in the Madeira Archipelago (North-East Atlantic). *Afr. J. Mar. Sci.* 38, 151–160. doi: 10.2989/1814232x.2016.1167780

Dinis, A., Carvalho, A., Alves, F., Nicolau, C., Ribeiro, C., Kaufmann, M., et al. (2016b). Spatial and temporal distribution of bottlenose dolphins, *Tursiops truncatus*, in the *Madeira archipelago*, NE Atlantic. *Arquipélago. Life Mar. Sci.* 33, 45–54.

Dinis, A., Marques, R., Dias, L., Sousa, D., Gomes, C., Abreu, N., et al. (2017). Site fidelity of Blainville's beaked whale (*Mesoplodon densirostris*) off Madeira Island (Northeast Atlantic). *Aquat. Mamm.* 43:387. doi: 10.1578/am.43.4.2017.387

Dinis, A., Molina, C., Tobeña, M., Sambolino, A., Hartman, K., Fernandez, M., et al. (2021). Large-scale movements of common bottlenose dolphins in the Atlantic: dolphins with an international courtyard. *PeerJ* 9:e11069. doi: 10.7717/peerj.11069

Doty, M. S., and Oguri, M. (1956). The island mass effect. *ICES J. Mar. Sci.* 22, 33–37.

Dufois, F., Hardman-Mountford, N. J., Greenwood, J., Richardson, A. J., Feng, M., and Matear, R. J. (2016). Anticyclonic eddies are more productive than cyclonic eddies in subtropical gyres because of winter mixing. *Sci. Adv.* 2:e1600282. doi: 10.1126/sciadv.1600282

Embling, C. B., Walters, A. E. M., and Dolman, S. J. (2015). How much effort is enough? The power of citizen science to monitor trends in coastal cetacean species. *Glob. Ecol. Conserv.* 3, 867–877. doi: 10.1016/j.gecco.2015.04.003

Evans, K., and Hindell, M. A. (2004). The diet of sperm whales (*Physeter macrocephalus*) in southern Australian waters. *ICES J. Mar. Sci.* 61, 1313–1329. doi: 10.1016/j.icesjms.2004.07.026

Fernandez, M., Yesson, C., Gannier, A., Miller, P. I., and Azevedo, J. M. N. (2017). The importance of temporal resolution for niche modelling in dynamic marine environments. *J. Biogeogr.* 44, 2816–2827. doi: 10.1111/jbi.13080

Fernandez, M., Yesson, C., Gannier, A., Miller, P. I., and Azevedo, J. M. N. (2018). A matter of timing: how temporal scale selection influences cetacean ecological niche modelling. *Mar. Ecol. Prog. Ser.* 595, 217–231. doi: 10.3354/meps12551

Fletcher, R. J. Jr., Hefley, T. J., Robertson, E. P., Zuckerberg, B., McCleery, R. A., and Dorazio, R. M. (2019). A practical guide for combining data to model species distributions. *Ecology* 100:e02710. doi: 10.1002/ecy.2710

Freitas, L., Dinis, A., Alves, F., and Nobrega, F. (2004). *Relatório dos Resultados Científicos do Projecto Para a Conservação dos Cetáceos no Arquipélago da Madeira. Report to the European Commission*. Madeira: Museu da Baleia da Madeira.

Freitas, L., Dinis, A., Nicolau, C., Ribeiro, C., and Alves, F. (2012). New records of cetacean species for Madeira Archipelago with an updated checklist. *Bol. Mus. Mun. Funchal.* 62, 25–43.

Guisan, A., Weiss, S. B., and Weiss, A. D. (1999). GLM versus CCA spatial modeling of plant species distribution. *Plant Ecol.* 143, 107–122.

Hausner, A., Samhouri, J. F., Hazen, E. L., Delgerjargal, D., and Abrahms, B. (2021). Dynamic strategies offer potential to reduce lethal ship collisions with large whales under changing climate conditions. *Mar. Policy* 130:104565. doi: 10.1016/j.marpol.2021.104565

Henckel, L., Bradter, U., Jönsson, M., Isaac, N. J., and Snäll, T. (2020). Assessing the usefulness of citizen science data for habitat suitability modelling: opportunistic reporting versus sampling based on a systematic protocol. *Divers. Distrib.* 26, 1276–1290. doi: 10.1111/ddi.13128

Jefferson, T. A., Webber, M. A., and Pitman, R. L. (2011). *Marine Mammals of the World: A Comprehensive Guide to Their Identification*. Amsterdam: Elsevier.

Kato, H., and Perrin, W. F. (2018). "Bryde's whales *Balaenoptera edeni*," in *Encyclopedia of Marine Mammals*, 3rd Edn, eds B. Würsig, J. G. M. Thewissen, and K. Kovacs (London: Academic Press), 143–145.

Kerosky, S. M., Širović, A., Roche, L. K., Baumann-Pickering, S., Wiggins, S. M., and Hildebrand, J. A. (2012). Bryde's whale seasonal range expansion and increasing presence in the Southern California Bight from 2000 to 2010. *Deep Sea Res. Pt. I* 65, 125–132. doi: 10.1016/j.dsr.2012.03.013

Lobo, J. M., Jiménez-Valverde, A., and Real, R. (2008). AUC: a misleading measure of the performance of predictive distribution models. *Glob. Ecol. Biogeogr.* 17, 145–151. doi: 10.1111/j.1466-8238.2007.00358.x

Macleod, C. D. (2000). Review of the distribution of *Mesoplodon* species (order Cetacea, family Ziphiidae) in the North Atlantic. *Mamm. Rev.* 30, 1–8. doi: 10.1046/j.1365-2907.2000.00057.x

Mann, K., and Lazier, J. (1991). *Dynamics of Marine Ecosystems: Biological–Physical Interactions in the Oceans*. London: Blackwell.

Merow, C., Smith, M. J., and Silander, J. A. Jr. (2013). A practical guide to MaxEnt for modeling species' distributions: what it does, and why inputs and settings matter. *Ecography* 36, 1058–1069. doi: 10.1111/j.1600-0587.2013.07872.x

Moore, S. E., Waite, J. M., Mazzuca, L. L., and Hobbs, R. C. (2000). Mysticete whale abundance and observations of prey associations on the central Bering Shelf. *J. Cet. Res. Manage* 2, 227–234.

Moors-Murphy, H. B. (2014). Submarine canyons as important habitat for cetaceans, with special reference to the Gully: a review. *Deep Sea Res. II* 104, 6–19. doi: 10.1016/j.dsr2.2013.12.016

Naimi, B. (2015). *usdm: Uncertainty Analysis for Species Distribution Models. R Package Version 1*.

Norris, K., Terry, A., Hansford, J. P., and Turvey, S. T. (2020). Biodiversity conservation and the earth system: mind the gap. *Trends Ecol. Evol.* 35, 919–926. doi: 10.1016/j.tree.2020.06.010

Owen, K., Andrews, R. D., Baird, R. W., Schorr, G. S., and Webster, D. L. (2019). Lunar cycles influence the diving behavior and habitat use of short-finned pilot whales around the main Hawaiian Islands. *Mar. Ecol. Prog. Ser.* 629, 193–206. doi: 10.3354/meps13123

Peterson, A. T., Papeş, M., and Soberón, J. (2008). Rethinking receiver operating characteristic analysis applications in ecological niche modeling. *Ecol. Model.* 213, 63–72. doi: 10.1016/j.ecolmodel.2007.11.008

Phillips, S. J., Anderson, R. P., and Schapire, R. E. (2006). Maximum entropy modeling of species geographic distributions. *Ecol. Model.* 190, 231–259. doi: 10.1016/j.ecolmodel.2005.03.026

Pirotta, E., Brotons, J. M., Cerdà, M., Bakkers, S., and Rendell, L. E. (2020). Multi-scale analysis reveals changing distribution patterns and the influence of social structure on the habitat use of an endangered marine predator, the sperm whale *Physeter macrocephalus* in the Western Mediterranean Sea. *Deep Sea Res. Pt. I* 155:103169. doi: 10.1016/j.dsr.2019.103169

Radosavljevic, A., and Anderson, R. P. (2014). Making better Maxent models of species distributions: complexity, overfitting and evaluation. *J. Biogeogr.* 41, 629–643. doi: 10.1111/jbi.12227

Redfern, J. V., Ferguson, M. C., Becker, E. A., Hyrenbach, K. D., Good, C., Barlow, J., et al. (2006). Techniques for cetacean–habitat modeling. *Mar. Ecol. Prog. Ser.* 310, 271–295. doi: 10.3354/meps310271

Ritter, F., and Brederlau, B. (1999). Behavioural observations of dense beaked whales (*Mesoplodon densirostris*) off La Gomera, Canary Islands (1995-1997). *Aquat. Mamm.* 25, 55–62.

Robbins, J. R., Babey, L., and Embling, C. B. (2019). Citizen science in the marine environment: a case-study estimating common dolphin densities in the north-east Atlantic. *PeerJ* 8:e8335. doi: 10.7717/peerj.8335

Rodríguez, J. P., Brotons, L., Bustamante, J., and Seoane, J. (2007). The application of predictive modelling of species distribution to biodiversity conservation. *Divers. Distrib.* 13, 243–251. doi: 10.1111/j.1472-4642.2007.00356.x

Roman, J., Estes, J. A., Morissette, L., Smith, C., Costa, D., McCarthy, J., et al. (2014). Whales as marine ecosystem engineers. *Front. Ecol. Environ.* 12, 377–385. doi: 10.1890/130220

Sangrà, P., Pascual, A., Rodríguez-Santana, Á., Machín, F., Mason, E., McWilliams, J. C., et al. (2009). The Canary Eddy Corridor: A major pathway for long-lived eddies in the subtropical North Atlantic. *Deep Sea Res. Part I: Oceanogr. Res. Pap.* 56, 2100–2114. doi: 10.1016/j.dsr.2009.08.008

Schorr, G. S., Baird, R. W., Hanson, M. B., Webster, D. L., McSweeney, D. J., and Andrews, R. D. (2009). Movements of satellite-tagged Blainville's beaked whales off the island of Hawaii. *Endanger. Species Res.* 10, 203–213. doi: 10.3354/esr00229

Scott, B. E., Sharples, J., Ross, O. N., Wang, J., Pierce, G. J., and Camphuysen, C. J. (2010). Sub-surface hotspots in shallow seas: fine-scale limited locations of top predator foraging habitat indicated by tidal mixing and sub-surface chlorophyll. *Mar. Ecol. Prog. Ser.* 408, 207–226. doi: 10.3354/meps08552

Shmueli, G. (2010). To explain or to predict? *Stat. Sci.* 25, 289–310.

Silva, M. A., Prieto, R., Cascão, I., Seabra, M. I., Machete, M., Baumgartner, M. F., et al. (2014). Spatial and temporal distribution of cetaceans in the mid-Atlantic waters around the Azores. *Mar. Biol. Res.* 10, 123–137. doi: 10.1080/17451000.2013.793814

Silva, M. A., Prieto, R., Jonsen, I., Baumgartner, M. F., and Santos, R. S. (2013). North Atlantic blue and fin whales suspend their spring migration to forage in middle latitudes: building up energy reserves for the journey? *PLoS One* 8:e76507. doi: 10.1371/journal.pone.0076507

Soto, N. A., Johnson, M. P., Madsen, P. T., Díaz, F., Domínguez, I., Brito, A., et al. (2008). Cheetahs of the deep sea: deep foraging sprints in short-finned pilot whales off Tenerife (Canary Islands). *J. Anim. Ecol.* 77, 936–947. doi: 10.1111/j.1365-2656.2008.01393.x

Steiner, L., Silva, M. A., Zereba, J., and Leal, M. J. (2008). Bryde's whales, *Balaenoptera edeni*, observed in the Azores: a new species record for the region. *Mar. Biodivers. Rec.* 1:e66.

Thorne, L. H., Foley, H. J., Baird, R. W., Webster, D. L., Swaim, Z. T., and Read, A. J. (2017). Movement and foraging behavior of short-finned pilot whales in the Mid-Atlantic Bight: importance of bathymetric features and implications for management. *Mar. Ecol. Prog. Ser.* 584, 245–257. doi: 10.3354/meps12371

Thuiller, W., Brotons, L., Araújo, M. B., and Lavorel, S. (2004). Effects of restricting environmental range of data to project current and future species distributions. *Ecography* 27, 165–172. doi: 10.1111/j.0906-7590.2004.03673.x

Tyne, J. A., Loneragan, N. R., Johnston, D. W., Pollock, K. H., Williams, R., and Bejder, L. (2016). Evaluating monitoring methods for cetaceans. *Biol. Conserv.* 201, 252–260. doi: 10.1016/j.biocon.2016.07.024

Warren, D. L., and Seifert, S. N. (2011). Ecological niche modeling in Maxent: the importance of model complexity and the performance of model selection criteria. *Ecol. Appl.* 21, 335–342. doi: 10.1890/10-1171.1

Weiss, A. D. (2001). "Topographic positions and landforms analysis (Poster)," in *Proceedings of the ESRI International User Conference*, San Diego, CA.

Williams, J. W., and Jackson, S. T. (2007). Novel climates, no-analog communities, and ecological surprises. *Front. Ecol. Environ.*, 475–482. doi: 10.1890/070037

Wright, D. J., and Heyman, W. H. (2008). Introduction to the special issue: marine and coastal GIS for geomorphology, habitat mapping, and marine reserves. *Mar. Geod.* 31, 223–230. doi: 10.1080/01490410802466306

Conflict of Interest: J-CF and PT were employed by Lobosonda - Madeira Whale Watching.

The remaining authors declare that the research was conducted in the absence of any commercial or financial relationships that could be construed as a potential conflict of interest.

frontiers in Marine Science

ORIGINAL RESEARCH
published: 07 September 2021
doi: 10.3389/fmars.2021.697741

Investigations Exploring the Use of an Unstructured-Grid, Finite-Volume Modelling Approach to Simulate Coastal Circulation in Remote Island Settings—Case Study Region, Vanuatu/New Caledonia

Serena Blyth Lee[1,2], Fan Zhang[3], Charles James Lemckert[1,4] and Rodger Tomlinson[1]*

[1] Coastal and Marine Research Centre, Griffith University, Gold Coast, QLD, Australia, [2] Climate Action Beacon, Griffith University, Gold Coast, QLD, Australia, [3] Southern Marine Science and Engineering Guangdong Laboratory (Zhuhai), Zhuhai, China, [4] School of Design and the Built Environment and Centre for Applied Water Science, University of Canberra, Canberra, ACT, Australia

OPEN ACCESS

Edited by:
Rui Caldeira, Agência Regional para o Desenvolvimento da Investigação Tecnologia e Inovação (ARDITI), Portugal

Reviewed by:
Shiqiang Yan, City University of London, United Kingdom
Milena Menna, National Institute of Oceanography and Applied Geophysics (Italy), Italy
Michela De Dominicis, National Oceanography Centre, United Kingdom

***Correspondence:**
Serena Blyth Lee
serena.lee@griffith.edu.au

Specialty section:
This article was submitted to Coastal Ocean Processes, a section of the journal Frontiers in Marine Science

Received: *20 April 2021*
Accepted: *24 June 2021*
Published: *07 September 2021*

Citation:
Lee SB, Zhang F, Lemckert CJ and Tomlinson R (2021) Investigations Exploring the Use of an Unstructured-Grid, Finite-Volume Modelling Approach to Simulate Coastal Circulation in Remote Island Settings—Case Study Region, Vanuatu/New Caledonia. Front. Mar. Sci. 8:697741. doi: 10.3389/fmars.2021.697741

Understanding coastal circulation and how it may alter in the future is important in island settings, especially in the South West Pacific, where communities rely heavily upon marine resources, and where sea level rise (SLR) is higher than the global average. In this study we explore the use of an unstructured-mesh finite-volume modelling approach to assist in filling the knowledge gaps with respect to coastal circulation in remote island locations—selecting the Vanuatu and New Caledonia archipelagos as our example study site. Past limited observations and modelling studies are leveraged to construct and verify a regional/coastal ocean model based on the Finite-Volume Community Ocean Model (FVCOM). Following verification with respect to tidal behaviour, we investigate how changes in wind speed and direction, and SLR, alter coastal water levels and coastal currents. Results showed tidal residual circulation was typically associated with flow separation at headlands and islands. Trade winds had negligible effect on water levels at the coast, however, wind-residual circulation was sensitive to both wind speed and direction. Wind-residual currents were typically strongest close to coastlines. Wind residual circulation patterns were strongly influenced by Ekman flow, while island blocking, topographic steering and geostrophic currents also appear to influence current patterns. Tidal amplitudes and phases were unchanged due to SLR of up to 2 m, while maximum current speeds altered by as much as 20 cm/s within some coastal embayments. Non-linear relationships between SLR and maximum current speeds were seen at some coastal reef platform sites. Under higher sea levels, tidal residual currents altered by less than ±2 cm/s which is relatively significant given maximum tidal residual current speeds are typically below 10 cm/s. Our findings indicate that under higher sea levels, coastal processes governing sediment transport, pollutant dispersal and larval transport are likely to alter, which may have implications for coastal environments

and ecosystems. Given winds influence coastal circulation and subsequent coastal processes, changes in trade winds due to climate change may act to further alter coastal processes. It is felt that the current modelling approach can be applied to other regions to help fill critical knowledge gaps.

Keywords: sea level rise, residual, circulation, tidal, constituents

INTRODUCTION

Lack of data documenting present-day coastal circulation in many remote islands impedes accurate prediction of how coastal environments and marine resources will fair under future oceanic and atmospheric conditions. Decisions regarding the allocation of coastal hazards zones, placement of infrastructure, future site development to accommodate expanding populations, and the management of natural resources, requires fine-scale (∼0.01–1 km resolution) process understanding. While desirable, it is not financially feasible to undertake comprehensive field surveys documenting coastal circulation at every island location. Over recent decades, whilst improved understanding of how sea levels vary over broad scales (tens of km) in remote island regions has been garnered from global modelling studies and satellite observation platforms, detailed understanding of coastal circulation and subsequent coastal processes necessary for making informed coastal planning decisions at these locations is often lacking. A principal limitation in our ability to predict coastal sea level variability is coarse model resolution and coarse bathymetry (Jevrejeva et al., 2019).

Remote Pacific Island communities rely heavily upon marine resources as a source of food, wealth and cultural identity, and coastal zones are intensely utilised for residential and economic activities (Andrew et al., 2019). Lack of understanding with respect to present-day coastal circulation impedes accurate prediction of how coastal environments and marine resources will fair under future oceanic and atmospheric conditions. In order to understand how these changes will affect remote Pacific Island communities, higher resolution modelling and monitoring is necessary.

In the absence of comprehensive field observations describing coastal circulation and coastal processes, well-constructed numerical models provide a useful tool to help fill data gaps. In this study we construct and employ an unstructured-mesh Finite-Volume Community Ocean Model (FVCOM) detailed in Chen et al. (2006) to investigate coastal circulation across the Vanuatu/New Caledonia region of the South West Pacific Ocean. Observations from tide gauges and previous limited coastal monitoring and modelling studies are leveraged, to verify the model with respect to tides, and to identify strengths and limitations of the model setup. Following verification, the model is used to investigate how changes in trade winds, and changes in mean sea level, alter water levels and currents across the region and select coastal locations.

Site Description

The Vanuatu archipelago contains 83 islands, spread between latitudes 13°S–21°S, and longitudes 166°E–170°E (**Figure 1**). While 65 islands are inhabited, only 14 islands have surface areas exceeding 100 km^2. The islands of Vanuatu and New Caledonia have complex shoreline environments, comprised of a mix of fringing reefs and lagoons, coarse white sand beaches, fine volcanic black sand beaches, uplifted reef limestone terraces, soft sedimentary cliffs, and coastal plains. Small sections of coastline have been modified using hard engineered seawalls or gabion cages filled with oyster shells. The majority of shoreline environments across the islands, however, are unmodified. The majority of land sits higher than 5 m elevation, well beyond worst-case sea level rise (SLR) projections. However, the main populations centres are located in coastal areas, and major infrastructure such as airports and roads are situated in low-lying coastal land or reclaimed land. Fisheries play a vital role for island communities providing both food security and employment (David, 2016). Consequently, people's health, wellbeing and livelihoods are strongly connected with coastal and marine resources. For these reasons, climate change and SLR still pose a significant threat, to island communities, despite the limited extent of low-lying (>5 m elevation) coastal land.

Vanuatu lies just east of the New Hebrides/Vanuatu Trench, where water depths exceed 7,000 m. The islands of New Caledonia lie west of the Trench (**Figure 1a**) and are divided into four main groups, Grande Terre, the main island, and largest island in our model domain, the Loyalty Islands west of Grande Terre, the Belep Islands north west of Grande Terre, the Ilse of Pines south east of Grande Terre and the Chesterfield Islands, located over 500 km to the east of Grande Terre and which falls outside the model domain used in this study.

The majority of islands in the region are fringed by coral reef/lagoon systems. Within lagoons, water depths are typically <50 m. Beyond reefs, topography is very steep, rapidly descending to over 1,000 m a few hundred metres past outer reefs (**Figure 1a**).

The predominant trade wind direction is from the South East, and meteorological events such as Tropical Cyclones typically form in lower latitudes, tracking south, south-west. The islands act as an obstruction to the broad-scale ocean circulation, due to the Southern Equatorial Current (SEC) bifurcating around the islands (**Figure 1a**), forming boundary currents and western zonal jets at the northern and southern ends of islands/island groups (Cravatte et al., 2015). While relatively little is known about the variability of these currents and jets, research cruises undertaken in waters between New Caledonia and Vanuatu as part of the Southwest Pacific Ocean Circulation and Climate Experiment (SPICE) project (Ganachaud et al., 2014), have documented their presence and general pathways. A schematic representation of the known currents and jets flowing in our region of interest is presented in **Figure 1a**.

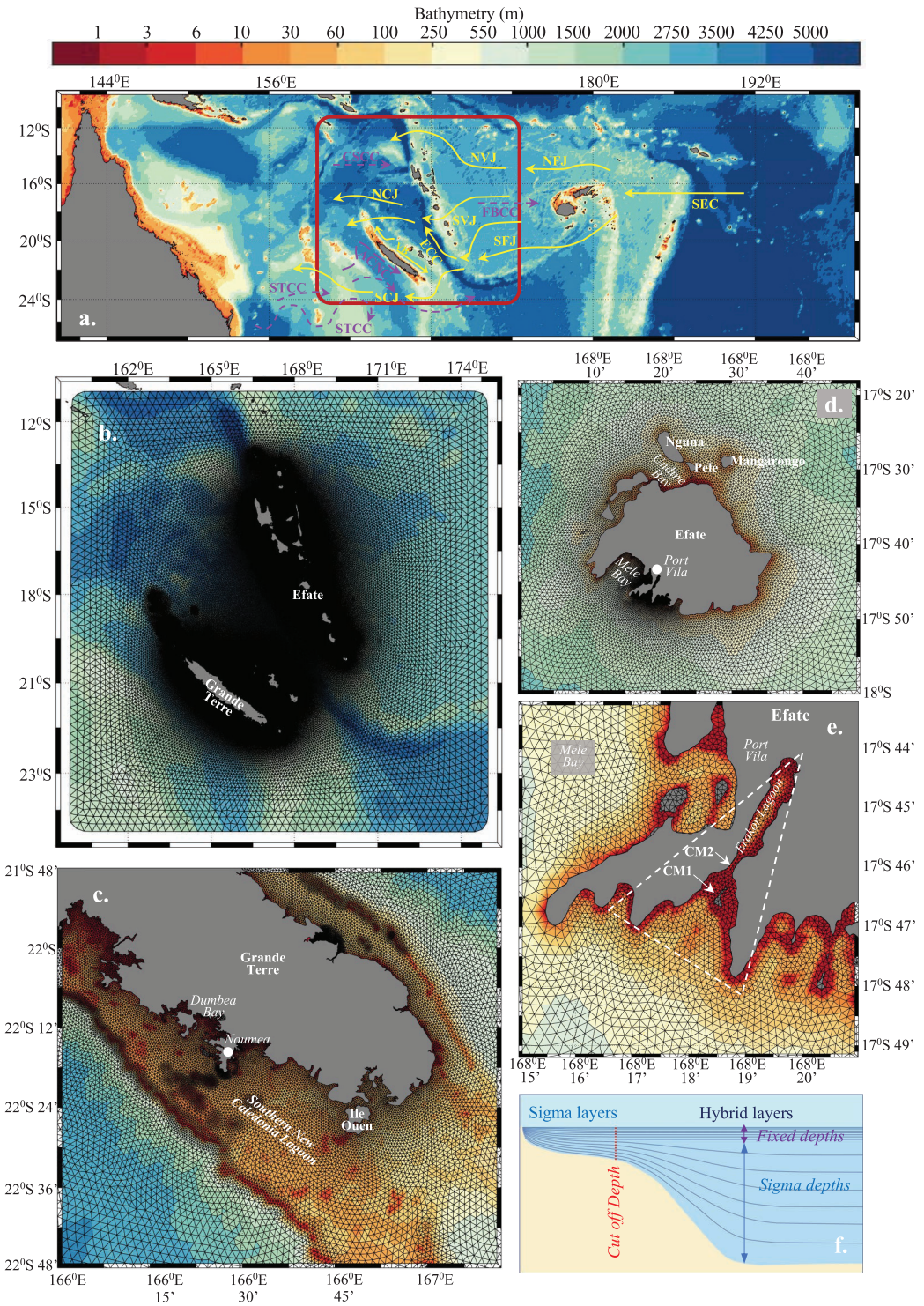

FIGURE 1 | Site map and bathymetry of the ocean region investigated, covering the Vanuatu and New Caledonia archipelagos **(a)**. The model domain extent is shown highlighted in the dark red rectangle. Yellow arrows represent regional currents associated with the passage of the Southern Equatorial Current (SEC) through the archipelagos and purple dashed arrows represent counter currents in the region. Indicated are the North/South Fiji Jets (NFJ/SFJ), North/South Vanuatu Jets (NVJ/SVJ), North/South Caledonia Jets (NCJ/SCJ), East Caledonia Current (ECC), the Vauban Current (VC), the SubTropical Counter Current (STCC), Coral Sea Counter Current (CSCC), Alis Current of New Caledonia (ACNC), and the Fiji Basin Counter Current (FBCC). The Van-Fvcom model grid constructed for the study **(b)** overlying bathymetry. Excerpts of the Van-Fvcom model grid covering southern Grande Terre **(c)**, Efate Island **(d)** and Erakor Lagoon, Efate Island **(e)** overlying bathymetry. Erakor Lagoon is highlighted in the dashed white triangle **(e)**. The legend shown at the top of the figure applies to panels **(a–e)**. Visual description of the hybrid vertical layer system employed by the Van-Fvcom model **(f)**.

Local circulation features such as upwelling, downwelling, and near-coastal currents result from the interaction between island topography, ocean currents, and atmospheric winds, with the strength of these processes being influenced by island orientation with respect to wind and ocean current direction (Cravatte et al., 2015). Hénin and Cresswell (2005) investigated upwelling and downwelling using satellite observations and *in situ* observations obtained from four outer reef locations surrounding Grande Terre, New Caledonia. The modelling experiments undertaken by Marchesiello et al. (2010), explored upwelling/downwelling events around New Caledonia, however, exchange processes between oceanic and lagoon waters were not addressed.

With respect to SLR, analysis of satellite altimetry data for the period 1993–2018, calculated the global mean rate of SLR to be 3.1 ± 0.3 mm/year (WCRP Global Sea Level Budget Group, 2018). Over this same period, in the remote South Pacific Island region, the rate of SLR ranged from ∼ 3 to 5 mm/year, and was ∼4 mm/year in the Vanuatu/New Caledonia region (Hamlington et al., 2020). Port Vila, Vanuatu, and Noumea, New Caledonia were included in a study investigating relationships between SLR and tidal characteristics based upon analysis of tide gauge records (Devlin et al., 2017). These same two locations were included in a global modelling study by Pickering et al. (2017) investigating the effect future SLR (0.5–10 m) would have on future Highest Astronomical Tide (HAT) levels, and M2 and K1 amplitudes. The last IPCC 5 report presented ensemble CMIP5 projections of SLR due to four different emission scenarios, projecting up to 0.98 m global mean sea level (GMSL) rise by 2100 under the highest emission scenario (Church et al., 2013). For the Vanuatu/New Caledonia region, future sea level in 2100 was projected to range by up to 10% from GMSL (Church et al., 2013). Hermans et al. (2021) used the same methodology previously employed to generate CMIP5 ensemble future SLR values, estimating GMSL under the highest emission scenario (SSP5-RECP 8.5) will increase by up to 1.05 m by 2100, relative to 1986–2005 levels. To enable cross comparison instability of the Antarctic ice sheet is not accounted for in the results presented by Hermans et al. (2021) and thus these results likely under-predict future sea level for this scenario. Similar analysis of ensemble CMIP6 data estimating regional SLR are presently not available, however, it is anticipated that similar variations of up to 10% from global values might be expected. In an effort to provide useful information for risk averse stakeholders, such as coastal planners and managers of critical infrastructure, Dayan et al. (2021) conducted an assessment of high-end sea level scenarios (HESs), providing maps of regional HESs projections. From this analysis, if temperatures stabilised at 2°C above pre-industrial levels by 2100, HESs in the Vanuatu/New Caledonia region was estimated to increase by between 1 and 1.2 m, under the "likely" (17–83%) range, increasing to 1.8–2 m under the "credible" (5–95%) range. If temperatures stabilised at 5°C over this same period HES increased to 2–2.2 m and 3.5–3.8 m under the "likely" and "credible" ranges respectively (Dayan et al., 2021).

While progress has been made with respect to understanding regional circulation processes in the South West Pacific, and processes influencing sea level trends, near-coastal circulation for the majority of Pacific Islands, including the islands of Vanuatu and much of New Caledonia, remains poorly understood. As a consequence, our ability to predict how coastal circulation and coastal water levels will alter under future ocean conditions is limited. By constructing a numerical model capable of resolving circulation processes within coastal waterways, we aim to begin to address these challenges.

METHODOLOGY

To better infer how climate change (predicted at large scale in low-resolution climate models) will influence island ecosystems and coastal processes, these poorly-understood, complex, near-coastal circulations and their relationship to large-scale ocean circulation must be better understood. Further, attempts to replicate the exchange between oceanic and coastal waters, including lagoon waters, is necessary in order to capture the full range of processes influencing near-shore sea levels and coastal processes. Therefore, in this study we construct an unstructured mesh, triangular cell grid, that encompasses a wide region (∼13.5° latitude, ∼15° longitude), but whose resolution nearshore is sufficiently fine (∼100 m), to resolve complex island shoreline geometry. In this way we endeavour to improve understanding of coastal circulation in this relatively under-studied region, where communities rely heavily on marine resources and ecosystems.

In this study we focus purely on tidal circulation, wind driven circulation, and how SLR might modify tidal characteristics and coastal currents, excluding the important role of regional circulation, which will be addressed in future modelling studies. It is recognised that wind-wave processes play an important role in coastal circulation, however, these processes are not addressed in this paper. For the purpose of this paper, the term "coastal" is used to describe shallow (depth <∼100 m) water environments within barrier-reef lagoon systems, or for islands with fringing reefs and steep near-shore topography, "coastal" is taken to mean waters within a few kilometres of shorelines.

Model Description

The Finite Volume Coastal Ocean Model (FVCOM; Chen et al., 2006) is used to configure a coupled coastal-ocean model for the Vanuatu and New Caledonia archipelagos, hereafter referred to as Van-Fvcom. For the simulations performed in this study, the model is run in three-dimensional barotropic mode. The following governing equations for momentum and continuity are solved by the FVCOM model:

$$\frac{\partial u}{\partial t}+u\frac{\partial u}{\partial x}+v\frac{\partial u}{\partial y}+w\frac{\partial u}{\partial z}-fv=-\frac{1}{\rho_0}\frac{\partial\left(p+p_a\right)}{\partial x}+\frac{\partial}{\partial z}\left(K_m\frac{\partial u}{\partial z}\right)+\frac{\partial}{\partial x}\left(K_h\frac{\partial u}{\partial x}\right)+\frac{\partial}{\partial y}\left(K_h\frac{\partial u}{\partial y}\right) \quad (1)$$

$$\frac{\partial v}{\partial t}+u\frac{\partial v}{\partial x}+v\frac{\partial v}{\partial y}+w\frac{\partial v}{\partial z}+fu=-\frac{1}{\rho_0}\frac{\partial\left(p+p_a\right)}{\partial y}+\frac{\partial}{\partial z}\left(K_m\frac{\partial v}{\partial z}\right)+\frac{\partial}{\partial x}\left(K_h\frac{\partial v}{\partial x}\right)+\frac{\partial}{\partial y}\left(K_h\frac{\partial v}{\partial y}\right) \quad (2)$$

$$0 = -\frac{1}{\rho_0}\frac{\partial p}{\partial z} - g \tag{3}$$

$$\frac{\partial u}{\partial x} + \frac{\partial v}{\partial y} + \frac{\partial w}{\partial z} = 0 \tag{4}$$

where u, v, and w represent the velocity components in the x (eastward), y (northward), and z (vertical) directions, respectively, f is the Coriolis parameter, p_a is air pressure at the sea surface, p is the hydrostatic pressure, ρ_0 is the reference water density, K_m and K_h are the vertical and horizontal eddy viscosity and g is gravitational acceleration. The direct effect of the tidal-generating force within the model domain is not considered.

The open ocean boundary encircles the model domain, with the distance between islands of interest and open boundaries exceeding three hundred kilometres. A single land cell separates the beginning and end of the open ocean boundary, positioned over Rennell Island (160.264°E, 11.663°S) (**Figures 1b–e**). In the vertical direction 26 levels were employed using a hybrid scheme. The hybrid scheme used stretched sigma coordinates for all levels in waters <100 m deep, while for deeper waters the first six upper layers employed fixed layer thicknesses of 2.5, 5.0, 7.5, 10, 10, and 10 m (from the surface layer to the sixth layer, respectively) and evenly distributed sigma coordinates for the remaining levels. A simplified visualisation of a hybrid layer scheme is shown in **Figure 1f**.

Initially it was intended that full resolution coastline files obtained from the global self-consistent, hierarchical, high-resolution geography database (Wessel and Smith, 1996), version 2.3.7 released in 2017, would be used to generate model grid land boundaries for the islands of Vanuatu and New Caledonia. However, it was found that the island shorelines positions from this dataset contained an offset of a few hundred metres, relative to satellite images, coral reef extent data from the Millennial Coral Reef Mapping project [Spalding et al., 2001; IMaRS-USF and Institut de Recherche pour le Developpement (IRD), 2005; Institute for Marine Remote Sensing-University of South Florida (IMaRS-USF)., 2005; UNEP-WCMC et al., 2010], and LiDAR data, despite all datasets reportedly using the WGS 84 the coordinate system. Such small offsets are unlikely to cause irregularities in coarser resolution (>500 m) fixed-grid regional models, however, given our model is attempting to resolve coastal lagoon systems, the data discrepancy posed a challenge. This challenge was made more difficult by a lack of high resolution (<500 m) elevation data available in this region, from which a consistent shoreline might be generated based upon elevation contours. After attempts to align the different datasets were unable to resolve the discrepancies, new shoreline data were generated, by manually digitised island shorelines using google earth. For the purpose of this study, shoreline polyline vertices were placed on the landward side of the land/water interface identified in satellite images. This was done in order so as to allow the movement of water overland in response to changing water levels. Given the majority of island shorelines have narrow coastal fringes, the shoreline was typically positioned within 50 m of the land/water interface. In areas covered by mangroves, the shoreline was placed landward of the mangrove area where possible. Mangroves typically occupy low-lying land, including intertidal flats, likely to become inundated during the tidal cycle and under higher sea levels, justifying their inclusion in the model domain. It should be noted, however, the influence mangroves may have on the movement of water due to friction and obstruction of flow, was not accounted for in this study. When constructing the Van-Fvcom grid, cell vertices, were positioned along the digitised shorelines thus capturing the complex geometry of the coastal waterways (**Figure 1**). Coastal waters are resolved applying grid resolutions of between 0.1 and 1.2 km along island shorelines. Higher resolutions (∼0.1 km) are employed in locations where high-resolution (∼5 m × 5 m) coastal bathymetry and elevation data were available (e.g., **Figures 1d,e**). While the model grid was constructed to closely follow coastlines, a lack of sufficient blended coastal elevation/bathymetry data at most locations limits our ability to replicate intertidal processes across all island shorelines, however, as improved data becomes available these data can be incorporated into the model. Similarly, while a concerted effort was made to resolve coastal reef/lagoons systems, the lack of high-resolution (<100 m) data capturing bathymetry in these geometrically complex systems likely limits our ability to accurately represent all processes governing circulation within reef waters. To allow flow over land in response to water level variations due to tidal processes and applied SLR, wetting and drying was implemented, using a using a cut-off water depth of 10 cm to trigger a cell becoming wet or dry. Using this regime grid cells on low-lying (<2 m HAT) coastal land, or in intertidal zones only become active when the water level exceeds the cut-off water depth. As such the shoreline moves in response to water level. Flow around small islands (<1 km across) incorporated in the model grid is accounted for via elevation, since cells whose elevation exceeds the minimum water depth remain dry during simulations.

High-resolution (∼5 m horizontal resolution) blended coastal elevation/bathymetry data for coastal waters of Southern Efate Island, and Southern Espiritu Santo Island are obtained from the Vanuatu Meteorology and Geo-Hazards Department. High resolution (∼5 m horizontal resolution) bathymetry data for Port Resolution, Tanna Island are obtained from the UK Hydrographic Office. For the remaining areas, bathymetry and coastal topography relied upon the GEBCO 15 arc second data (GEBCO Compilation Group, 2020), supplemented with data documented in nautical charts. Given GEBCO data poorly resolves coastal bathymetry and elevations, cells depths around islands reliant upon these data were manually edited to better match depths documented in nautical charts. While rudimentary, this methodology was necessary given the absence of adequate near-shore bathymetry and elevation data currently available in this remote island region.

At the offshore open boundary, tidal elevations are prescribed using eight tidal constituents (M_2, S_2, N_2, K_2, K_1, O_1, P_1, and Q_1) according to the Oregon State University global tidal model, TPXO9-atlas (Egbert and Erofeeva, 2002). At the ocean bed, a quadratic stress is exerted assuming a logarithmic bottom boundary layer. There is little understanding of the spatial variability in bed characteristics in our model region. For this study variable bottom roughness is applied, setting maximum bottom roughness heights (z_0) of 2.5 cm in shallow waters

(depths <50 m) decreasing to 1 mm in the deep ocean (depths >200 m). Sensitivity tests conducted applying uniform bottom roughness between 0.01 and 2.5 cm showed predicted water levels and currents were generally insensitive to changes in bottom roughness values ranging from 0.1 to 2.5 cm.

When investigating changes in coastal circulation, particularly maximum current speeds and residual circulation, three example sites are used to discuss coastal results. The sites selected include southern Grande Terre, New Caledonia, Efate Island Vanuatu, and Erakor Lagoon, near Port Vila on the south-western side of Efate Island. Southern Grande Terre, encompasses the Southern New Caledonia Lagoon, a relatively well-studied reef/lagoon system, on the south-western side of Grande Terre. Efate Island lies in central Vanuatu, housing the national capital Port Vila. Erakor Lagoon is a small urbanised reef/lagoon system near Port Vila where some focussed coastal process studies have been undertaken (Faivre et al., 2020).

Numerical Experiments

Tidal Behaviour

Model runs are conducted to verify the model's ability to replicate tidal characteristics. Simulations run from July 2015 to December 2016. Water level observation data at 11 tide gauges located within the model domain, were obtained from the IOC Sea Level Station Monitoring Facility [Flanders Marine Institute (VLIZ) and Intergovernmental Oceanographic Commission (IOC), 2021] and the University of Hawaii Sea Level Centre (Caldwelal et al., 2015). Four tide gauges are located on Vanuatu islands, and seven tide gauges are located on New Caledonia islands. The quality of observations at 9 of the 11 locations is not deemed to be research quality, the two exceptions are Port Vila in Vanuatu and Noumea in New Caledonia. Both sites have been included in the GLOSS tide gauge network. The water level data are provided in raw form, and as such, are affected by non-tidal influences, including atmospheric pressure, wind, and buoyancy related contributions, as well as contributions due to changes in regional circulation associated with ENSO cycles. In order to remove non-tidal influences, constituent analysis was performed on the raw observations using the U-tide program (Codiga, 2011), with the subsequent constituent amplitudes and phases used to predict tidal water levels at each location. The resulting tidal water level time series were compared with Van-Fvcom predicted water levels extracted at grid cells nearest tide gauge locations, satisfying the criteria that the grid cell depth >3 m to avoid the selection of intertidal grid cells. Constituent analysis of predicted water levels were compared with observed constituent data to determine the accuracy with which the model replicated observed tidal characteristics. Constituent data reported at an additional ten temporary water level monitoring sites within the Southern New Caledonia Lagoon (SNC Lagoon) were also compared with tidal constituents calculated from Van-Fvcom model water levels extracted nearest these locations.

Following verification with respect to tidal water levels, the Van-Fvcom model was used to predict tidal water levels at 12 unmonitored locations across Vanuatu. Results of constituent analysis for the five main tidal constituents (M2, K1, S2, N2, and O1) are reported for these 12 locations, to assist fill gaps in knowledge of tidal behaviour at unmonitored sites.

To understand the strengths and limitations of the Van-Fvcom model with respect to replication of currents in coastal waters, tidal currents extracted at grid points nearest to current meters are compared with observations. In New Caledonia, current observations were obtained at five sites within the SNC Lagoon (Douillet, 1998; Douillet et al., 2001). The only published study documenting tidal currents in coastal waters of Vanuatu, was undertaken in Erakor Lagoon, Efate Island by Faivre et al. (2020). Current velocity data from the same 58-days of the 60 day Van-Fvcom tidal simulation were analysed to determine maximum current speeds, and M2 tidal ellipses. Van-Fvcom M2 ellipses were mapped on top of maximum current speeds, and visually compared with ellipses documented in previous SNC Lagoon modelling studies (Douillet, 1998; Douillet et al., 2001). Maximum current speeds extracted from grid cells nearest to the CM1 and CM2 current meter sites in Erakor Lagoon (locations shown in **Figure 1e**) were compared with observed maximum currents speeds reported by Faivre et al. (2020).

Van-Fvcom maximum current speed data from tidal simulations are plotted for later comparison with simulations applying uniform wind fields in addition to tidal forcing, and simulations applying uniform SLR. Residual current speeds and directions were calculated for similar comparisons. In our study we do not address the influence of residual currents entering the model domain at the open boundary and only address internal circulatory residuals.

Wind Experiments

To investigate the sensitivity of coastal circulation to wind, nine 31-day simulations were run employing uniform 10, 20, and 40 km/h winds from the North East, East, and South East, to reflect predominant trade wind directions and speeds (light, moderate, and strong). Water levels were extracted at each tide gauge location and compared with tide-only simulations conducted over the same timeframe. The first 3 days of data were ignored to allow for model spinup, and the subsequent 28 days, covering two neap-spring tidal cycles analysed, to determine maximum depth-averaged current speeds (maxDA_curSp), and residual currents. The effect of the different wind regimes was investigated by calculating the difference in maxDA_curSp associated with each wind regime (Wind & Tide maxDA_curSp – Tide maxDA_curSp). To calculate residual currents due to wind only, 28-day mean eastward and northward currents were calculated at each grid cell for both tide-only and wind and tide simulations. The tide-only mean currents were then subtracted from wind and tide mean currents to obtain wind residual currents.

Sea Level Rise

To investigate the relationship between SLR and tidal behaviour, two different SLR experiments applying 1 and 2 m SLR were conducted. CMIP6-based global mean sea level (GMSL) ensemble projections estimate mean sea levels by 2100 will increase by 0.52–1.05 m relative to 1986–2005 levels, applying the SSP5-RCP8.5 scenario (Hermans et al., 2021). Altimetry sea level

observations between 2005 and 2016 indicate GMSL increased by nearly 4 cm over this period (Yi et al., 2017). Thus 1 m SLR reflects an upper estimate for GMSL relative to 2016 levels, which is the year used to represent present-day conditions in this study. It is recognised that this value likely does not fully account for contributions associated with the instability of the Antarctic ice sheet due to the assumptions made when generating the CMIP6 ensemble estimates (Hermans et al., 2021). The 2 m SLR value employed, reflects "credible" high-end scenarios of SLR by 2100, assuming 2°C warming relative to pre-industrial air temperatures, while also falling within the "likely" range assuming 5°C warming (Dayan et al., 2021), where high-end scenario values attempt to better account for the contribution of the Antarctic ice sheet. SLR values of 1 and 2 m were also chosen in this study to be consistent with other studies addressing the impact of SLR (e.g., Pelling and Green, 2013; Pickering et al., 2017).

For both simulations the additional SLR was uniformly added to tidal forcing at the open boundary and the model run for 60 days. The first ten simulation days were ignored to allow for model spin-up. Predicted water levels were extracted at tide gauge locations, and tidal constituent analysis performed to determine if 1–2 m SLR altered tidal constituent amplitudes and phases, thus changing tidal behaviour. Following this determination, maxDA_curSp and residual currents for the two SLR scenarios were compared to baseline (0 m SLR) maxDA_curSp and residual currents, to establish how SLR might alter circulation.

RESULTS

Tidal Water Level Verification

Modelled water levels show strong agreement with observed water levels (**Figure 2**). Tidal constituent analysis comparisons also show strong agreement (**Table 1**) with respect to both amplitudes and phases. Tidal behaviour across the region is dominated by the M2 constituent, whose amplitudes are approximately double K1 and S2 amplitudes, and approximately four times N2 and O1 amplitudes (**Table 1**). For the M2 constituent, mean difference between observed and predicted amplitudes and phases across all 11 tide gauge sites was 2.0 cm and 4.8°, respectively. Maximum differences in M2 amplitudes and phases were 4.3 cm and 24°, at Litzlitz (**Table 1** and **Figure 2C**). For the K1 constituent, mean difference between observed and predicted amplitudes and phases across all 11 sites was 1.9 cm and 12.7°, respectively. Maximum difference in K1 amplitude was 4.1 cm at Tanna Island (**Table 1** and **Figure 2E**) and maximum difference in K1 phase was 24.8°, at Thio (**Table 1** and **Figure 2H**).

Additional comparison with data acquired from ten temporary water level gauges deployed within the Southern New Caledonia Lagoon demonstrate the ability of the Van-Fvcom model to replicate tidal characteristics within the barrier reef lagoon system (**Table 2**). Despite the complex lagoon bathymetry, observed and predicted tidal constituent amplitudes showed close agreement (mean constituent amplitude difference <4 cm). For M2 and S2 constituents mean phase difference = 36° and 9°, respectively. Given the close agreement between M2 and S2 tidal constituents at the 10 temporary lagoon monitoring sites and the close agreement at the permanent tide gauge station in Noumea, we are confident that the model performs well and replicates tidal characteristics in this geometrically complex lagoon system.

Tidal characteristics were well replicated across the model domain enabling the Van-Fvcom model to be used to determine tidal constituent amplitudes and phases at 12 unmonitored Vanuatu locations (white diamonds **Figure 2A**). Results of tidal constituent analysis at these locations are provided in **Table 1**.

Tidal Currents

Analysis of predicted maximum depth averaged current speeds over the whole domain indicate highest tidal current speeds typically occur over reef/lagoon systems and between narrow passages between islands (**Figure 3a**). Compared to water levels, current speeds vary over smaller spatial scales in geometrically complex environments like reef/lagoon systems. To test Van-Fvcom's ability to replicate tidal currents we compare maximum current speeds and M2 tidal ellipses with those reported in previous modelling studies in the Southern New Caledonia Lagoon (Douillet, 1998; Douillet et al., 2001). Visual comparisons show similar results with respect to both current magnitudes and M2 tidal ellipses, despite differences in model setup. The previous modelling studies of the SNC Lagoon system, used a fixed resolution (1 km × 1 km) grid, oriented NW/SE between latitudes 22° 05′ S and 22° 40′ S and longitudes 166° 05′ E and 166° 50′ E, employing uniform bathymetry (depth = 50 m) in the southern extent of the model domain (Douillet, 1998; Douillet et al., 2001).

Within the SNC Lagoon, north of 22° 30′ S, Van-Fvcom maximum current speeds reached approximately 20 cm/s (**Figure 4a**), agreeing with the findings reported by Douillet (1998). South of 22° 30′ S, current speeds increased beyond 50 cm/s (**Figure 4a**). Maximum currents speeds approached 1 m/s in the narrow Canal Woodin, between Grande Terre and Ile Ouen. Similar high currents speeds appear to be predicted in Canal Woodin, based upon modelled M2 tidal ellipses presented by Douillet et al. (2001). Agreement between modelled and measured tidal constituent analysis in the SNC Lagoon show a closer agreement for the fixed-grid model than the Van-Fvcom model (**Table 2**). The fixed-grid model also reports closer agreement with respect to currents than was achieved in our simulations.

Maximum tidal current speeds and M2 tidal ellipses predicted around Efate Island are shown in **Figure 5a**. This scale however, does not clearly indicate current speed variability within the narrow Erakor Lagoon, where current meters for the Faivre et al., 2020 study were located. Within Erakor Lagoon, on Efate Island, the location of two current meters, labelled CM1 and CM2, are indicated on **Figures 1e**, **6a**. Model predicted maximum current speeds were close to observed values at the CM2 current meter site (model = 56 cm/s, CM2 = ∼59 cm/s). The coastline contracts near CM2, forming a relatively narrow channel (<150 m wide along its narrowest section). The Van-Fvcom model, predicts highest current speeds through the constriction, relative to surrounding lagoon waters (**Figure 6a**). At CM1, maximum

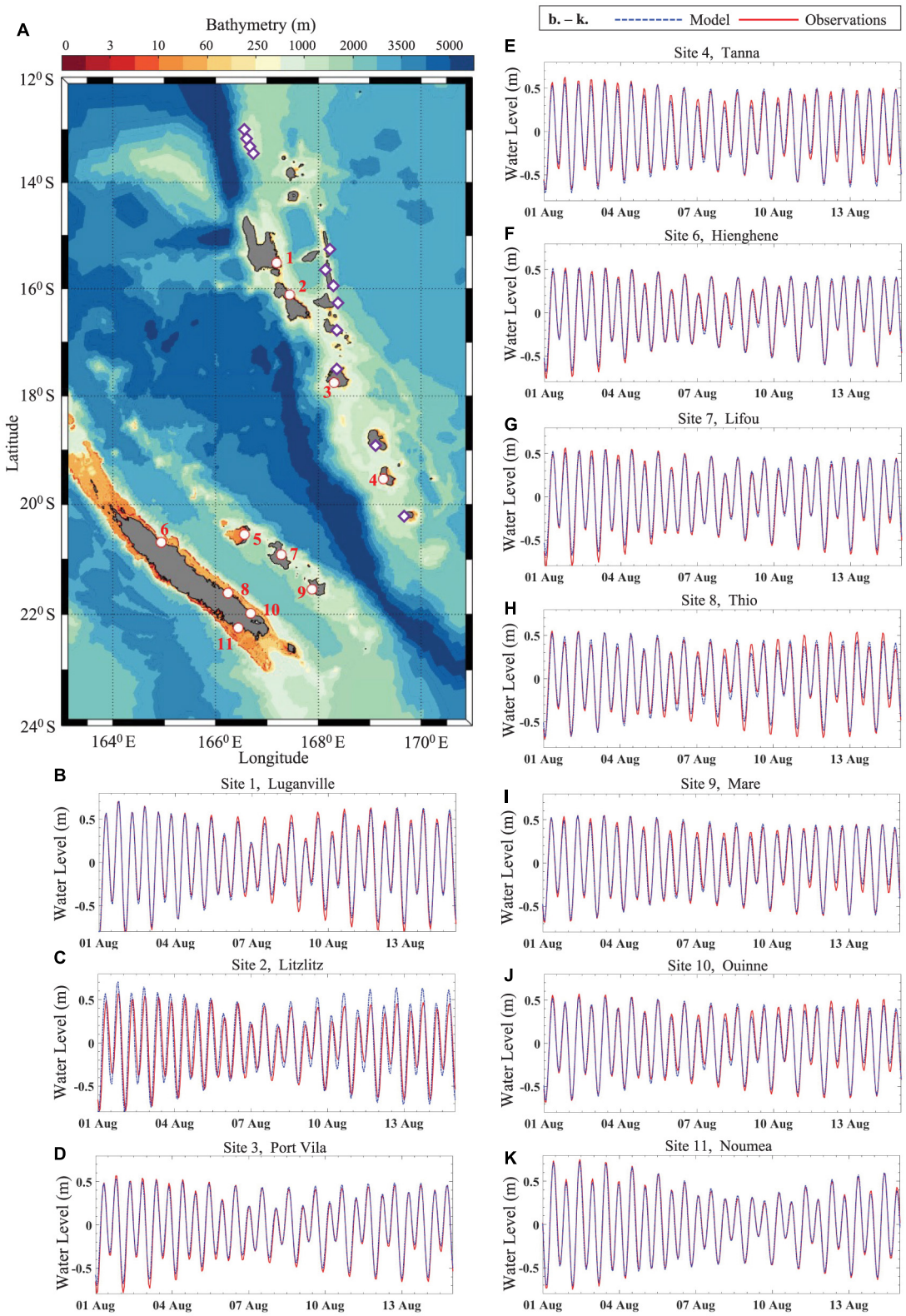

FIGURE 2 | Site map of tide gauge locations across Vanuatu and New Caledonia **(A)**. Tide gauge locations are highlighted using red and white circle markers, with red site number labels. Unmonitored locations where tidal characteristics were extracted are depicted using purple and white diamonds. Comparison between modelled water levels (blue) and observations (red) at ten of the eleven tide gauge locations **(B–K)** shown in panel **(A)**.

TABLE 1 | Results of observed and model predicted tidal constituent analysis, and predicted tidal constituents at unmonitored coastal locations (locations shown in **Figure 2A**).

Tidal Constituent Amplitude Comparison (cm)

	SITE 1, Luganville			SITE 2, Litzlitz			SITE 3, Port Vila			SITE 4, Tanna			SITE 5, Ouvea			SITE 6, Hienghene		
	Mod	Obs	Error	Mod	Obs	Error	Mod	Obs	Error	Mod	Obs	Error	Mod	Obs	Error	Mod	Obs	Error
M2	40.8	42.4	1.6	41.5	36.6	4.8	34.9	36.1	1.3	39.3	41.5	2.2	36.0	37.9	2.0	33.5	34.6	1.1
K1	16.7	20.6	3.9	16.5	21.2	4.7	17.0	15.3	1.7	15.5	11.6	3.8	16.9	15.3	1.5	17.6	17.0	0.6
S2	17.9	14.7	3.2	17.8	6.0	11.8	11.8	11.1	0.7	11.0	10.1	0.9	11.2	9.1	2.1	11.4	9.5	1.9
N2	10.8	9.4	1.5	11.1	7.9	3.2	8.5	8.4	0.1	9.6	8.2	1.4	8.9	9.3	0.4	8.4	7.8	0.6
O1	8.1	9.1	1.0	8.1	8.4	0.3	8.0	8.3	0.4	7.2	6.5	0.6	7.8	8.9	1.1	8.2	8.2	0.1

	SITE 7, Lifou			SITE 8, Thio			SITE 9, Mare			SITE 10, Ouinne			SITE 11, Noumea			Mean Diff (cm)	
	Mod	Obs	Error	Mod	Obs	Error	Mod	Obs	Error	Mod	Obs	Error	Mod	Obs	Error	Constituent	Error
M2	36.9	38.3	1.5	35.6	36.6	1.1	37.4	37.7	0.3	35.9	37.2	1.3	40.5	40.9	0.4	M2	1.6
K1	16.0	16.0	0.0	16.5	17.9	1.4	15.3	12.0	3.3	16.0	15.9	0.2	15.4	14.1	1.3	K1	2.0
S2	10.1	8.7	1.4	9.7	7.6	2.1	9.4	7.0	2.4	8.9	7.2	1.7	17.3	14.3	3.0	S2	2.8
N2	9.2	8.9	0.3	8.9	8.6	0.3	8.9	9.6	0.7	8.9	8.3	0.5	7.4	6.6	0.8	N2	0.9
O1	7.4	8.5	1.1	7.7	8.1	0.5	7.0	6.6	0.4	7.5	7.1	0.4	6.7	6.6	0.1	O1	0.5

Tidal Constituent Phase Comparison (degrees)

	SITE 1, Luganville			SITE 2, Litzlitz			SITE 3, Port Vila			SITE 4, Tanna			SITE 5, Ouvea			SITE 6, Hienghene		
	Mod	Obs	Error	Mod	Obs	Error	Mod	Obs	Error	Mod	Obs	Error	Mod	Obs	Error	Mod	Obs	Error
M2	180.2	181.8	1.7	179.5	217.5	38.0	200.7	206.1	5.4	205.6	208.7	3.1	211.1	216.5	5.4	212.7	216.2	3.5
K1	56.7	46.2	10.6	56.9	28.0	28.9	54.7	36.3	18.4	53.1	48.9	4.3	48.9	23.2	25.7	48.0	35.1	12.9
S2	194.4	179.5	14.9	193.2	218.7	25.5	223.0	214.6	8.3	232.6	220.8	11.8	233.2	211.3	22.0	231.5	218.4	13.1
N2	168.5	167.5	1.1	167.3	200.4	33.1	182.1	189.7	7.7	182.2	198.0	15.8	191.1	202.2	11.1	195.2	198.1	2.8
O1	19.0	21.5	2.5	19.0	7.5	11.4	14.8	16.8	2.0	13.2	21.3	8.1	8.2	11.7	3.5	7.2	13.6	6.3

	SITE 7, Lifou			SITE 8, Thio			SITE 9, Mare			SITE 10, Ouinne			SITE 11, Noumea			Mean Diff (degrees)	
	Mod	Obs	Error	Mod	Obs	Error	Mod	Obs	Error	Mod	Obs	Error	Mod	Obs	Error	Constituent	Error
M2	210.5	213.2	2.6	214.0	214.6	0.6	216.4	220.3	3.8	215.7	222.0	6.3	266.4	269.8	2.7	M2	6.7
K1	48.3	39.2	9.1	49.2	20.1	29.1	47.3	43.7	3.6	45.4	30.0	15.4	39.0	28.1	9.0	K1	15.2
S2	234.4	216.9	17.4	237.0	208.1	28.9	249.7	229.9	19.7	242.5	223.5	19.0	313.2	304.9	5.9	S2	17.0
N2	187.4	191.7	4.2	191.0	186.2	4.8	190.3	199.9	9.6	190.3	196.3	6.0	253.9	257.0	0.1	N2	8.8
O1	7.5	14.5	7.0	4.9	3.2	1.6	5.5	9.4	4.0	3.7	5.1	1.4	349.8	355.5	2.4	O1	4.6

Tidal Constituents at unmonitored locations - based upon Van-Fvcom model results

	Eramango 169.02 E 18.82 S		Aneghowhat 169.78 E 20.23 S		Tikilas 168.38 E 17.48 S		Endu Pahakol 168.25 E 16.26 S		Tongoa 168.53 E 16.91 S		Ranon 168.27 E 15.92 S	
	Amp	Phase	Amp	Phase	Amp	Phase	Amp	Phase	Amp	Phase	Amp	Phase
M2	38.9	202.4	41.0	207.1	34.8	199.2	44.0	181.0	37.8	188.2	44.2	179.9
K1	18.0	26.9	16.6	25.9	19.3	27.7	17.4	31.1	18.5	31.3	17.5	31.6
S2	9.2	186.8	7.5	194.4	9.5	184.5	14.1	158.9	10.5	166.5	14.4	158.3
N2	7.8	184.4	8.2	184.8	6.9	184.4	9.7	168.7	8.0	171.9	9.8	167.9
O1	7.3	19.0	6.7	17.8	7.8	20.1	7.4	24.9	7.7	24.2	7.4	25.6

	Nambwarangiut 168.13 E 15.6 S		Baitora 168.11 E 15.2 S		Toga 166.7 E 13.4 S		Lo 166.64 E 13.3 S		Metoma 166.6 E 13.2 S		Hiu 166.59 E 13.1 S	
	Amp	Phase	Amp	Phase	Amp	Phase	Amp	Phase	Amp	Phase	Amp	Phase
M2	41.8	180.3	41.8	179.0	36.0	174.9	37.0	174.4	35.0	174.1	37.5	173.1
K1	18.5	31.1	18.6	31.2	20.2	32.8	20.0	32.7	20.6	32.7	20.0	32.6
S2	14.4	161.9	14.7	161.3	14.2	161.0	14.7	161.2	14.0	162.4	15.1	160.3
N2	9.0	170.0	8.9	169.5	7.4	168.8	7.7	168.5	7.1	168.7	7.7	167.8
O1	7.8	24.7	7.9	24.9	8.6	26.1	8.5	26.0	8.7	26.4	8.6	25.9

current speeds are under-predicted by Van-Fvcom, reaching ∼30 cm/s during the simulation, while observed currents speeds reach ∼65 cm/s. CM1 is located in a narrow (∼ 50 m wide) reef channel between adjacent reef platforms (Faivre et al., 2020). It was initially thought that water depth settings used for reef platforms may be partly responsible for the under-prediction of current speeds at CM1. Whilst reef platforms in the vicinity of CM1 typically have sharp drop offs, with seaward edges becoming exposed during low tide, in the Van-Fvcom model water depths for grid cells at the seaward edge of platforms were set to 2 m.

TABLE 2 | Southern New Caledonia Lagoon tidal constituent amplitudes and phases at tide gauges (T21–T421).

	T21 Amplitudes				T21 Phase				T22 Amplitudes				T22 Phase			
	Mod	Obs	Error	Douil	Mod	Obs	Error	Douil	Mod	Obs	Error	Douil	Mod	Obs	Error	Douil
M2	34.3	35.4	1.1	35.6	259.5	222.1	37.4	221.7	38.0	38.2	0.2	38.1	264.7	223.2	41.5	223.7
K1	17.4	13.6	3.8		13.3	191.9	178.6		17.3	13.6	3.7		12.8	191.8	179.0	
S2	8.9	11.8	2.9	11.7	285.9	277.1	8.8	277.7	10.7	12.6	1.9	12.6	283.9	272.9	11.0	273.9
O1	7.0	6.6	0.4		356.9	149.1	207.8		6.8	6.6	0.2		356.1	149.3	206.8	

	T23 Amplitudes				T23 Phase				T25 Amplitudes				T25 Phase			
	Mod	Obs	Error	Douil	Mod	Obs	Error	Douil	Mod	Obs	Error	Douil	Mod	Obs	Error	Douil
M2	38.2	38.6	0.5	38.6	266.0	227.0	39.0	227.0	37.5	37.7	0.2	37.7	264.6	228.9	35.7	228.9
K1	17.3	13.3	4.0		12.5	190.2	177.8		17.1	13.8	3.3		12.5	191.1	178.6	
S2	11.1	13.6	2.6	13.6	284.8	272.0	12.8	272.0	10.6	13.8	3.2	13.8	285.2	267.5	17.7	267.7
O1	6.8	6.4	0.4		355.5	148.5	207.0		6.8	6.8	0.0		355.5	152.8	202.7	

	T90 Amplitudes				T90 Phase				T156 Amplitudes				T156 Phase			
	Mod	Obs	Error	Douil	Mod	Obs	Error	Douil	Mod	Obs	Error	Douil	Mod	Obs	Error	Douil
M2	41.2	40.9	0.3	40.3	269.6	228.1	41.5	228.9	33.5	42.3	8.8	42.7	263.4	234.1	29.3	234.4
K1	18.0	13.8	4.2		14.0	190.4	176.4		17.5	15.0	2.5		13.4	184.0	170.6	
S2	12.3	14.1	1.8	14.3	284.8	274.8	10.0	274.2	9.4	13.5	4.1	15.5	291.3	280.3	11.0	273.9
O1	6.9	6.9	0.0		357.9	148.5	209.4		6.9	6.7	0.2		356.8	160.9	195.9	

	T158 Amplitudes				T158 Phase				T229 Amplitudes				T229 Phase			
	Mod	Obs	Error	Douil	Mod	Obs	Error	Douil	Mod	Obs	Error	Douil	Mod	Obs	Error	Douil
M2	31.1	37.6	6.5	37.1	244.4	226.8	17.6	227.1	33.0	30.8	2.2	31.4	253.4	211.3	42.1	214.0
K1	17.5	13.6	3.9		13.7	191.5	177.8		17.4	13.8	3.6		13.4	192.8	179.4	
S2	5.6	12.5	6.9	12.9	275.1	284.5	9.4	279.6	7.5	8.2	0.7	8.3	281.8	282.2	0.4	282.6
O1	7.2	6.8	0.4		358.8	145.5	213.3		7.1	7.0	0.1		357.7	147.3	210.4	

	T278 Amplitudes				T278 Phase				T421, Amplitudes				T421 Phase			
	Mod	Obs	Error	Douil	Mod	Obs	Error	Douil	Mod	Obs	Error	Douil	Mod	Obs	Error	Douil
M2	35.7	33.7	2.0	34.1	258.3	218.1	40.2	218.1	38.4	39.7	1.3	39.1	266.5	228.0	38.5	227.1
K1	17.1	12.6	4.5		12.9	190.3	177.4		17.4	13.5	3.9		12.7	191.5	178.8	
S2	9.1	10.3	1.2	10.6	282.6	280.0	2.6	278.8	11.2	13.8	2.6	13.6	284.8	275.4	9.4	273.3
O1	6.9	6.1	0.8		356.9	149.8	207.1		6.8	6.7	0.1		355.8	143.7	212.1	

Mean Diff	
Const Amp	Error
M2	2.3
K1	3.7
S2	2.8
O1	0.3

Mean Diff	
Const Phase	Error
M2	36.3
K1	177.4
S2	9.3
O1	207.2

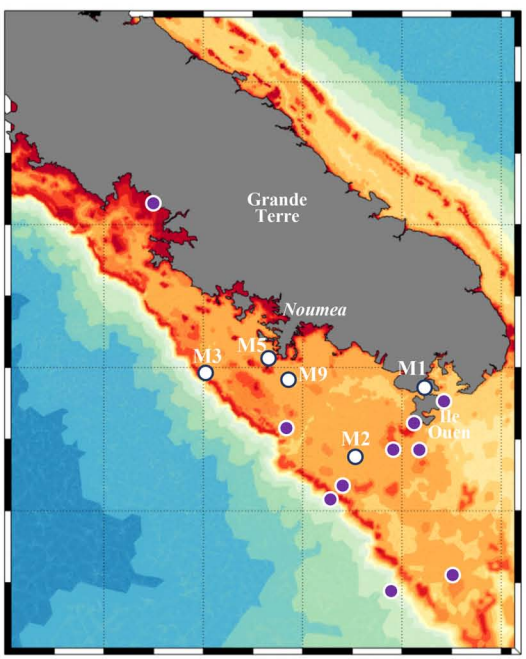

	M1				M2			
	Mod	Obs	Error	Douil	Mod	Obs	Error	Douil
M2 maj	38.3	17.8	20.5	22.0	17.0	10.8	6.2	14.0
M2 min	-0.1	-3.5	3.4	1.3	0.0	-0.1	0.1	0.4
M2 inclin	10.0	25.8	-15.8	58.7	205.1	111.1	94.0	115.3
S2 maj	13.6	6.9	6.7	6.9	5.9	4.0	1.9	4.9
S2 min	0.0	-0.9	0.9	-0.3	-0.9	-1.2	0.3	-1.2
S2 inclin	28.6	18.9	9.7	59.2	177.0	113.0	64.0	118.7

	M3				M5			
	Mod	Obs	Error	Douil	Mod	Obs	Error	Douil
M2 maj	5.4	28.0	-22.6	23.9	12.3	13.9	-1.6	12.8
M2 min	1.5	1.0	0.5	0.6	0.7	0.3	0.4	-0.5
M2 inclin	187.0	38.3	148.7	45.2	196.7	164.7	32.0	141.9
S2 maj	2.1	9.9	-7.8	9.7	5.1	3.4	1.7	3.8
S2 min	0.0	0.0	0.0	-0.4	0.1	-0.2	0.3	0.1
S2 inclin	55.3	36.8	18.5	42.2	138.3	151.6	-13.3	139.4

	M9			
	Mod	Obs	Error	Douil
M2 maj	5.0	4.0	1.0	4.9
M2 min	0.1	0.0	0.1	0.4
M2 inclin	194.6	132.6	62.0	115.1
S2 maj	2.1	1.5	0.6	1.6
S2 min	-0.4	-0.3	-0.1	-0.8
S2 inclin	2.7	111.0	-108.3	109.0

In this way cells adjacent to the channel did not become dry during low-tide. These depth setting were employed to allow the use of 1–2 s timesteps for simulations. To test the sensitivity of modelled currents to reef exposure at this location, a simulation was conducted whereby water level was reduced by 1 m, allowing more cells on the reef platform to dry during low tides, however, maximum current speeds at CM1 did not significantly improve, and maximum current speeds remained around 30 cm/s. Wind experiments discussed in detail in following sections increase maximum current speeds by less than 10 cm/s in the vicinity of CM1, and thus even under 40 km/h winds, Van-Fvcom maximum current speeds are underpredicted by ∼ 20 cm/s at this location.

Analysis of predicted maximum depth-averaged current speeds over the whole model domain indicate that tidal currents were typically fastest at north-western and south-eastern ends of islands (**Figure 3a**). In New Caledonia predicted tidal currents were fastest over the reefs and lagoons to the north/north west and south/south east of Grande Terre. For Vanuatu, fastest tidal currents also occur at the north/northwest and south/southeast tips of most islands, as well as between closely spaced islands (**Figure 3a**). Within the Southern New Caledonia Lagoon of Grande Terre, predicted tidal currents were fastest within two sections of the lagoon that extend from the south-eastern and south-western corners of Grand Terre, as well as in the narrow strait between Ile Ouen and Grande Terre (**Figure 4a**). Predicted maximum depth-averaged tidal current speeds reduced to less than 10 cm/s within coastal embayments (**Figure 4a**). Around Efate Island, fastest tidal currents were predicted in waters to the southeast of Efate, and to the north of Nguna Island, as well as between Efate, Pele, and Mangarongo Islands (**Figure 5a**). Within Erakor Lagoon, on the southwestern side of Efate Island, predicted tidal currents were fastest within the constriction in the lagoon (**Figure 6a**) as discussed earlier.

Wind Experiments

Water Levels

For all wind experiments, tidal water levels showed negligible (<1 cm) response to wind forcing (not shown). Extreme meteorological events such as Tropical Cyclone Pam (2015) can cause water levels to alter by up to 0.6 m. Winds during TC Pam exceeded 160 km/h, however, the majority of storm surge was due to low atmospheric pressure (Nishijima et al., 2015). While regional ocean circulation, driven by global wind systems, does alter the position of mean water over daily, and monthly timeframes, our results indicate that local wind forcing by trade winds within the model domain does not significantly alter coastal water levels at tide gauge stations.

Maximum Depth-Averaged Current Speeds

Between islands, changes under NE winds showed a mixed response, while coastal maxDA_curSp mainly increased (**Figures 3d–f**). Under E winds maxDA_curSp around and between islands mainly increased. Larger responses typically occurred on windward, southern, and northern sides of islands (**Figures 3g–i**). Under SE winds maxDA_curSp demonstrated a clear response, increasing along the axis of the wind. Both the Vanuatu and New Caledonia archipelagos are approximately orientated in a SE direction (**Figures 3j–l**) which likely contributes to larger response to SE winds, compared with NE and E winds. Coastal waters where the largest change in maxDA_curSp occur correspond to shallower areas of lagoon/reef systems.

Within coastal waters in southern Grande Terre, New Caledonia maxDA_curSp typically increased in response to increasing wind speed. The largest increases in maxDA_curSp are seen under SE winds (**Figures 4g–i**), and smallest changes occur under NE winds (**Figures 4d–f**). Under 40 km/h wind conditions maxDA_curSp increased by up to a factor of 2, within the Southern New Caledonia Lagoon.

In coastal waters around Efate, overall patterns with respect to changes in maxDA_curSp are similar under NE, E, and SE winds (**Figures 5d–l**). This is likely due to the more circular shape of Efate Island, compared to other islands such as Grande Terre, New Caledonia. Within Mele Bay, located on the southwestern side of Efate island, maxDA_curSp increase most significantly close to the coast, on the northern and western sides of the bay (**Figures 5d–l**).

Near Erakor Lagoon, Port Vila, on Efate Island, increasing wind speeds typically increased maxDA_curSp (**Figures 6d–l**). MaxDA_curSp increased most significantly under SE winds, while NE winds resulted in the least change. Under NE winds the largest change in maxDA_curSp were seen in waters running along the southeast shores of Mele Bay. Under E winds, maxDA_curSp increased on both the SE shores of Mele, and the SW shores of Erakor Lagoon, as well as waters immediately south of Erakor Lagoon. Under SE winds shallow waters over reefs and adjacent to shorelines showed the largest increases in maxDA_curSp, while within the upper Erakor Lagoon maxDA_curSp changed to a lesser degree, compared with those generated by NE and E winds (**Figures 6d–l**).

Residual Currents

Tidal residual currents are persistent features associated with the local bottom or coastal topography, which alter in response to the strength of the semidiurnal tides over regular spring neap cycles (Robinson, 1983). Small-scale eddies (1–10 km) are commonly observed in coastal waters in the vicinity of headlands or islands, driven by oscillatory tidal flow, forming on alternate sides of islands or headlands with the reversal of the tide (Signell and Geyer, 1991). For our model domain tidal residual currents are most significant in coastal waters due to the interaction of irregular shorelines and tidal flow (**Figures 7a**, **8a**, **9a**, **10a**). In open ocean waters, tidal residual current patterns are complex, with numerous meanders and cyclonic/anti-cyclonic eddies. Between the Vanuatu and New Caledonia islands, tidal residual flow appears to be influenced by topographic steering with north-westward flowing residual currents aligning with the Vanuatu (New Hebrides) Trench (**Figure 7a**). While residual current patterns in open ocean waters are complex, current speeds are relatively low (<0.5 cm/s) (**Figure 7a**) compared to coastal residual currents (up to ∼15 cm/s) (**Figures 8a**, **9a**, **10a**).

The application of trade winds from the NE, E and SE generated Ekman flow as demonstrated by wind residual circulation streamline directions (**Figures 7d–l**). In open ocean

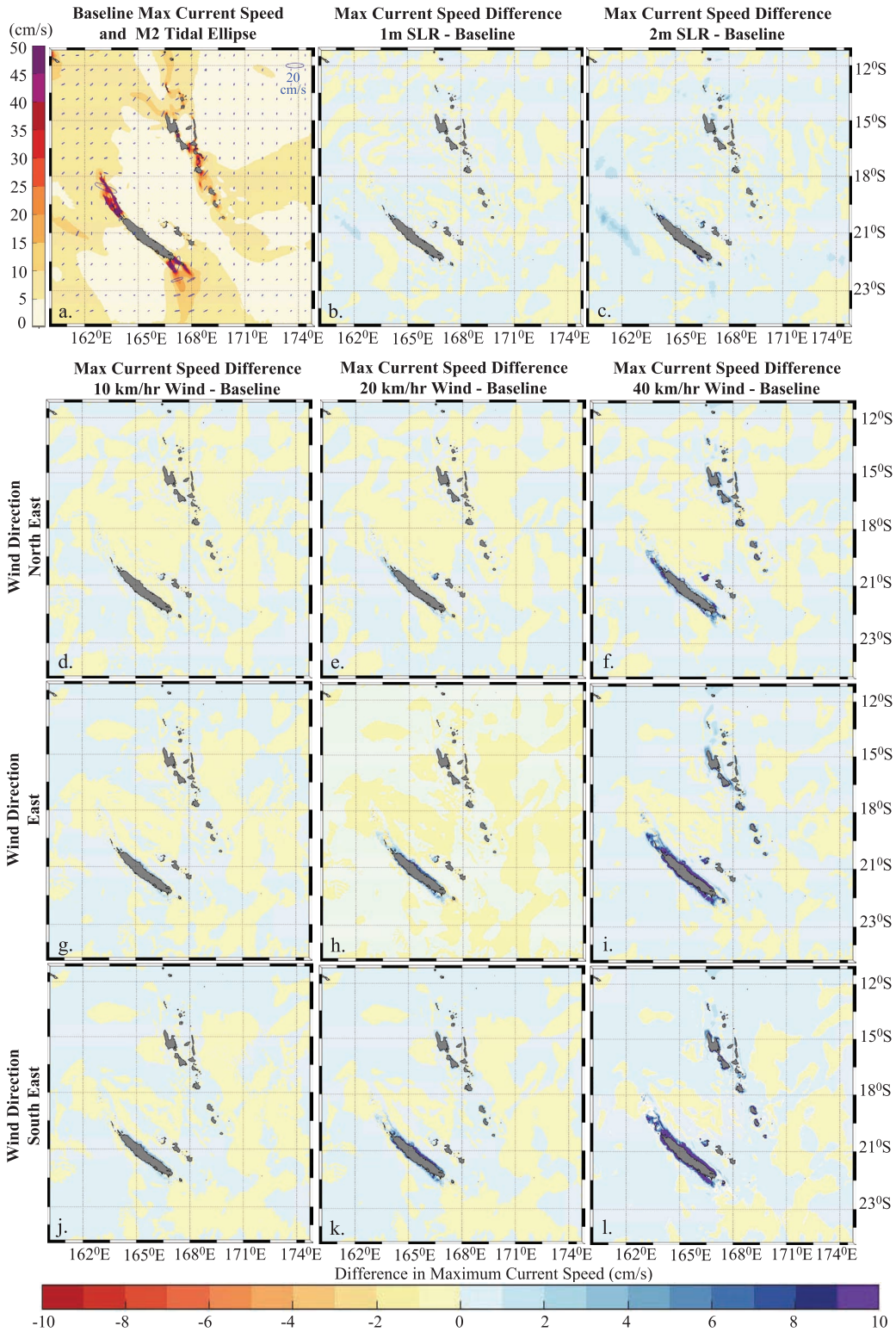

FIGURE 3 | Baseline maximum depth-averaged current speeds (cm/s) across the whole model domain shown underlying M2 tidal ellipses **(a)**. Change in maximum depth-averaged current speeds (cm/s) under 1 m SLR **(b)** and 2 m SLR **(c)**. Change in maximum depth-averaged current speed (cm/s) under 10 km/h **(d)**, 20 km/h **(e)**, and 40 km/h **(f)** northeast winds. Change in maximum depth-averaged current speed (cm/s) under 10 km/h **(g)**, 20 km/h **(h)**, and 40 km/h **(i)** east winds. Change in maximum depth-averaged current speed (cm/s) under 10 km/h **(j)**, 20 km/h **(k)**, and 40 km/h **(l)** southeast winds. Latitudes are displayed to the right of panels **(c,f,i,l)**. Longitude for all panels are displayed below panels **(j–l)**.

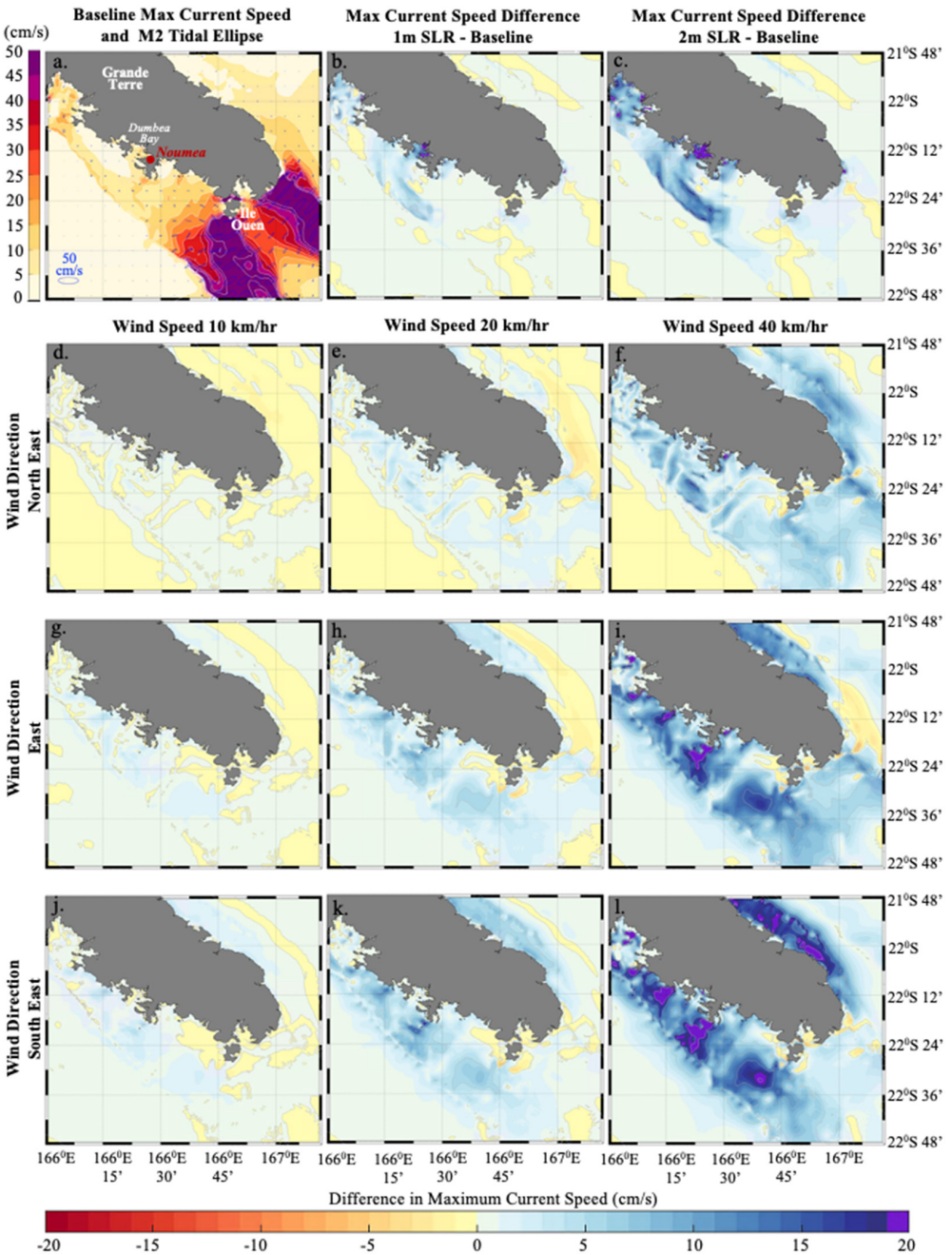

FIGURE 4 | Baseline maximum depth-averaged current speeds (cm/s) for southern Grande Terre, New Caledonia, shown underlying M2 tidal ellipses, with white isolines at 5 cm/s intervals **(a)**. Change in maximum depth-averaged current speeds (cm/s) under 1 m SLR **(b)** and 2 m SLR **(c)**. Change in maximum depth-averaged current speed (cm/s) under 10 km/h **(d)**, 20 km/h **(e)**, and 40 km/h **(f)** northeast winds. Change in maximum depth-averaged current speed under 10 km/h **(g)**, 20 km/h **(h)**, and 40 km/h **(i)** east winds. Change in maximum depth-averaged current speed under 10 km/h **(j)**, 20 km/h **(k)**, and 40 km/h **(l)** southeast winds. Light grey isolines **(b–l)** indicate 5 cm/s intervals. Latitudes are displayed to the right of panels **(c,f,i,l)**. Longitude for all panels are displayed below panels **(j–l)**.

waters, current speeds associated with wind residual circulation remain relatively low (0–5 cm/s, under 40 km/h winds). The direction of wind residual currents was consistent for simulations employing the same wind direction, with residual current speeds increasing in response to higher wind speed (**Figures 7d–l**). In addition to currents flowing approximately perpendicular to the wind direction, residual current patterns reveal the formation of anti-cyclonic eddies in open ocean waters, particularly east of 171°E, and complex meandering flow on the leeward side of islands (**Figures 7d–l**).

Within coastal waters of Grande Terre, tidal residual currents typically flow NW parallel to the shoreline along the eastern

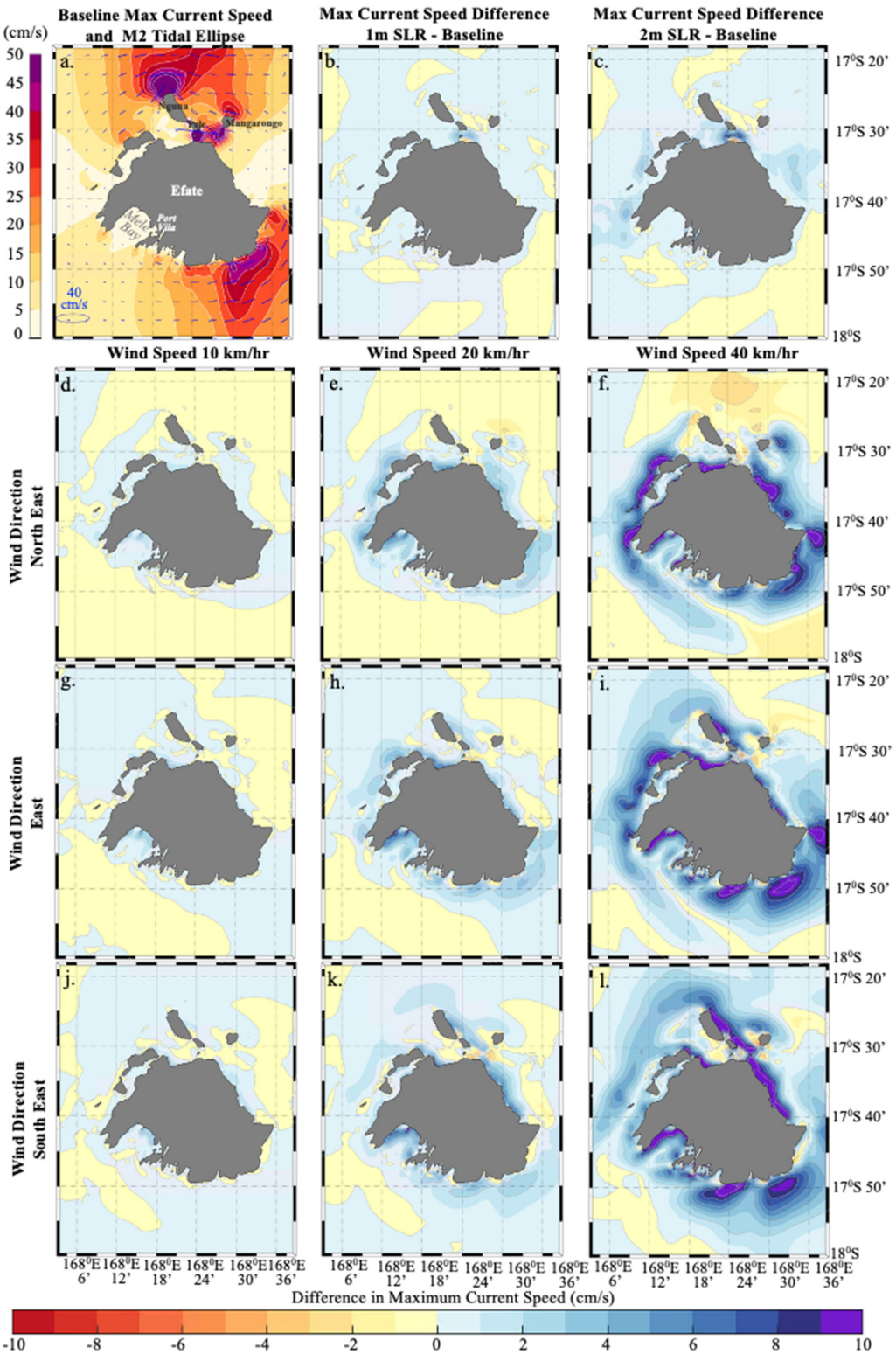

FIGURE 5 | Baseline maximum depth-averaged current speeds around Efate Island, Vanuatu shown underlying M2 tidal ellipses, with white isolines at 5 cm/s intervals **(a)**. Change in maximum depth-averaged current speeds (cm/s) under 1 m SLR **(b)** and 2 m SLR **(c)**. Change in maximum depth-averaged current speed (cm/s) under 10 km/h **(d)**, 20 km/h **(e)**, and 40 km/h **(f)** northeast winds. Change in maximum depth-averaged current speed under 10 km/h **(g)**, 20 km/h **(h)**, and 40 km/h **(i)** east winds. Change in maximum depth-averaged current speed under 10 km/h **(j)**, 20 km/h **(k)**, and 40 km/h **(l)** southeast winds. Light grey isolines **(b–l)** indicate 2 cm/s intervals. Latitudes are displayed to the right of panels **(c,f,i,l)**. Longitude for all panels are displayed below panels **(j–l)**.

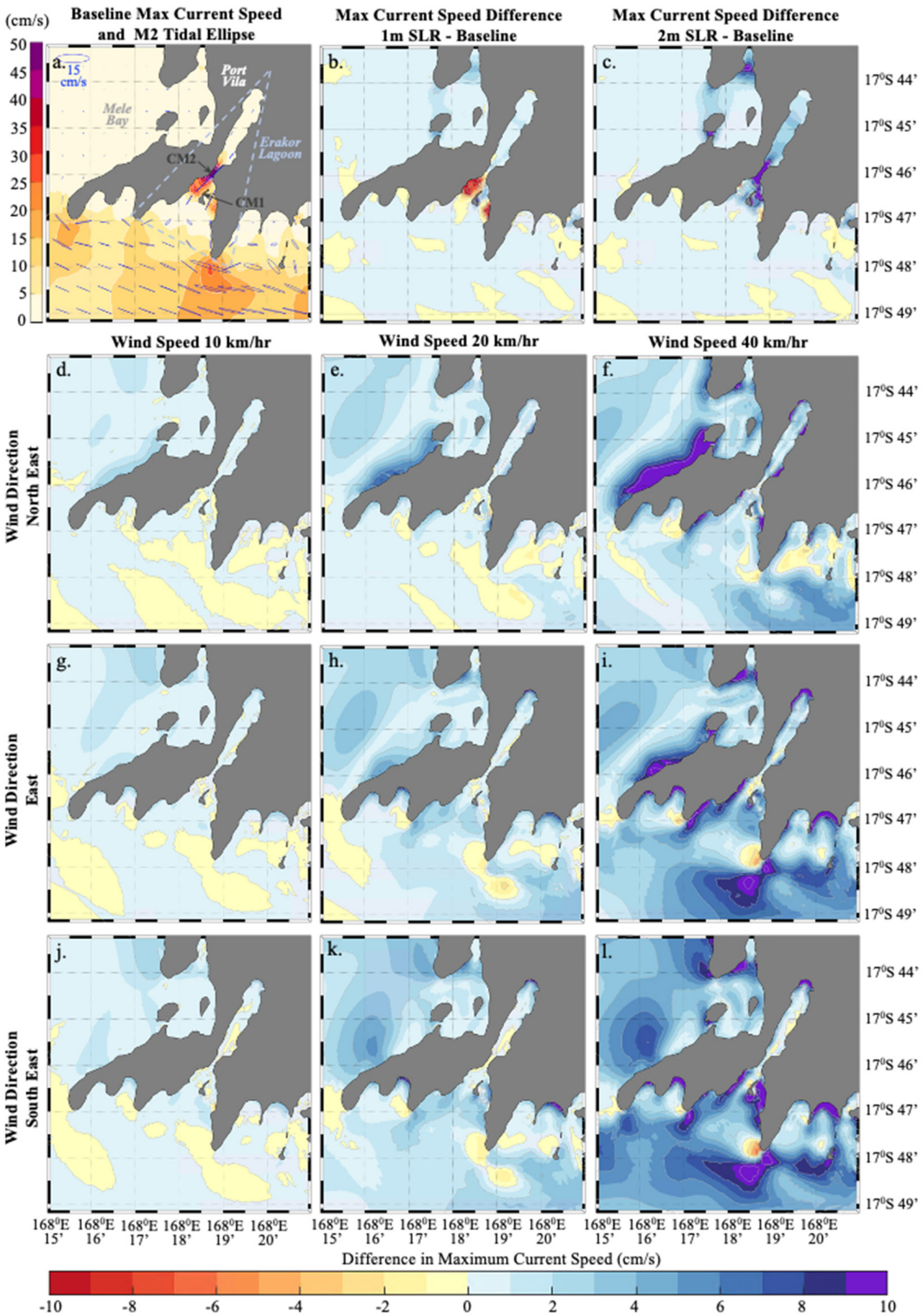

FIGURE 6 | Baseline maximum depth-averaged current speeds focussing on Erakor Lagoon, southwest Efate Island, shown underlying M2 tidal ellipses, with white isolines at 5 cm/s intervals **(a)**. Change in maximum depth-averaged current speeds (cm/s) under 1 m SLR **(b)** and 2 m SLR **(c)**. Change in maximum depth-averaged current speed (cm/s) under 10 km/h **(d)**, 20 km/h **(e)**, and 40 km/h **(f)** northeast winds. Change in maximum depth-averaged current speed under 10 km/h **(g)**, 20 km/h **(h)**, and 40 km/h **(i)** east winds. Change in maximum depth-averaged current speed under 10 km/h **(j)**, 20 km/h **(k)**, and 40 km/h **(l)** southeast winds. Light grey isolines **(b–l)** indicate 2 cm/s intervals. Latitudes are displayed to the right of panels **(c,f,i,l)**. Longitude for all panels are displayed below panels **(j–l)**.

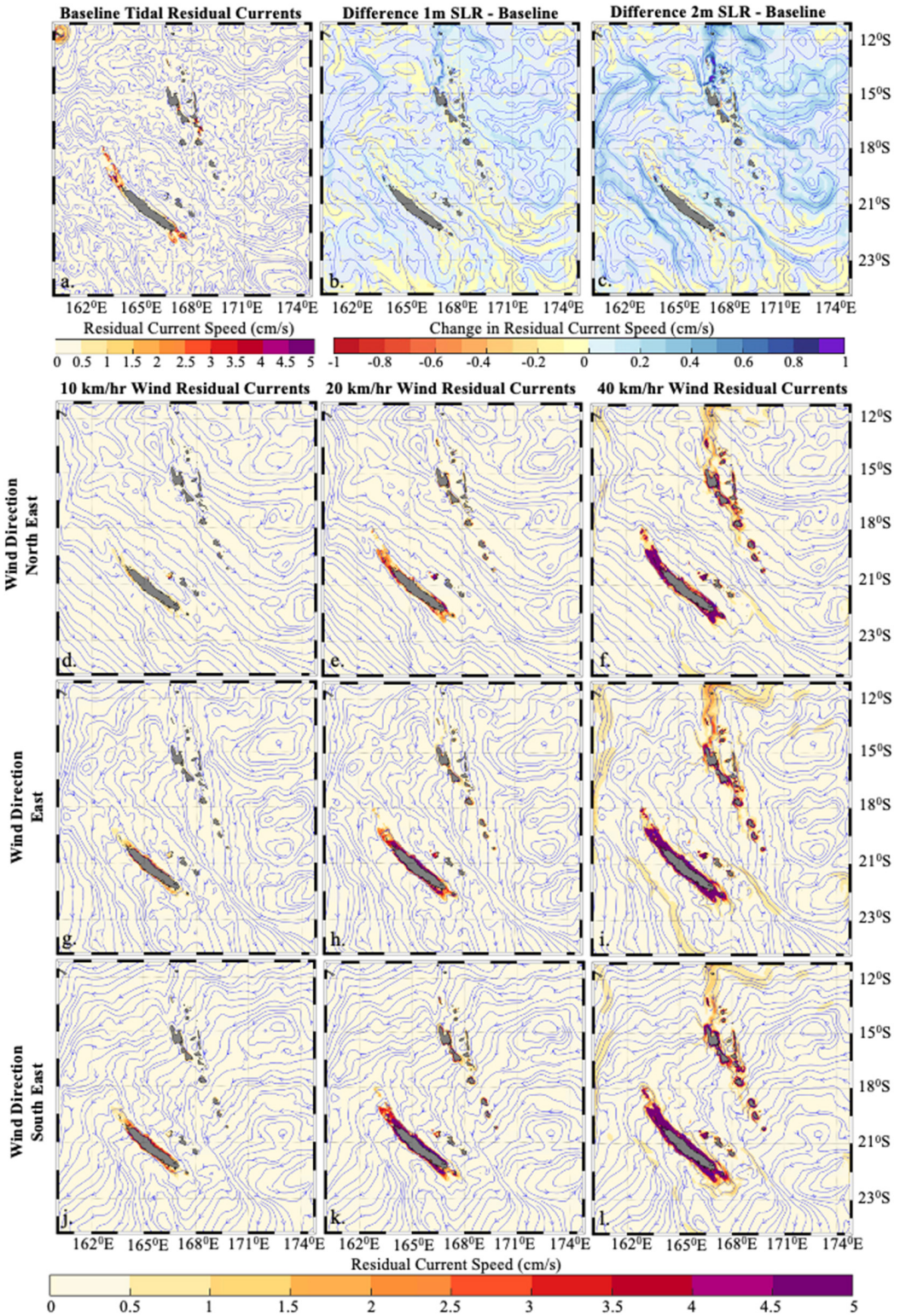

FIGURE 7 | Tidal residual current speeds (cm/s), with current patterns indicated by streamlines, across the whole model domain **(a)**. Change in residual current speeds (cm/s) and patterns under 1 m SLR **(b)** and 2 m SLR **(c)**. Wind residual current speeds (cm/s) and patterns under 10 km/h **(d)**, 20 km/h **(e)**, and 40 km/h **(f)** northeast winds. Wind residual current speeds (cm/s) and patterns under 10 km/h **(g)**, 20 km/h **(h)**, and 40 km/h **(i)** east winds. Wind residual current speeds (cm/s) and patterns under 10 km/h **(j)**, 20 km/h **(k)**, and 40 km/h **(l)** southeast winds. Latitudes are displayed to the right of panels **(c,f,i,l)**. Longitude for all panels are displayed below panels **(a–c,j–l)**.

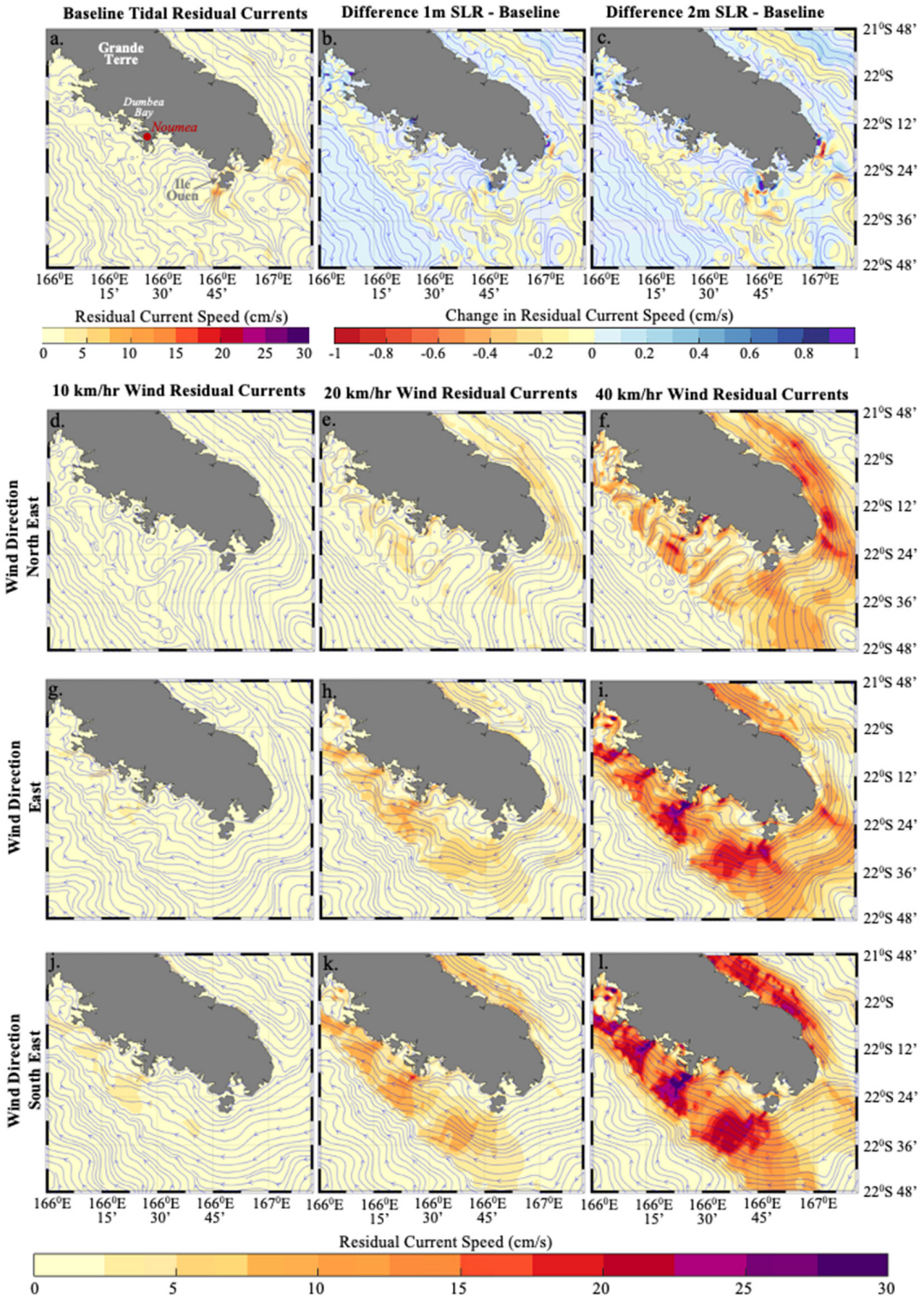

FIGURE 8 | Tidal residual current speeds (cm/s), with current patterns indicated by streamlines for southern Grande Terre, New Caledonia **(a)**. Change in residual current speeds (cm/s) and patterns under 1 m SLR **(b)** and 2 m SLR **(c)**. Wind residual current speeds (cm/s) and patterns under 10 km/h **(d)**, 20 km/h **(e)**, and 40 km/h **(f)** northeast winds. Wind residual current speeds (cm/s) and patterns under 10 km/h **(g)**, 20 km/h **(h)**, and 40 km/h **(i)** east winds. Wind residual current speeds (cm/s) and patterns under 10 km/h **(j)**, 20 km/h **(k)**, and 40 km/h **(l)** southeast winds. Latitudes are displayed to the right of panels **(c,f,i,l)**. Longitude for all panels are displayed below panels **(a–c,j–l)**.

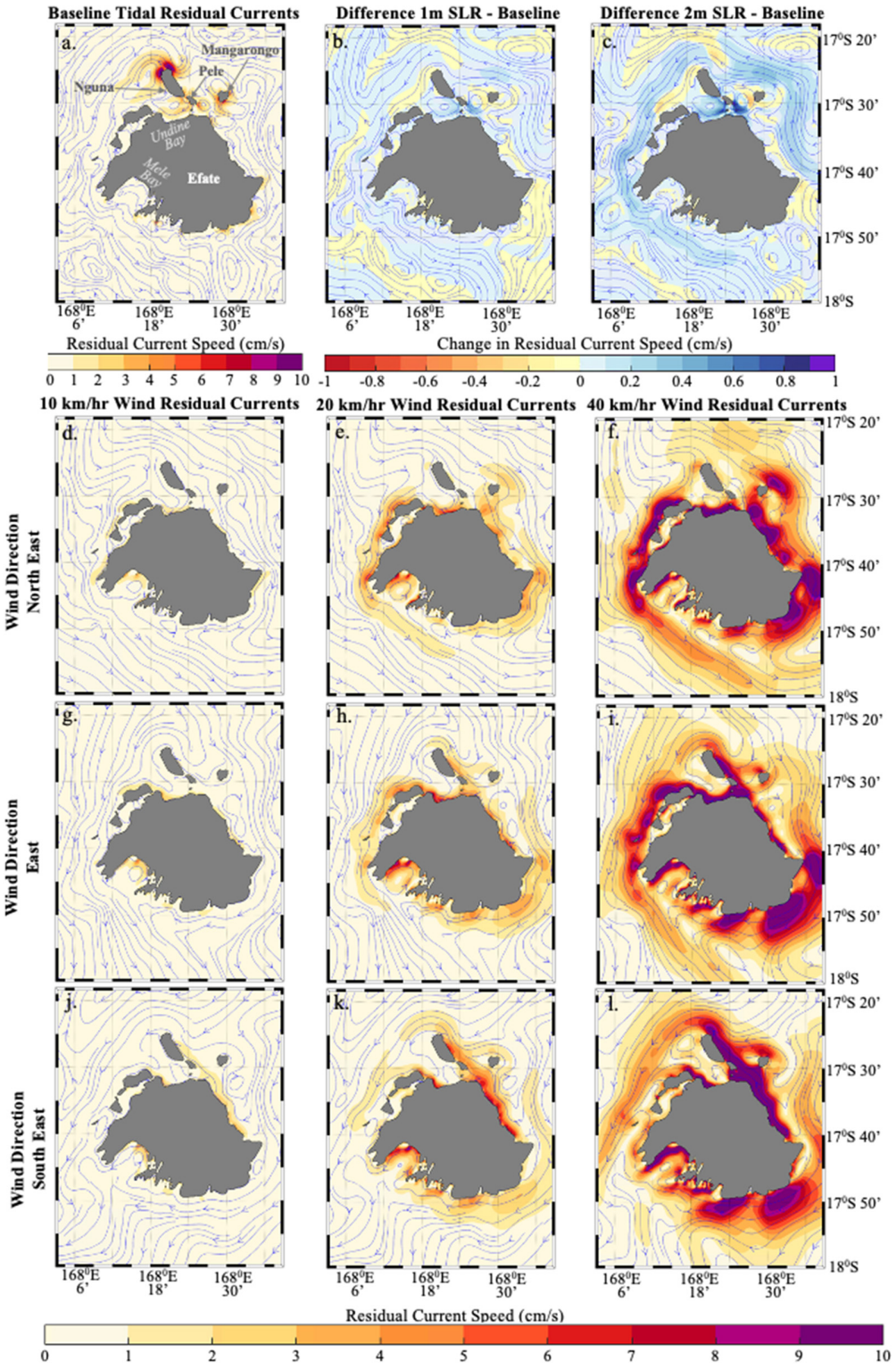

FIGURE 9 | Tidal residual current speeds, with current patterns indicated by streamlines, around Efate Island, Vanuatu **(a)**. Change in residual current speeds (cm/s) and patterns under 1 m SLR **(b)** and 2 m SLR **(c)**. Wind residual current speeds (cm/s) and patterns under 10 km/h **(d)**, 20 km/h **(e)**, and 40 km/h **(f)** northeast winds. Wind residual current speeds (cm/s) and patterns under 10 km/h **(g)**, 20 km/h **(h)**, and 40 km/h **(i)** east winds. Wind residual current speeds (cm/s) and patterns under 10 km/h **(j)**, 20 km/h **(k)**, and 40 km/h **(l)** southeast winds. Latitudes are displayed to the right of panels **(c,f,i,l)**. Longitude for all panels are displayed below panels **(a–c,j–l)**.

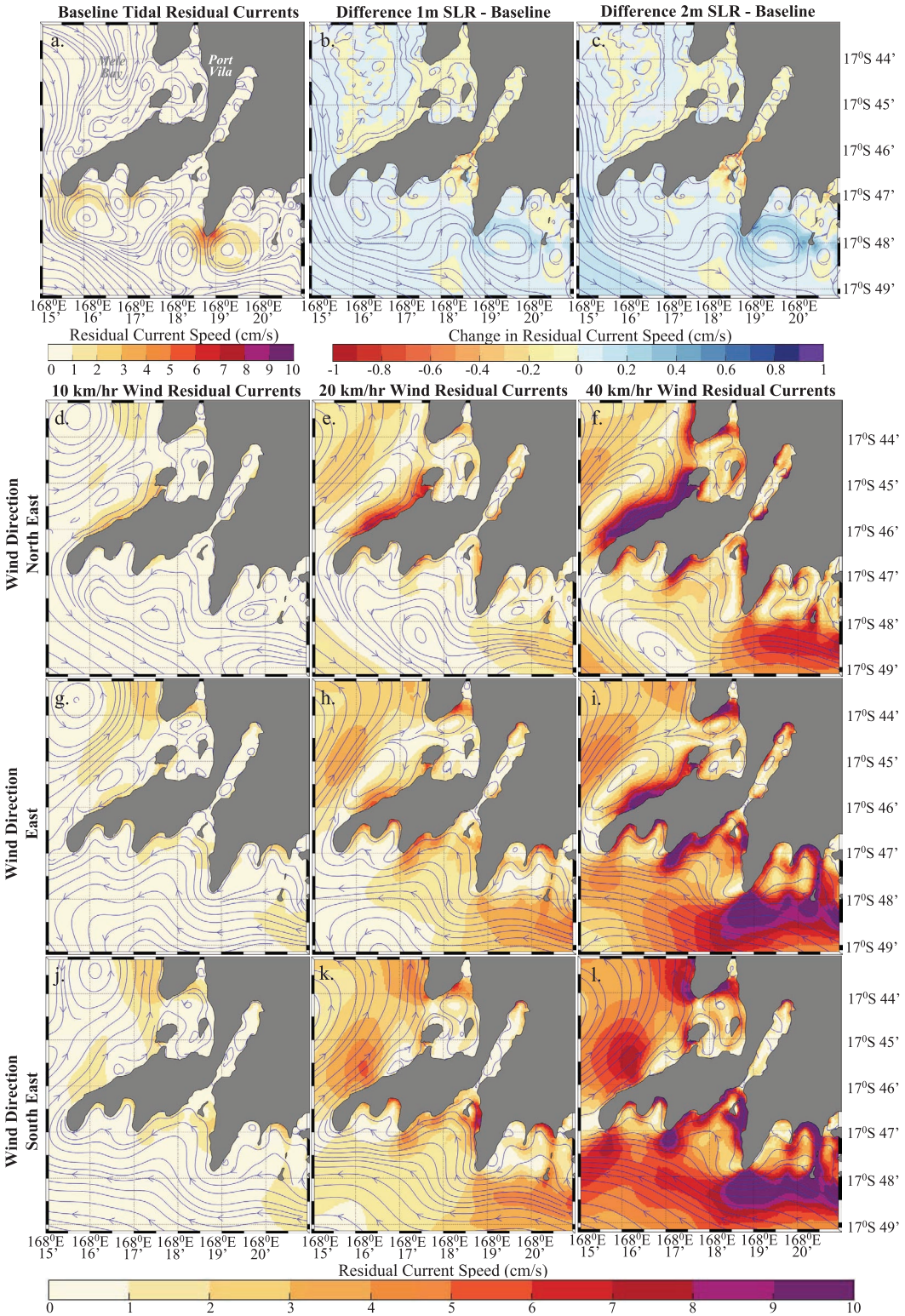

FIGURE 10 | Tidal residual current speeds, with current patterns indicated by streamlines, focussing on Erakor Lagoon, southwest Efate Island **(a)**. Change in residual current speeds (cm/s) and patterns under 1 m SLR **(b)** and 2 m SLR **(c)**. Wind residual current speeds (cm/s) and patterns under 10 km/h **(d)**, 20 km/h **(e)**, and 40 km/h **(f)** northeast winds. Wind residual current speeds (cm/s) and patterns under 10 km/h **(g)**, 20 km/h **(h)**, and 40 km/h **(i)** east winds. Wind residual current speeds (cm/s) and patterns under 10 km/h **(j)**, 20 km/h **(k)**, and 40 km/h **(l)** southeast winds. Latitudes are displayed to the right of panels **(c,f,i,l)**. Longitude for all panels are displayed below panels **(a–c,j–l)**.

side of the island, turning west in coastal waters north of Grande Terre, before flowing SW down the western side of the island. Within lagoon wates of southern Grande Terre, the north-westward flowing tidal residual currents along the eastern shoreline, reach speeds of up to 3.5 cm/s near the outer reef edge. Between the eastern outer reef and the shoreline, tidal residual current speeds range from 0.5 to 2 cm/s and follow a more meandering path, with an overall north-westerly flow (**Figure 8a**). In coastal waters of the Southern New Caledonia Lagoon, on the southwestern side of Grande Terre, tidal residual current speeds are most significant (up to ∼13 cm/s) near Ile Ouen, where cyclonic and anticyclone eddies form (**Figure 8a**). Within lagoon waters north of Ile Ouen, tidal residual current speeds are typically less than 2.5 cm/s, with the higher speeds occurring close to shore, near headlands and small islands. NE wind residual currents typically flowed SE, in line with currents in deep water adjacent to Grande Terre (**Figures 7d–f**, **8d–f**), however currents within lagoon waters on the western side were more meandering, compared to those on the east (**Figures 8d–f**). Under E and SE winds, coastal wind residual currents flowed NW within lagoon waters on both the eastern and western sides of Grande Terre. On the eastern side of Grande Terre, currents in deep water, beyond the lagoon, flowed SE. On the western side of Grande Terre, north-westward currents extended well beyond lagoon waters, before eventually turning south/southwest (for E/SE winds, respectively) a few hundred kilometres west of Grande Terre (**Figures 7g–l**, **8g–l**). Wind-residual current speeds increased in response to higher wind speeds for all three wind directions. The fastest residual current speeds were generated by winds blowing from the SE, followed by E, then NE. Residual current speeds under 40 km/h winds reached 56, 49, and 31 cm/s for SE, E, and NE winds, respectively.

In coastal waters of Efate Island, tidal residual circulation largely flows in an anticlockwise direction around the island. Fastest tidal residual currents are generated near headlands and islands, and appear strongest north of Efate Island in the vicinity of Nguna, Mangaronga, Pele, and Islands. Cyclonic and anticyclonic eddies form either side of Nguna Island, reaching speeds of up to 6 cm/s at the northern tip of Nguna Island (**Figure 9a**). A clockwise eddy is also generated within Undine Bay (**Figure 9a**). NE wind residual currents flow SE, splitting at Nguna Island, with currents continuing to flow S/SE on the eastern side of Efate, while west of Nguna Island currents flow south-west, parallel to the coastline, before turning southeast again at the western-most point of Efate Island, outside Mele Bay. Clockwise circulation occurs within Undine Bay, and anticyclonic circulation occurs within Mele Bay (**Figures 9d–f**). E wind residual currents flow S either side of Efate Island. Close to north Efate, the southerly flow is interrupted by the small islands, which cause the currents to flow westward, following the topography. At Nguna island currents flow SW, turning S/SE at the western tip of Efate. On the southern side of the island currents flowing down the eastern side of the island turn southwest, following the coastline, bending west before turning southeast just south of Mele Bay. Within Undine Bay, circulation is clockwise, and within Mele Bay circulation is anticlockwise (**Figures 9g–i**). SE wind residual currents flow SW around Efate, splitting to flow either side of the island north of Mangaronga Island. Within Undine Bay a smaller anticlockwise eddy forms west of Pele Island which interacts with flow generated in the wake of Nguna Island. Within Mele Bay, anticyclonic circulation persists (**Figures 9j–l**). Under all three wind directions, wind residual currents were typically strongest close to shore.

In the vicinity of Erakor Lagoon, Efate, the anticlockwise tidal residual currents circumnavigating Efate Island (shown in **Figure 9a**) interact with complex shoreline geometry, generating cyclonic and anticyclonic eddies either side of headlands and within embayments (**Figures 9a**, **10a**). Tidal residual current speeds largely fell between 0 and 2 cm/s inside embayments, exceeding 5 cm/s at the tips of headlands (**Figure 10a**). Being located on the southwestern side of Efate Island, the embayments shown in **Figure 10** do not experience the full force of winds from the NE, E, or SE, however winds from all three directions generated significant residual currents. Unlike tidal residual currents, wind residual currents were typically fastest along shorelines within embayments, rather than at the tips of headlands. Strong wind residual currents (>10 cm/s, under 40 km/h winds) also consistently flowed in waters just south of Erakor Lagoon (**Figures 10d–l**, east of 168° 18′ E, and south of 17° 48′ S) for all three wind directions.

Sea Level Rise Experiments

Tidal Constituents

Applying uniform sea level at the model open boundary resulted in negligible change in tidal constituent amplitudes and phases relative to baseline (0 m SLR) values. Both 1 and 2 m SLR scenario constituent amplitudes and phases altered by less than 1 mm and 0.2 degrees relative to baseline values across all eleven tide gauge locations. Pickering et al. (2017) investigated changing tidal constituent amplitudes and mean high water levels across the Pacific Basic under a 2 m SLR scenario, finding little change (±1 cm) in the Vanuatu/New Caledonia region.

Maximum Depth-Averaged Current Speeds

Whilst tidal amplitudes and phases were not impacted by 1–2 m SLR, maxDA_curSp diverged from baseline values in response to higher sea levels, with speeds mostly increasing with SLR (**Figures 3b,c**). The most significant changes are seen in coastal waters, and over remote reef/lagoon environments (**Figures 3b,c**).

Within lagoon waters surrounding southern Grande Terre, under 1 m SLR, maxDA_curSp increased by more than 20 cm/s inside Dumbea Bay, near Noumea (**Figure 4b**). Under 2 m SLR, areas where current speeds increased by 20 cm/s expanded (**Figure 4c**). MaxDA_curSp in outer sections of the Southern New Caledonia Lagoon, also showed a strong positive response to higher sea levels (green/blue areas, **Figures 4b,c**), increasing by 5–20 cm/s under 2 m SLR.

In waters surrounding Efate Island, changes were less significant than for Grande Terre, particularly for the 1m SLR scenario (**Figures 5b,c**). Changes in maxDA_curSp fell within ±10 cm/s of baseline conditions, and were mostly positive,

with the exception of two Efate locations where current speeds decreased under 1m SLR (red and orange areas **Figure 5b**).

Figure 6b displays a closer view of Erakor Lagoon on the south-western side of Efate, where maxDA_curSp were seen to reduce under 1 m SLR. Under 2 m SLR, the area within Erakor Lagoon, where current speeds reduced significantly decreased, and area where current speeds increased expanded. At this location the relationship between maxDA_curSp and SLR is non-linear.

Residual Currents

Increasing sea level by up to 2 m caused tidal residual current speeds to alter by between −0.5 and +1 cm/s over the majority of the model domain (**Figures 7b,c**). As with changes in maxDA_curSp, the highest degree of change (up to ±2.5 cm/s) occurred in coastal waters, within a few kilometres of island shorelines and remote open ocean reefs (**Figures 7b,c**, **8b,c**, **9b,c**, **10b,c**). Overall, tidal residual current patterns under 1 and 2 m SLR conditions are similar to those under present-day water levels. Within the lagoon waters of southern Grande Terre, changes in tidal residual currents showed a variable response, both with respect to speed and direction (**Figures 8b,c**). Around Efate Island, SLR largely enhanced the anticlockwise tidal residual circulation (**Figures 9b,c**). Within Erakor Lagoon, on the south-western side of Efate Island, tidal residual current speeds decreased in response to higher sea levels, whilst outside the lagoon, near headlands, eddy circulation was enhanced (**Figures 10b,c**).

DISCUSSION

Tide gauge observations at nine of the eleven locations are not quality controlled (Port Vila and Noumea are the two quality-controlled sites). Errors in tide gauge observations may contribute to differences between observed and model-predicted tidal water level time series, and tidal constituents. At Litzlitz water level time series are approximately 1 h out of phase (**Figure 2C**). Data from different years were used to perform tidal constituent analysis and subsequent observed tidal water level time series, however the temporal offset between model and observed tidal water level time series did not alter. When differences at this location where first identified during model runs using a preliminary iteration of the Van-Fvcom grid, it was thought that differences from observations at this location may be due to insufficient grid resolution. Improvements were made increasing the grid resolution from Grid resolution in this area was initially ∼500 m. In an effort to improve model representation of the coastal embayment containing the Litzlitz tidal gauge, grid resolution was increased to ∼350 m, which improved replication of tidal amplitudes (not shown), however phase differences between modelled and observed water levels did not significantly alter. Higher grid resolution (∼100 m) may be necessary at this location, however, such improvements must be accompanied by higher resolution (<100 m) bathymetry data, which at present is not available at this site. Alternatively human error converting from local time to GMT, may be responsible for model/observation phase differences at this location, as the tide gauge data is not quality controlled. Aside from these differences the model performs well and replicates tidal characteristics across the model domain. In the absence of observations, the tidal constituents determined from model predicted water levels may be used to generate tidal water level data at unmonitored coastal locations within the model domain. This information may assist shipping, since these islands are heavily reliant upon shipping for the transportation of goods, but some docks may be difficult to access during low tide due to the presence of barrier and fringing reefs.

While point current measurements are difficult to reproduce in the Van-Fvcom regional/coastal model due to the complexity of reef/lagoon bathymetry, the replication of previously modelled M2 tidal ellipse data, and close agreement at sites where coastline complexity is captured (CM2, Erakor lagoon) provide confidence the Van-Fvcom model adequately replicates overall tidal circulation in this complex region. Currents due to wind waves may contribute to the under-prediction of maximum current speeds at the CM1 site in Erakor Lagoon. The horizontal grid resolution, which is ∼80 m in this section of the grid, may also contribute to the lower current speeds predicted at this location. To this end, higher resolution, site specific coastal models are necessary to capture the full variability of coastal currents within these highly spatially variable reef/lagoon environments. With respect to the higher agreement achieved by the fixed-grid New Caledonia model (Douillet, 1998) relative to the Van-Fvcom model, factors which may contribute to the higher discrepancy are: the much larger Van-Fvcom model domain; the distant location of open boundary forcing; differences in methodologies employed to generate tidal forcing at the open boundary; lack of calibration with respect to currents; and the inclusion of variable wind forcing in the fixed-grid model, while the Van-Fvcom verification runs were forced solely by tidal processes. Results achieved by Van-Fvcom tidal simulations demonstrate that the model is an appropriate tool for investigating circulation at scales larger than ∼100 m. As higher resolution coastal bathymetry data become available and computational capacity increases, the accuracy with which future unstructured-mesh models covering the region are able to replicate current meter observations will likely improve. Despite the limitations discussed, given the overall strong performance of the Van-Fvcom model with respect to tidal characteristics, the regional/coastal model would prove extremely useful in providing boundary conditions to drive higher-resolution, site specific coastal process models.

Local wind forcing by weak to strong trade winds within the model domain do not significantly alter coastal water levels at tide gauge stations, however, coastal currents are sensitive to trade winds (**Figures 3–10**). The shape and orientation of islands with respect to wind direction strongly influenced the degree to which wind altered maximum current speeds in coastal waters (**Figures 3–6**). This is evident in the different responses seen for Efate compared with Grande Terre. Grande Terre, having an elongated shape (∼400 km long, ∼60 km wide),

oriented northwest/southeast, showed a reduced response to winds from the NE on both windward and leeward sides of the island, compared with winds from the E and SE (**Figures 4d–l**). While overall changes in maximum current speeds due to wind around Efate were less than those seen around Grande Terre, magnitudes were similar for the three wind directions (**Figures 5d–l**). This is a reflection of its smaller size and more circular shape (∼ 50 km long, ∼50 km wide). Differences in wind residual current patterns (**Figures 7–10**) further demonstrate the influence of island shape on coastal circulation. While Ekman flow is evident from residual circulation plots for all three wind directions, Ekman processes dominate residual circulation for NE wind events. Both the New Caledonia and Vanuatu archipelagos lie along a NW/SE orientation, which aligns with the direction of Ekman flow due to NE winds. As such, Ekman currents generated by NE winds experience less interruption by the topography, compared to Ekman currents generated by E and SE winds (**Figures 7d–f**). East winds generate southward Ekman currents, however, residual circulation patterns were more complex, likely due the higher degree of blocking along the N/S axis by islands. In relatively open water, between Vanuatu and New Caledonia, rather than flowing directly south, residual currents flowed SE, aligning with the orientation of both island chains and the deep Vanuatu trench (**Figures 7g–i**). Below Grande Terre, an irregular anticyclonic eddy forms which facilitates NW residual current flow in western Grande Terre coastal waters (**Figures 7g–i**, **8g–i**). West of 163°E, residual circulation is dominated by Ekman processes, flowing south (**Figures 7g–i**). South east winds generated SW flowing Ekman currents. Despite the Vanuatu islands lying perpendicular to the Ekman current flow, north of 17°S, residual circulation largely follows a SE path, showing little diversion due to blocking by islands (**Figures 7j–l**). Between Vanuatu and New Caledonia, below 17°S, residual currents bend to the SE, again aligning with the orientation of the Vanuatu Trench. On the western side of Grande Terre, an anticyclonic eddy forms which generates NW residual currents close to shore. West of 163°E, residual circulation is once more dominated by Ekman processes, flowing SE (**Figures 7j–l**). Under all three wind directions a series of large anticyclonic eddies form in the eastern half of the model domain, in deep ocean waters (**Figures 7d–l**). Here we attribute residual circulation to geostrophic currents set up in response to Ekman flow from winds with an easterly component, since all the eddies rotate in an anticlockwise direction. Geostrophic processes also likely contribute to the eddy which forms south of Grande Terre, since sea surface height anomalies correspond strongly with streamline shapes (**Supplementary Material 1**). Further experiments testing the effect of uniform bathymetry and presence/absence of islands would help explain these features more fully. With respect to coastal circulation, wind-residual current results shown in **Figures 8–10**, demonstrate the important role wind-driven circulation has on near-shore currents, and thus coastal processes.

Tidal constituents did not noticeably alter under higher sea level conditions. This contrasts with the findings of Devlin et al. (2017), at least at Port Vila, Vanuatu, where M2 and K1 amplitudes were reported to alter by 8.25 ±1.95, and −1.17 ± 0.5 cm per m SLR respectively. At Noumea change in M2 amplitude was not statistically significant, and change in K1 amplitude was 2.7 ± 1.01 cm per m SLR (Devlin et al., 2017). Despite changes in M2 and K1 constituents, change in HAT was not statistically significant at Vanuatu and New Caledonia locations (Devlin et al., 2017). The differences between our findings and those of Devlin et al. (2017) are likely due to the fact that our model experiments did not account for basin-scale changes in tidal characteristics in model forcing, which are likely to be evident in tidal gauge data. In a global tidal modelling study investigating the impact of SLR on tides, Pickering et al. (2017) found SLR of 1 and 2 m had relatively little effect on mean water levels in the New Caledonia/Vanuatu region. Under 2 m SLR, mean high water levels altered by ∼0 – 1 cm (Pickering et al., 2017). These results are similar to our findings. Taking these studies as a whole, results indicate that relative SLR is unlikely to be significantly affected by changing tidal characteristics under higher sea levels at Vanuatu and New Caledonia coastal locations. As tidal gauge and satellite altimetry records extend in time, a clearer picture with respect to changing tidal behaviour in this region will be obtained.

While future tidal amplitudes and phases did not alter, analysis of maximum and residual currents under SLR show changes in coastal currents should be taken into account when investigating how coastal environments will alter in the future. Changes in maximum depth-averaged currents speeds were greatest under 2 m SLR conditions, and the spatial distribution of areas that experienced the greatest change differed from those due to wind (**Figures 3b,c**, **4b,c**, **5b,c, 6b,c**). Within the Southern New Caledonia Lagoon, the largest changes correspond to upper embayments and shallower sections within the lagoon (purple shaded areas **Figures 4b,c**). In coastal waters of Efate, the two locations which showed a reduction in maximum depth-averaged current speed due to SLR, correspond to shallow fringing reef environments (yellow/orange shaded areas **Figures 5b,c**, **6b,c**). The reduction at these sites is likely due to water depths increasing by approximately an order of magnitude under 1m SLR (e.g., from ∼0.1 m at low tide to ∼1.1 m at low tide under 1 m SLR), resulting in lower depth-averaged current speeds. In shallow water (∼<3 m) dissipation of tidal energy appears to exceed potential increases in tidal energy associated with the increase in tidal prism due to 1m SLR. Within Erakor Lagoon, under 2 m SLR water depth over the majority of the reef platforms exceeds 3 m, and increased tidal energy due to the larger tidal prism appears to dominate reduction in tidal energy due to dissipation in shallow water (<3 m), leading to predominantly positive changes in maxDA_curSp in Erakor Lagoon (**Figure 6c**). The results in Erakor Lagoon indicate that the representation of the reef is very important when determining the impact changing sea levels will have on coastal processes in fringing reef locations. Significant changes in current speeds alter coastal processes including sediment transport regimes, tidal flushing rates, pollutant dispersal and larval transport. Further analysis is needed to determine how model depth settings over reef environments may alter response to SLR at other coastal locations within our model domain, to

better understand the variety of responses different locations will experience in the future. While the magnitude of change in residual current speeds due to SLR is small relative to those seen due to wind conditions, these small changes still have the potential to influence sediment transport erosion and deposition patterns, due to the sustained nature of tide-generated residual currents.

In the scenarios tested, it was assumed that the underlying morphology would remain unchanged. In the context of Vanuatu and New Caledonia, this includes the assumption that the shape and height of coral reefs will not alter between present-day and 2100. Given the tectonic activity present in this region, coupled with the rapid development of some coastal sites, and lack of data regarding reef growth/damage, this assumption is limited. Nevertheless, results presented provide important insights which may assist future modelling efforts exploring impacts associated with changing sea levels in this region.

Interannual and interdecadal sea level variability is of the order ±0.1 m in the Western South Pacific Ocean, and is determined by large-scale ocean dynamics (Kumar et al., 2018). As such, changes in current speeds and residual circulation caused by interannual sea level variability are likely to be relatively small, given the limited response seen under +1 m SLR (**Figures 3b**, **10b**). Sites likely to be most sensitive to sea level variations due to regional circulation are shallow reef platforms near narrow deeper channels, as well as coastal embayments where higher water levels act to alter the tidal prism. The effect baroclinic processes and the transfer of kinetic energy associated with the jets and boundary currents, have on coastal circulation in lagoons and embayments is presently unknown. The role these processes play in island coastal waters will be the focus of future modelling studies employing the Van-Fvcom model, in an effort to better understand how regional ocean processes affect coastal processes in remote island locations.

CONCLUSION

The model setup employed in this study adequately replicated tidal characteristics at coastal sites across the region and is an appropriate tool for predicting tidal behaviour at unmonitored coastal locations within the model domain. While point current meter data were difficult to replicate within spatially variable reef/lagoon environments, overall current patterns match those of previous studies.

Coastal waters and waters between closely spaced islands were most sensitive to changes in current speeds and residual current patterns associated with changes in wind speed and direction, and due to changes in sea level. Within reef/lagoon systems the largest changes in maximum depth-averaged current speeds due to wind corresponded with shallower sections of the waterways.

Wind-residual current speeds were sensitive to changes in wind speed. Strong winds (up to 40 km/h) generated coastal residual currents whose magnitudes were significantly larger (up to an order of magnitude) than those associated with tidal-residual currents. Wind-residual current patterns depended upon wind direction, with circulating patterns showing little alteration due to changing wind speed. Wind residual circulation appears to be influenced by Ekman processes, geostrophic currents, and topographic steering, with the influence of each process varying across the region. Future simulations will employ spatially and temporally varying wind fields to determine how realistic wind-residual current patterns and magnitudes vary from those due to the uniform wind fields employed in this study.

Sea level rise of up to 2 m SLR did not significantly alter tidal amplitudes and phases at Vanuatu and New Caledonia coastal sites. Changes in maximum current speeds due to SLR were sensitive to the presence of reef platforms. For reef platforms that were exposed, or close to becoming exposed at low tide under 0 m SLR, response to SLR was non-linear. Sections of reef platforms experienced reduced current speeds under 1m SLR and increasing current speeds under 2 m SLR. The sensitivity of modelled currents within reef/lagoon systems to the assumptions made regarding reef bathymetry require further research, and comprehensive sensitivity studies are necessary to accurately predict how SLR will alter coastal processes in these environments.

Tidal-residual current patterns were little altered by changes in sea level and changes in tidal-residual current speeds ranged from 0 and ±2.5 cm/s. Model results demonstrate that coastal circulation was more sensitive to changes in wind than changes in sea level. Given the sustained nature of tidal processes, when compared with the variability of wind, the impact of higher sea levels on maximum current speeds and residual circulation still needs to be taken into consideration when investigating the impact climate change will have on island coastal communities and ecosystems.

Given the important role regional circulation processes play in the SW Pacific region, it is vital to investigate exchange processes between oceanic and lagoon waters. While preliminary, the modelling experiments undertaken in this study demonstrate the potential value of using unstructured-mesh finite volume modelling approaches to investigate circulation in geometrically complex environments covering large regions. Further this study justifies the future use of the Van-Fvcom model to investigate more complex ocean processes in remote island regions. While this paper addresses circulation, future coastal/ocean modelling studies will need to examine the influence of regional ocean circulation, nutrient, pollutant and fishery distribution patterns, and their impacts on existing systems and communities, to better understand the full range of impacts associated with changing climate.

DATA AVAILABILITY STATEMENT

Model outputs generated during the current study are available from the corresponding author upon reasonable request, with permission of the Director of the Griffith Climate Action Beacon.

AUTHOR CONTRIBUTIONS

SL, CL, and RT contributed to conception and design of the study. SL constructed the model upon which the study is based and FZ assisted identify and rectify errors in model setup and input files. SL analysed model results with assistance from FZ who provided expertise with respect to tidal analysis. SL wrote the first draft of the manuscript. All authors contributed to manuscript revision, read, and approved the submitted version.

FUNDING

This research was supported by a grant from a private charitable trust.

ACKNOWLEDGMENTS

This research was undertaken with the assistance of resources and services from the National Computational Infrastructure (NCI), which is supported by the Australian Government, through support from the Queensland Cyber Infrastructure Foundation (QCIF). Many thanks to Andrew Ross and Jianhua Qi for patiently answering all queries relating to FVCOM. Thanks to John Luick for providing assistance applying phase corrections for tidal constituent data used to force the FVCOM model. We wish to acknowledge the Vanuatu Meteorology and Geo-Hazards Department and the UK Hydrographic Office for the provision of bathymetry data. This research was undertaken through an MOU with the Tafea Provincial Government and under a research agreement with the Vanuatu National Cultural Centre representing the Government of the Republic of Vanuatu and the local community.

SUPPLEMENTARY MATERIAL

The Supplementary Material for this article can be found online at: https://www.frontiersin.org/articles/10.3389/fmars.2021.697741/full#supplementary-material

Supplementary Material 1 | Plots to illustrate the potential influence of geostrophic currents **(a)** and topographic steering and island blocking **(b)** on wind-residual current patterns. Sea surface height anomaly **(a)** reflects the mean value calculated over the same timeframe used to calculate wind residual currents. Latitudes are shown to the left of panels with longitude displayed below.

REFERENCES

Andrew, N. L., Bright, P., de la Rua, L., Teoh, S. J., and Vickers, M. (2019). Coastal proximity of populations in 22 Pacific island countries and Territories. *PLoS One* 14:e0223249.

Caldwelal, P. C., Merrifield, M. A., and Thompson, P. R. (2015). *Sea Level Measured by Tide Gauges from Global Oceans — the Joint Archive for Sea Level holdings (NCEI Accession 0019568), Version 5.5*.

Chen, C., Beardsley, R., and Cowles, G. (2006). An unstructured-grid Finite-Volume Coastal Ocean Model (FVCOM) system. *Oceanography* 19, 78–89. doi: 10.5670/oceanog.2006.92

Church, J. A., Clark, P. U., Cazenave, A., Gregory, J. M., Jevrejeva, S., and Levermann, A. (2013). "Sea level change," in *Climate Change 2013: the Physical Science Basis. Contribution of Working Group I to the Fifth Assessment Report of the Intergovernmental Panel on Climate Change*, eds T. F. Stocker, D. Qin, and G.-K. Plattner (Cambridge: Cambridge University Press).

Codiga, D. L. (2011). *Unified Tidal Analysis and Prediction Using the UTide Matlab Functions*. Technical Report 2011-01. Narragansett, RI: University of Rhode Island. TechnicalReport201101.

Cravatte, S., Kestenare, E., Eldin, G., Ganachaud, A., Lefèvre, J., Marin, F., et al. (2015). Regional circulation around New Caledonia from two decades of observations. *J. Mar. Syst.* 148, 249–271. doi: 10.1016/j.jmarsys.2015.03.004

David, G. (2016). "The challenge of sustainability for Pacific Island village fisheries, a historical perspective," in *Fisheries in the Pacific: the Challenges of Governance and Sustainability*, [online] (Marseille: Pacific-credo Publications). doi: 10.4000/books.pacific.446 ISBN: 9782956398165.

Devlin, A. T., Jay, D. A., Zaron, E. D., Talke, S. A., Pan, J., and Lin, H. (2017). Tidal variability related to sea level variability in the Pacific Ocean. *J. Geophys. Res. Oceans* 122, 8445–8463. doi: 10.1002/2017JC013165

Douillet, P. (1998). Tidal dynamics of the south-west lagoon of New Caledonia: observations and 2D numerical modelling. *Oceanologica Acta* 21, 69–79. doi: 10.1016/S0399-1784(98)80050-9

Douillet, P., Ouillon, S., and Cordier, E. (2001). A numerical model for fine suspended sediment transport in the south-west lagoon of New-Caledonia. *Coral Reefs* 20, 361–372. doi: 10.1007/s00338-001-0193-6

Dayan, H., Le Cozannet, G., Speich, S., and Thiéblemont, R., (2021). High-End scenarios of sea-level rise for coastal risk-averse stakeholders. *Front. Mar. Sci.* 8:569992. doi: 10.3389/fmars.2021.569992

Egbert, G., and Erofeeva, S. (2002). Efficient inverse modeling of barotropic ocean tides. *J. Atmos. Oceanic Technol.* 19, 183–204. doi: 10.1175/1520-0426(2002)019<0183:EIMOBO>2.0.CO;2

Faivre, G., Vieira da Silva, G., Aimbie, J., Ware, D., Tomlinson, R., Mackey, B., et al. (2020). "Coastal processes within a coral reef lagoon system: Erakor lagoon, Efate Island, Vanuatu," in *Global Coastal Issues of 2020*, eds G. Malvárez and F. Navas (Florida: Coconut Creek).

Flanders Marine Institute (VLIZ) and Intergovernmental Oceanographic Commission (IOC) (2021). *Sea Level Station Monitoring Facility*. Available online at: http://www.ioc-sealevelmonitoring.org (accessed August 16, 2021). doi: 10.14284/482

Ganachaud, A., Cravatte, S., Melet, A., Schiller, A., Holbrook, N. J., Slyon, B. M., et al. (2014). The Southwest Pacific Ocean circulation and climate experiment (SPICE). *J. Geophys. Res. Oceans* 119, 7660–7686. doi: 10.1002/2013JC009678

GEBCO Compilation Group (2020). *GEBCO 2020 Grid*. Liverpool: British Oceanographic Data Centre.

Hamlington, B. D., Frederikse, T., Nerem, R. S., Fasullo, J. T., and Adhikari, S. (2020). Investigating the acceleration of regional sea level rise during the satellite altimeter era. *Geophys. Res. Lett.* 47:e2019GL086528.

Hénin, C., and Cresswell, G. R. (2005). Upwelling along the western barrier reef of New Caledonia. *Mar. Freshw. Res.* 56, 1005–1010. doi: 10.1071/MF04266

Hermans, T. H. J., Gregory, J. M., Palmer, M. D., Ringer, M. A., Katsman, C. A., and Slangen, A. B. A. (2021). Projecting global mean sea-level change using CMIP6 models. *Geophys. Res. Lett.* 48:e2020GL092064.

IMaRS-USF and Institut de Recherche pour le Developpement (IRD) (2005). *Millennium Coral Reef Mapping Project. Validated Maps*. Cambridge: UNEP World Conservation Monitoring Centre.

Institute for Marine Remote Sensing-University of South Florida (IMaRS-USF). (2005). *Millennium Coral Reef Mapping Project. Unvalidated Maps. these Maps are Unendorsed by IRD, but Were Further Interpreted by UNEP World Conservation Monitoring Centre*. Cambridge: UNEP World Conservation Monitoring Centre.

Jevrejeva, S., Frederikse, T., Kopp, R. E., Le Cozannet, G., Jackson, L. P., and van de Wal, E. S. W. (2019). Probabilistic sea level projections at the coast by 2100. *Surv. Geophys.* 40, 1673–1696. doi: 10.1007/s10712-019-09550-y

Kumar, V., Melet, A., Meyssignac, B., Ganachaud, A., Kessler, W. S., Singh, A., et al. (2018). Reconstruction of local sea levels at South West Pacific Islands - a multiple linear regression approach (1988–2014). *J. Geophys. Res. Oceans* 123, 1502–1518. doi: 10.1002/2017JC013053

Marchesiello, P., Lefèvre, J., Vega, A., Couvelard, X., and Menkes, C. (2010). Coastal upwelling, circulation and heat balance around New Caledonia's barrier reef. *Mar. Pollut. Bull.* 61, 432–448. doi: 10.1016/j.marpolbul.2010.06.043

Nishijima, K., Mori, N., Yasuda, T., Shimura, T., Gogon, J. T., Gibson, D., et al. (2015). *DPRI-VMGD Joint Survey for Cyclone Pam Damages*. Available Online at: http://www.taifu.dpri.kyoto-u.ac.jp/wp-content/uploads/2015/05/DPRI-VMGD-survey-first-report-Final.pdf (aaccessed October 20, 2015).

Pelling, H. E., and Green, J. A. M. (2013). Sea leve rise and tidal power plants in the Gulf of Maine. *J. Geophys. Res. Oceans* 118, 2863–2873. doi: 10.1002/jgrc.20221

Pickering, M. D., Horsburgh, K. J., Blundell, J. R., Hirschi, J. J.-M., Nicholls, R. J., Verlaan, M., et al. (2017). The impact of future sea-level rise on the global tides. *Cont. Shelf Res.* 142, 50–68. doi: 10.1016/j.csr.2017.02.004

Robinson, I. S. (1983). "Chapter 7 tidally induced residual flows," in *Elsevier Oceanography Series*, ed. B. Johns (Amsterdam: Elsevier).

Signell, R. P., and Geyer, R. (1991). Transient eddy formation around headlands. *J. Geophys. Res.* 96, 2561–2575. doi: 10.1029/90JC02029

Spalding, M. D., Ravilious, C., and Green, E. P. (2001). *World Atlas of Coral Reefs*. Berkeley, CA: The University of California Press.

UNEP-WCMC, WorldFish Centre, WRI, and TNC (2010). *Global Distribution of Warm-Water Coral Reefs, Compiled from Multiple Sources (listed in "Coral_Source.mdb"), and Including IMaRS-USF and IRD (2005), IMaRS-USF (2005) and Spalding et al. (2001)*. Cambridge: UNEP World Conservation Monitoring Centre.

WCRP Global Sea Level Budget Group (2018). Global sea-level budget 1993–present. *Earth Syst. Sci. Data* 10, 1551–159018. doi: 10.5194/essd-10-1551-2018

Wessel, P., and Smith, W. H. F. (1996). A global, self-consistent, hierarchical, high-resolution shoreline database. *J. Geophys. Res.* 101, 8741–8743. doi: 10.1029/96JB00104

Yi, S., Heki, K., and Qian, A. (2017). Acceleration in the global mean sea level rise: 2005–2015. *Geophys. Res. Lett.* 44, 11,905–11,913. doi: 10.1002/2017GL076129

Conflict of Interest: The authors declare that the research was conducted in the absence of any commercial or financial relationships that could be construed as a potential conflict of interest.

Publisher's Note: All claims expressed in this article are solely those of the authors and do not necessarily represent those of their affiliated organizations, or those of the publisher, the editors and the reviewers. Any product that may be evaluated in this article, or claim that may be made by its manufacturer, is not guaranteed or endorsed by the publisher.

frontiers in Marine Science

ORIGINAL RESEARCH
published: 06 January 2022
doi: 10.3389/fmars.2021.749638

Impact of Flash Flood Events on the Coastal Waters Around Madeira Island: The "Land Mass Effect"

Alexandra Rosa[1], Cláudio Cardoso[1,2], Rui Vieira[1], Ricardo Faria[1], Ana R. Oliveira[3], Gabriel Navarro[4] and Rui M. A. Caldeira[1,2]*

[1] Observatório Oceânico da Madeira, Agência Regional para o Desenvolvimento da Investigação, Tecnologia e Inovação, Funchal, Portugal, [2] Instituto Dom Luiz, Faculdade de Ciências, Universidade de Lisboa, Lisbon, Portugal, [3] Centro de Ciência e Tecnologia do Ambiente e do Mar (MARETEC-LARSyS), Instituto Superior Técnico, Universidade de Lisboa, Lisbon, Portugal, [4] Grupo de Ecología y Gestión Costera, Instituto de Ciencias Marinas de Andalucía, Consejo Superior de Investigaciones Científicas, Puerto Real, Spain

The Island Mass Effect has been primarily attributed to nutrient enhancement of waters surrounding oceanic islands due to physical processes, whereas the role of land runoff has seldom been considered. Land runoff can be particularly relevant in mountainous islands, highly susceptible to torrential rainfall that rapidly leads to flash floods. Madeira Island, located in the Northeast Atlantic Ocean, is historically known for its flash flood events, when steep streams transport high volumes of water and terrigenous material downstream. A 22-year analysis of satellite data revealed that a recent catastrophic flash flood (20 February 2010) was responsible for the most significant concentration of non-algal Suspended Particulate Matter (SPM) and Chlorophyll-a at the coast. In this context, our study aims to understand the impact of the February 2010 flash flood events on coastal waters, by assessing the impact of spatial and temporal variability of wind, precipitation, and river discharges. Two specific flash floods events are investigated in detail (2 and 20 February 2010), which coincided with northeasterly and southwesterly winds, respectively. Given the lack of *in situ* data documenting these events, a coupled air-sea-land numerical framework was used, including hydrological modeling. The dynamics of the modeled river plumes induced by flash floods were strongly influenced by the wind regimes subsequently affecting coastal circulation, which may help to explain the differences between observed SPM and Chlorophyll-a distributions. Model simulations showed that during northeasterly winds, coastal confinement of the buoyant river plume persisted on the island's north coast, preventing offshore transport of SPM. This mechanism may have contributed to favorable conditions for phytoplankton growth, as captured by satellite-derived Chlorophyll-a in the northeastern coastal waters. On the island's south coast, strong ocean currents generated in the eastern island flank promoted strong vertical shear, contributing to vertical mixing. During southwesterly winds, coastal confinement of the plume with strong vertical density gradient was observed on the south side. The switch to eastward winds spread the south river plume offshore, forming a filament of high Chlorophyll-a extending 70 km offshore. Our framework demonstrates a novel methodology to investigate ocean productivity around remote islands with sparse or absent field observations.

Keywords: oceanic island, Island Mass Effect, extreme precipitation, flash floods, small mountainous rivers, river plumes dynamics, coupled numerical modeling, hydrological modeling

OPEN ACCESS

Edited by:
Yang Yang,
Nanjing Normal University, China

Reviewed by:
Rui Salgado,
Universidade de Évora, Portugal
Alfredo L. Aretxabaleta,
United States Geological Survey (USGS), United States
Serena Blyth Lee,
Griffith University, Australia

****Correspondence:***
Alexandra Rosa
alexandra.rosa@oom.arditi.pt

Specialty section:
This article was submitted to Coastal Ocean Processes, a section of the journal Frontiers in Marine Science

Received: *29 July 2021*
Accepted: *03 December 2021*
Published: *06 January 2022*

Citation:
Rosa A, Cardoso C, Vieira R, Faria R, Oliveira AR, Navarro G and Caldeira RMA (2022) Impact of Flash Flood Events on the Coastal Waters Around Madeira Island: The "Land Mass Effect". Front. Mar. Sci. 8:749638. doi: 10.3389/fmars.2021.749638

INTRODUCTION

Deep ocean islands are often characterized by pristine and remote ecosystems that support important socio-economic activities and provide resilience to local communities. From an ecological point of view, oceanic islands are characterized as biodiversity hotspots. This biological enhancement is strongly associated with the interaction of the wind and ocean currents with the islands, which can induce physical perturbations in the atmospheric and oceanic flows and ultimately boost phytoplankton growth in the surrounding environment. This concept is coined in the literature as the Island Mass Effect (IME). IME was first introduced by Doty and Oguri (1956) to explain the consistent increase of primary productivity on the windward waters of Oahu Island in the Hawaiian Archipelago, relative to offshore waters. Since then, this phenomenon has been intensively investigated and detected in several island-reef ecosystems around the world. In the South Pacific, IME processes were investigated by Jones (1962), Dandonneau and Charpy (1985), Signorini et al. (1999), Martinez and Maamaatuaiahutapu (2004), Andrade et al. (2014), Raapoto et al. (2018, 2019), Cassianides et al. (2020), James et al. (2020), and Messié et al. (2020). In the North Pacific, IME was investigated in the vicinity of the Kuroshio current (Hasegawa et al., 2004; Hasegawa, 2019) and within the Southern California Bight (Caldeira et al., 2005). In the Equatorial Pacific, IME was investigated around the Galápagos Archipelago (Palacios, 2002). In the Indian, IME was studied around the Prince Edward Islands (Perissinotto et al., 2000). IME processes in the North Atlantic Ocean were investigated around Gran Canaria Island (Arístegui et al., 1997) and Madeira Island (Caldeira et al., 2002). Island-induced physical processes, such as the formation of wakes, eddies, internal waves, fronts, and upwelling cells, are some of the features linked to the IME (Leichter et al., 1998, 2003; Signorini et al., 1999; Caldeira et al., 2002; Palacios, 2002; Hasegawa et al., 2004; Hasegawa, 2019). These processes are responsible for the increase of nutrients and consequent enhancement of the primary productivity in the vicinity of oceanic islands, supporting the upper trophic levels and, as a consequence, the distribution of fishing activities in these areas (Chassot et al., 2010; Gove et al., 2016).

Notwithstanding the current IME studies, the processes that occur at the land-sea boundary have been less addressed in the scientific literature. The processes include the role of benthic mechanisms, such as accumulation of inorganic nutrients by benthic algae and further nutrients remineralization (Doty and Oguri, 1956) and nutrient-enrich waters associated with hydrothermal fluxes (Signorini et al., 1999). The input of nutrients from submarine groundwater discharges (Street et al., 2008; Tait et al., 2014; Moosdorf et al., 2015) and from island surface runoff (Dandonneau and Charpy, 1985; Bell, 1992; Perissinotto et al., 2000; Messié et al., 2020) have also been demonstrated to contribute to IME. Island surface runoff is particularly important in mountainous islands. With rugged relief and complex river networks flowing through narrow and steep valleys, these islands are naturally vulnerable to extreme precipitation events and consequent torrential and rapid streamflow. During such events, flow in these small rivers—characterized by relatively small watersheds and a low baseflow (Kao and Milliman, 2008; Osadchiev and Korshenko, 2017)—drastically increases. As a consequence, high runoff events often transport large amounts of terrigenous sediments/nutrients (Milliman and Syvitski, 1992; Liu et al., 2013; Wang et al., 2020) and solid material (e.g., mud, rocks, blocks, wreckage) to the coastal environment, often leading to floods (Vieira et al., 2018). Such torrential discharge often generates buoyant river plumes that are easily identified by the high levels of suspended matter that spread from river mouths and mix with the surrounding oceanic waters. According to Osadchiev and Zavialov (2020), the formation, mixing, and spreading of buoyant river plumes depends on several factors that may be divided into two groups: (i) site characteristics, such as the geometry of the coastline and river mouths, bathymetry, and latitude-dependent Coriolis force (Chao and Boicourt, 1986; Simpson, 1997; Garvine, 1999; Horner-Devine et al., 2006, 2015; McCabe et al., 2009; Warrick and Farnsworth, 2017); and (ii) external forcing mechanisms, such as river flow, wind, coastal currents, tides, waves, and water column stratification (Fong and Geyer, 2001, 2002; Yankovsky et al., 2001; Wu et al., 2011; Korotenko et al., 2014; Osadchiev, 2018; Yuan et al., 2018; Zhao et al., 2018; Marta-Almeida et al., 2020). Thus, the land-sea discharges of freshwater, terrigenous sediments, nutrients, suspended matter, and anthropogenic contaminants or pollutants affect the physical, chemical, biological, and geological processes in the coastal environment (Milliman and Syvitski, 1992; Meybeck et al., 2003; Brodie et al., 2010; Hilton et al., 2011; Bao et al., 2015; Osadchiev et al., 2017; Warrick and Farnsworth, 2017; Osadchiev, 2018; Osadchiev and Zavialov, 2020).

In Madeira, a mountainous island located in the Northeast Atlantic Ocean, the frequent occurrence of flash flood events currently represents the most significant natural hazard (Fragoso et al., 2012; Vieira et al., 2018). The most recent catastrophic flash flood event occurred on 20 February 2010, causing numerous human casualties and substantial economic loss (∼1.4 billion euros; Baioni, 2011; Fragoso et al., 2012), mainly in the capital city, Funchal, located in the southern region. Several scientific studies addressed this specific event (Luna et al., 2011; Couto et al., 2012; Fragoso et al., 2012; Levizzani et al., 2013; Lira et al., 2013; Nguyen et al., 2013; Teixeira et al., 2014; Dasari and Salgado, 2015; Lopes et al., 2020). In simple terms, the 20 February flash flood event was caused by a large-scale atmospheric phenomenon associated with a southwesterly front embedded in a low-pressure system over the Azores Archipelago, intensified by an anomalous sea surface temperature gradient across the Atlantic Ocean (Luna et al., 2011; Fragoso et al., 2012). On 20 February, an atmospheric river extending the entire length of the North Atlantic Ocean is also responsible for the increased humidity in the lower atmospheric levels (Couto et al., 2012). As this frontal weather system passed over the island from the southwest, the orographic uplift associated with the island led to heavy precipitation (Luna et al., 2011; Couto et al., 2012; Fragoso et al., 2012; Levizzani et al., 2013). Considering that atmospheric rivers are linked to extreme precipitation events in Madeira (Couto et al., 2015; Ramos et al., 2018a) and that the frequency

of these phenomena is expected to increase due to climate change (Ramos et al., 2016), extreme precipitation and flooding events are expected to become an important contributor to the local coastal waters. In addition to the persistent high rainfall during the preceding winter months, an intense precipitation event on 2 February 2010 resulted in saturation of the soil which prevented further infiltration, and accelerated surface runoff and subsequent river flow, ultimately causing flash floods downstream (Fragoso et al., 2012; Nguyen et al., 2013). The 2 February event was caused by a low-pressure system centered between Madeira and Canary Islands, but atmospheric rivers were not detected (Couto et al., 2012). Besides the studies that focused on the meteorological (Luna et al., 2011; Couto et al., 2012; Fragoso et al., 2012; Levizzani et al., 2013; Teixeira et al., 2014; Dasari and Salgado, 2015) and geomorphological (Lira et al., 2013; Nguyen et al., 2013; Lopes et al., 2020) aspects of these events, the impacts of the extreme discharges of freshwater and land-based material into the coastal area are undocumented.

A long-term analysis (22 years) of monthly-averaged satellite-based measurements of the sea surface (non-algal) Suspended Particulate Matter (SPM) and Chlorophyll-a (Chla) concentrations highlight the potential impact these high discharge events have on coastal marine waters, in which maximum SPM (1.2 g m^{-3}) and Chla (0.5 mg m^{-3}) concentrations occur concurrently with the February 2010 floods (**Figures 1A,B**). This is further supported by the significantly higher values of monthly-averaged SPM (>2 g m^{-3}) and Chla (1 mg m^{-3}) near the coast (**Figures 1C,D**, respectively). Typical concentrations reported around the island are characteristic of an oligotrophic marine ecosystem with nutrient-poor waters and low Chla concentrations (average of 0.15 mg m^{-3}, red line in **Figure 1B**; Longhurst et al., 1995; Caldeira et al., 2002; Narciso et al., 2019; Schäfer et al., 2020). A past study focused on the IME around Madeira Island hypothesized upwelling as the main mechanism responsible for high Chla concentrations, while island runoff and river discharges were considered to have a weak contribution (Caldeira et al., 2002). However, the long-term analysis indicates that episodes of enhanced SPM and Chla concentrations related to island runoff are likely frequent, as shown by the concurrent trends in SPM and Chla with precipitation values (identified by black arrows in **Figure 1B**).

This study aims to investigate the impact of two different flash flood events (on the 2nd and 20th of February 2010) on the coastal waters around Madeira Island, focusing on the spatial and temporal variability of the forcing mechanisms (i.e., wind, precipitation, and river discharges). In the absence of field observations capturing these two events, a numerical framework coupling the air-sea-land interfaces was used to theoretically investigate how the dynamics of the plumes might influence coastal circulation and help to explain the different SPM and Chla concentration distributions observed in the days after the flash flood events (**Figure 2**).

The manuscript is organized as follows: section "Study Area" is dedicated to the description of the study area. Section "Data and Methods" describes (i) the observational datasets used for model validation, (ii) the numerical models, their implementation, and the atmospheric model validation, and (iii) the kinematic parameters calculated to investigate the stratification and mixing of the water column. The results focused on the temporal variability of the forcing mechanisms and its impact on the coastal waters around Madeira Island are presented and discussed in section "Results and Discussion." Lastly, the main conclusions are summarized in section "Conclusion".

STUDY AREA

Madeira Island is in the Northeast Atlantic Ocean 750 km west of the Northwestern African coast and 850 km southwest of Portugal (**Figure 3A**). Madeira is the largest and most populated island (∼260,000 inhabitants) of the Archipelago, with an area of 741 km^2 and 1,861 m maximum altitude. Porto Santo Island (45 km to the northeast) is also populated (∼5,000 inhabitants). In contrast, the islands and small islets that constitute the Desertas Islands (20 km to the southeast; **Figure 3B**) and Selvagens Islands (300 km to the south; not shown) are uninhabited natural reserves. Madeira Island supports diverse socio-economic activities, such as fishing, aquaculture, agriculture, and tourism—the most important economic sector (hosting over one million visitors per year; Vieira et al., 2018). From a biodiversity viewpoint, the archipelago is recognized for its marine biodiversity, with several marine reserves and Natural Parks as part of the Natura 2000 network and UNESCO world heritage area.

Madeira is approximately 58 km in length, oriented in the northwest-southeast direction, with a maximum width of 23 km (**Figure 3C**). The island has a complex topography, with a mountainous ridge extending along the center. Given its location, at the eastern boundary of the North Atlantic Subtropical Gyre, the climate is mainly controlled by the Azores subtropical high-pressure system interacting with its topography. The high terrain acts as a perpendicular barrier to the prevailing northeastern trade winds (Caldeira et al., 2002; Prada et al., 2009; Gorricha et al., 2012; Alves et al., 2020; Belo-Pereira and Santos, 2020). As a result, many microclimates form within the island (Espinosa et al., 2021). Specifically, higher precipitation and lower air temperatures prevail in the northern slope (a more humid region), while the opposite pattern occurs in the southern slope, characterized as a dryer region (Caldeira et al., 2002; Prada et al., 2009). In addition, its topography causes an orographic effect on cloud formation, in which precipitation increases with altitude (Gorricha et al., 2012; Espinosa and Portela, 2020).

From the central mountainous ridge to the coast, there are very deep, narrow, and steep valleys formed by erosional processes associated with torrential river flow caused by historical extreme precipitation events (Rodrigues et al., 2006). Most of the valleys form a typical U-shaped profile, characteristic of a young geomorphology (Prada et al., 2005a; Rodrigues et al., 2006). The hydrological network is characterized by a radial pattern typical of volcanic islands, with more than 100 small drainage basins and a mean drainage density of 5.2 km^{-1}. From those drainage basins, Ribeira da Janela (R1), Ribeira de São Roque do Faial (R2), Ribeira Brava (R3), Ribeira dos Socorridos (R4), Ribeira de São Vicente (R5), Ribeira de São Jorge (R6), and Ribeira de Machico (R7) are the most important with respect to runoff (see **Figure 3C**

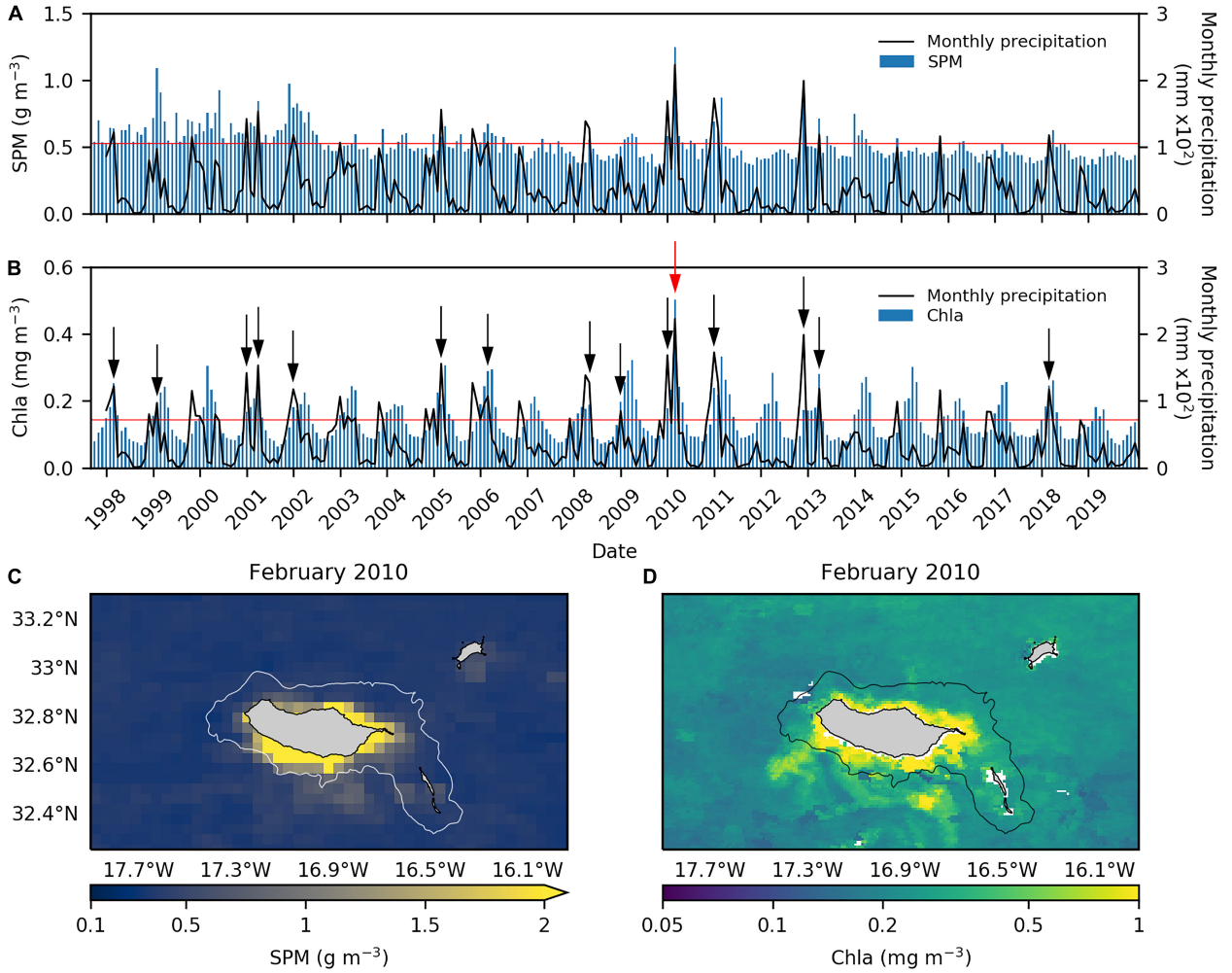

FIGURE 1 | Monthly variability of **(A)** non-algal Suspended Particulate Matter (SPM; g m^{-3}) and **(B)** Chlorophyll-a (Chla; mg m^{-3}) concentrations at the inner shelf area (calculated with values within the -2000 m isobath, represented by the white and black line in **C,D**, respectively) between September 1997 and December 2019 based on satellite data along with monthly accumulated precipitation recorded at 9 meteorological stations distributed over the island (black line). The red line represents the mean, and the black arrows in **(B)** indicate anomalous Chla concentrations associated with runoff episodes. Satellite images of the regional area of Madeira Archipelago representing the monthly average of **(C)** SPM and **(D)** Chla concentrations for the specific episode of February 2010, when the maximum of concentrations occurred (red arrow in **B**).

for location of rivers outlets and its drainage basins), with river catchment areas ranging between 52 and 24 km^2 (**Table 1**). Due to the high-altitude origin (mostly > 1,600 m), high drainage density (4.4–5.5 km^{-1}), and steep slopes (26°–40°; **Table 1**), these rivers are characterized by high torrential flow and high sediment erosion rates during episodes of heavy rain (Rodrigues et al., 2006). For the geometric characteristics of the remaining rivers of the island, please refer to **Supplementary Table 1**. The rivers that drain into the northern coast have a continuous flow—associated with higher rainfall, larger drainage basins, and higher groundwater supply—while river flow in the southern region is intermittent (Prada et al., 2005a).

Maps for land use (Carta de Ocupação do Solo da Região Autónoma da Madeira de 2007—COSRAM, **Figure 4B**) estimates that the majority (77%, ~ 70 km^2) of Madeira Island is covered by forests and natural/semi-natural areas. Agriculture/agroforestry is the next largest land use category, covering 15% (~110 km^2) of the island. Urban/artificial land use covers 8% (~61 km^2) of land, and wetlands and water bodies comprise 1% (~4 km^2; **Figure 4B**). In terms of soil properties, maps for soil type (Ricardo et al., 1992) show that 19 types of soil are present on the island, with Umbric Andosols (40%) and Dystric Rough Terrain (32%) being the dominant soil types (details provided in **Supplementary Table 2** and **Supplementary Figure 1**).

The insular shelf of Madeira is relatively narrow and steep, rapidly dropping from 200 to 500 m within ~10 km from the coastline (**Figure 3C**). An underwater ridge of ~100 m depth connects Madeira to the Desertas Islands (**Figure 3B**). The coastal circulation is influenced by semidiurnal tides, with an average tidal amplitude of ~2

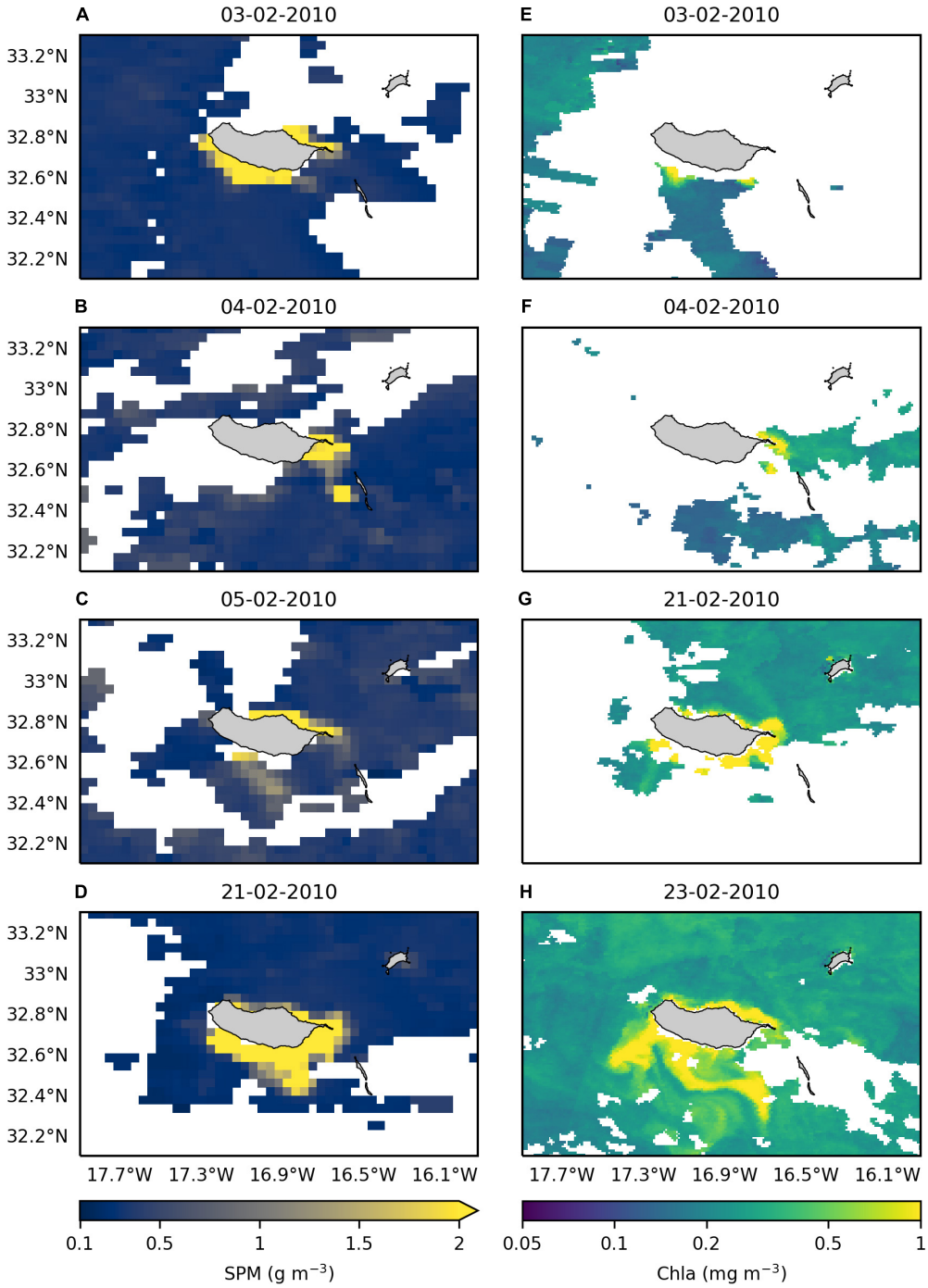

FIGURE 2 | Satellite images of the regional area of Madeira Archipelago. Daily averages of **(A–D)** non-algal Suspended Particulate Matter (SPM; g m^{-3}) and **(E–H)** Chlorophyll-a (Chla; mg m^{-3}) concentrations for specific days of February 2010.

m (Canning-Clode et al., 2008). Salinity surrounding the island is typically 36.5 PSU (Caldeira et al., 2002; Narciso et al., 2019).

Previous studies in this region focused on atmospheric and oceanic island processes, combining the use of medium-high resolution numerical models (Caldeira and Sangrà, 2012; Couvelard et al., 2012; Caldeira and Tomé, 2013; Nunalee and Basu, 2014; Pullen et al., 2017b; Alves et al., 2021; Miranda et al., 2021), with *in situ* and satellite data (Caldeira et al., 2001, 2002, 2014; Grubišic et al., 2015; Alves et al., 2020; Azevedo et al., 2021). These studies revealed the complexity and variety of oceanic and atmospheric interactive processes which occur around the

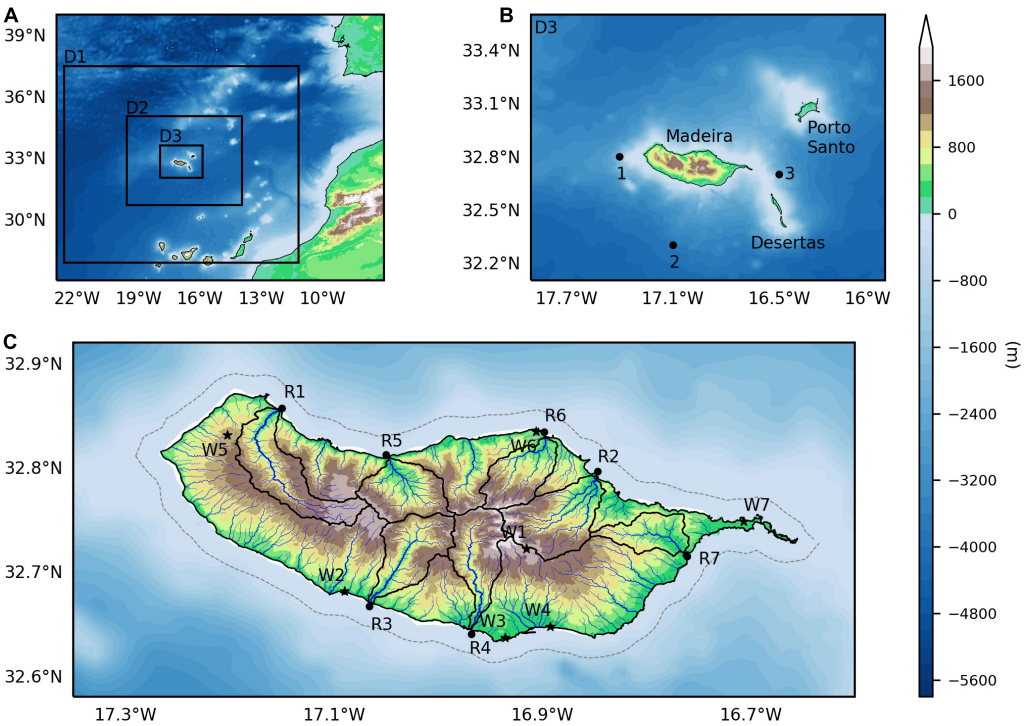

FIGURE 3 | Map of the study area showing the topography and bathymetry retrieved from the Shuttle Radar Topography Mission (SRTM). **(A)** Representation of the three nested COAWST model domains (black boxes D1, D2, and D3, corresponding to 9, 3, and 1 km resolution, respectively). **(B)** Model domain D3 encompassing the regional area of Madeira Archipelago (Selvagens are not shown), where numbers correspond to locations used for model validation. **(C)** Madeira Island showing: (i) the drainage network (blue lines), with identification of the main river outlets (R1—Ribeira da Janela, R2—Ribeira de São Roque do Faial, R3—Ribeira Brava, R4—Ribeira dos Socorridos, R5—Ribeira de São Vicente, R6—Ribeira de São Jorge, R7—Ribeira de Machico; black circles) and its drainage basins (delimited by black lines); (ii) the location of the meteorological stations deployed by IPMA (Portuguese Institute for Sea and Atmosphere; black stars W1–W7) used for model validation; (iii) the location where vertical transects parallel to the north and south coast were performed (gray dashed lines).

TABLE 1 | Geometric characteristics (orientation, area, maximum altitude, main river length, total network length, drainage density and mean drainage slope) of the main rivers of Madeira Island.

River	Orientation	Area (km^2)	Maximum altitude (m)	Main river length (km)	Total network length (km)	Drainage density (km^{-1})	Mean drainage slope (°)
R1—Ribeira da Janela	North	51.7	1604	24.4	268.6	5.2	27.6
R2—Ribeira de São Roque do Faial	North	49.8	1859	15.7	243.4	4.9	36.0
R3—Ribeira Brava	South	41.0	1689	13.9	201.8	4.9	36.7
R4—Ribeira dos Socorridos	South	38.7	1857	18.5	169.3	4.4	40.3
R5—Ribeira de São Vicente	North	37.7	1720	10.8	207.9	5.5	34.7
R6—Ribeira de São Jorge	North	32.1	1854	11.1	155.4	4.8	34.8
R7—Ribeira de Machico	South	24.4	1079	13.4	140.0	5.7	26.2

Data was estimated based on the drainage network computed from the Digital Terrain Model (described in section "MOHID-Land, the Hydrological Model") using QGIS version 3.14.1 (www.qgis.org).

island, including the formation of von Kármán vortex streets, warm wakes, leeward eddies, and atmospheric jets that induce upwelling events.

DATA AND METHODS

Observational Datasets

Meteorological data for precipitation, wind, and air temperature measured every 10 min at seven stations distributed throughout the island (see **Figure 3C** for stations location) were used to validate the atmospheric model results obtained from the coupled (WRF) model simulations. These data were provided by the Portuguese Institute for Sea and Atmosphere (IPMA), with data available since 2007. The model simulations were quantitatively assessed based on statistical analysis (correlation coefficient-r, root-mean-square error-RMSE, and bias; **Table 2**) widely used to evaluate atmospheric model performance (e.g., Alves et al., 2020; Belo-Pereira and Santos, 2020). Additionally, precipitation data for 9 meteorological stations were obtained

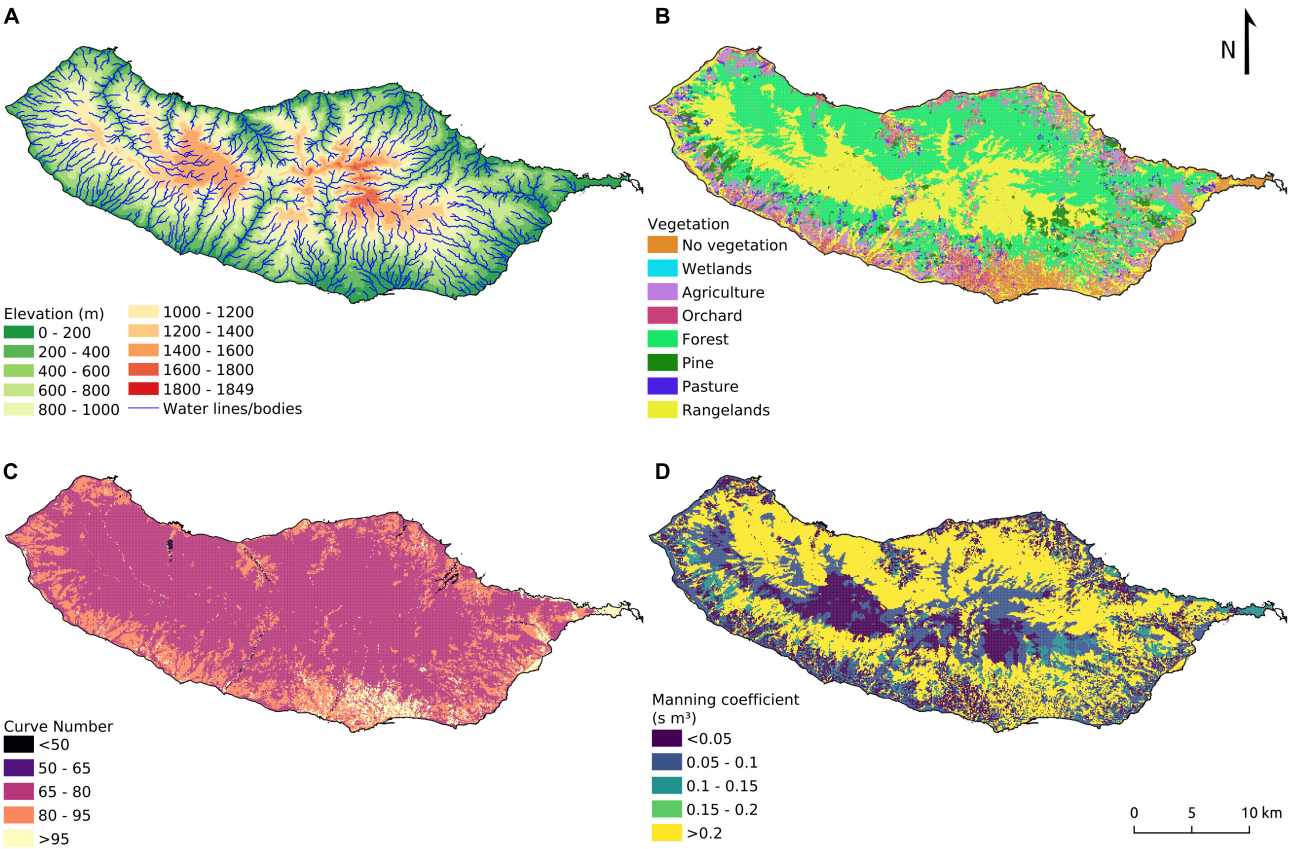

FIGURE 4 | Maps used in the hydrological simulations (MOHID-Land): **(A)** Digital Terrain Model with drainage network; **(B)** soil use; **(C)** curve number (CN-AMCII); **(D)** Manning coefficient.

from the Portuguese water resources database (SNIRH)[1] to be used in the long-term analysis of SPM and Chla (shown in **Figures 1A,B**).

The rivers in Madeira are very poorly gauged, as are most of the small rivers in the world (Hrachowitz et al., 2013; Osadchiev and Zavialov, 2020). This lack of data acquisition is often associated with the difficulty to ensure the adequate maintenance of the hydrometric network due to the sharp topography of the island and due to the frequent torrential flow occurring during intense rain episodes which often damage the equipment and sensors (Prada et al., 2005b). Data are only available for 13 hydrometric stations, located at upstream sections of some of the rivers (altitudes higher than 400 m) and for sporadic periods between 1985 and 2000. Therefore, hydrological data at the river outlets are not available, which did not allow for the validation of the hydrological model's outputs with *in situ* observations.

The accuracy of the offshore winds simulated by the coupled model was also assessed by analyzing 12.5 km resolution data from the Advanced SCATterometer (ASCAT) on MetOp-A, retrieved from a global ocean data product (WIND_GLO_WIND_L3_REP_OBSERVATIONS_012_005) provided by Copernicus Marine Service (CMEMS).[2] The statistical validation was made with satellite observations from the descending (between 10:00-11:00 UTC) and ascending passage (between 21:00 and 23:00 UTC), by comparing instantaneous values both at regional scales (spatially averaged for the model domain D3; **Figure 3B**) and at specific locations around Madeira Island (points 1, 2, and 3 in **Figure 3B**).

Daily and monthly composites of satellite-derived data for SPM and Chla concentrations were obtained from the CMEMS data catalog. The analysis of SPM was based on a Level 3 data product (OCEANCOLOUR_GLO_OPTICS_L3_REP_OBSERVATIONS_009_086) at 4 km spatial resolution. The satellite-derived Chla surface concentrations were based on a Level 4 data product (OCEANCOLOUR_ATL_CHL_L4_REP_OBSERVATIONS_009_091) at 1 km spatial resolution. Both datasets are blended gridded products and cover the period from 1997 to 2019. The usage of multi-mission products allow for an increased spatial and temporal coverage, especially relevant in regions where the analysis of satellite data is limited by cloud cover, such as over Madeira Island (Caldeira et al., 2002). Chla, SPM, and precipitation data were used to identify the periods associated

[1]https://snirh.apambiente.pt

[2]https://marine.copernicus.eu/

TABLE 2 | Statistics obtained from the comparison between hourly meteorological data (precipitation, wind speed, and air temperature), daily instantaneous satellite-derived winds (offshore stations), and model simulations between 1 and 28 February 2010.

Variable	Precipitation (mm h^{-1})			Wind speed (m s^{-1})			Air temperature (°C)		
Station	***r***	**RMSE**	**Bias**	***r***	**RMSE**	**Bias**	***r***	**RMSE**	**Bias**
W1—Chão do Areeiro	0.76	4.16	−0.49	0.83	4.39	2.42	0.86	1.44	−0.23
W2—Lugar de Baixo	0.48	2.32	0.48	0.51	3.94	2.63	0.85	1.11	−0.43
W3—Lido	0.68	1.77	0.37	0.69	5.34	4.05	0.62	1.27	0.17
W4—Funchal	0.66	2.47	0.30	0.72	3.59	2.38	0.85	0.95	0.01
W5—Lombo da Terça	0.23	3.93	0.26	0.90	2.79	−0.72	0.88	1.29	0.78
W6—São Jorge	0.61	2.14	0.06	0.63	4.04	2.15	0.85	1.16	−0.02
W7—Caniçal	0.53	2.03	0.13	0.72	3.64	1.70	0.79	1.75	1.43
Offshore—1	–	–	–	0.82/0.78	1.44/1.56	−0.27/ − 0.78	–	–	–
Offshore—2	–	–	–	0.96/0.84	1.43/1.59	0.47/ − 0.69	–	–	–
Offshore—3	–	–	–	0.94/0.81	2.25/1.64	−1.74/ − 0.29	–	–	–

Left and right values for offshore stations correspond to descending and ascending satellite passage results, respectively.

with runoff events (black arrows in **Figure 1B**) and to assess the impact of the February 2010 flash flood events on primary productivity and turbidity around the island (regional monthly mean shown in **Figures 1C,D** and daily means in **Figure 2**).

COAWST Modeling Framework

The physical processes of the ocean and atmosphere were simulated using the Coupled Ocean-Atmosphere-Waves-Sediment Transport (COAWST), a two-way coupled numerical system, currently operational for Madeira Archipelago[3] (Vieira et al., in preparation). COAWST includes the modeling of ocean circulation (Regional Ocean Modelling System—ROMS), atmosphere (Weather Research and Forecasting—WRF), and waves (Simulating WAves Nearshore—SWAN). COAWST is implemented following a downscaling technique, which consists in simulating at a regional scale, based on information provided by a larger domain, enabling the extension of operational global forecasting capabilities to local scales (Caldeira et al., 2016). Boundary conditions are provided from larger and coarser domains to their subdomains and vice-versa. In the present study, three nested domains were implemented (black boxes D1, D2, and D3 in **Figure 3A**). The coarsest spatial resolution, 9 km, was applied to D1 (WRF), decreasing to 3 km for D2 (WRF, ROMS, SWAN) and 1 km for D3 (WRF, ROMS, SWAN). The highest resolution, innermost grid (D3) covers Madeira, Porto Santo, and Desertas Islands (**Figure 3B**). Model outputs are written every 24, 12, and 1 h for the D1, D2, and D3 domains, respectively. Models within the COAWST coupled system are integrated by the Model Coupling Toolkit (MCT), an open-source software that enables the two-way exchange of data between the models with minimum effort (Jacob et al., 2005; Larson et al., 2005). For the coupling of the models, the Spherical Coordinate Remapping, and Interpolation Package (SCRIP; Jones, 1999) was used to compute addresses and weights for remapping and interpolating fields between atmospheric and oceanic grids of different spatial resolution in spherical coordinates. For a detailed description of the COAWST coupling methodology, see Warner et al. (2010).

The exchange of variables between the models that comprise the COAWST modeling system occurred every 30 min, in which: (i) the atmospheric model WRF provided 10 m surface winds to ROMS and SWAN and atmospheric pressure, air relative humidity, 2 m atmospheric surface temperature, cloud fraction, precipitation and short-wave and long-wave net radiative fluxes to ROMS; (ii) the oceanic model ROMS provided SST to WRF and surface currents, free surface elevation and bathymetry to SWAN; and (iii) the wave model SWAN provided significant wave height and wavelength to WRF and ROMS, and wave direction, surface and bottom wave periods, percent of breaking waves, wave energy dissipation and bottom orbital velocity to ROMS (Warner et al., 2010). This numerical framework was recently applied to the Madeira Archipelago (Pullen et al., 2017a; Alves et al., 2020; Azevedo et al., 2021), demonstrating that the coupling between the atmosphere and the ocean significantly improved model results. A recent study employing the COAWST demonstrated improved performance with respect to the replication of heavy precipitation events compared with stand-alone atmospheric models (Ricchi et al., 2021). In the present study, a numerical simulation was performed using COAWST, starting on 15 January and ending on 28 February 2010, where the first 15 days were used for model spin-up, with the remaining 28 days used for the analysis presented herein.

Oceanic Model

ROMS is a free-surface, terrain-following, primitive equations model used to study the ocean response to physical forcings. Bathymetry used in the present study resulted from interpolation between ETOPO2 (Smith and Sandwell, 1997) and GEBCO8 (General Bathymetric Chart of the Oceans; Becker et al., 2009), with 2 arc-minute resolution (∼3 km) in offshore regions and 30 arc-second resolution (∼0.78 km) in coastal regions, respectively. The vertical domain was discretized to 40 sigma levels, increasing the vertical resolution near the sea surface and sea bottom. To force ROMS, initial and boundary conditions were obtained from a Hybrid Coordinate Ocean Model (HYCOM) Navy Coupled

[3]https://oom.arditi.pt/forecasts.php

Ocean Data Assimilation (NCODA) product (global 1/12° analysis), with approximately 9 km grid resolution and daily outputs. The parameterizations chosen included: (i) radiation and nudging for tracers (temperature and salinity) and baroclinic velocities (Marchesiello et al., 2001); (ii) Shchepetkin condition for barotropic velocities (Mason et al., 2010); (iii) Chapman explicit boundary condition for free-surface height (Chapman, 1985); (iv) Generic Length Scale (GLS) for vertical mixing (k–ε scheme; Umlauf and Burchard, 2003); and (v) tides, considering 10 tidal constituents (M2, S2, N2, K2, K1, O1, P1, Q1, Mf, Mm) from a global model (TPX07; Egbert and Erofeeva, 2002). At the riverine boundaries, salinity was set to 0 and water temperature and river flow was imposed based on 10-min hydrological simulation outputs performed with the MOHID-Land hydrological model. The model variables are spatially discretized on an Arakawa C-grid. Baroclinic timestep was set as 30 and 10 s for D2 and D3 domains, respectively. For each baroclinic timestep, 30 s barotropic timestep was defined. ROMS was successfully applied in previous studies focused on Madeira Island to investigate island-induced oceanic processes (Caldeira and Sangrà, 2012; Couvelard et al., 2012; Caldeira et al., 2016; Alves et al., 2021) and has also been used in idealized and realistic studies to investigate plume dynamics generated by the Columbia, Pearl, and South Brazilian rivers (Chen et al., 2009; Liu et al., 2009; Pan et al., 2014; Basdurak et al., 2020; Branch et al., 2020; Marta-Almeida et al., 2020). Despite the lack of *in situ* data to assess the accuracy of the coupled ROMS model outputs during February 2010, Vieira et al. (in preparation) are (at the time of publication) assessing the general capability of our numerical framework to represent island-scale geophysical processes, including warm wakes, storm events, and land runoff. Sea surface temperature, sea surface salinity, waves, and coastal currents compared well with data collected between 2018 and 2021. For more information on the numerical details of the ROMS model, the reader is referred to Shchepetkin and McWilliams (2005).

Atmospheric Model

WRF is a numerical model used for atmospheric research and operational forecasting. The WRF configuration used in the present study considers the non-hydrostatic terms and the second-order diffusion term to solve turbulence, except in the boundary layer where the turbulent flow is solved through the Smagorinsky scheme. The WRF parameterization comprised the following options: (i) WSM 6-class graupel scheme for cloud microphysics (Hong and Lim, 2006); (ii) Rapid Radiative Transfer Model for longwave and shortwave radiation (Mlawer et al., 1997); (iii) Eta similarity scheme for the surface layer (Janjic, 1996; Janjić, 2002); and (iv) Mellor-Yamada-Janjic scheme for the planetary boundary layer (Janjic, 1990, 1994). The vertical domain was discretized to 40 sigma levels. The initial and boundary conditions used to force the model were obtained from the NCEP (National Center for Environmental Prediction) FNL (Final) Operational Model Global Tropospheric Analyses, with 6 h interval outputs and 1° resolution. The Shuttle Radar Topography Mission (SRTM) was used as topographic data (Becker et al., 2009), with a horizontal resolution of 3 arc-second (∼90 m). Land use information was obtained from the Corine Land Cover 2006 (CLC-06) from USGS, National Center for Earth Resources Observation and Science (EROS; Büttner and Kosztra, 2007). CLC-06 classes were converted to 24 USGS classes and the classification table was obtained from De Meij and Vinuesa (2014). The use of SRTM and CLC-06 improved the topography and land-use representation and the calculation of topographically sensitive variables, such as wind speed, air temperature, and precipitation. The calculation time step was set to 45, 15, and 5 s for D1, D2, and D3 domains, respectively. Although with slightly different configurations, the stand-alone WRF was successfully implemented in Madeira Island in past studies (Couvelard et al., 2012; Caldeira and Tomé, 2013; Grubišic et al., 2015). For a detailed description of the WRF model, the reader is referred to Skamarock and Klemp (2008) and Skamarock et al. (2008).

Atmospheric Model Validation

The atmospheric model outputs for February 2010 were validated using hourly averaged data from seven meteorological stations. These stations are located at different altitudes: Chão do Areeiro (W1) is located at the central ridge; Lugar de Baixo (W2), Lido (W3), and Funchal (W4) are located at the southern region; Lombo da Terça (W5), São Jorge (W6) and Caniçal (W7) are located at the northwestern, northeastern and eastern regions, respectively (**Figure 3C**). Statistical validation between model results and observations are shown in **Table 2**. The comparison of modeled and *in situ* data for precipitation and wind speed are shown in **Figure 5**, while the air temperature is shown in **Supplementary Figure 2**. Offshore winds from numerical simulations were also compared with satellite data products and are shown in **Figure 6**.

Precipitation data recorded at the meteorological stations shows two periods of maximum rainfall depicted by the rain gauges (black line in **Figure 5**, left panels), on the 2nd and 20th of February. During the first episode, maximum rainfall occurred in São Jorge (W6) and Chão do Areeiro (W1) stations, reaching approximately 35 and 30 mm h^{-1}, respectively, while the remaining stations measured values between 9 and 27 mm h^{-1}. During the second event, precipitation was much higher than the values recorded on the 2nd of February, particularly in Chão do Areeiro (W1), Funchal (W4), Lugar de Baixo (W5), and Lido (W3) stations, with maximum values reaching 67, 51, 28 and 20 mm h^{-1}, respectively. COAWST replicated precipitation during both quiescent and high precipitation events with a high degree of accuracy at most stations, as suggested by the RMSE (<2.5 mm h^{-1}) and correlations coefficient values ($r > 0.5$; **Table 2**). Maximum agreement occurred at Lido (RMSE = 1.77, $r = 0.68$; W3) and maximum disagreement at Chão do Areeiro (RMSE = 4.16, $r = 0.76$; W1), followed by Lombo da Terça (RMSE = 3.93, $r = 0.23$; W5). Despite the strong correlation ($r = 0.76$) at Chão do Areeiro (W1), the model underestimated precipitation values over the entire period at this station (**Figure 5A**), as suggested by the negative bias (**Table 2**). At Lombo da Terça (W5), the model underestimated

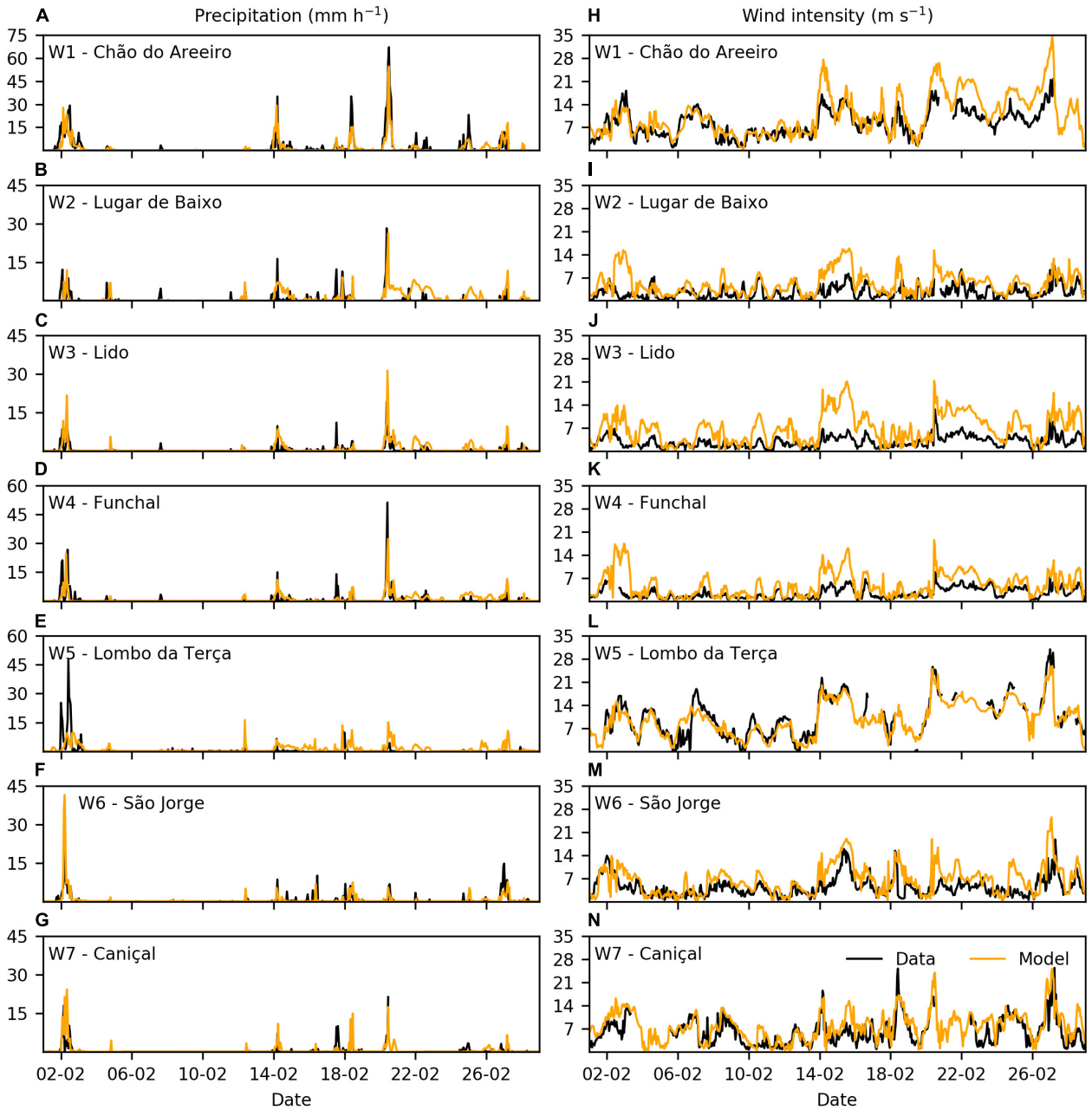

FIGURE 5 | Comparison between the data recorded by the meteorological stations (black line) and the COAWST model results (orange line) for **(A–G)** precipitation (mm h^{-1}; left panel) and **(H–N)** wind intensity (m s^{-1}; right panel) during February 2010. Note the changes on the precipitation scales.

precipitation in the first episode and overestimated in the second event (**Figure 5E**), showing an overall overestimation, as indicated by a bias of 0.26 (**Table 2**). We believe that this discrepancy between model results and observations is likely due to the complex topography and the model spatial grid resolution (1 km), which may not be able to reproduce the exact weather conditions at the station location. It is also important to note that the model results used for this comparison were extracted from the nearest grid point to the meteorological station, which may not be the exact same position. However, overall, the model performs well and strikes a good balance between model accuracy and computational cost. Model RMSE and correlation coefficient obtained in the present study are similar to previous studies (Luna et al., 2011; Teixeira et al., 2014; Dasari and Salgado, 2015).

Concerning wind, comparison of model results with *in situ* measurements demonstrates that the model represents the main spatial and temporal variability of the wind speed (**Figure 5**, right panels). Correlation coefficients (mostly ranged between 0.7

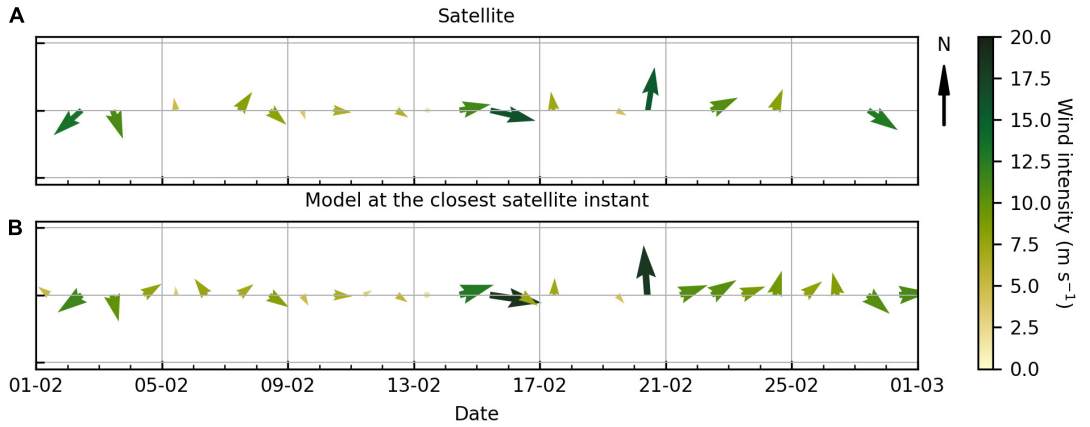

FIGURE 6 | Comparison of D3 domain spatial average of wind direction and intensity (m s^{-1}) from **(A)** ASCAT (descending satellite passage) and from **(B)** model simulations at the timestep closest to the time of the satellite passage.

and 0.9; **Table 2**) are similar or higher than those reported in previous studies (Pullen et al., 2017b; Alves et al., 2020; Belo-Pereira and Santos, 2020). However, RMSE are higher than those reported by Alves et al. (2020). The higher RMSE is associated with the fact that, in contrast to previous studies, our model was applied to replicate conditions during extreme weather, during which wind intensity and direction vary rapidly. Positive bias also indicates an overestimation of the wind speed by the model, except at Lombo da Terça station (W5) where the wind speed was underestimated (**Table 2**). **Figure 6** shows the comparison between the average offshore winds for the regional domain (D3; **Figure 3B**) obtained from descending satellite passage and from the model simulation at the closest satellite instants. As can be seen, the model represents well the main temporal variability patterns of the wind direction (as observed in **Figure 6**) and wind intensity ($r = 0.96$) computed for February 2010. Ascending satellite passage shows similar results ($r = 0.90$). The accuracy of the modeled surface wind was also assessed at three specific locations (points 1, 2, and 3 represented in **Figure 3B**), and are presented in **Table 2** for both descending and ascending satellite passages. Points 1 and 3 are located close to the regions of the atmospheric jets (Alves et al., 2020, 2021), and point 2 is in the southern region characterized by the frequent occurrence of warm wakes (Caldeira et al., 2002, 2016; Couvelard et al., 2012; Grubišic et al., 2015; Azevedo et al., 2021). In general, correlation coefficients were high (0.78–0.96) and RMSE values were low (mostly < 1.6 m s^{-1}; **Table 2**), showing the strong performance of the model with respect to representing the wind variability. The point located at the eastern atmospheric tip-jet (point 3) showed the worst comparisons, as indicated by the highest RMSE (2.25 and 1.64 m s^{-1} for descending and ascending satellite data, respectively), associated with an underestimation of the wind speed, as suggested by negative bias (**Table 2**). Despite that, WRF wind correlation coefficients reported in this study are identical to those reported in previous studies using ASCAT satellite data products at similar locations (Alves et al., 2020, 2021).

The main spatial and temporal air temperature was also closely replicated by COAWST, as shown in **Supplementary Figure 2**, and as suggested by strong correlation coefficients (mostly > 0.8), low RMSE (<1.3), and low bias (ranged between -0.43 and 0.78; **Table 2**). Sites with the largest divergence from observations were Caniçal (W7) and Chão do Areeiro (W1) stations, with RMSE of 1.75 and 1.44°C, respectively (**Table 2**). RMSE and correlation coefficient in the present study are similar or better than those reported in former studies (Pullen et al., 2017b; Alves et al., 2020).

While small discrepancy between model outputs and observations are present, the WRF model performs well considering the complexity of atmospheric processes interacting with highly variable topography and terrain. Reported RMSE and correlations in this study closely agree with those reported in previous studies providing confidence in the WRF to replicate precipitation, wind and air temperature.

Wave Model

SWAN is a state-of-the-art third-generation wave model designed to simulate the generation and propagation of waves in coastal shallow waters (Booij et al., 1999). Initial and boundary conditions for the wave height, period and direction were obtained from a global model product (multi_1.glo_30m) with 30 arc-minute grid resolution (~1 km) and outputs every 3 h, available at the NCEP database. The SWAN boundaries were divided into 10 directional bands and 25 frequencies (range: 0.04–1 Hz). The Taylor and Yelland (2001) formula was used for changes in sea surface roughness caused by waves. Timestep was set to 180 and 60 s for D2 and D3 domains, respectively.

MOHID-Land, the Hydrological Model

The hydrological simulations were performed using the MOHID-Land numerical code, a physically based, continuous and open-source model designed to study watershed dynamics and the transport of water quality tracers (Trancoso et al., 2009; Canuto et al., 2019; Oliveira et al., 2020). The model considers four mediums, the atmosphere (which provides the meteorological data, not explicitly simulated in MOHID-Land), porous media (i.e., soil), land surface, and drainage (i.e., river) network. The water circulates through the three latter compartments based

on mass and momentum conservation equations. MOHID-Land is based on finite volumes organized into a regular structured grid, rectangular or quadrangular in the horizontal domain, and Cartesian in the vertical domain. MOHID-Land has been applied to study several research topics, including (i) forecasts of freshwater quantity and quality to improve the management of coastal systems (Brito et al., 2015); (ii) the assessment of nutrient transport and turnover processes at the watershed scale (Epelde et al., 2016); (iii) water-exchanges between surface water and groundwater in floodplains (Bernard-Jannin et al., 2016); (iv) the contribution of flash floods episodes to the eutrophication in water reservoirs (Brito et al., 2017, 2018); (v) the improvement of the irrigation water management (Simionesei et al., 2016, 2018, 2020; Ramos et al., 2017, 2018b); and (vi) the influence of reservoir management on the river flow regime (Canuto et al., 2019). For a more detailed description of the model's architecture and sensitivity to parameterizations, the reader is referred to Trancoso et al. (2009) and Oliveira et al. (2020), respectively.

The configuration of MOHID-Land used in the present study relies on a rectangular grid with a 100 m horizontal resolution, meaning that all maps used for the calculation of surface and subsurface land runoff were resampled to a 100 m horizontal grid resolution, regardless of the original grid resolution. The Digital Terrain Model (DTM), used to derive the model's drainage network (**Figure 4A**) and other parameters (e.g., soil depth), was sampled through LIDAR surveying techniques with a 5 m horizontal spatial resolution and was provided by the DROTe (Direção Regional do Ordenamento do Território). The geometry of the river cross-sections was considered rectangular and was defined as a function of the drained area in each node (linearly interpolated between user-specified values, presented in **Supplementary Table 3**). Considering that the present study aims to simulate an extreme weather event, the Manning coefficient for the entire drainage network was set to a constant value of 0.035 $s.m^{-1/3}$, which according to Gonçalves (2016) is close to the optimum value estimated for three Madeiran rivers at peak discharge rate. Maps for land cover/land use (at 1:10,000 scale; COSRAM) and soil type (at 1:50,000 scale; Ricardo et al., 1992; **Supplementary Figure 1**) were also provided by DROTe.

In the present study, MOHID-Land calculated surface runoff and infiltration over different land uses with the runoff curve number (CN) method, based upon the methodology developed by the USDA Soil Conservation Service (1972). CN values can range from 0 to 100, in which high values are associated with less permeable soils and thus higher surface runoff. In practice, CN values estimated for Madeira assume that surface runoff and infiltration are dependent on the soil type and land use (e.g., Řehánek et al., 2019; Lopes et al., 2020). According to USDA Soil Conservation Service (1972), soils can be divided into four hydrologic groups from A to D, in which type A/D soil has the highest/lowest hydraulic conductivity and lowest/highest surface runoff potential. The definition of the soil hydrologic groups was done considering the soil texture (i.e., the relative proportion of sand, silt, and clay), following Sartori et al. (2009) (**Supplementary Table 2**). The CN values specific to each land use developed by the SCS were adapted to Portuguese soils by David (1976) and Correia (1983) (consulted in Oliveira, 2004). The resulting map was computed by merging the combined attributes of the hydrological soil type and land use (**Figure 4C**). As surface runoff and infiltration during a precipitation event is highly dependent on the soil's antecedent moisture condition (AMC), CN values can also be adjusted to dry (CN AMC I), moderately wet (CN AMC II) or wet (CN AMC III) conditions. MOHID-Land works with CN AMC II by default but adjusts CN values according to the accumulated precipitation in the previous 5 days.

Using the information on land use, the vegetation type (**Figure 4B**) was defined according to MOHID's vegetation database, and corresponding Manning coefficients (**Figure 4D**) were defined following Pestana et al. (2013). The porous media was divided into five grid layers, with a thickness of 0.3, 0.3, 0.4, 1.0, and 3.0 m (from surface to bottom). The soil depth in each cell varied according to the cell's slope, set between a maximum of 5 m (flat areas) and a minimum of 0.1 m (steep areas). For the vertical soil profile, the soil was divided into four horizons with specific hydraulic parameters: (a) 0–0.6 m (1st and 2nd soil grid layers), (b) 0.6–1.0 m (3rd soil grid layer), (c) 1.0–2.0 m (4th soil grid layer), and (d) 2.0–5.0 m (5th soil grid layer; **Supplementary Figure 3**). This means that horizon (a) included the first two grid layers, horizon (b) included the third layer, horizon (c) included the fourth layer, and horizon (d) included the bottom layer. The hydraulic parameters for each horizon were extracted from the multilayered European Soil Hydraulic Database (Tóth et al., 2017), which includes the Mualem–van Genuchten hydraulic parameters with a 250 m resolution (**Supplementary Table 4**). The vertical hydraulic conductivity in each cell results from the multiplication of the horizontal hydraulic conductivity (retrieved from Tóth et al., 2017) by a factor of 10, the initial water depth was set to 50% of the soil's depth.

Outputs from the coupled WRF model (within the COAWST numerical framework described and validated in section "Atmospheric Model Validation") were used to simulate MOHID's atmospheric forcing conditions (precipitation, temperature, wind, air humidity, and solar radiation). MOHID-Land's calculation timestep was dynamically adjusted (decreasing/increasing) according to the precipitation rate. The MOHID-Land simulation period was set between 10 December 2009 and 1 April 2010, where the first 2 months were used as model spin-up. The river discharge rate ($m^3\ s^{-1}$) and water temperature (°C) obtained from the hydrological simulations at 10-min timesteps were then used to force the oceanic model at the grid cells that were nearest to the actual river outlets (shown in **Figure 3C**). Given the spatial grid resolution of the oceanic model and the close proximity of the rivers, a total of 148 rivers were considered, which accounted for 96 riverine grid cells in the oceanic model. This model setup assumes that the land runoff due to high precipitation events predominantly flows abruptly *via* rivers, with sheet runoff making a negligible contribution to freshwater discharge from land. The numerical framework used in this study presents a significant advance for the scientific community mainly because the coupling of oceanic models with hydrological models is scarce (e.g., Dresback et al., 2013; Silva-Araya et al., 2018), especially when applied to insular systems with complex topography (e.g., Ogden, 2016). Despite

the lack of *in situ* data to validate the MOHID-Land outputs, past studies focused on the flash flood event of 20 February 2010 employed theoretical methodologies for the calculation of peak river discharge and showed similar results with the present study, with river discharge rates ranging from ∼200 to 600 $m^3\ s^{-1}$ in the large rivers (Oliveira et al., 2011; Caetano, 2014; Lousada and Loures, 2020). Still, there is a need to investigate model sensitivity to different hydrological scenarios when river gauge data becomes available.

Kinematic Parameters

To investigate the impact of the river plumes on coastal waters, two kinematic parameters were computed to study the stratification and mixing of the water column, the Brunt–Väisälä buoyancy frequency (N^2) and Richardson Number (R_i), respectively. These two parameters have previously been employed to investigate stratification and mixing processes in coastal waters (Osadchiev, 2018; Ayouche et al., 2020, 2021; Basdurak et al., 2020; Sorgente et al., 2020).

The Brunt–Väisälä buoyancy frequency squared is defined as:

$$N^2 = -\frac{g}{\rho_0}\frac{\partial \rho}{\partial z}$$

where g is the gravitational acceleration (9.8 m s^{-2}), ρ_0 is the reference density, ρ is the density calculated from temperature and salinity model outputs and $\partial\rho/\partial z$ is the vertical density gradient (thus, at the surface, N^2 is equal to 0; Saldías et al., 2012). High Brunt–Väisälä values are indicative of vertical stratification.

The Richardson Number is defined as:

$$R_i = \frac{N^2}{S^2}$$

where N^2 is the Brunt–Väisälä Frequency and S^2 is the vertical shear ($S^2 = (\partial_z u)^2 + (\partial_z v)^2$, where u and v corresponds to the eastward and northward velocities, respectively; Ayouche et al., 2020). R_i values lower than 0.25 are indicative of vertical mixing and therefore the kinetic energy of the flow surpasses vertical stratification (Smyth and Moum, 2000; Sanders and Garvine, 2001).

RESULTS AND DISCUSSION

The impact of flash floods events on coastal circulation and on ecosystem dynamics depends on the physical processes that control the spreading and mixing of buoyant river plumes (Horner-Devine et al., 2015). For example, the wind and ocean currents control the spreading, while the vertical shear controls the mixing of freshwater with oceanic waters, increasing salinity and decreasing concentrations of land-based material in the coastal plume (Horner-Devine et al., 2015). Bearing this in mind, the impact of the river discharges from the February 2010 flash floods on the coastal waters around Madeira Island is focused on the physical processes that mediated the plume's behavior. In this regard, the variability of atmospheric forcing mechanisms (i.e., precipitation and wind), river discharges, and sea surface salinity (i.e., stratification) for the entire month is first described. Subsequently, two specific flash floods events are studied in more detail to better understand the potential processes influencing the different SPM and Chla concentration observations (**Figure 2**). To this end, we used modeled salinity distributions as a proxy to investigate the transport of freshwater and associated terrigenous material, including nutrients, to coastal and offshore waters.

Temporal Variability of Atmospheric Forcing, River Discharges, and Sea Surface Salinity

Temporal variability of wind, precipitation, river discharges, and sea surface salinity for February 2010 is shown in **Figure 7**. To analyze the prevailing wind direction and intensity, the wind field obtained from the coupled physical model was spatially averaged for the regional domain (D3; **Figure 3B**). As observed in **Figure 7A**, wind speed and direction varied quite significantly over the study period, changing anti-clockwise from south to southeast during the first 6 days, then turning clockwise and remaining with a westward orientation most of the time (varying between southwest and northwest direction). During the two periods of maximum rainfall, which corresponds to the 2nd and 20th of February (black dashed lines in **Figure 7**), prevailing winds had a northeast and southwest direction, respectively, reaching speeds typical of stormy weather conditions (∼ 15 and 20 m s^{-1}, respectively). On these occasions, extreme volumes of rain fell over the island, such that the total daily precipitation during the 2nd and 20th of February 2010 accounted for 19 and 20% of the total monthly precipitation (blue line in **Figure 7B**). Hourly precipitation values higher than 0.5 mm h^{-1} prevailed 69% of the time.

As expected, river discharges simulated by the hydrological model responded rapidly to intense precipitation events, as suggested by the concurrent peaks of the river flow and precipitation (**Figure 7B**). This pattern is usually found in mountainous rivers characterized by small drainage basins and steep topography (Osadchiev et al., 2020). This is the case of the Kodor River (located in the northeastern region of the Black Sea), where the shape and size of its river plume are very dynamic and can change very quickly (Osadchiev et al., 2020). In Madeira, total river discharge rates ranged between 15 and 4,566 $m^3\ s^{-1}$, corresponding to a total freshwater volume of 4.8×10^8 m^3 that entered the coastal area during the entire month. Southern rivers accounted for 56% of total freshwater volume (2.7×10^8 m^3 *via* 77 rivers outlets), while 44% of total freshwater volume flowed from northern rivers (2.1×10^8 m^3 *via* 71 rivers outlets). South rivers reached a maximum combined discharge rate of 3,220 $m^3\ s^{-1}$, while north rivers reached a maximum combined discharge rate of 1,782 $m^3 s^{-1}$ (both peaks on 20th of February; red and black line in **Figure 7B**, respectively).

Hovmöller diagrams representative of sea surface salinity transects parallel to the south and north coast (see **Figure 3C** for transects location) are shown in **Figures 7C,D**, respectively. In general, salinity values were typical of oceanic waters (>36.5 PSU; Caldeira et al., 2002; Narciso et al., 2019). The

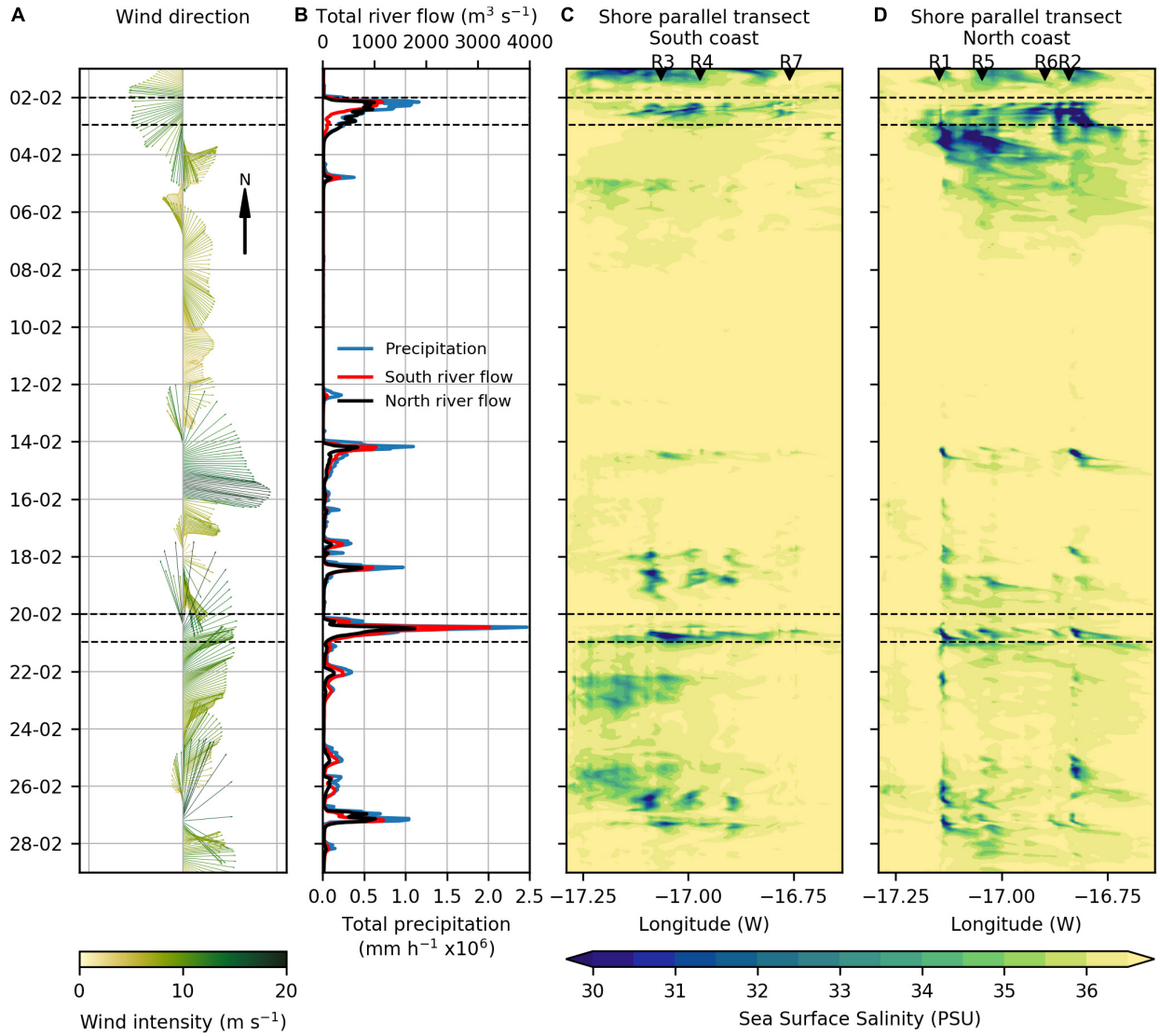

FIGURE 7 | (A) Spatial average of WRF model wind direction and intensity (m s^{-1}) for D3 domain, **(B)** total modeled river flow (m^3 s^{-1}) for rivers discharging in the south coast and north coast, along with the WRF model total precipitation (mm h^{-1}) calculated for the island (red, black and blue lines, respectively), Hovmöller diagrams for the modeled Sea Surface Salinity (PSU) obtained from the shore parallel transects along **(C)** the southern shoreline and **(D)** northern shoreline during February 2010. The shoreline transects are positioned around 2 km from the coast and labels R1–R7 indicate the position of the main river outlets (see **Figure 3C** for transects and river outlets location). Black dashed lines identify two flash flood events.

exceptions occurred during periods of strong precipitation and consequent intense river discharge, whereby salinity decreased to < 35 PSU (**Figures 7C,D**). Despite the occurrence of maximum precipitation and river discharges on the 20th of February (**Figure 7B**), the river plume at the surface showed a more persistent signature on the 2nd and 3rd of February on the northern coast, as indicated by low salinity values (<30 PSU; **Figures 7C,D**). Thus, two major hydrological events were identified: the 2nd of February, characterized by intense precipitation, high river discharges, moderate northeasterly winds forming a persistent river plume in the northern coast; and the 20th of February—the catastrophic flash flood event—characterized by extreme precipitation, extreme river discharges, strong southwesterly winds, and a less persistent surface river plume mainly affecting the southern coast. As such, we will focus on the plume dynamics and their impacts on the coastal waters during these two episodes.

Coastal Dynamics of River Plumes

Considering that freshwater discharges, wind, ocean currents, bathymetry, and coastal geometry are some of the primary factors that determine the shape and size of river plumes (Horner-Devine et al., 2015), here we discuss the dynamics of the plumes based on snapshots of surface maps representing the variability of precipitation, river flow, wind, ocean currents, and sea surface

salinity, while water column stratification and mixing processes are discussed based on vertical transects of salinity, Brunt–Väisälä Frequency and Richardson Number.

February 2nd, 2010—Northeasterly Winds

Snapshots of surface maps for the 2nd of February 2010 flash flood event are shown in **Figures 8A–D**. The wind field clearly reflects the orographic effects on the lower atmospheric level, frequently detected in Madeira Island (Couvelard et al., 2012; Caldeira and Tomé, 2013; Caldeira et al., 2014; Pullen et al., 2017b; Caldeira, 2018; Alves et al., 2020, 2021; Belo-Pereira and Santos, 2020). This pattern is particularly evident at 06:00 and 12:00 UTC, when moderate northeasterly winds ($\sim$15 m s^{-1}) intercepted the island's topography, inducing an intensification of the wind at the eastern and western flanks, and a deceleration in the southern (wake) side ($<$5 m s^{-1}; **Figures 8A,B**). These two tip-jets are frequently observed on the island flanks of Madeira, particularly during Summer (Alves et al., 2020). As the north component of the wind intensified to $\sim$ 17 m s^{-1}, orographic effects generated downslope airflow, resulting in stronger winds blowing offshore on the leeward side of the island, as captured at 21:00 UTC and at 6:00 UTC on 3 February (**Figures 8C,D**).

As a result of the northeastern winds converging to the eastern part of the mountainous ridge, the largest precipitation occurred over the eastern region of the island, reaching maximum values in the northeastern slopes (around 40 mm h^{-1}; **Figures 8A,B**). These results are in line with Couto et al. (2012) and reinforce the fact that rainfall distribution over Madeira is strongly controlled by the intensity and direction of the prevailing winds (Gouveia-Reis et al., 2016). At this time, four main rivers oriented to the northeastern and southeastern coastal areas rapidly responded to the intense precipitation, with calculated river flow increasing from 5 to a maximum of 300 m^3 s^{-1} (**Figures 8A,B**). In the northern region, the total river discharges were dominated by Ribeira de São Roque do Faial (R2) and Ribeira de São Jorge (R6), which accounted for 24 and 15%, respectively, of the total discharge in the north (**Figure 9A**). In the southern region, total river discharges were dominated by Ribeira de Machico (R7) and Ribeira dos Socorridos (R4), which constituted 15 and 11% of the total discharge in the south, respectively (**Figure 9B**). The remaining rivers had a small individual contribution to the total river flow in each region, which accounted for less than 10 and 8% of total north and south river discharge, respectively (gray lines in **Figures 9A,B**). However, while the minor rivers individually contribute little to total discharge in each region, cumulatively they account for approximately 61 and 74% of total north and south river discharge, respectively. The contribution small rivers make to discharge highlights the need of taking into account its cumulative contribution in the transport of land-based materials to the coastal environment in future studies, often neglected in other coastal regions (Osadchiev and Korshenko, 2017; Osadchiev and Zavialov, 2020).

Maps of modeled sea surface salinity illustrate the variability of the horizontal structure of the plumes, clearly demonstrating the impact of freshwater entering and interacting with the coastal ocean. Concurrent with maximum river flow (6:00 UTC), modeled low-salinity values near the river mouths suggests the presence of small-scale river plumes interacting with marine coastal waters (**Figure 8A**). As freshwater discharge from rivers continues, the individual surface plumes expand and spread offshore, almost reaching the 1,000 m isobath (**Figure 8B**). Collision and coalescence of the plumes is observed in the northern and southern regions (**Figure 8B**). The river plumes were mostly depicted by low salinity values at the inner shelf ($<$35 PSU between the coast and 1,000 m isobath), while offshore waters retained typical oceanic values ($>$36.5 PSU), inducing a strong horizontal salinity gradient and convergence zones at the plume's front (**Figure 8B**). Collisions and coalescence of river plumes is a phenomenon commonly found in coastal regions characterized by the presence of several small rivers in close proximity (Warrick and Farnsworth, 2017), for example, the Russian coast in the northeastern Black Sea (Osadchiev et al., 2020). Considering that individual plumes have different shapes and sizes, the interaction between plumes strongly controls the transport of river-borne materials at the coast (Warrick and Farnsworth, 2017; Osadchiev et al., 2020). Given that our model results suggest collision and coalescence of river plumes, the detailed investigation of the interaction between individual river plumes and their role on the land-based material fluxes (including terrigenous sediments and nutrients) should be explored in future studies.

Within 24 h following maximum precipitation, the persistence of the northern and southern river plumes generated by the 2 February event differed (**Figures 8C,D**). On the north coast, the river plume remained evident within 24 h (see **Supplementary Video 1**), possibly due to the continuous river flow and corresponding onshore winds (northeastern), which confined riverine water to the coast. However, when wind direction shifted from northeasterly to northerly, riverine water started to spread toward the south coast, driven by the coastal circulation, as shown by the lower-salinity filament contouring the eastern flank of the island (**Figure 8D** and **Supplementary Video 1**). On the south coast, the river plume weakened and dispersed within 15 h after maximum precipitation (see **Figures 8C,D**, and **Supplementary Video 1**).

Vertical cross-shore transects beginning at two main river outlets (NT1 and ST1 for R2—Ribeira de São Roque do Faial and R7—Ribeira de Machico, respectively; **Figure 8A**) illustrate the vertical variability of these plumes (**Figures 10–12**). A shallow freshwater mass was trapped in the first 2 m of the water column, extending 6 km and 10 km offshore for the NT1 and ST1 transects, respectively, while salinity remained relatively constant below the buoyant plume ($>$36.5 PSU; **Figures 10A,E**). The vertical salinity gradient also implied strong stratification at the surface, as indicated by high values of Brunt–Väisälä Frequency and low-density values ($<$26 sigma-t kg m^{-3}; **Figures 11A,E**). Brunt–Väisälä reached maximum values of 0.05 and 0.09 s^{-2} near the river mouths of Ribeira de São Roque do Faial (R2) and Ribeira de Machico (R7), respectively, similar to the values obtained in other stratified systems (Osadchiev, 2018; Mendes et al., 2021). Moreover, the strong vertical salinity gradient inhibited vertical mixing between the adjacent freshwater and oceanic water parcels, as suggested by Richardson Number $>$ 0.25 (**Figures 12A–F**).

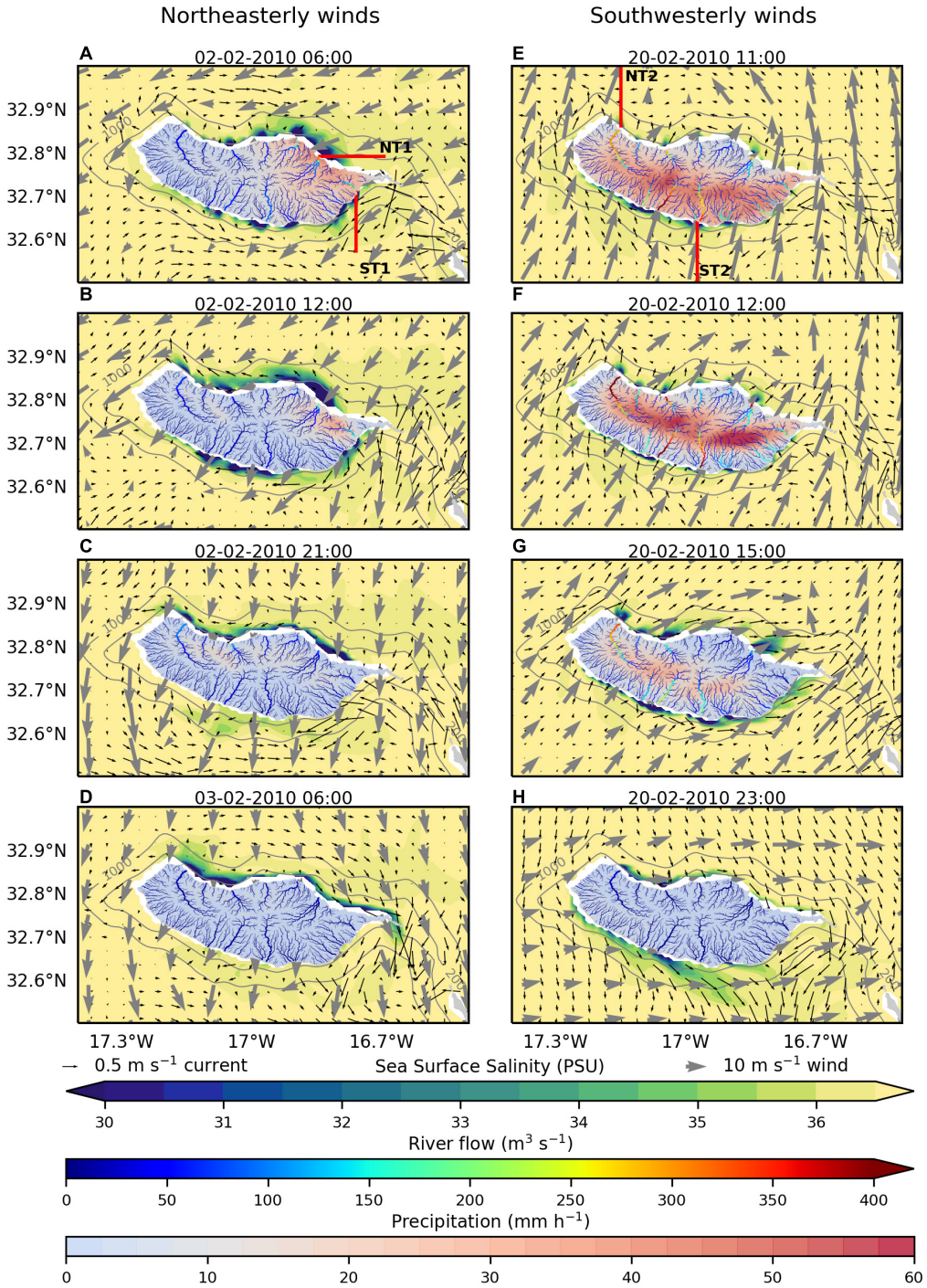

FIGURE 8 | Snapshots of the spatial variability of Sea Surface Salinity (PSU) along with surface currents (black arrows), wind (gray arrows), precipitation (mm h^{-1}), and river flow (m^3 s^{-1}) when **(A–D)** northeasterly (left panel) and **(E–H)** southwesterly (right panel) winds prevailed. See also **Supplementary Video 1**. The gray lines represent the bathymetric lines 200 and 1000 m. The red lines indicate the location of the vertical transects shown in **Figure 10**.

The coastal confinement of the plume on the north coast is also noticeable on the vertical cross-shore transects depicting modeled salinity (**Figures 10B–D**) and Brunt–Väisälä Frequency (**Figures 11B–D**). The river plume retreats from 6 km offshore at 6:00 UTC, to 4 km offshore 6 h later at 12:00 UTC, resulting in a deepening of the freshwater signal. This behavior is likely due to the persistent runoff (∼50 m^3 s^{-1}) and northeasterly wind regime, which contained the freshwater

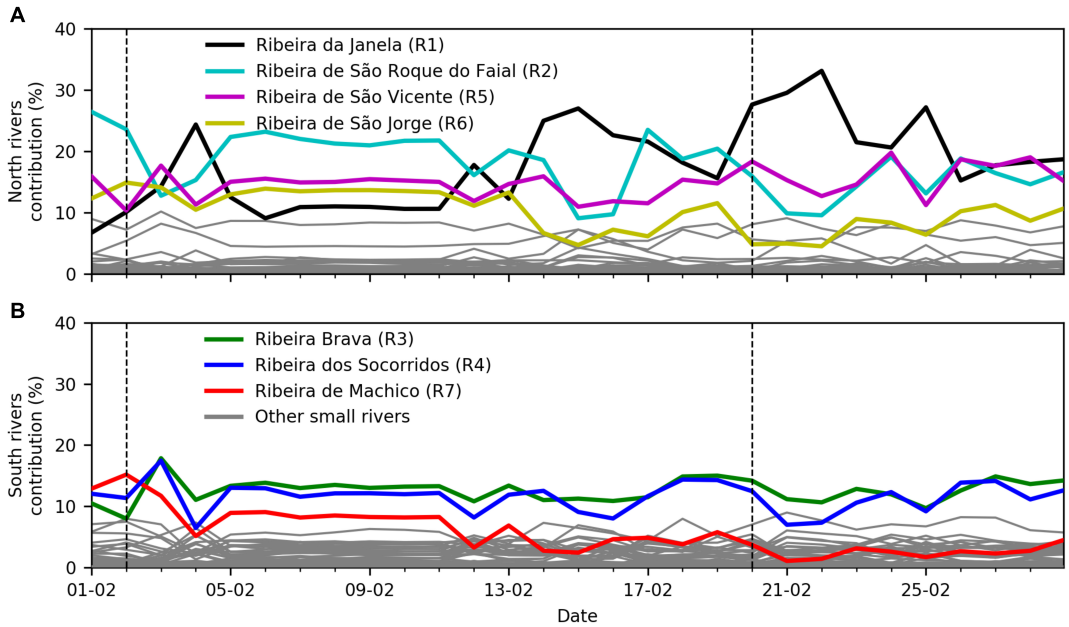

FIGURE 9 | Daily contribution of each river (%) to **(A)** the northern river discharges, and **(B)** the southern river discharges during February 2010. The main seven rivers are identified by different colors, while the remaining small rivers are identified by gray. The black dashed lines identify the days of the flash floods events (2nd and 20th of February 2010).

discharge within a confined region near the coast (**Figure 8C**). The effect of wind on plume confinement is also evident from vertical cross-shore transects depicting modeled zonal-current component (u), in which a negative current (westward) was predicted within the upper 10 m of the water column, while a positive current (eastward) was predicted below 10 m depth, at NT1 (see **Supplementary Figures 4A,B**). The confinement of freshwater at the coast together with strong stratification modified the coastal circulation and prevented the transport of river-borne material to offshore waters. This is evident from daily averaged satellite images of SPM, showing the retention of suspended matter at the coast up to 3 days after the flash flood (**Figures 2A–C**). We believe that this retention zone is characterized by a stable water column (**Figures 11B–D**), with the continuous input of nutrients from river discharges and the decrease in wind intensity (**Figure 7A** and **Supplementary Video 1**) and thus mixing (**Figures 12B–D**) favored phytoplankton growth, as evidenced by the high concentrations of Chla in the northeastern coastal waters observed 2 days after the flash flood (**Figure 2F**). It is suspected that this pattern occurs frequently. The prevailing northeast trade winds often lead to higher rainfall in the north (Caldeira et al., 2002; Prada et al., 2009), and subsequent higher river discharge and erosion, evidenced by the concave morphology of the northern coast compared with the convex morphology seen on the southern coast (**Figure 3C**; Rodrigues et al., 2006; Baioni, 2011), where rainfall is lower. Four of the main drainage basins are in the north (**Figure 3C** and **Table 1**), inducing the transport of large amounts of terrigenous material to the coastal environment during discharge events, which partially explains the brown and turbid appearance of the sea surface on the north side of the island (**Figures 2A–C**). This may also explain the high Chla concentrations often detected near the northern coast (Caldeira et al., 2002), however, more *in situ* observations are required to confirm such speculations.

On the southern side of Madeira Island, river discharges were weak ($\sim$20 m^3 s^{-1}), while tidal induced currents over the ridge that connects Madeira and Desertas Islands were relatively high ($>$0.5 m s^{-1}; **Figures 8C,D** and **Supplementary Figures 4G,H**). From an oceanographic perspective, this region is dynamic, with the recurrent generation of internal waves (Reis et al., in preparation) and upwelling episodes, as detected by cold and Chla-rich water masses in satellite-derived datasets (Caldeira et al., 2002) and *in situ* measurements (Caldeira et al., 2014). Such strong currents promoted a strong vertical shear, which reduced the Richardson Number to values $<$ 0.25 (**Figures 12G,H**) and contributed to the destratification of the water column (**Figures 10G,H**, **11G,H**). These oceanographic processes may have contributed to the offshore spreading of river-borne materials (**Figures 2A–C,E**).

February 20th, 2010—Southwesterly Winds

Surface maps for the 20th of February 2010 flash flood event are presented in **Figures 8E–H**. Similar to the previous episode, the intense southwesterly winds ($\sim$ 20 m s^{-1}) created two tip-jets at the island flanks and a downslope flow, as indicated by high speeds and changeable direction on the northeastern side (**Figures 8E–G**). Such a wind regime agrees with Couto et al. (2012) and Teixeira et al. (2014). Southwesterly winds prevailed until 18:00 UTC (**Supplementary Video 1**), after which

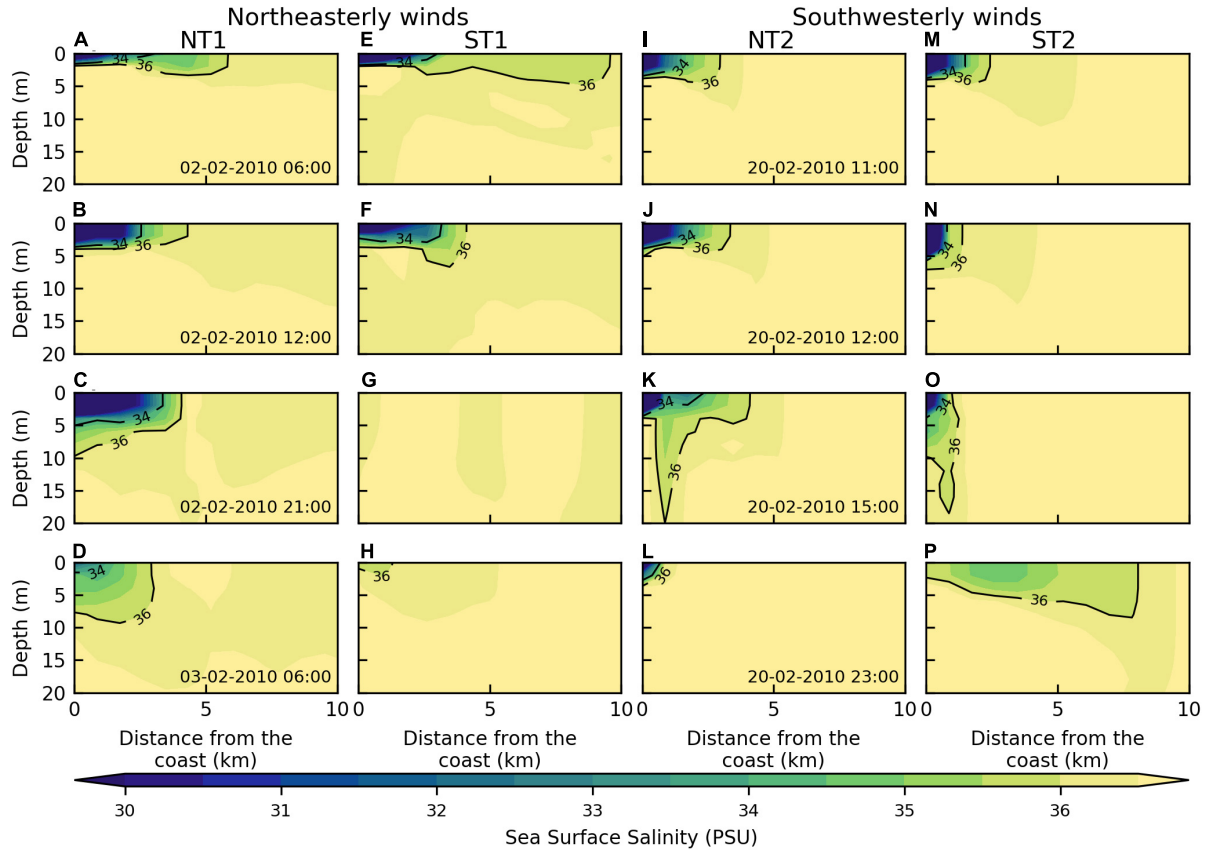

FIGURE 10 | Snapshots (same time steps as shown in **Figure 8**) of vertical variability of salinity with contours in transects **(A–D)** NT1 and **(E–H)** ST1 during northeasterly winds and **(I–L)** NT2 and **(M–P)** ST2 during southwesterly winds. See **Figure 8** for transect locations.

winds weakened and veered to the east, blowing parallel to the coast (**Figure 8H**).

On the 20th of February, extreme and persistent rainfall (>10 mm h^{-1} during 5–10 h) fell mostly over Madeira (Fragoso et al., 2012), but according to Couto et al. (2012), there could also be precipitation over the ocean south of the island. Our model results show that such rainfall started at ∼6:00 UTC (**Supplementary Video 1**) and intensified at 11:00 UTC (∼50 mm h^{-1}), affecting mainly the leeward (southern) side of the island, particularly Funchal and Ribeira Brava (**Figure 8E**). At 12:00 UTC, modeled rainfall reached maximum values in high-altitude regions (∼60 mm h^{-1}), in agreement with previous studies (Luna et al., 2011; Couto et al., 2012; Fragoso et al., 2012; Levizzani et al., 2013).

The discharge rates drastically increased during the period of maximum rainfall (11:00–12:00 UTC), reaching more than 400 m^3 s^{-1} (**Figures 8E,F** and **Supplementary Video 1**). Such a high discharge rate, together with the high amount of solid material moved by the torrential flow, contributed to the flooding of the surrounding areas (Lira et al., 2013; Nguyen et al., 2013; Lopes et al., 2020). This was the case for Ribeira Brava (R3) and Ribeira dos Socorridos (R4), which constituted 14 and 12% of the total river discharges in the southern region during that day (**Figure 9B**). In the northern region, the total river discharges were dominated by Ribeira da Janela (R1) and Ribeira de São Vicente (R5), which accounted for 28 and 18% of total river discharges, respectively (**Figure 9A**). The extreme precipitation and associated surface runoff caused landslides in the upstream sections of the rivers (Oliveira et al., 2011; Lira et al., 2013; Nguyen et al., 2013; Lopes et al., 2020), leading to severe erosion of the drainage basins and river channels. It was estimated that a sediment volume of 2.2–3.4 × 10^5 m^3 and 6.1–9.8 × 10^5 m^3 was eroded during this event in the Funchal drainage basins (corresponding to Ribeira de São João, Ribeira de Santa Luzia and Ribeira de João Gomes) and Ribeira Brava drainage basins, respectively (Lira et al., 2013). Part of the resulting terrigenous sediments and solid material were deposited in the downstream (urbanized) areas of Funchal and Ribeira Brava, causing severe damage to the local infrastructure (see Figures in Fragoso et al., 2012; Levizzani et al., 2013; Lira et al., 2013; Nguyen et al., 2013; Lourenço and Rodrigues, 2016). Nevertheless, high volumes of freshwater and land-based solid material were discharged to southern coastal waters (Lourenço and Rodrigues, 2016), resulting in the formation of a brown-colored freshwater plume significantly large and visible from space 3 days after the event (see **Figure 12** in Oliveira et al., 2011).

The dynamics of these river plumes are shown in the maps of modeled sea surface salinity (**Figures 8E–H**). During the

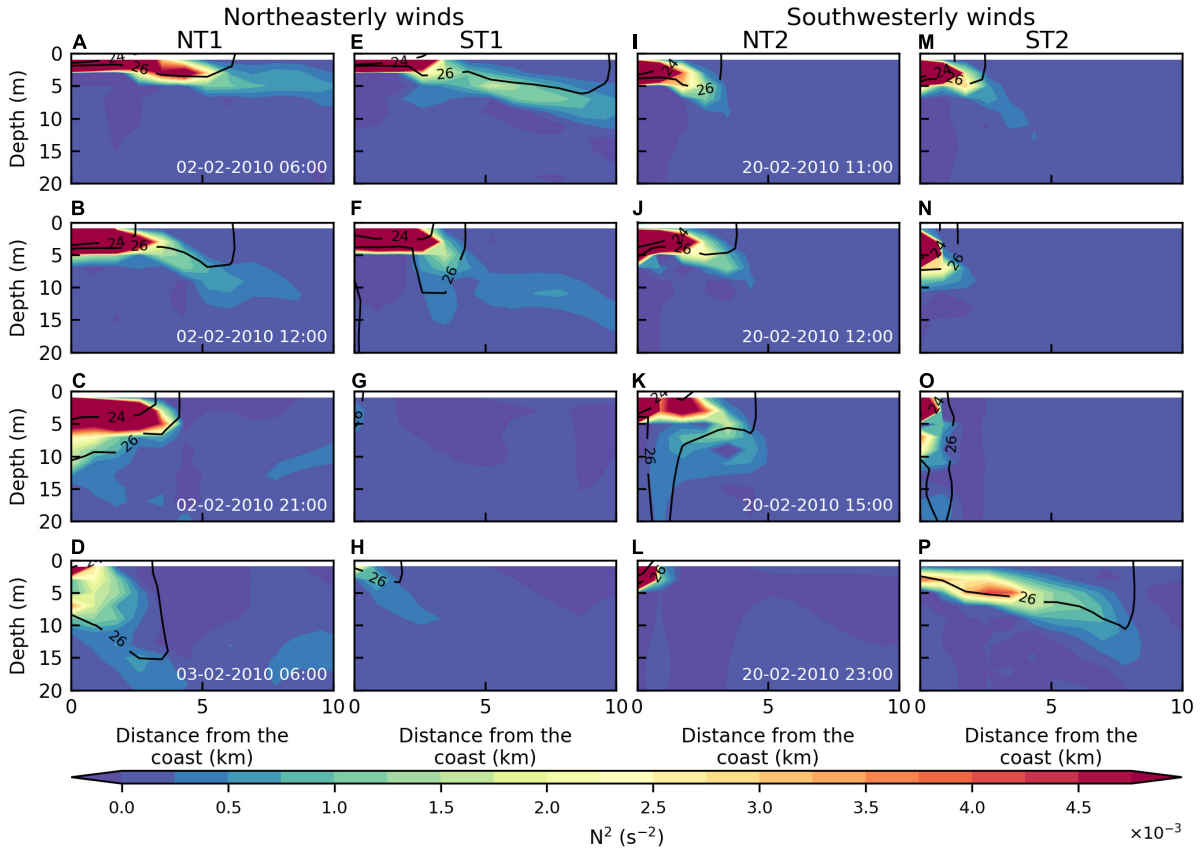

FIGURE 11 | Vertical variability of Brunt–Väisälä Frequency (10^{-3} s^{-2}) with density contours in transects **(A–D)** NT1 and **(E–H)** ST1 during northeasterly winds and **(I–L)** NT2 and **(M–P)** ST2 during southwesterly winds.

early stages of the event, collisions and coalescence of the nearby river plumes resulted in the formation of a thin surface layer with low salinity values (<35 PSU) spreading along the southern coast, while small, localized plumes are also depicted on the northern coast (**Figure 8E**). The combination of rapid river flow and persistent southwesterly winds seem to cause the offshore spreading of the northern plumes (going over the 200 m isobath), whereas the southern plumes remained confined to the coast (**Figure 8F**). A general eastward transport of the plumes was observed 3 h later, particularly for the northern plumes, most likely induced by the wind-driven coastal circulation (**Figure 8G**). When wind veered from the southwest to the west, an intensification of the southward flowing surface ocean currents on the southern side of the island (from ∼ 0.2 to 0.5 m s^{-1}) resulted in the rapid dispersion of the plume (**Figure 8H** and **Supplementary Video 1**). Collisions and coalescence of the plumes were predicted in northern coastal waters, which resulted in the formation of a thin freshwater surface layer along the coast (**Figures 8H**, **10L**). Thus, winds from the west seem to spread the southern river plumes offshore, while the northern river plumes remain confined against the coast. Satellite images of SPM showed very similar responses of the river plumes, verifying the ability of the present numerical framework configuration to represent the plume dynamics (**Figure 2D**).

Vertical cross-shore transects beginning at the river outlets of Ribeira da Janela (R1) and Ribeira dos Socorridos (R4; NT2 and ST2 marked in **Figure 8E**, respectively) further demonstrate the impact of the southwesterly winds on the spreading and mixing of the river plumes (**Figures 10–12**). Similar, to the northeasterly flash flood episode, modeled vertical cross-sections of salinity showed a shallow freshwater lense trapped in the first 4 m of the water column, extending 3 km offshore from the river mouth, overlying high salinity water (>36.5 PSU; **Figures 10I,M** for NT2 and ST2, respectively). Such a shallow river plume is likely associated with the steep topography of the island (**Figure 3C**) and the torrential rains, which cause abrupt discharges at the coast (**Figure 7B**). Shallow river plumes were also found in the steep coastal region of Russia, in which the rapid river discharges formed a hydraulic jump, resulting in the generation of internal waves (Osadchiev, 2018). Considering the similarities between small rivers in Madeira and Russia, internal waves may also be generated during torrential rainfall episodes in Madeira. At 11:00 UTC, the vertical gradient of salinity and density induced strong water column stratification, as confirmed by high values of Brunt–Väisälä (**Figures 11I,M**), reaching maximum values of 0.06 s^{-2} near the river mouths of Ribeira da Janela (R1) and Ribeira dos Socorridos (R4). At this time, vertical shear was not sufficiently strong to induce turbulent mixing between the

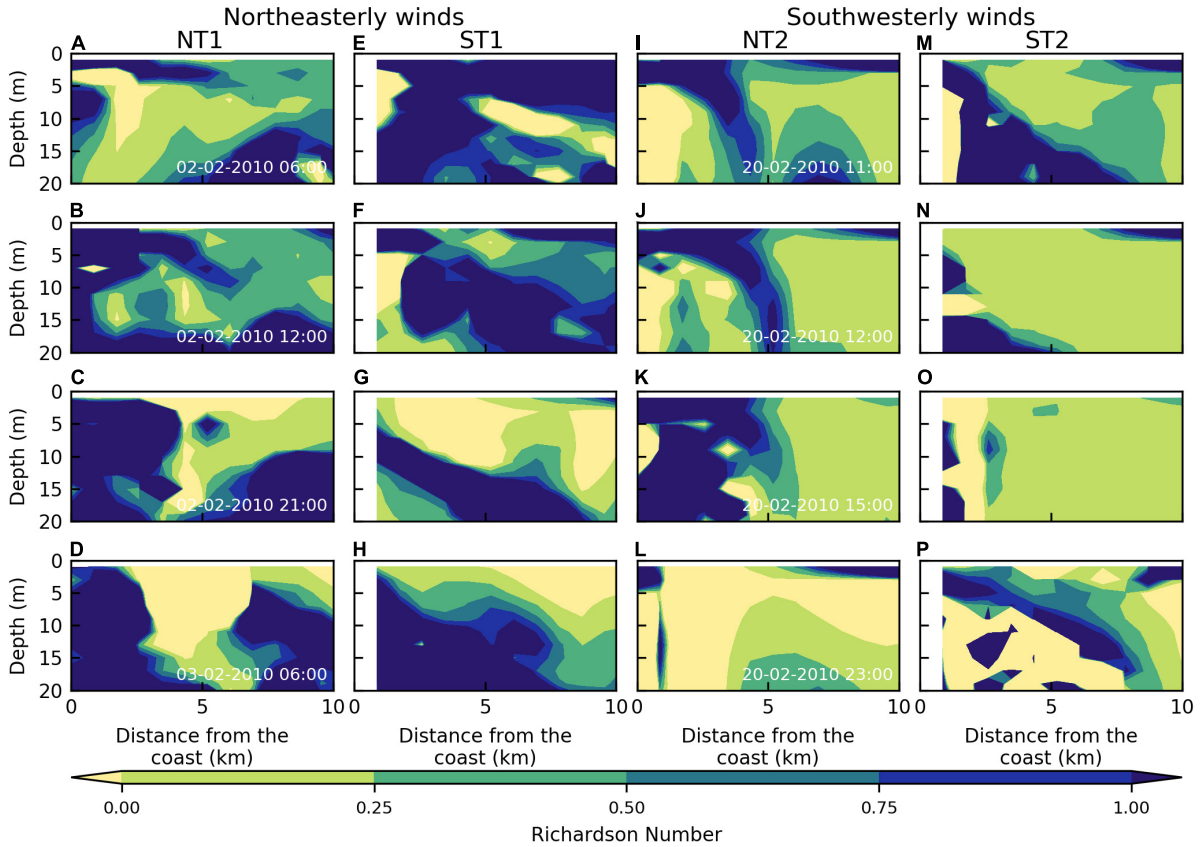

FIGURE 12 | Vertical variability of Richardson Number in transects **(A–D)** NT1 and **(E–H)** ST1 during northeasterly winds and **(I–L)** NT2 and **(M–P)** ST2 during southwesterly winds.

river plume and the oceanic waters, as indicated by Richardson Number > 0.25 near the river mouth (**Figures 12I,M**). Offshore waters were characterized by Richardson Number < 0.25, suggesting strong vertical mixing (**Figures 12I,M**), and constant values for salinity (**Figures 10I,M**) and Brunt–Väisälä Frequency (**Figures 11I,M**). The confinement of the southern river plumes against the coast is depicted in the vertical transects of salinity (**Figures 10M–O**) and Brunt–Väisälä Frequency (**Figures 11M–O**), where a retraction from 3 to 1 km away from the river outlet and a deepening of the plume to 20 m depth was observed. Such confinement is likely associated with the opposing wind flow (**Figures 8E–G**), acting to restrict offshore spreading of the plume (Zhao et al., 2018). During this same period, the northern river plumes tended to spread offshore (**Figures 8E–G**), likely facilitated by the offshore winds moving in the same direction as the plume front on the northern side of the island (Zhao et al., 2018). A similar wind-induced confinement/dispersion of the river plume in the north/south coast was observed on the 2nd of February (characterized by northeasterly winds), further highlighting the importance of the wind on the horizontal dispersion of the river plumes. Notwithstanding, one should note that the turbulent scheme used may favor the vertical mixing of the river plume (i.e., overmix; Li et al., 2005; Robertson and Dong, 2019) and thus weakening the horizontal dispersion of the northern (2nd of February; **Figures 12B–D**) and southern river plume (20th of February; **Figures 12N,O**). The shift in wind direction from southwest to the west (between 15:00 UTC and 23:00 UTC 20 February 2010; **Figures 8G,H**) impacted the dynamics of the modeled northern and southern river plumes. Under westerly winds, the horizontal extent of the northern river plume was limited by the strong landward (northerly) wind-driven currents (**Figure 8H**), pressing the plume against the northern coast (**Figures 10K,L**). Off the southern coast of Madeira, westerly winds and subsequently southward surface currents, caused modeled river plumes to spread farther offshore, extending ∼ 8 km from river outlets (**Figures 10P**, **11P**, **12P**). It is important to note that the dominant chemical weathering of basalt occurring in Madeira Island produces several types of soils (**Supplementary Figure 1**) rich in organic matter, nutrients (e.g., silicate), and trace metals (e.g., magnesium and iron; Van Der Weijden and Pacheco, 2003). Considering that all these elements regulate phytoplankton growth (Barcelos e Ramos et al., 2017), we believe that this buoyant river plume transported high amounts of land-based material and nutrients offshore (**Figure 2D**), which combined with the concurrent decrease in wind speed (**Figure 7A** and **Supplementary Video 1**) enhanced phytoplankton growth. This combination of processes is likely responsible for Chla-rich filament detected in satellite observations, which extended 70 km offshore 3 days after the 20 February 2010 flash flood event (**Figure 2H**). Given that salinity

has a chemically conservative character, it is often used as a tracer of a conservative mixing between freshwater and seawater. For conservative nutrients, salinity can be used as a proxy to indicate the mixing processes affecting nutrient distribution (Liss, 1976). In dynamic environments, such as the ocean, many physical and biogeochemical processes including coastal upwelling, biological processes (e.g., nutrient uptake), remineralization, desorption, and adsorption of nutrients on settling particles (e.g., Carstensen et al., 2020; Jiang et al., 2021) cause relationships between salinity and nutrient concentrations to deviate from conservative behavior. Therefore, the use of salinity as a proxy for land-based nutrient inputs may not fully reflect nutrient distributions. As such, we believe that the coupling of a biogeochemical model to investigate the implications of flood episodes on nutrient cycling should be considered in follow up studies.

CONCLUSION

This study investigated the impact of February 2010 flash floods on the coastal waters around Madeira Island, focusing on the processes driving the dynamics of the river plumes, responsible for favoring the maximum monthly-averaged Chla concentrations around the island over the last two decades (**Figure 1B**).

Based on coupled air-sea-land numerical simulations, our results demonstrate that the wind is the main mechanism controlling river plume dynamics and subsequent impact on the coastal waters. Onshore winds confined the plumes against the coast on both sides of the island. In particular, on 2 February 2010, onshore winds (northeasterly) confined the northern plumes (**Figures 8A–C**), which resulted in strong horizontal and vertical density gradients (**Figures 10A–C**, **11A–C**). Such confinement prevented the offshore transport of river-borne material (**Figures 2A–C**), favoring phytoplankton growth in inshore waters, as suggested by high concentrations of sea surface Chlorophyll-a in the northeastern region (**Figure 2F**). Considering the predominance of the impinging northeasterly winds, we believe that this retention zone is likely responsible for frequent localized eutrophication patches in the northeastern region of the island (Caldeira et al., 2002). On 20 February 2010 (the catastrophic flash flood event), onshore winds (southwesterly) caused confinement of the river plume characterized by a strong vertical density gradient in coastal waters on the south side of Madeira Island (**Figures 10M–O**, **11M–O**). Offshore winds (southwesterly) caused plumes to spread offshore, as suggested by the eastward drift of the plumes in coastal waters on the north side of the island (**Figures 8E–G**). Cross-shore winds (westerly) pressed the northern plumes against the coast, leading to the coalescence and collisions of the plumes, and to the formation of a thin freshwater lenses that spread along the coast (**Figure 8H**). However, the spreading of the buoyant river plume offshore was observed in the southern region (**Figure 8H**), forming a high Chlorophyll-a patch protruding 70 km away from the island (**Figure 2H**). The persistence of plumes was governed by the duration of rainfall, river discharges, and strong onshore winds, while offshore winds and strong tidal currents generated over the underwater ridge that connects Madeira to Desertas Islands facilitated the dispersion of the plume (**Figures 2**, **8**).

Overall, our numerical study suggests that the island's surface runoff associated with high rainfall events may indeed enhance the primary productivity of the coastal waters surrounding Madeira Island, as shown by the low salinity river plumes serving as a proxy for the land-based nutrient input on the two distinct precipitation events. The latter suggests that IME episodes related to land runoff can occur frequently. The finding of this study reinforces the important role of small mountainous rivers in the delivery of river-borne material to the coastal ocean, particularly during flash floods episodes, and subsequent on phytoplankton growth. In this sense, we deem this episode as the "Land Mass Effect."

Besides the strong likelihood that high runoff events make an important contribution to the primary productivity in Madeira's coastal waters, *in situ* measurements (e.g., river gauges, salinity, and nutrients) are required to assess the model configurations (including model sensitivity analysis to the coupling frequency, boundary conditions, and vertical turbulence schemes) and future numerical studies. The integration of such *in situ* data in the present numerical framework is expected to improve the model capacity to investigate the occurrence of localized phenomena in different spatial and temporal scales, including the generation of internal waves related to rapid river flow and processes of coalescence and collisions of the rivers of Madeira. As future work, the coupling of a biogeochemical model would help to investigate the implications of flood episodes on the nutrients cycling and on the phytoplankton communities around Madeira Island. One should also consider that similar processes may affect the productivity of coastal waters in other oceanic islands, and that more observational and numerical investigations are needed to quantify the relative contribution of land runoff on the productivity of island coastal waters.

DATA AVAILABILITY STATEMENT

The satellite datasets used in this study can be found in online repositories cited throughout the article. Upon request, the raw data supporting the conclusions of this article can be made available by the authors, without undue reservation.

AUTHOR CONTRIBUTIONS

AR performed the data analysis and wrote most of the manuscript. RC and CC designed the numerical framework and guided the investigation. RV performed the COAWST numerical simulations. CC performed the MOHID-Land simulations in collaboration with AO. RF performed the validation of the WRF atmospheric model. GN performed part of the analysis of satellite-derived data of Chlorophyll-a. All authors contributed to the writing of the manuscript and approved the final version.

FUNDING

This work was partially financed by the Oceanic Observatory of Madeira Project (M1420-01-0145-FEDER-000001-Observatório Oceânico da Madeira-OOM) and by the Fundação para a Ciência e Tecnologia (FCT) through IDL project (UIDB/50019/2020). The COAWST numerical simulations were performed on the Cirrus platform of FCT, I.P. Advanced Computing Project (CPCA/A2/6193/2020).

ACKNOWLEDGMENTS

We would like to thank IPMA (Portuguese Institute for Sea and Atmosphere) for providing access to the meteorological data used to validate the atmospheric model; DROTe (Direção Regional do Ordenamento do Território) for providing the topography and maps for soil types and land-use used in the numerical systems; and CESGA (Supercomputing Center of Galicia) for enabling some of the computational resources used to conduct the model simulations. We are particularly indebted to comments from the reviewers that substantially improved the first version of the manuscript. Serena Blyth Lee provided a detailed and thorough review, for which we are very grateful.

SUPPLEMENTARY MATERIAL

The Supplementary Material for this article can be found online at: https://www.frontiersin.org/articles/10.3389/fmars.2021.749638/full#supplementary-material

REFERENCES

Alves, J. M. R., Caldeira, R. M. A., and Miranda, P. M. A. (2020). Dynamics and oceanic response of the Madeira tip-jets. *Q. J. R. Meteorol. Soc.* 146, 3048–3063. doi: 10.1002/qj.3825

Alves, J. M. R., Tomé, R., Caldeira, R. M. A., Miranda, P. M. A., and Munoz-perez, J. J. (2021). Asymmetric ocean response to atmospheric forcing in an Island Wake: a 35-year high-resolution study. *Front. Mar. Sci.* 8:624392. doi: 10.3389/fmars.2021.624392

Andrade, I., Sangrà, P., Hormazabal, S., and Correa-Ramirez, M. (2014). Island mass effect in the Juan Fernández Archipelago (33°S), Southeastern Pacific. *Deep. Res. 1 Oceanogr. Res. Pap.* 84, 86–99. doi: 10.1016/j.dsr.2013.10.009

Arístegui, J., Tett, P., Hernández-Guerra, A., Basterretxea, G., Montero, M. F., Wild, K., et al. (1997). The influence of island-generated eddies on chlorophyll distribution: a study of mesoscale variation around Gran Canaria. *Deep Sea Res. 1 Oceanogr. Res. Pap.* 44, 71–96. doi: 10.1016/S0967-0637(96)00093-3

Ayouche, A., Carton, X., Charria, G., Theettens, S., and Ayoub, N. (2020). Instabilities and vertical mixing in river plumes: application to the Bay of Biscay. *Geophys. Astrophys. Fluid Dyn.* 114, 650–689. doi: 10.1080/03091929.2020.1814275

Ayouche, A., Charria, G., Carton, X., Ayoub, N., and Theetten, S. (2021). Non-linear processes in the gironde river plume (North-East Atlantic): instabilities and mixing. *Front. Mar. Sci.* 8:701773. doi: 10.3389/fmars.2021.701773

Azevedo, C. C., Camargo, C. M. L., Alves, J., and Caldeira, R. M. A. (2021). Convection and heat transfer in Island (Warm) wakes. *J. Phys. Oceanogr.* 51, 1187–1203. doi: 10.1175/JPO-D-20-0103.1

Baioni, D. (2011). Human activity and damaging landslides and floods on Madeira Island. *Nat. Hazards Earth Syst. Sci.* 11, 3035–3046. doi: 10.5194/nhess-11-3035-2011

Bao, H., Lee, T. Y., Huang, C., Feng, X., Dai, M., and Kao, S. J. (2015). Importance of Oceanian small mountainous rivers (SMRs) in global land-to-ocean output of lignin and modern biospheric carbon. *Sci. Rep.* 5:16217. doi: 10.1038/srep16217

Barcelos e Ramos, J., Schulz, K. G., Voss, M., Narciso, Á, Müller, M. N., Reis, F. V., et al. (2017). Nutrient-specific responses of a phytoplankton community: a case study of the North Atlantic Gyre, Azores. *J. Plankton Res.* 39, 744–761. doi: 10.1093/plankt/fbx025

Basdurak, N. B., Largier, J. L., and Nidzieko, N. J. (2020). Modeling the dynamics of small-scale river and creek plumes in tidal waters. *J. Geophys. Res. Ocean.* 125:e2019JC015737. doi: 10.1029/2019JC015737

Becker, J. J., Sandwell, D. T., Smith, W. H. F., Braud, J., Binder, B., Depner, J., et al. (2009). Global bathymetry and elevation data at 30 Arc seconds resolution: SRTM30_PLUS. *Mar. Geod.* 32, 355–371. doi: 10.1080/01490410903297766

Bell, P. R. F. (1992). Eutrophication and coral reefs-some examples in the Great Barrier Reef lagoon. *Water Res.* 26, 553–568. doi: 10.1016/0043-1354(92)90228-V

Belo-Pereira, M., and Santos, J. A. (2020). Air-traffic restrictions at the Madeira International Airport Due to adverse winds: links to synoptic-scale patterns and orographic effects. *Atmosphere* 11:1257. doi: 10.3390/atmos11111257

Bernard-Jannin, L., Brito, D., Sun, X., Jauch, E., Neves, R., Sauvage, S., et al. (2016). Spatially distributed modelling of surface water-groundwater exchanges during overbank flood events–a case study at the Garonne River. *Adv. Water Resour.* 94, 146–159. doi: 10.1016/j.advwatres.2016.05.008

Booij, N., Ris, R. C., and Holthuijsen, L. H. (1999). A third-generation wave model for coastal regions 1. Model description and validation. *J. Geophys. Res. Ocean.* 104, 7649–7666. doi: 10.1029/98JC02622

Branch, R. A., Horner-Devine, A. R., Kumar, N., and Poggioli, A. R. (2020). River plume Liftoff dynamics and surface expressions. *Water Resour. Res.* 56:e2019WR026475. doi: 10.1029/2019WR026475

Brito, D., Campuzano, F. J., Sobrinho, J., Fernandes, R., and Neves, R. (2015). Integrating operational watershed and coastal models for the Iberian Coast: watershed model implementation–a first approach. *Estuar. Coast. Shelf Sci.* 167, 138–146. doi: 10.1016/j.ecss.2015.10.022

Brito, D., Neves, R., Branco, M. A., Gonçalves, M. C., and Ramos, T. B. (2017). Modeling flood dynamics in a temporary river draining to an eutrophic reservoir in southeast Portugal. *Environ. Earth Sci.* 76:377. doi: 10.1007/s12665-017-6713-7

Brito, D., Ramos, T. B., Gonçalves, M. C., Morais, M., and Neves, R. (2018). Integrated modelling for water quality management in a eutrophic reservoir in south-eastern Portugal. *Environ. Earth Sci.* 77:40. doi: 10.1007/s12665-017-7221-5

Brodie, J., Schroeder, T., Rohde, K., Faithful, J., Masters, B., Dekker, A., et al. (2010). Dispersal of suspended sediments and nutrients in the Great Barrier Reef lagoon during river-discharge events: conclusions from satellite remote sensing and concurrent flood-plume sampling. *Mar. Freshw. Res.* 61, 651–664. doi: 10.1071/MF08030

Büttner, G., and Kosztra, B. (2007). CLC2006 technical guidelines. *Eur. Environ. Agency Tech. Rep.* 1:70.

Caetano, C. (2014). *Avaliação do Risco de Aluviões das Ribeiras da Ilha da Madeira*. Master's thesis. Lisboa: Instituto Superior Técnico de Lisboa.

Caldeira, R., Couvelard, X., Vieira, R., Lucas, C., Sala, I., and Casanova, I. V. (2016). Challenges of building an operational ocean forecasting system for small island regions: regional to local. *J. Oper. Oceanogr.* 9:12. doi: 10.1080/1755876X.2016.1205304

Caldeira, R. M. A. (2018). *Island Wakes*, 3rd Edn. Amsterdam: Elsevier Inc. doi: 10.1016/B978-0-12-409548-9.11614-8

Caldeira, R. M. A., Groom, S., Miller, P., Pilgrim, D., and Nezlin, N. P. (2002). Sea-surface signatures of the island mass effect phenomena around Madeira Island, Northeast Atlantic. *Remote Sens. Environ.* 80, 336–360. doi: 10.1016/S0034-4257(01)00316-9

Caldeira, R. M. A., Marchesiello, P., Nezlin, N. P., DiGiacomo, P. M., and McWilliams, J. C. (2005). Island wakes in the Southern California Bight. *J. Geophys. Res. Ocean.* 110, 1–20. doi: 10.1029/2004JC002675

Caldeira, R. M. A., Russell, P., and Amorim, A. (2001). Evidence of an unproductive coastal front in Baía D'Abra, an embayment on the southeast of Madeira Island, Portugal. *Bull. Mar. Sci.* 69, 1057–1072.

Caldeira, R. M. A., and Sangrà, P. (2012). Complex geophysical wake flows Madeira archipelago case study. *Ocean Dyn.* 62, 683–700. doi: 10.1007/s10236-012-0528-6

Caldeira, R. M. A., Stegner, A., Couvelard, X., Araújo, I. B., Testor, P., and Lorenzo, A. (2014). Evolution of an oceanic anticyclone in the lee of Madeira Island: *in situ* and remote sensing survey. *J. Geophys. Res. Ocean.* 119, 1195–1216. doi: 10.1002/2013JC009493

Caldeira, R. M. A., and Tomé, R. (2013). Wake response to an ocean-feedback mechanism: Madeira Island case study. *Boundary Layer Meteorol.* 148, 419–436. doi: 10.1007/s10546-013-9817-y

Canning-Clode, J., Kaufmann, M., Molis, M., Wahl, M., and Lenz, M. (2008). Influence of disturbance and nutrient enrichment on early successional fouling communities in an oligotrophic marine system. *Mar. Ecol.* 29, 115–124. doi: 10.1111/j.1439-0485.2007.00210.x

Canuto, N., Ramos, T. B., Oliveira, A. R., Simionesei, L., Basso, M., and Neves, R. (2019). Influence of reservoir management on Guadiana streamflow regime. *J. Hydrol. Reg. Stud.* 25:100628. doi: 10.1016/j.ejrh.2019.100628

Carstensen, J., Conley, D. J., Almroth-Rosell, E., Asmala, E., Bonsdorff, E., Fleming-Lehtinen, V., et al. (2020). Factors regulating the coastal nutrient filter in the Baltic Sea. *Ambio* 49, 1194–1210. doi: 10.1007/s13280-019-01282-y

Cassianides, A., Martinez, E., Maes, C., Carton, X., and Gorgues, T. (2020). Monitoring the influence of the mesoscale ocean dynamics on phytoplanktonic plumes around the Marquesas Islands using multi-satellite missions. *Remote Sens.* 12:2520. doi: 10.3390/RS12162520

Chao, S.-Y., and Boicourt, W. C. (1986). Onset of estuarine plumes. *J. Phys. Oceanogr.* 16, 2137–2149. doi: 10.1175/1520-04851986016<2137:OOEP<2.0.CO;2

Chapman, D. C. (1985). Numerical treatment of cross-shelf open boundaries in a barotropic coastal ocean model. *J. Phys. Ocean.* 15, 1060–1075. doi: 10.1175/1520-04851985015<1060:ntocso<2.0.co;2

Chassot, E., Bonhommeau, S., Dulvy, N. K., Mélin, F., Watson, R., Gascuel, D., et al. (2010). Global marine primary production constrains fisheries catches. *Ecol. Lett.* 13, 495–505. doi: 10.1111/j.1461-0248.2010.01443.x

Chen, F., MacDonald, D. G., and Hetland, R. D. (2009). Lateral spreading of a near-field river plume: observations and numerical simulations. *J. Geophys. Res. Ocean.* 114, 1–12. doi: 10.1029/2008JC004893

Correia, F. N. (1983). "Alguns procedimentos adaptados pelo soil conservation service na determinação de Caudais de Cheia em Pequenas Bacias Naturais e Urbanas," in *Proceedings of the Seminário 290 "Contribuição para o Cálculo de Drenagem de Águas Pluviais em Zonas Urbanas*, (Lisboa: Laboratório Nacional de Engenharia Civil).

Couto, F. T., Salgado, R., and Costa, M. J. (2012). Analysis of intense rainfall events on Madeira Island during the 2009/2010 winter. *Nat. Hazards Earth Syst. Sci.* 12, 2225–2240. doi: 10.5194/nhess-12-2225-2012

Couto, F. T., Salgado, R., Costa, M. J., and Prior, V. (2015). Precipitation in the Madeira Island over a 10-year period and the meridional water vapour transport during the winter seasons. *Int. J. Climatol.* 35, 3748–3759. doi: 10.1002/joc.4243

Couvelard, X., Caldeira, R. M. A., Araújo, I. B., and Tomé, R. (2012). Wind mediated vorticity-generation and eddy-confinement, leeward of the Madeira Island: 2008 numerical case study. *Dyn. Atmos. Ocean.* 58, 128–149. doi: 10.1016/j.dynatmoce.2012.09.005

Dandonneau, Y., and Charpy, L. (1985). An empirical approach to the island mass effect in the south tropical Pacific based on sea surface chlorophyll concentrations. *Deep Sea Res. A Oceanogr. Res. Pap.* 32, 707–721. doi: 10.1016/0198-0149(85)90074-3

Dasari, H. P., and Salgado, R. (2015). Numerical modelling of heavy rainfall event over Madeira Island in Portugal: sensitivity to different micro physical processes. *Meteorol. Appl.* 22, 113–127. doi: 10.1002/met.1375

David, J. S. (1976). *Drenagem de Estradas, Caminhos de ferro e Aeródromos. Estudo Hidrogeológico. Determinação de Caudais de Ponta de cheia em Pequenas Bacias Hidrográficas*. Lisboa: Laboratório Nacional de Engenharia Civil, SH-DHF.

De Meij, A., and Vinuesa, J. F. (2014). Impact of SRTM and corine land cover data on meteorological parameters using WRF. *Atmos. Res.* 143, 351–370. doi: 10.1016/j.atmosres.2014.03.004

Doty, M. S., and Oguri, M. (1956). The island mass effect. *ICES J. Mar. Sci.* 22, 33–37. doi: 10.1093/icesjms/22.1.33

Dresback, K. M., Fleming, J. G., Blanton, B. O., Kaiser, C., Gourley, J. J., Tromble, E. M., et al. (2013). Skill assessment of a real-time forecast system utilizing a coupled hydrologic and coastal hydrodynamic model during Hurricane Irene (2011). *Cont. Shelf Res.* 71, 78–94. doi: 10.1016/j.csr.2013.10.007

Egbert, G. D., and Erofeeva, S. Y. (2002). Efficient inverse modeling of barotropic ocean tides. *J. Atmos. Ocean. Technol.* 19, 183–204. doi: 10.1175/1520-04262002019<0183:EIMOBO<2.0.CO;2

Epelde, A. M., Antiguedad, I., Brito, D., Jauch, E., Neves, R., Garneau, C., et al. (2016). Different modelling approaches to evaluate nitrogen transport and turnover at the watershed scale. *J. Hydrol.* 539, 478–494. doi: 10.1016/j.jhydrol.2016.05.066

Espinosa, L. A., and Portela, M. M. (2020). Rainfall trends over a small island teleconnected to the North Atlantic oscillation–the case of Madeira Island, Portugal. *Water Resour. Manag.* 34, 4449–4467. doi: 10.1007/s11269-020-02668-4

Espinosa, L. A., Portela, M. M., Filho, J. D. P., and Zelenakova, M. (2021). Bivariate modelling of a teleconnection index and extreme rainfall in a small North Atlantic Island. *Climate* 9, 1–21. doi: 10.3390/cli9050086

Fong, D. A., and Geyer, W. R. (2001). Response of a river plume during an upwelling favorable wind event. *J. Geophys. Res. Ocean.* 106, 1067–1084. doi: 10.1029/2000JC900134

Fong, D. A., and Geyer, W. R. (2002). The alongshore transport of freshwater in a surface-trapped river plume. *Br. J. Oral Maxillofac. Surg.* 23, 251–258. doi: 10.1175/1520-04852002032<0957:TATOFI<2.0.CO;2

Fragoso, M., Trigo, R. M., Pinto, J. G., Lopes, S., Lopes, A., Ulbrich, S., et al. (2012). The 20 February 2010 Madeira flash-floods: synoptic analysis and extreme rainfall assessment. *Nat. Hazards Earth Syst. Sci.* 12, 715–730. doi: 10.5194/nhess-12-715-2012

Garvine, R. W. (1999). Penetration of buoyant coastal discharge onto the continental shelf: a numerical model experiment. *J. Phys. Oceanogr.* 29, 1892–1909. doi: 10.1175/1520-04851999029<1892:pobcdo<2.0.co;2

Gonçalves, J. A. V. (2016). *Caracterização do Coeficiente de Rugosidade e seu Efeito no Escoamento em Canais Naturais Simulação e modelação (à escala) no laboratório de hidráulica Aplicação às ribeiras do Funchal. Master's thesis*. Funchal: University of Madeira.

Gorricha, J., Lobo, V., and Costa, A. C. (2012). "Spatial characterization of extreme precipitation in Madeira Island using geostatistical procedures and a 3D SOM," in *Proceedings of the GEOProcessing 2012. The Fourth International Conference on Advanced Geographic Information Systems, Applications, and Services*, Valencia, 98–104.

Gouveia-Reis, D., Guerreiro Lopes, L., and Mendonça, S. (2016). A dependence modelling study of extreme rainfall in Madeira Island. *Phys. Chem. Earth A/B/C* 94, 85–93. doi: 10.1016/j.pce.2015.11.006

Gove, J. M., McManus, M. A., Neuheimer, A. B., Polovina, J. J., Drazen, J. C., Smith, C. R., et al. (2016). Near-island biological hotspots in barren ocean basins. *Nat. Commun.* 7:10581. doi: 10.1038/ncomms10581

Grubišic, V., Sachsperger, J., and Caldeira, R. M. A. (2015). Atmospheric wake of madeira: first aerial observations and numerical simulations. *J. Atmos. Sci.* 72, 4755–4776. doi: 10.1175/JAS-D-14-0251.1

Hasegawa, D. (2019). "Island mass effect," in *Kuroshio Current: Physical, Biogeochemical, and Ecosystem Dynamics*, eds T. Nagai, H. Saito, K. Suzuki, and T. Motomitsu (Washington, DC: American Geophysical Union (AGU)), 163–174. doi: 10.1002/9781119428428.ch10

Hasegawa, D., Yamazaki, H., Lueck, R. G., and Seuront, L. (2004). How islands stir and fertilize the upper ocean. *Geophys. Res. Lett.* 31, 2–5. doi: 10.1029/2004GL020143

Hilton, R. G., Galy, A., Hovius, N., Horng, M. J., and Chen, H. (2011). Efficient transport of fossil organic carbon to the ocean by steep mountain rivers: an orogenic carbon sequestration mechanism. *Geology* 39, 71–74. doi: 10.1130/G31352.1

Hong, S.-Y., and Lim, J.-O. J. (2006). The WRF single-moment 6-class microphysics scheme (WSM6). *Asia Pac. J. Atmos. Sci.* 42, 129–151.

Horner-Devine, A. R., Fong, D. A., Monismith, S. G., and Maxworthy, T. (2006). Laboratory experiments simulating a coastal river inflow. *J. Fluid Mech.* 555, 203–232. doi: 10.1017/S0022112006008937

Horner-Devine, A. R., Hetland, R. D., and MacDonald, D. G. (2015). Mixing and transport in coastal river plumes. *Annu. Rev. Fluid Mech.* 47, 569–594. doi: 10.1146/annurev-fluid-010313-141408

Hrachowitz, M., Savenije, H. H. G., Blöschl, G., McDonnell, J. J., Sivapalan, M., Pomeroy, J. W., et al. (2013). A decade of predictions in ungauged basins (PUB)-a review. *Hydrol. Sci. J.* 58, 1198–1255. doi: 10.1080/02626667.2013.803183

Jacob, R., Larson, J., and Ong, E. (2005). M × N communication and parallel interpolation in community climate system model version 3 using the model coupling toolkit. *Int. J. High Perform. Comput. Appl.* 19, 293–307. doi: 10.1177/1094342005056116

James, A. K., Washburn, L., Gotschalk, C., Maritorena, S., Alldredge, A., Nelson, C. E., et al. (2020). An island mass effect resolved near Mo'orea, French Polynesia. *Front. Mar. Sci.* 7:16. doi: 10.3389/fmars.2020.00016

Janjic, Z. I. (1990). The step-mountain coordinate: physical package. *Mon. Weather Rev.* 118, 1429–1443. doi: 10.1175/1520-04931990118<1429:TSMCPP<2.0.CO;2

Janjic, Z. I. (1994). The step-mountain eta coordinate model: further developments of the convection, viscous sublayer, and turbulence closure schemes. *Mon. Weather Rev.* 122, 927–945. doi: 10.1175/1520-04931994122<0927:TSMECM<2.0.CO;2

Janjic, Z. I. (1996). "The surface layer in the NCEP eta model," in *Proceedings of the 11th Conference on Numerical Weather Prediction*, Norfolk, VA, 354–355. doi: 10.1371/journal.pone.0117082

Janjić, Z. I. (2002). *Nonsingular Implementation of the Mellor-Yamada level 2.5 Scheme in the NCEP Meso Model*. NCEP Office Note 437. College Park, MD: 61.

Jiang, Z.-P., Tong, Y., Tong, M., Yuan, J., Cao, Q., and Pan, Y. (2021). The effects of suspended particulate matter, nutrient, and salinity on the growth of *Amphidinium carterae* under estuary environmental conditions. *Front. Mar. Sci.* 8:690764. doi: 10.3389/fmars.2021.690764

Jones, E. C. (1962). Evidence of an island effect upon the standing crop of zooplankton near the marquesas islands, central pacific. *ICES J. Mar. Sci.* 27, 223–231. doi: 10.1093/icesjms/27.3.223

Jones, P. W. (1999). First- and second-order conservative remapping schemes for grids in spherical coordinates. *Mon. Weather Rev.* 127, 2204–2210. doi: 10.1175/1520-04931999127<2204:FASOCR<2.0.CO;2

Kao, S. J., and Milliman, J. D. (2008). Water and sediment discharge from small mountainous rivers, Taiwan: the roles of lithology, episodic events, and human activities. *J. Geol.* 116, 431–448. doi: 10.1086/590921

Korotenko, K. A., Osadchiev, A. A., Zavialov, P. O., Kao, R. C., and Ding, C. F. (2014). Effects of bottom topography on dynamics of river discharges in tidal regions: case study of twin plumes in Taiwan Strait. *Ocean Sci.* 10, 863–879. doi: 10.5194/os-10-863-2014

Larson, J., Jacob, R., and Ong, E. (2005). The model coupling toolkit: a new Fortran90 Toolkit for building multiphysics parallel coupled models. *Int. J. High Perform. Comput. Appl.* 19, 277–292. doi: 10.1177/10943420050056115

Leichter, J. J., Shellenbarger, G., Genovese, J. S., and Wing, R. S. (1998). Breaking internal waves on a Florida (USA) coral reef: a plankton pump at work? *Mar. Ecol. Prog. Ser.* 166, 83–97. doi: 10.3354/meps166083

Leichter, J. J., Stewart, H. L., and Miller, S. L. (2003). Episodic nutrient transport to Florida coral reefs. *Limnol. Oceanogr.* 48, 1394–1407. doi: 10.4319/lo.2003.48.4.1394

Levizzani, V., Laviola, S., Cattani, E., and Costa, M. J. (2013). Extreme precipitation on the Island of Madeira on 20 February 2010 as seen by satellite passive microwave sounders. *Eur. J. Remote Sens.* 46, 475–489. doi: 10.5721/EuJRS20134628

Li, M., Zhong, L., and Boicourt, W. C. (2005). Simulations of Chesapeake Bay estuary: sensitivity to turbulence mixing parameterizations and comparison with observations. *J. Geophys. Res. Ocean.* 110, 1–22. doi: 10.1029/2004JC002585

Lira, C., Lousada, M., Falcão, A. P., Gonçalves, A. B., Heleno, S., Matias, M. P., et al. (2013). The 20 February 2010 Madeira Island flash-floods: VHR satellite imagery processing in support of landslide inventory and sediment budget assessment. *Nat. Hazards Earth Syst. Sci.* 13, 709–719. doi: 10.5194/nhess-13-709-2013

Liss, P. S. (1976). "Conservative and non-conservative behaviour of dissolved constituents during estuarine mixing," in *Estuarine Chemistry*, eds J. D. Burton and P. S. Liss (London: Academic Press), 93–130.

Liu, J. T., Kao, S. J., Huh, C. A., and Hung, C. C. (2013). Gravity flows associated with flood events and carbon burial: Taiwan as instructional source area. *Ann. Rev. Mar. Sci.* 5, 48–68. doi: 10.1146/annurev-marine-121211-172307

Liu, Y., MacCready, P., Hickey, B. M., Dever, E. P., Kosro, P. M., and Banas, N. S. (2009). Evaluation of a coastal ocean circulation model for the Columbia river plume in summer 2004. *J. Geophys. Res. Ocean.* 114, 1–23. doi: 10.1029/2008JC004929

Longhurst, A., Sathyendranath, S., Platt, T., and Caverhill, C. (1995). An estimate of global primary production in the ocean from satellite radiometer data. *J. Plankton Res.* 17, 1245–1271. doi: 10.1093/plankt/17.6.1245

Lopes, S., Fragoso, M., and Lopes, A. (2020). Heavy rainfall events and mass movements in the funchal area (Madeira, Portugal): spatial analysis and susceptibility assessment. *Atmosphere* 11:104. doi: 10.3390/atmos11010104

Lourenço, S. D. N., and Rodrigues, D. M. M. (2016). "The 2010 flash floods in Madeira Island: characteristics and the role of soil water repellency in future events," in *Proceedings of the XVI European Conference on Soil Mechanics and Geotechnical Engineering*, (London: British Geotechnical Association), 4. doi: 10.1680/ecsmge.60678.vol4.266

Lousada, S., and Loures, L. (2020). Modelling torrential rain flows in urban territories: floods - natural channels (the case study of Madeira Island). *Am. J. Water Sci. Eng.* 6:17. doi: 10.11648/j.ajwse.20200601.13

Luna, T., Rocha, A., Carvalho, A. C., Ferreira, J. A., and Sousa, J. (2011). Modelling the extreme precipitation event over Madeira Island on 20 February 2010. *Nat. Hazards Earth Syst. Sci.* 11, 2437–2452. doi: 10.5194/nhess-11-2437-2011

Marchesiello, P., McWilliams, J. C., and Shchepetkin, A. (2001). Open boundary conditions for long-term integration of regional oceanic models. *Ocean Model.* 3, 1–20. doi: 10.1016/S1463-5003(00)00013-5

Marta-Almeida, M., Dalbosco, A., Franco, D., and Ruiz-Villarreal, M. (2020). Dynamics of river plumes in the South Brazilian Bight and South Brazil. *Ocean Dyn.* 71, 59–80. doi: 10.1007/s10236-020-01397-x

Martinez, E., and Maamaatuaiahutapu, K. (2004). Island mass effect in the Marquesas Islands: time variation. *Geophys. Res. Lett.* 31, 1–4. doi: 10.1029/2004GL020682

Mason, E., Molemaker, J., Shchepetkin, A. F., Colas, F., McWilliams, J. C., and Sangrà, P. (2010). Procedures for offline grid nesting in regional ocean models. *Ocean Model.* 35, 1–15. doi: 10.1016/j.ocemod.2010.05.007

McCabe, R. M., MacCready, P., and Hickey, B. M. (2009). Ebb-tide dynamics and spreading of a large river plume. *J. Phys. Oceanogr.* 39, 2839–2856. doi: 10.1175/2009JPO4061.1

Mendes, R., da Silva, J. C. B., Magalhaes, J. M., St-Denis, B., Bourgault, D., Pinto, J., et al. (2021). On the generation of internal waves by river plumes in subcritical initial conditions. *Sci. Rep.* 11:1963. doi: 10.1038/s41598-021-81464-5

Messié, M., Petrenko, A., Doglioli, A. M., Aldebert, C., Martinez, E., Koenig, G., et al. (2020). The delayed island mass effect: how islands can remotely trigger blooms in the oligotrophic ocean. *Geophys. Res. Lett.* 47, 1–10. doi: 10.1029/2019GL085282

Meybeck, M., Laroche, L., Dürr, H. H., and Syvitski, J. P. M. (2003). Global variability of daily total suspended solids and their fluxes in rivers. *Glob. Planet. Change* 39, 65–93. doi: 10.1016/S0921-8181(03)00018-3

Milliman, J. D., and Syvitski, J. P. M. (1992). Geomorphic/tectonic control of sediment discharge to the ocean: the importance of small mountainous rivers. *J. Geol.* 100, 525–544. doi: 10.1086/629606

Miranda, P. M. A., Tomé, R., Frois, L., Nogueira, M., Alves, J. M. R., Prior, V., et al. (2021). Speed-up of the Madeira tip jets in the ERA5 climate highlights the decadal variability of the Atlantic subtropics. *Q. J. R. Meteorol. Soc.* 147, 679–690. doi: 10.1002/qj.3940

Mlawer, E. J., Taubman, S. J., Brown, P. D., Iacono, M. J., and Clough, S. A. (1997). Radiative transfer for inhomogeneous atmospheres: RRTM, a validated correlated-k model for the longwave. *J. Geophys. Res. Atmos.* 102, 16663–16682. doi: 10.1029/97jd00237

Moosdorf, N., Stieglitz, T., Waska, H., Dürr, H. H., and Hartmann, J. (2015). Submarine groundwater discharge from tropical islands: a review. *Grundwasser* 20, 53–67. doi: 10.1007/s00767-014-0275-3

Narciso, Á, Caldeira, R., Reis, J., Hoppenrath, M., Cachão, M., and Kaufmann, M. (2019). The effect of a transient frontal zone on the spatial distribution of extant coccolithophores around the Madeira archipelago (Northeast Atlantic). *Estuar. Coast. Shelf Sci.* 223, 25–38. doi: 10.1016/j.ecss.2019.04.014

Nguyen, H. T., Wiatr, T., Fernández-Steeger, T. M., Reicherter, K., Rodrigues, D. M. M., and Azzam, R. (2013). Landslide hazard and cascading effects following the extreme rainfall event on Madeira Island (February 2010). *Nat. Hazards* 65, 635–652. doi: 10.1007/s11069-012-0387-y

Nunalee, C. G., and Basu, S. (2014). On the periodicity of atmospheric von Kármán vortex streets. *Environ. Fluid Mech.* 14, 1335–1355. doi: 10.1007/s10652-014-9340-9

Ogden, F. L. (2016). Evidence of equilibrium peak runoff rates in steep tropical terrain on the island of Dominica during Tropical Storm Erika, August 27, 2015. *J. Hydrol.* 542, 35–46. doi: 10.1016/j.jhydrol.2016.08.041

Oliveira, A. R., Ramos, T. B., Simionesei, L., Pinto, L., and Neves, R. (2020). Sensitivity analysis of the MOHID-land hydrological model: a case study of the Ulla River Basin. *Water* 12:3258. doi: 10.3390/w12113258

Oliveira, M. M. (2004). *"Recarga de Águas Subterrâneas: Métodos de Avaliação". Dissertação de doutoramento em Geologia (hidrogeologia)*. Lisboa: Universidade de Lisboa e Laboratório Nacional de Engenharia Civil, 440.

Oliveira, R. P., Almeida, A. B., Sousa, J., Pereira, M. J., Portela, M. M., Coutinho, M. A., et al. (2011). "Avaliação do risco de aluviões na Ilha da Madeira," in *Proceedings of the 10? Simpósio de Hidráulica e Recursos Hídricos dos Países de Língua Oficial Portuguesa*, Porto de Galinhas.

Osadchiev, A., Barymova, A., Sedakov, R., Zhiba, R., and Dbar, R. (2020). Spatial structure, short-temporal variability, and dynamical features of small river plumes as observed by aerial drones: case study of the Kodor and Bzyp river plumes. *Remote Sens.* 12:3079. doi: 10.3390/RS12183079

Osadchiev, A., and Korshenko, E. (2017). Small river plumes off the northeastern coast of the Black Sea under average climatic and flooding discharge conditions. *Ocean Sci.* 13, 465–482. doi: 10.5194/os-13-465-2017

Osadchiev, A., and Zavialov, P. (2020). "Structure and dynamics of plumes generated by small rivers," in *Estuaries and Coastal Zones–Dynamics and Response to Environmental Changes*, eds J. Pan and A. Devlin (London: IntechOpen). doi: 10.5772/intechopen.87843

Osadchiev, A. A. (2018). Small mountainous rivers generate high-frequency internal waves in coastal ocean. *Sci. Rep.* 8:16609. doi: 10.1038/s41598-018-35070-7

Osadchiev, A. A., Izhitskiy, A. S., Zavialov, P. O., Kremenetskiy, V. V., Polukhin, A. A., Pelevin, V. V., et al. (2017). Structure of the buoyant plume formed by Ob and Yenisei river discharge in the southern part of the Kara Sea during summer and autumn. *J. Geophys. Res. Ocean.* 122, 1–22. doi: 10.1002/2016JC012603

Palacios, D. M. (2002). Factors influencing the island-mass effect of the Galápagos Archipelago. *Geophys. Res. Lett.* 29, 1–4. doi: 10.1029/2002GL016232

Pan, J., Gu, Y., and Wang, D. (2014). Observations and numerical modeling of the Pearl River plume in summer season. *J. Geophys. Res. Ocean.* 119, 2480–2500. doi: 10.1002/2013JC009042

Perissinotto, R., Lutjeharms, J. R. E., and Van Ballegooyen, R. C. (2000). Biological-physical interactions and pelagic productivity at the Prince Edward Islands, Southern Ocean. *J. Mar. Syst.* 24, 327–341. doi: 10.1016/S0924-7963(99)00093-7

Pestana, R., Matias, M., Canelas, R., Araújo, A., Roque, D., van Zeller, E., et al. (2013). "Calibration Of 2D hydraulic inundation models in the floodplain region of the Lower Tagus River," in *Proceedings of the ESA Living Planet Symposium*, Edimburgh, 9–13.

Prada, S., Menezes de Sequeira, M., Figueira, C., and da Silva, M. O. (2009). Fog precipitation and rainfall interception in the natural forests of Madeira Island (Portugal). *Agric. For. Meteorol.* 149, 1179–1187. doi: 10.1016/j.agrformet.2009.02.010

Prada, S. N., da Silva, M. O., and Cruz, J. V. (2005a). Groundwater behaviour in Madeira, volcanic island (Portugal). *Hydrogeol. J.* 13, 800–812. doi: 10.1007/s10040-005-0448-3

Prada, S., Perestrelo, A., Sequeira, M., Nunes, A., Figueira, C., and Cruz, J. V. (2005b). "Disponibilidades hídricas da ilha da Madeira," in *Projecto AQUAMAC – Técnicas e Métodos para a Gestão da Água na Macaronésia*, eds A. Ortega, L. V. Peña, and G. M. Rodríguez (Las Palmas: Consejo Insular de Aguas de Lanzarote), 261–294.

Pullen, J., Allard, R., Seo, H., Miller, A. J., Chen, S. Y., Pezzi, L. P., et al. (2017a). Coupled ocean–atmosphere forecasting at short and medium time scales. *J. Mar. Res.* 75, 877–921. doi: 10.1357/002224017823523991

Pullen, J., Caldeira, R., Doyle, J. D., May, P., and Tomé, R. (2017b). Modeling the air-sea feedback system of Madeira Island. *J. Adv. Model. Earth Syst.* 6, 513–526. doi: 10.1002/2016MS000861

Raapoto, H., Martinez, E., Petrenko, A., Doglioli, A., Gorgues, T., Sauzède, R., et al. (2019). Role of iron in the Marquesas Island mass effect. *J. Geophys. Res. Ocean.* 124, 7781–7796. doi: 10.1029/2019JC015275

Raapoto, H., Martinez, E., Petrenko, A., Doglioli, A. M., and Maes, C. (2018). Modeling the wake of the Marquesas archipelago. *J. Geophys. Res. Ocean.* 123, 1213–1228. doi: 10.1002/2017JC013285

Ramos, A. M., Tomé, R., Trigo, R. M., Liberato, M. L. R., and Pinto, J. G. (2016). Projected changes in atmospheric rivers affecting Europe in CMIP5 models. *Geophys. Res. Lett.* 43, 9315–9323. doi: 10.1002/2016GL070634

Ramos, A. M., Trigo, R. M., Tomé, R., and Liberato, M. L. R. (2018a). Impacts of atmospheric rivers in extreme precipitation on the European Macaronesian Islands. *Atmosphere* 9:325. doi: 10.3390/atmos9080325

Ramos, T. B., Simionesei, L., Jauch, E., Almeida, C., and Neves, R. (2017). Modelling soil water and maize growth dynamics influenced by shallow groundwater conditions in the Sorraia Valley region, Portugal. *Agric. Water Manag.* 185, 27–42. doi: 10.1016/j.agwat.2017.02.007

Ramos, T. B., Simionesei, L., Oliveira, A. R., Darouich, H., and Neves, R. (2018b). Assessing the impact of LAI data assimilation on simulations of the soil water balance and maize development using MOHID-Land. *Water* 10:1367. doi: 10.3390/w10101367

Řehánek, T., Podhorányi, M., and Křenek, J. (2019). Parameter recalculation for a rainfall-runoff model with a focus on runoff curve numbers. *Geoscape* 13, 132–140. doi: 10.2478/geosc-2019-0013

Ricardo, R. P., Câmara, E. M. S., and Ferreira, M. A. M. (1992). *Carta dos Solos da Ilha da Madeira (1:50,000)*. Lisboa: Secretaria Regional de Economia, Direcção Regional de Agricultura da Madeira.

Ricchi, A., Bonaldo, D., Cioni, G., Carniel, S., and Miglietta, M. M. (2021). Simulation of a flash flood event over the Adriatic Sea with a high resolution atmosphere–ocean–wave coupled system. *Sci. Rep.* 11: 9388. doi: 10.1038/s41598-021-88476-1

Robertson, R., and Dong, C. (2019). An evaluation of the performance of vertical mixing parameterizations for tidal mixing in the regional ocean modeling system (ROMS). *Geosci. Lett.* 6, 1–18. doi: 10.1186/s40562-019-0146-y

Rodrigues, A., Oliveira, A., Fonseca, R., Taborda, R., and Cascalho, J. (2006). Sedimentary dynamics of the southern shelf of Madeira (Portugal). *J. Coast. Res.* 1, 454–458.

Saldías, G. S., Sobarzo, M., Largier, J., Moffat, C., and Letelier, R. (2012). Seasonal variability of turbid river plumes off central Chile based on high-resolution MODIS imagery. *Remote Sens. Environ.* 123, 220–233. doi: 10.1016/j.rse.2012.03.010

Sanders, T. M., and Garvine, R. W. (2001). Fresh water delivery to the continental shelf and subsequent mixing: an observational study. *J. Geophys. Res. Ocean.* 106, 27087–27101. doi: 10.1029/2001jc000802

Sartori, A., Genovez, A. M., and Neto, F. L. (2009). "Tentative Hydrologic soil Classification for Tropical Soils," in *Proceedings of the 16th IAHR-APD Congress and 3rd Symposium of IAHR-ISHS*, Nanjing, 199–204. doi: 10.1007/978-3-540-89465-0_37

Schäfer, S., Monteiro, J., Castro, N., Gizzi, F., Henriques, F., Ramalhosa, P., et al. (2020). Lost and found: a new hope for the seagrass *Cymodocea nodosa* in the marine ecosystem of a subtropical Atlantic Island. *Reg. Stud. Mar. Sci.* 41:101575. doi: 10.1016/j.rsma.2020.101575

Shchepetkin, A. F., and McWilliams, J. C. (2005). The regional oceanic modeling system (ROMS): a split-explicit, free-surface, topography-following-coordinate oceanic model. *Ocean Model.* 9, 347–404. doi: 10.1016/j.ocemod.2004.08.002

Signorini, S. R., McClain, C. R., and Dandonneau, Y. (1999). Mixing and phytoplankton bloom in the wake of the Marquesas Islands. *Geophys. Res. Lett.* 26, 3121–3124. doi: 10.1029/1999GL010470

Silva-Araya, W. F., Santiago-Collazo, F. L., Gonzalez-Lopez, J., and Maldonado-Maldonado, J. (2018). Dynamic modeling of surface runoff and storm surge during hurricane and tropical storm events. *Hydrology* 5, 1–28. doi: 10.3390/hydrology5010013

Simionesei, L., Ramos, T. B., Brito, D., Jauch, E., Leitão, P. C., Almeida, C., et al. (2016). Numerical simulation of soil water dynamics under stationary sprinkler irrigation with mohid-land. *Irrig. Drain.* 65, 98–111. doi: 10.1002/ird.1944

Simionesei, L., Ramos, T. B., Oliveira, A. R., Jongen, M., Darouich, H., Weber, K., et al. (2018). Modeling soilwater dynamics and pasture growth in the montado ecosystem using MOHID land. *Water* 10, 1–19. doi: 10.3390/w10040489

Simionesei, L., Ramos, T. B., Palma, J., Oliveira, A. R., and Neves, R. (2020). IrrigaSys: a web-based irrigation decision support system based on open source data and technology. *Comput. Electron. Agric.* 178:105822. doi: 10.1016/j.compag.2020.105822

Simpson, J. H. (1997). Physical processes in the ROFI regime. *Oceanogr. Lit. Rev.* 45, 6. doi: 10.1016/S0924-7963(96)00085-1

Skamarock, W. C., and Klemp, J. B. (2008). A time-split nonhydrostatic atmospheric model for weather research and forecasting applications. *J. Comput. Phys.* 227, 3465–3485. doi: 10.1016/j.jcp.2007.01.037

Skamarock, W. C., Klemp, J. B., Dudhia, J., Gill, D. O., Barker, D. M., Wang, W., et al. (2008). *A Description of the Advanced Research WRF version 3*. NCAR Technical note-475+ STR. Boulder, CO: National Center for Atmospheric Research. doi: 10.5065/D68S4MVH

Smith, W. H. F., and Sandwell, D. T. (1997). Global sea floor topography from satellite altimetry and ship depth soundings. *Science* 277, 1956–1962. doi: 10.1126/science.277.5334.1956

Smyth, W. D., and Moum, J. N. (2000). Anisotropy of turbulence in stably stratified mixing layers. *Phys. Fluids* 12, 1343–1362. doi: 10.1063/1.870386

Sorgente, R., Di Maio, A., Pessini, F., Ribotti, A., Bonomo, S., Perilli, A., et al. (2020). Impact of freshwater inflow from the Volturno river on coastal circulation. *Front. Mar. Sci.* 7:293. doi: 10.3389/fmars.2020.00293

Street, J. H., Knee, K. L., Grossman, E. E., and Paytan, A. (2008). Submarine groundwater discharge and nutrient addition to the coastal zone and coral reefs of leeward Hawai'i. *Mar. Chem.* 109, 355–376. doi: 10.1016/j.marchem.2007.08.009

Tait, D. R., Erler, D. V., Santos, I. R., Cyronak, T. J., Morgenstern, U., and Eyre, B. D. (2014). The influence of groundwater inputs and age on nutrient dynamics in a coral reef lagoon. *Mar. Chem.* 166, 36–47. doi: 10.1016/j.marchem.2014.08.004

Taylor, P. K., and Yelland, M. J. (2001). The dependence of sea surface roughness on the height and steepness of the waves. *J. Phys. Oceanogr.* 31, 572–590. doi: 10.1175/1520-04852001031<0572:TDOSSR<2.0.CO;2

Teixeira, J. C., Carvalho, A. C., Carvalho, M. J., Luna, T., and Rocha, A. (2014). Sensitivity of the WRF model to the lower boundary in an extreme precipitation event-Madeira island case study. *Nat. Hazards Earth Syst. Sci.* 14, 2009–2025. doi: 10.5194/nhess-14-2009-2014

Tóth, B., Weynants, M., Pásztor, L., and Hengl, T. (2017). 3D soil hydraulic database of Europe at 250 m resolution. *Hydrol. Process.* 31, 2662–2666. doi: 10.1002/hyp.11203

Trancoso, A. R., Braunschweig, F., Chambel Leitão, P., Obermann, M., and Neves, R. (2009). An advanced modelling tool for simulating complex river systems. *Sci. Total Environ.* 407, 3004–3016. doi: 10.1016/j.scitotenv.2009.01.015

Umlauf, L., and Burchard, H. (2003). A generic length-scale equation for geophysical turbulence models. *J. Mar. Res.* 61, 235–265. doi: 10.1357/002224003322005087

USDA Soil Conservation Service (1972). *National Engineering Handbook, Section 4: Hydrology, Chapters 4–10*. Washington, DC: USDA Soil Conservation Service, 762.

Van Der Weijden, C. H., and Pacheco, F. A. L. (2003). Hydrochemistry, weathering and weathering rates on Madeira island. *J. Hydrol.* 283, 122–145. doi: 10.1016/S0022-1694(03)00245-2

Vieira, I., Barreto, V., Figueira, C., Lousada, S., and Prada, S. (2018). The use of detention basins to reduce flash flood hazard in small and steep volcanic watersheds–a simulation from Madeira Island. *J. Flood Risk Manag.* 11, S930–S942. doi: 10.1111/jfr3.12285

Wang, A., Wei, B., Xiang, Y., Li, Y., Hassan, M. H. A., Hoe, L. K., et al. (2020). Transport mechanism and fate of terrestrial materials delivered by a small tropical mountainous river: a case study of the Kelantan River, Malaysia. *Mar. Geol.* 430:106344. doi: 10.1016/j.margeo.2020.106344

Warner, J. C., Armstrong, B., He, R., and Zambon, J. B. (2010). Development of a coupled ocean – atmosphere – wave – sediment transport (COAWST) modeling system. *Ocean Modell.* 35, 230–244. doi: 10.1016/j.ocemod.2010.07.010

Warrick, J. A., and Farnsworth, K. L. (2017). Coastal river plumes: collisions and coalescence. *Prog. Oceanogr.* 151, 245–260. doi: 10.1016/j.pocean.2016.11.008

Wu, H., Zhu, J., Shen, J., and Wang, H. (2011). Tidal modulation on the Changjiang River plume in summer. *J. Geophys. Res. Ocean.* 116, 1–21. doi: 10.1029/2011JC007209

Yankovsky, A. E., Hickey, B. M., and Münchow, A. K. (2001). Impact of variable inflow on the dynamics of a coastal buoyant plume. *J. Geophys. Res. Ocean.* 106, 19809–19824. doi: 10.1029/2001jc000792

Yuan, Y., Horner-Devine, A. R., Avener, M., and Bevan, S. (2018). The role of periodically varying discharge on river plume structure and transport. *Cont. Shelf Res.* 158, 15–25. doi: 10.1016/j.csr.2018.02.009

Zhao, J., Gong, W., and Shen, J. (2018). The effect of wind on the dispersal of a tropical small river plume. *Front. Earth Sci.* 12:170–190. doi: 10.1007/s11707-016-0628-6

Conflict of Interest: The authors declare that the research was conducted in the absence of any commercial or financial relationships that could be construed as a potential conflict of interest.

Publisher's Note: All claims expressed in this article are solely those of the authors and do not necessarily represent those of their affiliated organizations, or those of the publisher, the editors and the reviewers. Any product that may be evaluated in this article, or claim that may be made by its manufacturer, is not guaranteed or endorsed by the publisher.

Advantages of publishing in Frontiers

OPEN ACCESS
Articles are free to read for greatest visibility and readership

FAST PUBLICATION
Around 90 days from submission to decision

HIGH QUALITY PEER-REVIEW
Rigorous, collaborative, and constructive peer-review

TRANSPARENT PEER-REVIEW
Editors and reviewers acknowledged by name on published articles

Frontiers
Avenue du Tribunal-Fédéral 34
1005 Lausanne | Switzerland

Visit us: www.frontiersin.org
Contact us: frontiersin.org/about/contact

REPRODUCIBILITY OF RESEARCH
Support open data and methods to enhance research reproducibility

DIGITAL PUBLISHING
Articles designed for optimal readership across devices

FOLLOW US
@frontiersin

IMPACT METRICS
Advanced article metrics track visibility across digital media

EXTENSIVE PROMOTION
Marketing and promotion of impactful research

LOOP RESEARCH NETWORK
Our network increases your article's readership